AD-A174 451 CONSTITUTIVE MODELLING OF CONCRETE AND ROCKS UNDER MULTIAXIAL COMPRESSIVE (U) ARIZONA UNIV TUCSON DEPT OF CIVIL ENGINEERING M R SALAMI ET AL 04 SEP 86 1/5

UNCLASSIFIED AFOSR-TR-86-2014 AFOSR-83-0256 F/G 8/7 NL

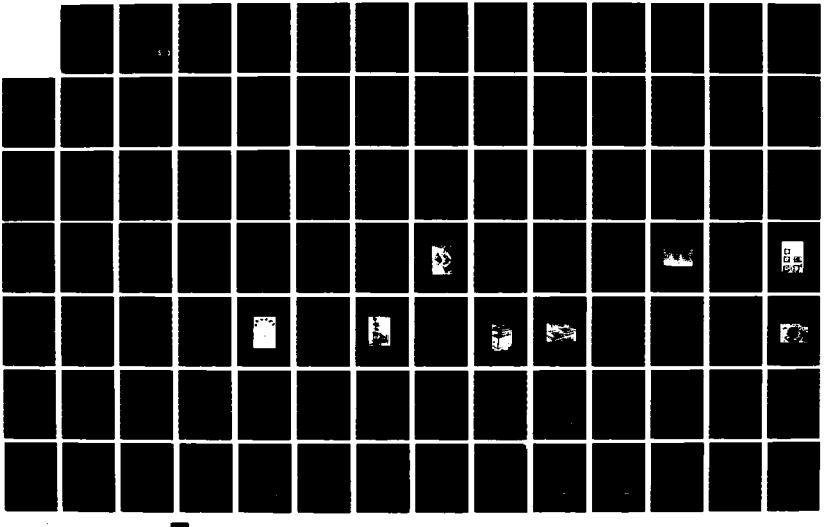

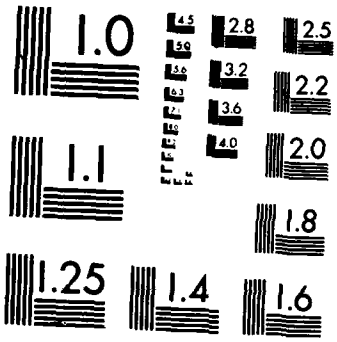

CONSTITUTIVE MODELLING OF CONCRETE AND ROCKS UNDER MULTIAXIAL COMPRESSIVE LOADINGS

by

M. R. Salami and C. S. Desai

Submitted to

Air Force Office of Scientific Research (AFOSR)
Bolling AFB, D. C. 20332

Grant No. 830256

Department of Civil Engineering and Engineering Mechanics
University of Arizona
Tucson, Arizona 85721

January 1986

UNCLASSIFIED

SECURITY CLASSIFICATION OF THIS PAGE

ADA174451

REPORT DOCUMENTATION PAGE

1a. REPORT SECURITY CLASSIFICATION	1b. RESTRICTIVE MARKINGS
2a. SECURITY CLASSIFICATION AUTHORITY	3. DISTRIBUTION/AVAILABILITY OF REPORT
2b. DECLASSIFICATION/DOWNGRADING SCHEDULE	Approved for public release; distribution unlimited
4. PERFORMING ORGANIZATION REPORT NUMBER(S)	5. MONITORING ORGANIZATION REPORT NUMBER(S) AFOSR-TR- 86-2014
6a. NAME OF PERFORMING ORGANIZATION: UNIVERSITY OF ARIZONA; 6b. OFFICE SYMBOL (If applicable):	7a. NAME OF MONITORING ORGANIZATION: AFOSR
6c. ADDRESS (City, State and ZIP Code): DEPT. OF CIVIL ENGR. & ENGR. MECHANICS, TUCSON, AZ 85721	7b. ADDRESS (City, State and ZIP Code): same as 8c
8a. NAME OF FUNDING/SPONSORING ORGANIZATION: AIR FORCE OFFICE OF SCIENTIFIC RESEARCH; 8b. OFFICE SYMBOL (If applicable): AFOSR/NA	9. PROCUREMENT INSTRUMENT IDENTIFICATION NUMBER: AFOSR-83-0256
8c. ADDRESS (City, State and ZIP Code): BOLLING AFB, DC 20332 Building 410	10. SOURCE OF FUNDING NOS.

PROGRAM ELEMENT NO.	PROJECT NO.	TASK NO.	WORK UNIT NO.
61102F	2302	C1	

11. TITLE (Include Security Classification): CONSTITUTIVE MODELLING OF JOINTS UNDER CYCLIC LOADING (UNCLASSIFIED)

12. PERSONAL AUTHOR(S): DESAI, C. S. AND SALAMI, M. R.

13a. TYPE OF REPORT	13b. TIME COVERED	14. DATE OF REPORT (Yr., Mo., Day)	15. PAGE COUNT
INTERIM	FROM Jan. 85 TO Jan. 86	1986, September 4	406

16. SUPPLEMENTARY NOTATION

17. COSATI CODES		
FIELD	GROUP	SUB. GR.

18. SUBJECT TERMS (Continue on reverse if necessary and identify by block number): JOINTS, CONSTITUTIVE MODELLING, CYCLIC LOADING, LABORATORY TESTING, ELASTIC AND ELASTIC-PLASTIC MODELS, VERIFICATION, BOUNDARY VALUE PROBLEMS Rock

19. ABSTRACT (Continue on reverse if necessary and identify by block number)

The research envisages development of constitutive models for joints in rock (concrete) subjected to cyclic loads. The objective is to implement the models in (numerical) solutions of boundary value problems involving solids and joints subjected to dynamic loads such as blasts and earthquake. Hence, it is appropriate to develop models for both the joints and the intact or solid (concrete) media in which the joints occur. The first and the subsequent report(s) contain description of mathematical details, laboratory testing and verification of models proposed for the joints. This report contains description of a new hierarchical plasticity-based constitutive model, laboratory testing using a multiaxial device and verification for the intact concrete used in the investigation.

20. DISTRIBUTION/AVAILABILITY OF ABSTRACT	21. ABSTRACT SECURITY CLASSIFICATION
UNCLASSIFIED/UNLIMITED ☒ SAME AS RPT. ☐ DTIC USERS ☐	UNCLASSIFIED

22a. NAME OF RESPONSIBLE INDIVIDUAL	22b. TELEPHONE NUMBER (Include Area Code)	22c. OFFICE SYMBOL
DR SPENCER T WU	202-767-4935	AFOSR/NA

DD FORM 1473, 83 APR EDITION OF 1 JAN 73 IS OBSOLETE.

PREFACE

This report contains development and application of a generalized constitutive model for geologic materials such as concrete and rock. The model is defined based on comprehensive laboratory tests using a multiaxial test device. One of the concretes used is the same as that considered for simulation of static and cyclic behavior of joints supported by Grant No. 830256 from the Air Force Office of Scientific Research (AFOSR), Bolling AFB. The model is also applied to characterize behavior of some rocks; this was partly supported by Grant No. CEE 8215344 from the National Science Foundation, Washington, D. C.

This report is submitted as a part of the accomplishments during 1985 for the AFOSR grant, which is monitored by Col. H. D. Hokanson and Dr. Spencer Wu. The principal investigator for the project is Dr. C. S. Desai.

TABLE OF CONTENTS

TABLE OF CONTENTS -- Continued

TABLE OF CONTENTS -- Continued

TABLE OF CONTENTS -- Continued

TABLE OF CONTENTS -- Continued

LIST OF ILLUSTRATIONS

LIST OF ILLUSTRATIONS -- Continued

LIST OF ILLUSTRATIONS -- Continued

LIST OF ILLUSTRATIONS -- Continued

LIST OF ILLUSTRATIONS -- Continued

LIST OF ILLUSTRATIONS -- Continued

LIST OF ILLUSTRATIONS -- Continued

LIST OF ILLUSTRATIONS -- Continued

LIST OF ILLUSTRATIONS -- Continued

LIST OF ILLUSTRATIONS -- Continued

LIST OF ILLUSTRATIONS -- Continued

LIST OF ILLUSTRATIONS -- Continued

LIST OF ILLUSTRATIONS -- Continued

LIST OF ILLUSTRATIONS -- Continued

LIST OF ILLUSTRATIONS -- Continued

LIST OF ILLUSTRATIONS -- Continued

LIST OF ILLUSTRATIONS -- Continued

LIST OF ILLUSTRATIONS -- Continued

LIST OF ILLUSTRATIONS -- Continued

LIST OF ILLUSTRATIONS -- Continued

LIST OF ILLUSTRATIONS -- Continued

LIST OF TABLES

ABSTRACT

Characterization of stress-deformation behavior of concrete and rocks have been a subject of active research for a long time. Linear elastic, nonlinear (piecewise) linear elastic, elastic-plastic and endochronic models have been proposed and used by various investigators and the literature on the subjects is very wide. A review of various models together with their implementation is numerical (finite element) procedures is presented in Ref. [77].

The primary objective of the present study is to develop a generalized constitutive model based on the theory of plasticity. Although such a model can be used for a wide range of materials, in this dissertation its appli ations to plain concrete and rocks are emphasised.

One of the main objectives of this dissertation is to study constitutive behavior of concrete and soapstone under multiaxial load histories by using a truly triaxial or multiaxial testing device. The truly triaxial device is capable of applying a general three-dimensional state of stress. Samples can be tested along any three dimensional stress path. Therefore, constitutive behavior of concrete and soapstone can be studied under all possible states of stress.

The conventional, octahedral, proportional loading and circular stress test series are conducted using the truly triaxial cubical device. For meaningful results, samples with consistent initial properties are essential. In order to produce samples with uniform initial properties such as density, equipment and procedures are developed to standardize the sample preparation process.

The test data is used to determine the material constants associated with the proposed constitutive model. The model is then verified by back-predicting the stress-strain curves obtained from the laboratory.

CHAPTER 1

INTRODUCTION

1.1 General

Characterization of stress-deformation behavior of concrete and rocks has been a subject of active research for a long time. Linear elastic, nonlinear (piecewise linear) elastic, elastic-plastic and endochronic models have been proposed and used by various investigators and the literature on the subjects is very wide. A review of various models together with their implementation in numerical (finite element) procedures is presented in Ref. [77].

The primary objective of the present study is to develop a generalized constitutive model based on the theory of plasticity. Although such a model can be used for a wide range of materials, in this dissertation its applications to plain concrete and rocks are emphasised.

One of the main objectives of this dissertation is to study constitutive behavior of concrete and soapstone under multiaxial load histories by using a truly triaxial or multiaxial testing device. The truly triaxial device is capable of applying a general three-dimensional state of stress. Samples can be tested along any three dimensional stress path. Therefore, the constitutive behavior of concrete and soapstone can be studied under all possible states of stress.

The conventional, octahedral, proportional loading and circular stress test series are conducted using the truly triaxial cubical device. For meaningful results, samples with consistent initial properties are essential. In order to produce samples with uniform initial properties such as density, equipment and procedures are developed to standardize the sample preparation process.

1.2 Scope and Objective of Investigation

The first objective of this investigation is to obtain information regarding the material properties of plain concrete and rocks subjected to multiaxial compressive stresses, the purpose being to formulate constitutive relations for stress analysis of structures constructed of these materials.

Pressure sensitive materials such as plain concrete and rocks often show nonlinear and inelastic response when subjected to external loads. Thus, the theory of plasticity can be effectively used to characterize the constitutive behavior of concrete and rocks.

A large number of constitutive models are available at this time for concrete and rocks. However, many of these models have inherent drawbacks. Thus, there is need for new developments in this area.

A new constitutive model is employed to describe both ultimate failure and yielding of concrete and rocks. Both

ultimate failure and yielding are defined by a single yield surface. Hence the model is easier to implement for numerical computations.

The preciseness of solution of boundary value problems using any constitutive model is highly dependent upon the values of the material constants. As a result, appropriate laboratory tests are necessary to determine these material constants.

The model should agree with all the experimental evidence regarding the shapes of yield surfaces on various planes. The model proposed here is expressed in terms of J_1, J_{2D} and J_{3D} deviatoric (invariants of stress) with hardening defined by using various measures of plastic strains. Some of the important assumptions of the proposed model are stated below:

(1) The material is initially isotropic and undergoes isotropic hardening during plastic deformation.

(2) Deformations are small enough to disregard the nonlinear terms of the strain displacement relations.

(3) Elastic and plastic deformation are uncoupled.

(4) The system is considered to be under isothermal conditions.

(5) The rate of loading is slow enough to disregard the inertia effects.

The second objective is to determine the material constants associated with the proposed model by using laboratory test data for a number of different plain concretes and rocks.

Finally, it is necessary to verify the proposed constitutive model with respect to the laboratory test data. The material constants associated with the model are determined from the laboratory tests. The proposed model is then used to back-predict the stress-strain response curves, ultimate failures envelopes for different planes, ultimate strengths and volume change responses under different stress paths from which the material constants are determined. Also the model us used to back predict some stress paths which are not used for finding the material constants.

1.3 Summaries of Various Chapters

Following this introductory chapter, Chapter 2 contains full details of the research program including description of materials tested, mix design and procedure, sample preparation multiaxial test apparatus, testing program and testing procedure.

Chapters 3 and 4 contain the stress-strain response curves under different stress path tests and strength, from multiaxial tests with 4.0 in. (10.16 cm) cubical specimens for concrete and soapstone, respectively.

Chapter 5 is devoted to describing some fundamentals of the theory of plasticity and the reviewing some of the existing plasticity-based constitutive models for concrete and rocks.

Chapter 6 contains the proposed constitutive model based on the theory of plasticity. This is followed by the description of the hardening behavior during inelastic deformations. Chapter 6 also describes the general procedure to determine the material constants associated with the proposed model. Material constants are determined for eight different type of concretes and rocks.

Chapter 7 contains the verification of the model with respect to the laboratory test data.

Finally, a summary of the current work, conclusions and recommendations for future work are presented in Chapter 8.

CHAPTER 2

RESEARCH PROGRAM

2.1 Introduction

The experimental program followed was designed to contribute to understanding the behavior of plain concrete and rock (soapstone) responses to general and complex load histories. For an analytical formulation to successfully model the stress-strain responses of plain concrete and soapstone to an arbitrary stress path, the constitutive relations of the material must be well defined. The characteristics of behavior of plain concrete and rocks during loading, unloading, and reloading must be understood and defined before any such modelling can be successfully realized.

The other main purpose of the experimental work was to determine the behavior and strength of the plain concrete and soapstone under low confining pressures subjected to multiaxial compressive stresses.

This chapter describes the different stages of the experimental program.

2.2 Description of Materials Tested

2.2.1 Concrete

Mix Design and Uniaxial Strength:

The plain concrete mix proportions by weight were as follows:

Cement: Sand: Gravel = 1.00:3.26:2.90

Cement: Water = 1.33

Fine Aggregate Gradation

Sieve No.	Particle Size (mm)	Percent Finer
4	4.75	97.6
10	2.00	89.3
20	0.85	52.24
40	0.425	23.3
60	0.250	8.13
140	0.106	0.0
200	0.075	0.0

Fineness Modulus = 2.65

Coarse Aggregate Gradation

Sieve	Percent Finer
1/2	71.454
3/8	26.455
4	0.531
10	0.244
20	0.202
40	0.176
60	0.164
140	0.117

The fine and coarse aggregate gradations fall within the limits required by ASTMC33 - Section 4.1 and TABLE 2 [1], respectively.

Two batches of this mix design were prepared. For both batches the average uniaxial compressive strength of plain con-

crete was approximately 2.85 ksi (19.63 Mpa) verifying the similarities of the two batches. Based on this comparison, cubes from each batch were selected randomly throughout the testing program.

Casting and Curing Procedures:

In order to reproduce identical mixes, a standard for casting and curing of specimens to be used for the multiaxial tests was established.

A cube mold was constructed of plexiglass and accommodated the casting of 4 to 6 cubes at one time. A typical mold is shown in Fig. 2.1.

The constituents for the mix (cement, aggregate, and water) in the proportions as outlined in previous section were weighed. All the aggregates and half of the water were placed in the mixer and rotated for 5 minutes to produce a uniformly graded sand, and to allow the aggregate to absorb the water during the mixing process. The remaining water and cement were then put in the mixer, and rotated for another 5 minutes.

Thirty 4.05 in. (10.29 cm) cubes, and eighteen 6x12 in. (15.24x30.48 cm) control cylinders were cast from each batch.

The mix was immediately placed into the molds and vibrated. This vibration was continued until it was felt that uniformity of the specimen had been achieved and that the entrapped air had surfaced in order to minimize air voids.

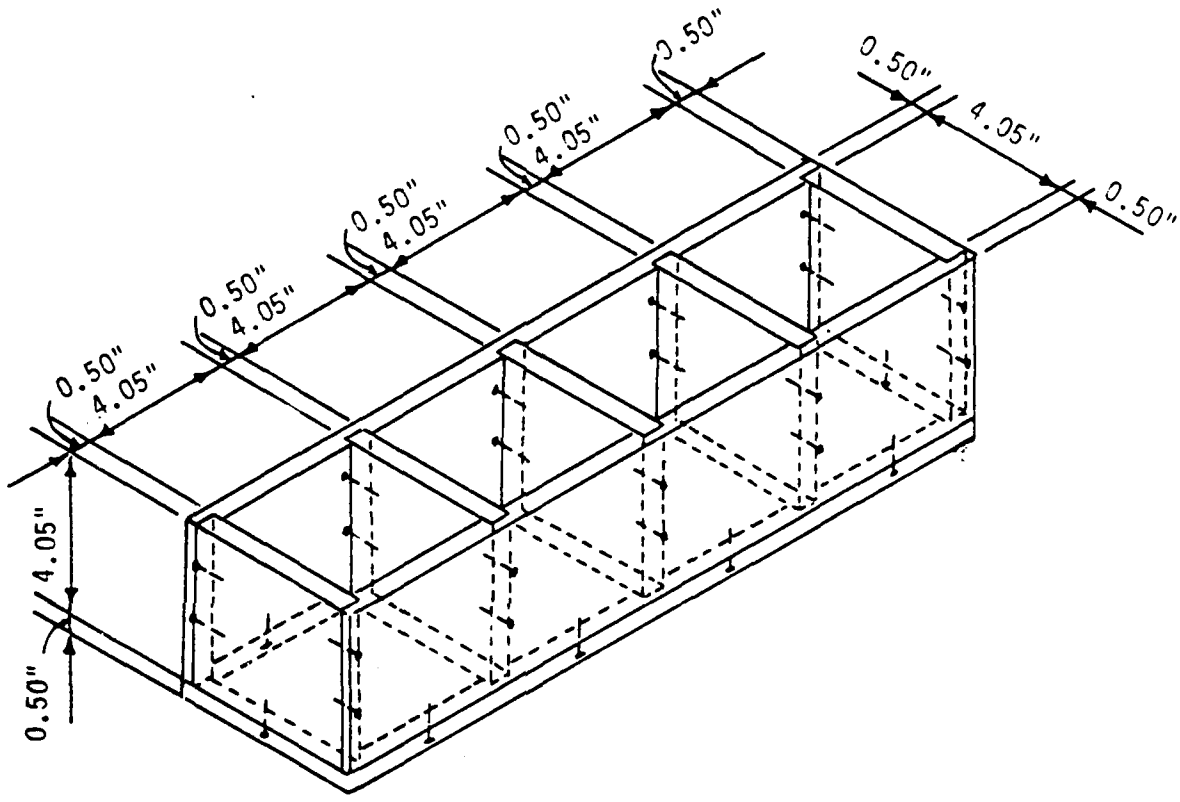

Figure 2.1. Plexiglass Cube Mold

After 24 hours of dry curing, the molds were stripped and placed in a 100% humidity room for 28 days. The specimen was then removed and prepared for testing.

The initial size of specimens was 4.05x4.05/4.05 in. (10.29x10.29x10.29 cm) the additional thickness of 0.05 in. (0.13 cm) was later removed by using a diamond grinding machine. This was done in order to adhere to the strict tolerance of 4x4x4 in. (10.16x10.16x10.16 cm) dimension of the specimens to be used in cubical testing device.

Sample Preparation:

As previously discussed, all specimens were ground to the size of 4.00x4.00x4.00 in. (10.16x10.16x10.16 cm). After the grinding, air voids near the surfaces could be avoided. Since these air voids would lead to a penetration of the flexible membranes under pressure resulting in their rupture, all surfaces of the specimens were sandblasted and refilled with a concrete (or plastic) filler material (Durham's Rock Hard Water Putty). This was allowed to harden and dry for 24 hours. After drying, the puttied surfaces were sanded, reputtied and finished with fine sandpaper. The average initial density of all cubical specimens was 153.9 lb/ft^3 (2.55 gr/cm^3). The control cylinders were capped with sulfur on the upper and

the lower surfaces and tested by using standard uniaxial testing equipment and by following appropriate procedures [1].

2.2.2 Soapstone

Composition, Use and Location of Material:

"Soapstone" is a general term used to describe a metamorphic rock composed essentially of the mineral talc, a soft hydrous magnesium silicate mineral. The mineral talc, $Mg_6(Si_8O_{20})(OH)_4$, and the rock soapstone are extremely versatile materials and have a number of uses as industrial products. Talc's extreme softness (1 on Mohs' scale of hardness), the ease with which it can be ground into an ultrafine, white powder, its chemical inertness, high fusion point, low water absorption, low shrinkage when fired, low electrical and thermal conductivity, and high reflectivity make it useful as a ceramic tile base, paint extender, filler in rubber, paper, roofing, plastic, construction use -- buildings, chimneys, etc.

In 1967, Steatite of Southern Oregon, Inc., founded by John H. Pugh of Grants Pass, began selectively mining pieces of soapstone from a landslide deposit on Powell Creek near Williams Oregon. The main source now is in the upper Applegate-Squaw Creek-Elliot Creek Ridge area in Southern Jackson County in Oregon [59].

Geology of Area[1]

Talc and soapstone deposits occur mainly with altered igneous rocks or in metamorphosed dolomite. The known southwestern Oregon occurrences are all associated with serpentinized ultramatic rocks and are typical of this type of deposit. They occur as sheared lenses within or salvages on serpentinites. The talc alteration varies from thin salvages to complete replacement of the serpentinite mars [59].

The talc and associated magnesium-bearing minerals are formed by the reaction of serpentinite with carbon dioxide or with sliceous country rocks in a suitable temperature and pressure environment. *The deposits along Elliot Creek Ridge* are in lenses and irregular pod-shaped masses of altered serpentinite within rocks mapped as older schists and schists of pre-Mesozoic age. Metamorphic age of these rocks, determined by potassium-argon analysis of muscovite, is 141 m.y., or late Jurassic. Because the outcrops of altered serpentinite which contain the soapstone deposits are slightly more resistant to erosion than the surrounding schist, they form rough, craggy knobs and ridges at or near the crest of Elliot Creek Ridge. Soapstone exposed at the surface is found as thin to thick salvages on the edges and as pods within the medium-grained, greenish metaser - pentinite.

---

[1] This section is rewritten in part from Ref. [59].

Sample Preparation:

Blocks of good quality soapstone weighing up to several tons are removed and trucked to a staging area at Divident Bar on Squaw Creek, about 2.5 miles from the mine, where they are sorted, sized, and cut into blocks for shipping. Basic equipment at the staging area is a front-end loader for moving large blocks, gang saw, band saw, and table trim saw. Marketing, packaging, and shipping are done from a small shop at the Pugh resident in Grants Pass.

For the experimental purpose herein, all specimens were taken from a single block of soapstone. For multiaxial testing 4x4x4 in. (10.16x10.16x10.16 cm) cubical specimen were cut (by a local company) and shipped for our purpose to the department of Civil Engineering and Engineering Mechanics at the University of Arizona in Tucson. After arrival, all six surfaces of the specimens were sanded and refilled with a plastic filler material (Durham's Rock Hard Water putty). This was allowed to harden and dry for about 24 hours. After drying, the puttied surfaces were sanded, reputtied and finished with fine sand paper. (Soapstone is a fairly good homogeneous and isotropic rock.)

Uniaxial compressive strength of soapstone is found to be about 1.2 ksi (8.27 MPa) under conventional triaxial com-

pression (CTC) test with confining pressure σ_0=0 in the multiaxial device. The average moisture content and density for all specimens were about 0.57% and 189.0 lb/ft^3 (3.17 gr/cm^3), respectively.

2.3 Multiaxial Test Apparatus

A detailed description of the test cell is given by Desai et al and Strue [20, 76]. The apparatus consists of a rigid cubical space frame and six walls that function as lids. Details of the device and an exploded view of the wall and testing arrangements are shown in Figs. 2.2 and 2.3 The openings in the frame form six similar cavities. Each of these cavities, together with the adjoining walls and a proper seal arrangement, act as pressure vessel.

The 4 in. cubical specimen is placed in the center of the space frame's cubical cavity, then sealed off by six walls which are bolted on the frame. The load is applied via a hydraulic pressure system where urethane membranes and pressure seals located on the inner face of each wall contain the hydraulic fluid pumped into the apparatus. Each set of opposing walls is connected to an individual pumping system which regulates the stress level on that axis. Thus the stresses on each of the three axes are independently controlled such that a stress with $\sigma_1=\sigma_2=\sigma_3$ can be achieved. Proximity-

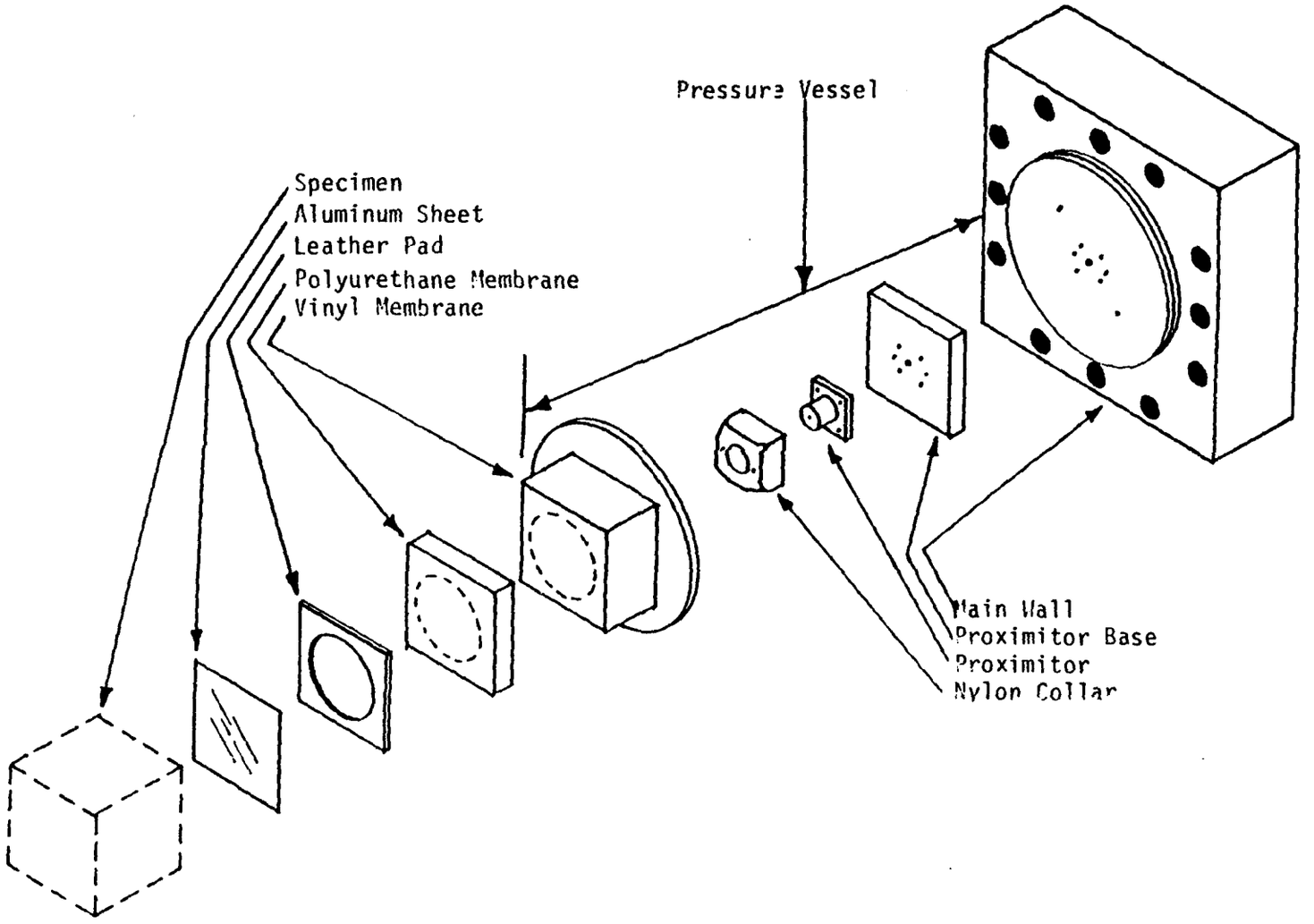

Figure 2.2. Exploded View of the Test Wall Cell.

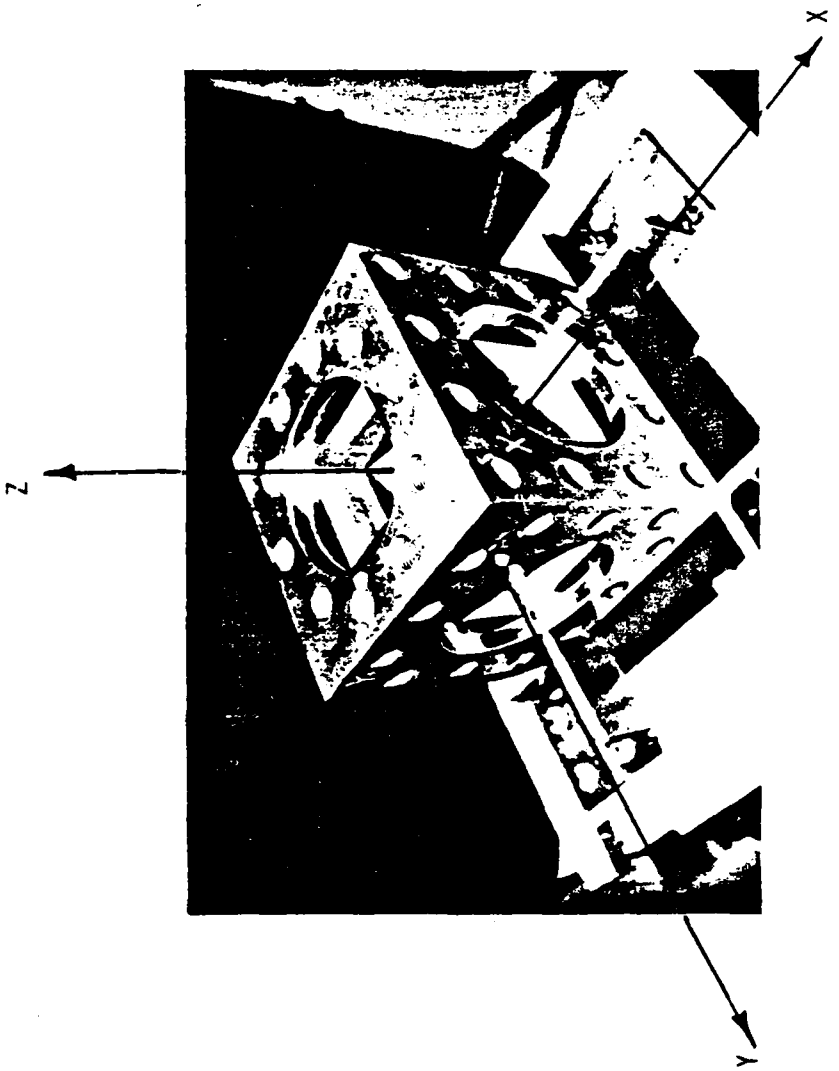

Figure 2.3. Frame of Multiaxial Cell

type transducers (probes) are used to measure the deformations in the three principal directions. All test data is monitored and plotted by computer later so the specimen behavior can be observed and analyzed.

2.3.1 Frame

The frame of the test cell, Fig. 2.3 was machined from 10 in. cubical block of VASCOMAX 250 CVM 18.5% nickel maraging steel. The steel offers exceptional ductility, a strength and hardness, all necessary material parameters considering the high stresses the equipment is subjected to after machining to the dimensions given in Fig. 2.4 the block underwent heat treating to obtain the mechanical properties quoted by the manufacture as: ultimate tensile strength, 264 ksi (1,820.28 MPa); yield strength at 0.2% offset, 255 ksi (1,758.23 MPa); elongation at ultimate - 13%; modulus of elasticity, 26, 500 ksi (1.83×10^5 MPa). Figure 2.4 shows detailed dimensions of the box frame. The test cell assembly procedure discussed in Section 2.4 is easily understood if the coordinate system shown in Fig. 2.2 is followed.

2.3.2 Walls

The walls covering the six faces on the cubical frame are built up of two components. The main frame of each wall was machined from 4 in. (10.16 cm) thick ALCLAD 7075-T6

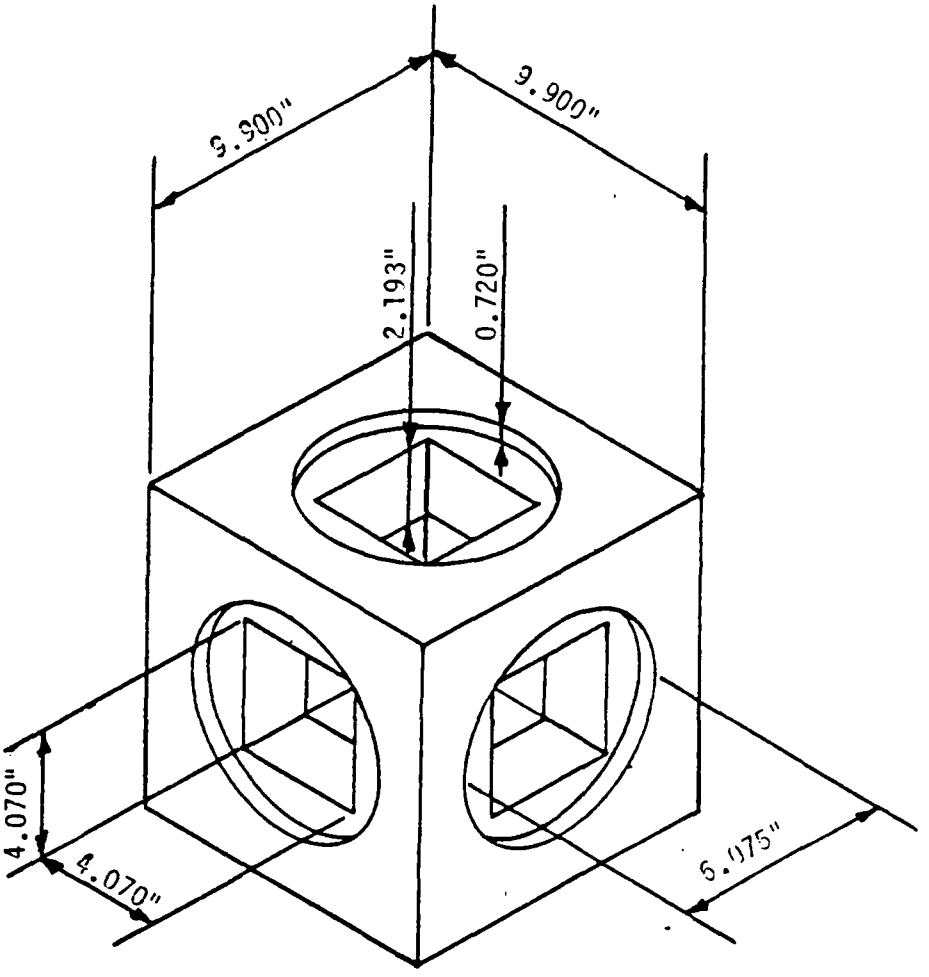

Figure 2.4. Dimensions of the Cell Frame

aluminum plate serve as the lids for the six pressure vessels and as a base for the displacement measuring probes. They contain the pressure seal devices and the hydraulic fluid inlet ports. The square top piece, bolted on the main wall, acts as a base for probe attachment. One of the two fluid ports serves as an inlet for the hydraulic fluid, the other as an outlet to bleed entrapped air from the pressure chambers or as a pressure chamber. A photograph of a typical wall is shown in Fig. 2.5

2.3.3 Seals

Details of the sealing system are shown in section in Fig. 2.6. Two O-ring grooves form the pressure seal between the wall and the frame. The inner groove, closest to the sample, hold the outer O-ring sleeve of the vinyl or polyurethane membrane. The outer groove and O-ring which is compressed to a maximum when the wall is assembled to the frame. The sealing capacity of this arrangement increases with cell pressure.

A polyurethane pad with a sleeve and a leather pad rest against the sample face, and transmit the fluid pressure from the membrane to the specimen. They are flexible enough to follow minor differential distortions on the specimen surface. These two pads also help to prevent a membrane extrusion from occurring when a large deviatoric stress is present between two adjacent pressure vessels. Fig. 2.7 shows the membrane, the

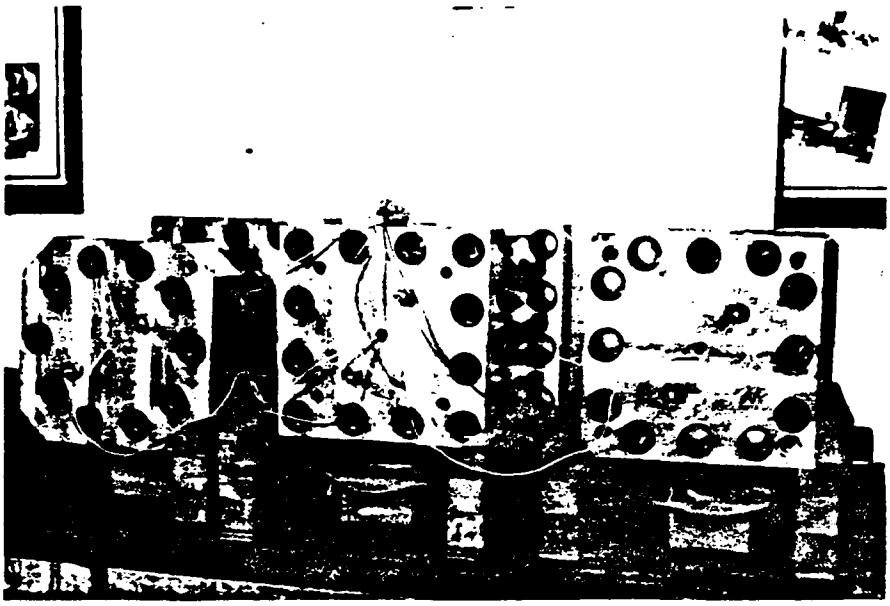

Figure 2.5. View of Typical Assembled Walls.

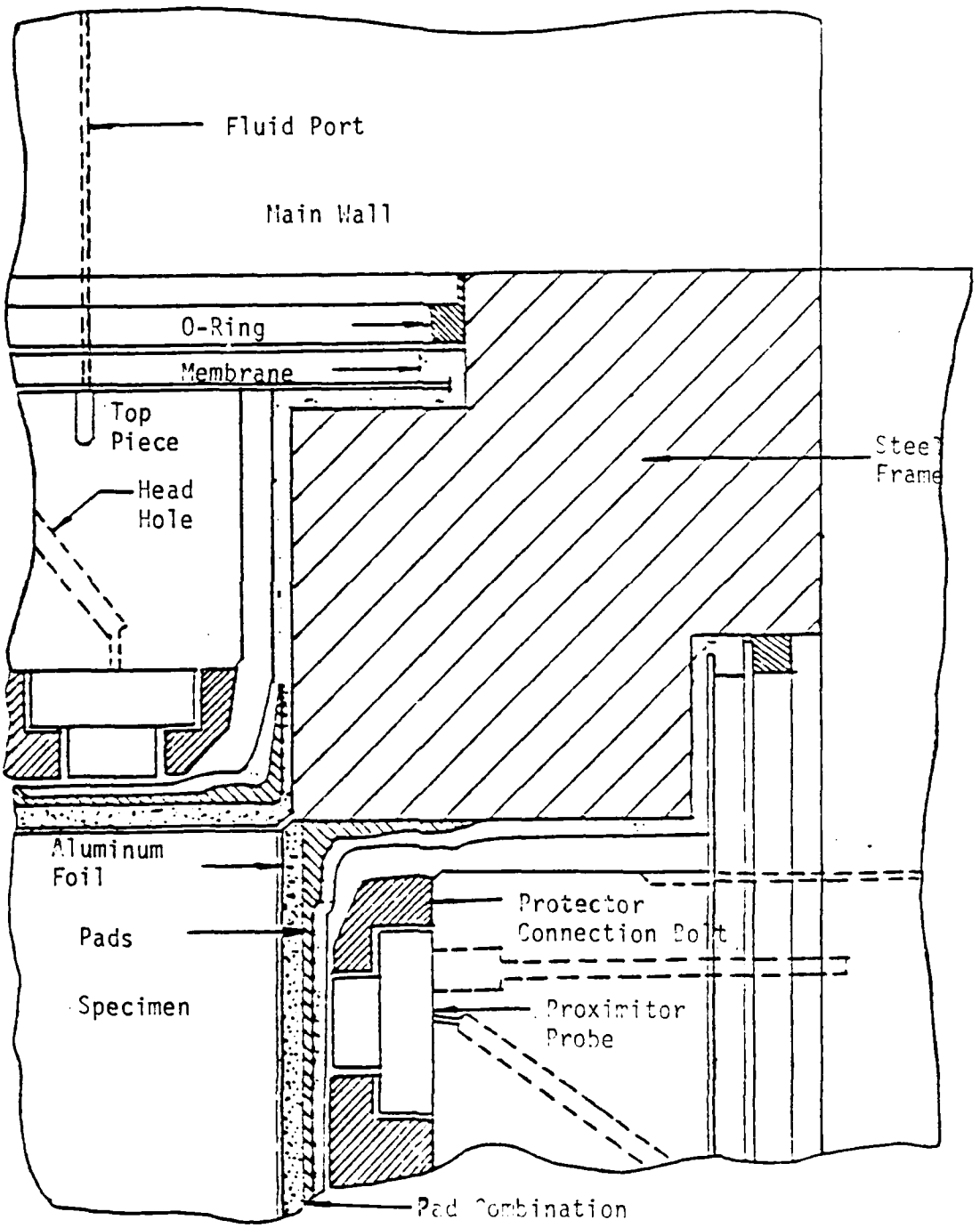

Figure 2.6. Pressure Seal Arrangement

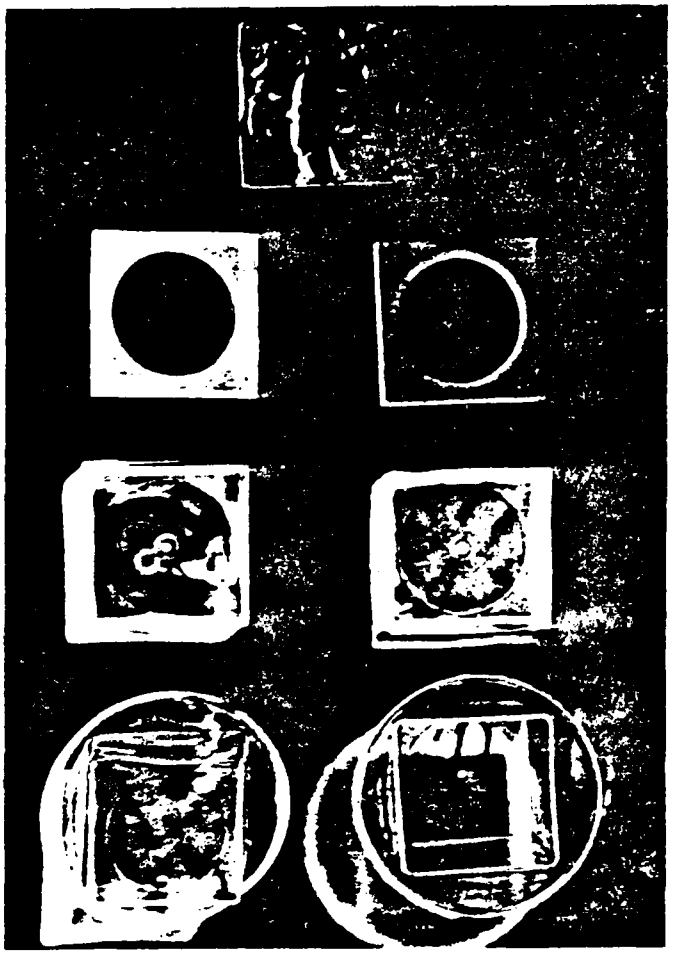

Figure 2.7. Top and Bottom Views of Polyurethane Membrane and Pad, Leather Pad and Aluminum Target.

polyurethane pad, the leather pad and the aluminum target.

The leather pads were made in-house from about 1/4 in. shoe leather to the approximate specifications given in Fig. 2.8.

First, the pads were cut and sanded to the 4.06 in. (10.31 cm) square dimension. They were then placed, one at a time, in a positioning fixture mounted in a turning lathe and the 3.62 in. (9.19 cm) outside diameter hole centered in the pad with a 45^{0} bevel, was cut through. Finally the 45^{0} bevel along the pad's edges was sanded to minimize the interference at the interfaces between leather pads of adjacent pressure vessels. After each test, these pads were checked and resanded to the 4.06 in. (10.31 cm) square dimension, and re-beveled, if necessary.

2.3.4 Pressure System

The hydraulic pressure that is applied to each of six sides of the cubical specimen is generated and controlled by a hydraulic system. A silicon fluid with a viscosity of 100 ctks is used as the pressurizing medium. Silicon liquid is pumped by positive displacement pumps. These three independently operated pumps, by suitable valving, can be used to produce any combination of the stresses in the direction of the three principal axes. Pressures are measured by Bourdon pressure gages 0-20 ksi

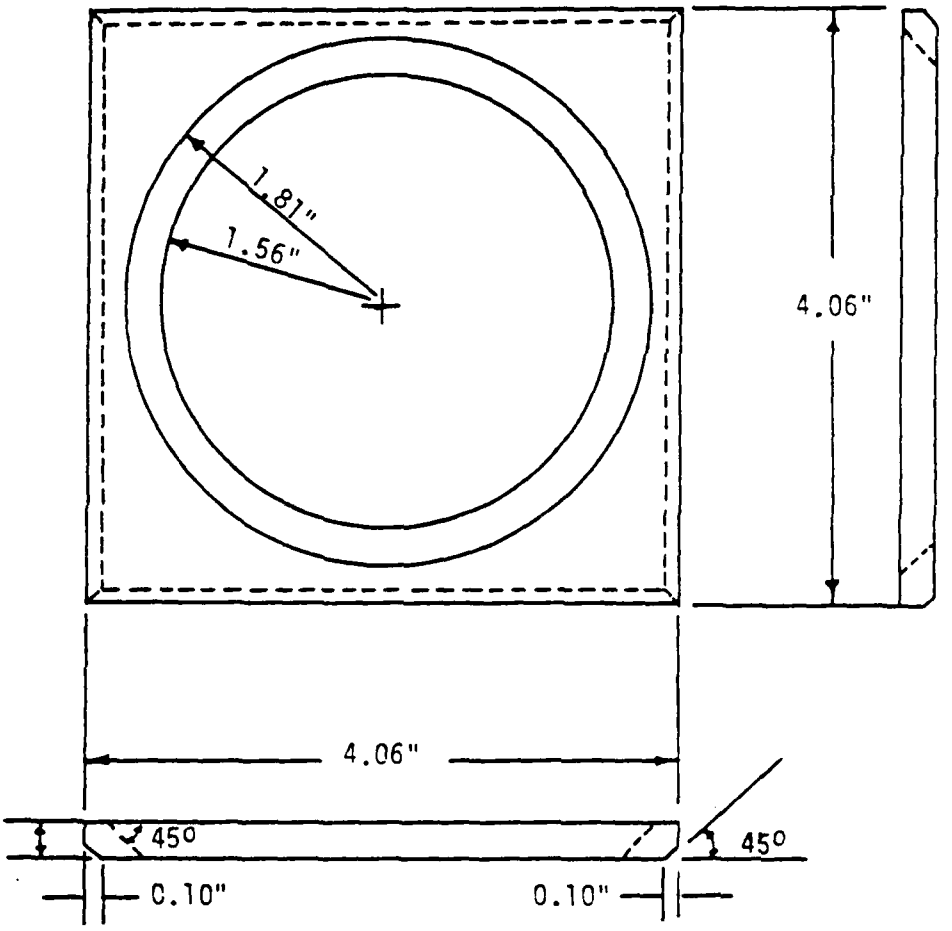

Figure 2.8. Leather Pad Dimensions (1.0 in. = 2.54 cm).

(137.9 MPa) range, fitted to each pump, Fig. 2.9. The pumps themselves with their drained valves act as pressure regulators. Valves are installed in the lines leading to the wall. A rapid filling arrangement is used to fill the membranes before the start of the experiment. Silicon liquid is forced into the membrane from a reservoir of liquid by compressed air. The same arrangement works backward in draining the liquid from the membranes, when vacuum is applied instead of compressed air.

2.3.5 Deformation Measurement System

Surface displacements on the specimen are measured by a Bently-Nevada proximitor probe system. The system is composed of two basic units; the probe, which is the sensing element, and the proximitor driver, which provides the excitation to the probe. The system works on inductive proximity principles and so does not have any physical contact with the specimen under test. The probes shown in Fig. 2.10 measure the distance between the specimen and a detector coil embedded in the tip of the probe. The test specimen is covered with a conducting aluminum foil, Fig. 2.3. The probes now have the foil as a well defined target to aim at. The vinyl membrane, silicon fluid and pad system occupies the space between the target and the probe tip. Presumably these are all non-conductive and dielectric.

The proximitor probes are calibrated in a special calibra-

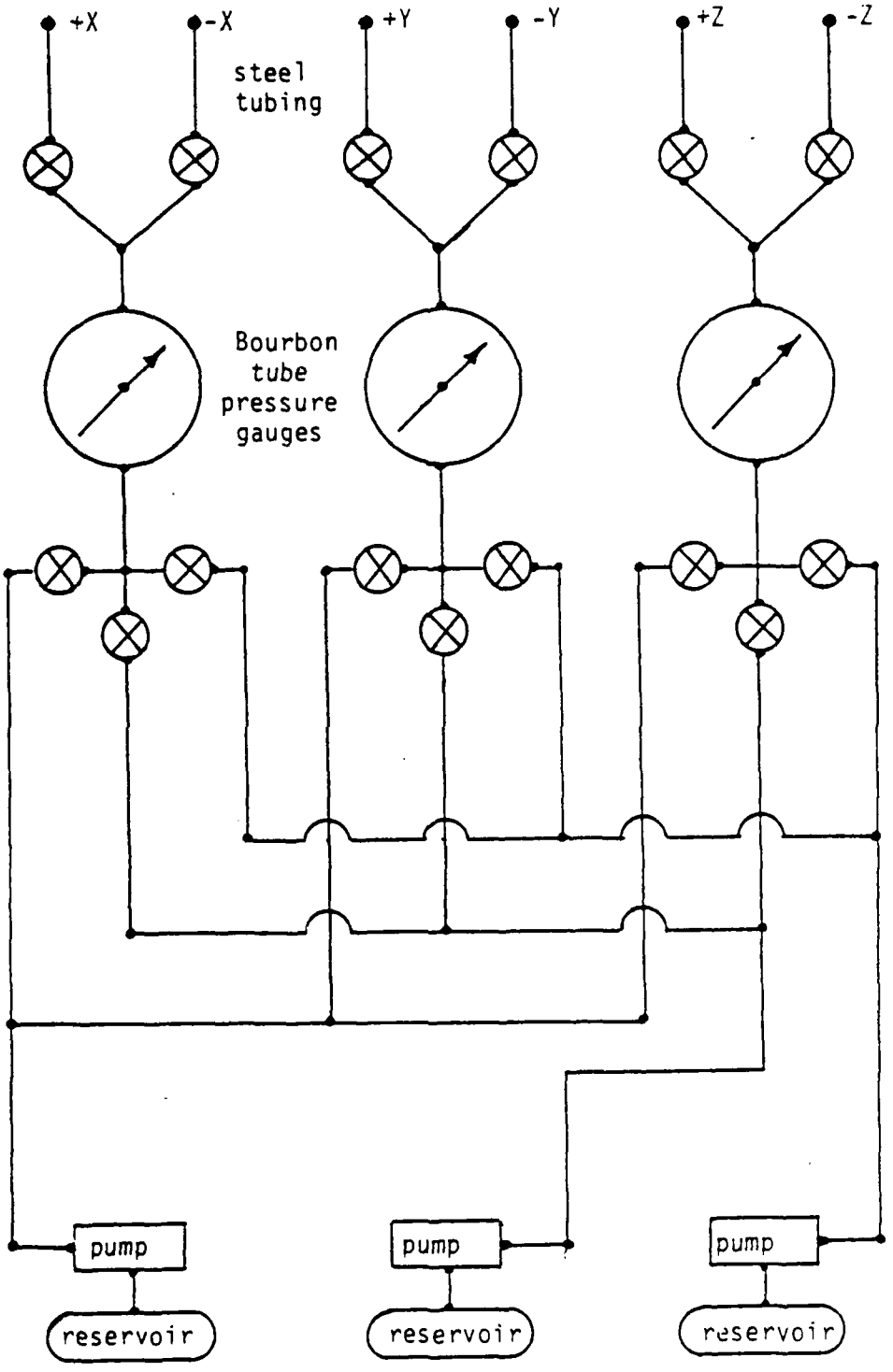

Figure 2.9. Hydraulic System Diagram.

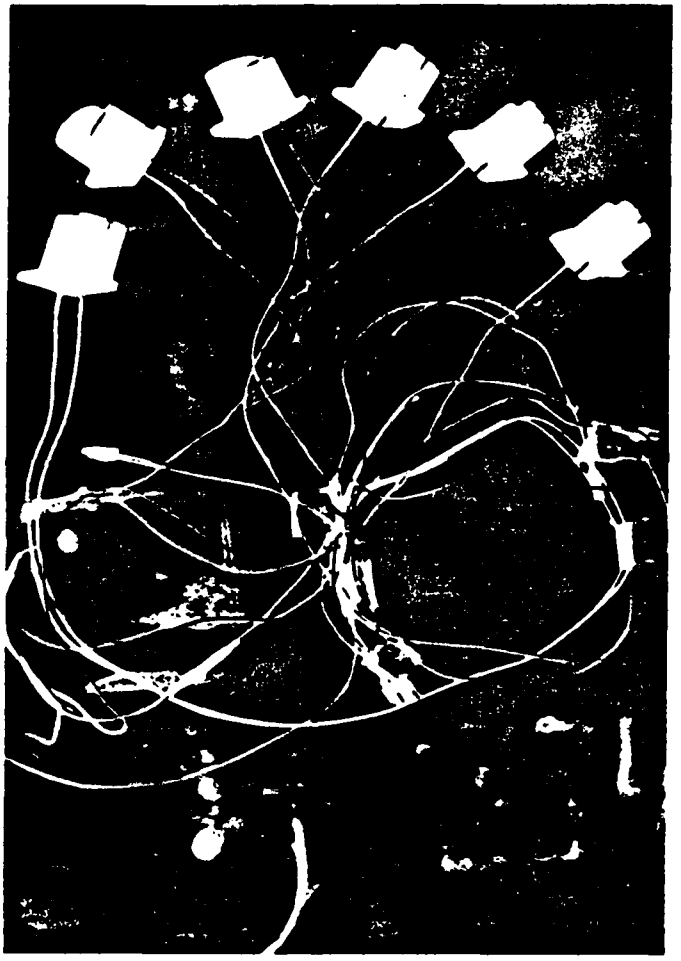

Figure 2.10. Proximitor Probes

tion setup, Fig. 2.11 before use in an experiment. The calibration setup is so designed that it simulates the action inside the pressure vessels. Readings are taken with the help of a dial gage connected to a target through a solid threaded aluminum rod. These calibration values are used to extrapolate the measured displacements in form of voltages during the experiment.

2.3.6 Multiaxial Test Cell Calibration

The multiaxial test cell has to be calibrated to determine the relation between cell deformations and pressure. Since the deformations of the cell that take place in the frame, bolts and walls are dependent on the manner of the assembly of the cell and the loadpath, the cell must be calibrated for each load path and has to be assembled for the test in the same manner as for the calibration. This includes the sequence of mounting the six faces and the tightening of the bolts. The calibration is performed with a 4.0 in. (10.16 cm) aluminum cube of known elastic constants which are $E = 10.4 \times 10^3$ ksi (71.71×10^3 MPa) and $\nu = 1/3$, respectively. Subtracting the known deformations of the elastic aluminum cube from the total deformations of the pressurized cell gives the deformations for the cell itself. These deformation data are stored in a test cell calibration array and are used for specific tests with the given stress path.

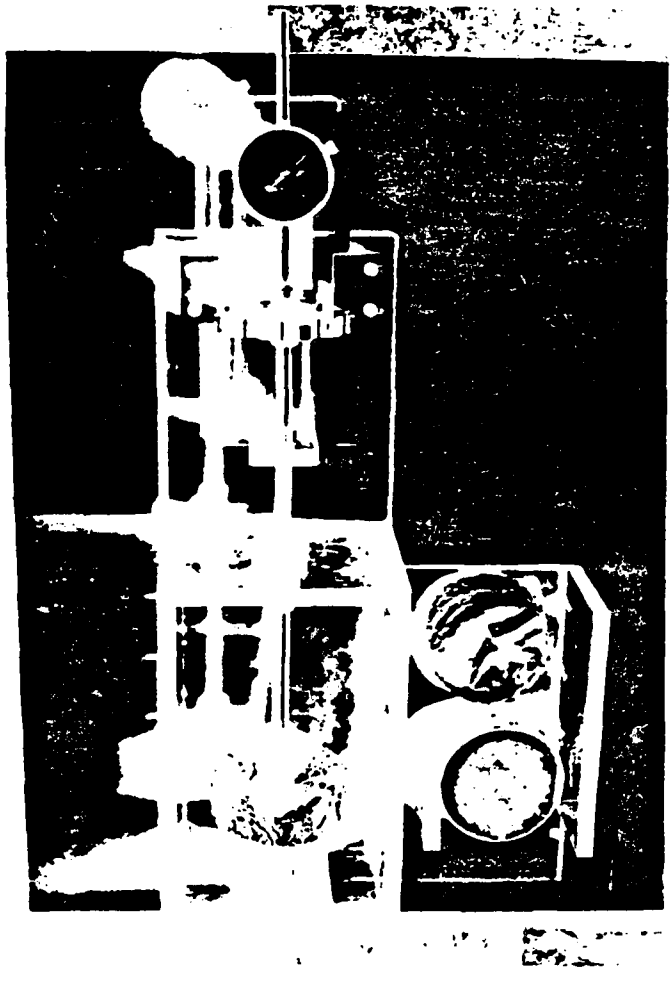

Figure 2.11. Proximity Probe Calibration Unit.

2.3.7 Data Acquisition System

Teh data acquisition system used for collecting the deformation produced by applying loads to the cubical specimens consists of the proximitor probes and the central data acquisition system which houses the proximitor drivers. All data reduction is done with a Hewlett-Packard 9825A calculator. The proximitor readings are monitored by means of scanner, voltmeter and then recorded and stored in the memory of the calculator. The recording sequence consists of the reading of six proximitors, one control proximitor to record electronic drift, preceded by three pressure readings. The recorded pressure and voltage readings are printed out on a paper tape. A constant scanner reading frequency is "set", so that each channel has equal time to "set" to a steady voltage. Figs. 2.12 and 2.13 show Hewlett-Packard central data acquisition system, computer and plotter.

2.4 Test Procedure

As previously discussed, the test cell is not perfrectly rigid and deformations do take place in the frame, walls, bolts, etc., when the specimen is stressed. Therefore, since the cell must be calibrated for these deformations, and in order to minimize the error that may occur in these deformations from test to test, a systematic manner of assembling the cell was established and strictly followed throughout all tests. This

Figure 2.12. Data Acquisition System.

Figure 2.13. Hewlett-Packard Computer and Plotter.

standard procedure also helped speed the assembly of the system. The wall mounting and bolt tightening sequences are first mentioned to avoid being repetitious later.

The walls were mounted to the box frame and bolted down in the following sequence: -Z, +Z; -Y, +Y; -X, +X. The aluminum targets, leather pads and polyurethane pads were inserted first and the corresponding aluminum walls with membranes attached were mounted; Fig. 2.2 demonstrates this. After opposing walls were placed, the four corner bolts for these walls were inserted and alternately tightened from wall to wall in a systematic manner such that the specimen remaned centered in the frame. Once these four bolts were snugged and the walls tightly in place, the bolts were torqued to 300 ft-lbs (406.8 N.m) using an indicating torque wrench. Then the remaining bolts were inserted and torqued to 300 ft-lbs (406.8 N.m) in a clockwise manner, starting at the top. Fig. 2.14 shows the bolt tightening sequence followed.

The Z-direction with specimen, targets, pads, membranes and walls were positioned and affixed, followed by the components in Y and X - directions according to the sequence described above.

With the test cell assembled, the hydraulic tubing was hooked up and the pressure cells filled with hydraulic fluid. The en-

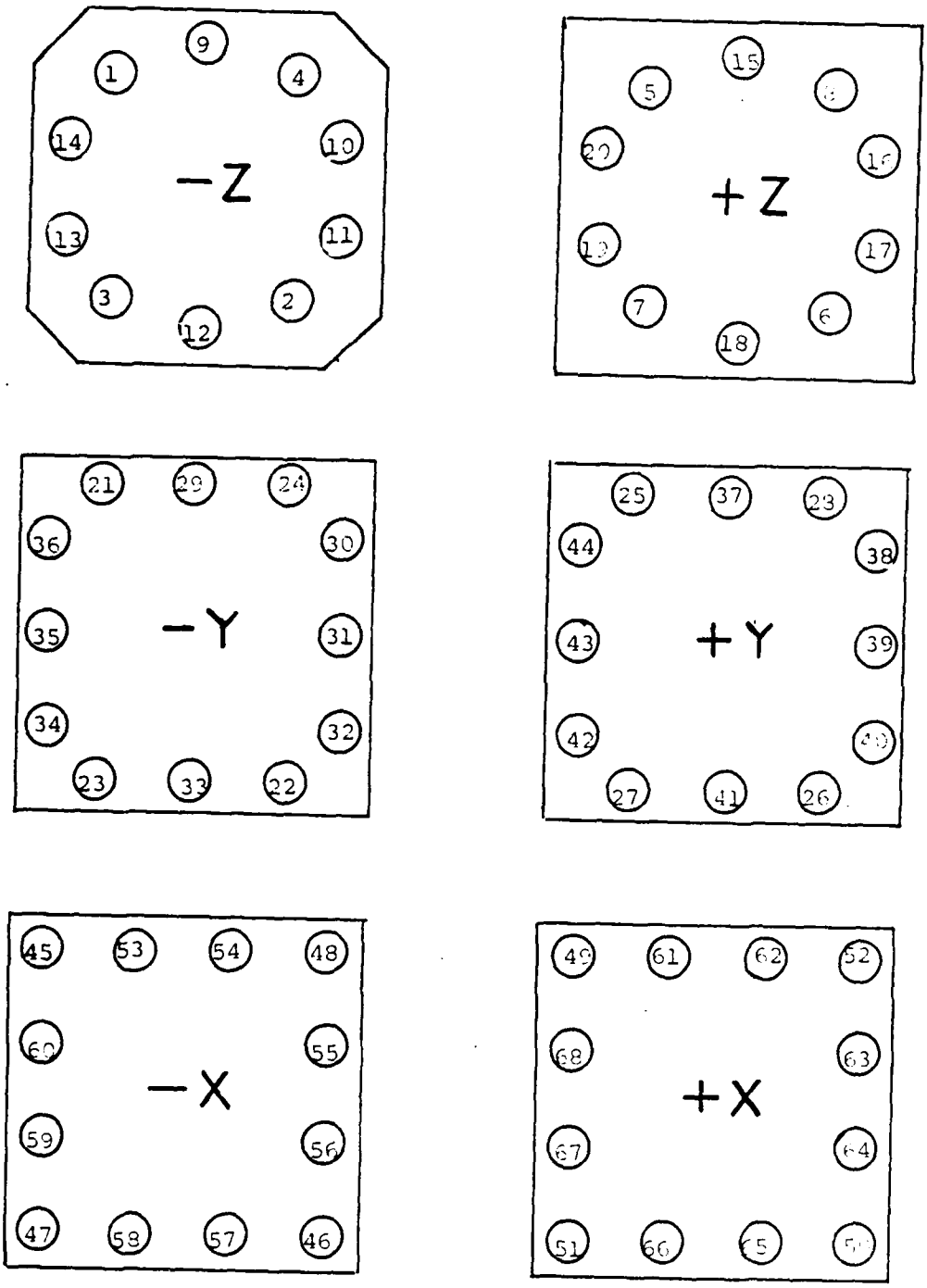

Figure 2.14. Bolt Tightening Sequence for the Box Faces and Respective Walls.

trapped air in the cells was then bled out of the system through the bleed holes. The coaxial cables from the central data acquisition system were then connected to their respective proximitor probe cables. An initial manual scan through the 6 proximitor channels indicated whether or not the test could be started. If necessary, as indicated by distorted proximitor voltage reading, the specimen dislocation could be remedied by carefully applying pressure to one or more sides, translating the specimen by required amounts. The data acquisition and analysis computer program was then loaded into the HP 9825A calculator's memory, and the test conducted. The assembled test cell is shown in Fig. 2.15

2.5 Test Program

The testing device is capable of applying loads following any arbitrary stress path. Figures 2.16a, 2.16b, 2.16c show the schematic of the commonly used stress paths in 3-D stress space. octahedral plane and triaxial plane, respectively. Thus, it is ideally suited for testing geological material such as a concrete and rocks because their stress-strain responses are highly path dependent. As a result, the parameters obtained from such test data would be more representative of the field conditions compared to Conventional Cylindrical Triaxial tests in which only a limited number of stress paths are possible. In the following, each test series is described separately.

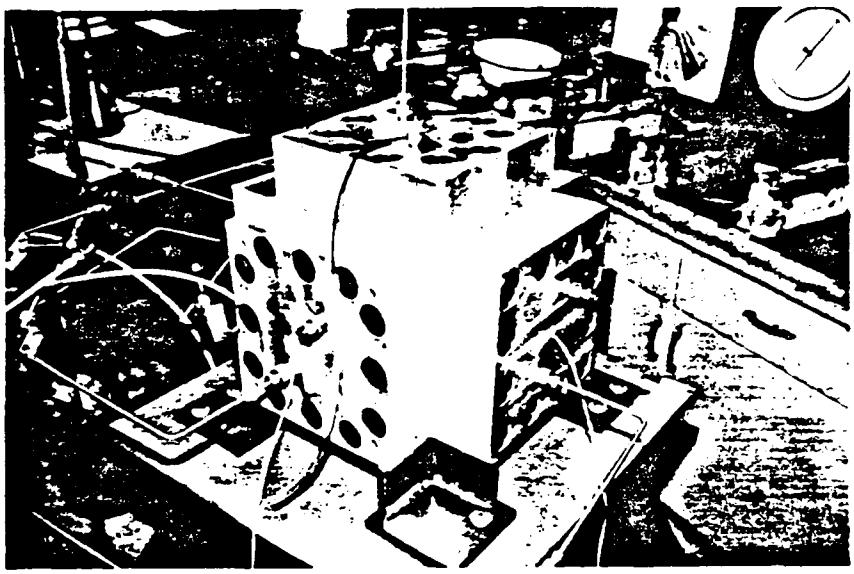

Figure 2.15. Fully Assembled Cell During Testing.

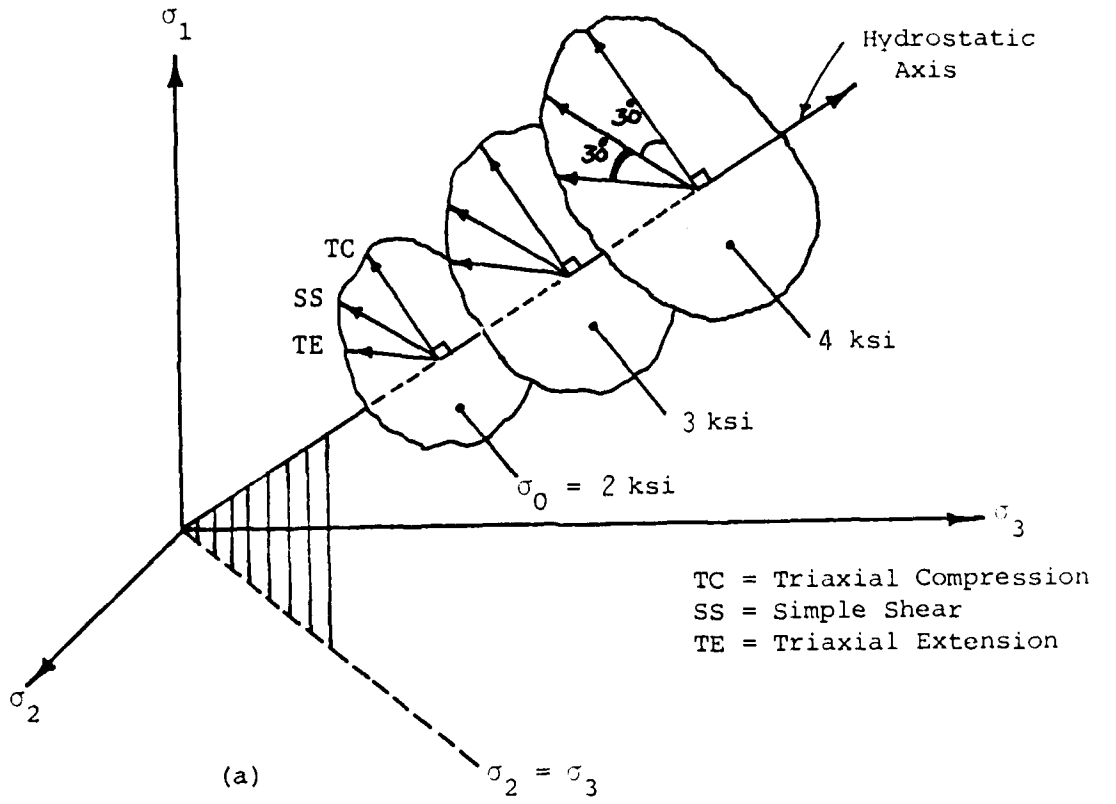

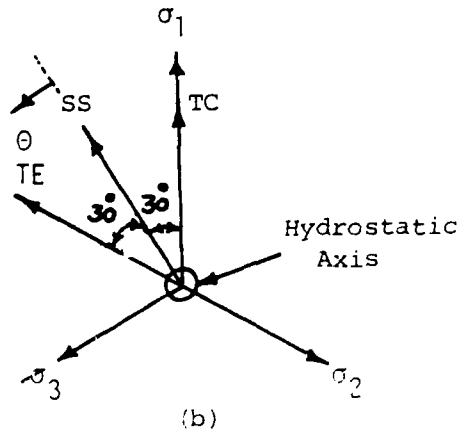

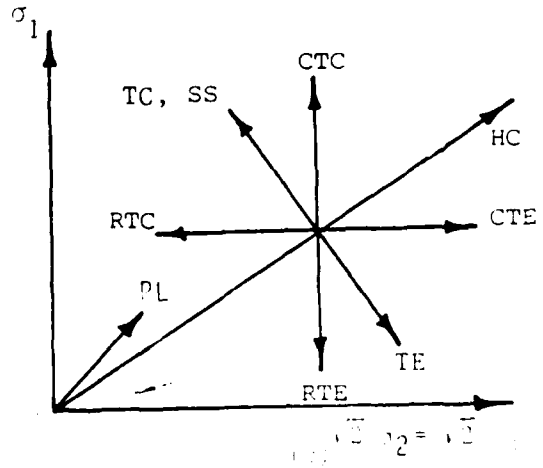

Figure 2.16. Schematic of the Commonly Used Stress Paths in (a) 3-D Stress Space; (b) Octahedral Plane; (c) Triaxial Plane. (Compression Stresses Positive).

2.5.1 Stress Paths on Triaxial Plane

The main purpose of this test series was to collect stress-strain and strength information of 4.0 in. (10.16 cm) cubical specimens tested in the Truly Triaxial device under triaxial loading conditions with low and high stress levels in order to determine the constitutive relations and strength of the material for triaxial compressive stress states. These triaxial tests were conducted by loading the specimen hydrostatically to a confining pressure equal to one of five selected levels, σ_o = 1,2,3,4 or 7.5 ksi (6.85, 13.79, 20.685, 27.58 or 51.713 MPa), and then subsequently following monotonic shear stress path to stay on the triaxial plane along various directions as shown in Fig. 2.16c. The data acquired during these tests consist of the stress-strain response in each loading direction as well as the ultimate (failure).

Also the hydrostatic compression (HC) loading, with maximum confining pressure of σ_o = 8 ksi (55.16 MPa), tests used to acquire information about the volumetric behavior.

Stress-strain and strength results of these tests are presented in Chapters 3 and 4 for concrete and soapstone, respectively.

2.5.2 Stress Paths on Octahedral Plane

The main objective of this series was to collect stress-

strain and strength information of 4.0 in. (10.16 cm) cubical specimens tested in the cubical device under triaxial loading conditions in order to determine the constitutive relation of material for traixial compressive stress states. These triaxial tests were conducted by loading the specimen hydrostatically to the octahedral normal stress, as low as possible, equal to one of three selected levels σ_{oct} = 2,3 or 4 ksi (13.79, 20.675 or 27.58 MPa), and then subsequently following a monotonic shear stress path to stay on the octahedral plane along either Triaxial Compression (TC), Simple Shear (SS) or Triaxial Extension (TE) direction as shown in Figs. 2.16b and 2.16c thus inducting a change in only the octahedral shear stress (τ_{oct}) along these paths. Through examination of the ultimate data in triaxial plane in Chapters 3 and 4, one can see that if tests had been conducted along the TE stress path at confining pressure lower than 2 ksi (13.79 MPa), they would have ended before the specimens failed because tensile stresses would have beeen required, which was impossible at the time this research was conducted.

The superposition of a pure shear stress on an initial hydrostatic state permits the investigation of the effect of three-dimensional shear stress state on the stress-strain relations of the material. The data acquired during these tests consist of the stress-strain response in each loading direction

as well as the ultimate failure data. By assuming isotropy of the material, the shape of the ultimate failure envelope for the three octahedral planes is determined from the ultimate (failure) data by loading along these monotonic stress paths.

Stress-strain and strength results of these tests are presented in Chapters 3 and 4 for concrete and soapstone, respectively.

2.5.3 Proportional Loading Paths

In an attempt to gather additional information regarding the behavior of plain concrete subjected to proportional loading, these tests were conducted. Proportional loading tests were conducted such that the ratio of $R = \frac{\sigma_2}{\sigma_2} = \frac{\sigma_3}{\sigma_1}$ remain the same during the change in loading. Two ratios of R = 1/3 and 2/3 were selected here.

Stress-strain response of these tests for the concrete are presented in Chapter 3.

2.5.4 Circular Stress Path Tests

The circular stress path shown in Fig. 2.17 illustrates the type of test done in this test series. The stress path was selected in order to gain information about the effects of the third stress invariant. Characteristic of circular stress path is the fact the first and second stress invariants are held constant with only the third stress invariant varying during the loading

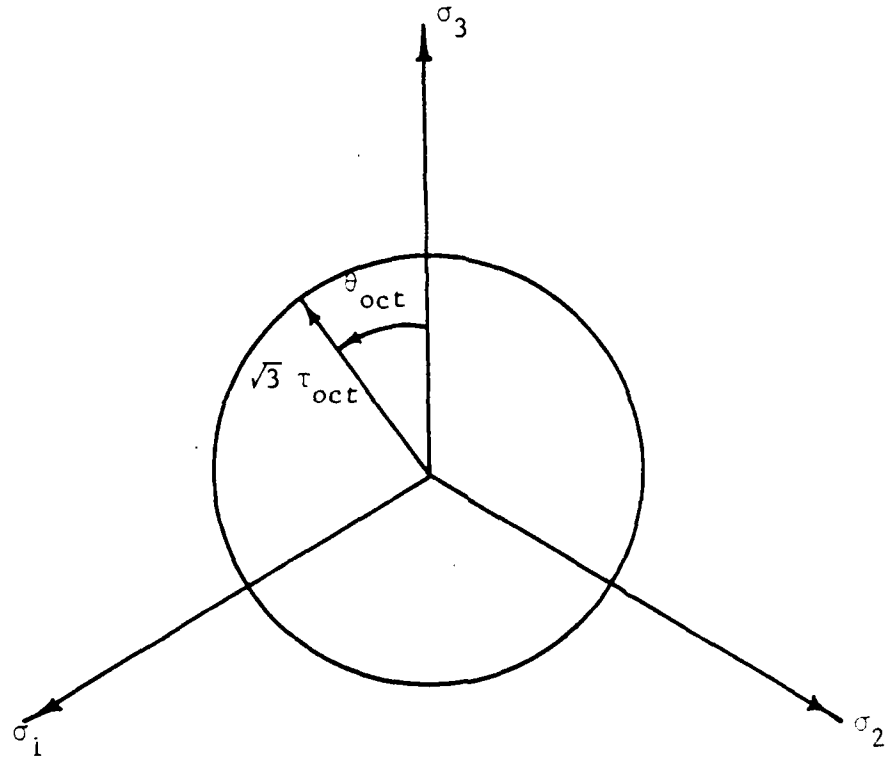

$$\sigma_1 = \frac{\tau_{oct}}{\sqrt{2}} (-\cos \theta_{oct} + \sqrt{3} \sin \theta_{oct}) + \sigma_{oct}$$

$$\sigma_2 = \frac{\tau_{oct}}{\sqrt{2}} (-\cos t_{oct} - \sqrt{3} \sin \theta_{oct}) + \sigma_{oct}$$

$$\sigma_3 = \sqrt{2}\ \tau_{oct} \cos \theta_{oct} + \sigma_{oct}$$

Figure 2.17. Circular Stress Path with Principal Stress Relations Given.

sequence. Isolation of the third stress invariant in this way allows its effects to be clearly identified.

Tests of this type were performed in the 4.0 ksi (27.58 MPa) deviatoric plane. From the ultimate (failure) data that were obtained in the section 2.5.2 tests, values of the octahedral shear stress, that is radii of the circle, were selected. This was done in such a way that the circular stress path remained sufficiently far below the ultimate strength of the concrete and soapstone in order that significant damage of the concrete and soapstone specimens and microcracking, would not result during the loading sequence.

A value of 10^{o} for the incremental octahedral stress angle, Θ_{oct}, was selected for these tests.

Stress-strain response of these tests are presented in Chapters 3 and 4 for concrete and soapstone, respectively.

CHAPTER 3

TEST SERIES AND RESULTS ON PLAIN CONCRETE

3.1 Introduction

Various stress paths and their abbreviations used in testing program are shown in Fig. 2.16. These include Hydrostatic Compression (HC), Conventional Triaxial Compression (CTC), Reduced Triaxial Extension (RTE), Triaxial Compression (TC), Triaxial Extension (TE), Simple Shear (SS) paths, Proportional Loading (PL), Circular Stress Path (CSP) and Arbitrary on CTC Path (AP test paths. These test series were conducted to determine the behavior of plain concrete under three dimensional states of stress.

The triaxial plane is the plane in the principal stress space (σ_1, σ_2, σ_3) which bisects σ_2 - σ_3 axes and is coplanar with the σ_1 - axis. In the conventional triaxial device, only two principal stress can be varied. Therefore, on the triaxial plane, two of the three principal stresses are equal.

3.2 Preliminary Test Series

The details of the preliminary test series for cylindrical specimens are shown in TABLE 3.1 where the specimen type and test condition are given along with the specimen numbers, the age at which they were tested and the strength results. All tests were

TABLE 3.1
PRELIMINARY TEST PROGRAM
SPECIMEN TYPE: 6x12 in. (15.24x30.48 cm) CYLINDER
TEST CONDITION: UNCONFINED COMPRESSION

DESIGNATION		CASTING DATE	TESTING DATE	AGE AT TESTING	f'_c
SERIES	SP.NO.	MO/DA/YR	MO/DA/YR	(DAYS)	(ksi)*
BATCH NO. 1	A1	2/2/84	2/9/84	7	1.50
	A2		2/9/84	7	1.60
	A3		2/9/84	7	1.55
	B1		2/16/84	14	2.12
	B2		2/16/84	14	2.12
	B3		2/16/84	14	2.10
	C1		2/30/84	28	2.85
	C2		2/30/84	28	2.86
	C3		2/30/84	28	2.83
	D1		3/22/84	50	3.18
	D2		3/22/84	50	3.00
	D3		3/22/84	50	3.12
BATCH NO. 2	E1	2/28/84	3/3/84	7	1.55
	E2		3/3/84	7	1.58
	E3		3/3/84	7	1.58
	F1		3/10/84	14	2.2
	F2		3/10/84	14	2.1
	F3		3/10/84	14	2.3
	G1		3/24/84	28	2.88
	G2		3/24/84	28	2.84
	G3		3/24/84	28	2.82
	H1		4/16/84	50	3.0
	H2		4/16/84	50	3.12
	H3		4/16/84	50	3.13

*1.0 psi = 6.89 kPa

conducted in triplicate. Notice that the unconfined compression tests for the cylinders were conducted at varying specimen ages of 7, 14, 28 and 50 days. This was done to observe the effect of specimen age on strength after the curing period of 7 days in the humidity room and the remaining time in air in order to determine if after 50 days of curing, full strength was achieved such that the cubical tests could be conducted without the variability of increasing strength with age coming into play.

3.3 Results from Various Tests

3.3.1 Hydrostatic Compression (HC)

The results of the two replicate HC tests are presented in Figs. 3.1a, 3.1b, 3.2a, 3.2b. Increments of load (stresses) of the same magnitude are applied on all six faces of the specimen. It is seen from Fig. 3.1a, 3.2a that the strain in the vertical direction is substantially less than the strains in the lateral directions. This may be due to the fact that the plain concrete is made by pouring and vibrating the concrete mixed in vertical direction. There are four unloading-reloading cycles in each test. Average slopes of the unloading-reloading curves is used to calculate the elastic parameters as well as the plastic part of the total strain. Figures 3.1b and 3.2b show the mean pressure vs. volumetric strain curves. The elastic (unloading-reloading) bulk modulus appears to remain almost constant throughout the test at about 487.86 ksi (3363.80 MPa).

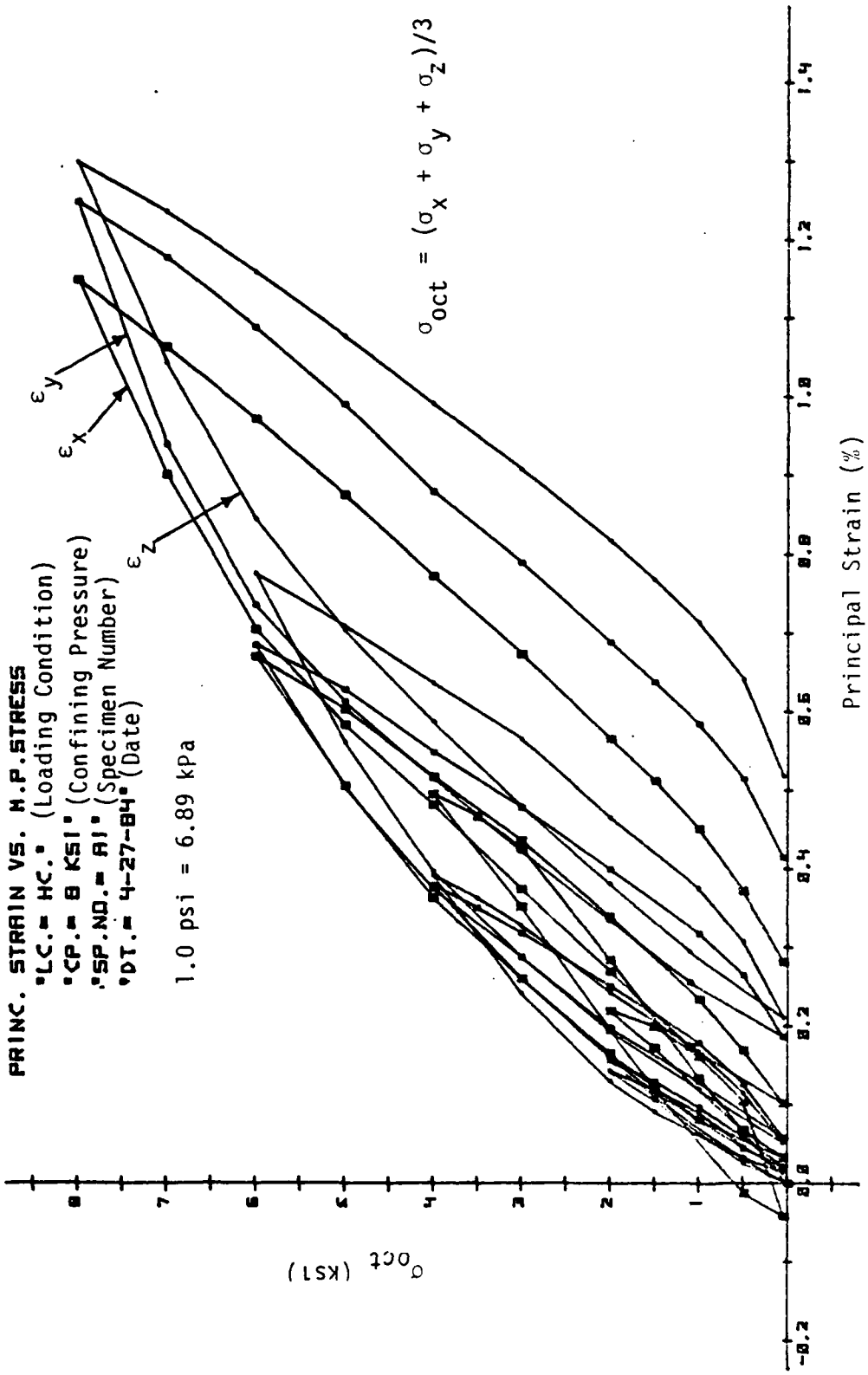

Figure 3.1a. Stress-Strain Response Curves for Hydrostatic Compression Test.

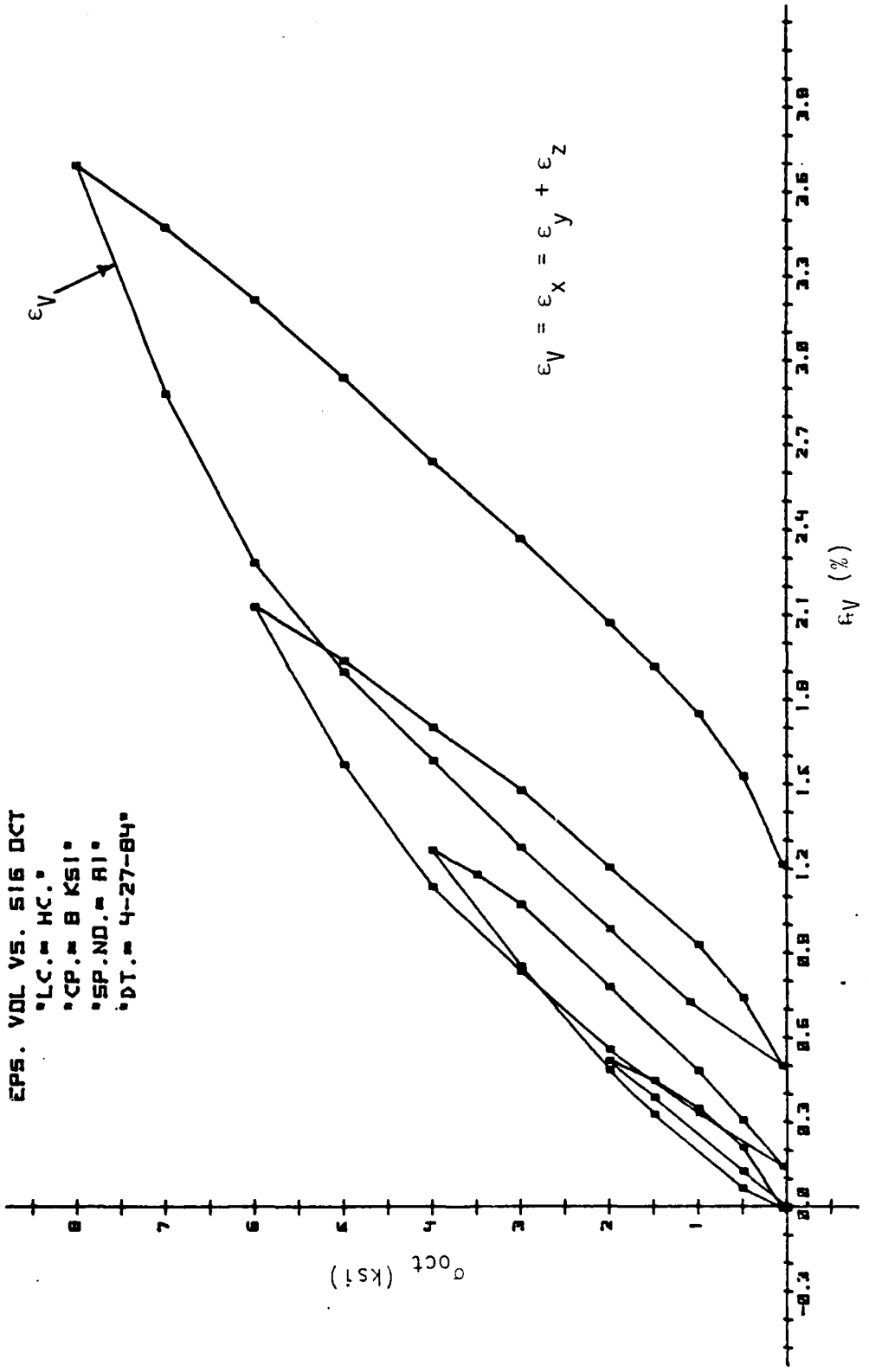

Figure 3.1b. Average Stress-Strain Response Curve for Hydrostatic Compression Test.

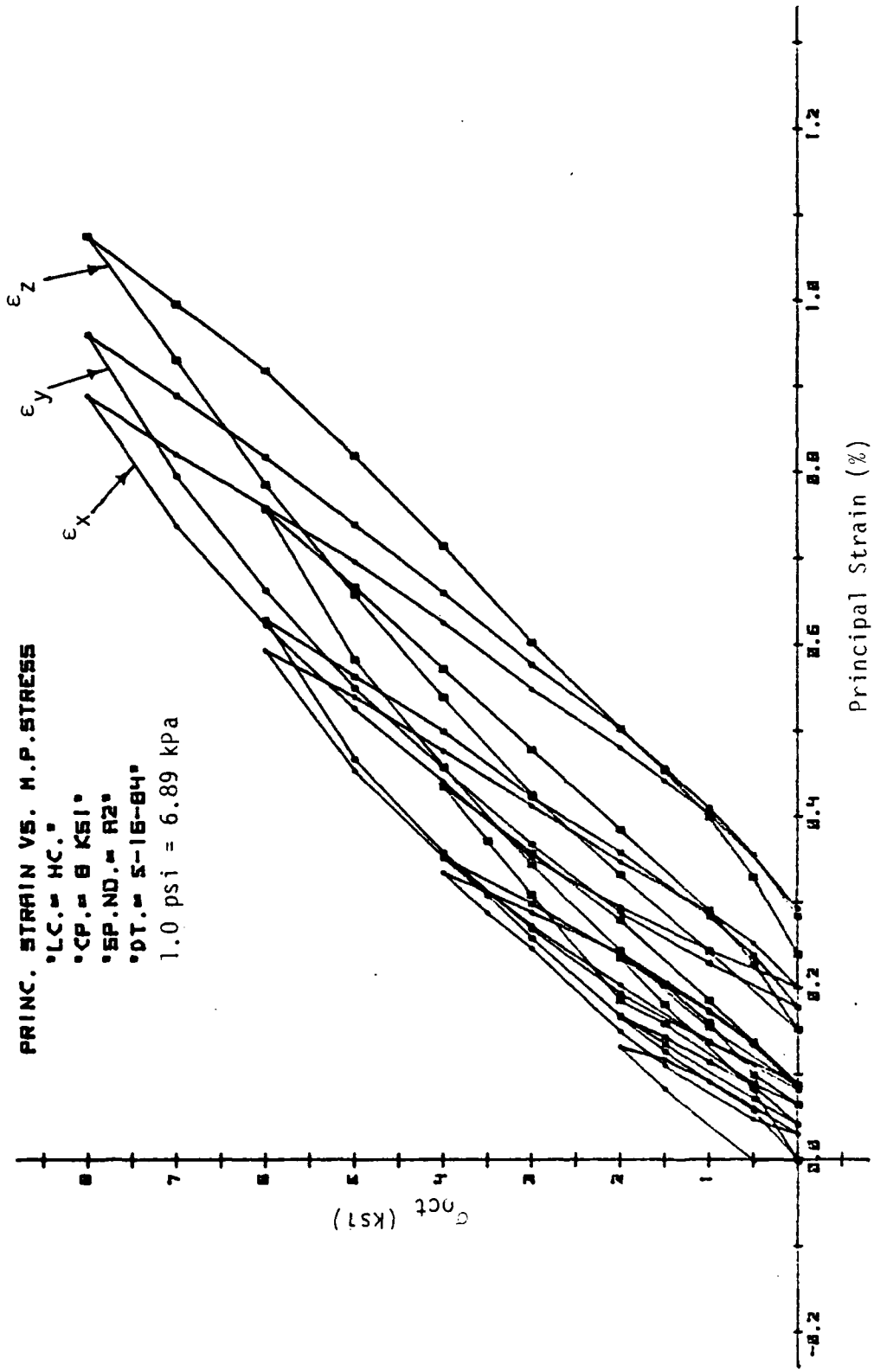

Figure 3.2a. Stress-Strain Response Curves for Hydrostatic Compression Test.

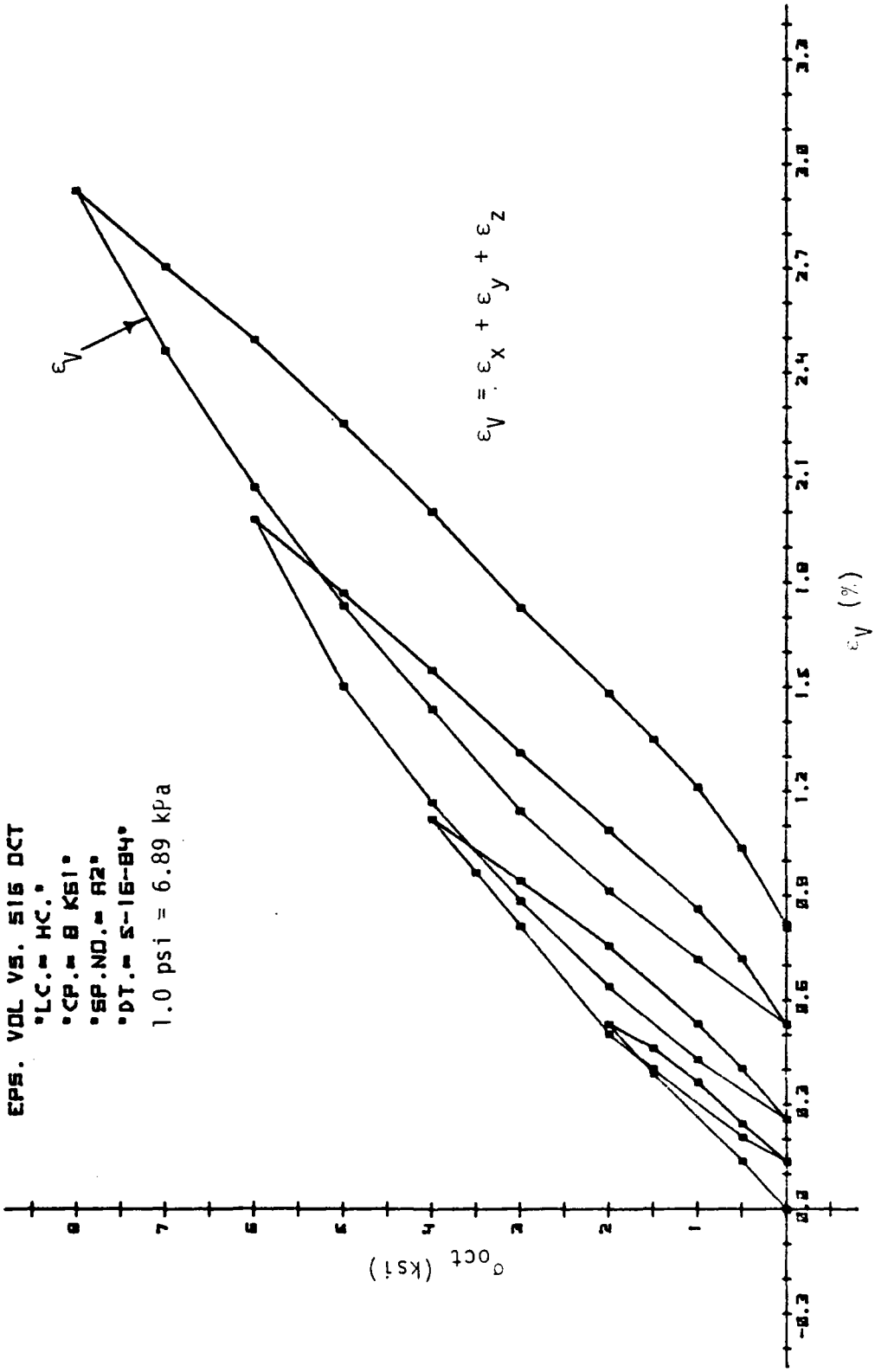

Figure 3.2b. Average Stress-Strain Response Curve for Hydrostatic Compression Test.

3.3.2 Conventional Triaxial Compression (CTC)

Figures 3.3 to 3.14 show the stress-strain responses for four Conventional Triaxial Compression (CTC) tests at confining pressures of 0.0, 1.0, 2.0 and 3.0 ksi (0.0, 6895.0, 13.79 and 20.685 MPa) respectively. In these tests, the stresses in lateral directions, σ_2 and σ_3 are kept constant (equal to the confining pressure, σ_0), while the vertical stress σ_1 is increased in small increments. There are three unloading-reloading cycles in each test. A part of these tests is intended to study the concrete response at low confining pressure.

The Z direction corresponds to the direction of sample vibration (compaction); this can explain the high degree of isotropy exhibited in the x and y directions, as shown in the octahedral shear stress vs. strain plots of all four tests. From these plots it is evident that the sample strength increases with initial confining pressure as expected for frictional materials.

3.3.3 Reduced Triaxial Extension (RTE)

The results of the RTE test are presented in Fig. 3.15 and 3.16. In the RTE test, the stresses in the x and y directions were held constant at the initial hydrostatic pressure 7.5 ksi (51.71 MPa) while the stress in the Z direction was reduced. The degree of isotropy in x and y direction is similar for this test as in the previous tests, in Figs. 3.3-3.14, as shown in Fig. 3.15.

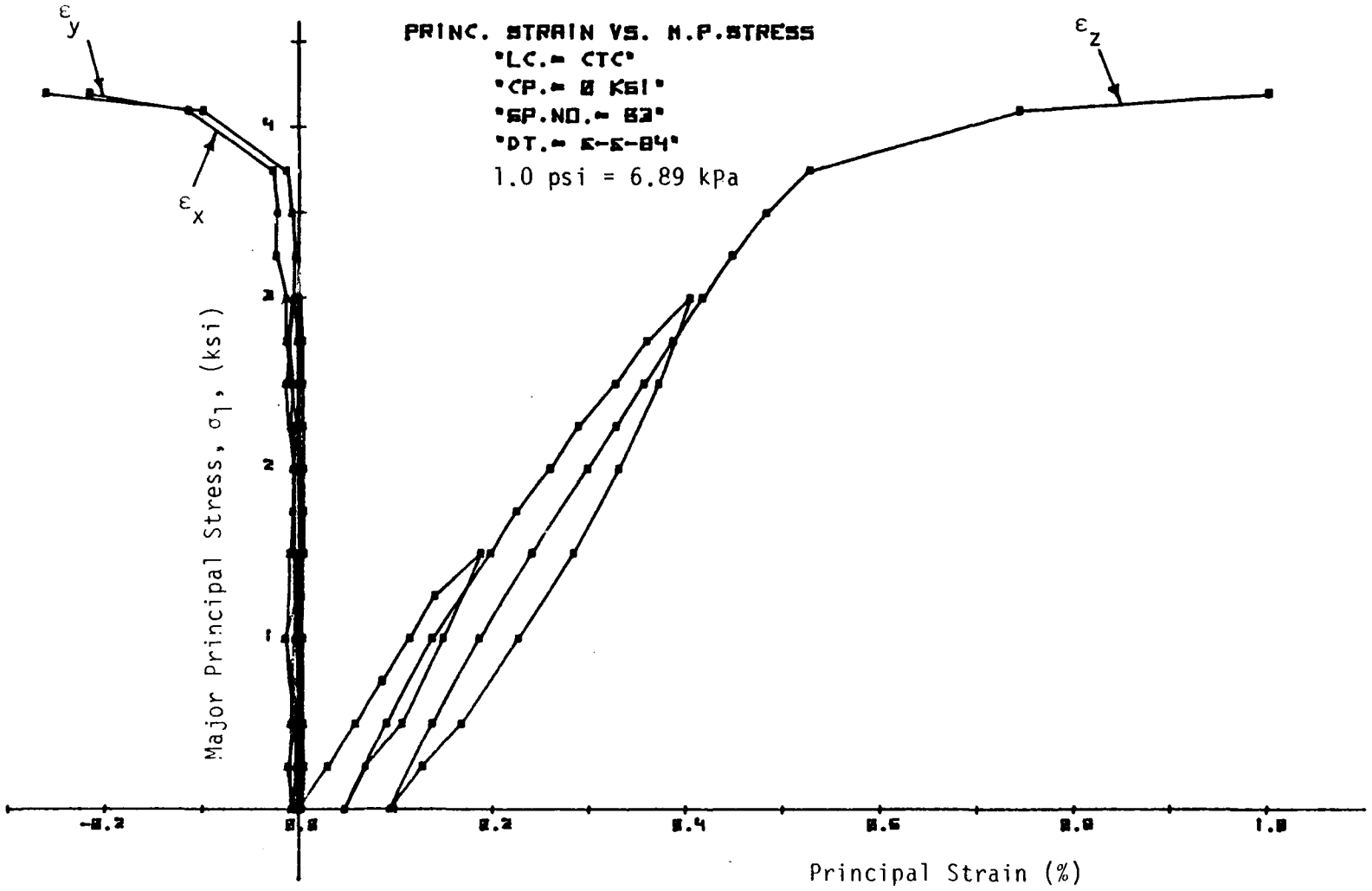

Figure 3.3. Stress-Strain Response Curves for Conventional Triaxial Compression Test.

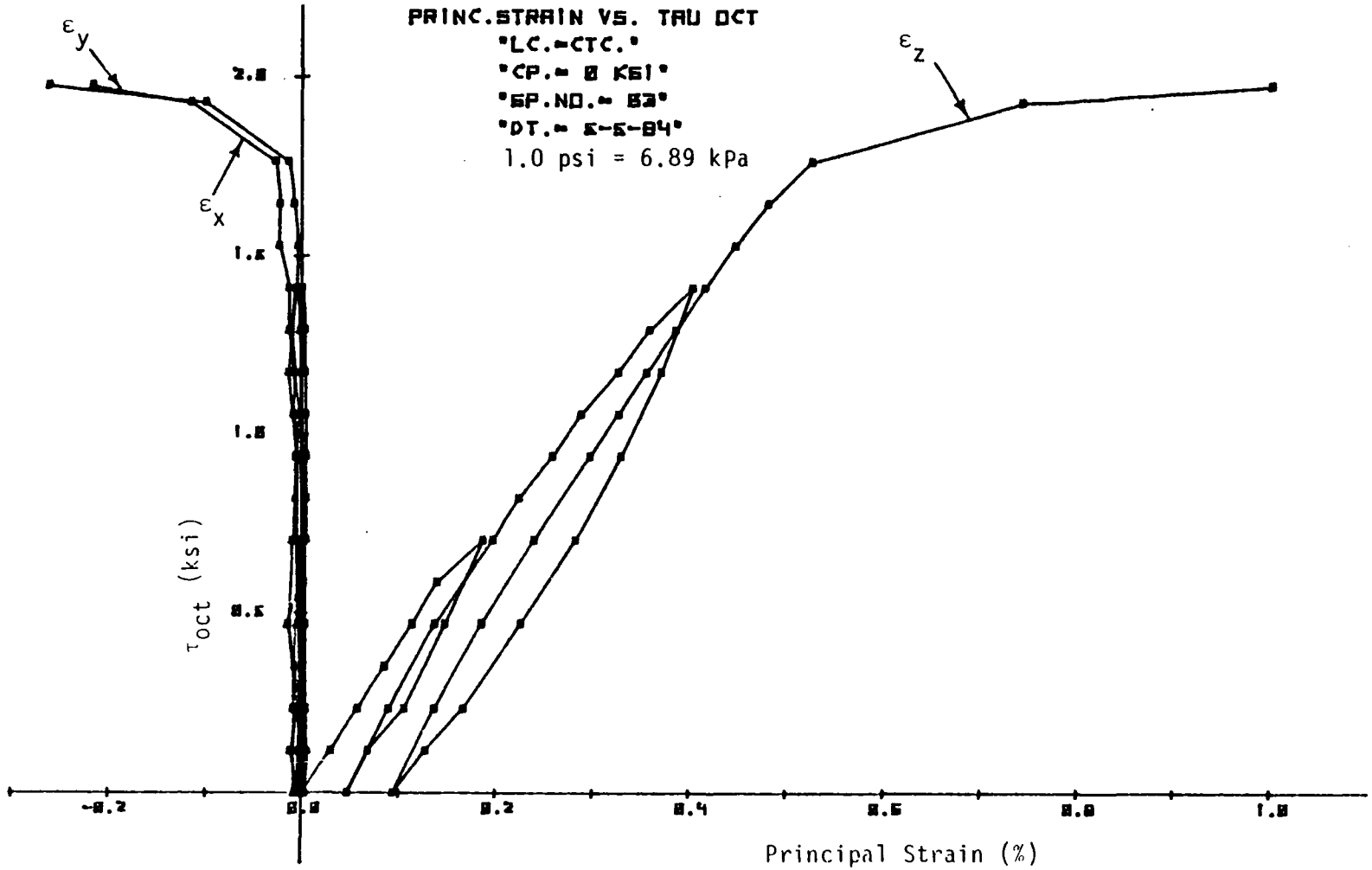

Figure 3.4. Stress-Strain Response Curves for Conventional Triaxial Compression Test.

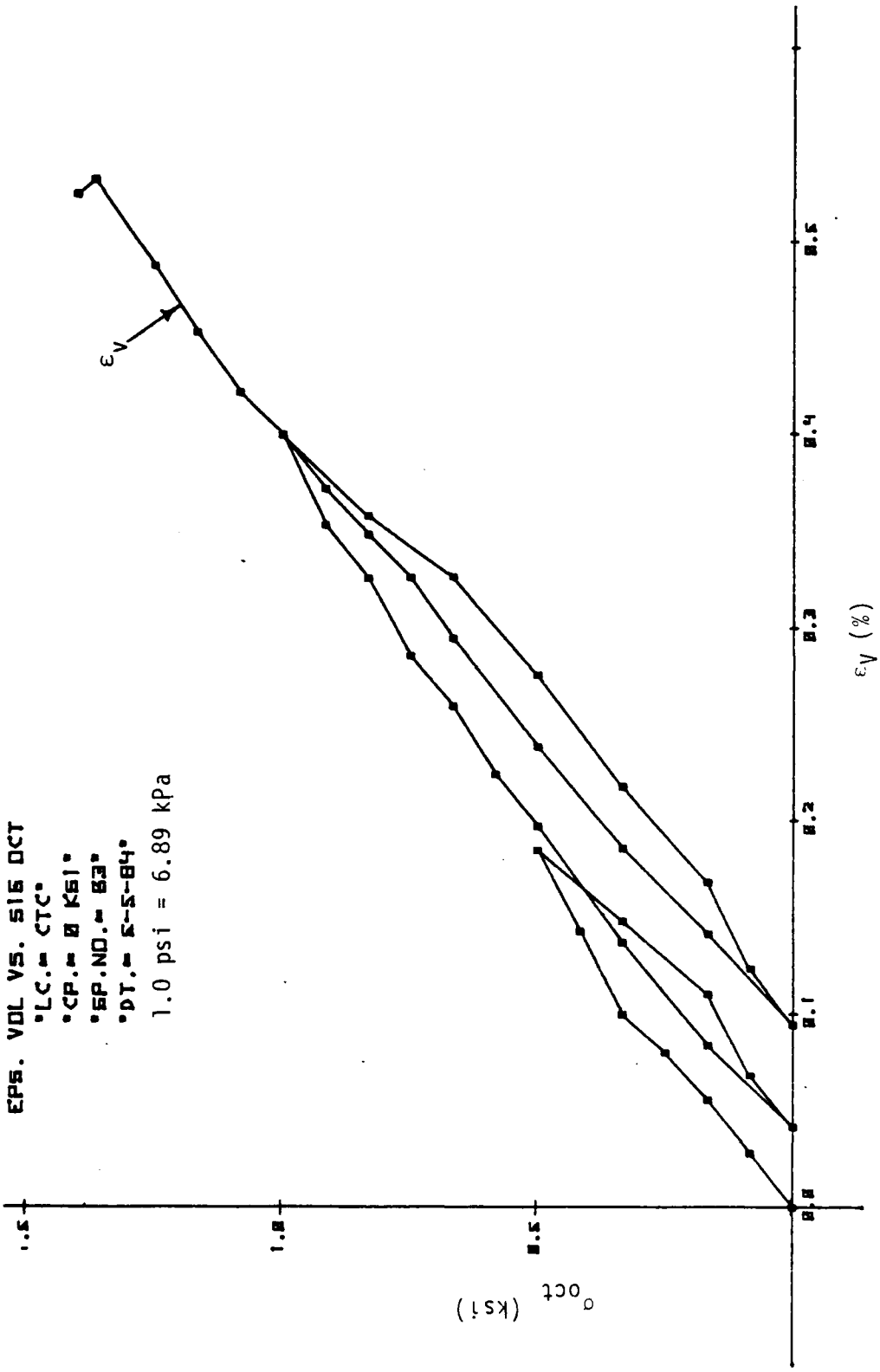

Figure 3.5. Average Stress-Volumetric Strain Response Curve for Conventional Triaxial Compression Test.

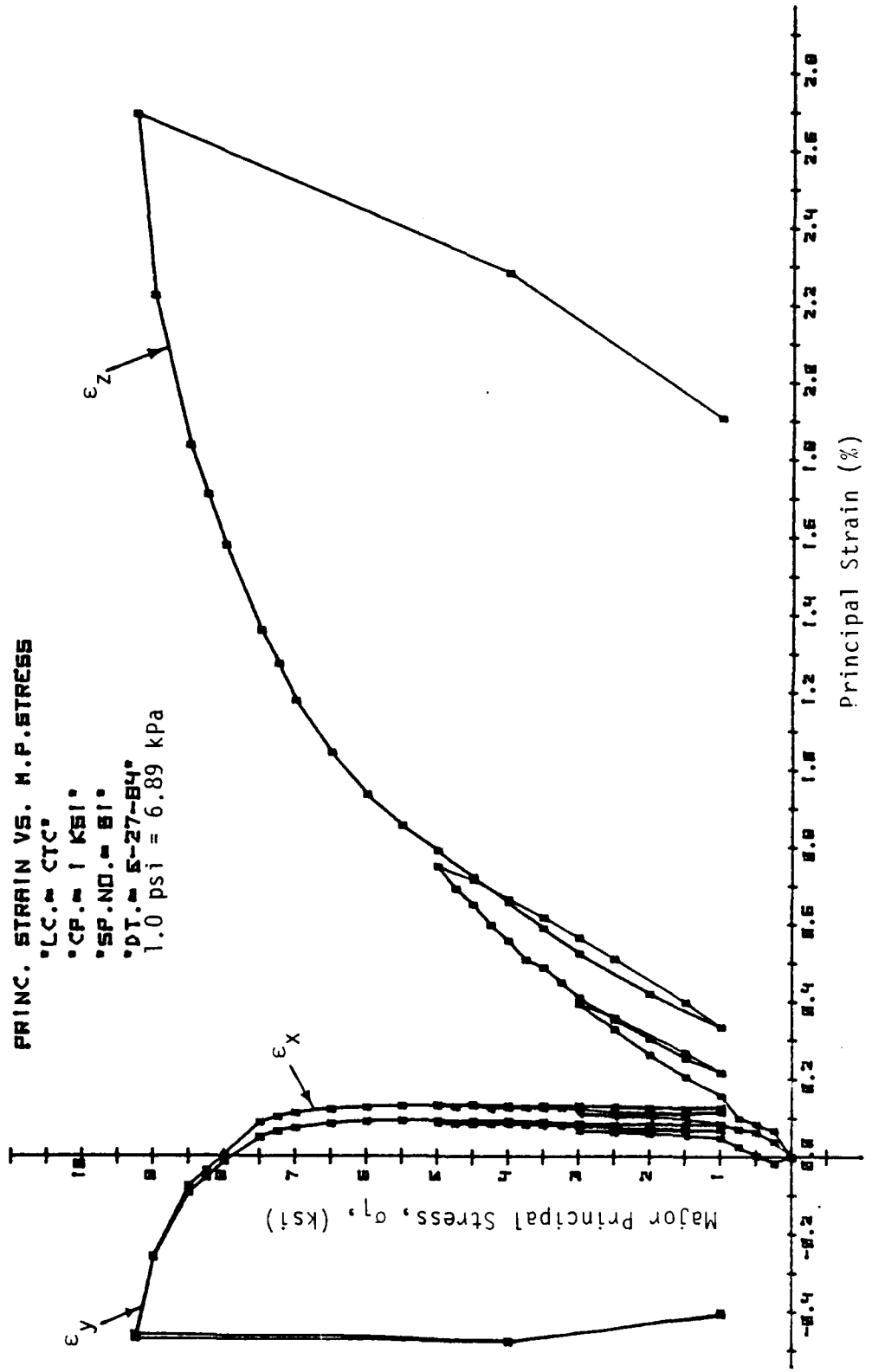

Figure 3.6. Stress-Strain Response Curves for Conventional Triaxial Compression Test.

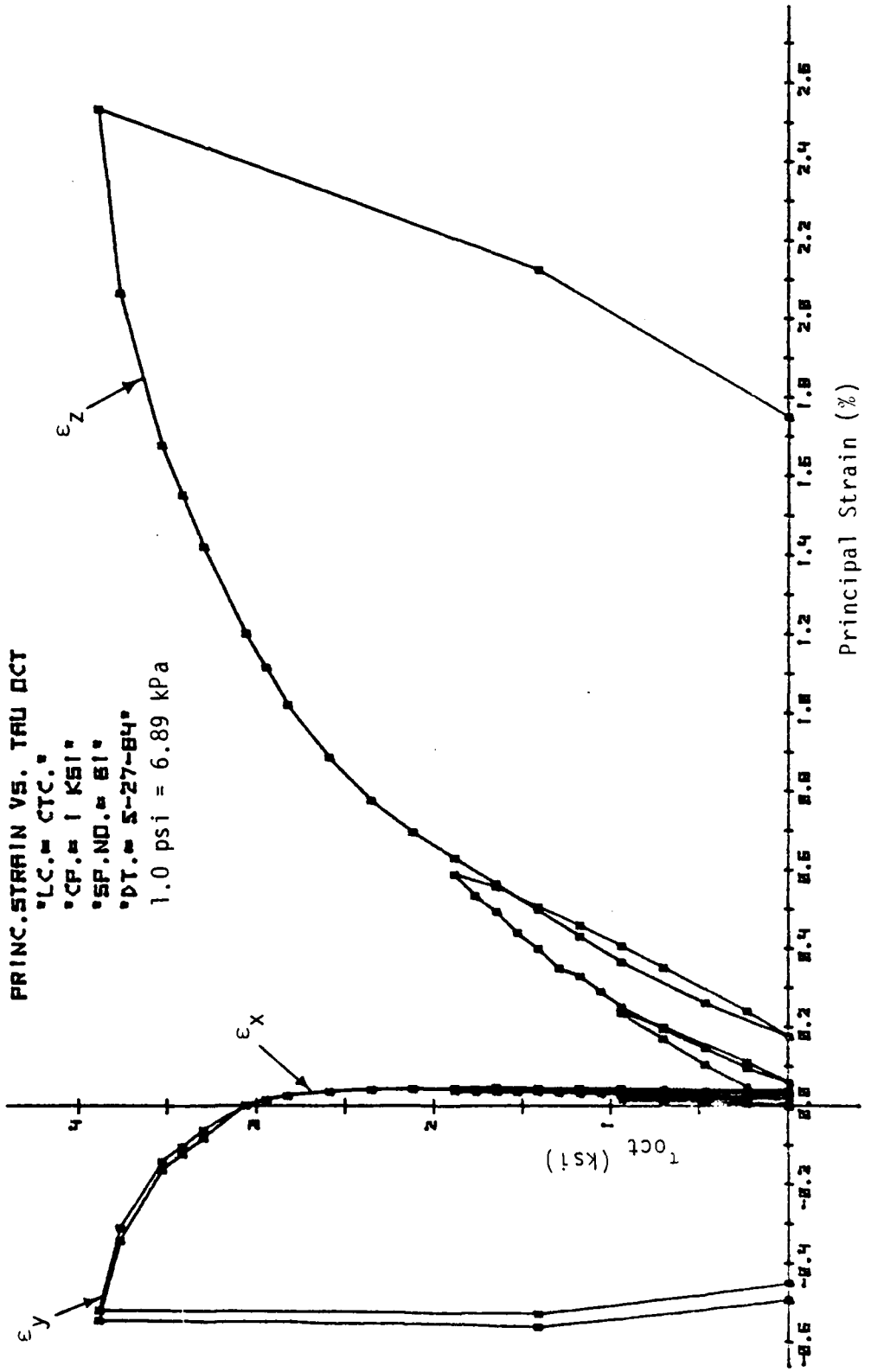

Figure 3.7. Stress-Strain Response Curves for Conventional Triaxial Compression Test.

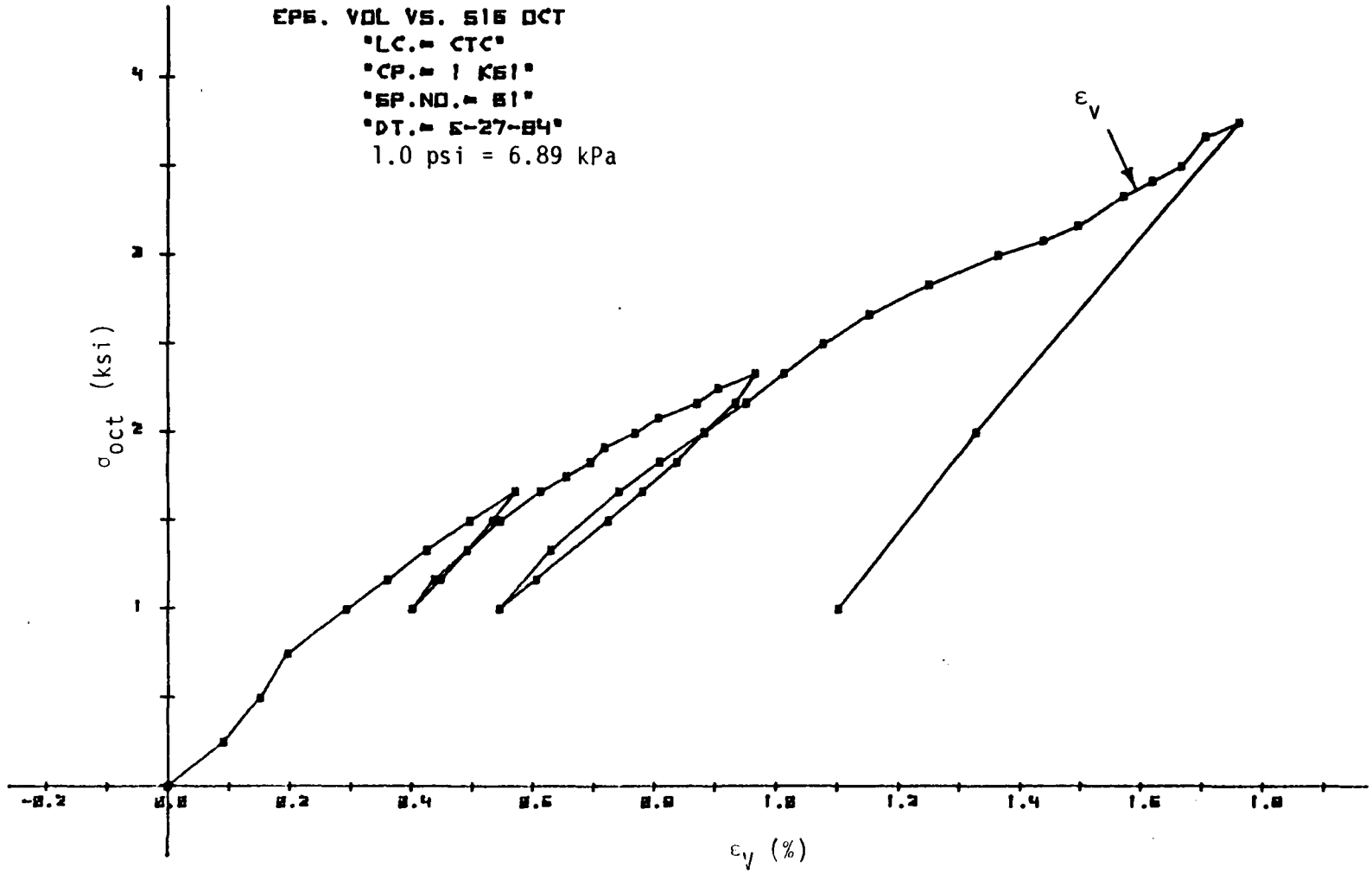

Figure 3.8. Average Stress-Volumetric Strain Response Curve for Conventional Triaxial Compression Test.

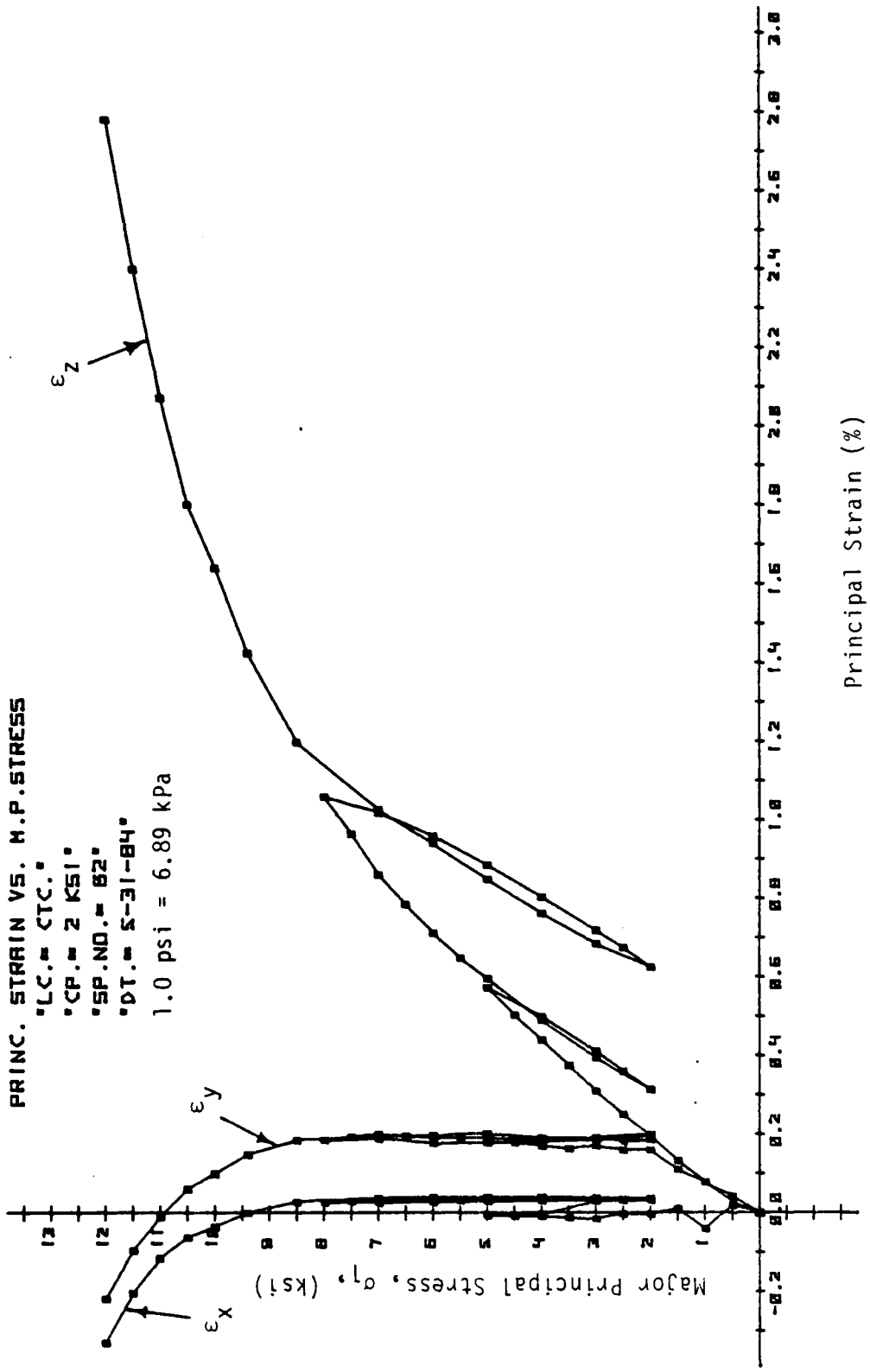

Figure 3.9. Stress-Strain Response Curves for Conventional Triaxial Compression Test.

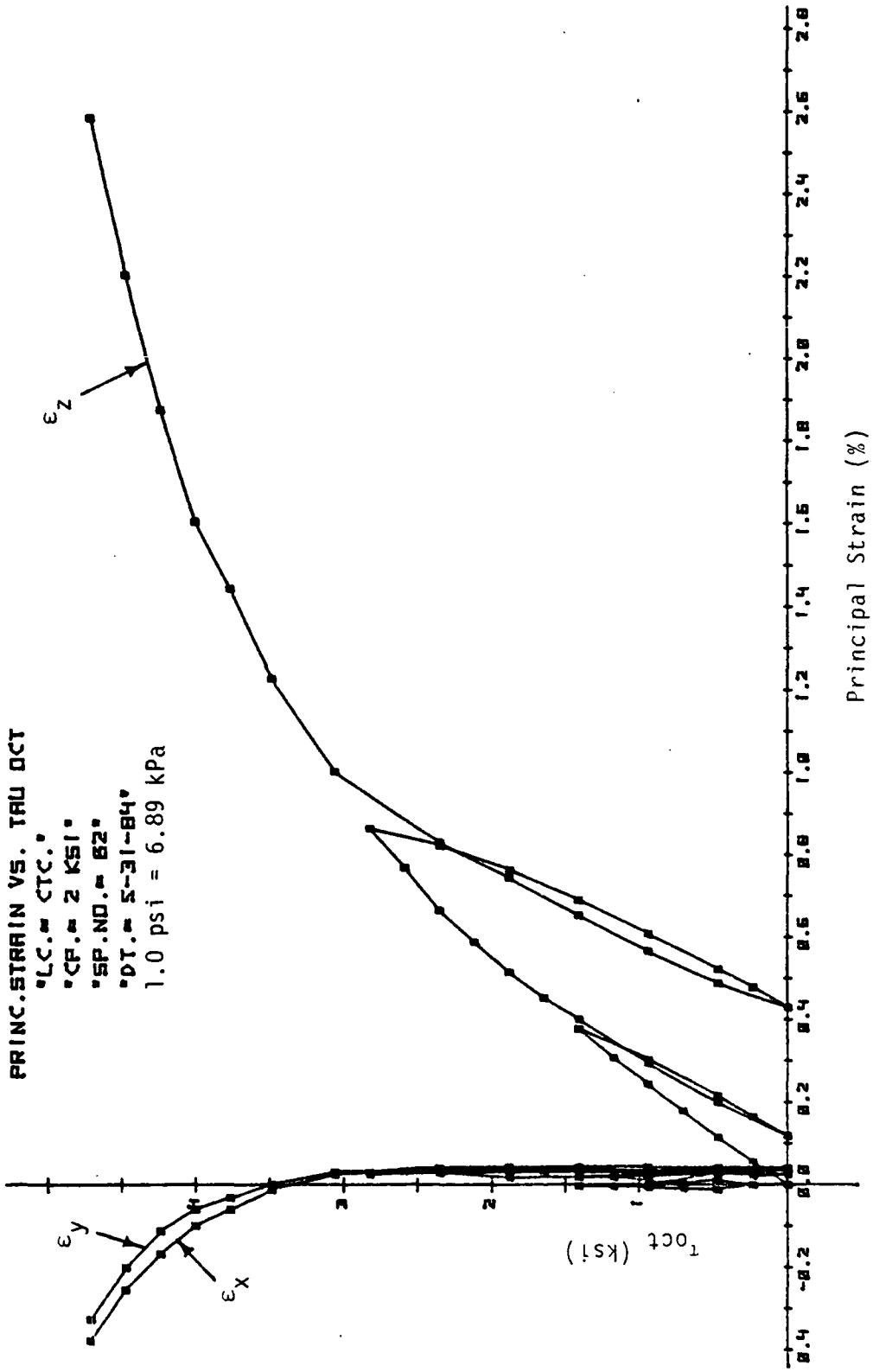

Figure 3.10. Stress-Strain Response Curves for Conventional Triaxial Compression Test.

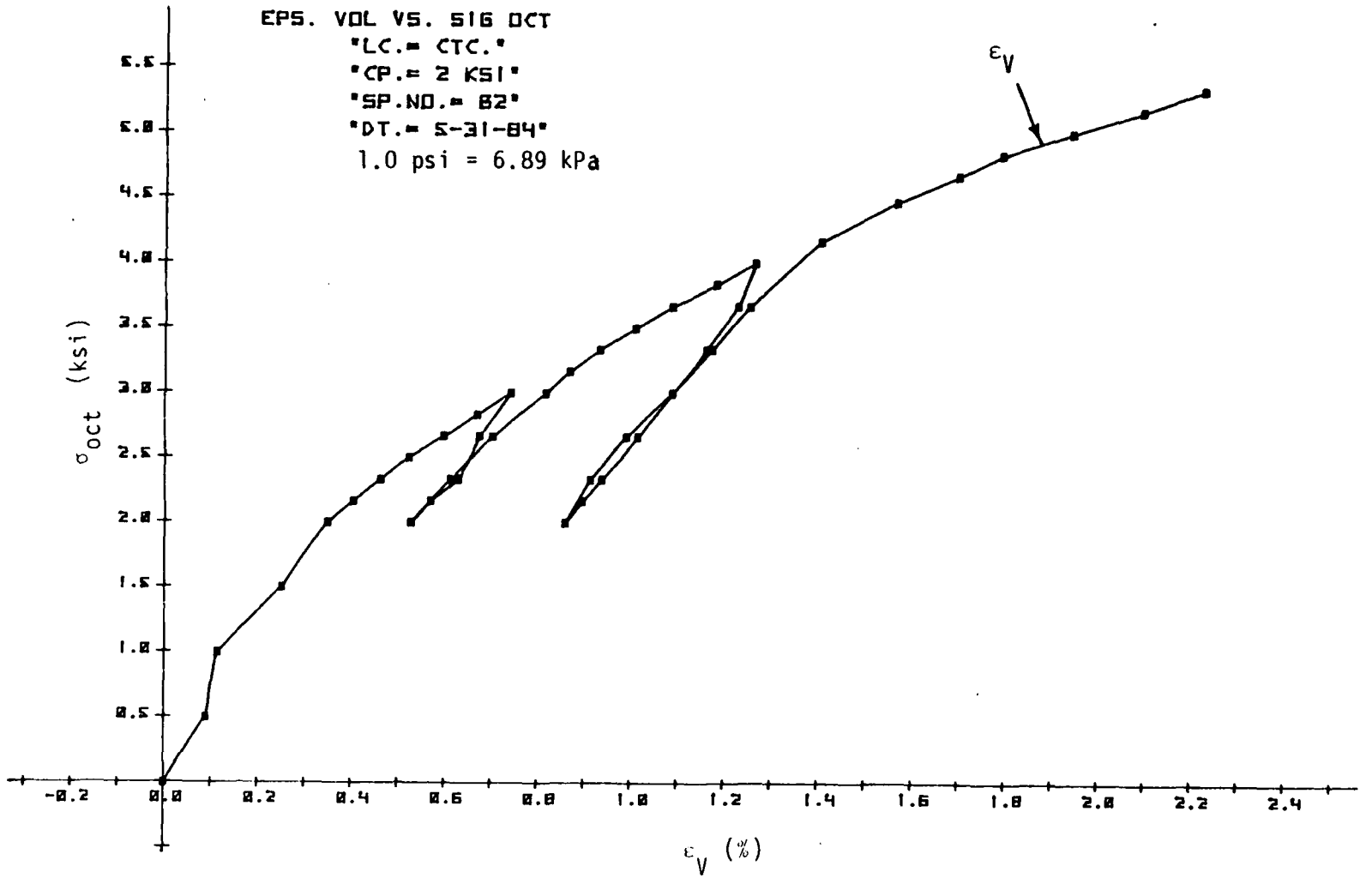

Figure 3.11. Average Stress-Volumetric Strain Response Curve for Conventional Triaxial Compression Test.

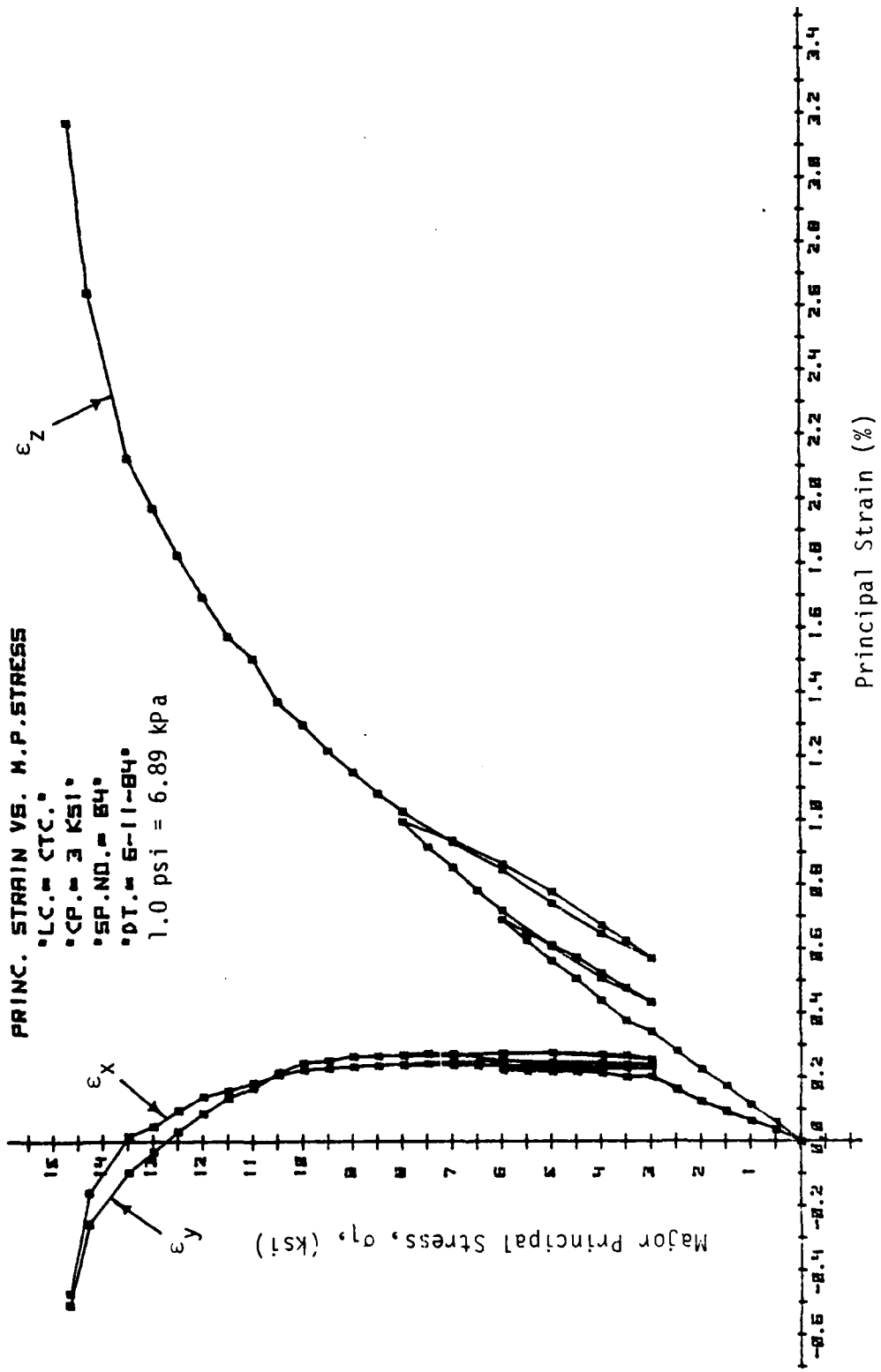

Figure 3.12. Stress-Strain Response Curves for Conventional Compression Test.

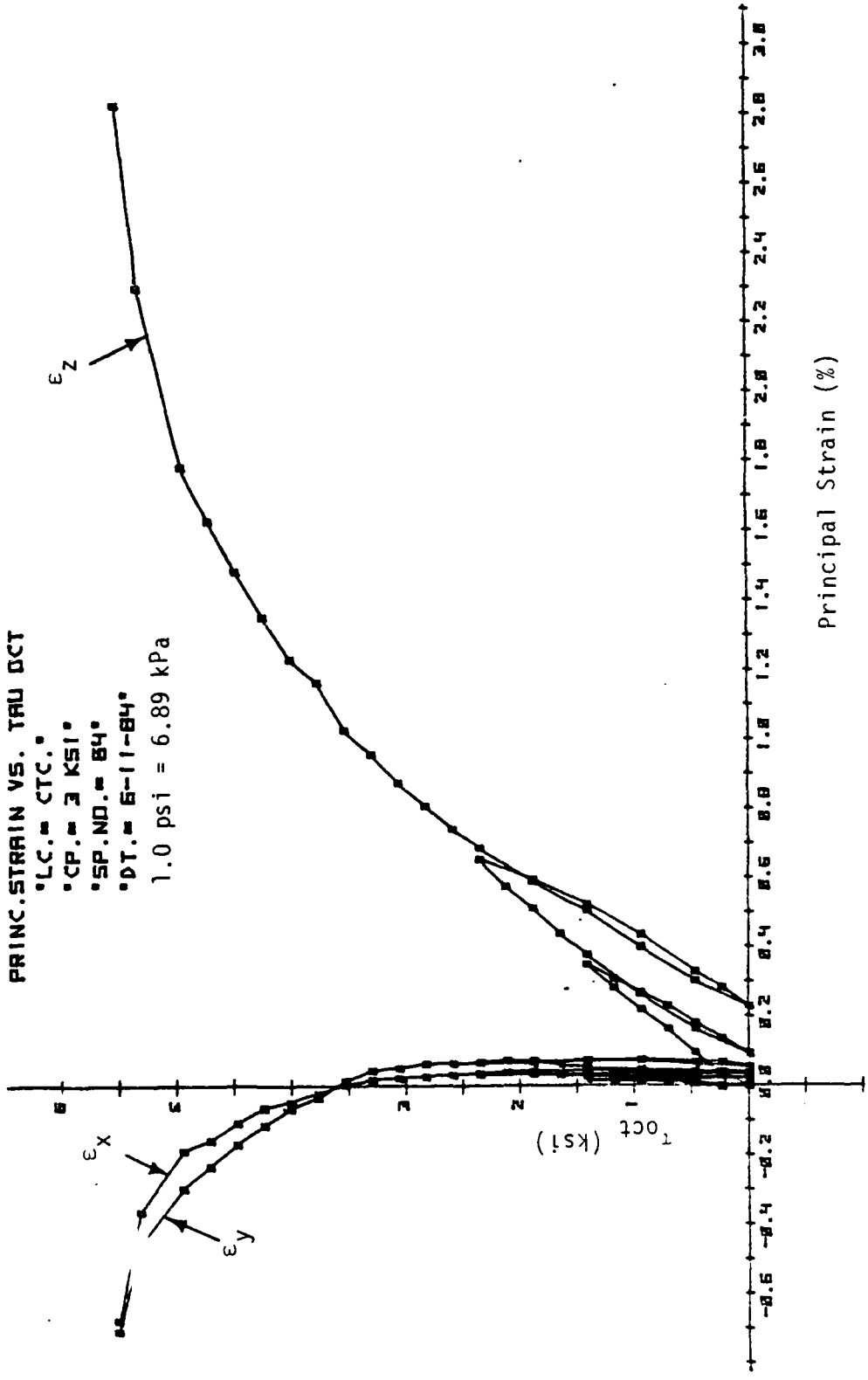

Figure 3.13. Stress-Strain Response Curves for Conventional Compression Test.

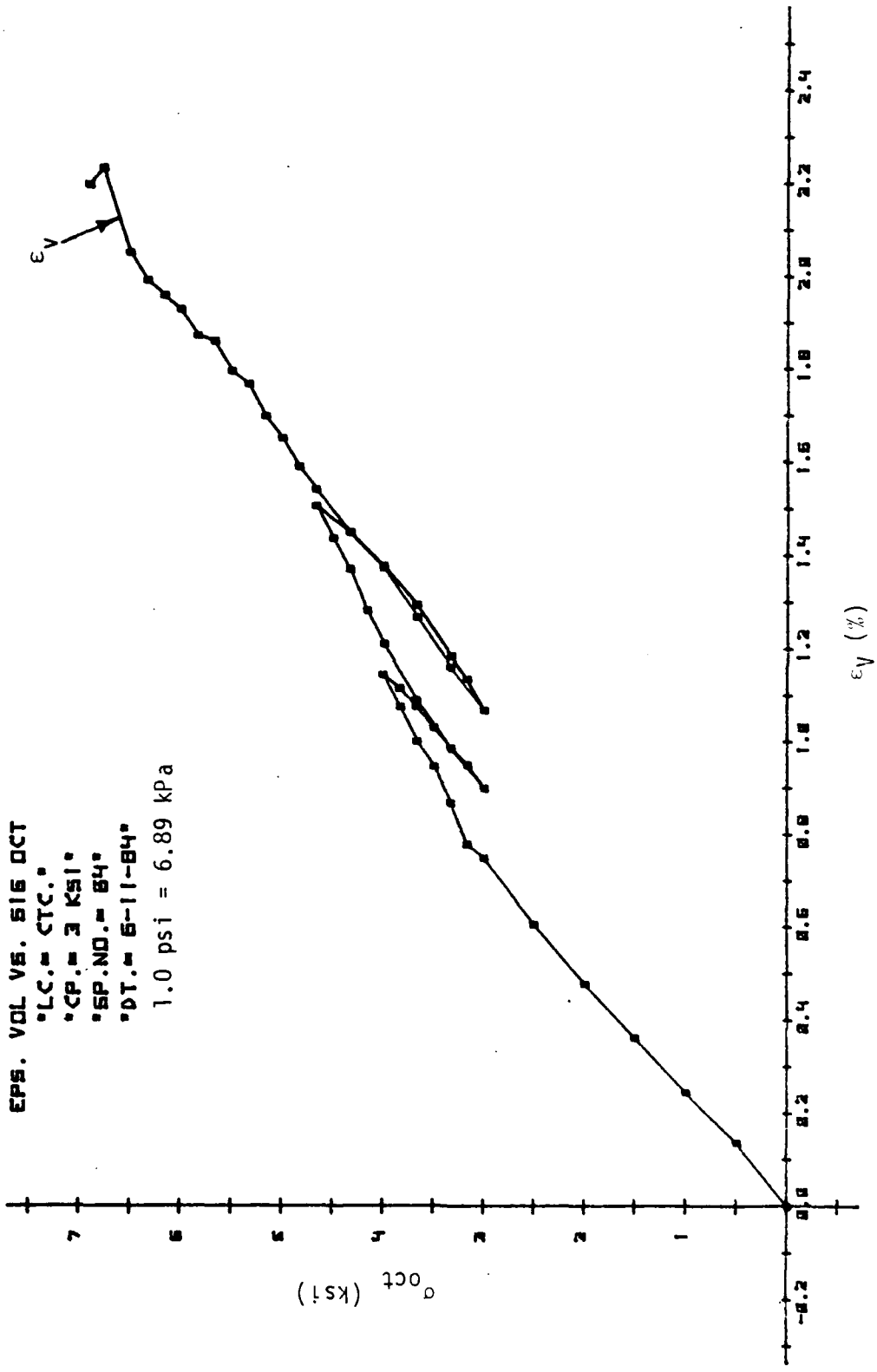

Figure 3.14 Stress-Volumetric Strain Response Curve for Conventional Triaxial Compression Test.

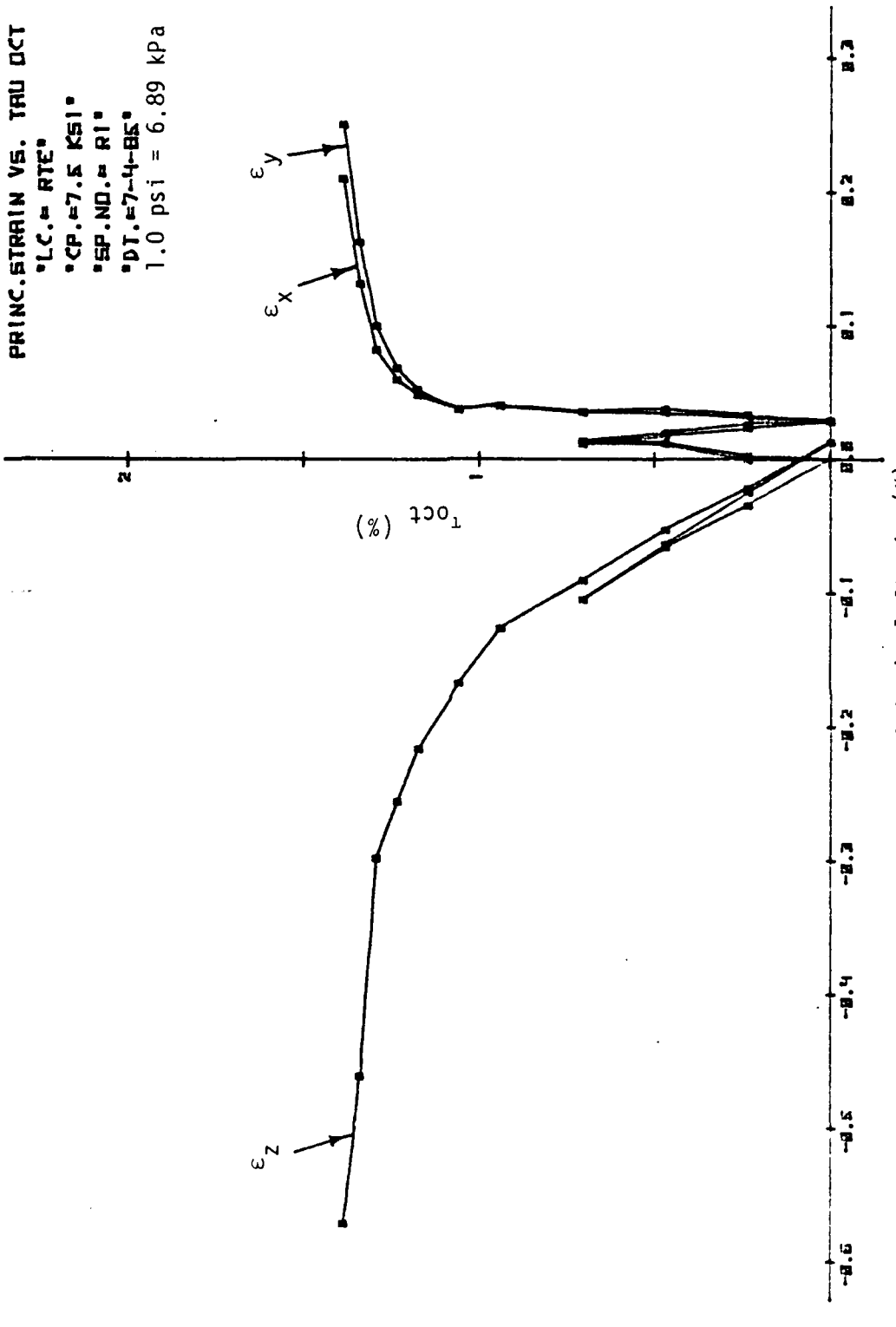

Figure 3.15. Stress-Strain Response Curves for Reduced Triaxial Compression Test.

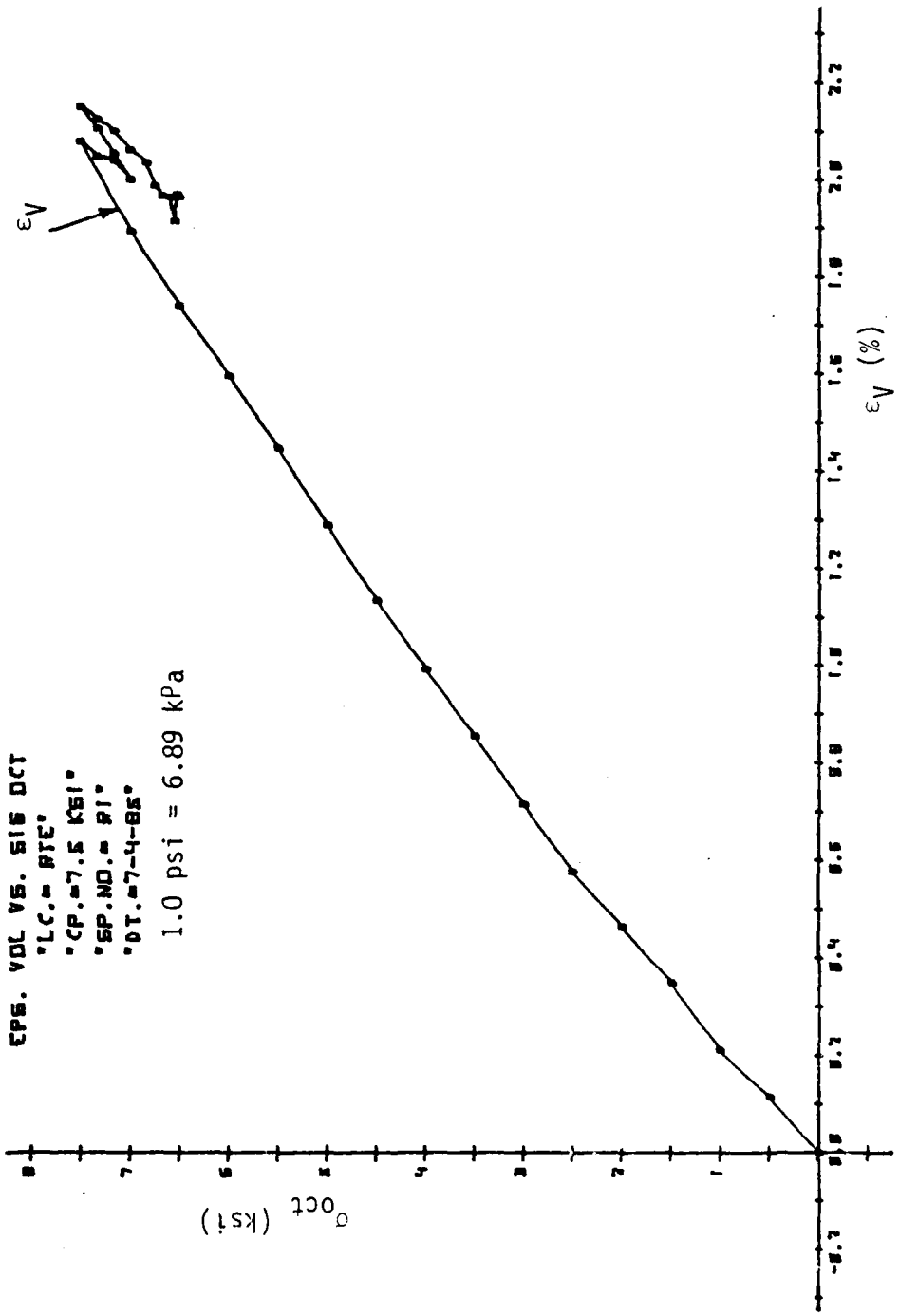

Figure 3.16. Stress-Volumetric Strain Response Curve for Reduced Triaxial Compression Test

AD-A174 451 CONSTITUTIVE MODELLING OF CONCRETE AND ROCKS UNDER MULTIAXIAL COMPRESSIVE (U) ARIZONA UNIV TUCSON DEPT OF CIVIL ENGINEERING M R SALAMI ET AL 04 SEP 86 2/5

UNCLASSIFIED AFOSR-TR-86-2014 AFOSR-83-0256 F/G 8/7 NL

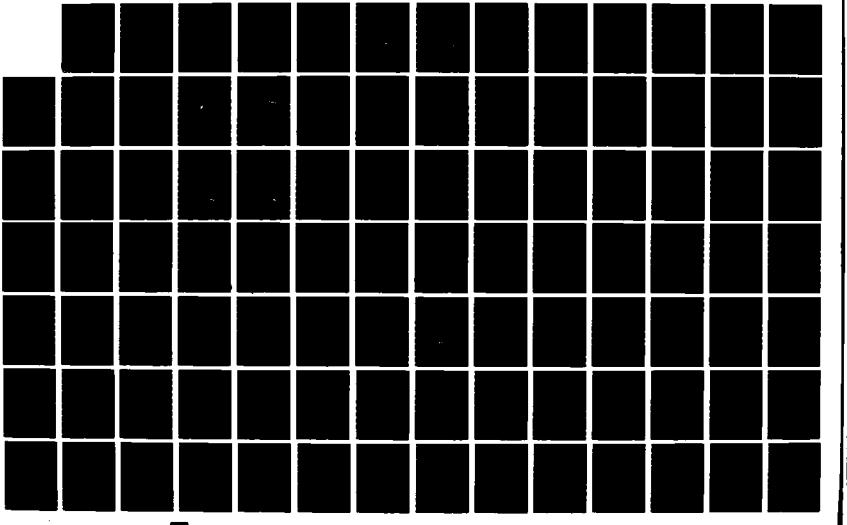

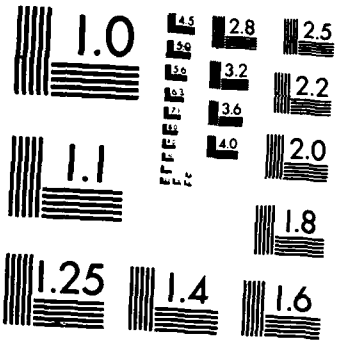

As part of the graphs show the three principal strains ε_i (i = 1,2,3) and ε_v plotted against the major principal stress σ_1; in these graphs, the stress axis is labeled "Major Principal Stress." In all the tests excepting the Hydrostatic Compression (HC) test, the three principal strains ε_i (i = 1,2,3) are plotted as a function of the octahedral shear stress, τ_{oct}. Thus, the plastic strains for each principal strain can be calculated very easily.

3.4 Test Series on the Octahedral Plane

This series consists of five tests, intended to explore the concrete response to triaxial load cycles and to provide data to locate yield surfaces on an octahedral plane from $\theta=-30^o$ to $\theta=30^o$, where θ = Lode angle. The testing program consisted of 2 TC, 1 SS and 2 TE, Fig. 2.16, tests with initial hydrostatic pressure of $\sigma_0 = J_1/3$ = 2.0, 3.0, 4.0, 4.5 and 5.0 ksi (13.79, 20.69, 27.58, 31.03 and 34.48 MPa). All specimens were first loaded in HC up to σ_0 and then subjected to deviatoric cyclic loading along TC, SS and TE paths with increasing octahedral shear stress, τ_{oct}, to ultimate conditions.

3.4.1 Triaxial Compression (TC)

Figures 3.17 to 3.22 show the stress-strain responses for two triaxial compression (TC) tests at confining pressures of 2.0 and 3.0 ksi (13.79 and 20.69 mpa), respectively. In the TC stress path, major principal stress σ_1 is increased while the minor principal

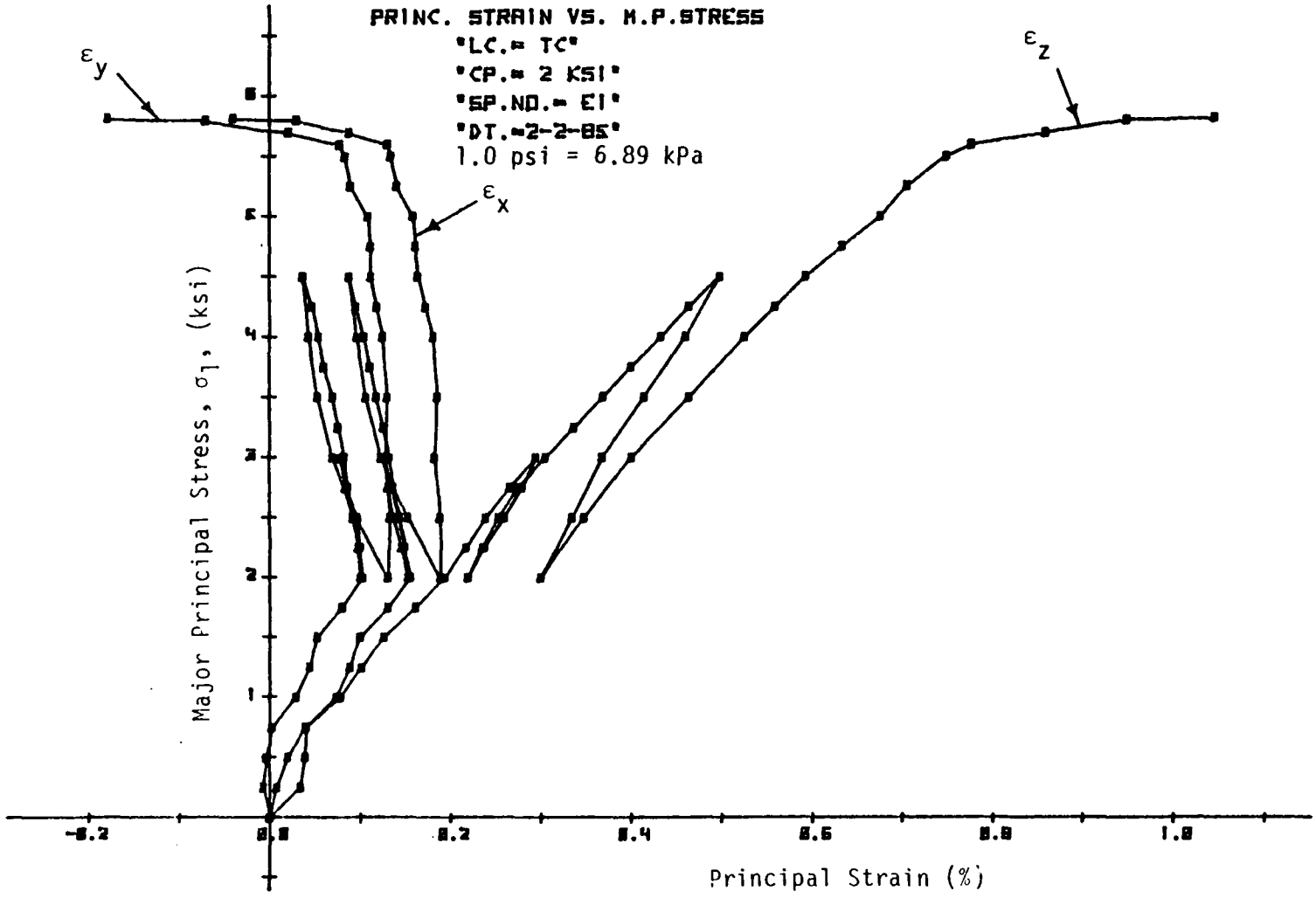

Figure 3.17. Stress-Strain Response Curves for Triaxial Compression Test.

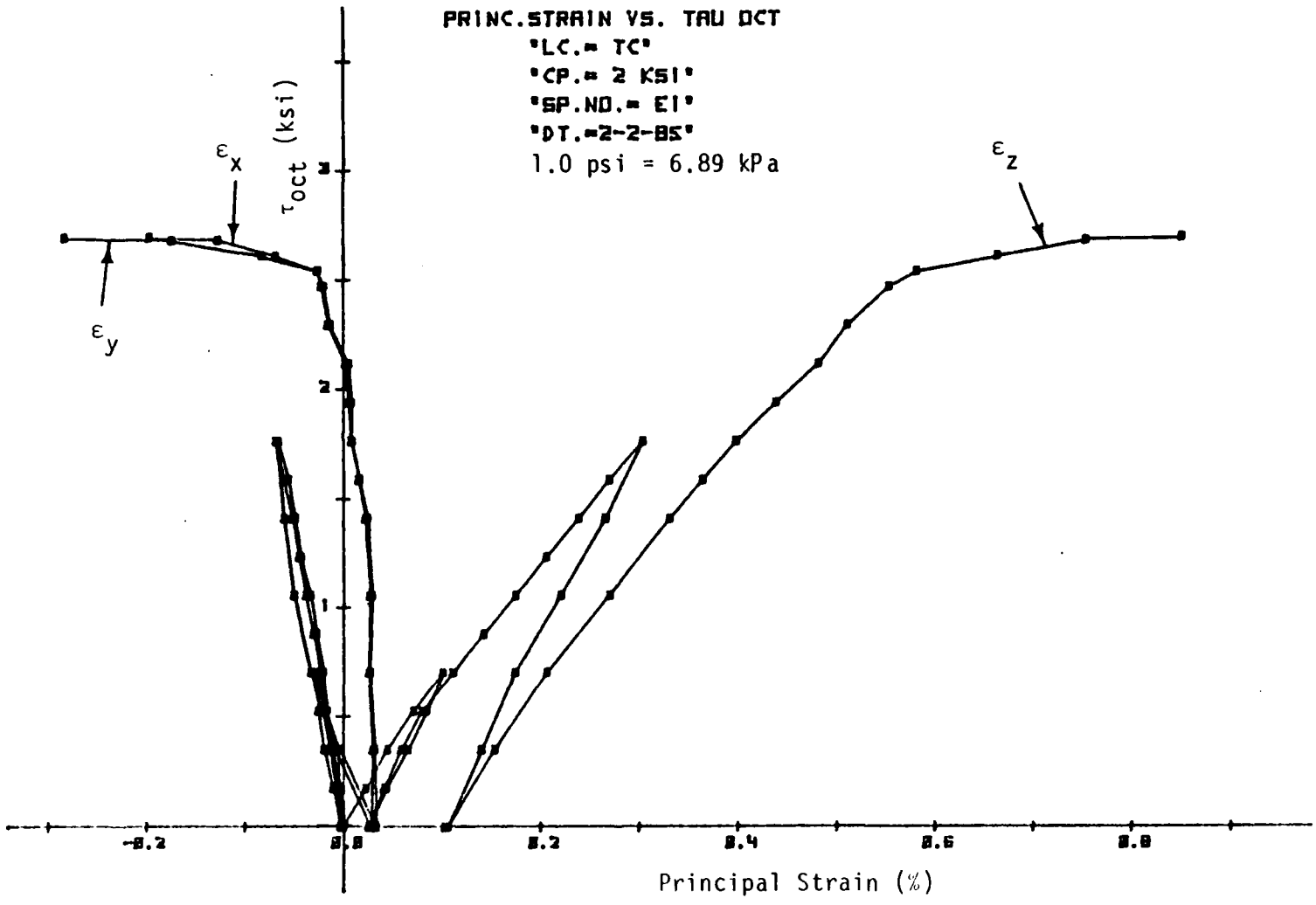

Figure 3.18. Stress-Strain Response Curves for Triaxial Compression Test.

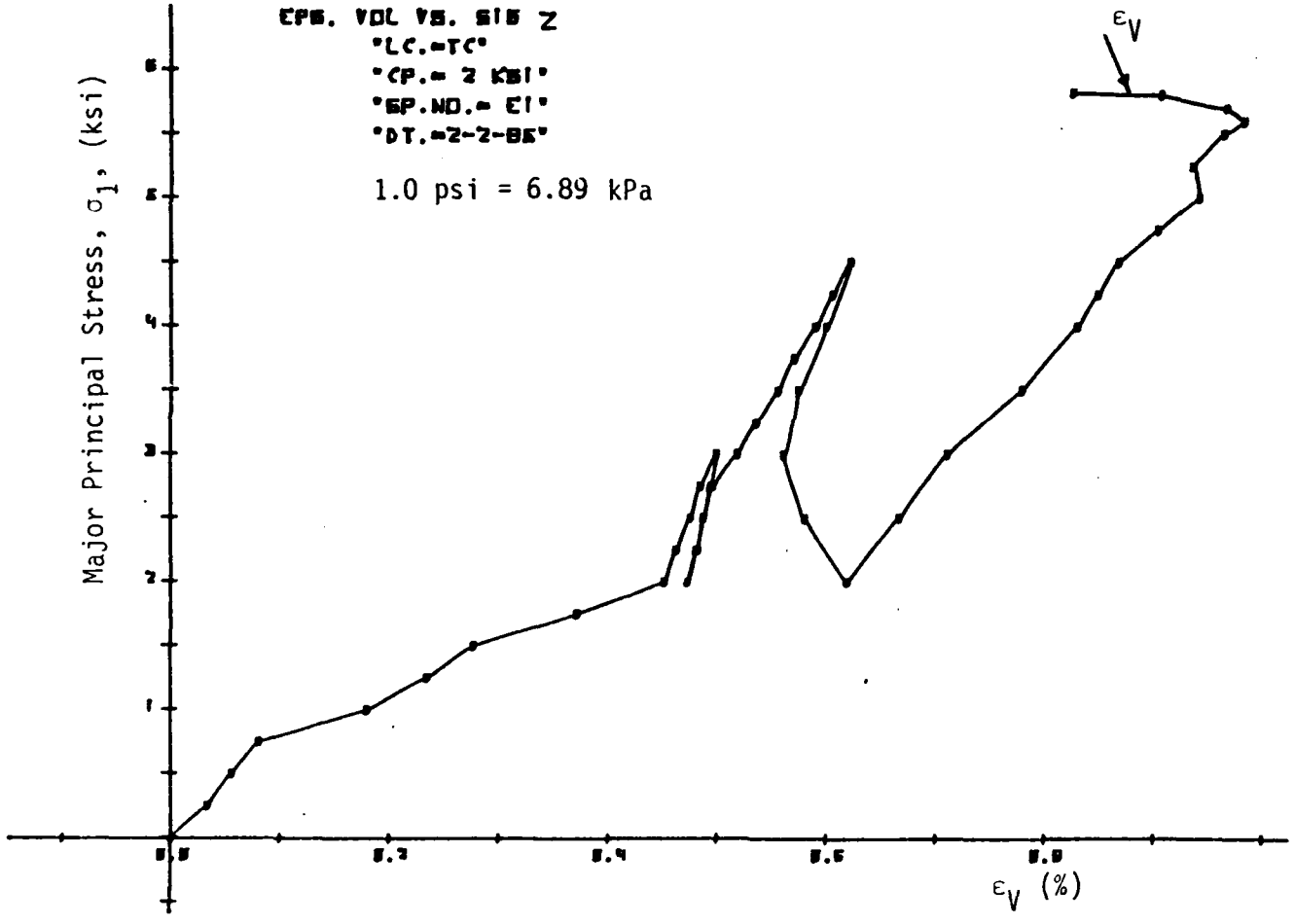

Figure 3.19. Stress-Volumetric Strain Response Curve for Triaxial Compression Test

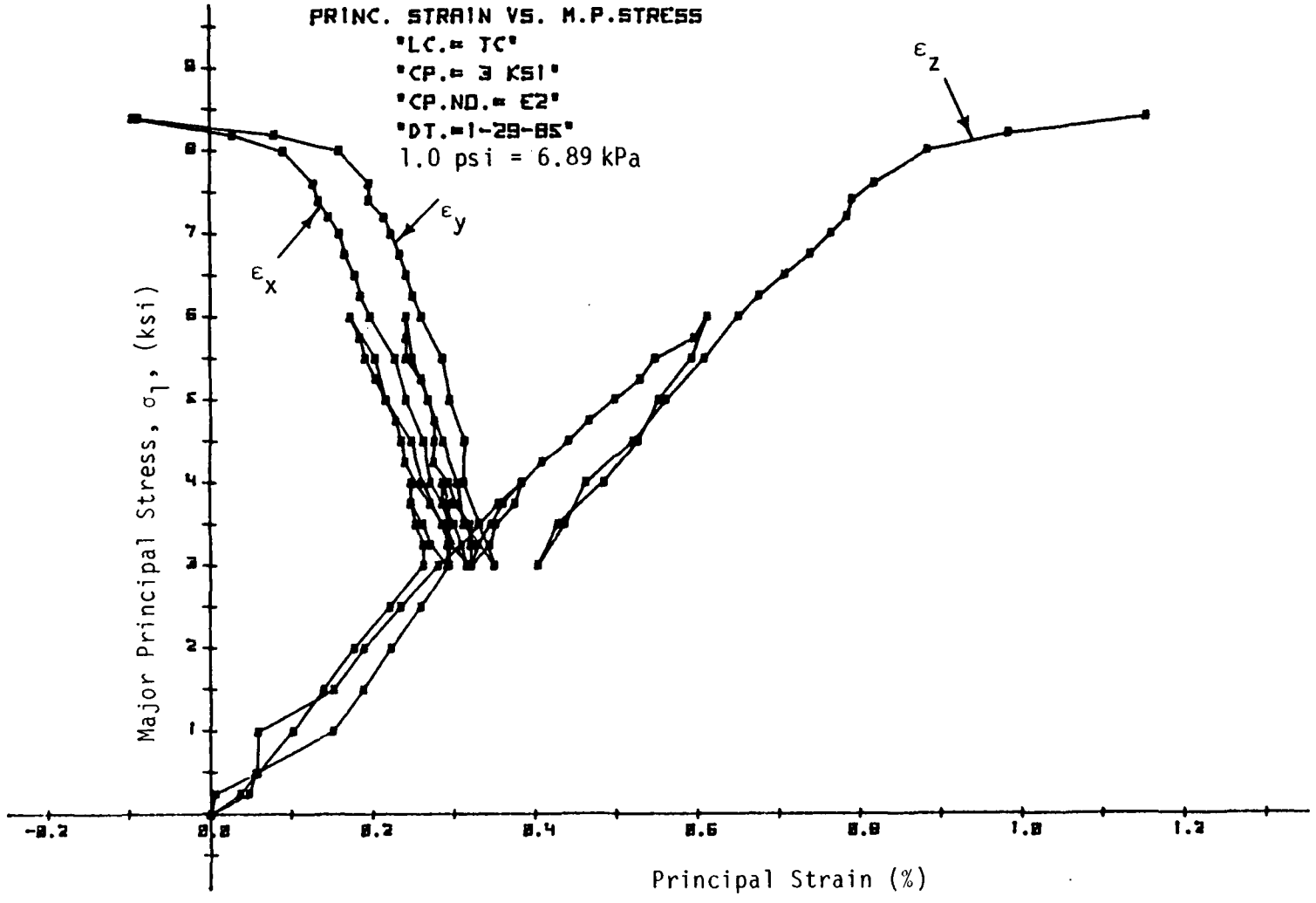

Figure 3.20. Stress-Strain Response Curves for Triaxial Compression Test.

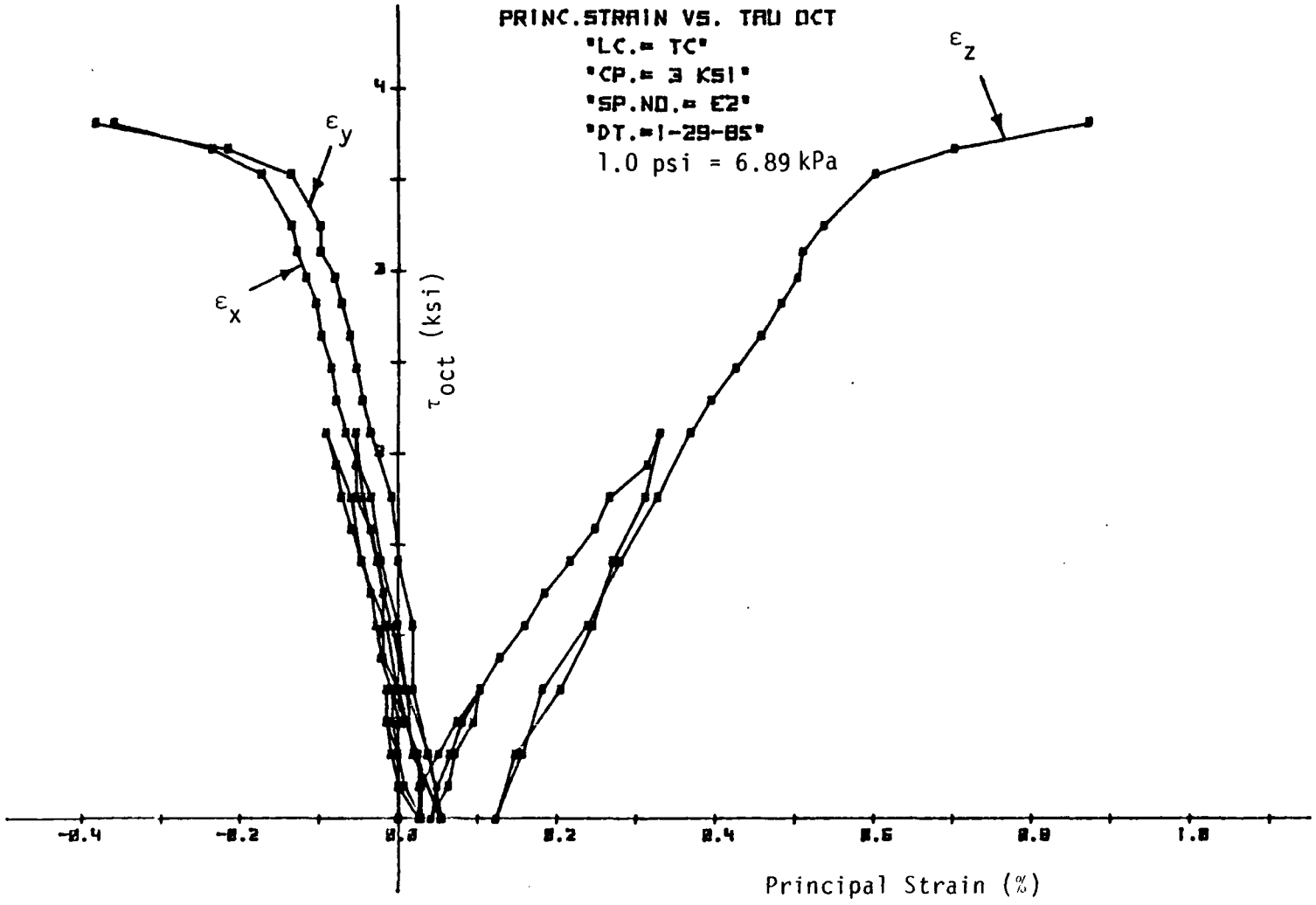

Figure 3.21. Stress-Strain Response Curves for Triaxial Compression Test.

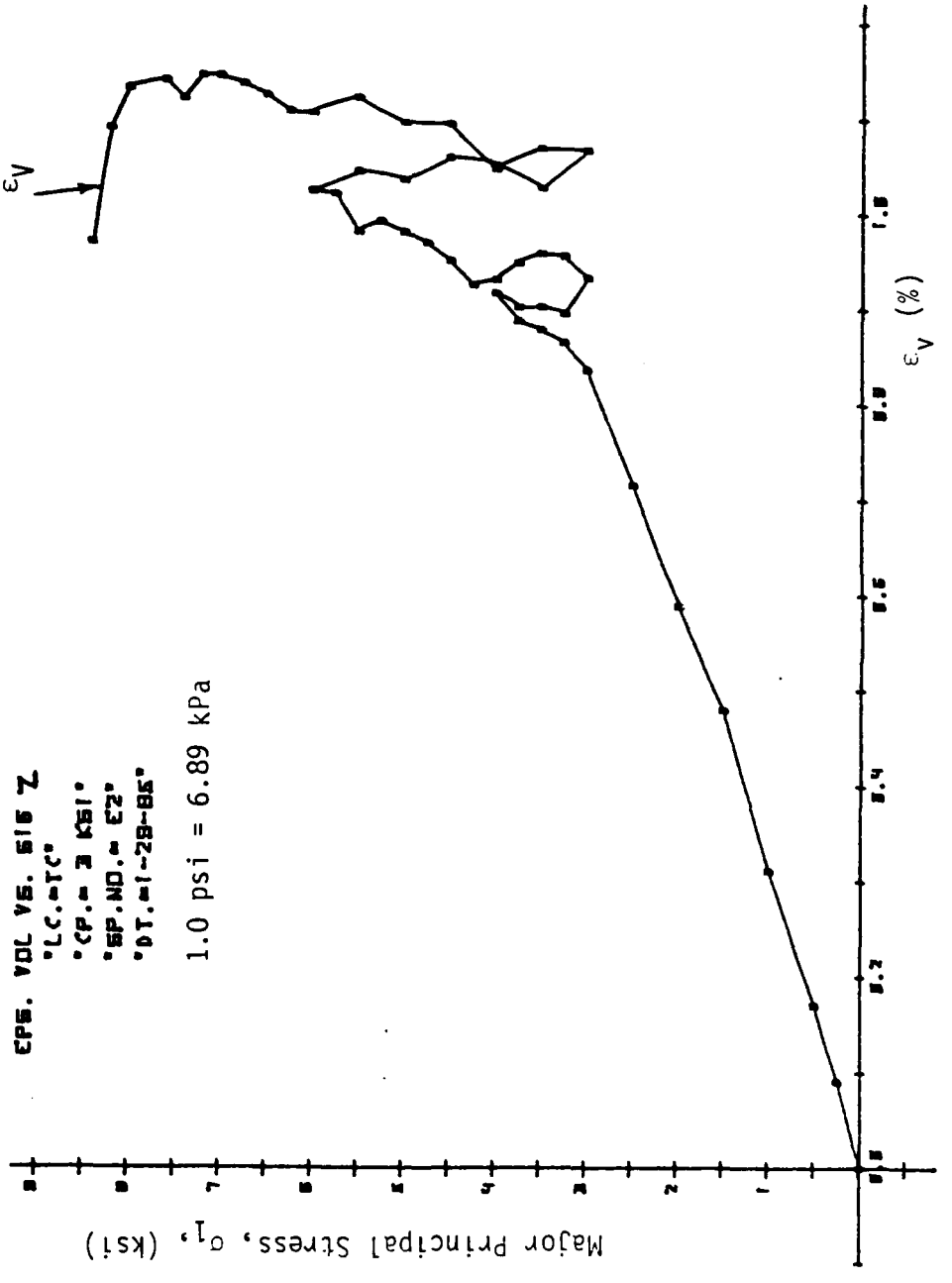

Figure 3.22. Stress-Volumetric Strain Response Curve for Triaxial Compression Test

stresses σ_2 and σ_3 are decreased. The increment of the major principal stress, $\Delta\sigma_1$ is double that of the decrement $\Delta\sigma_2 = \Delta\sigma_3$ of the minor principal stress. Thus σ_{oct} remains constant because $\Delta\sigma_1 = 2\Delta\sigma_2$. As with other stress paths in the octahedral plane, this separates the effects of hydrostatic and deviatoric stress components.

Since σ_2 and σ_3 are equal, ε_2 and ε_3 should also be equal for isotropic behavior. One can see the good agreement between these strains (ε_x and ε_y in this case) from Figs. 3.17 to 3.22. During TC, the volumetric behavior is compressive and nearly linear just prior to dilation, then becomes expansive. This phenomenon occurring under shear distortion at constant confining pressure is usually observed for concrete behavior. Gerstle et al [34] observed similar behavior to occur for plain concrete. The deviatoric stress-strain behavior is stiffer for low confining pressure (σ_o) than it is for high.

3.4.2 Simple Shear (SS)

The state of stress of a specimen under simple shear refers to an octahedral plane normal to the space diagonal at a given hydrostatic stress level, $\sigma_{oct} = 1/3\ (\sigma_1+\sigma_2+\sigma_3)$. Intermediate principal stress, σ_2 is kept constant, but the major and minor principal stress, σ_1 and σ_3 are increased and decreased respectively by the same amount so that σ_{oct} remains constant. Figs. 3.23 to 3.25 show the stress-strain responses for Simple Shear (SS) test at confining pressure 4.5 ksi (31.03 MPa).

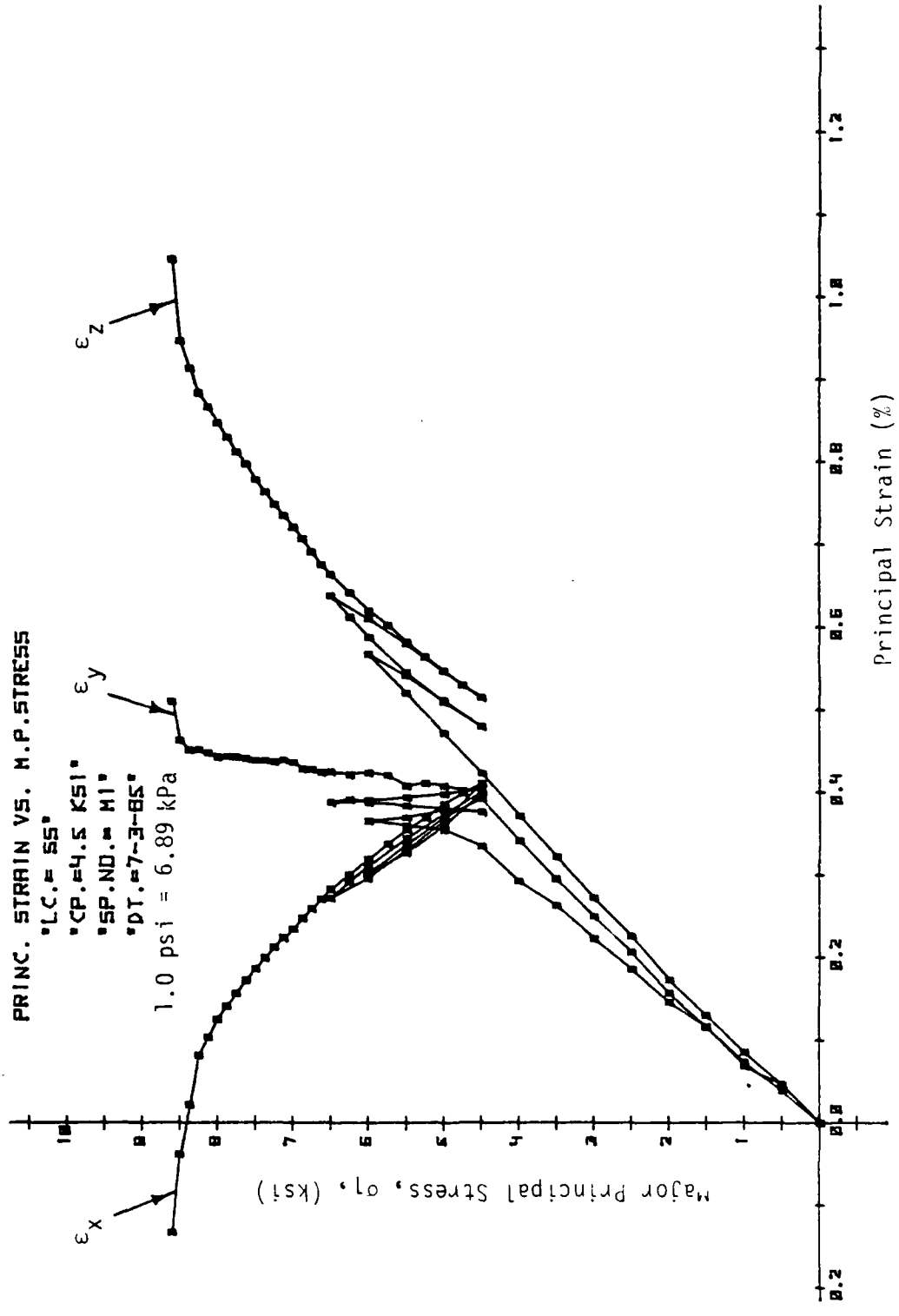

Figure 3.23. Stress-Strain Response Curves for Simple Shear Test.

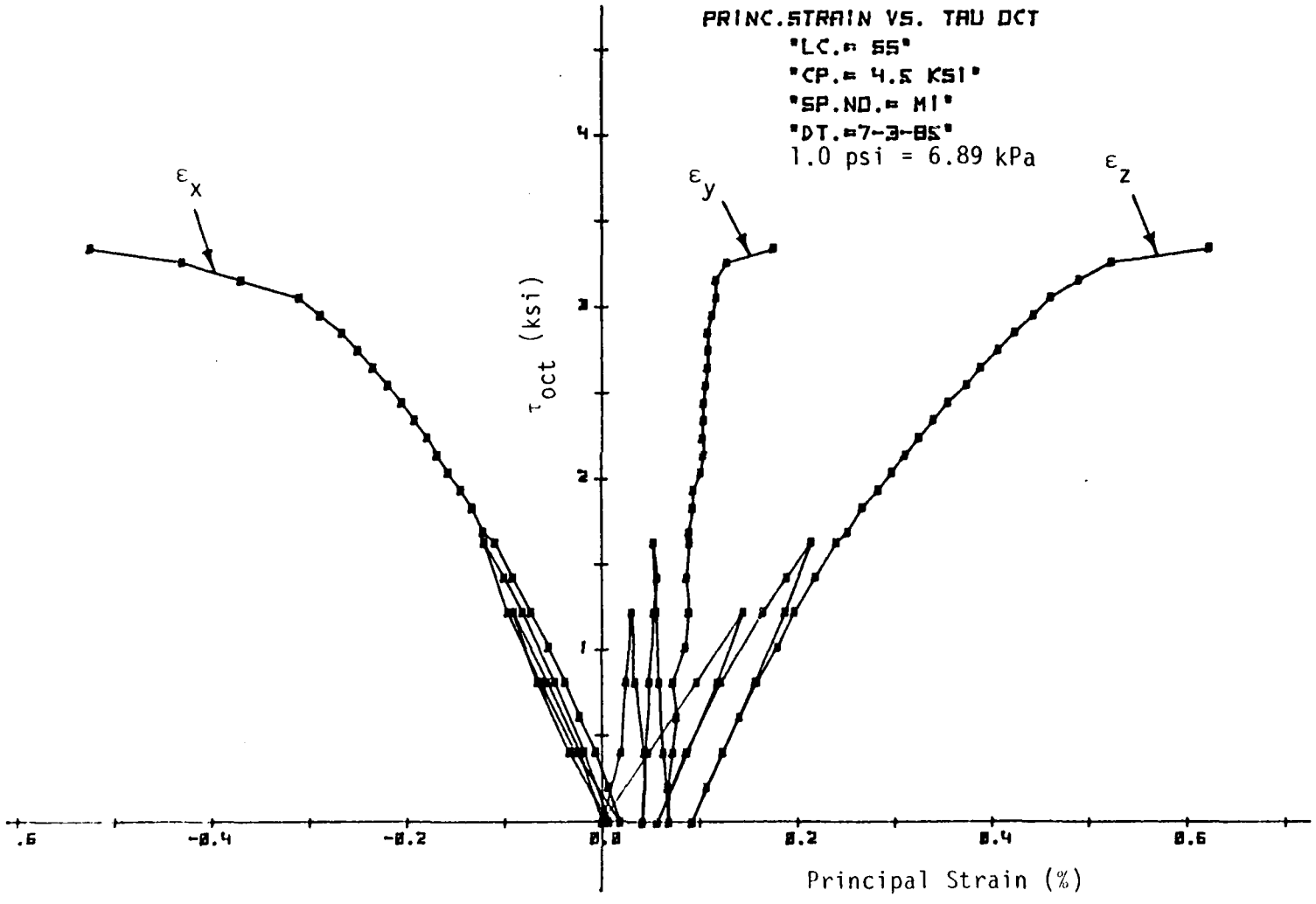

Figure 3.24. Stress-Strain Response Curves for Simple Shear Test.

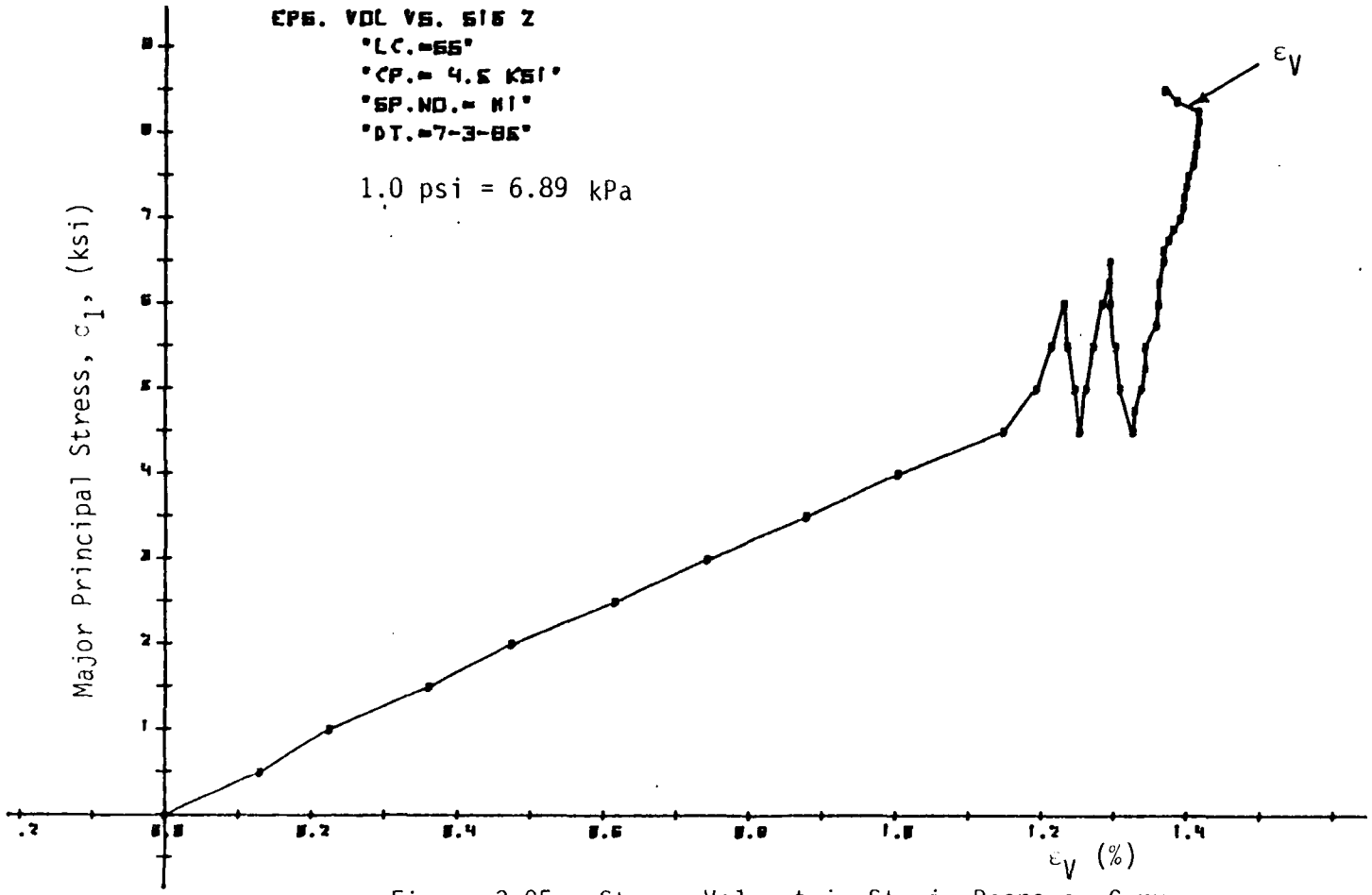

Figure 3.25. Stress-Volumetric Strain Response Curve for Simple Shear Test

It is significant to note that the intermediate strain is slightly compressive, Figs. 2.23 to 2.24.

3.4.3 Triaxial Extension (TE)

Figures 3.26 to 3.31 show the stress-strain responses for two Triaxial Extension (TE) tests at confining pressures of 4.0 and 5.0 ksi (27.58 and 34.48 MPa , respectively. In the TE stress path, σ_1 and σ_2 are increased equally while σ_3 is decreased to maintain σ_0 at a constant level. Since σ_1 and σ_2 are equal, ε_1 and ε_2 should also be equal for isotropic material. As in TC results for ε_2 and ε_3, one can see good agreement between ε_1 and ε_2 (ε_x and ε_y in this case) for TE tests from the individual results, the difference stemming from the HC portion. As in the other tests (TC and SS), the volumetric behavior is compressive and nearly linear up to the point of dilation. But immediately after dilation of the specimen, rapid expansion in the volumetric behavior takes place, as if the specimen were splitting in half and coming apart.

In all the tests, the three principal strains [illegible] and ε_v are plotted against the major principal stress, [illegible] octahedral shear stress, τ_{oct}.

3.5 Octahedral Stress-Strain Relations

The octahedral normal and shear stress τ_{oct} and [illegible]

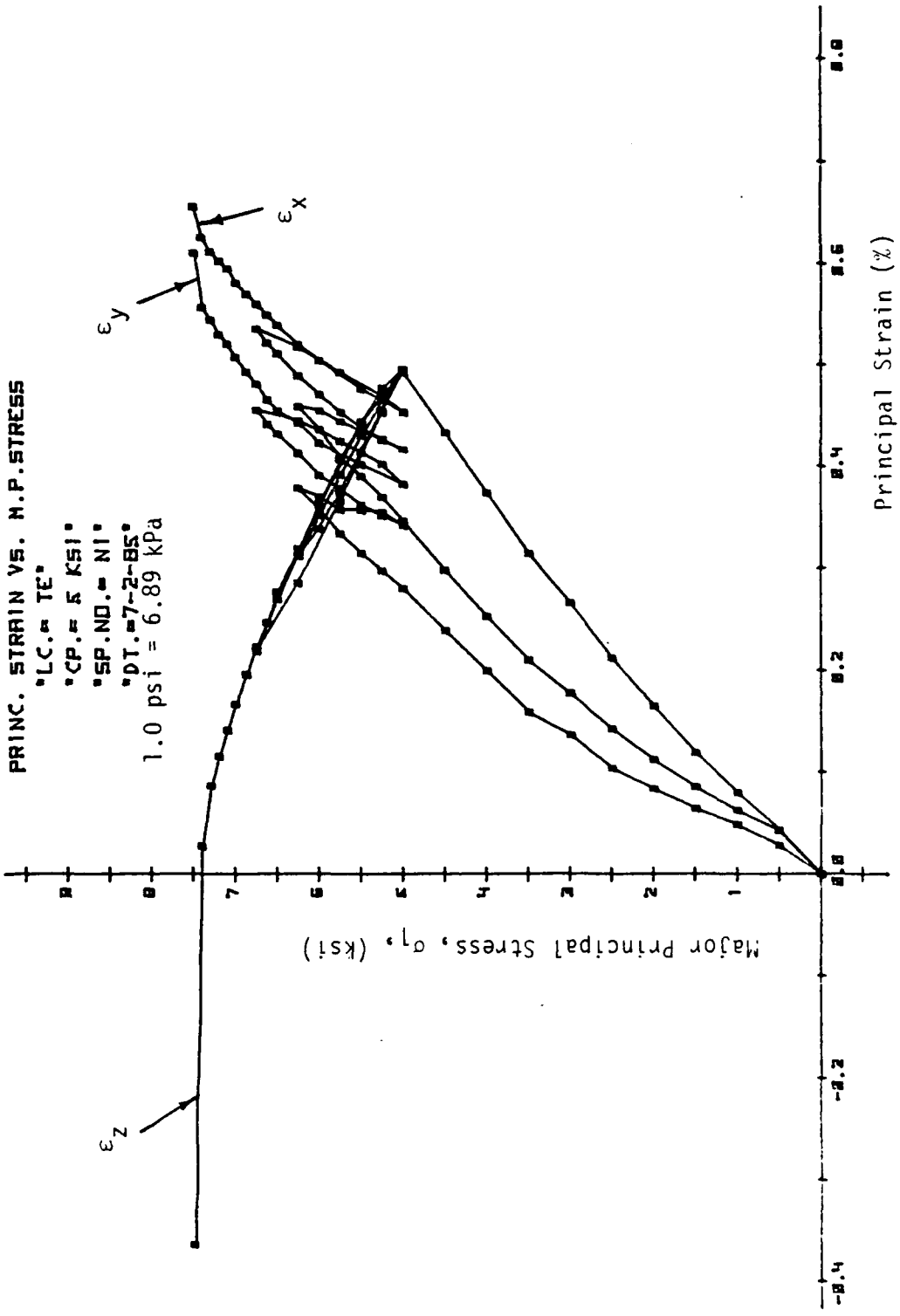

Figure 3.26. Stress-Strain Response Curves for Triaxial Extension Test.

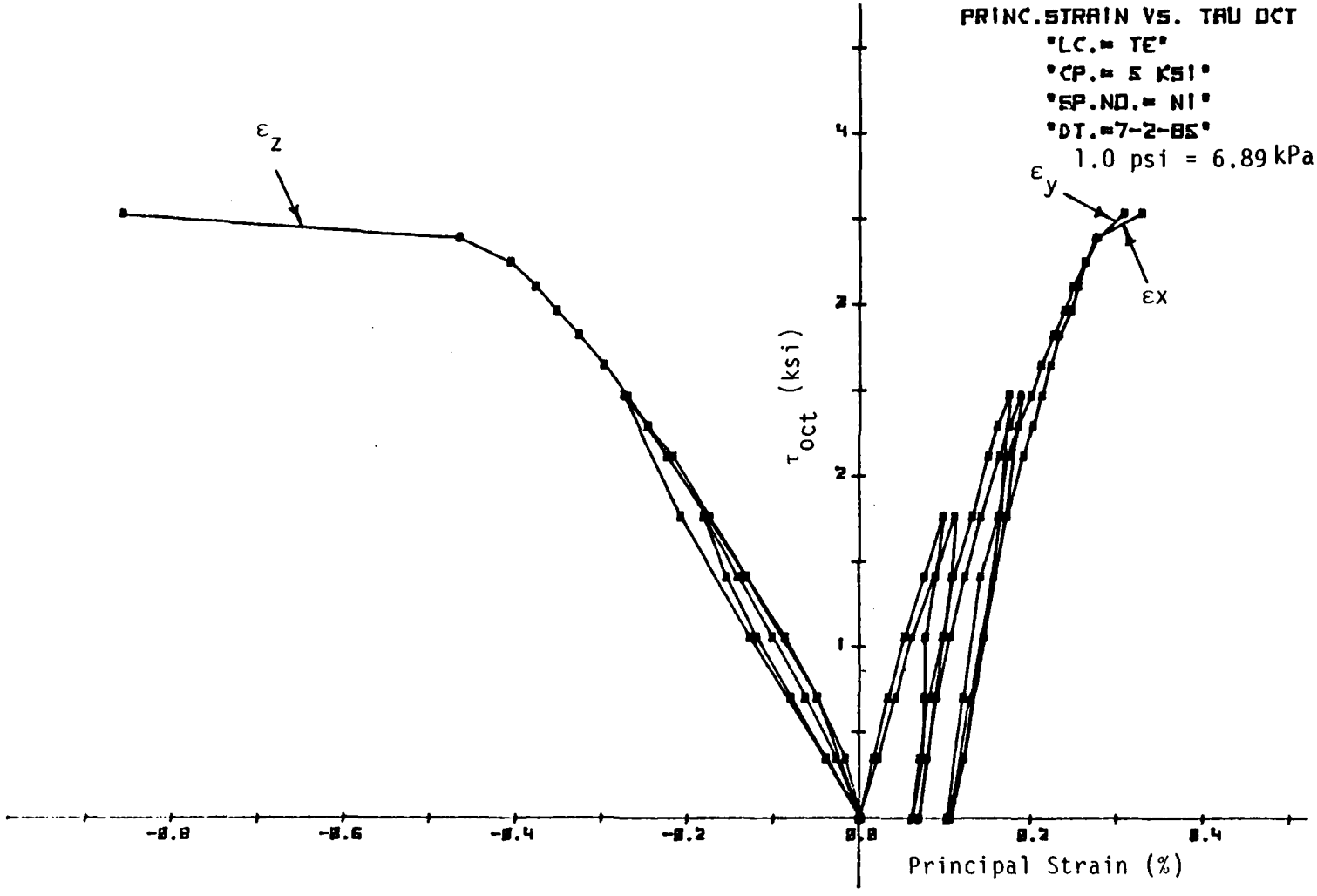

Figure 3.27. Stress-Strain Response Curves for Triaxial Extension Test.

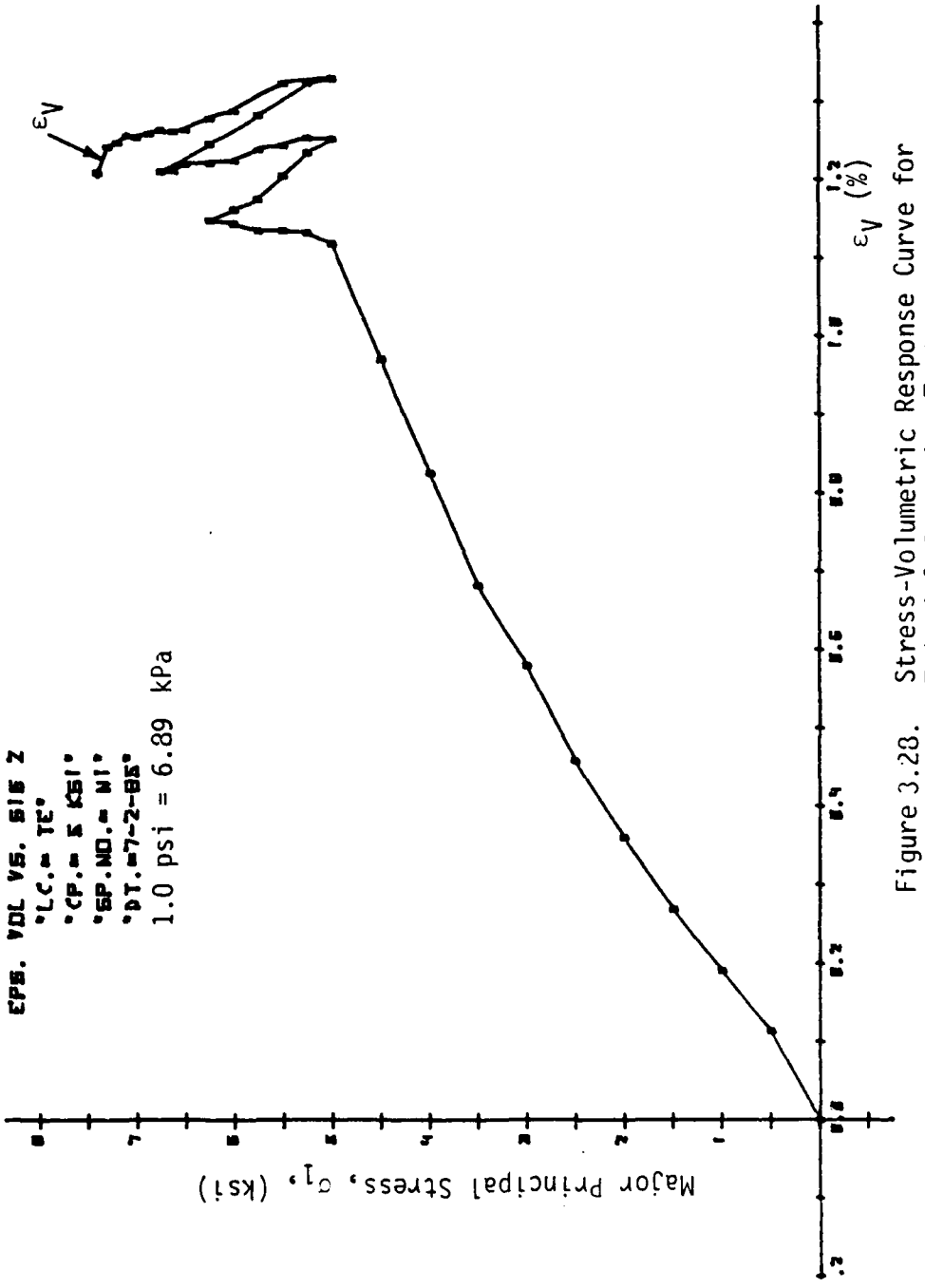

Figure 3.28. Stress-Volumetric Response Curve for Triaxial Extension Test

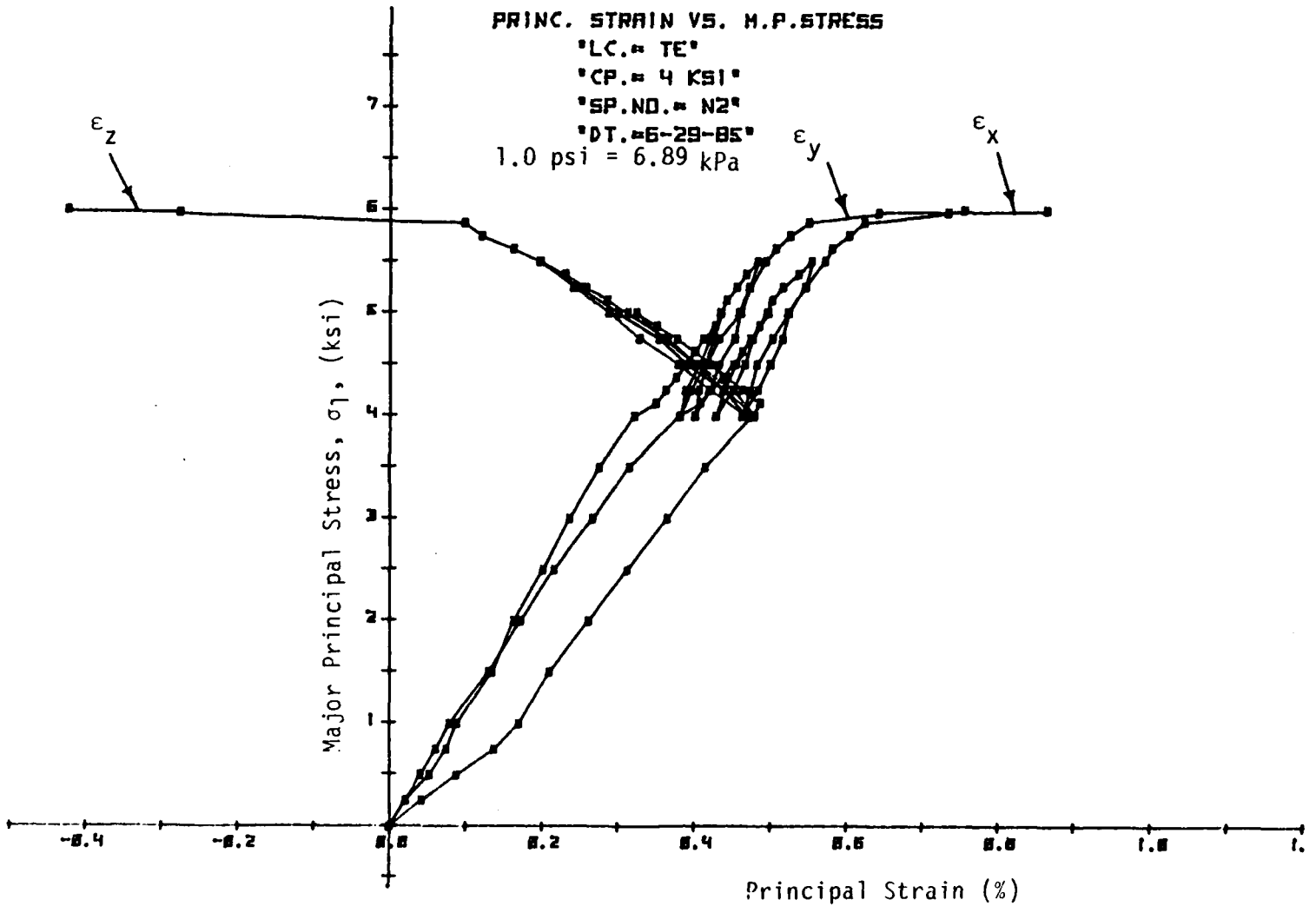

Figure 3.29. Stress-Strain Response Curves for Triaxial Extension Test.

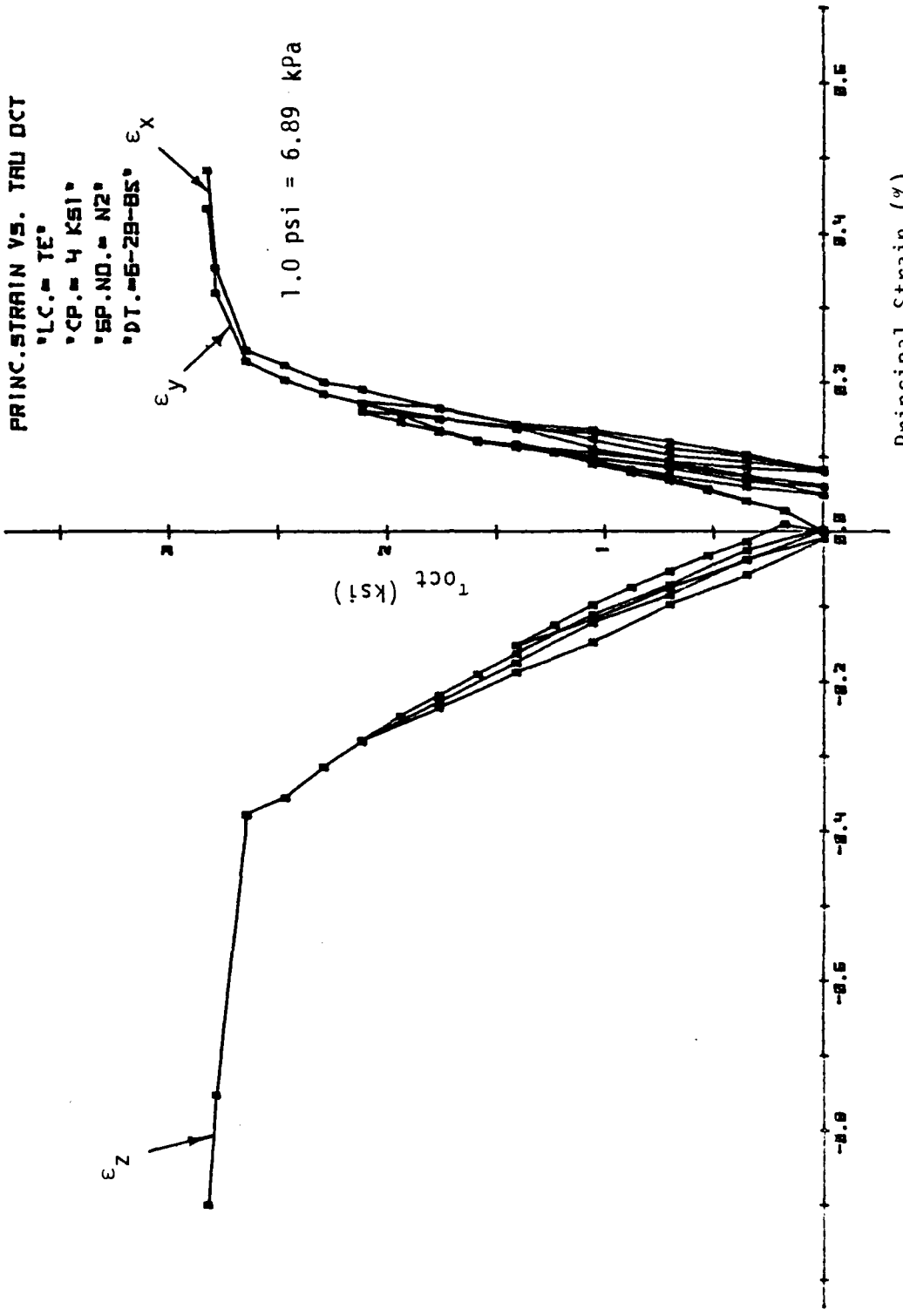

Figure 3.30. Stress-Strain Response Curves for Triaxial Extension Test.

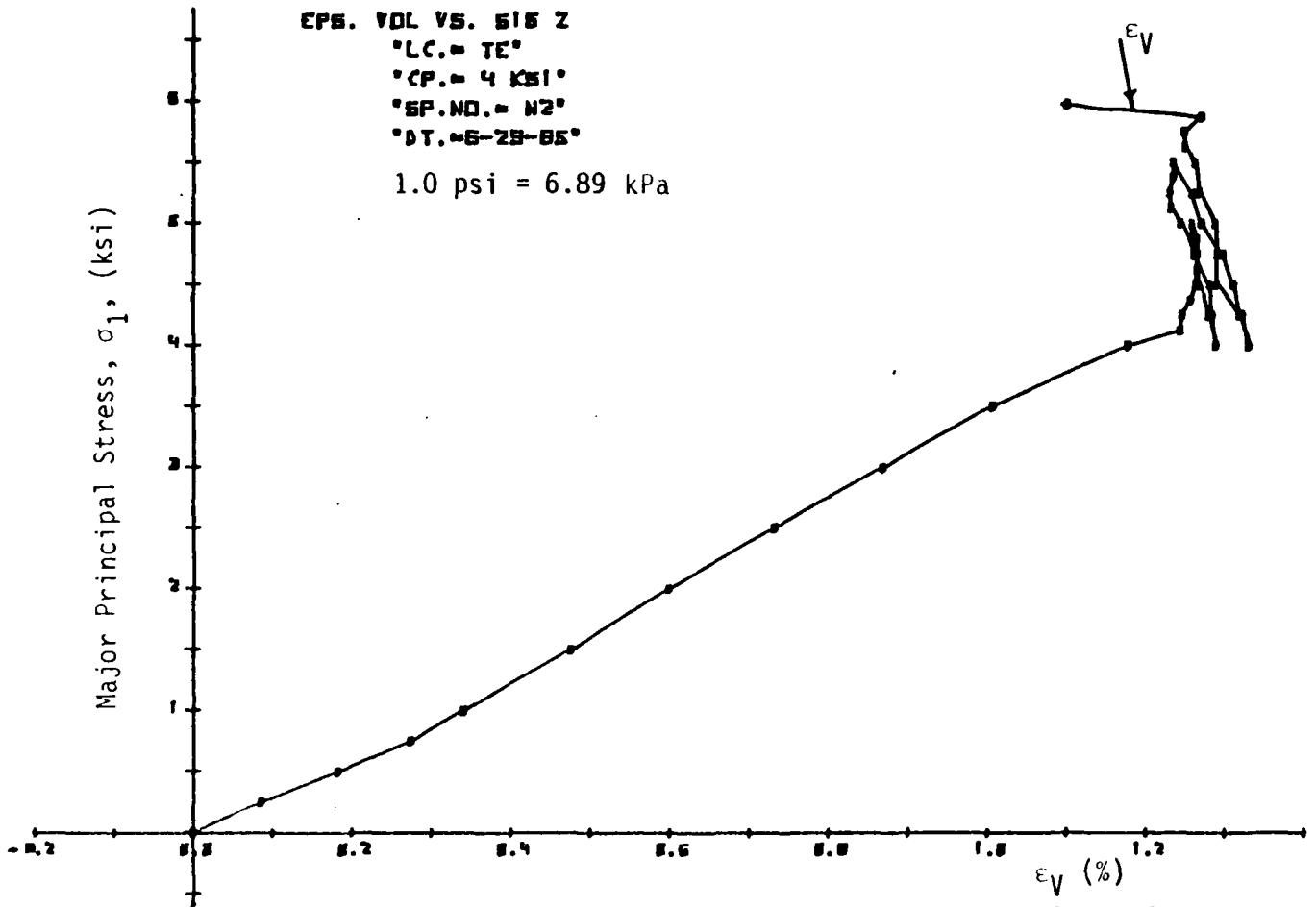

Figure 3.31. Stress-Volumetric Strain Response Curve for Triaxial Extension Test

the octahedral normal and shear strains ε_{oct} and γ_{oct} are represented in terms of principal stresses and strains by the following relations:

$$\sigma_{oct} = 1/3\ (\sigma_1 + \sigma_2 + \sigma_3) \tag{3.1a}$$

$$\tau_{oct} = 1/3\ \sqrt{(\sigma_1 - \sigma_2)^2 + (\sigma_2 - \sigma_3)^2 + (\sigma_3 - \sigma_1)^2} \tag{3.1b}$$

$$\varepsilon_{oct} = 1/3\ (\varepsilon_1 + \varepsilon_2 + \varepsilon_3) \tag{3.1c}$$

$$\gamma_{oct} = 1/3\ \sqrt{(\varepsilon_1 - \varepsilon_2)^2 + (\varepsilon_2 - \varepsilon_3)^2 + (\varepsilon_3 - \varepsilon_1)^2} \tag{3.1d}$$

The octahedral stress-strain curves obtained from CTC, RET, TC, SS and TE tests are plotted individually in Figs. 3.32 to 3.41, respectively. The (unloading) slope of the τ_{oct} - γ_{oct} curve is two times the shear modulus, G, and is determined from these tests to be 440.36 ksi (3036.28 MPa).

3.6 Proportional Loading (PL)

The proportional loading tests are conducted such that the ratio of $R = \frac{\sigma_2}{\sigma_1} = \frac{\sigma_3}{\sigma_1}$ remains the same during the change in loading. Two different load ratios, R, were followed (R=1/3 and R=2/3). The deformational response of the specimen under proportional loading was monitored at intervals of 250.0 psi (1723.75 kPa). Figs. 3.42 and 3.43 show the stress-strain responses for the two proportional loading (R=1/3 and R=2/3) tests, respectively. Since σ_2 and σ_3 are equal, ε_2 and ε_3 should also be equal for isotropic behavior. One can see the good agreement between these strains from the individual results. None of the PL tests reached

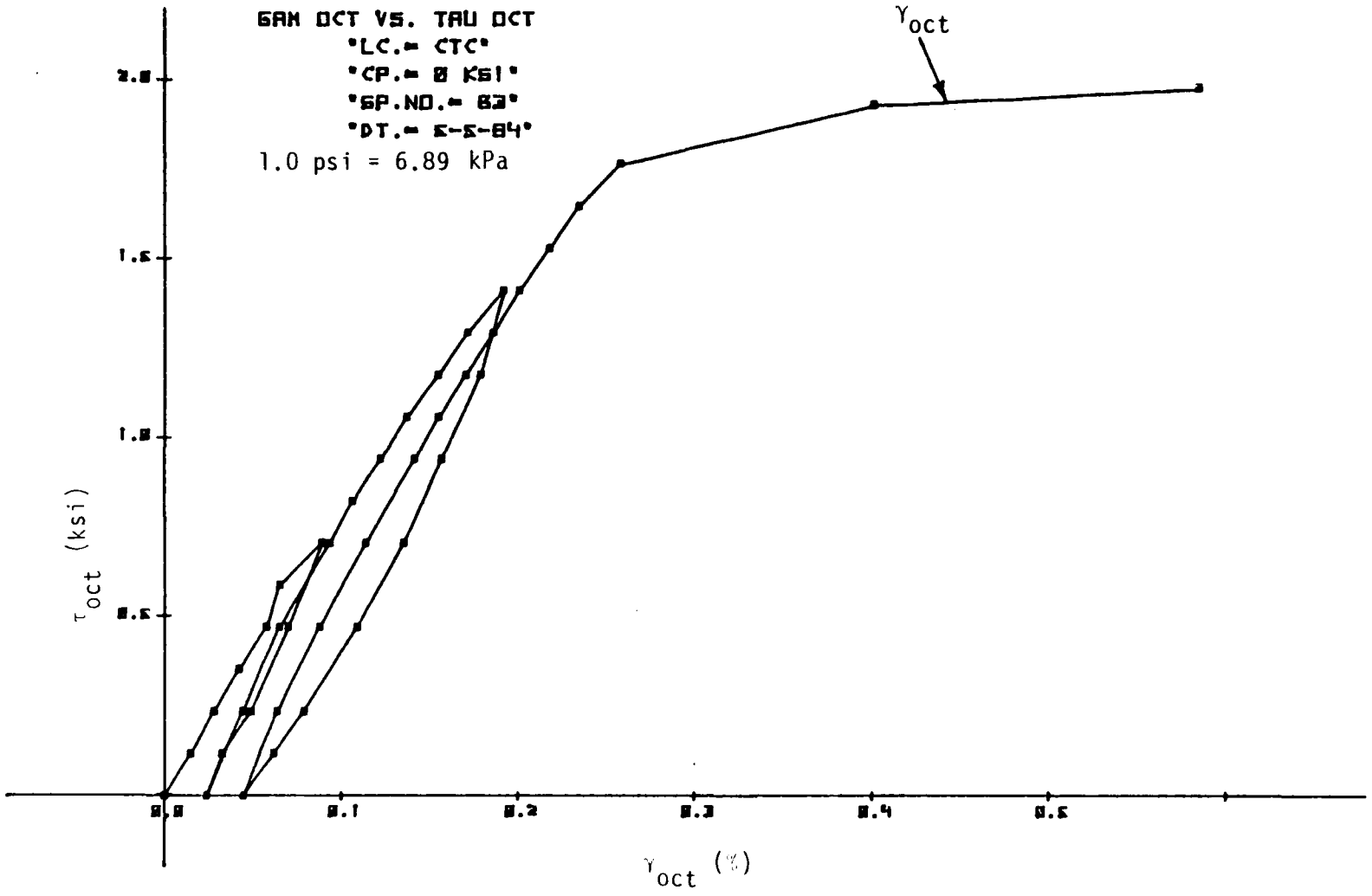

Figure 3.32. Octahedral Stress-Strain Response Curve for Conventional Triaxial Compression Test.

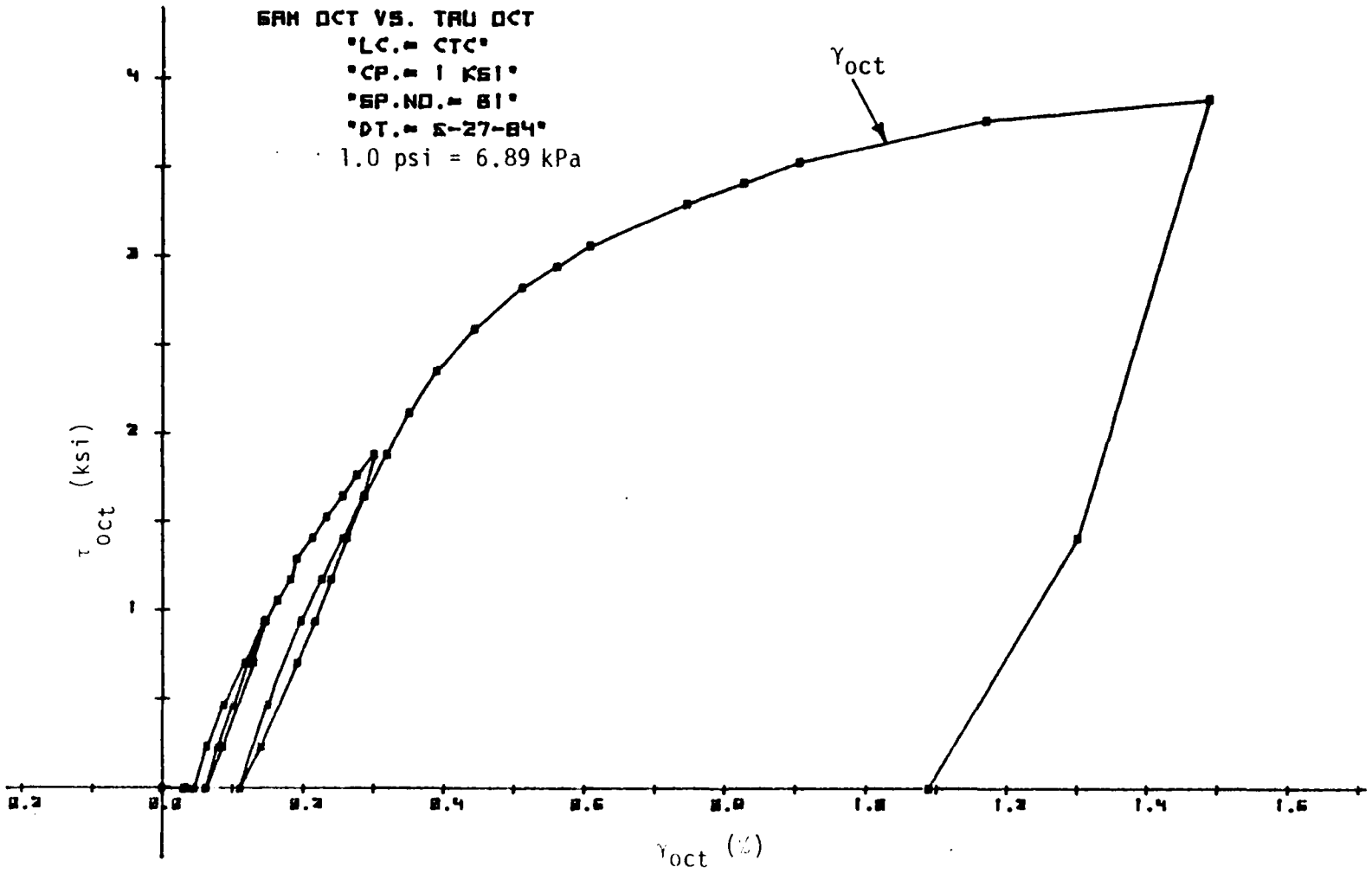

Figure 3.33. Octahedral Stress-Strain Response Curve for Conventional Triaxial Compression Test.

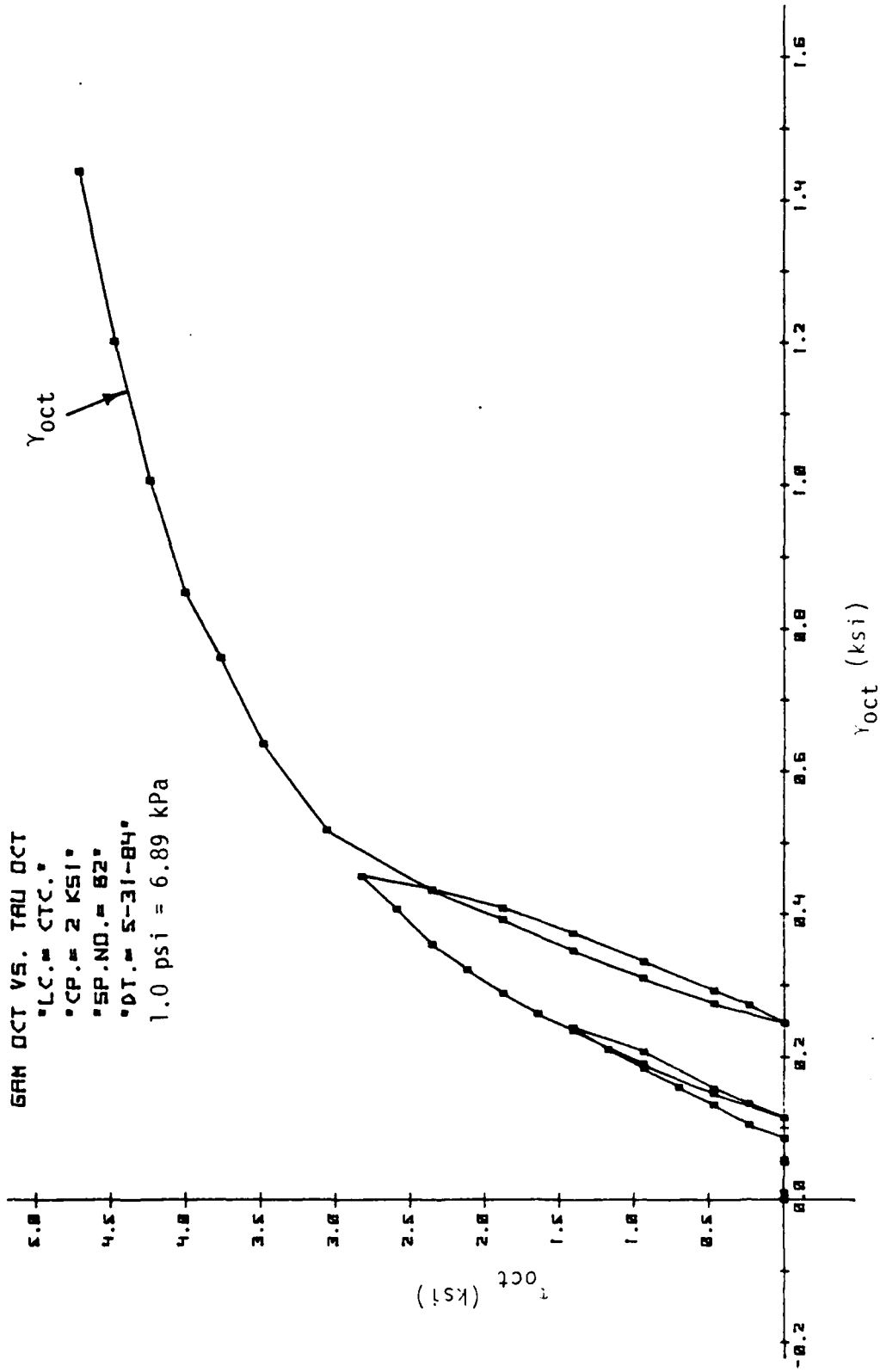

Figure 3.34. Octahedral Stress-Strain Response Curve for Conventional Triaxial Compression Test.

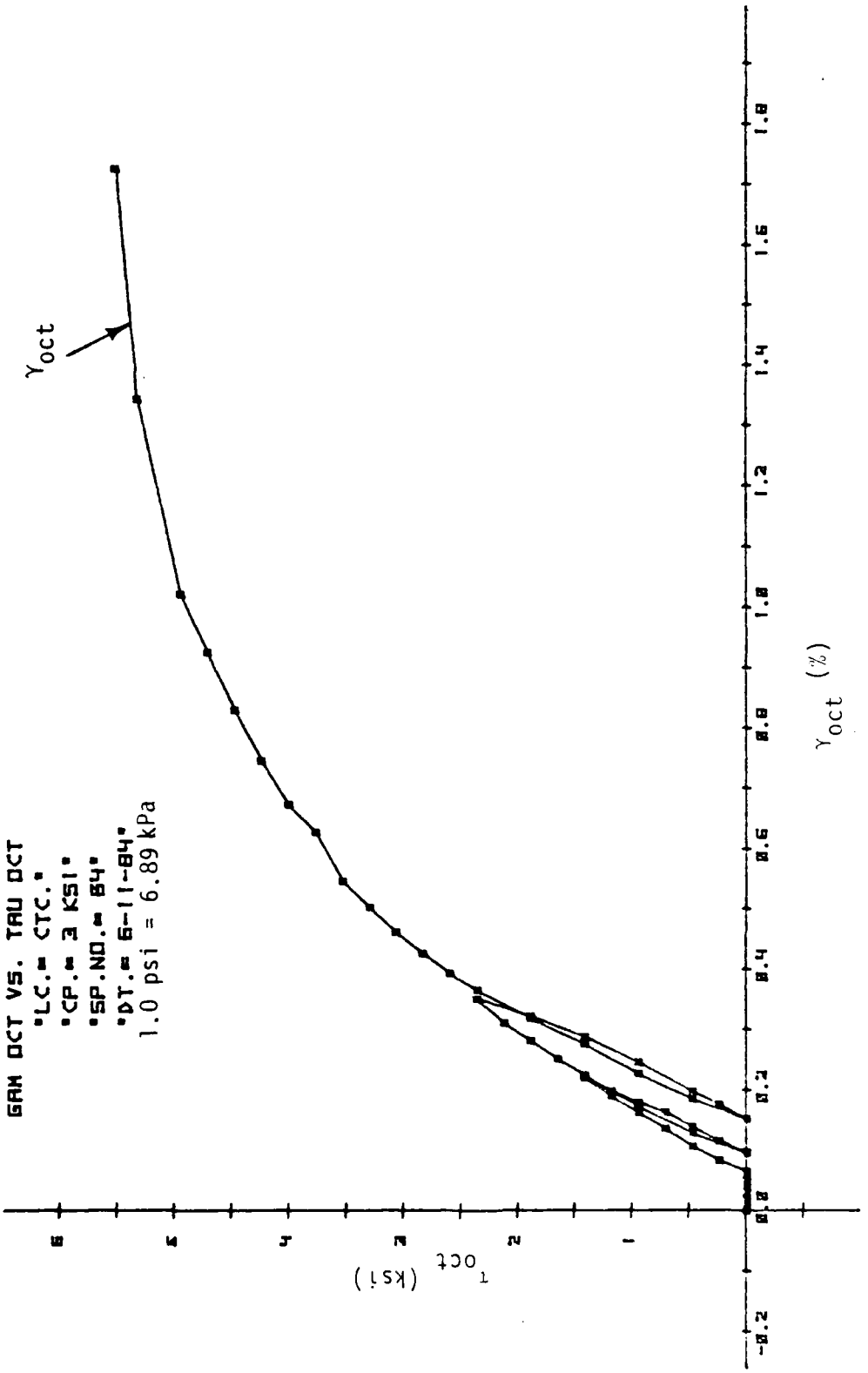

Figure 3.35. Octahedral Stress-Strain Response Curve for Conventional Triaxial Test.

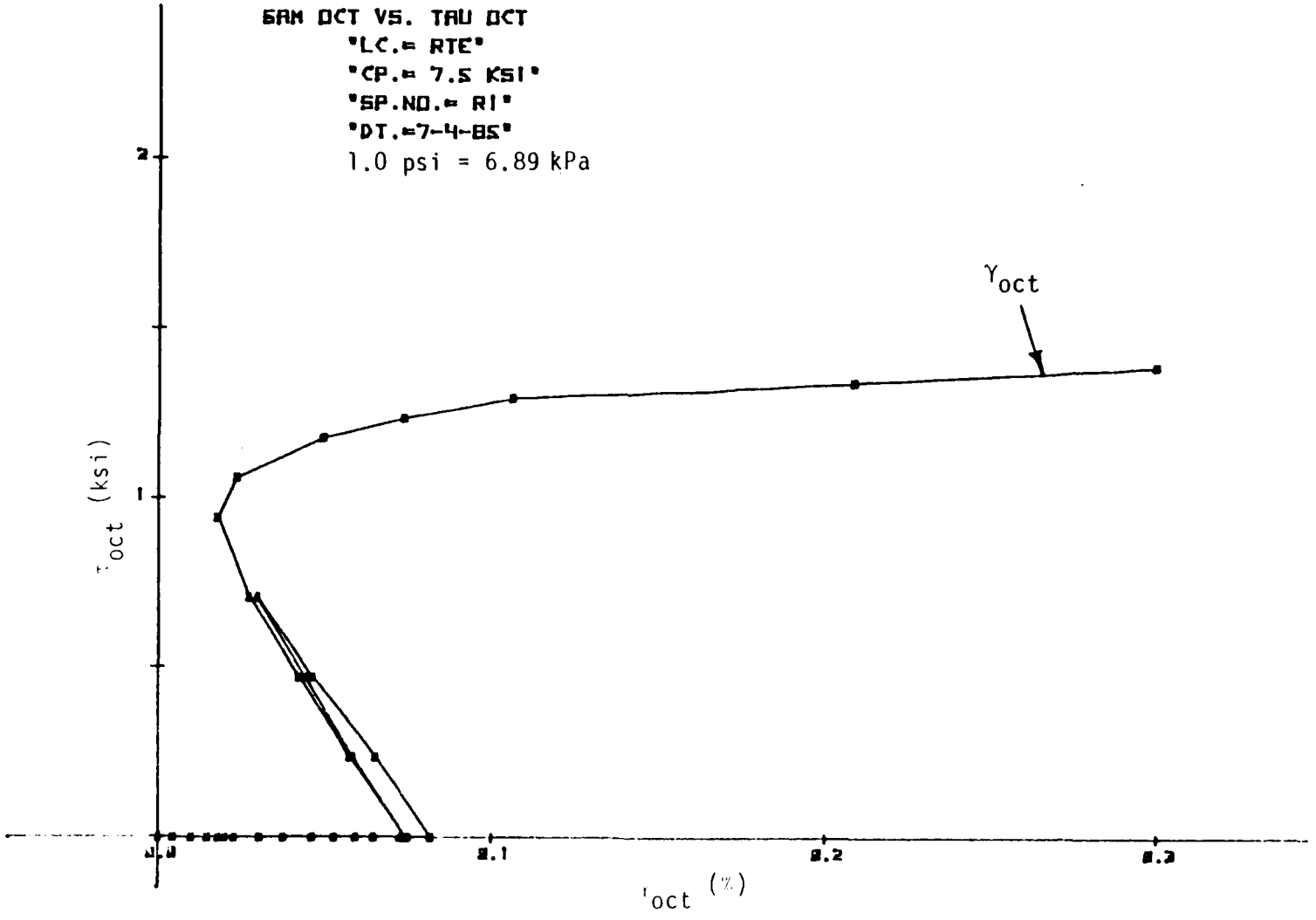

Figure 3.36. Octahedral Stress-Strain Response for Reduced Triaxial Compression Test.

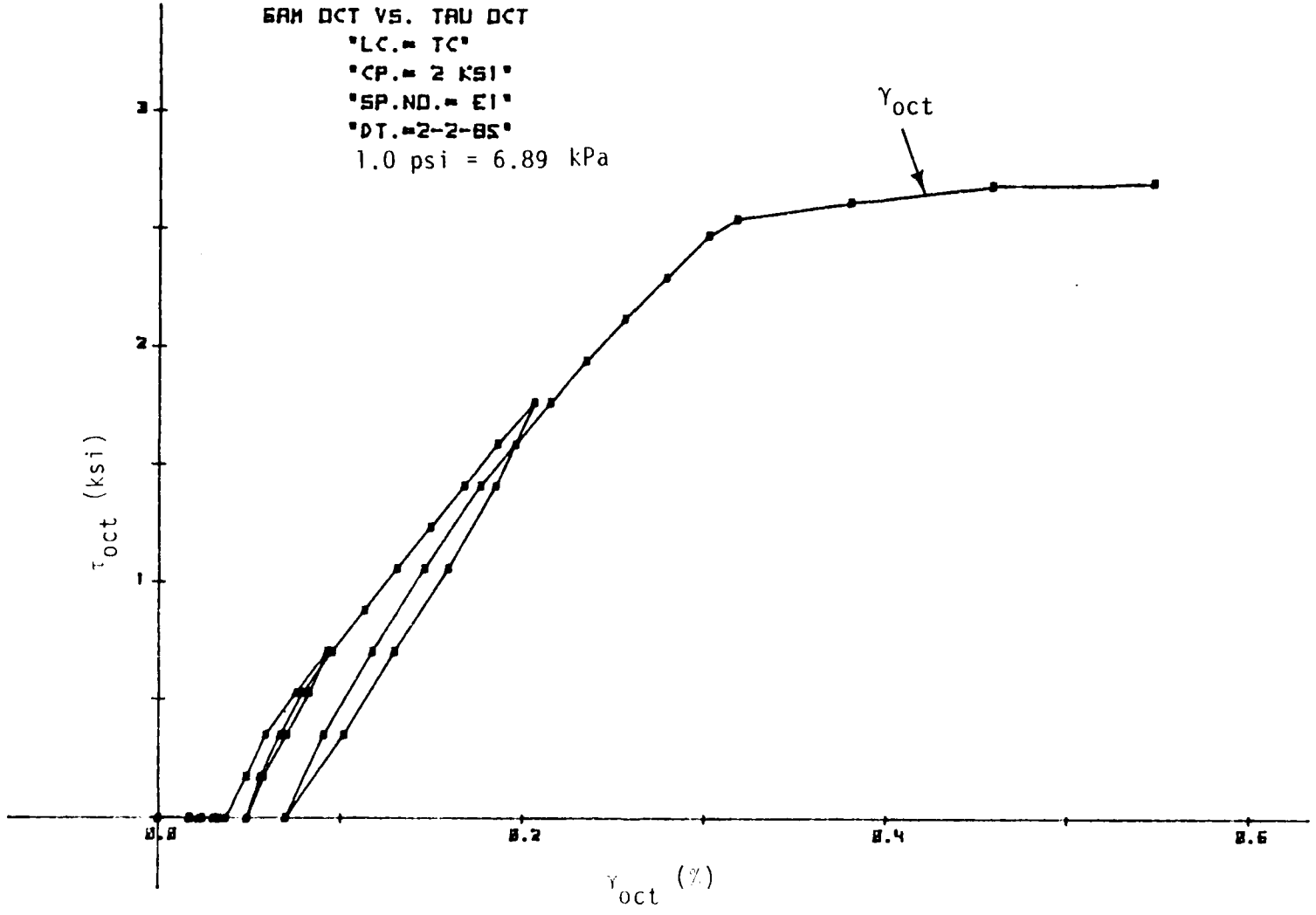

Figure 3.37. Octahedral Stress-Strain Response Curve for Triaxial Compression Test.

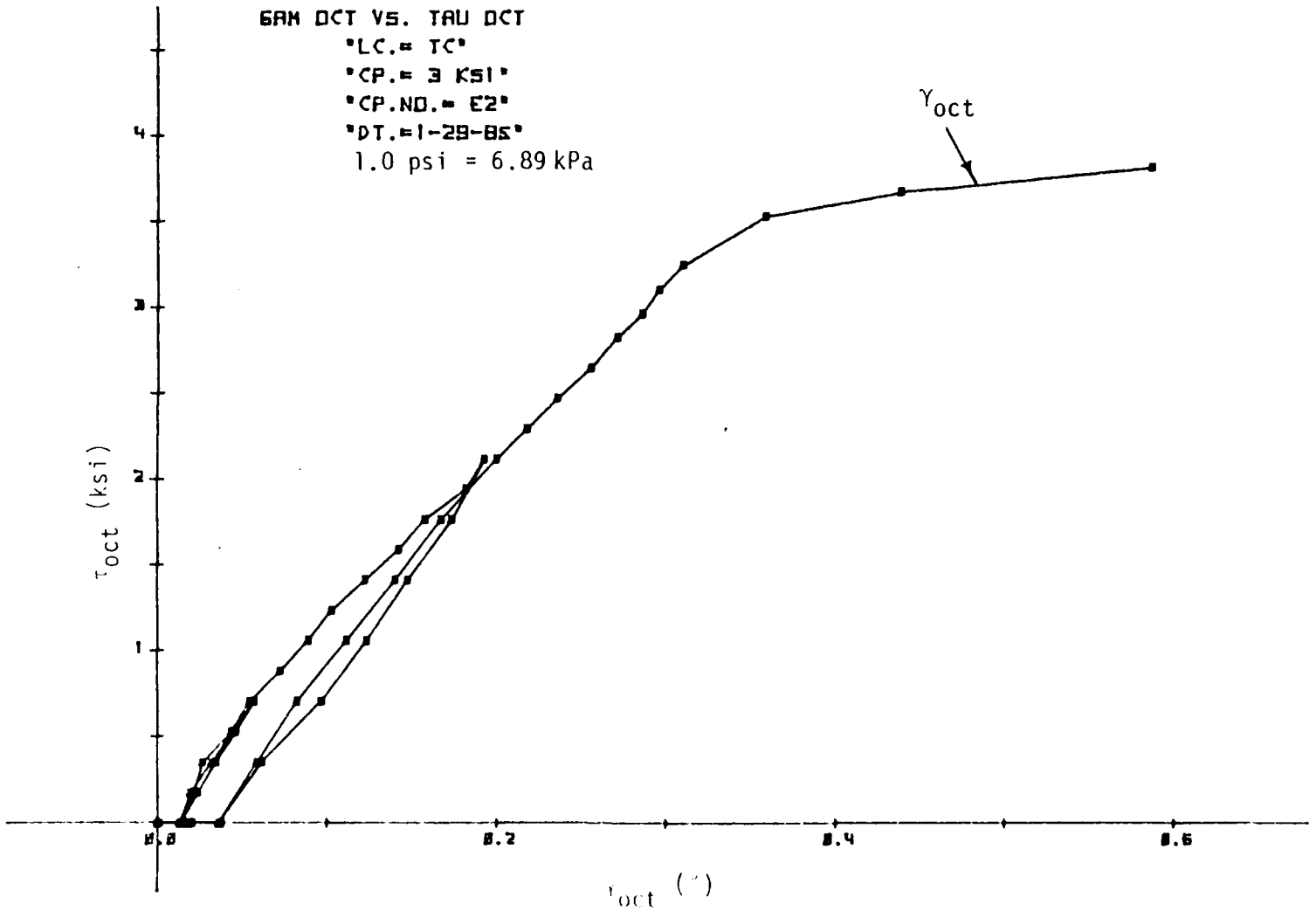

Figure 3.38. Octahedral Stress-Strain Response Curve for Triaxial Compression Test.

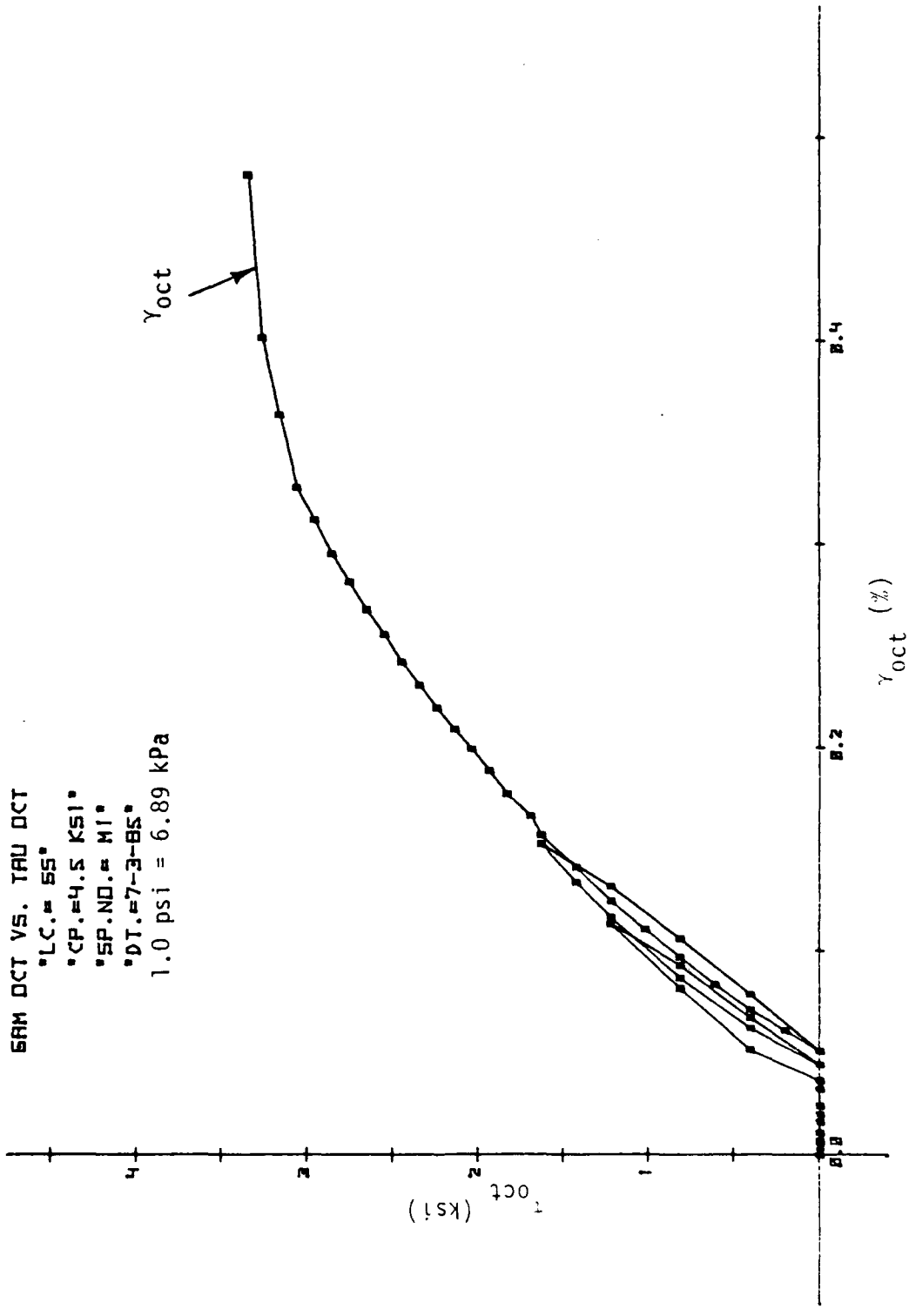

Figure 3.39. Octahedral Stress-Strain Response Curve for Simple Shear Test.

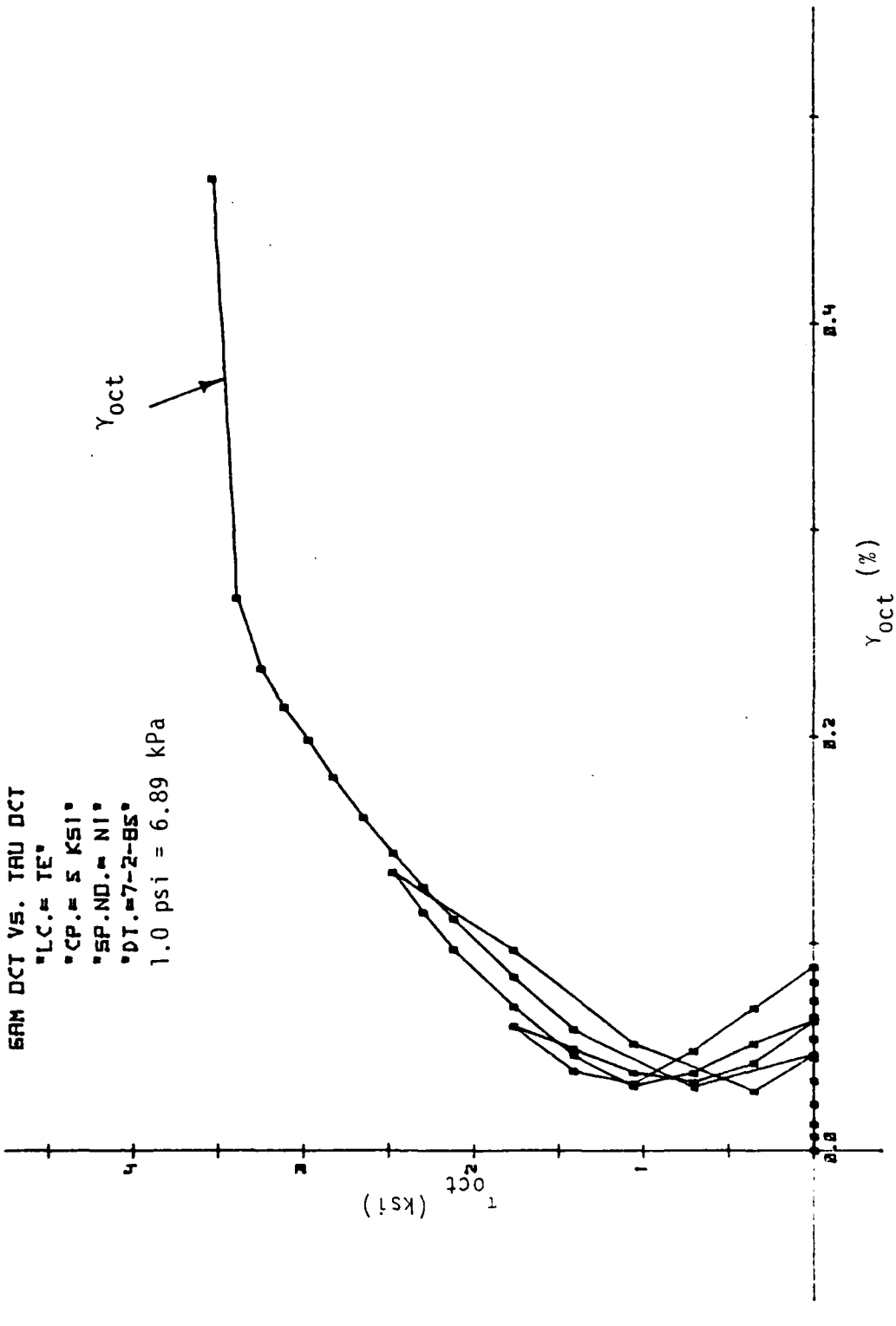

Figure 3.40. Octahedral Stress-Strain Response Curve for Triaxial Extension Test.

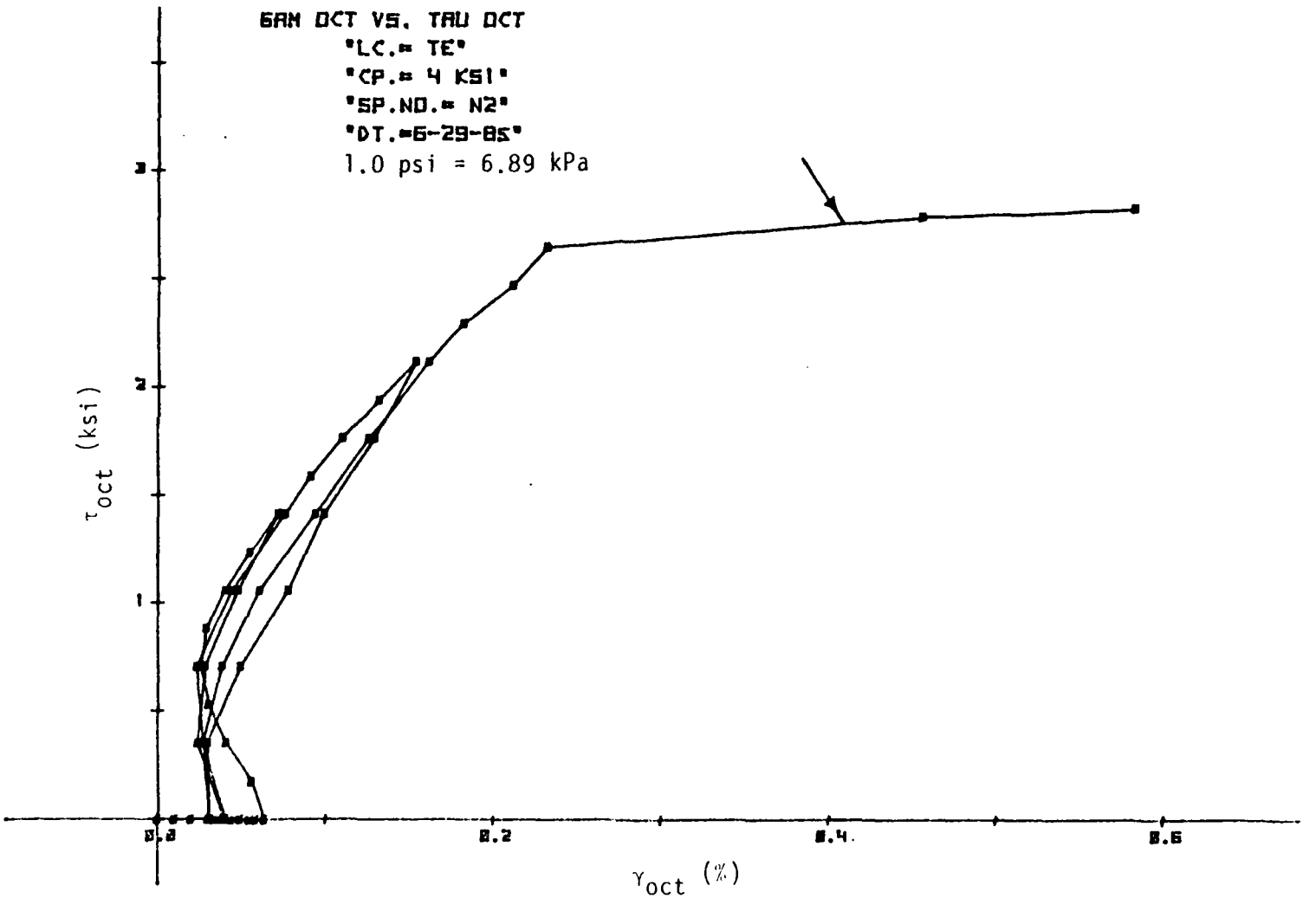

Figure 3.41. Octahedral Stress-Strain Response Curve for Triaxial Extension Test.

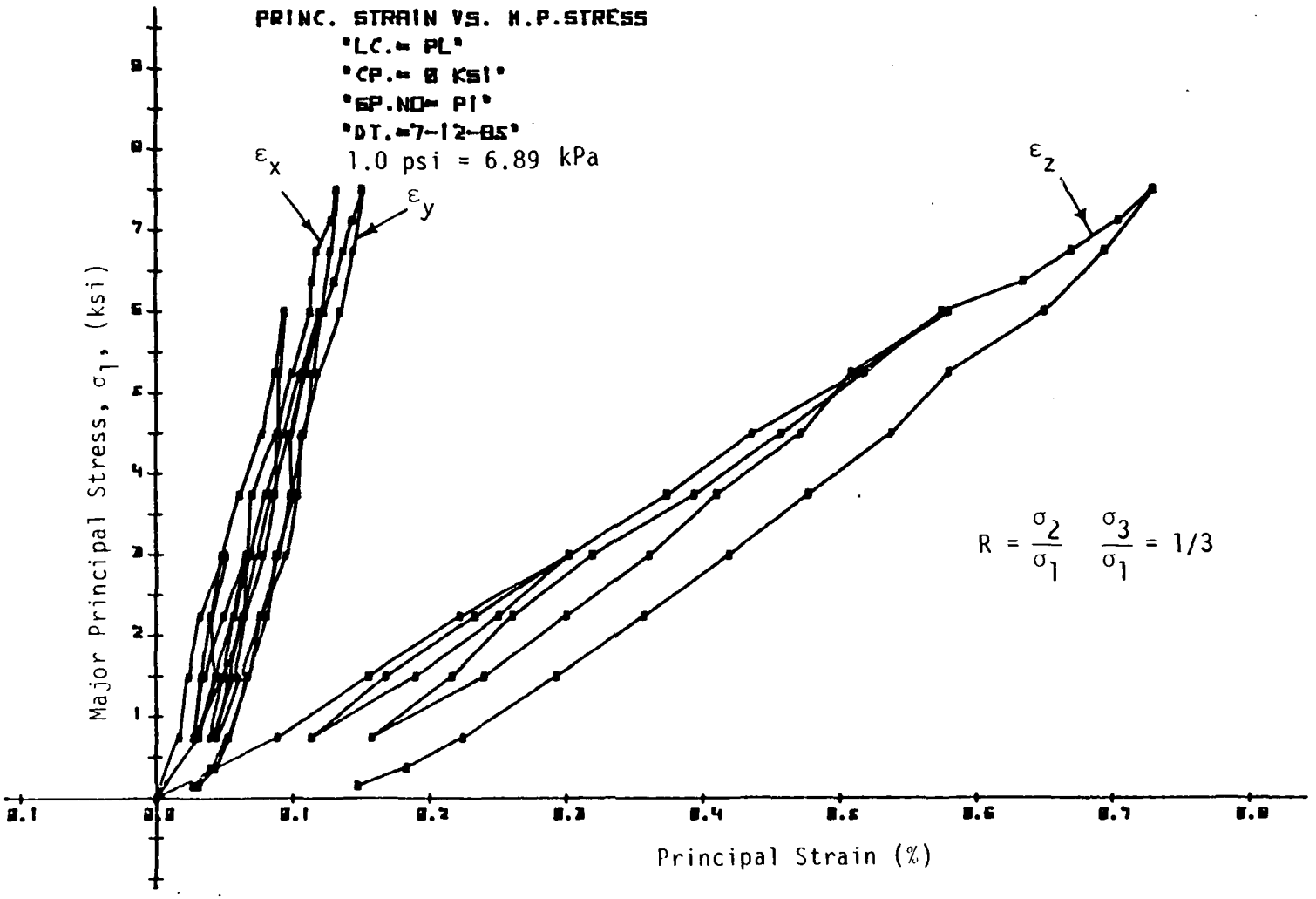

Figure 3.42. Stress-Strain Response Curves for Proporportional Loading Test.

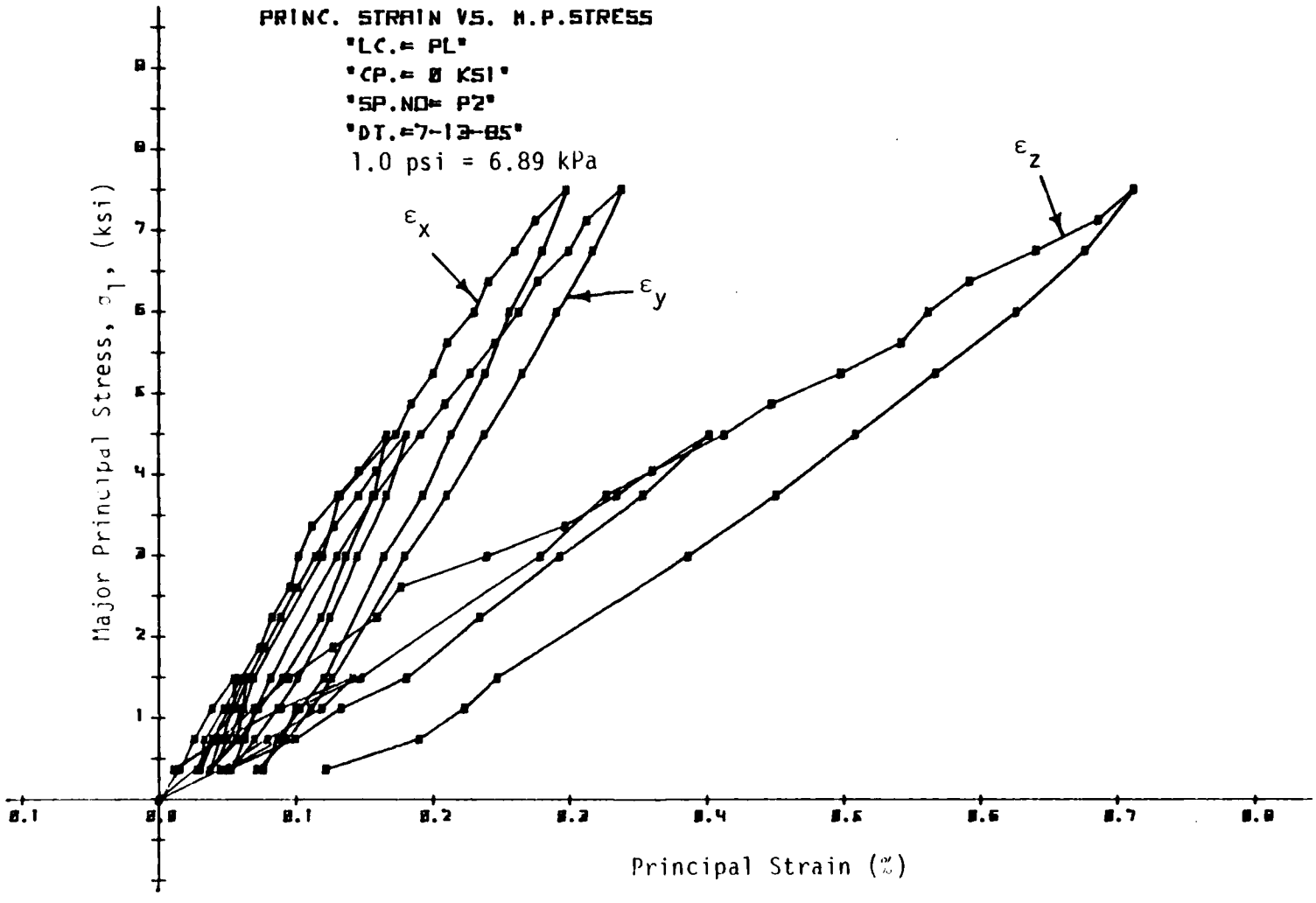

Figure 3.43. Stress-Strain Response Curves for Proportional Loading Test (R = 2/3).

an ultimate strength plateau indicating failure.

3.7 Circular Stress Paths (CSP)

The circular stress path was selected in order to gain information about the effects of the third stress invariant. Tests of this type were performed in 4.0 ksi (27.58 MPa) deviatoric planes. These tests involve hydrostatic, monotonic loading to specified deviator plane, followed by stress deviation along the triaxial compression path to the specified circle. The circular stress paths consist of 10 degree load steps. From the failure data that were obtained in the triaxial plane test series and octahedral plane test series, value of octahedral shear stress, radii of the circle, were selected. This was done in such a way that the circular stress path remained sufficiently far from the ultimate strength of the concrete in order that damage of the concrete specimen, microcracking, would not result during the loading sequence.

Figures 3.44 and 3.45 show the stress-strain responses for two circular stress paths (CSP) tests at confining pressures of 4 ksi (27.58 MPa) and octahedral shear stress, τ_{oct}, of 1 and 1.5 ksi (6.895 and 10.34 MPa), respectively. The graphs of these circular paths show the major principal stress, σ_1 plotted against the three principal strains. Figures 3.46 and 3.47 show the three principal strains plotted against the angle of similarity θ_{oct}, measured counter-clockwise from the triaxially

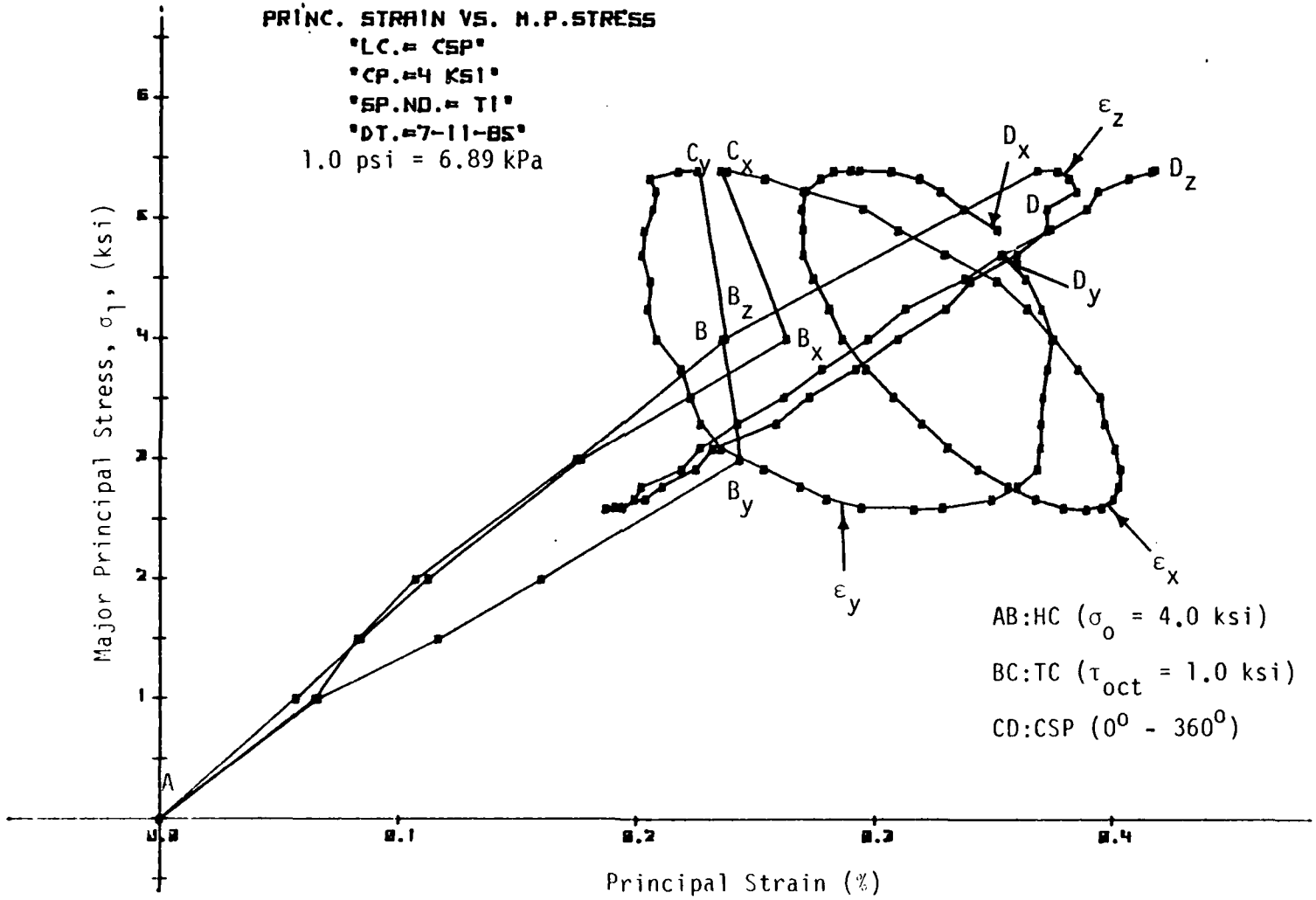

Figure 3.44. Stress-Strain Response Curves for Circular Stress Path Test.

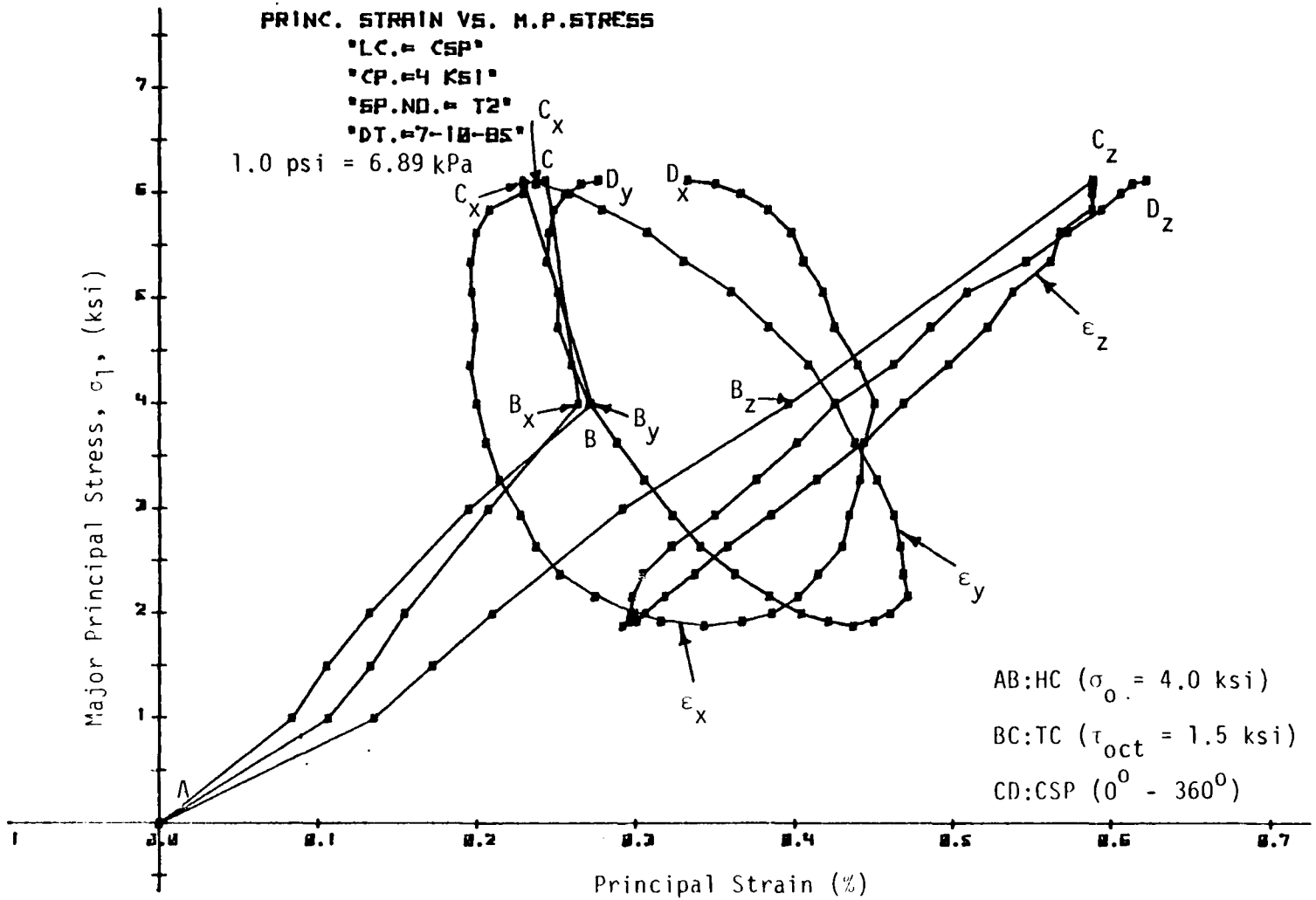

Figure 3.45. Stress-Strain Response Curves for Circular Stress Path Test.

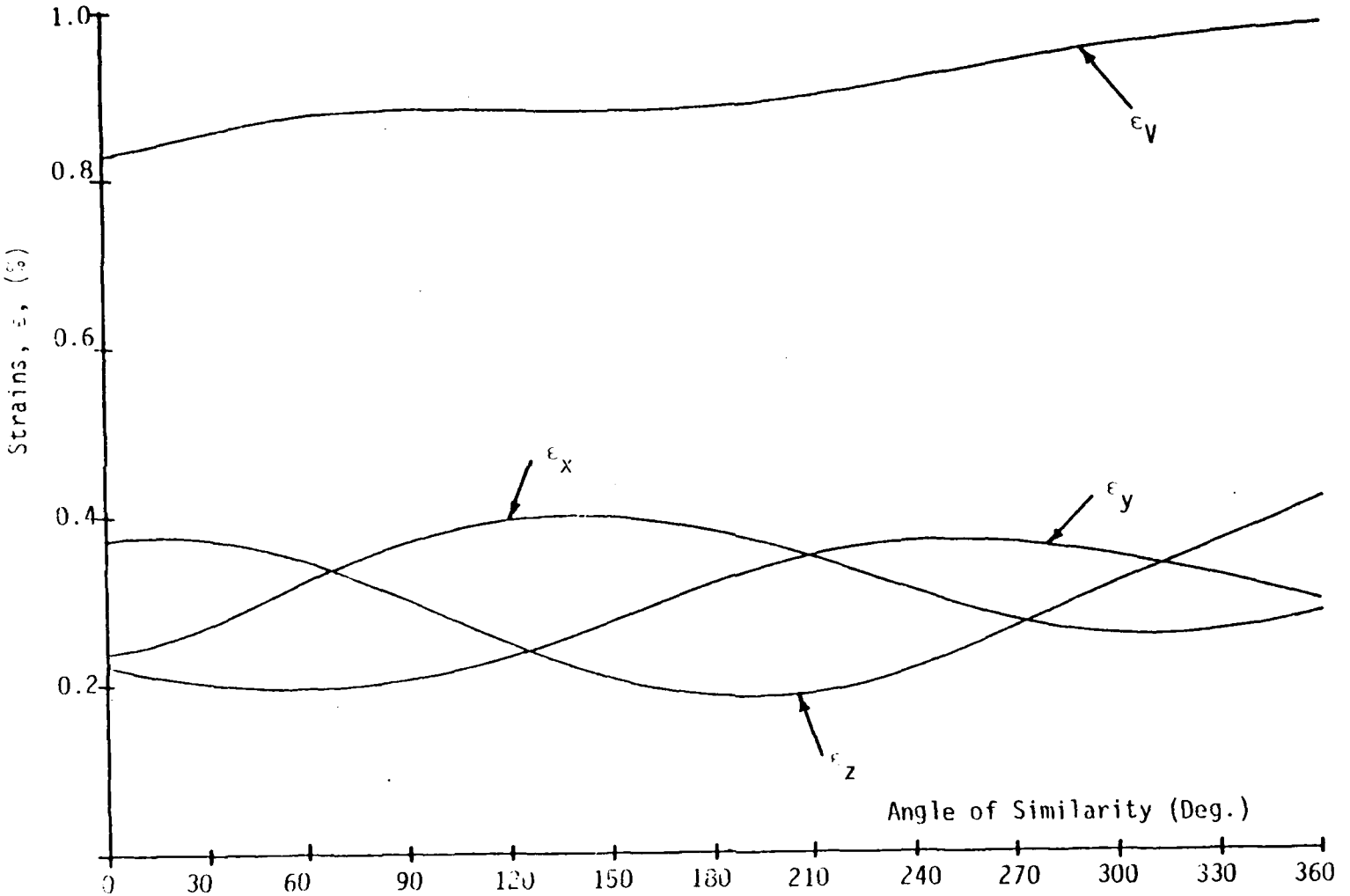

Figure 3.46. Strain-Angle of Similarity Response Curve for Circular Stress Path Test (σ_{oct} = 4.0 ksi and τ_{oct} = 1.0 ksi), (1.0 psi = 6.89 kPa).

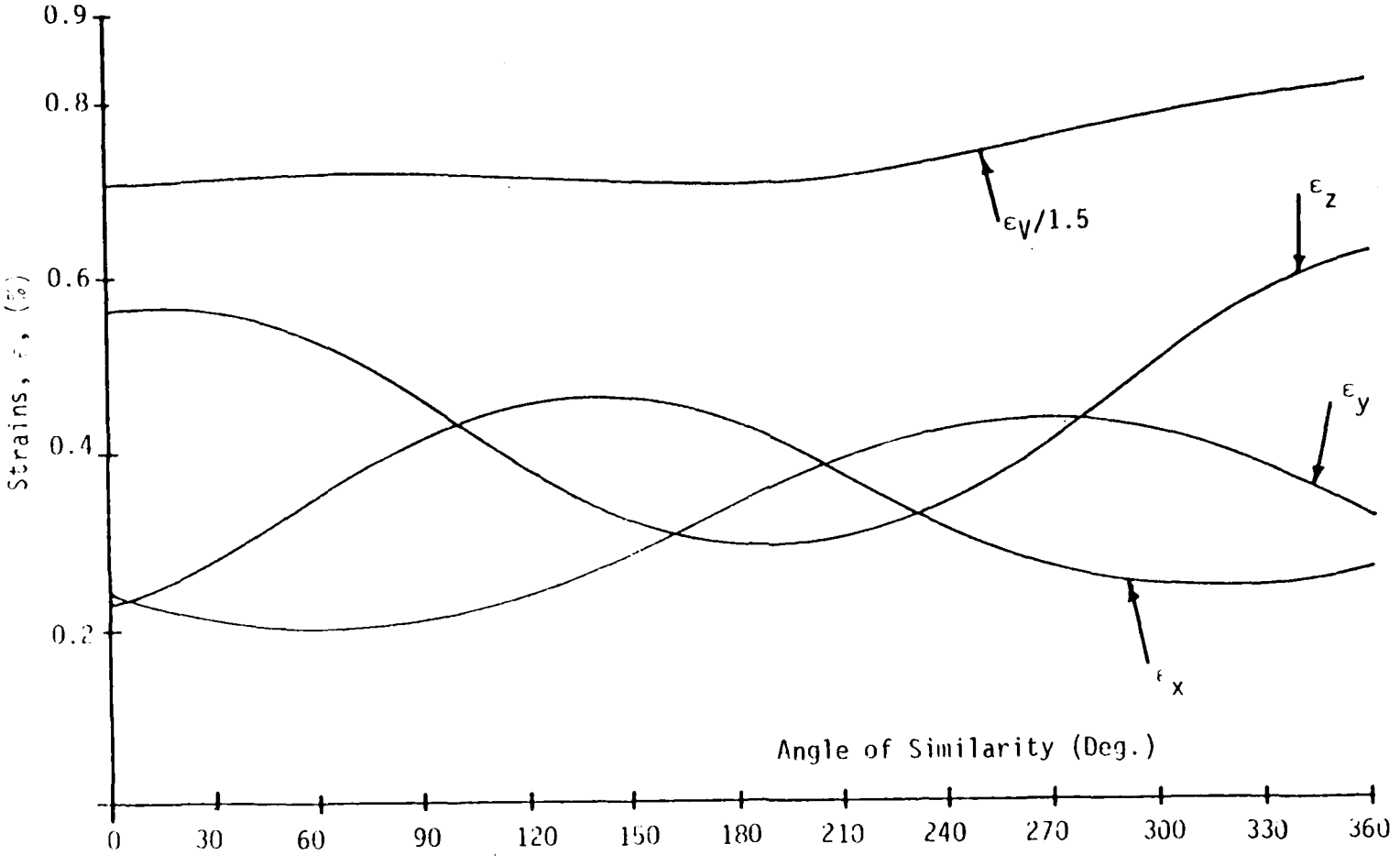

Figure 3.47. Strain-Angle of Similarity Response Curve for Circular Stress Path Test (σ_{oct} = 4.0 ksi at τ_{oct} = 1.5 ksi), (1.0 psi = 6.89 kPa)

compressive axis in the deviatoric plane.

3.8 Arbitrary Stress Path (ASP)

Figures 3.48 show the stress-strain responses for arbitrary stress path (ASP) test at three different confining pressures of 1.0, 2.0 and 3.0 ksi (6.895, 13.79 and 20.69 MPa) on the same specimen. This specimen was loaded cyclically along the hydrostatic axis with gradually increasing σ_o up to 1.0 ksi (6.895 MPa), and then cycled along CTC path with gradually increasing σ_{oct} to near failure, and then unloaded to original confining pressure, σ_o, 1.0 ksi (6.895 MPa). Similarly, CTC test was repeated with confining pressures, σ_o, of 2.0 and 3.0 ksi (13.69 and 20.69 MPa).

3.9 Ultimate Failure (Strength)

The ultimate condition is defined as the asymptotic value of the stress in the stress-strain response curve, as shown in Fig. 3.49. Since the cubical testing apparatus is a stress-controlled device, not being as stiff as one would like, some of the specimens did not dilate because of brittle failures occurring (usually a corner or edge failure). Therefore no failure stresses were recorded for these specimens. However, in some of the tests, slight increases in shear stress (τ_{oct}) were applied beyond the point of dilation. Of the 20 specimens tested, 10 reached failure (the stress state at which dilation occurs as shown in Fig. 3.49). TABLE 3.2 lists the ultimate data for these specimens. Failed samples are shown in APPENDIX A. Figures 3.50 to 3.52 show the

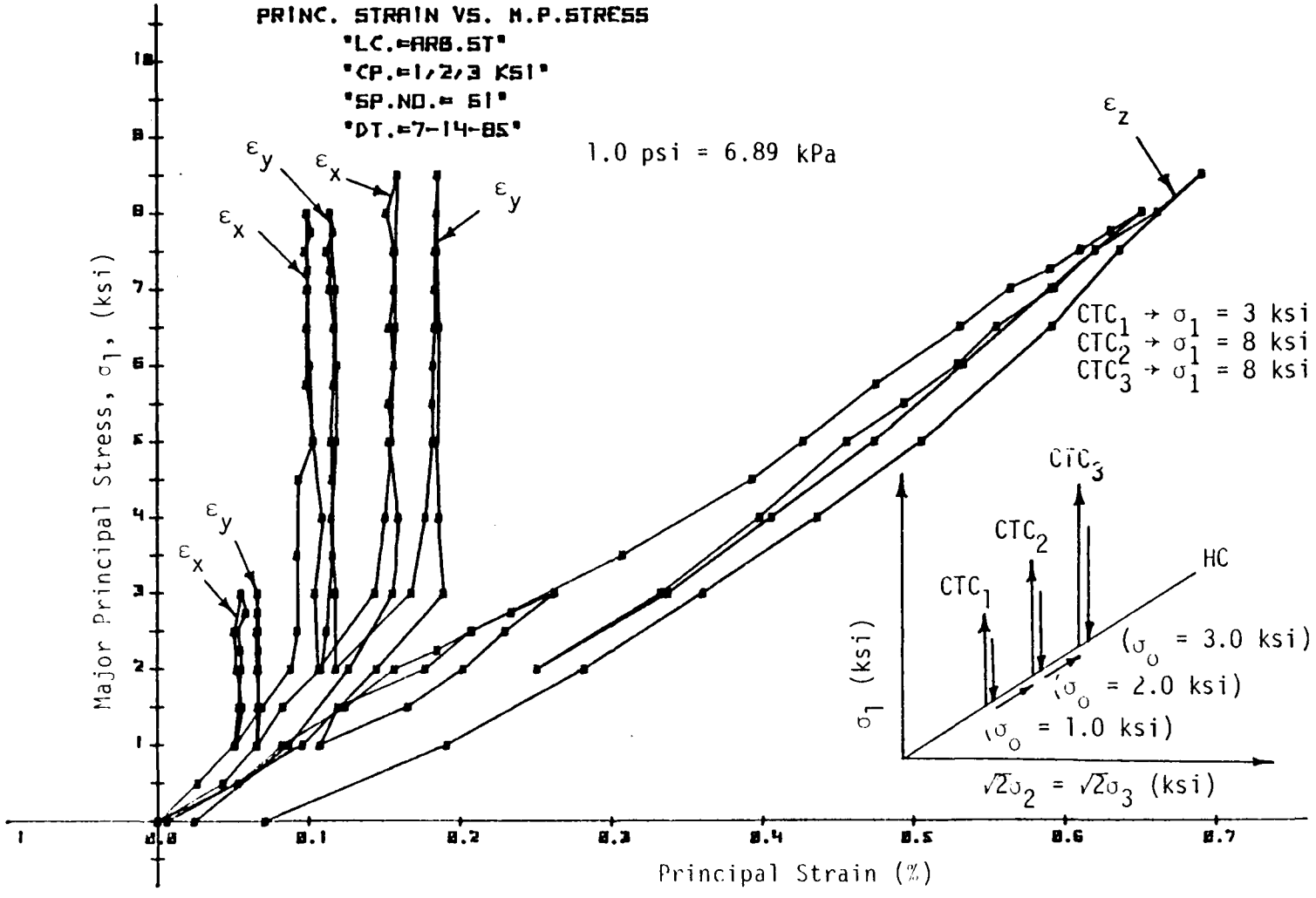

Figure 3.48. Stress-Strain Response Curves for Arbitrary Stress Path Test Under Different Confining Pressure (σ_o = 1.0, 2.0, and 3.0 ksi).

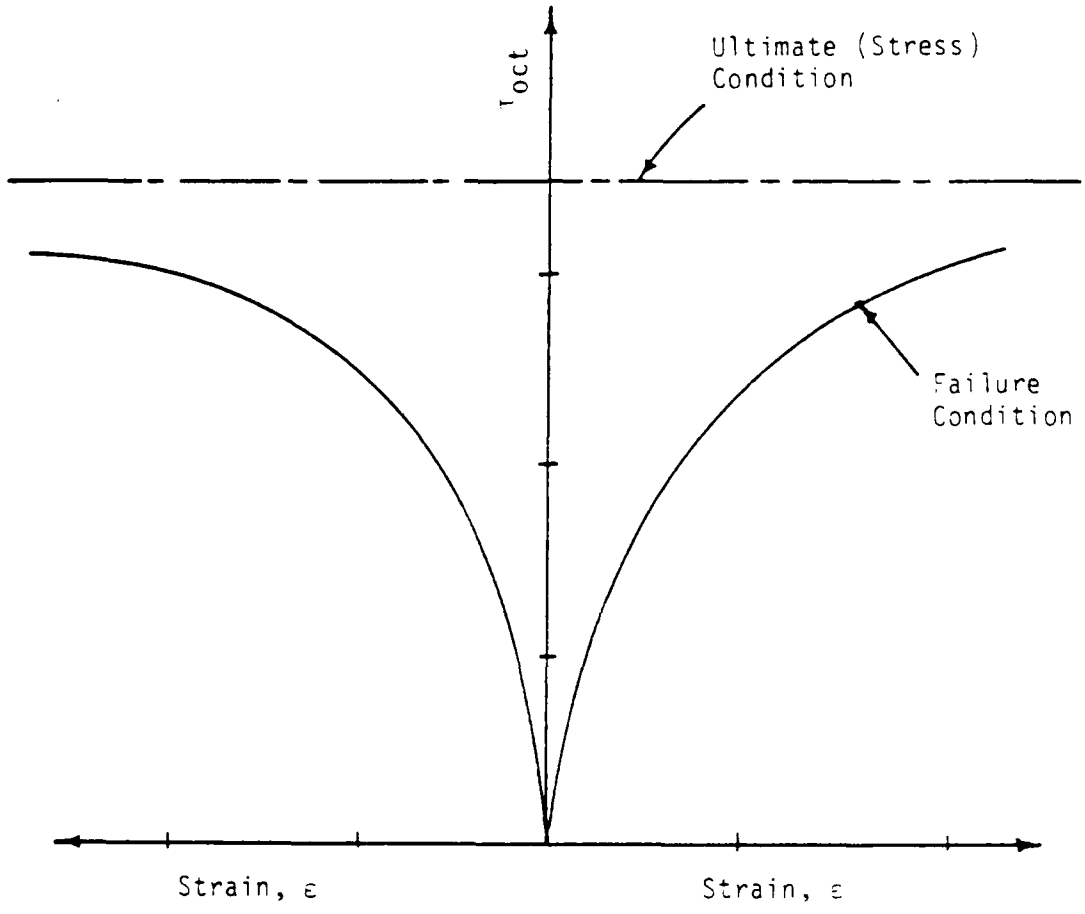

Figure 3.49. Ultimate Condition Shown for a Typical Stress-Strain Response.

TABLE 3.2

ULTIMATE DATA FOR PLAIN CONCRETE

(Compressive Stresses Positive)

Load Path (Fig. 2.16)	Spec. No.	σ_1 (ksi)	σ_2 (ksi)	σ_3 (ksi)	σ_{oct} (ksi)	τ_{oct} (ksi)	J_1* (ksi)	$\sqrt{J_{2D}}$ (ksi)
Conventional Triaxial Compression (CTC)		σ_z	σ_x	σ_y				
	B_3	4.5033	0.0	0.0	1.5011	2.12	4.5033	2.6
	B_1	10.47	1.0	1.0	4.16	4.47	12.47	5.47
	B_2	13.951	2.0	2.0	5.8337	5.47	17.50	6.70
	B_4	17.371	3.0	3.0	7.4803	6.78	22.44	8.30
Triaxial Compression (TC)		σ_z	σ_x	σ_y				
	E_1	6.02	-0.01	-0.01	2.0	2.84	7.18	3.48
	E_2	8.40	0.3	0.3	3.0	3.82	10.18	4.68
Simple Shear (SS)		σ_z	σ_x	σ_y				
	M_1	9.42	-0.42	4.5	4.5	4.02	14.68	4.92
Triaxial Extension (TE)		σ_z	σ_x	σ_y				
	N_2	6.2979	6.2979	-.5957	4.0	3.25	13.18	3.98
	N_1	7.875	7.875	-.7504	5.0	4.07	16.18	4.98
	N_3	9.3198	9.3198	-.6395	6.0	4.69	19.18	5.75
Reduced Triaxial Extension (RTE)		σ_z	σ_x	σ_y				
	R_1	7.5	7.5	4.55	6.517	1.47	20.[illegible]3	1.8.

*1.0 psi = 6.89 kPa

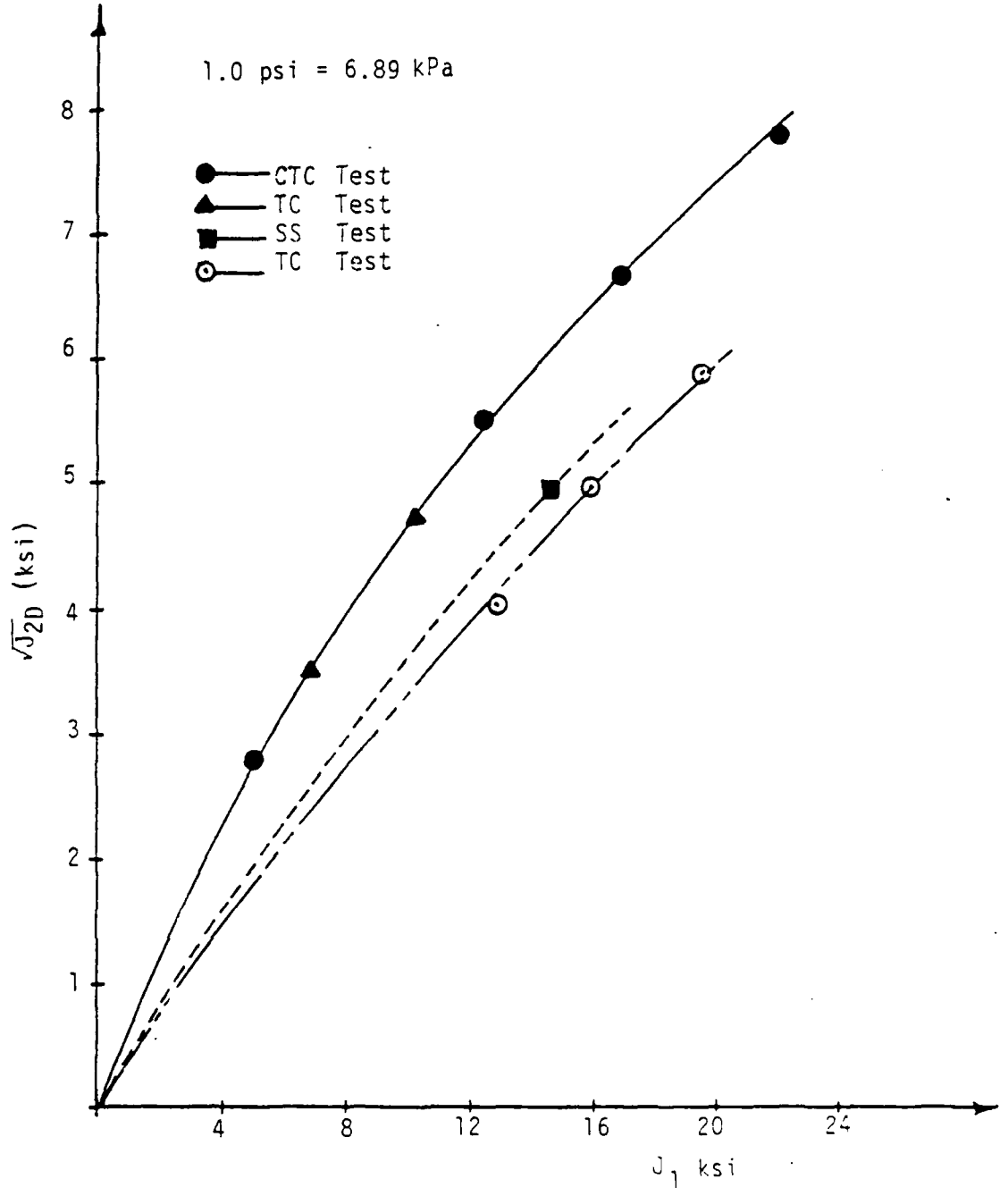

Figure 3.50. Observed Ultimate Surfaces in $\sqrt{J_{2D}} - J_1$ Plane for Plain Concrete

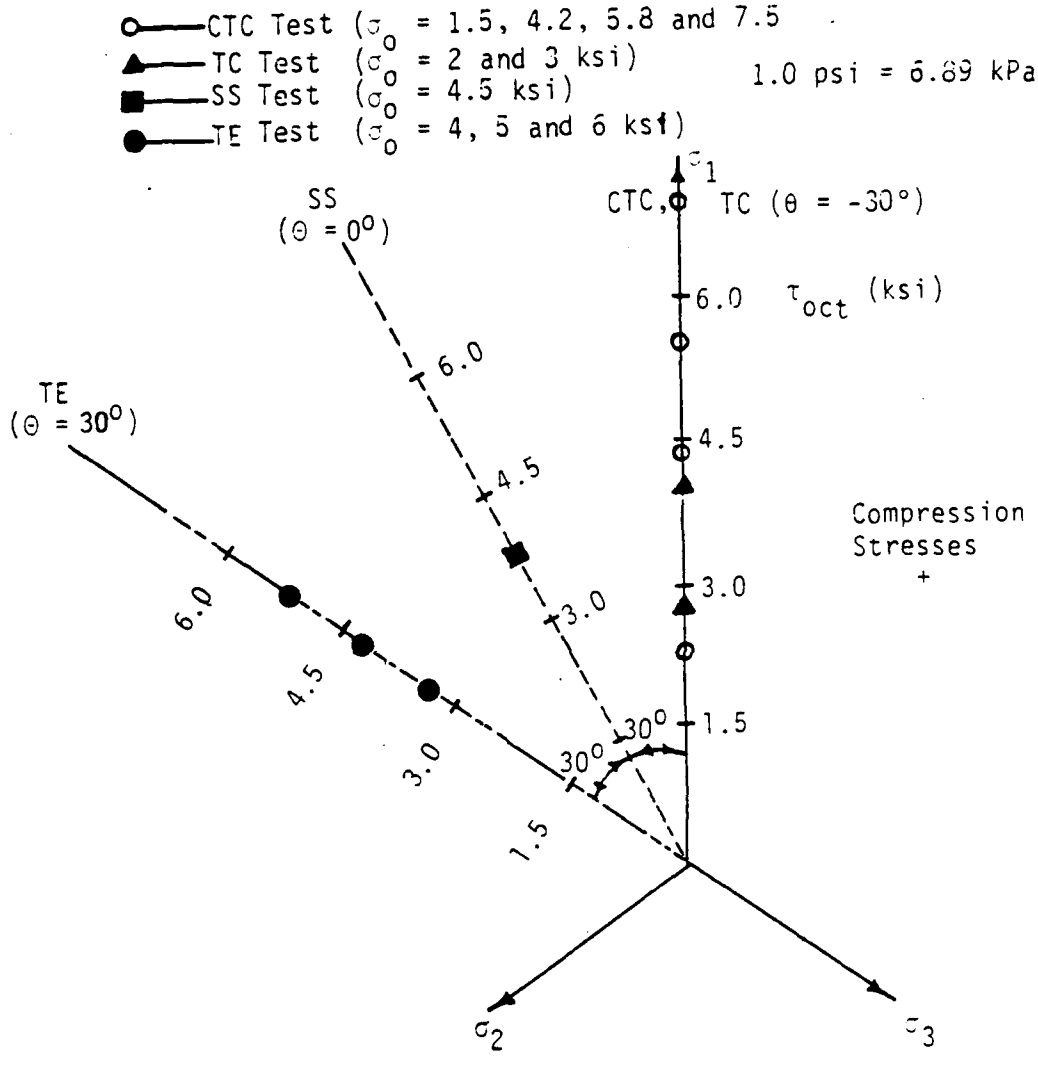

Figure 3.51. Observed Ultimate States in Octahedral Plane for Plain Concrete.

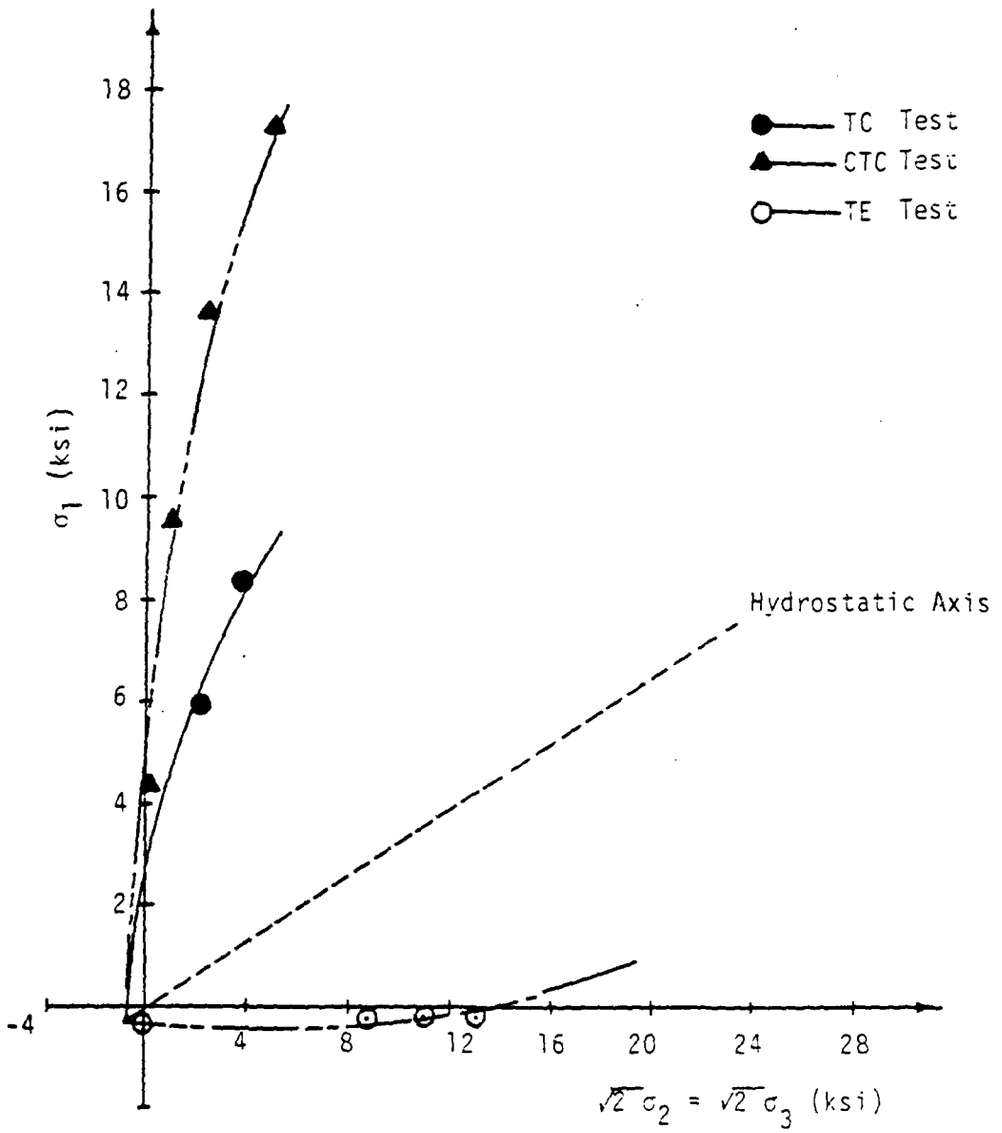

Figure 3.52. Observed Ultimate Surfaces in Triaxial Plane for Plain Concrete.

plots of the data in $\sqrt{J_{2D}}$ - J_1 octahedral or deviatoric and triaxial planes, respectively.

Notice in TABLE 3.2 that x,y,z directions of the specimens do not always correspond to the 1,2,3 principal directions. For CTC, TC and SS tests, σ_z, σ_x and σ_y correspond to σ_1, σ_2 and σ_3 respectively. The reason for the differences is to be consistent with the sign convention employed in the conventional cylindrical triaxial test for CTC, TC, RTE and TE paths. The SS path is not possible in conventional triaxial tests, therefore the SS sign convention was arbitrarily chosen to be the same as the CTC and TC's. The SS data is not plotted in Fig. 3.52 simply because the SS stress path does not lie in the triaxial plane. Also CTC stress path does not lie in octahedral plane.

Several conclusions can be drawn from examination of the strength results shown in Figs. 3.50 - 3.52.

i) The octahedral shear strength of plain concrete specimens is strongly dependent upon the stress path (Θ or J_3). In the tests with constant hydrostatic or confining pressure ($\sigma_0 = J_1/3$), the order of strength from the largest to the smallest is CTC, TC, SS, and TE. Had the strengths proven to be independent of the stress path, the three lines through the strength data in Fig. 3.50 would lie atop each other and a Drucker-Prager shaped envelope would have resulted.

ii) There is a direct relationship between strength and confining pressure (see Fig. 3.50).

iii) The ultimate envelopes in the octahedral planes (Fig. 3.5) are non-circular, i.e. they depend on stress path (Θ). Many researchers, including Gerstle, et al [33], have observed similar results for plain concrete. Had the plain concrete results proven to be independent of the stress path, the ultimate data would plot as circles in the octahedral planes. If the results had been independent of hydrostatic pressure, the ultimate envelopes would be identical for varying hydrostatic pressure. With some thought and imagination, one can see that the plain concrete ultimate surface that will develop is basically cone-shaped, having a non-circular cross-section, similar to one shown in Fig. 5.6. Any ultimate (failure) criteria used to predict the strength behavior of the plain concrete must include the effects of stress path (Θ) and hydrostatic pressure (σ_0).

iv) Finally, through examination of the data in the triaxial plane (Fig. 3.52) and in TABLE 3.2 one can see that if the tests had been conducted along TE stress path at confining pressures lower than about 4 ksi (27.58 MPa), they would have ended

before the specimens failed because tensile stresses would have been required, which are impossible to achieve with the present device.

CHAPTER 4

TEST SERIES AND RESULTS ON SOAPSTONE

4.1 Introduction

Tests are conducted on soapstone in HC, CTC, TC, SS, TE and CSP states and the stress-strain responses together with the discussion of test results are presented here.

4.2 Triaxial Plane Test Series

4.2.1 Hydrostatic Compression (HC)

The results of the HC test are presented in Figs. 4.1a, 4.1b, 4.1c and 4.1d. In the HC test, increments of 250 to 750 psi (1723.75 to 5171.25 kPa) were simultaneously applied to each face. The sample was loaded to 1.5 ksi (10.34 MPa) unloaded to zero; (initial confining pressure); reloaded to 4.5 ksi (31.03 MPa) unloaded to zero; and again reloaded to 8 ksi (55.16 MPa) finally unloaded to zero.

There are four unloading-reloading cycles in HC. The slope of the unloading-reloading curves are used to calculate the elastic parameters as well as the plastic part of total strain. Figure 4.1d shows the mean pressure - volumetric strain curves. The elastic bulk modulus appear to remain almost constant throughout the test at 449.51 ksi (3099.37 MPa). The material demonstrates

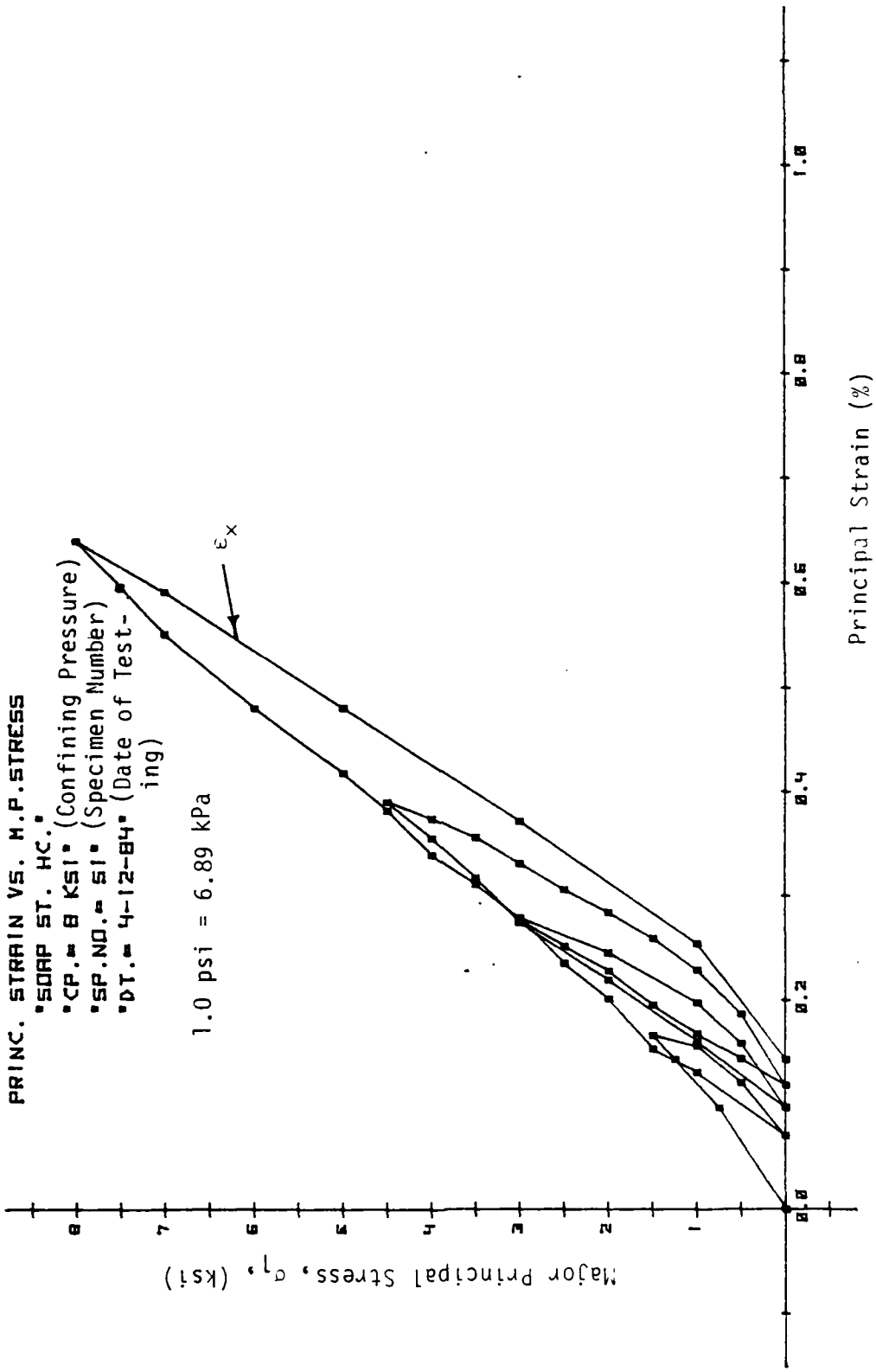

Figure 4.1a. Stress-Strain Response Curve for Hydrostatic Compression Test.

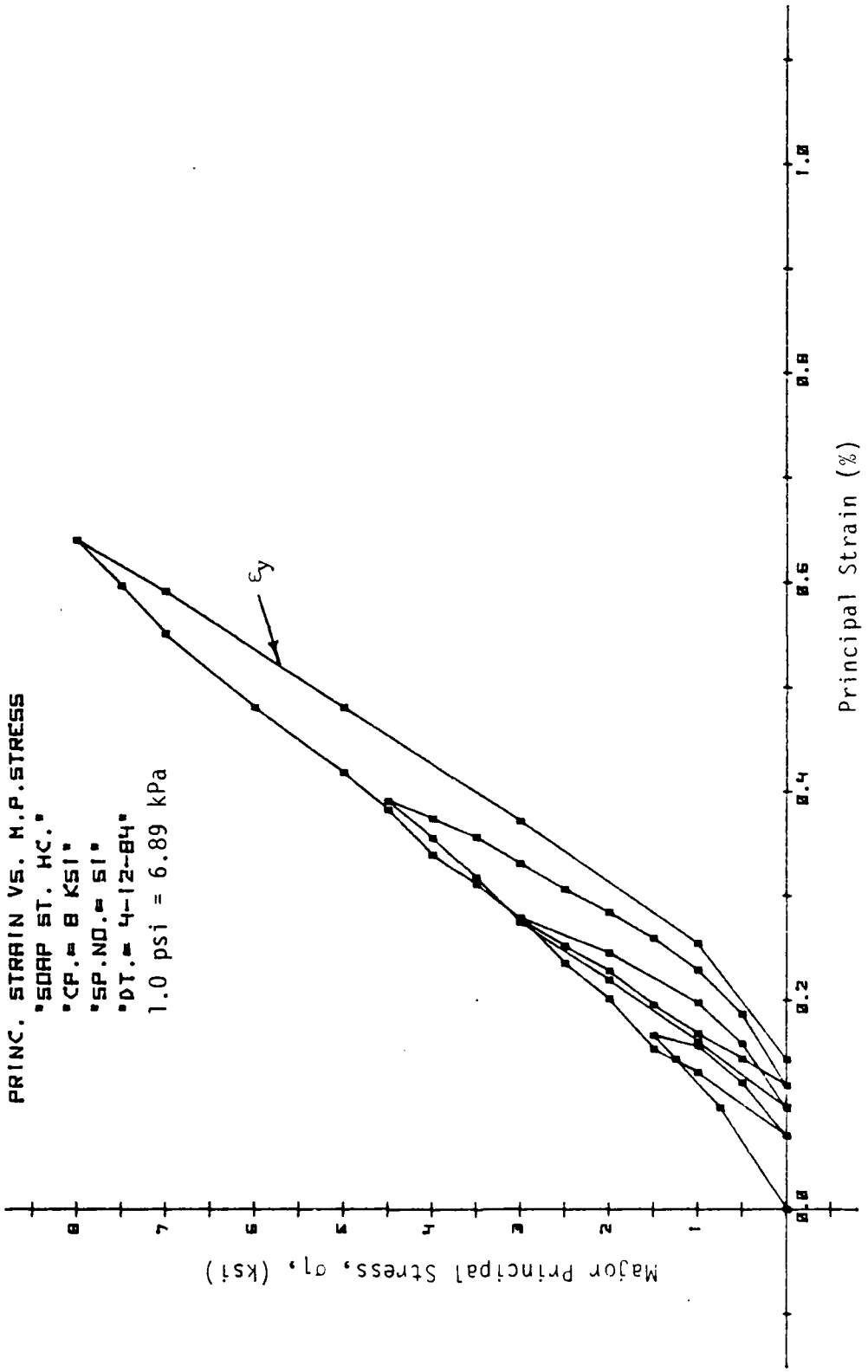

Figure 4.1b. Stress-Strain Response Curve for Hydrostatic Compression Test.

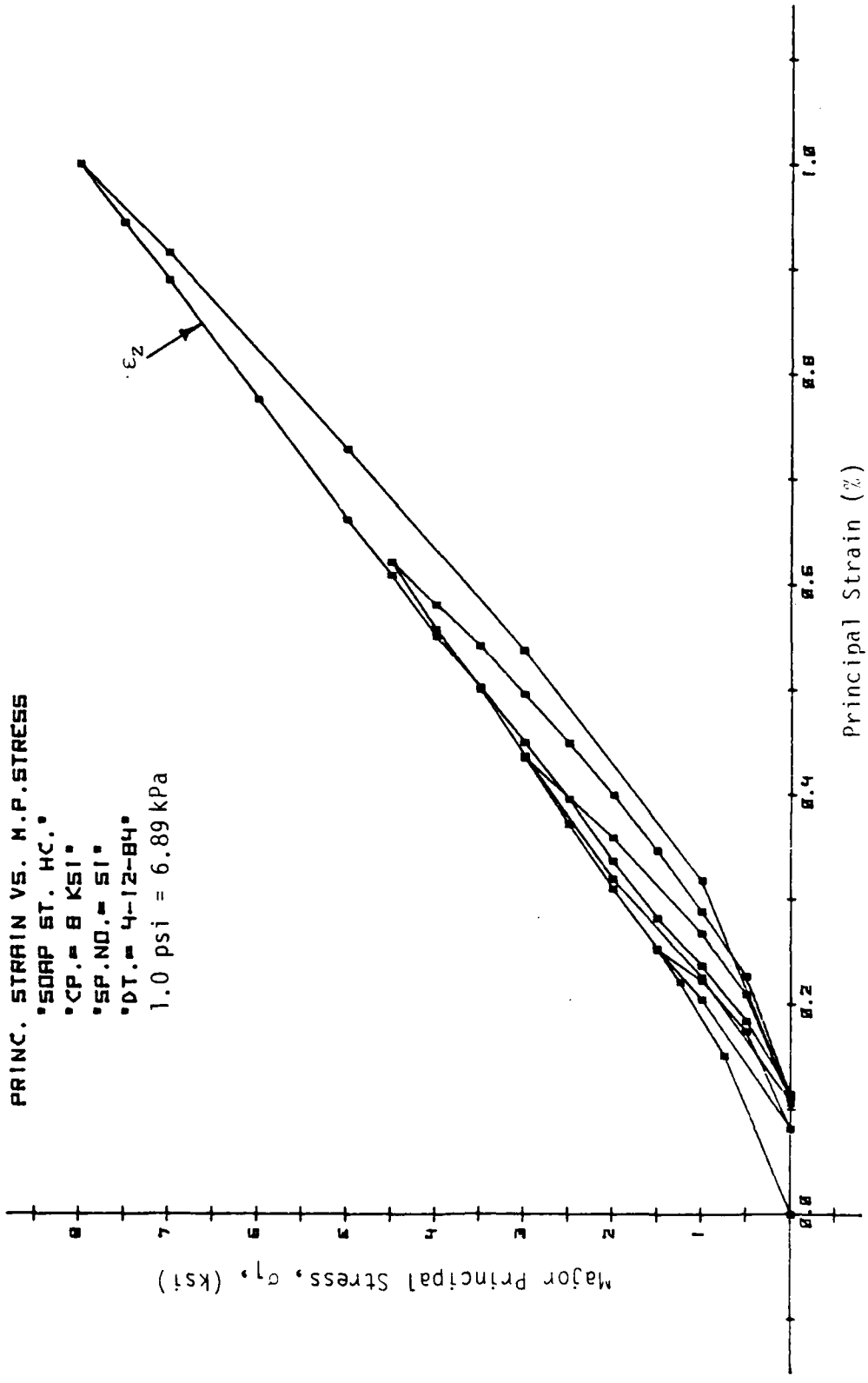

Figure 4.1c. Stress-Strain Response Curve for Hydrostatic Compression Test.

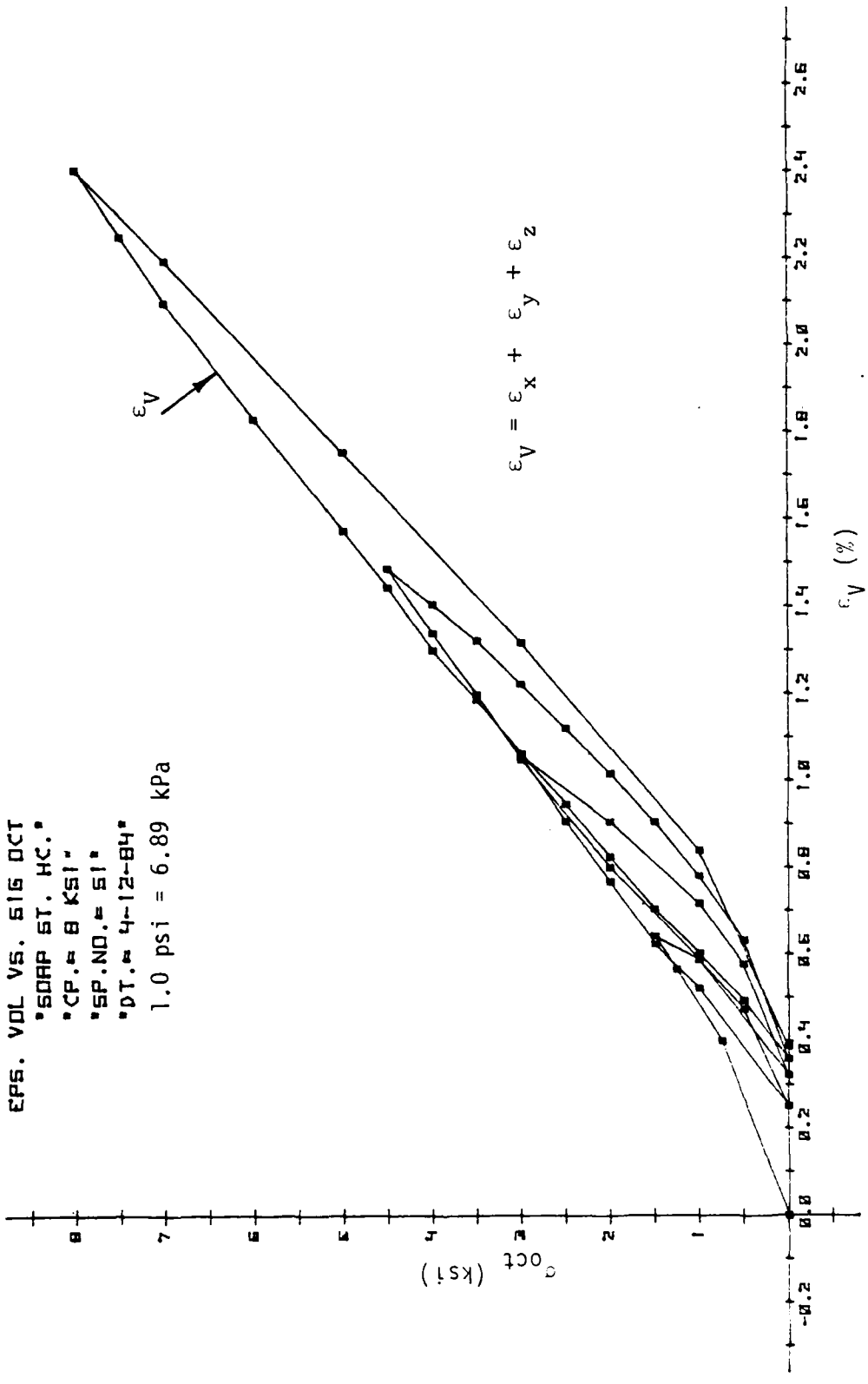

Figure 4.1d. Average Stress-Volumetric Strain Response Curve for Hydrostatic Compression Test.

fairly good isotropy in x and y direction as seen from the principal stress-strain curves.

4.2.2 Conventional Triaxial Compression (CTC)

Figure 4.2 to 4.10 show the stress-strain responses for CTC tests at confining pressures of 1.0, 2.0 and 3.0 ksi (6.895, 13.79 20.685 MPa), respectively. From these plots it is evident that the sample strength increases with initial strength plateau indicating failure. The tests are terminated when they reach that level.

4.3 Test Series on the Octahedral Plane

This series consists of nine tests, intended to explore the soapstone response to triaxial load cycle and to provide data to locate yield surface on an octahedral plane from $\theta=-30^{o}$ to $\theta=30^{o}$.

4.3.1 Triaxial Compression (TC)

The stress-strain curves for TC tests for σ_o = 2.0, 3.0 and 4.0 ksi (13.97, 20.69 and 27.58 MPa), are shown in Figs. 4.11 to 4.19. The test is conducted by increasing σ_1 and decreasing both σ_2 and σ_3 by equal amounts so that the value of σ_o remains constant. The sample is initially loaded to hydrostatic pressure of the desired value of σ_o, and then TC path is followed. The ultimate state is well-defined in these tests.

Since σ_2 and σ_3 are equal, ε_2 and ε_3 should also be equal for isotropic behavior, one can see a good agreement between these strains from Figs. 4.11 to 4.19.

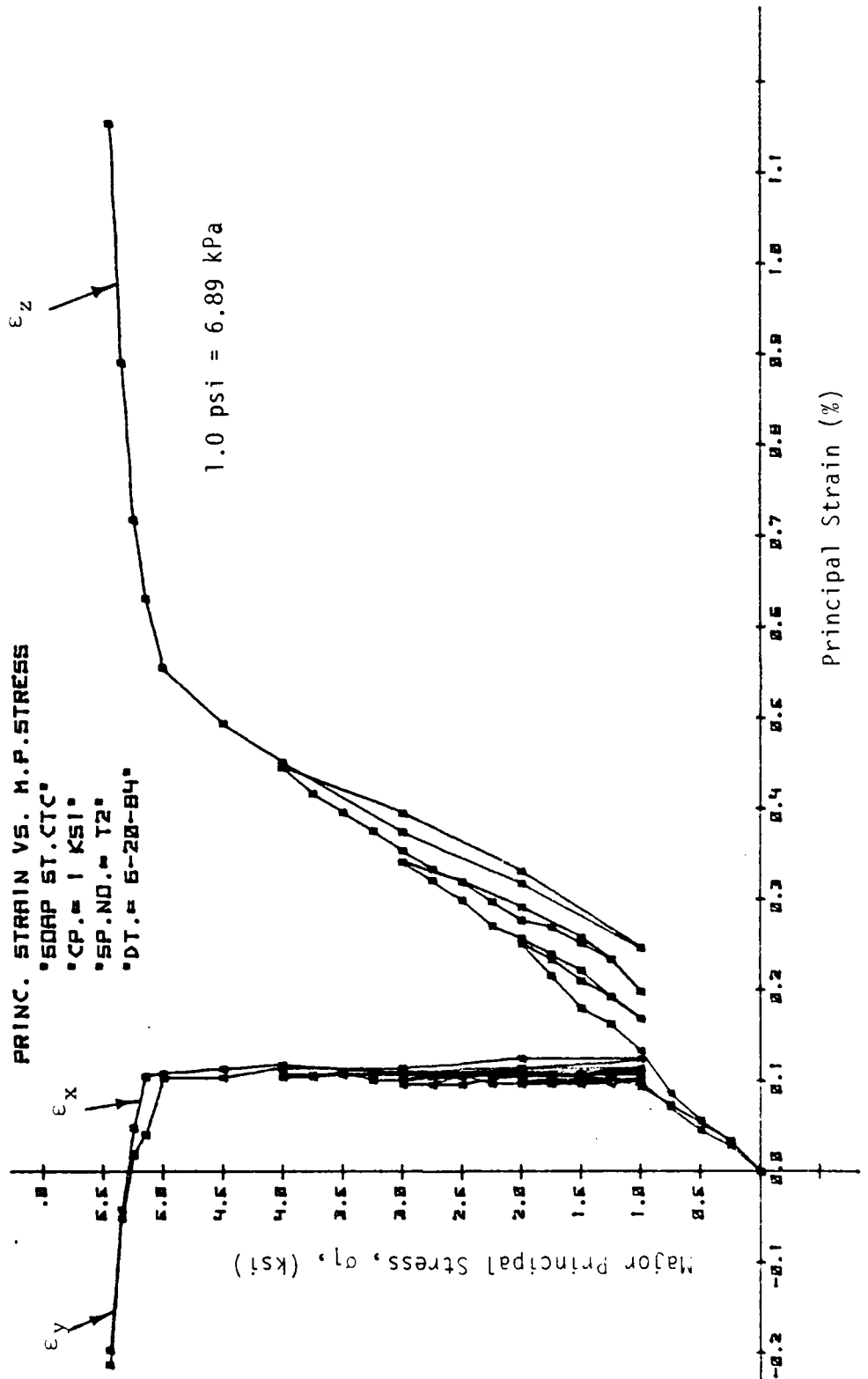

Figure 4.2. Stress-Strain Response Curves for Conventional Triaxial Compression Test.

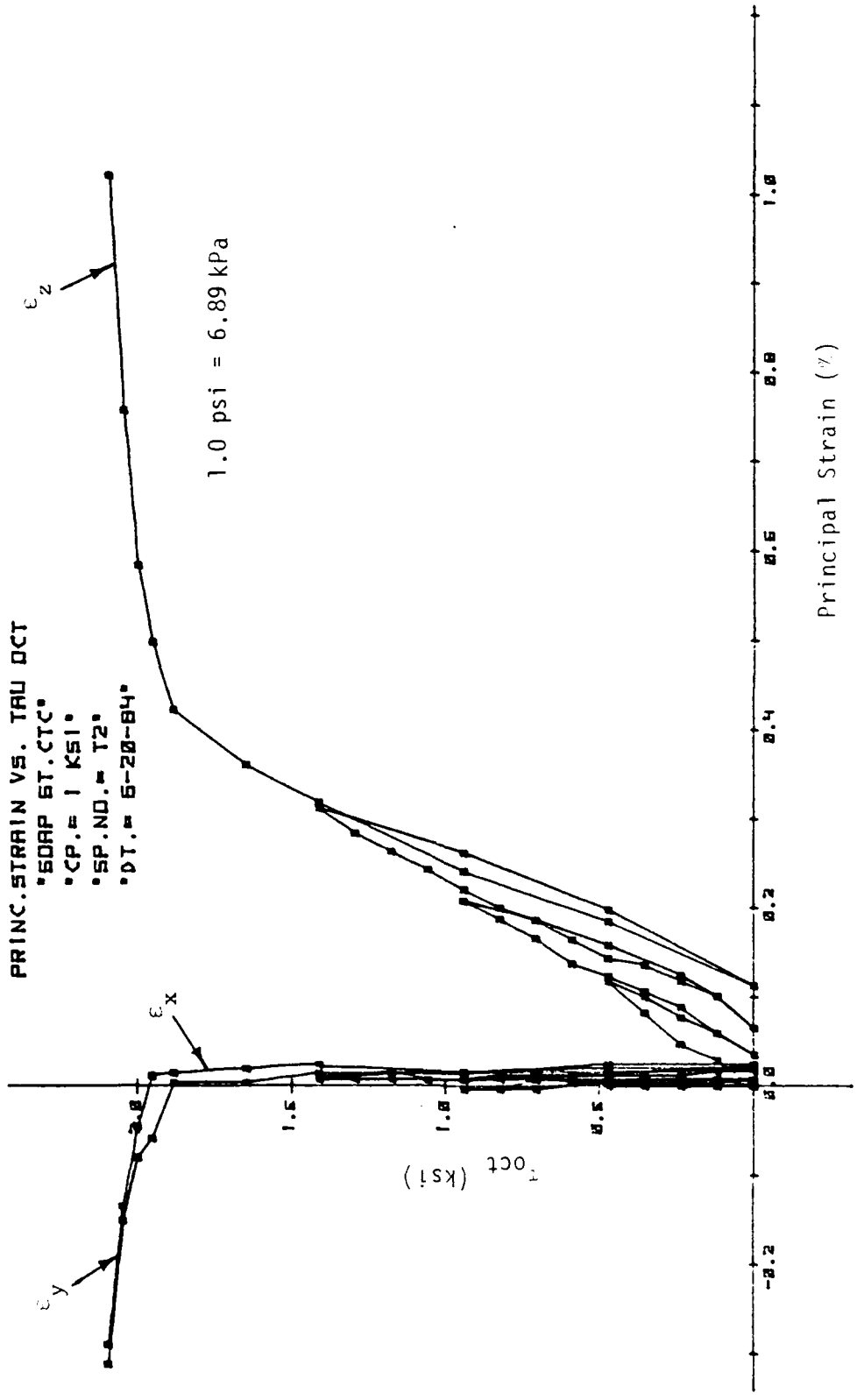

Figure 4.3. Stress-Strain Response Curves for Conventional Triaxial Compression Test.

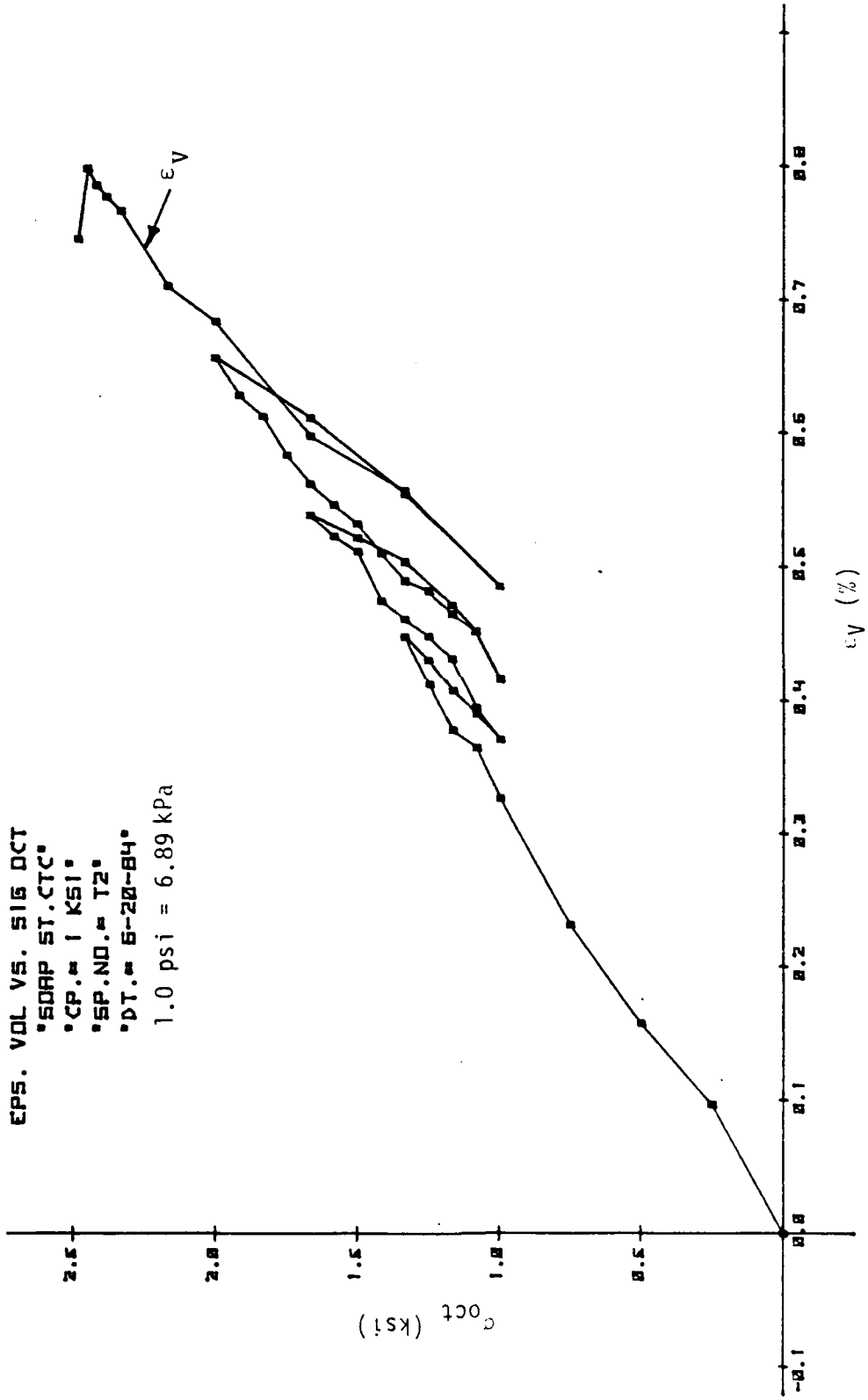

Figure 4.4. Average Stress-Volumetric Strain Response Curve for Conventional Triaxial Compression Test.

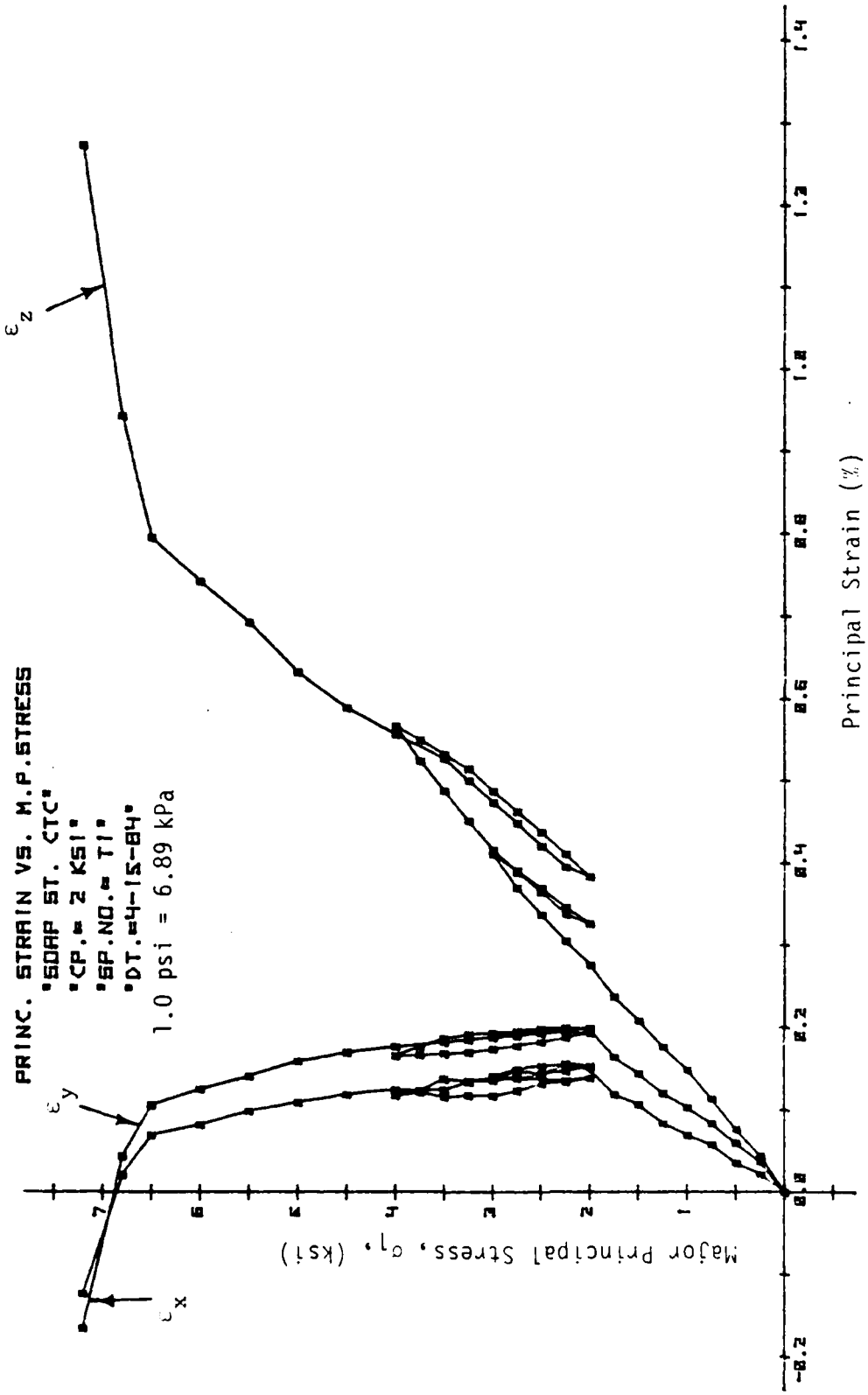

Figure 4.5. Stress-Strain Response Curves for Conventional Triaxial Compression Test.

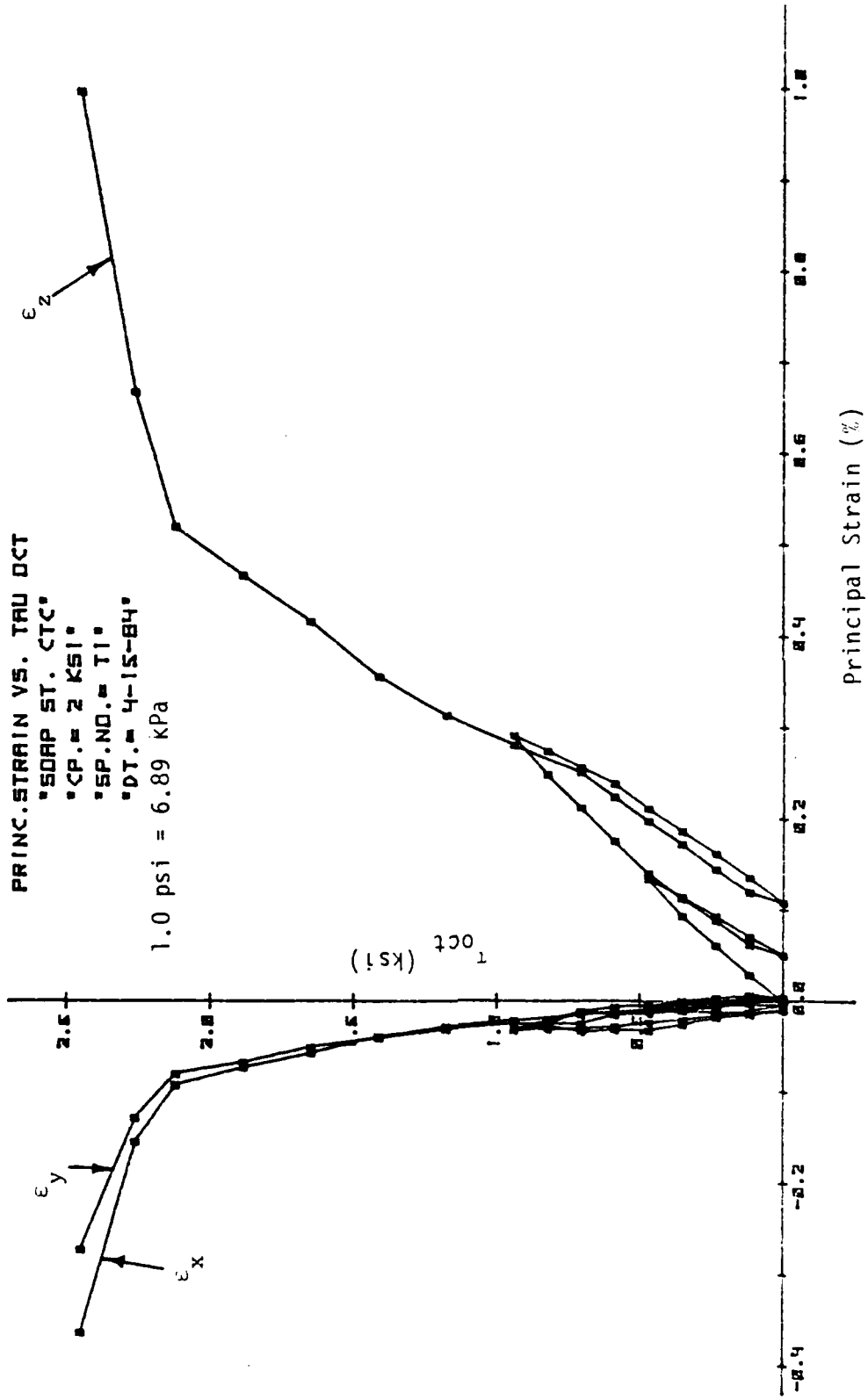

Figure 4.6. Stress-Strain Response Curves for Conventional Triaxial Compression Test.

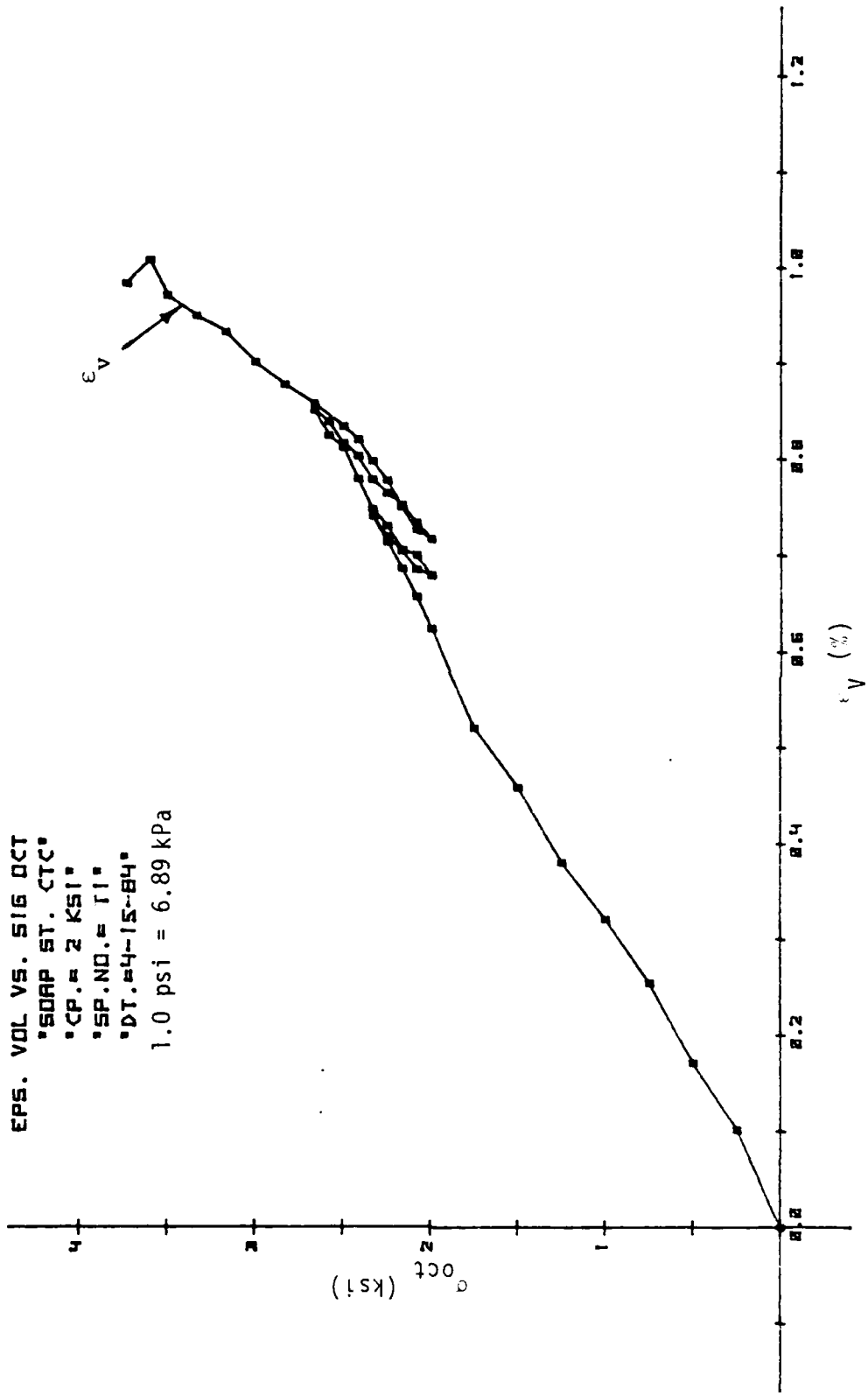

Figure 4.7. Average Stress-Volumetric Strain Response Curve for Conventional Triaxial Compression Test.

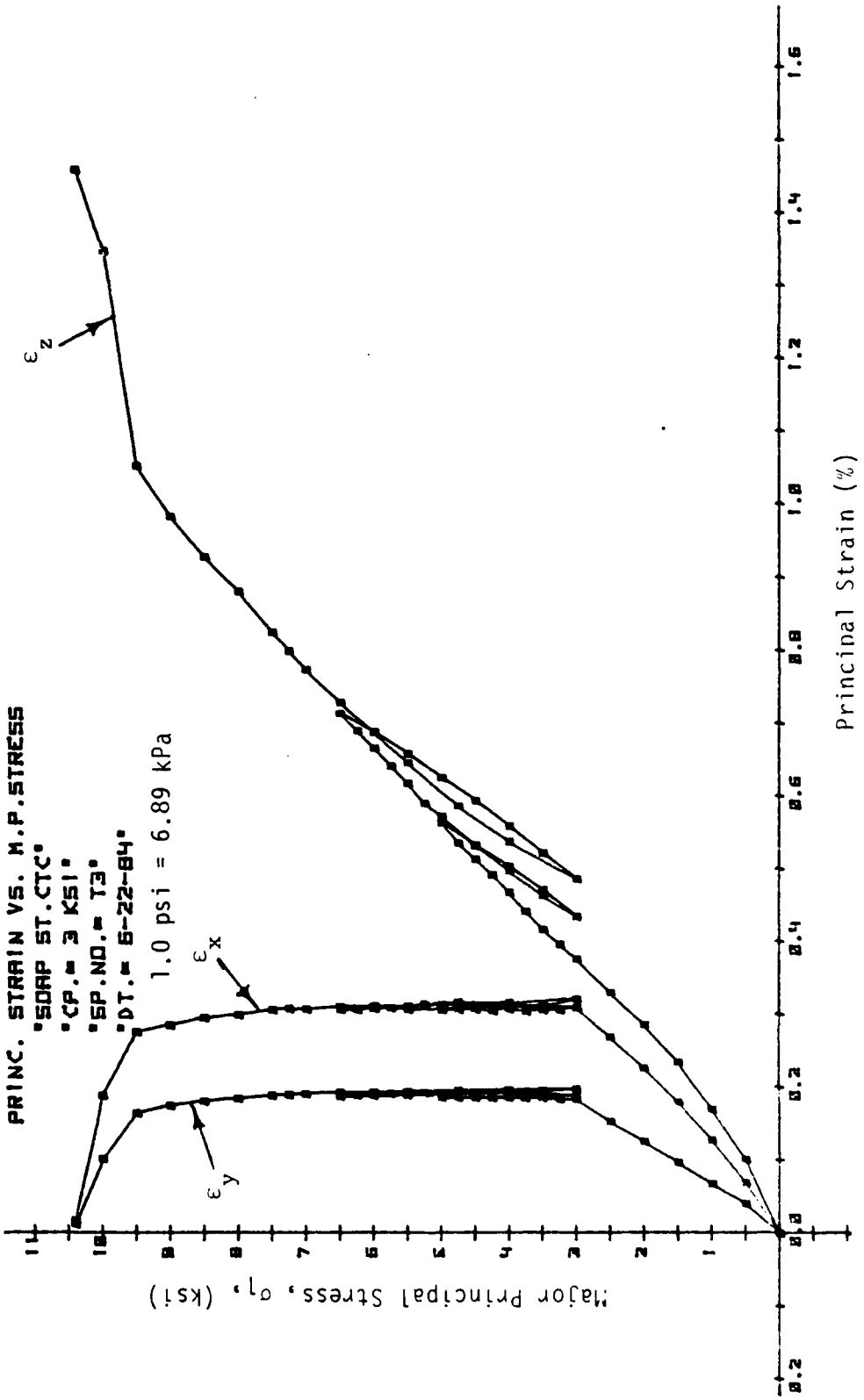

Figure 4.8. Stress-Strain Response Curves for Conventional Triaxial Compression Test.

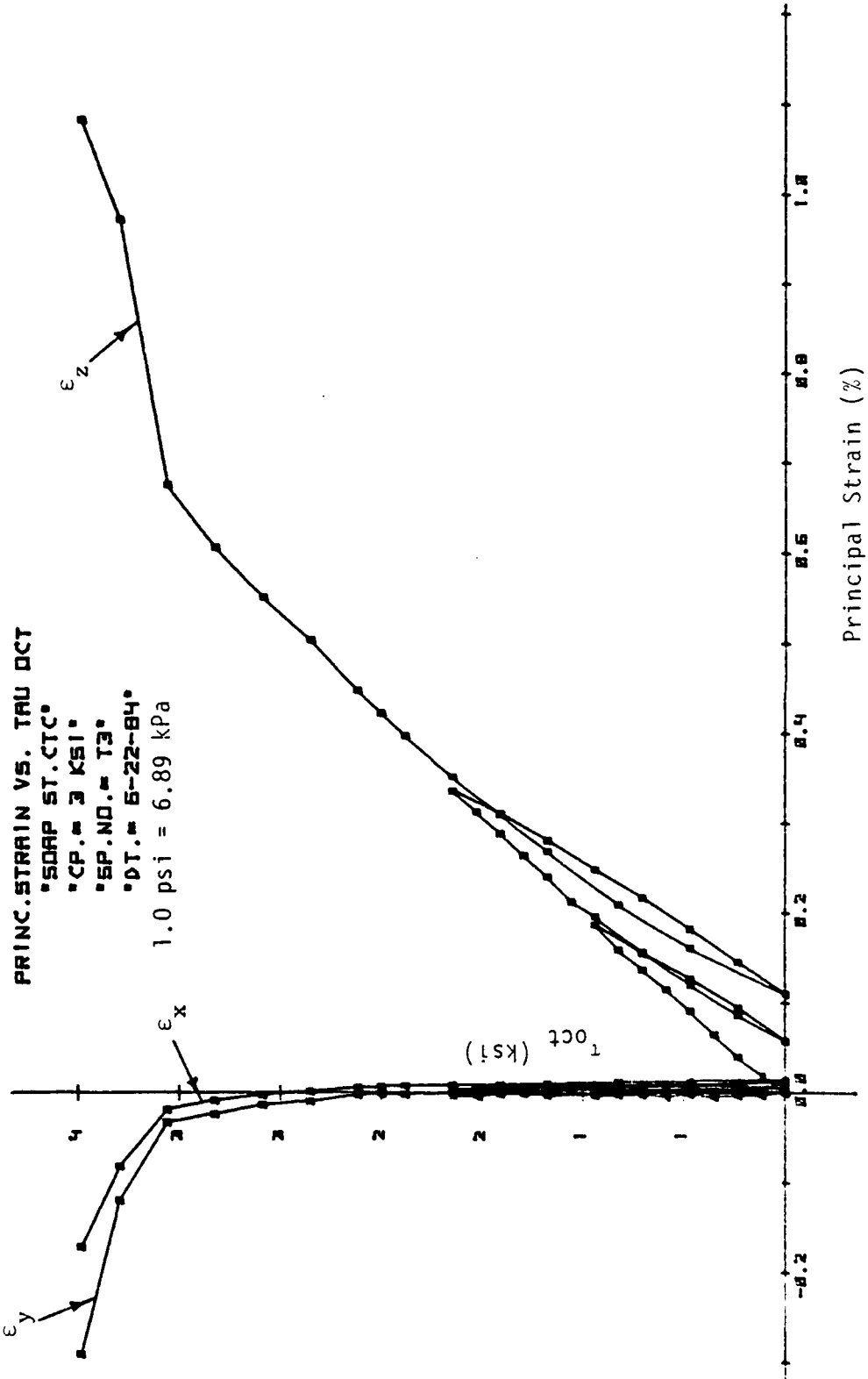

Figure 4.9. Stress-Strain Response Curves for Conventional Triaxial Compression Test.

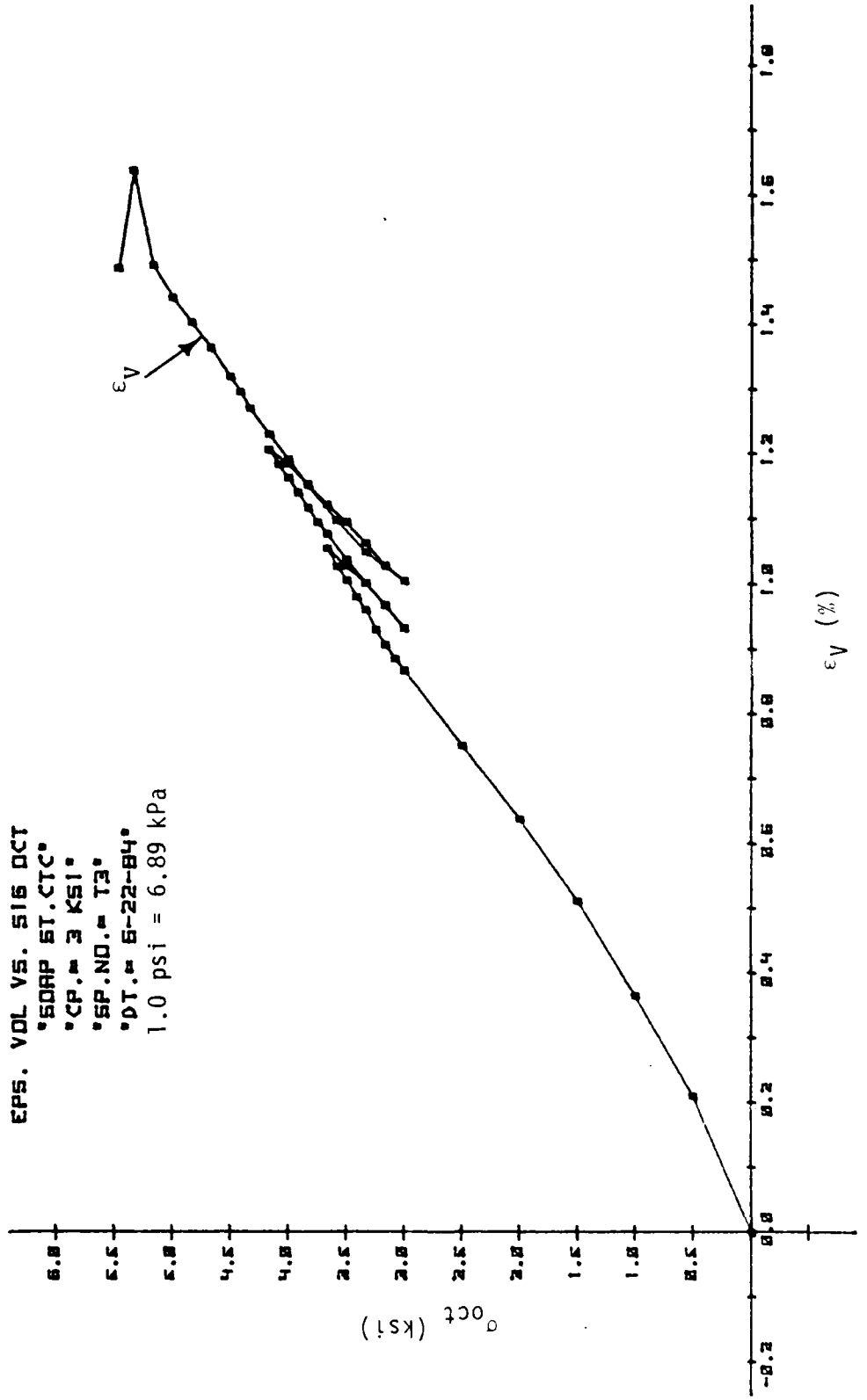

Figure 4.12. Average Stress-Volumetric Strain Response Curve for Conventional Traixial Compression Test.

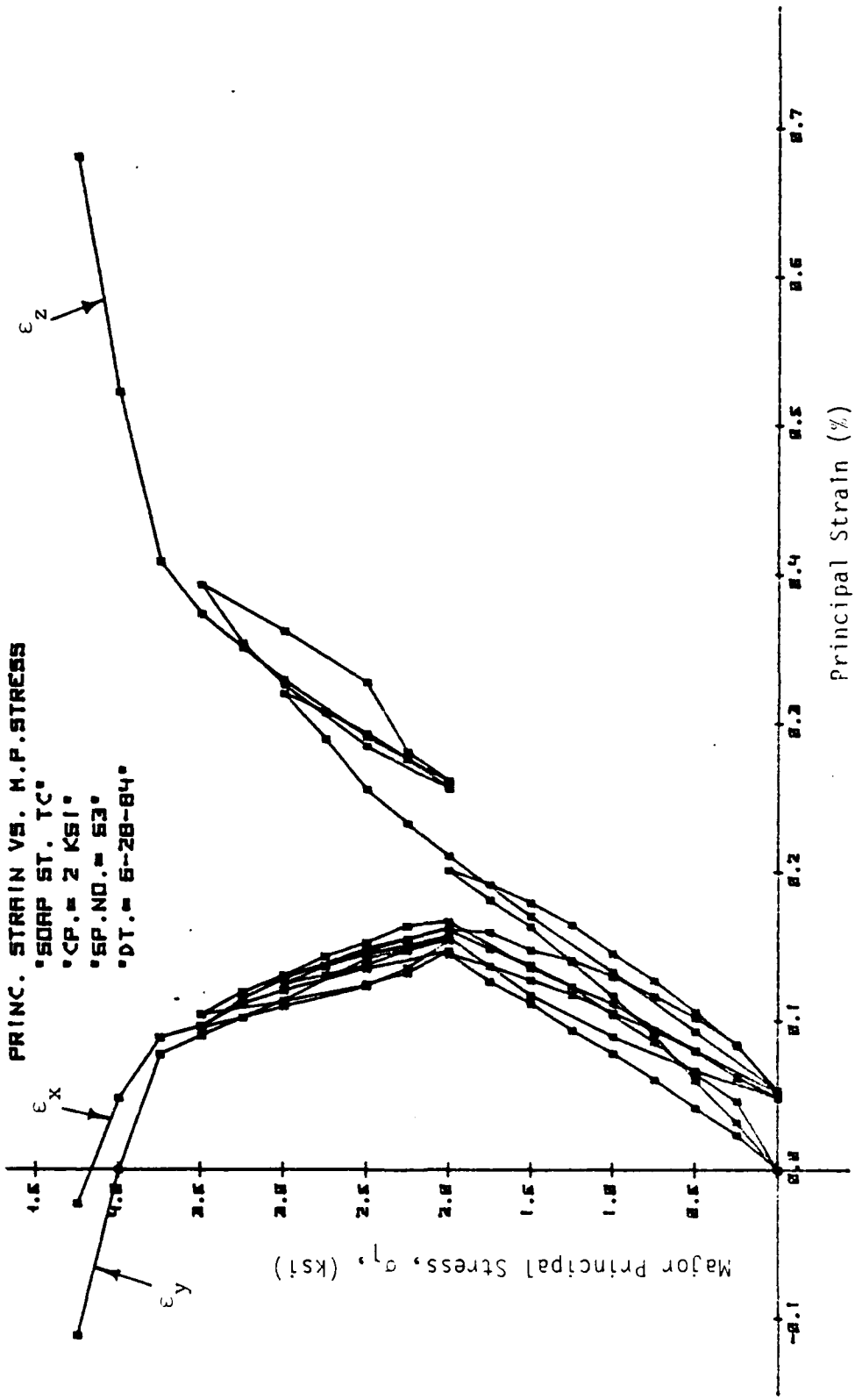

Figure 4.11. Stress-Strain Response Curves for Triaxial Compression Test.

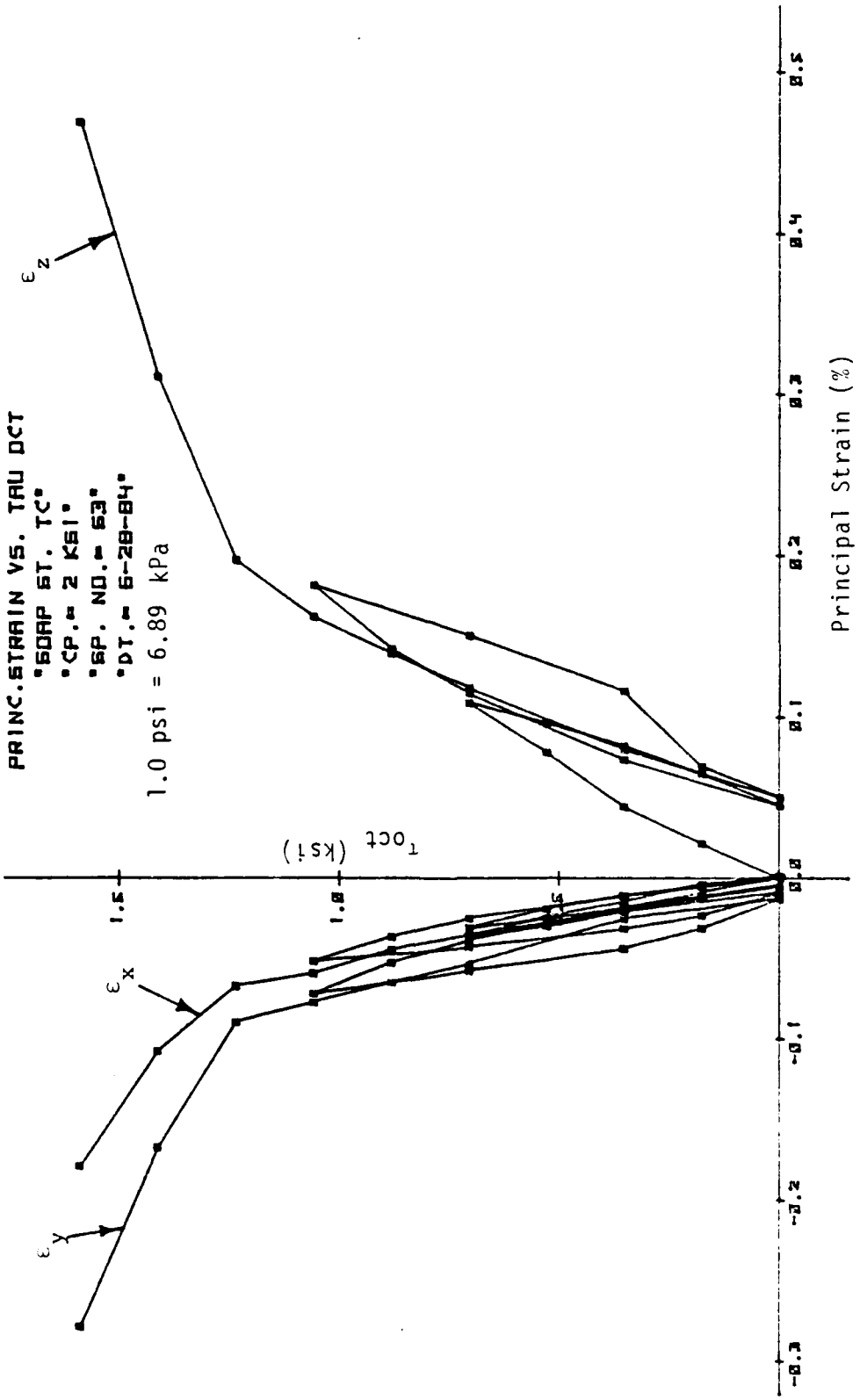

Figure 4.12. Stress-Strain Response Curves for Triaxial Compression Test.

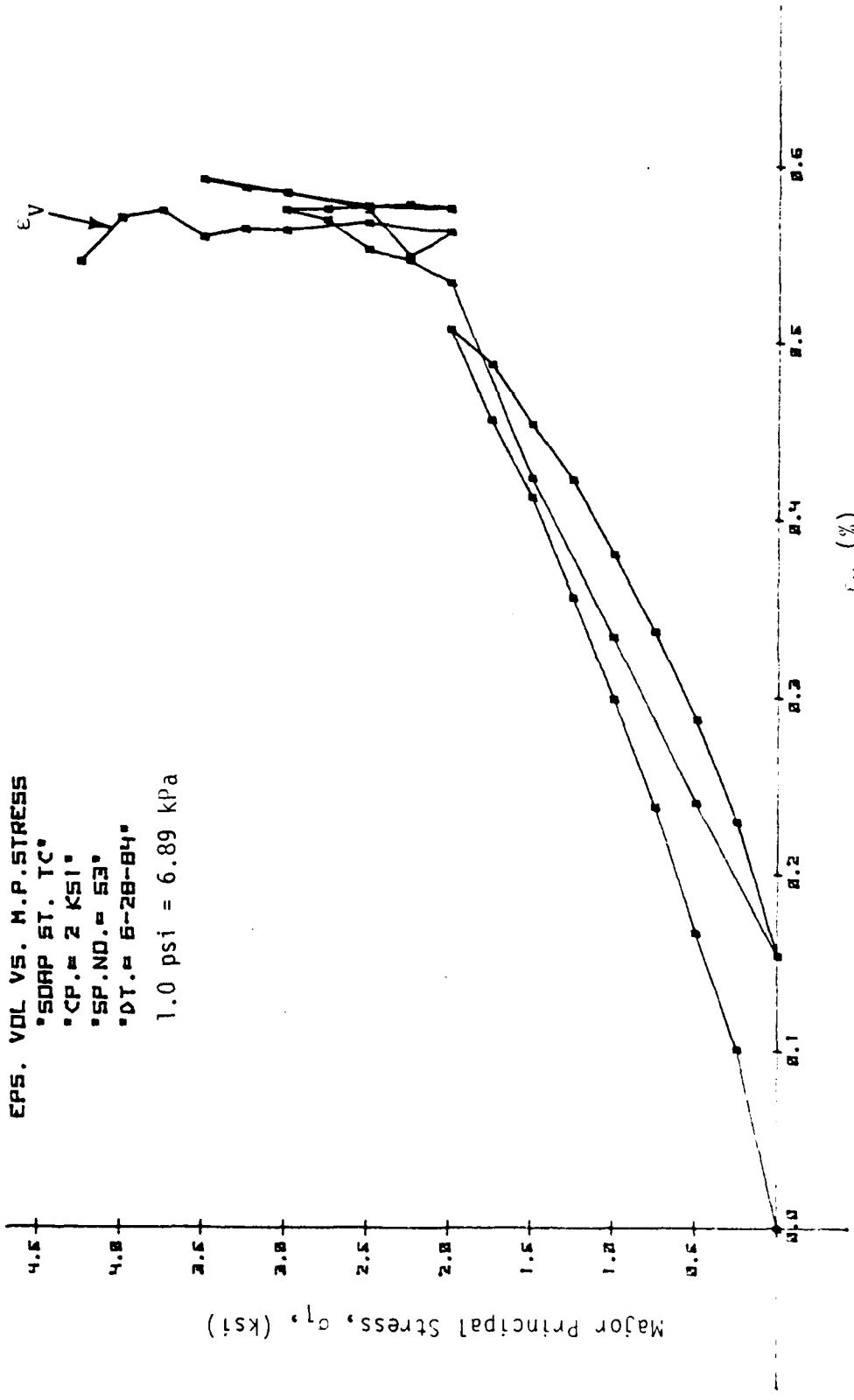

Figure 4.13. Stress-Volumetric Strain Response Curve for Triaxial Compression Test.

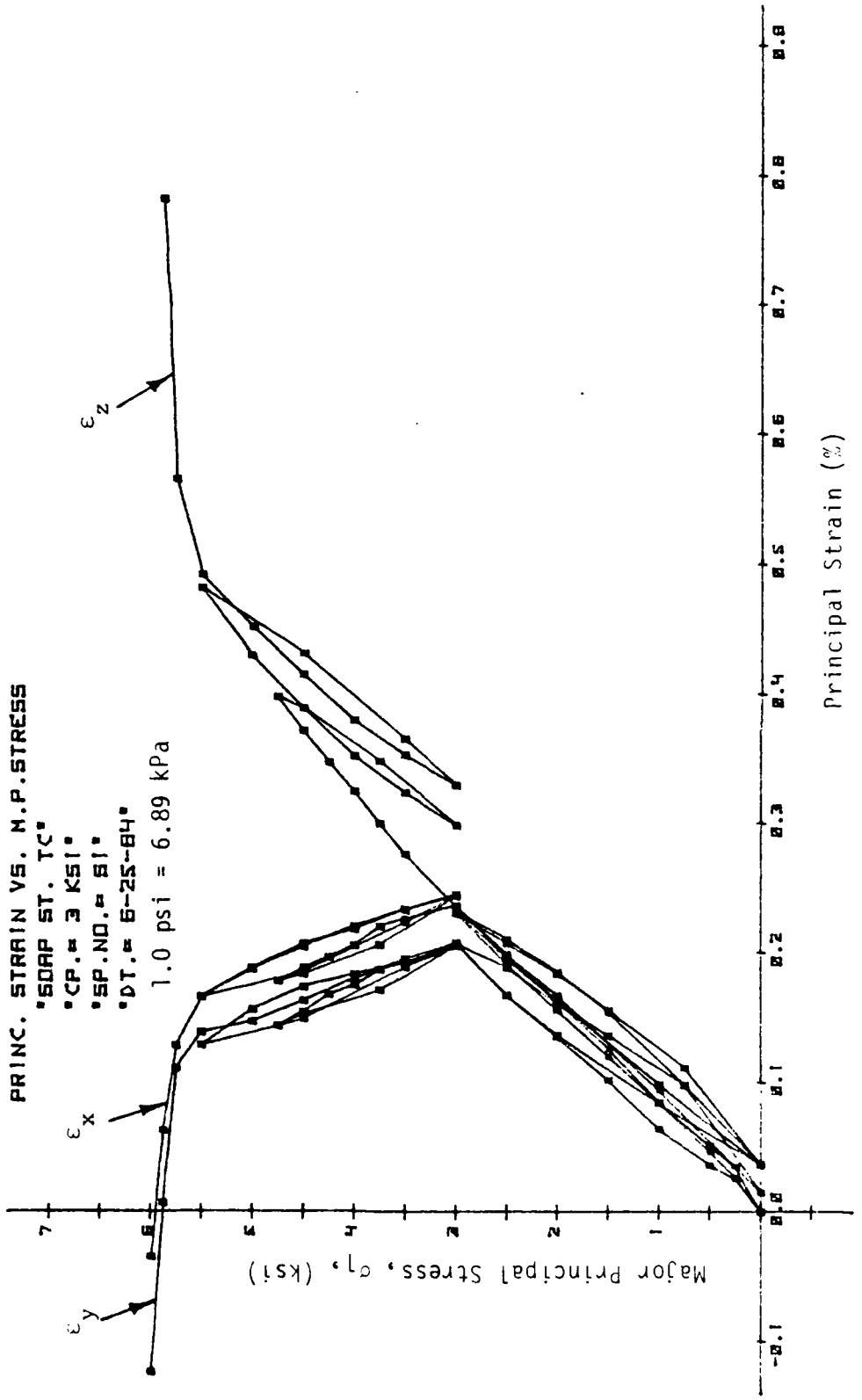

Figure 4.14. Stress-Strain Response Curves for Triaxial Compression Test.

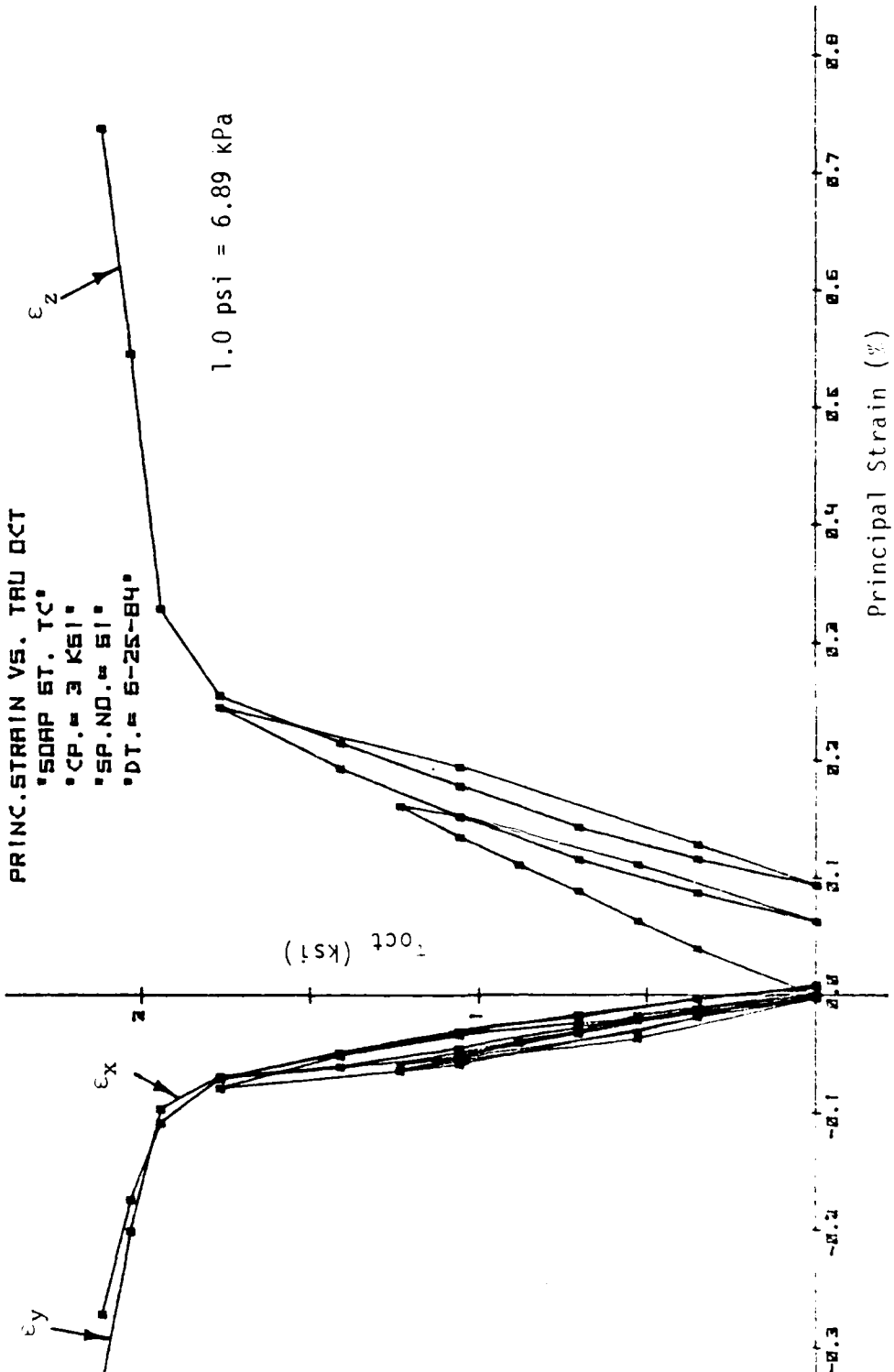

Figure 4.15. Stress-Strain Response Curves for Triaxial Compression Test.

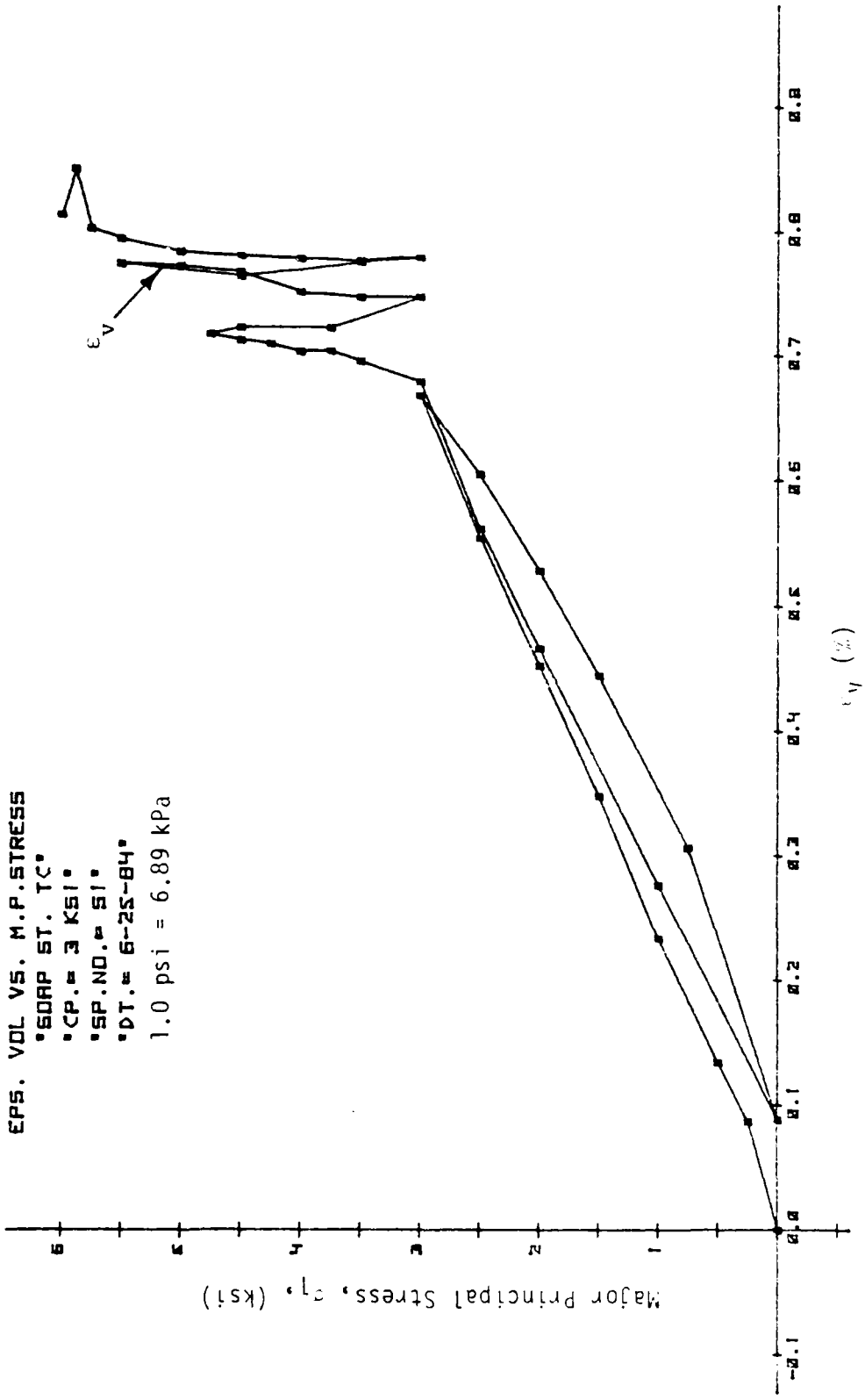

Figure 4.16. Stress-Volumetric Strain Response Curve for Triaxial Compression Test.

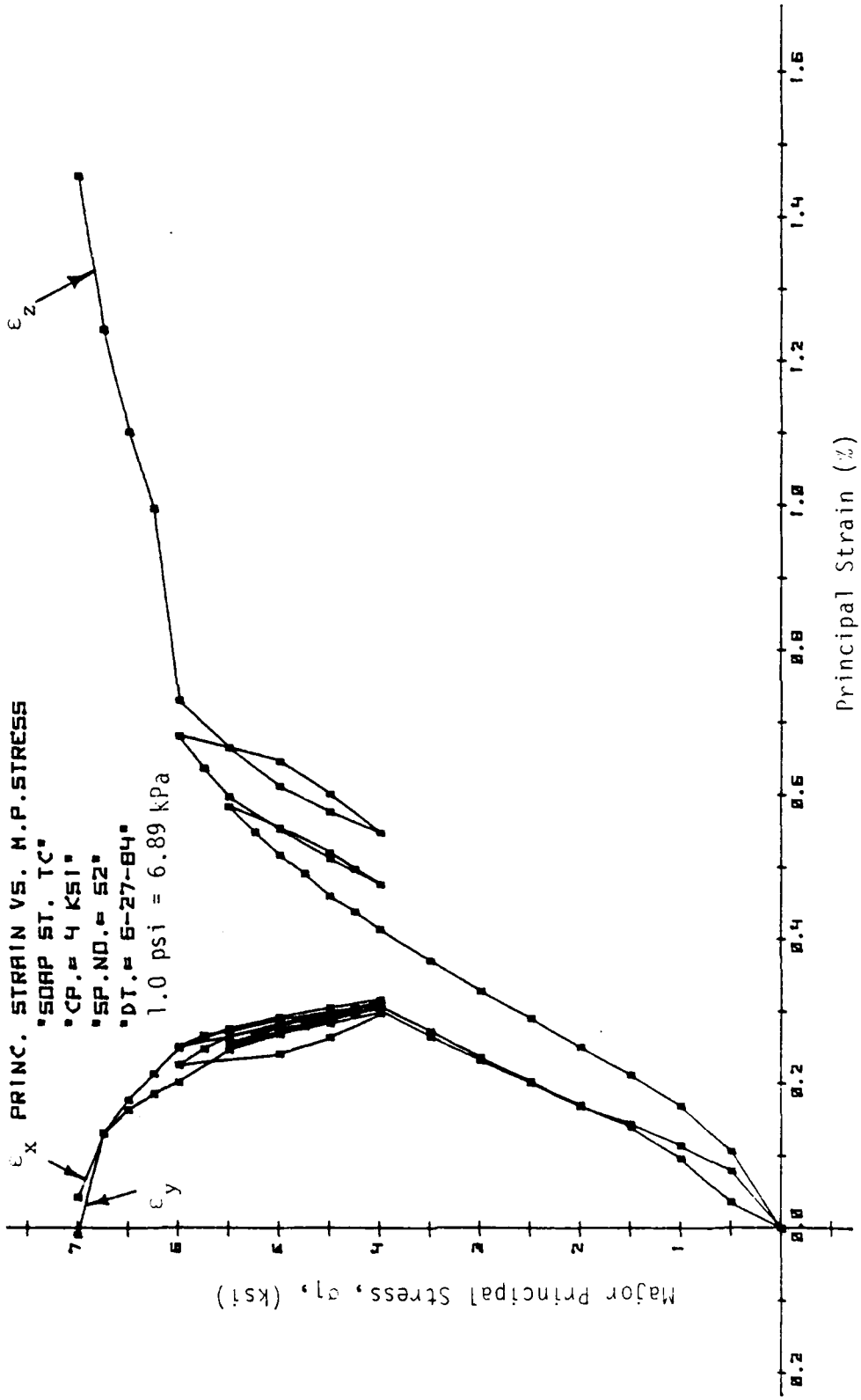

Figure 4.17. Stress-Strain Response Curves for Triaxial Compression Test.

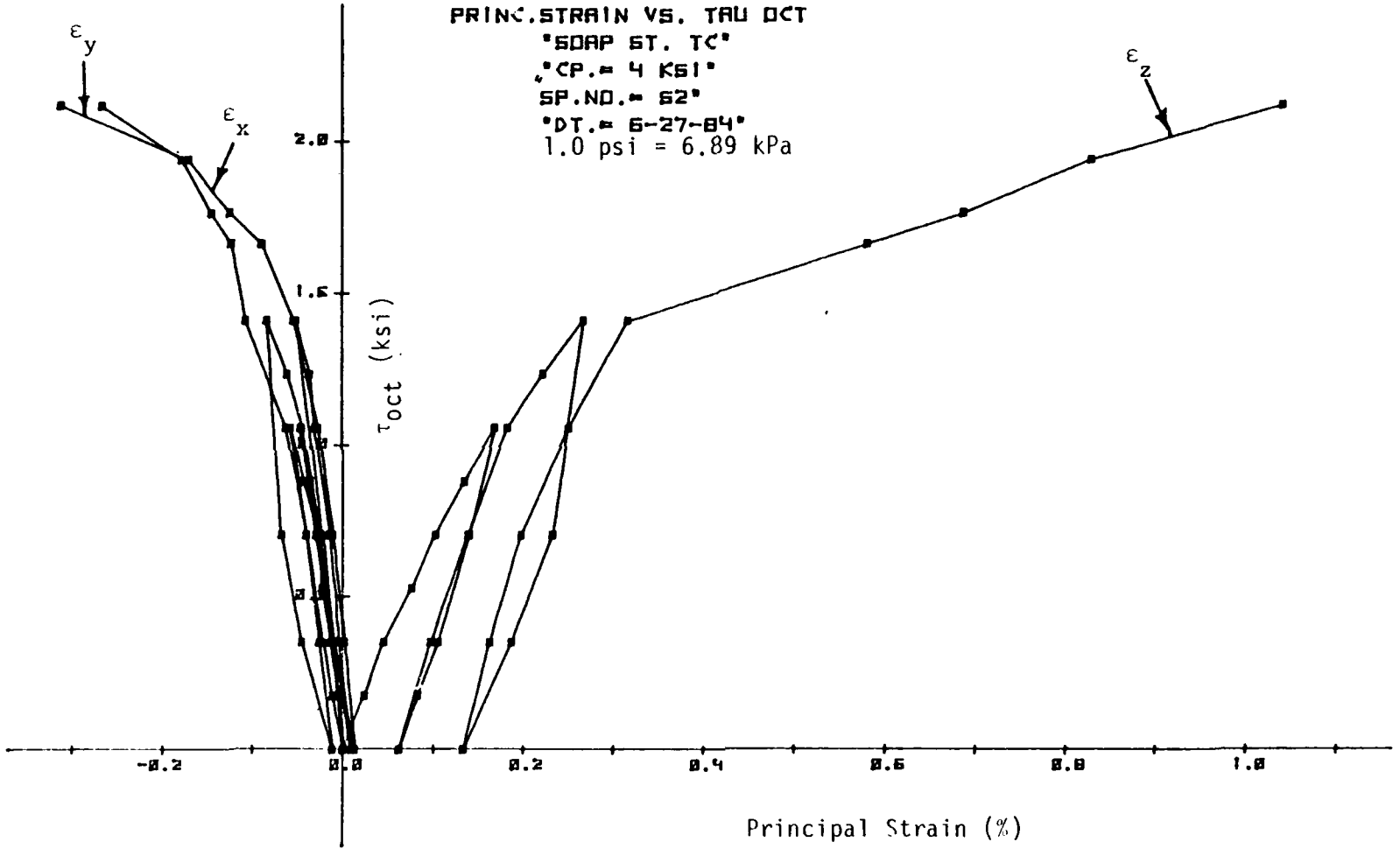

Figure 4.18. Stress-Strain Response Curves for Triaxial Compression Test.

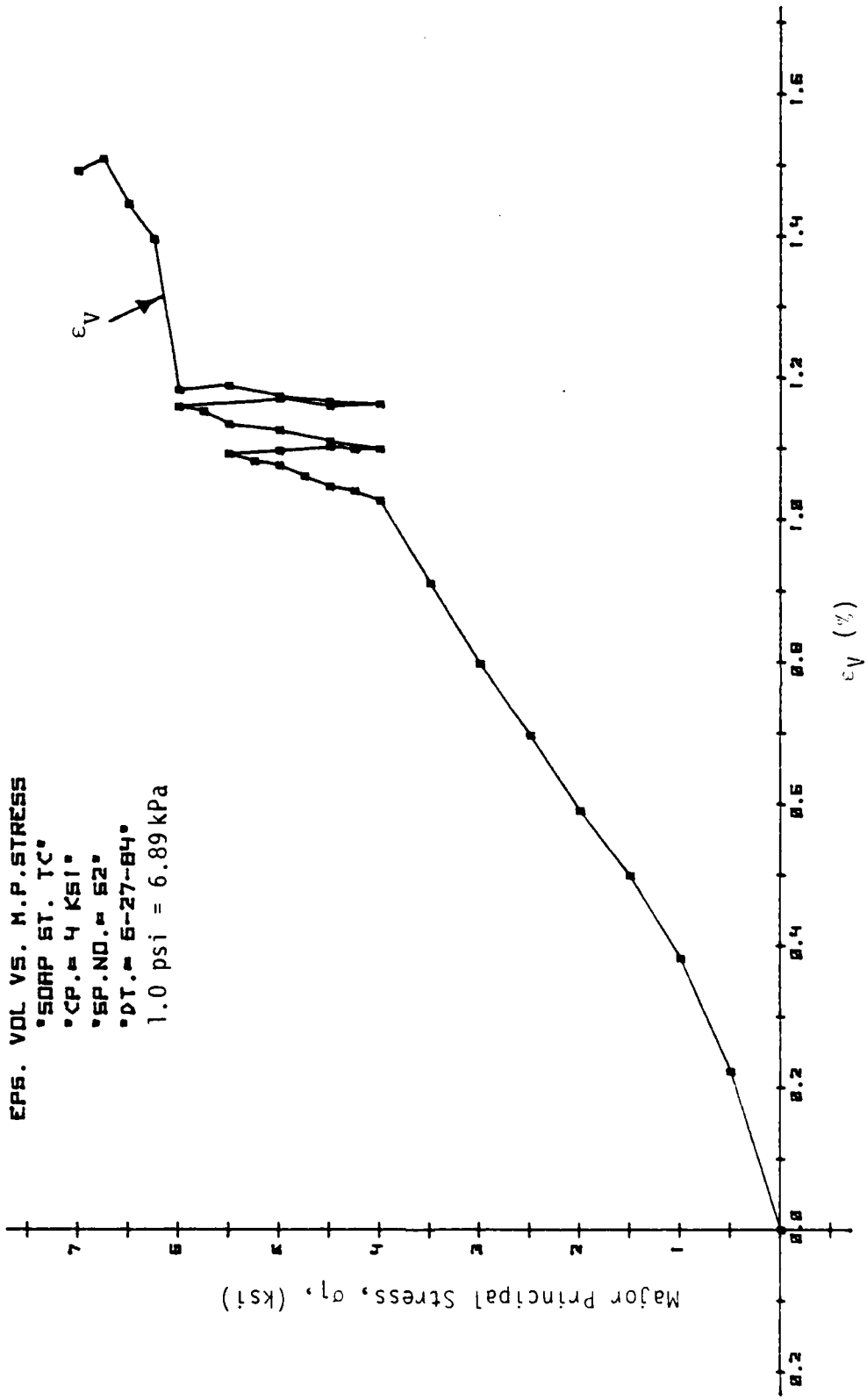

Figure 4.19. Stress-Volumetric Strain Response Curve for Compression Triaxial Test.

4.3.2 Simple Shear (SS)

Simple shear tests on soapstone samples are run with σ_o = 3.0 and 4.0 ksi (20.69 and 27.58 MPa). Intermediate principal stress (σ_2) is kept constant equal to the value of σ_o. The major and minor principal stresses σ_1 and σ_3 are increased and decreased respectively by equal amount so that σ_o remains constant. The stress-strain responses obtained from these two tests are shown in Figs. 4.20 to 4.25. In two cases it is observed that the intermediate principal strain is slightly compressive. A well-defined ultimate strength level is reached in two tests.

4.3.3 Triaxial Extension (TE)

In the TE test, σ_3 and σ_2 are increased while σ_1 is reduced to maintain σ_o at a constant level. Figures 4.26 to 4.31 show the stress-strain responses for two TE tests at σ_o = 3.0 and 4.0 ksi (20.69 and 27.58 MPa) respectively. Since σ_1 and σ_2 are equal, ε_1 and ε_2 should also be equal for isotropic behavior. One can see a good agreement between these strains from Figs. 4.26 to 4.31.

4.4 Octahedral Stress-Strain Relation

The octahedral normal and shear stresses σ_{oct} and τ_{oct}, and the octahedral normal and shear strains ε_{oct} and γ_{oct} are defined in Eqs. (3.1) in terms of principal stress and strains. The octahedral stress-strain curves obtained from CTC, TC, SS and TE tests

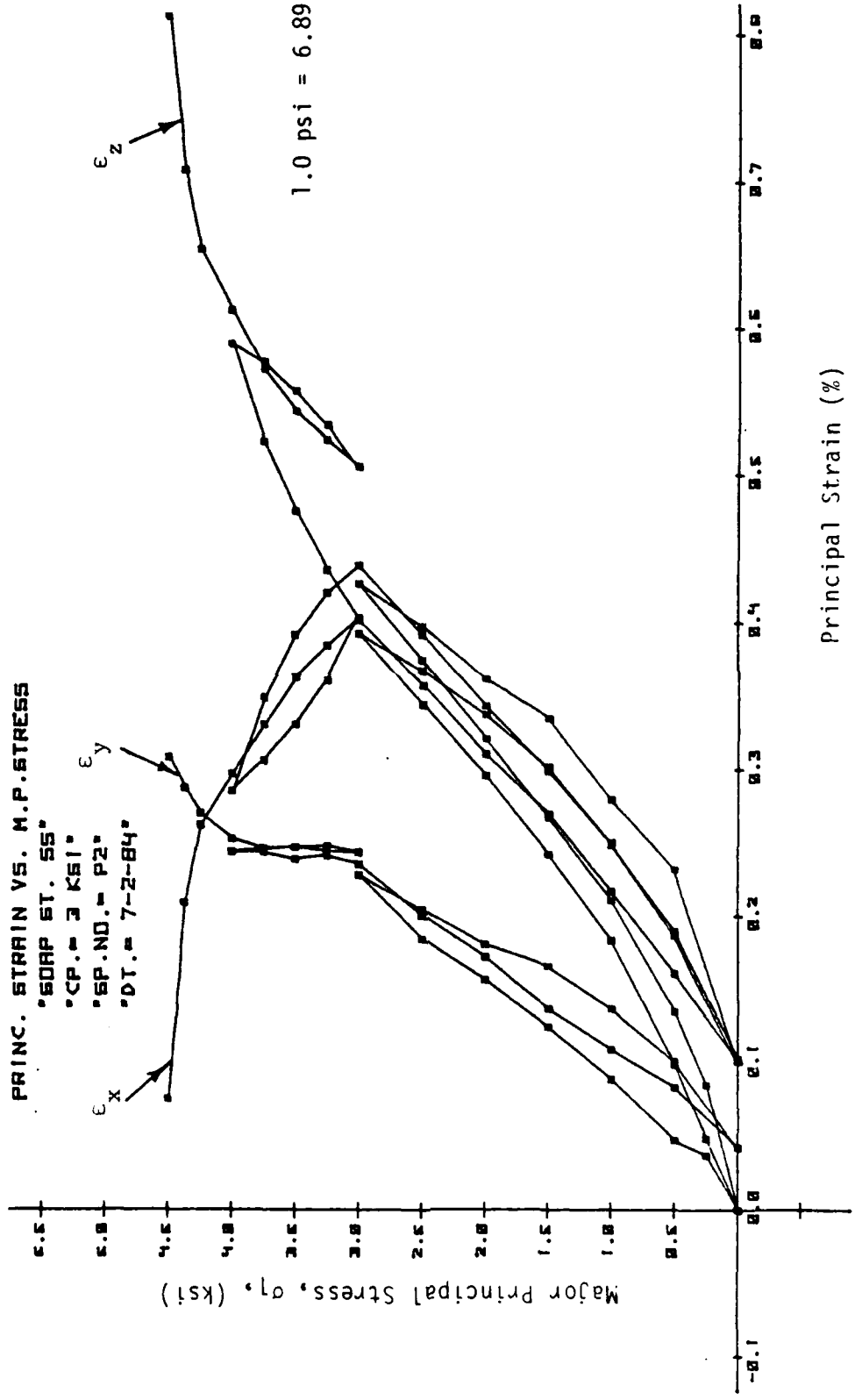

Figure 4.20. Stress-Strain Response Curves for Simple Shear Test.

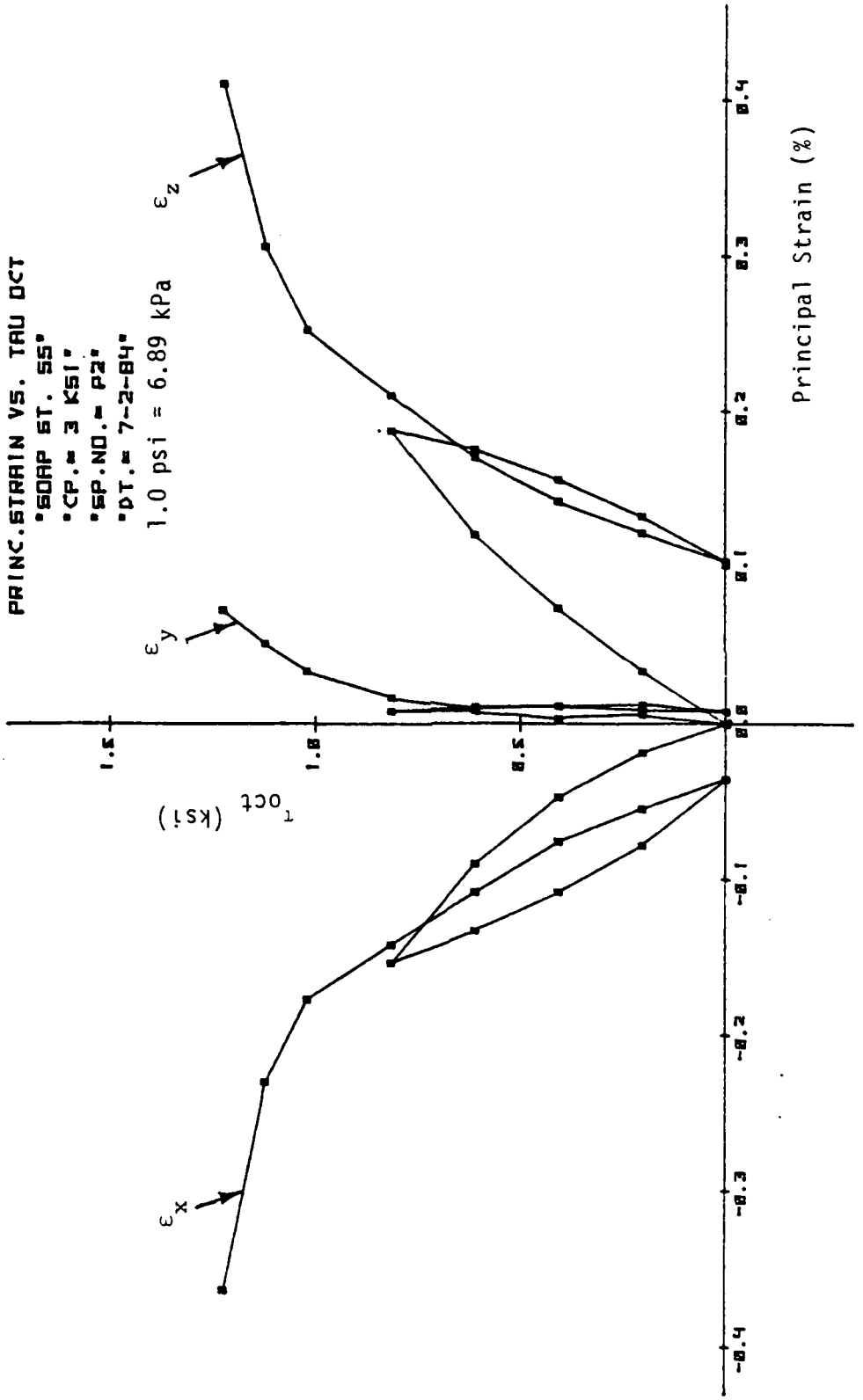

Figure 4.21. Stress-Strain Response Curves for Simple Shear Test.

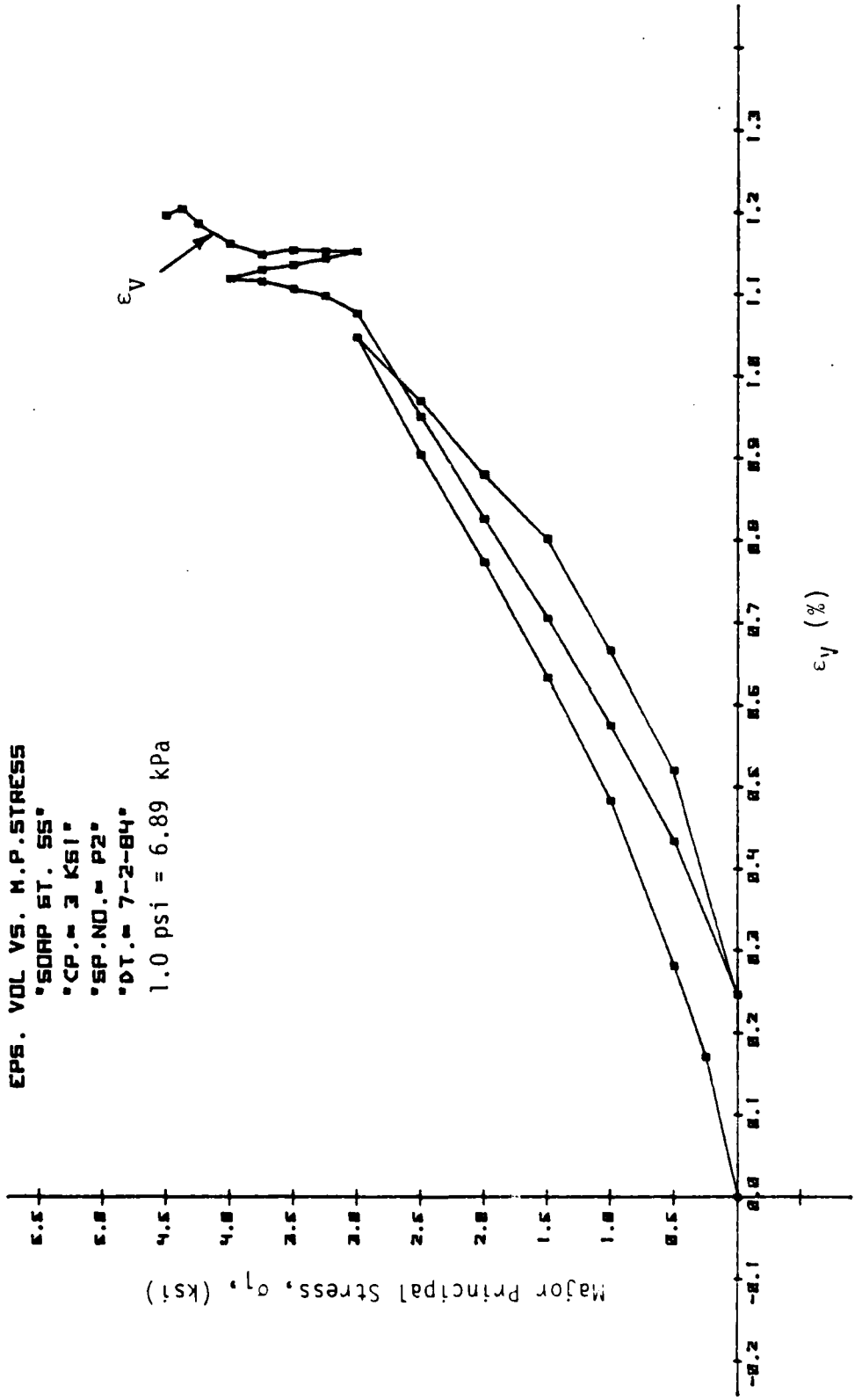

Figure 4.22. Stress-Volumetric Strain Response Curve for Simple Shear Test.

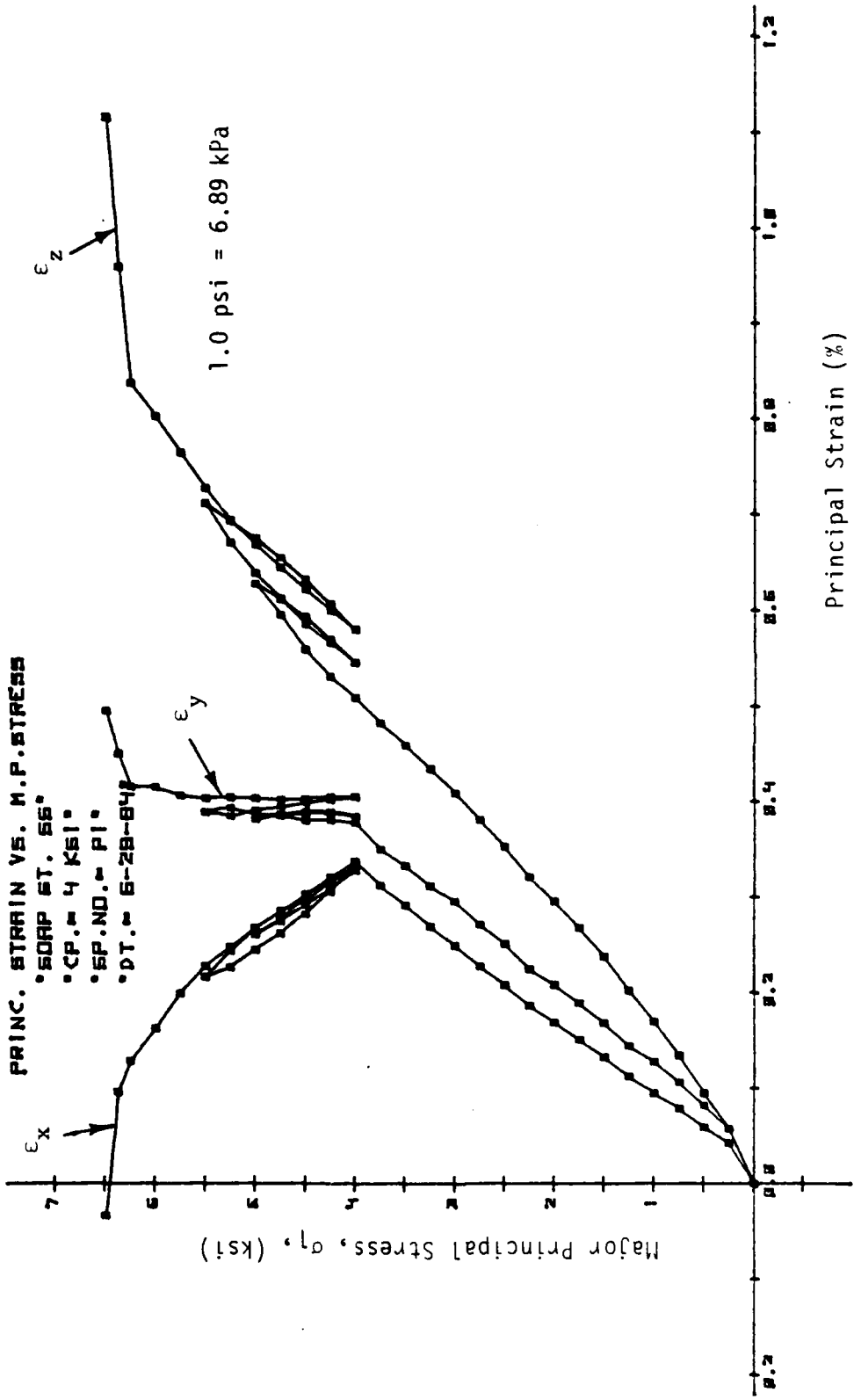

Figure 4.23. Stress-Strain Response Curves for Simple Shear Test.

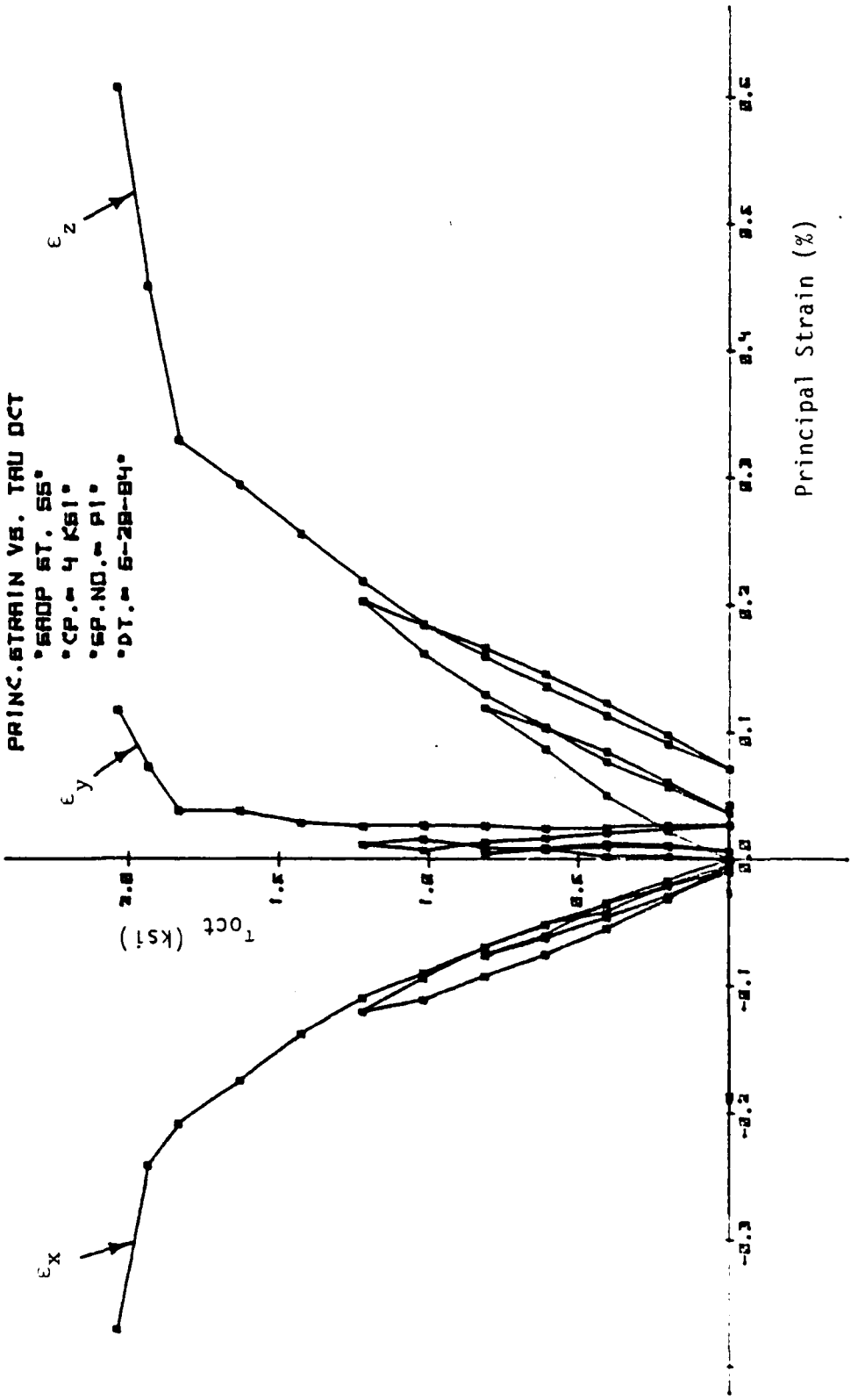

Figure 4.24. Stress-Strain Response Curves for Simple Shear Test.

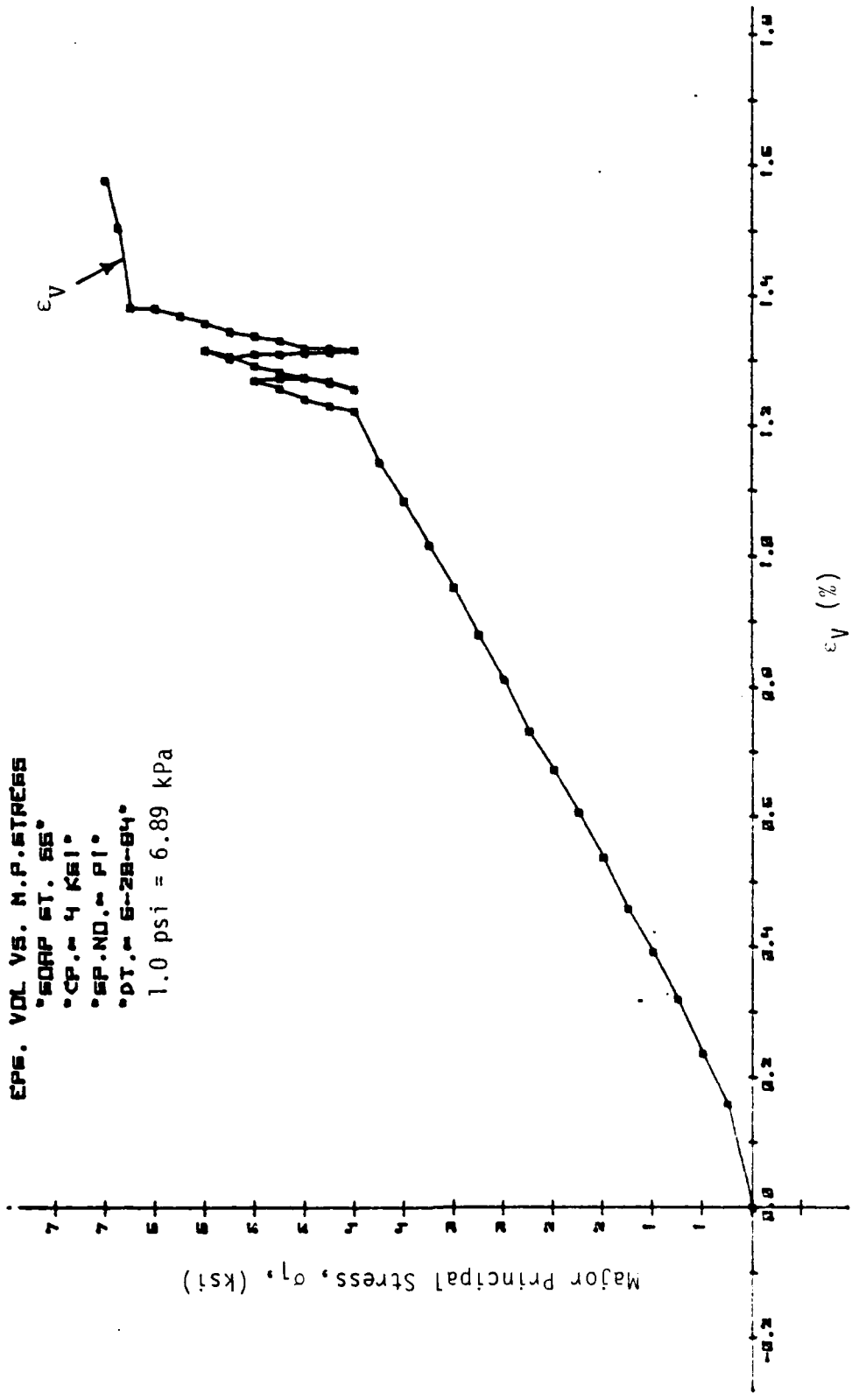

Figure 4.25. Stress-Volumetric Strain Response Curve for Simple Shear Test.

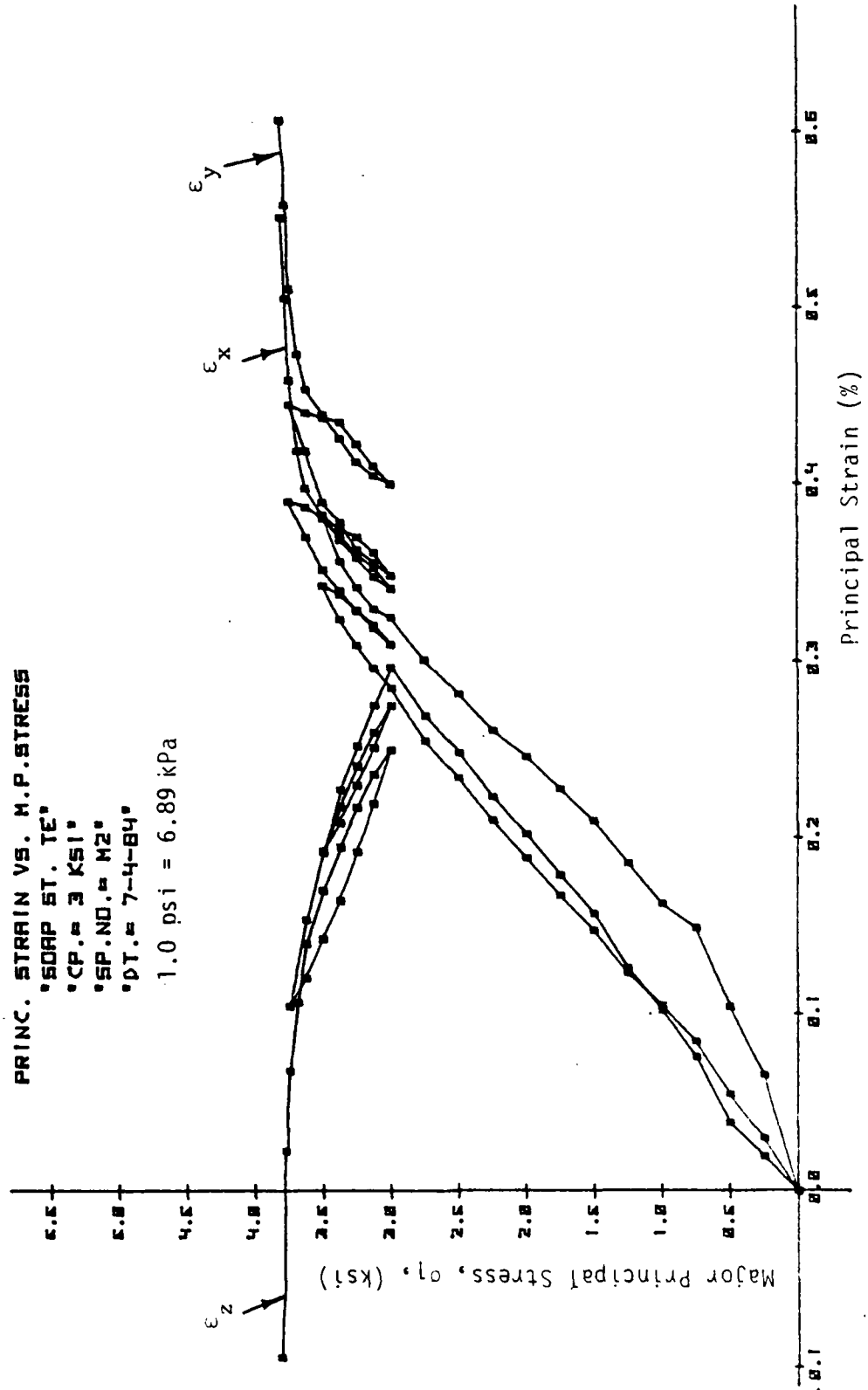

Figure 4.26. Stress-Strain Response Curves for Triaxial Extension Tests.

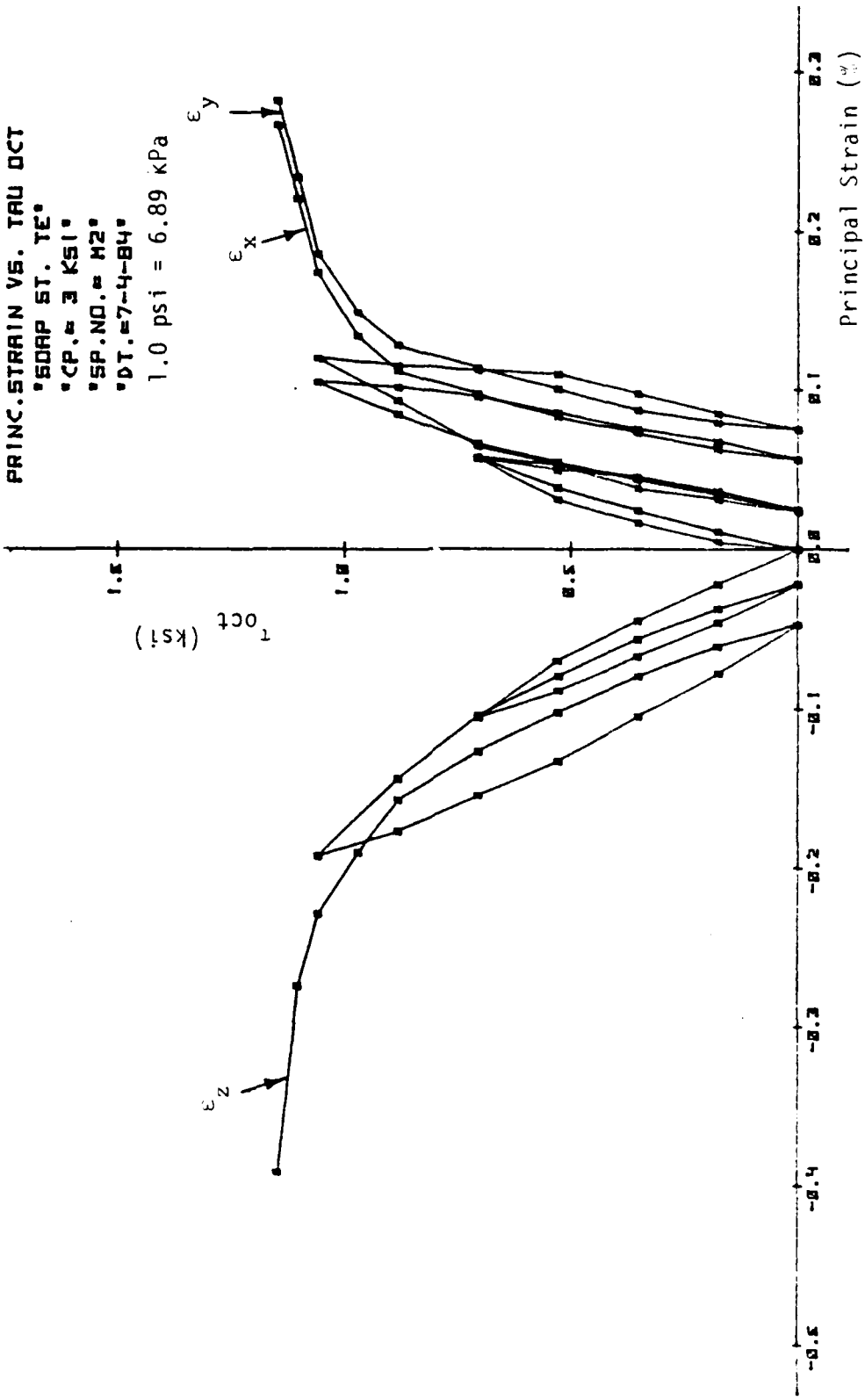

Figure 4.27. Stress-Strain Response Curves for Triaxial Extension Test.

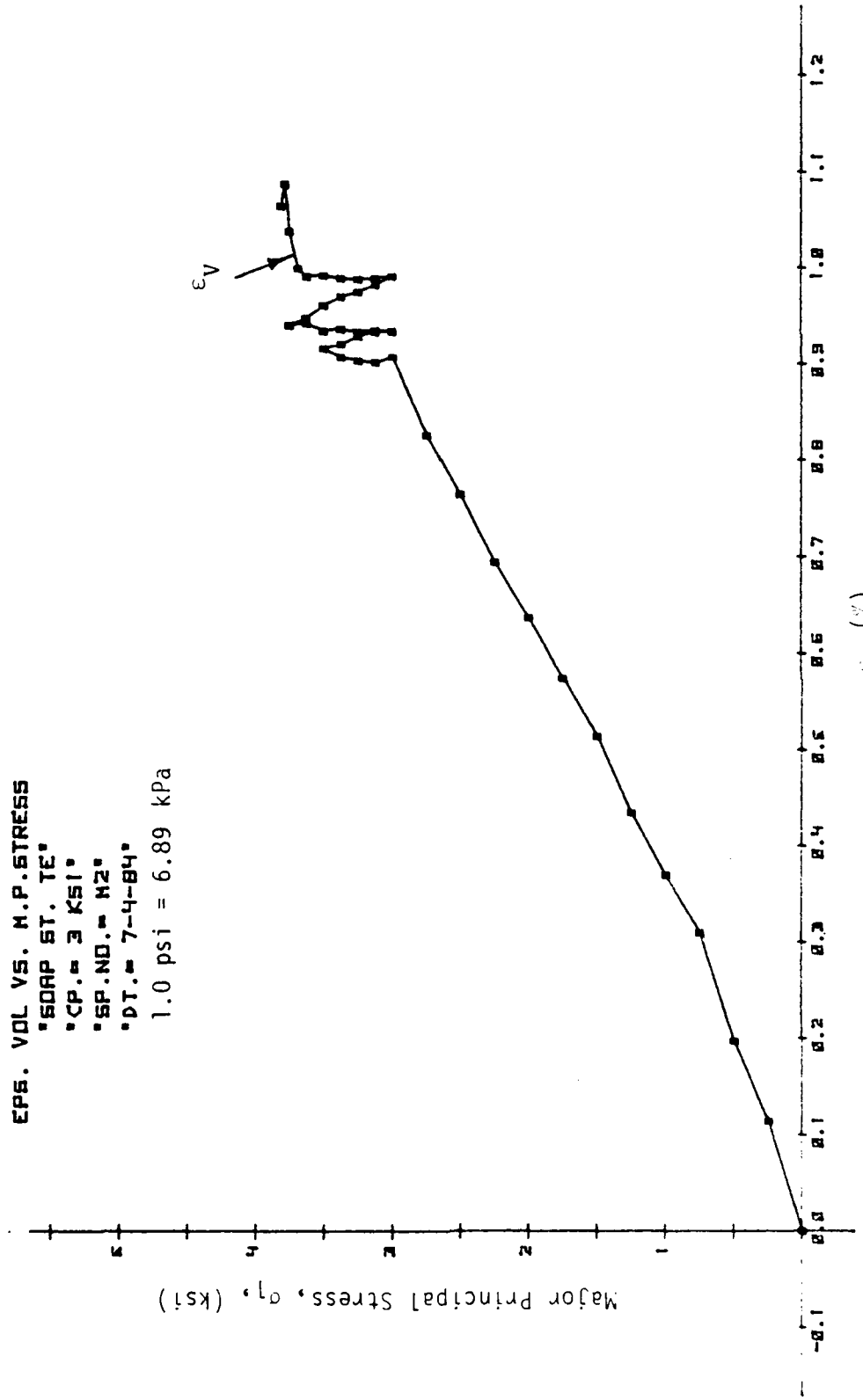

Figure 4.28. Stress-Volumetric Strain Response Curve for Triaxial Extension Test.

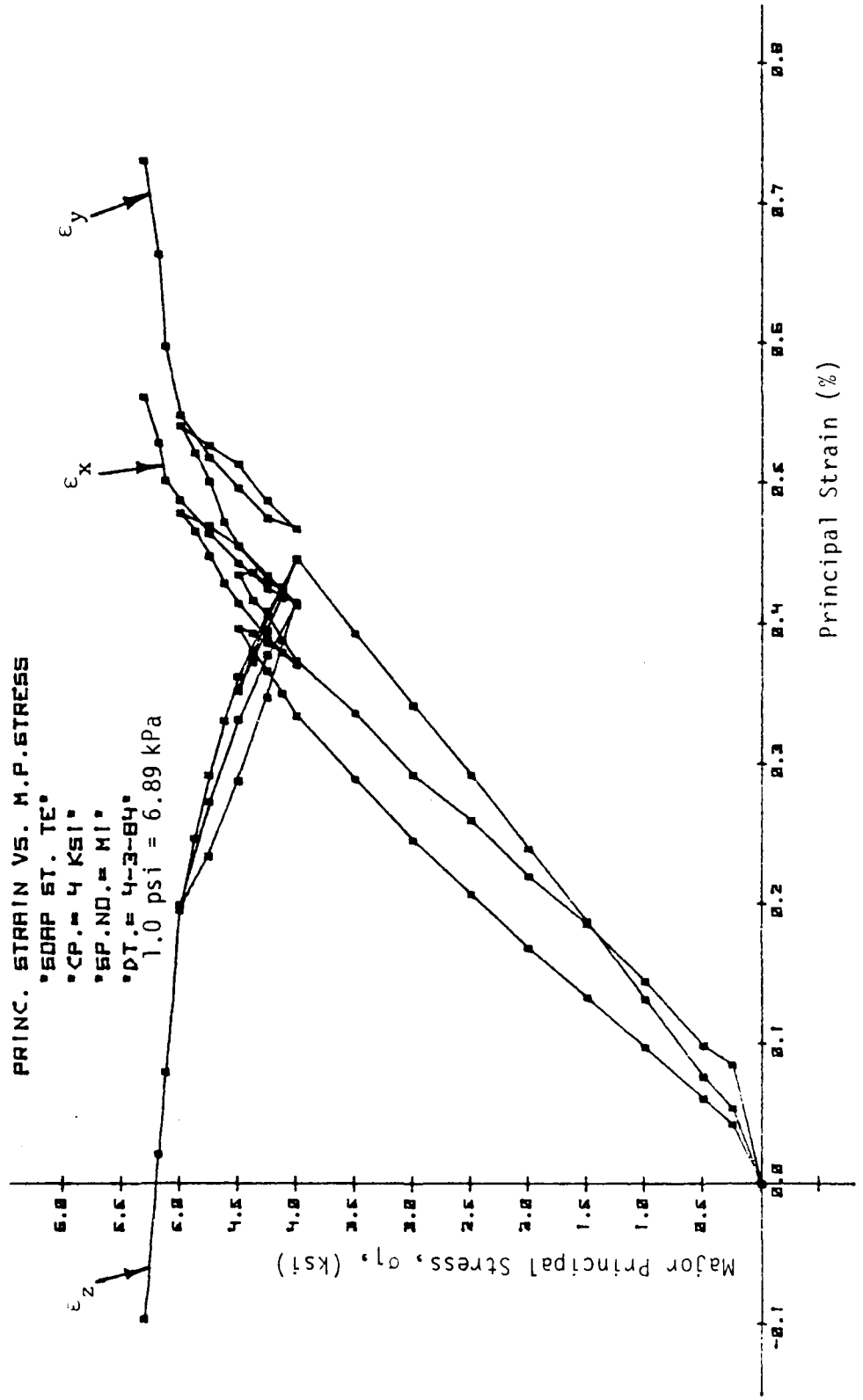

Figure 4.29. Stress-Strain Response Curves for Triaxial Extension Test.

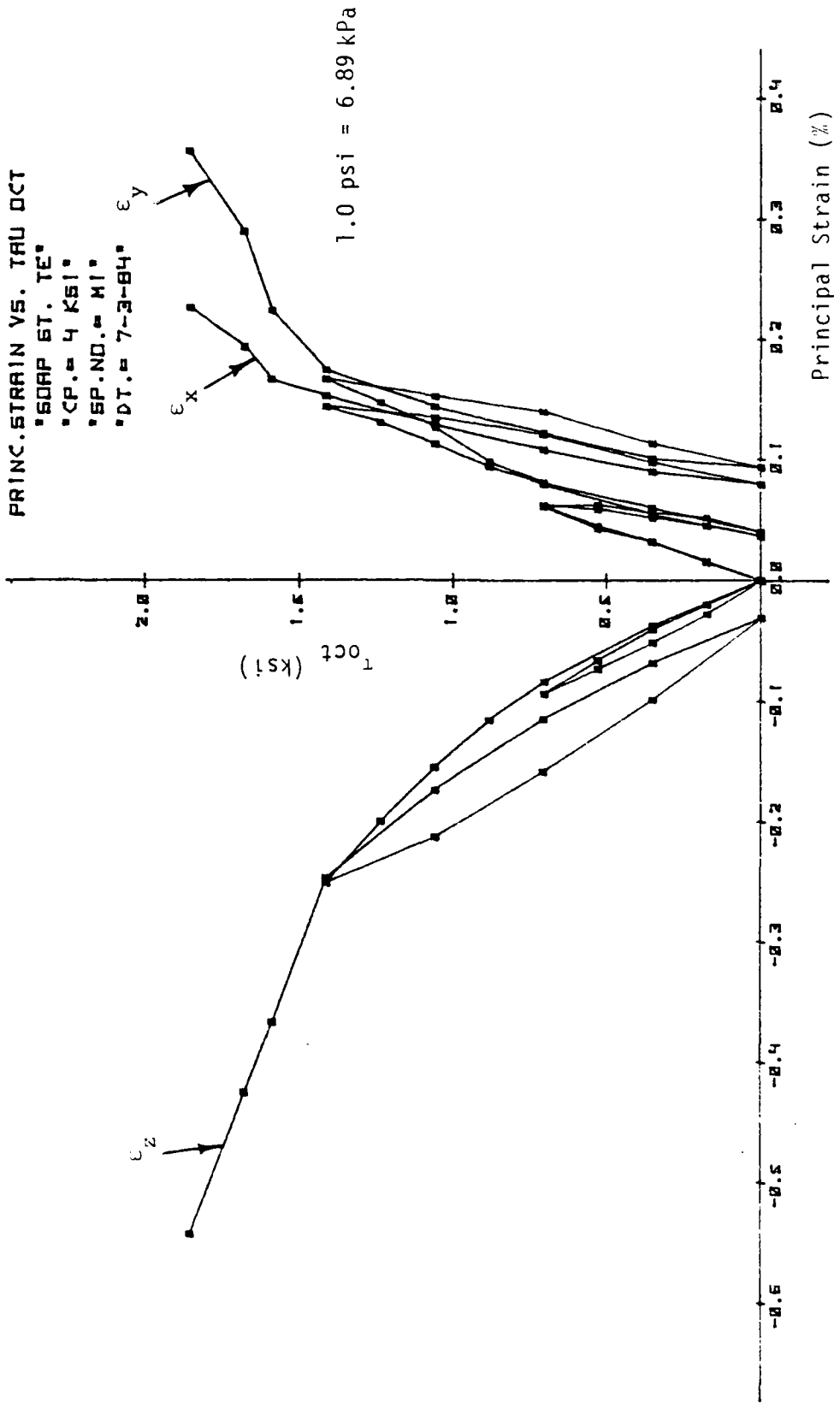

Figure 4.30. Stress-Strain Response Curves for Triaxial Extension Test.

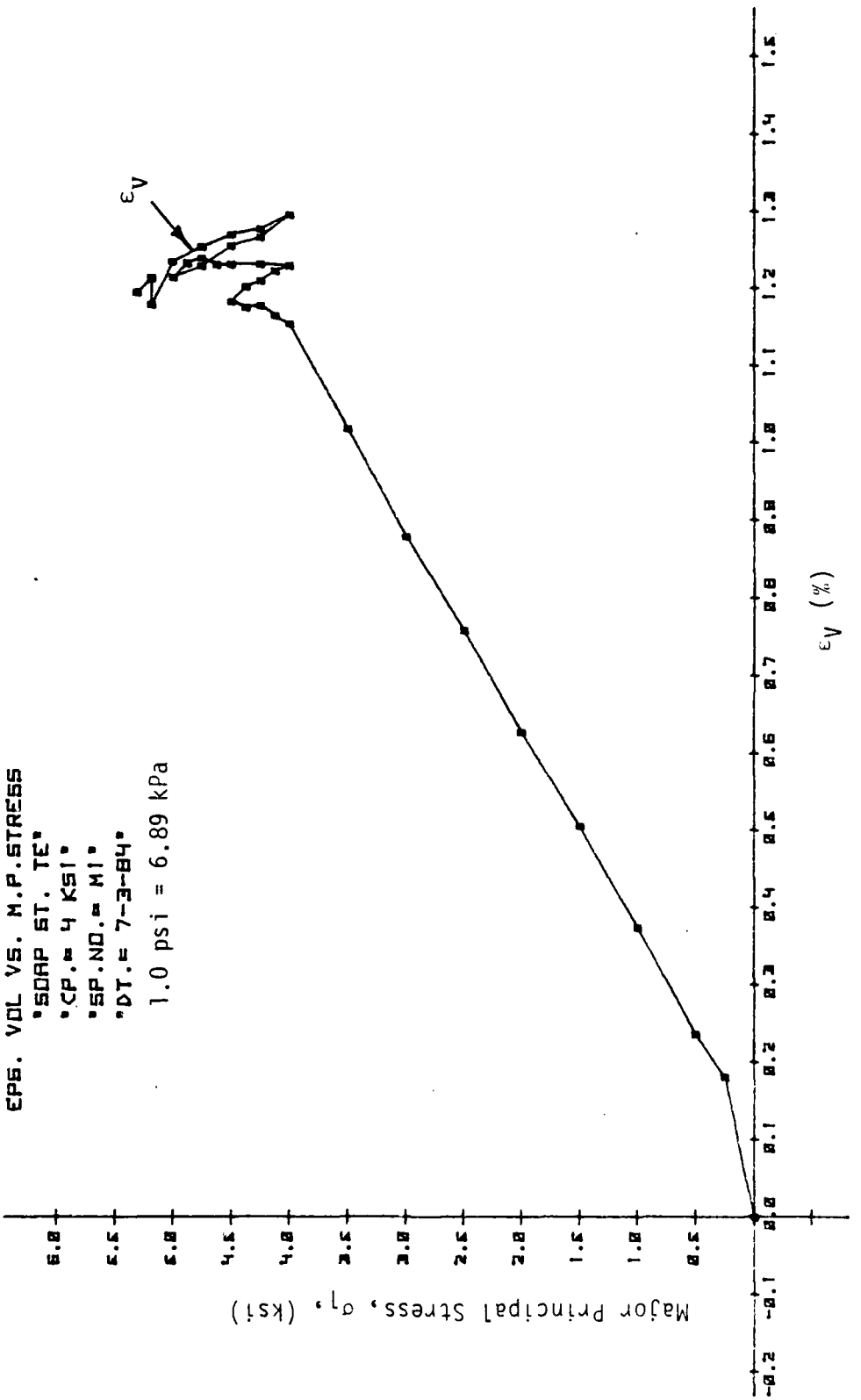

Figure 4.31. Stress-Volumetric Strain Response Curve for Triaxial Extension Test.

are plotted individually in Figs. 4.32 to 4.40. The slope of the τ_{oct} and γ_{oct} curve is two times shear modulus G. The average shear modulus, G, is determined from these tests to be 614.99 ksi (4240.4 MPa).

4.5 Circular Stress Path (CSP

Figure 4.41 show the stress-strain responses for circular stress path (csp) test at confining pressure of 4.0 ksi (27.58 MPa) and octahedral shear stress, τ_{oct}, of 1.0 ksi (6.895 MPa). The graph of this circular path shows the major principal stress σ_1, plotted against the three principal strains. Figure 4.42 shows the three principal strains plotted aggainst the angle of similarity Θ_{oct}.

4.6 Ultimate Failure (Strength)

The ultimate condition is defined by asymplotic value of the stress in the stress-strain response curve, as shown in Fig. 3.49 of the 15 specimens tested, 13 reached failure. TABLE 4.1 lists the ultimate data for these specimens. Failed samples are shown in APPENDIX B. Figures 4.43 to 4.45 show the plots of data in $J_1 - \sqrt{J_{2D}}$, octahedral and triaxial planes, respectively.

Several conclusions can be drawn from examination of the strength results shown in Figs. 4.43 to 4.45.

i) The octahedral shear strength of soapstone specimens is strongly dependent upon the stress path (Θ or J_3), (see Fig. 4.43).

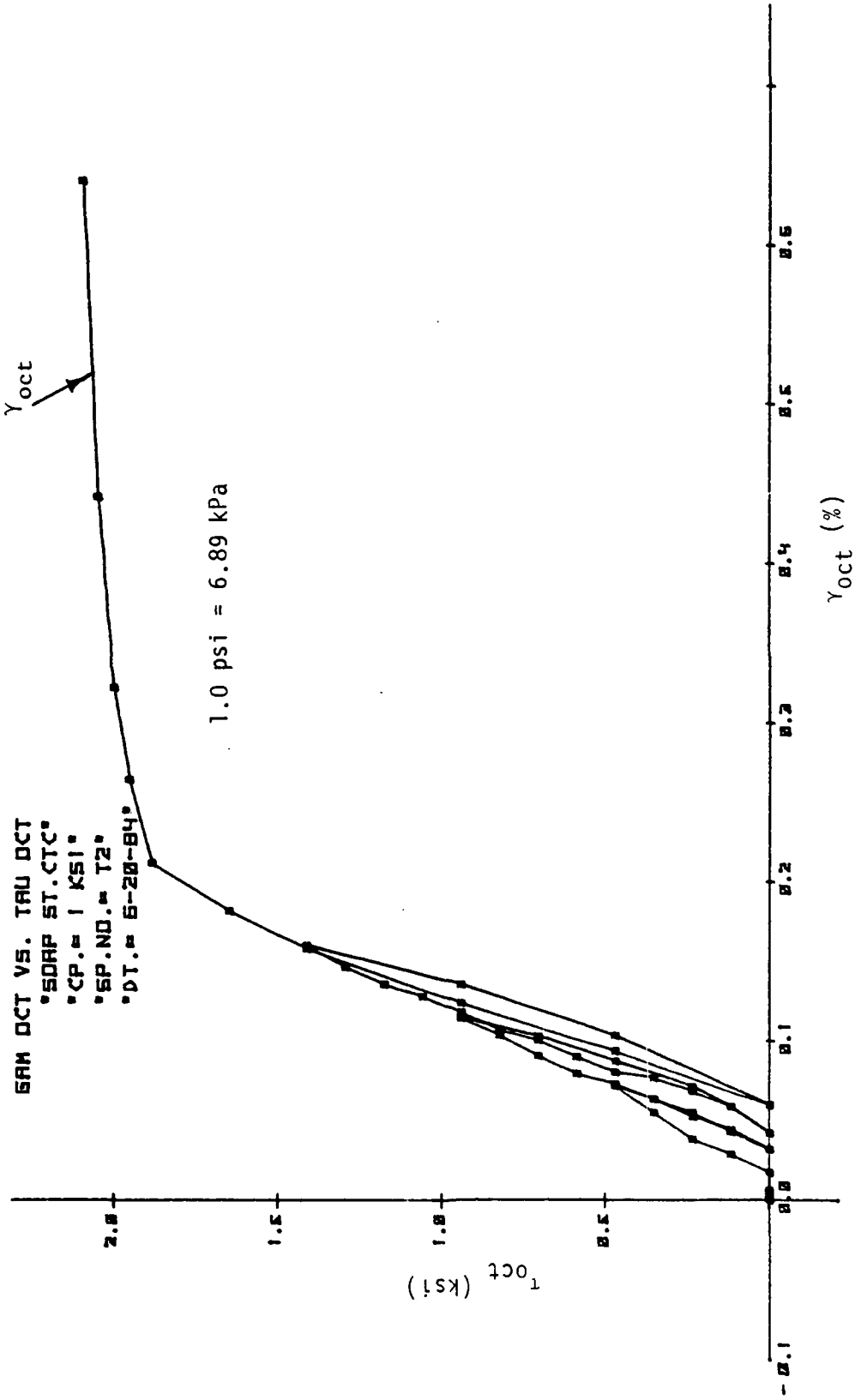

Figure 4.32. Octahedral Stress-Strain Response Curve for Conventional Triaxial Compression Test.

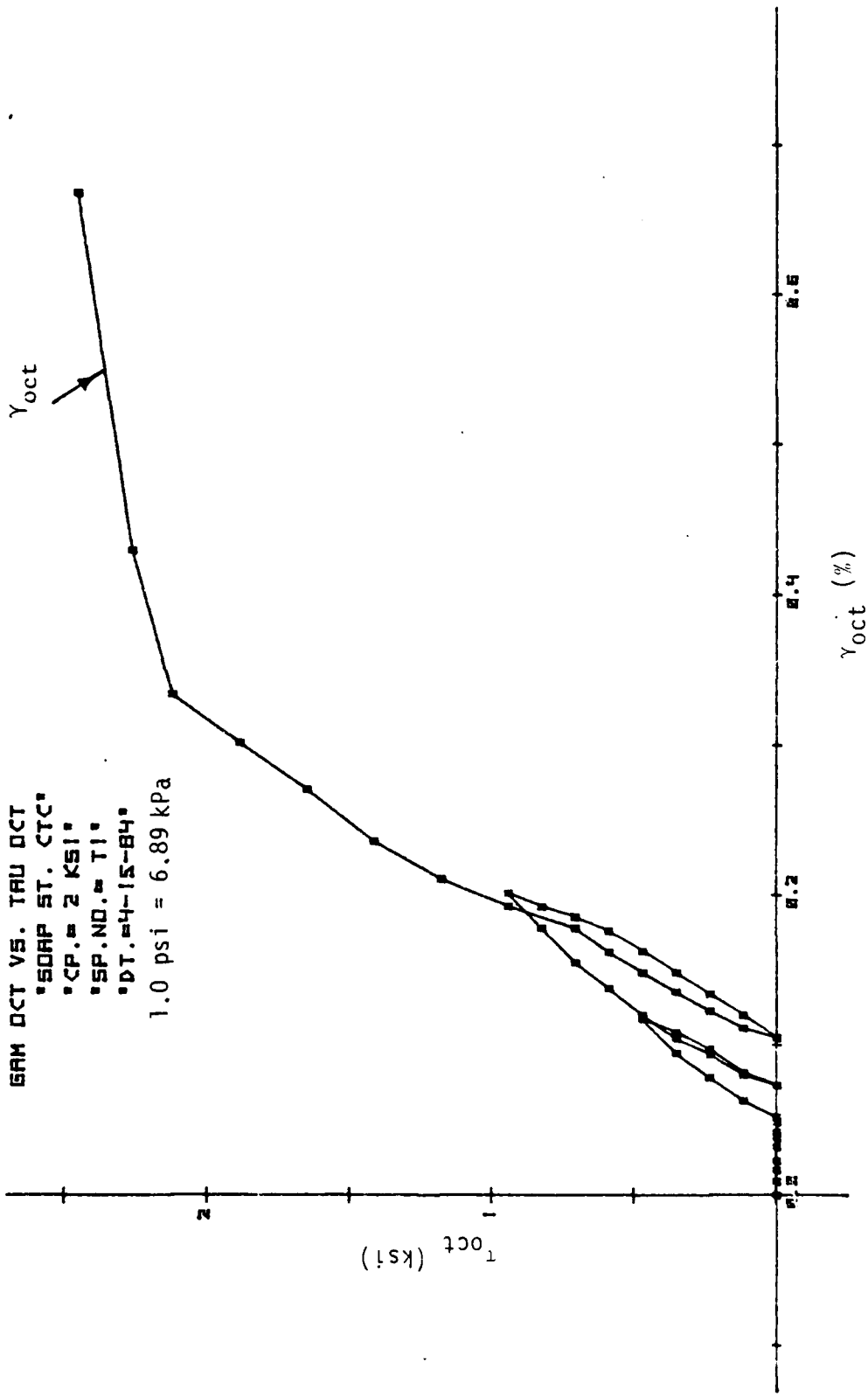

Figure 4.33. Octahedral Stress-Strain Response Curve for Conventional Triaxial Compression Test.

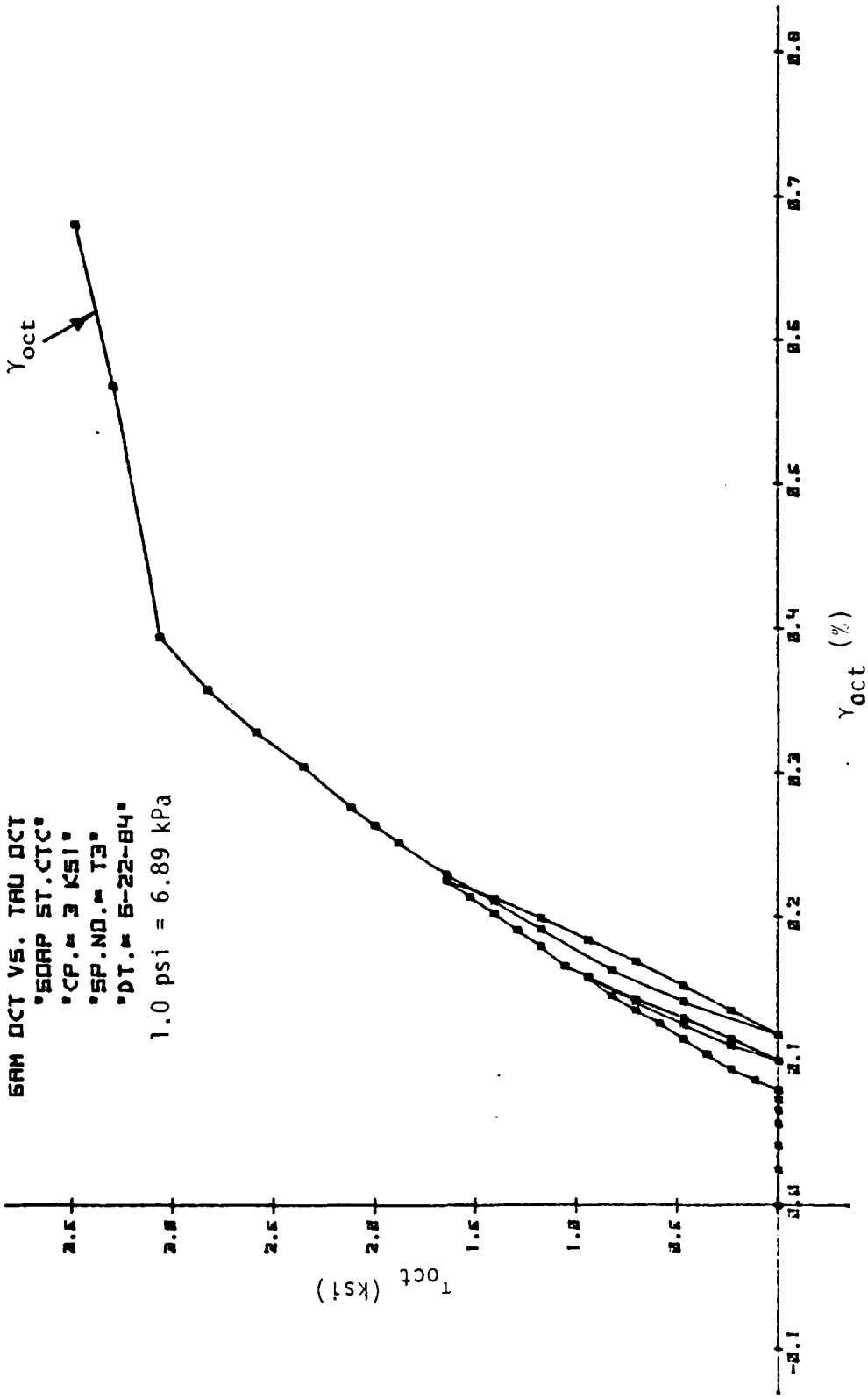

Figure 4.34. Octahedral Stress-Strain Response Curve for Conventional Triaxial Compression Test.

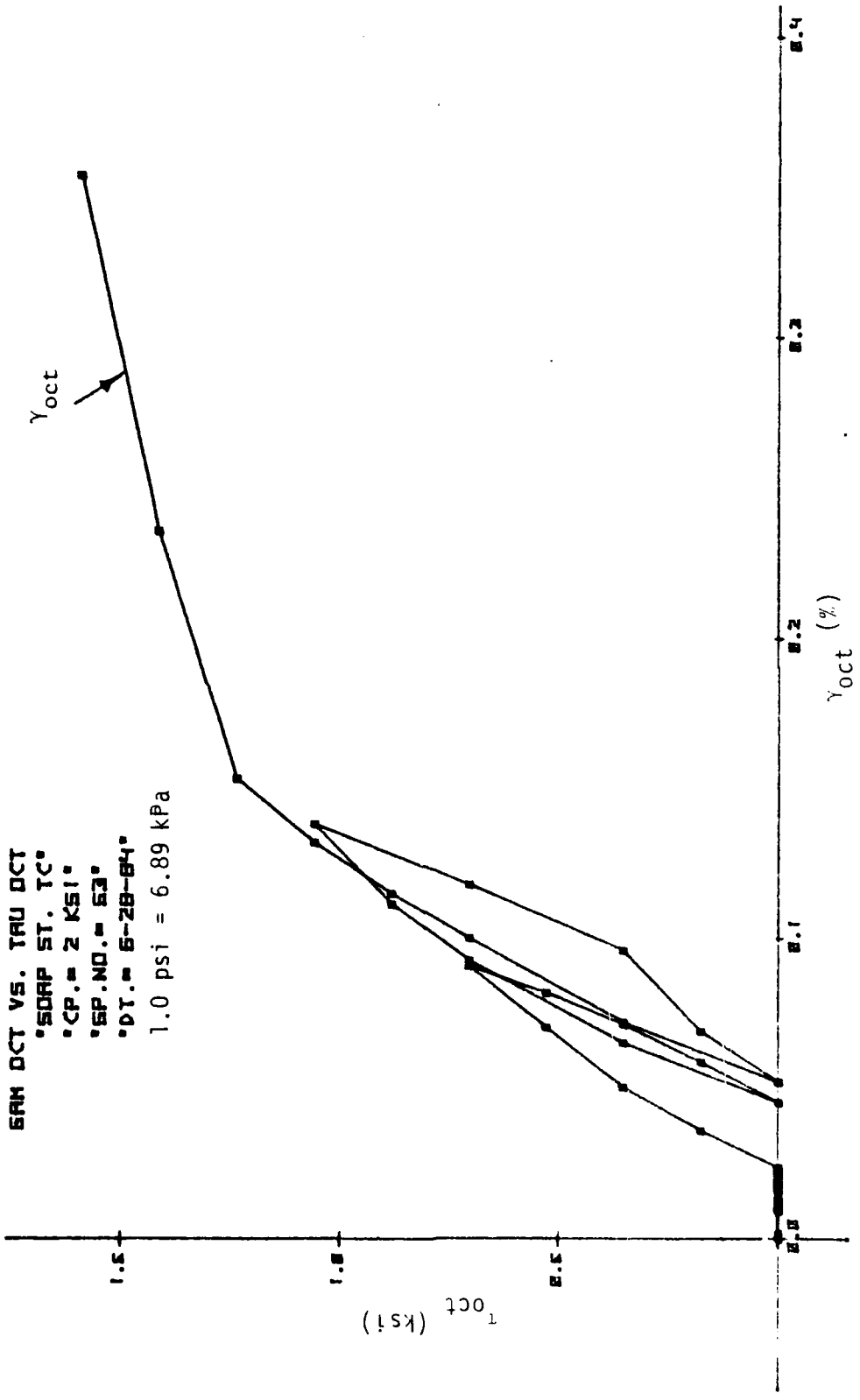

Figure 4.35. Octahedral Stress-Strain Response Curve for Conventional Triaxial Compression Test.

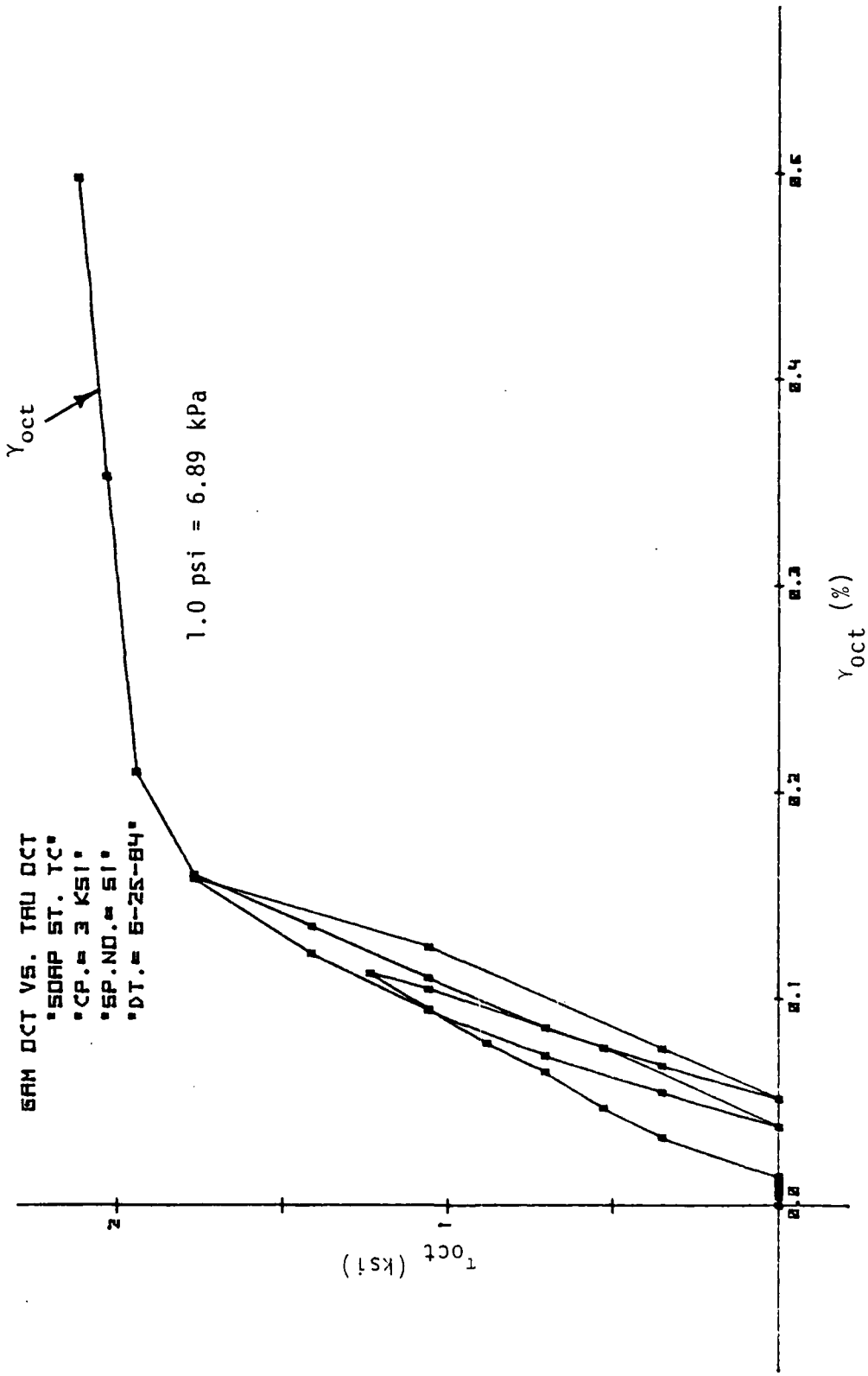

Figure 4.36. Octahedral Stress-Strain Response Curve for Triaxial Compression Test.

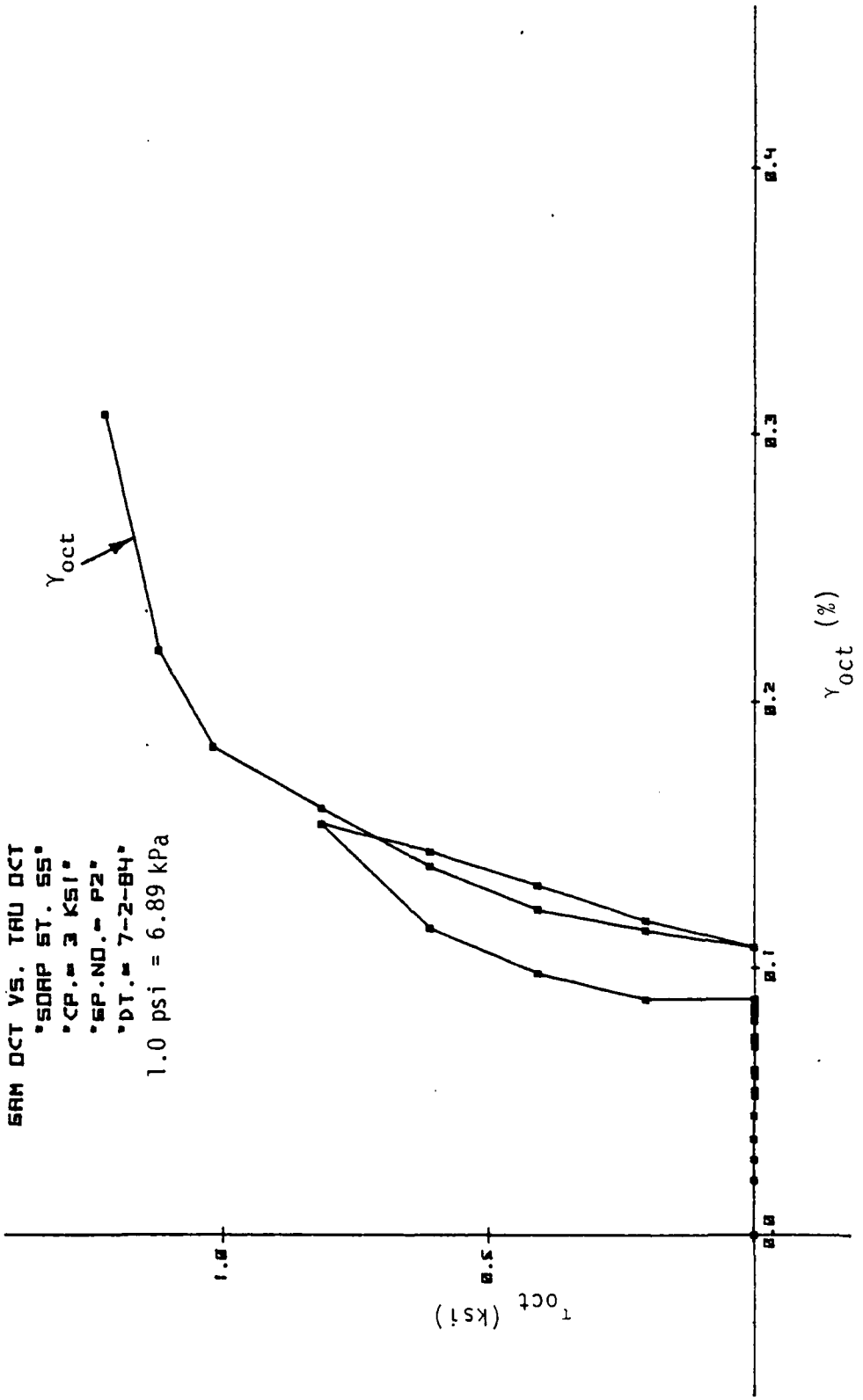

Figure 4.37. Octahedral Stress-Strain Response Curve for Simple Shear Test.

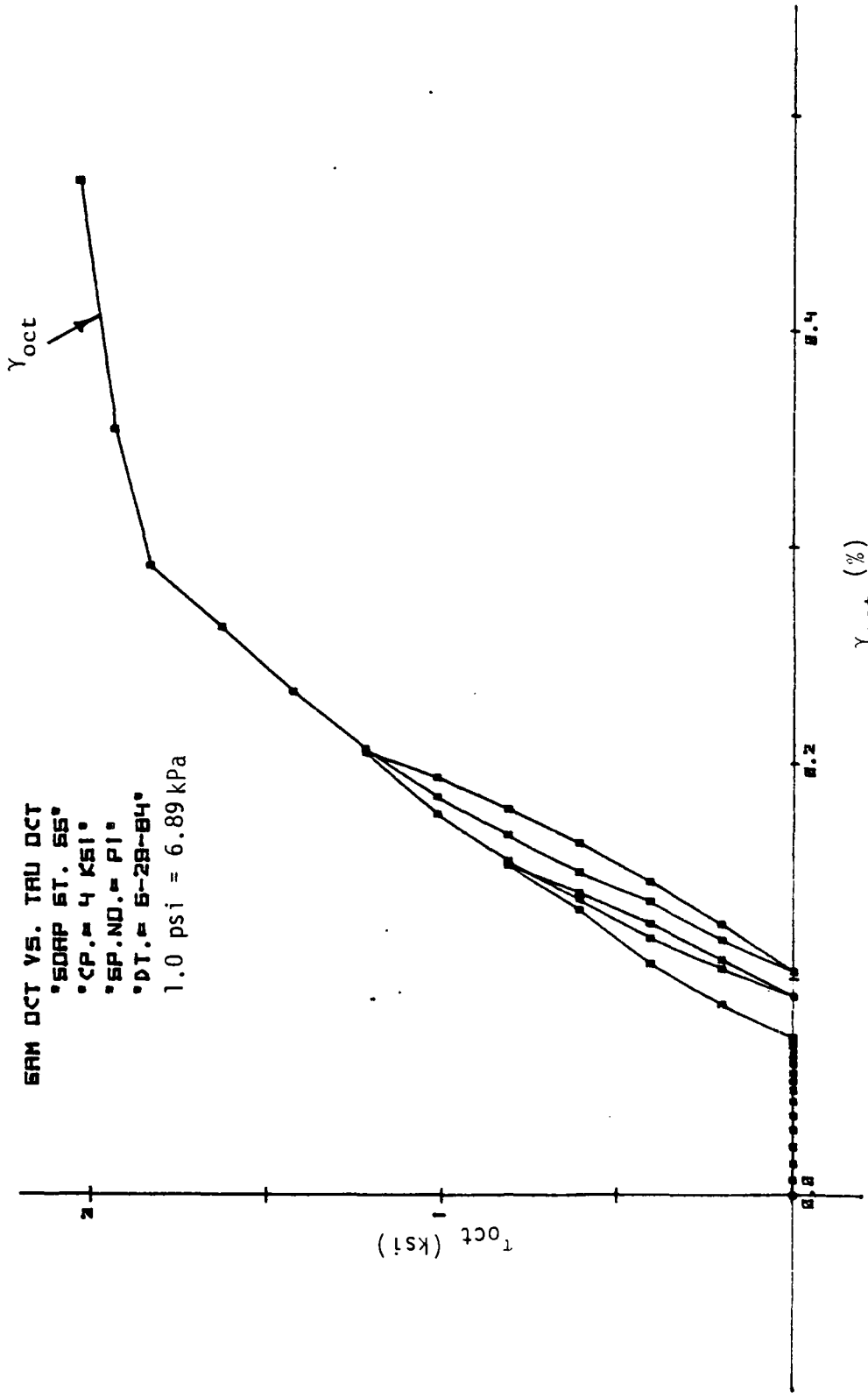

Figure 4.38. Octahedral Stress-Strain Response Curve for Simple Shear Test.

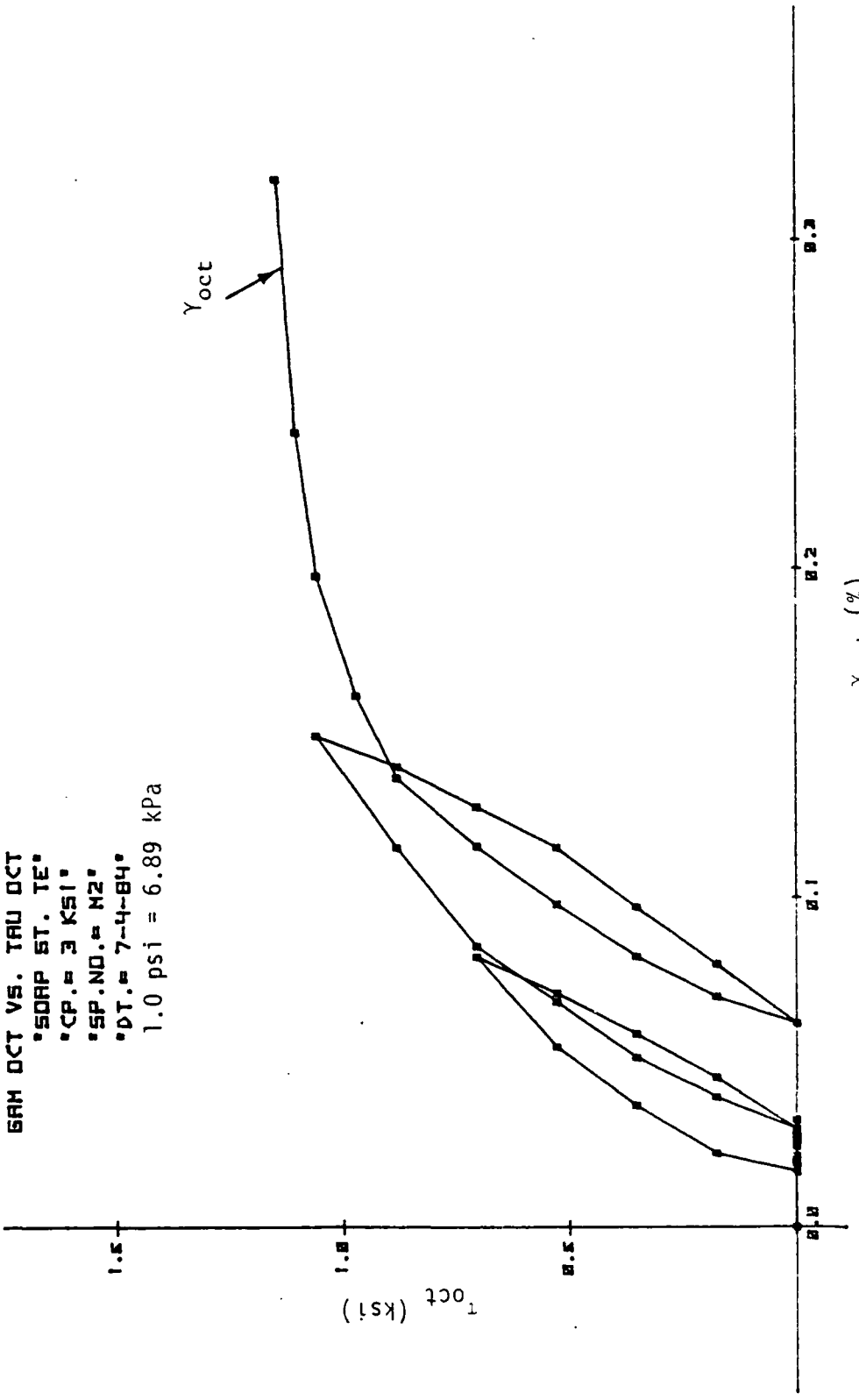

Figure 4.39. Octahedral Stress-Strain Response Curve for Triaxial Extension Test.

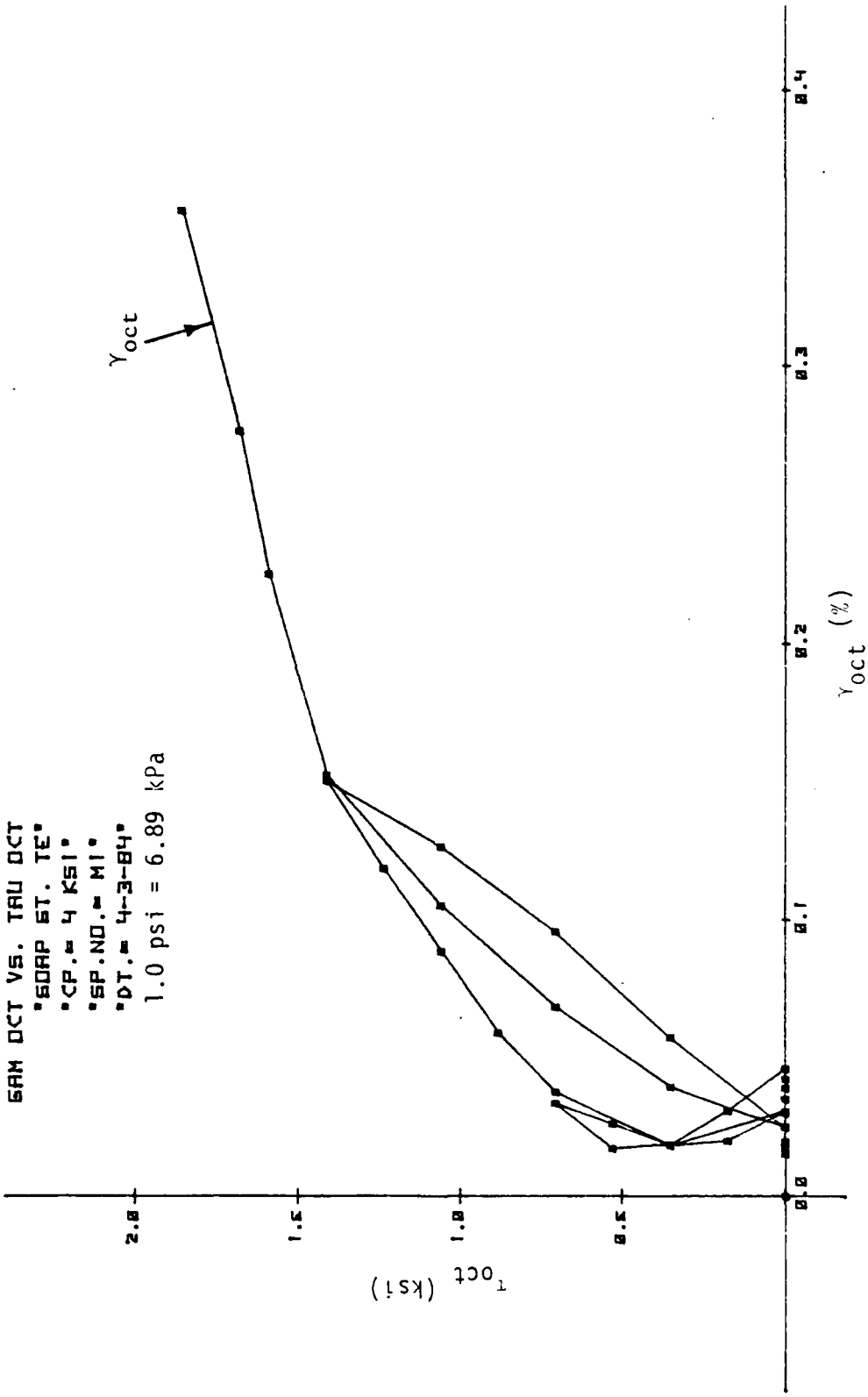

Figure 4.40. Octahedral Stress-Strain Response Curve for Triaxial Extension Test.

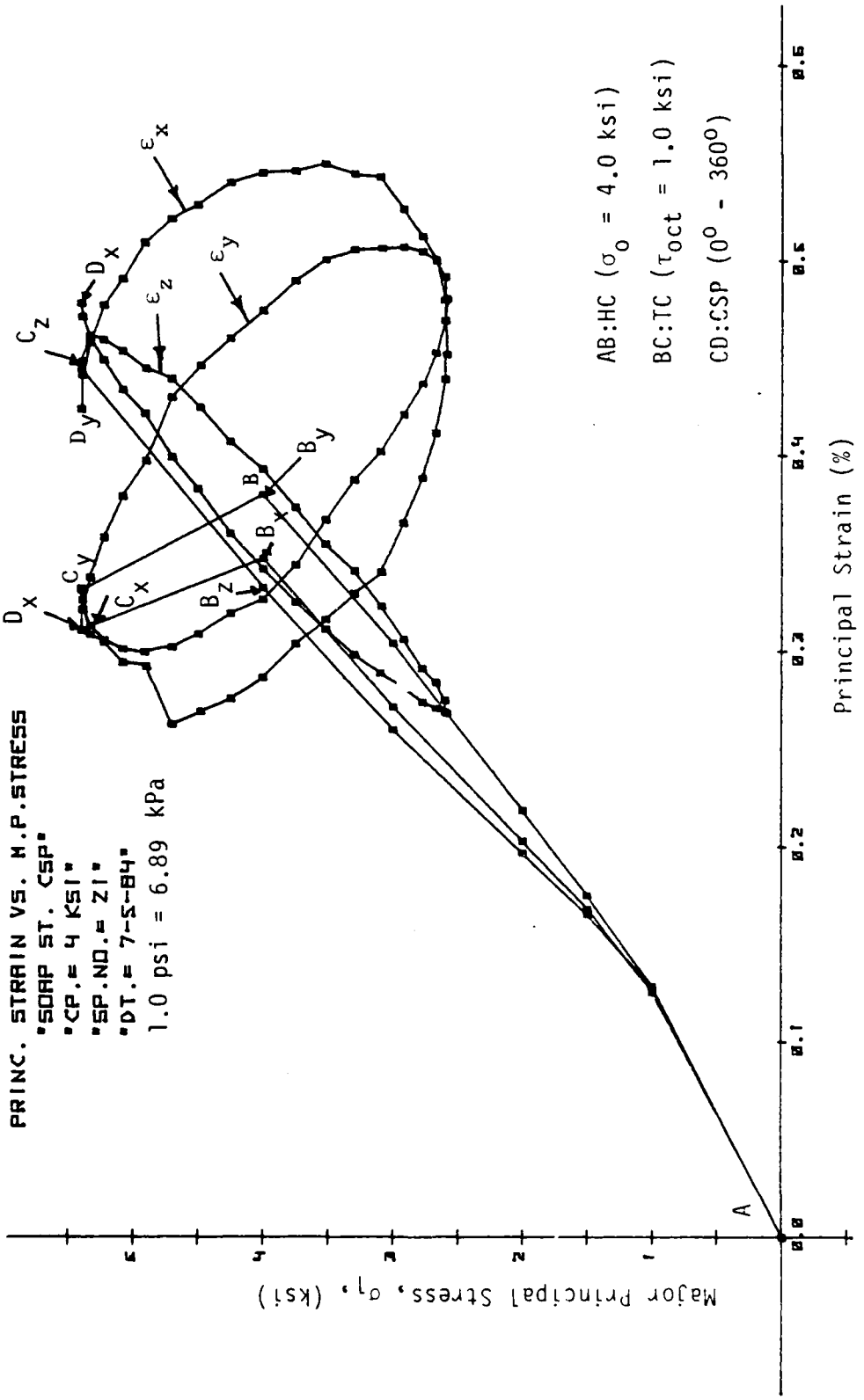

Figure 4.41. Stress-Strain Response Curves for Circular Stress Path Test.

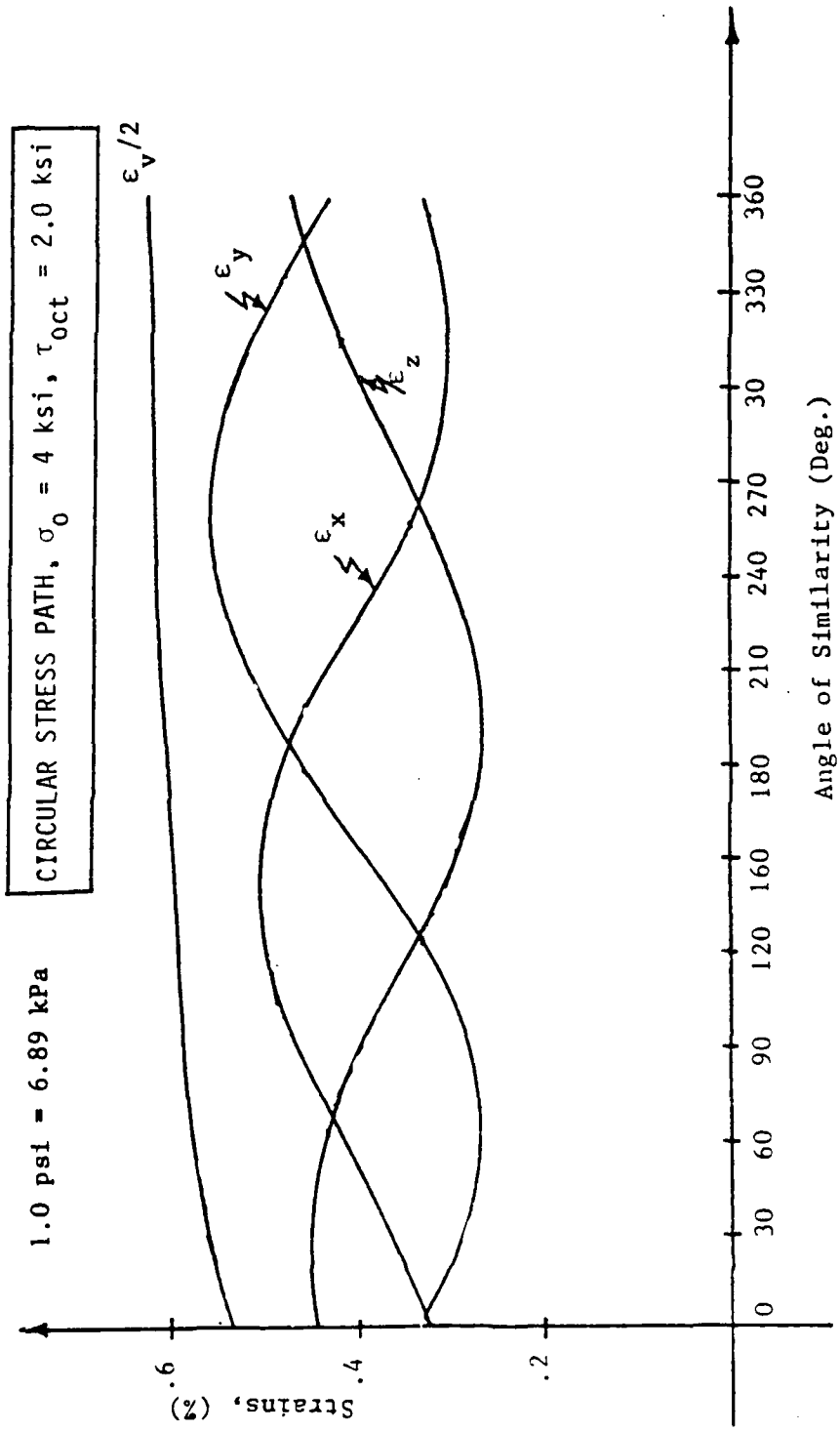

Figure 4.42. Strain-Angle of Similarity Response Curve for Circular Stress Path, (σ_o = 4.0 ksi and $\tau_{oct} \doteq$ 1.0 ksi).

TABLE 4.1

ULTIMATE DATA FOR SOAPSTONE

(Compression Stress Positive)

Load Path (Fig. 2.16)	Spec. No.	σ_1 * (psi)	σ_2 (psi)	σ_3 (psi)	σ_{oct} (psi)	τ_{oct} (psi)	J_1 (psi)	$\sqrt{J_{2D}}$ (psi)
Conventional Triaxial Compression (CTC)		σ_z	σ_x	σ_y				
	T_4	1200	0	0	400	566	1200	693
	T_2	5561	1000	1000	2520	2150	7561	2633
	T_1	7834	2000	2000	3945	2750	11834	3368
	T_3	10425	3000	3000	5475	3500	16425	4287
Triaxial Compression (TC) ($\Theta = 60^o$)		σ_z	σ_x	σ_y				
	S_3	4334	833	833	2000	1650	6000	2021
	S_1	6182	1409	1409	3000	2250	9000	2756
	S_2	7394	2303	2303	4000	2400	12000	2939
Simple Shear (SS) ($\Theta = 60^o$)		σ_z	σ_x	σ_y				
	P_3	3409	592	2000	2000	1150	6000	1409
	P_2	4776	1224	3000	3000	1450	9000	1776
	P_1	6548	1453	4000	4000	2080	12000	2548
Triaxial Extension (TE) ($\Theta = 0^o$)		σ_z	σ_x	σ_y				
	M_3	2743	2743	515	2000	1050	6000	1286
	M_2	3955	3955	1091.	3000	1350	9000	1653
	M_1	5308	5308	1384	4000	1850	12000	2266

*1.0 psi = 6.89 kPa

AD-A174 451 CONSTITUTIVE MODELLING OF CONCRETE AND ROCKS UNDER MULTIAXIAL COMPRESSIVE (U) ARIZONA UNIV TUCSON DEPT OF CIVIL ENGINEERING M R SALAMI ET AL 04 SEP 86 3/5

UNCLASSIFIED AFOSR-TR-86-2014 AFOSR-83-0256 F/G 8/7 NL

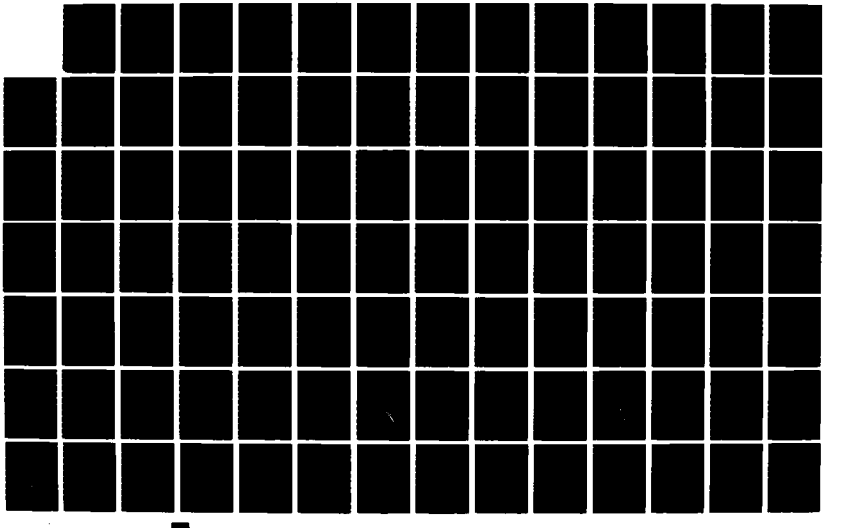

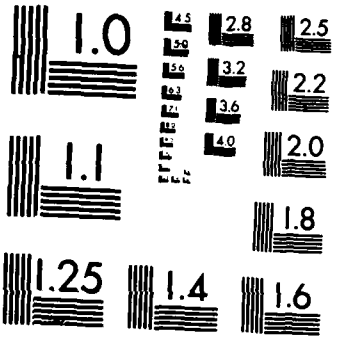

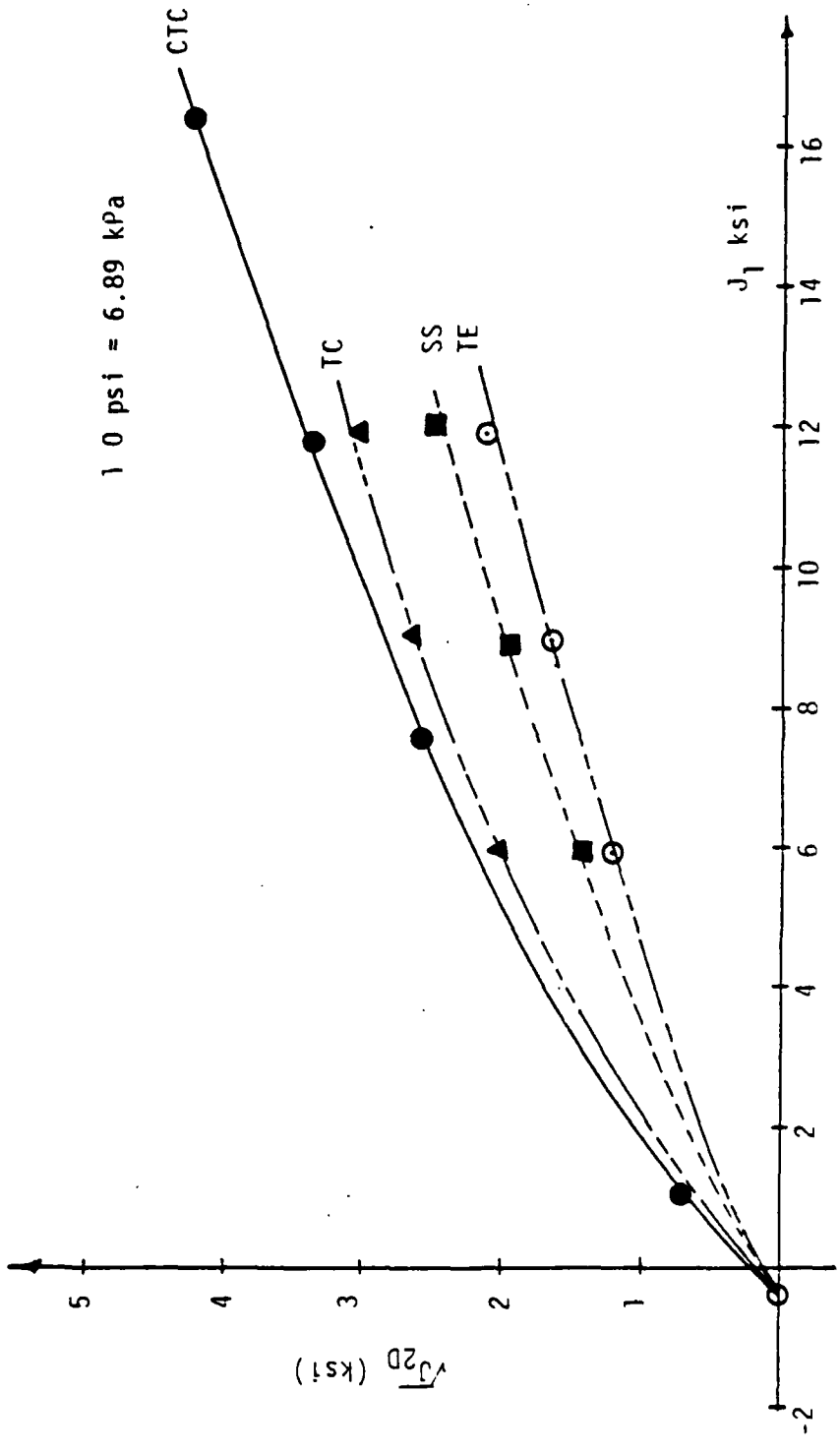

Figure 4.43. Observed Ultimate Surfaces in $\sqrt{J_{2D}} - J_1$ Plane.

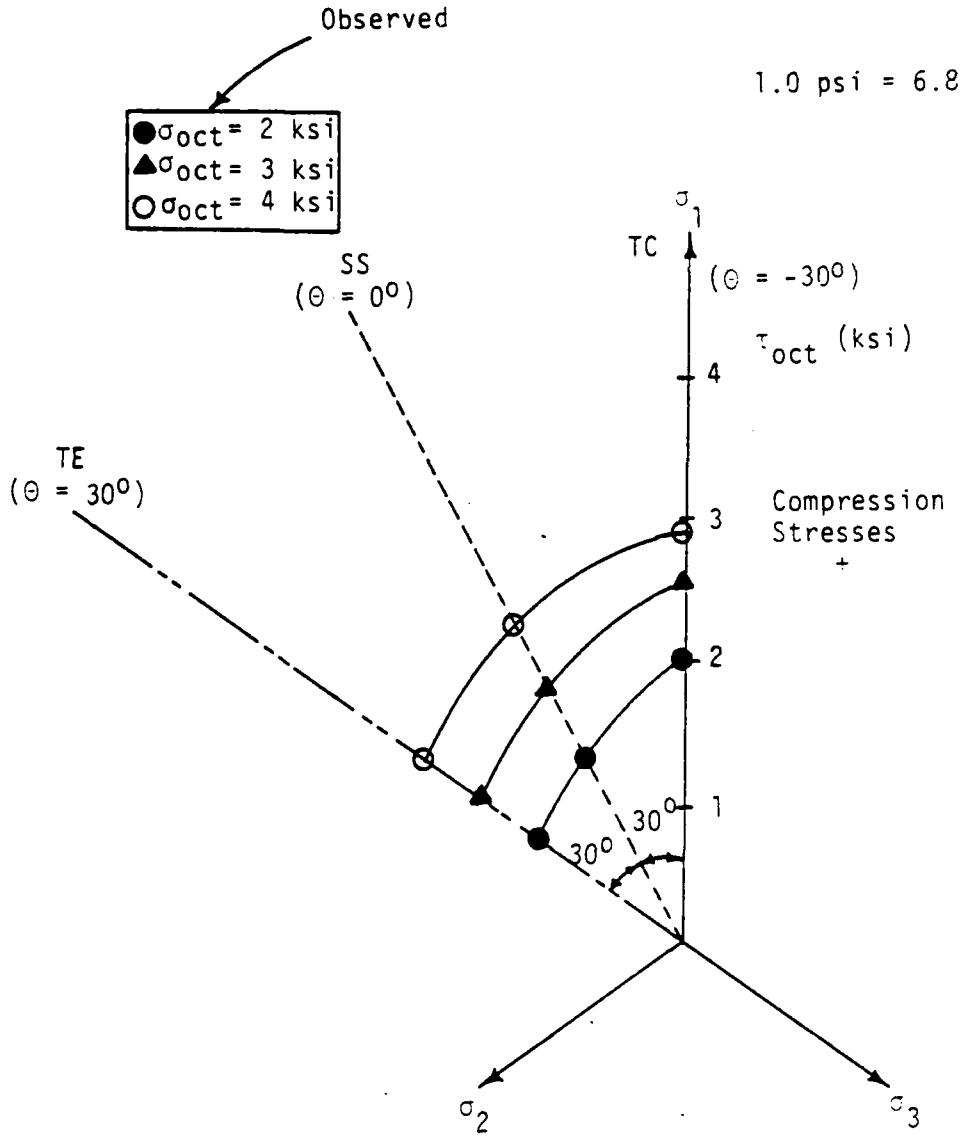

Figure 4.44. Observed Ultimate Surfaces in Octahedral Plane for Soapstone.

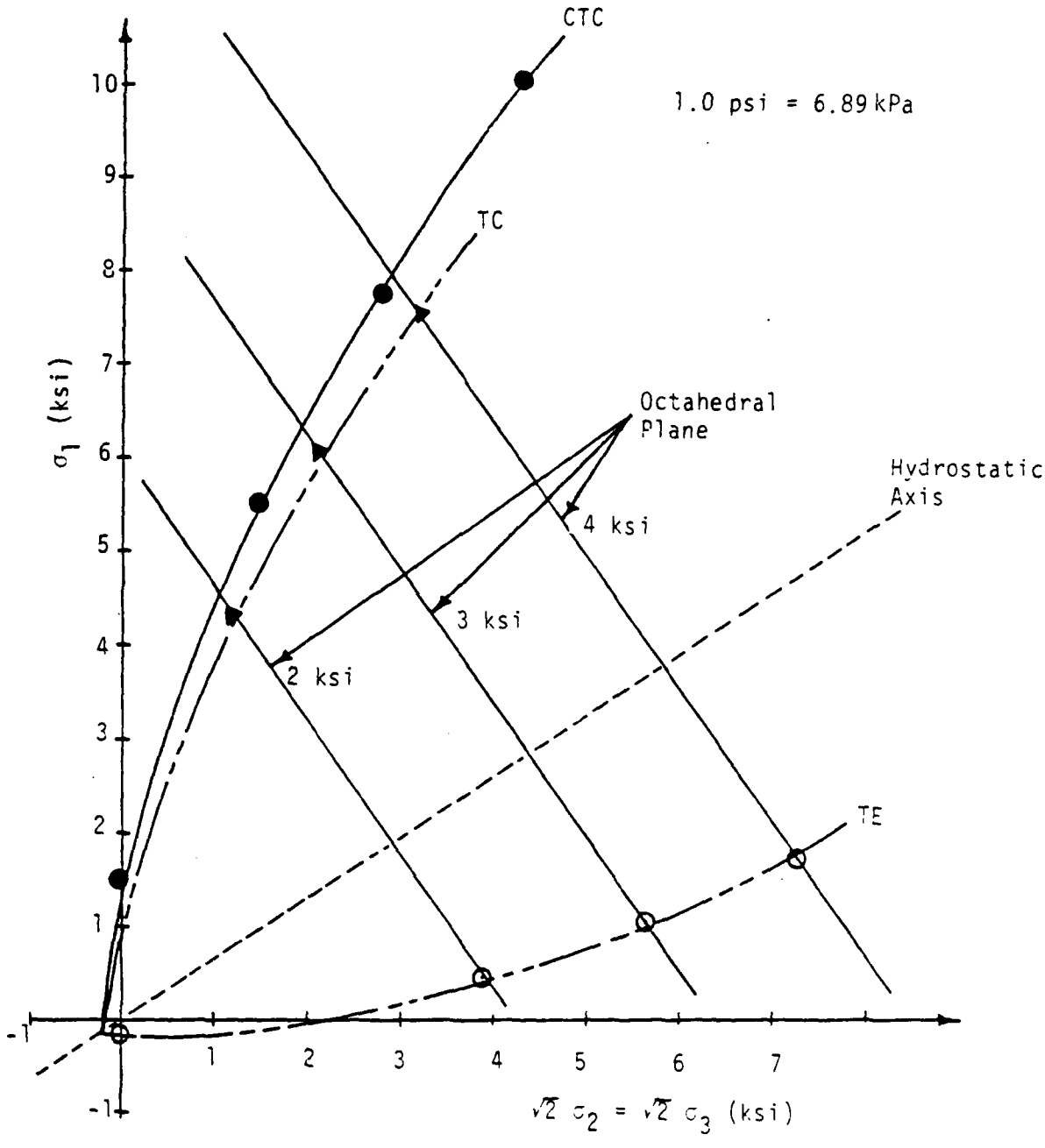

Figure 4.45. Observed Ultimate Surfaces in Triaxial Plane for Soapstone.

ii) There is a direct relationship between strength and confining pressure $\sigma_o = J_1/3$.

iii) The ultimate envelopes in the octahedral planes are non circular, i.e. they depend on stress path (Θ).

iv) Finally, any ultimate (failure) criteria used to predict the strength behavior of soapstone must include the effects of the tensile stresses as shown in Fig. 4.45.

CHAPTER 5

A REVIEW OF EXISTING LITERATURE

5.1 Introduction

In the first part of this chapter, some fundamentals of theory of plasticity are presented. This will be followed by the plasticity models developed to characterize nonlinear and inelastic behavior of geological materials.

5.2 Some Fundamentals of Plasticity Theory

Theory of plasticity describes the rate independent, nonlinear, inelastic responses of materials. Formulation of a constitutive law for engineering materials based on the theory of plasticity includes the following four elements:

i) Yield condition

ii) Stress-elastic strain relationship

iii) Flow rule

iv) Hardening rule

These phases will be explained in the following sections.

5.2.1 Yield condition

The yield criterion can be defined as the limit of elastic deformations expressed by a combination of states of stress. For a one-dimensional state of stress, the yield criterion can be easily visualized. Consider the uniaxial stress-strain curve for metal

under simple tension as shown in Fig. 5.1 when the load is increased gradually, the material behaves elastically up to point A, and regains the original state if the load is removed. When the stress level goes beyond point A, the material experiences irreversible straining. If the metal specimen is stressed beyond point A, say up to B, and then unloaded, there will be some permanent or irrecoverable deformation in the body, and the material is said to have undergone plastic deformations. It can be seen from Fig. 5.1 when the specimen is loaded from A to B, both elastic and plastic deformations will occur, and this is known as elastoplastic behavior. The point A on the stress-strain curve is called the elastic limit and the corresponding stress level is called the yield stress and denoted by σ_y as shown in Fig. 5.1. Thus, for a uniaxial stress-deformation problem, the yield condition can be expressed as:

$$F = \sigma - \sigma_y = 0 \tag{5.1}$$

where σ is the state of stress at any state of loading history. Although yield condition for uniaxial case is quite simple. However, under multiaxial states of stress, this becomes complicated, and a mathematical expression involving all stresses is often required. Establishment of this mathematical expression, known as the yield criterion, has to be done based on experimental observations.

In view of the complexities involved in yielding of materials under three-dimensional states of stress, it is con-

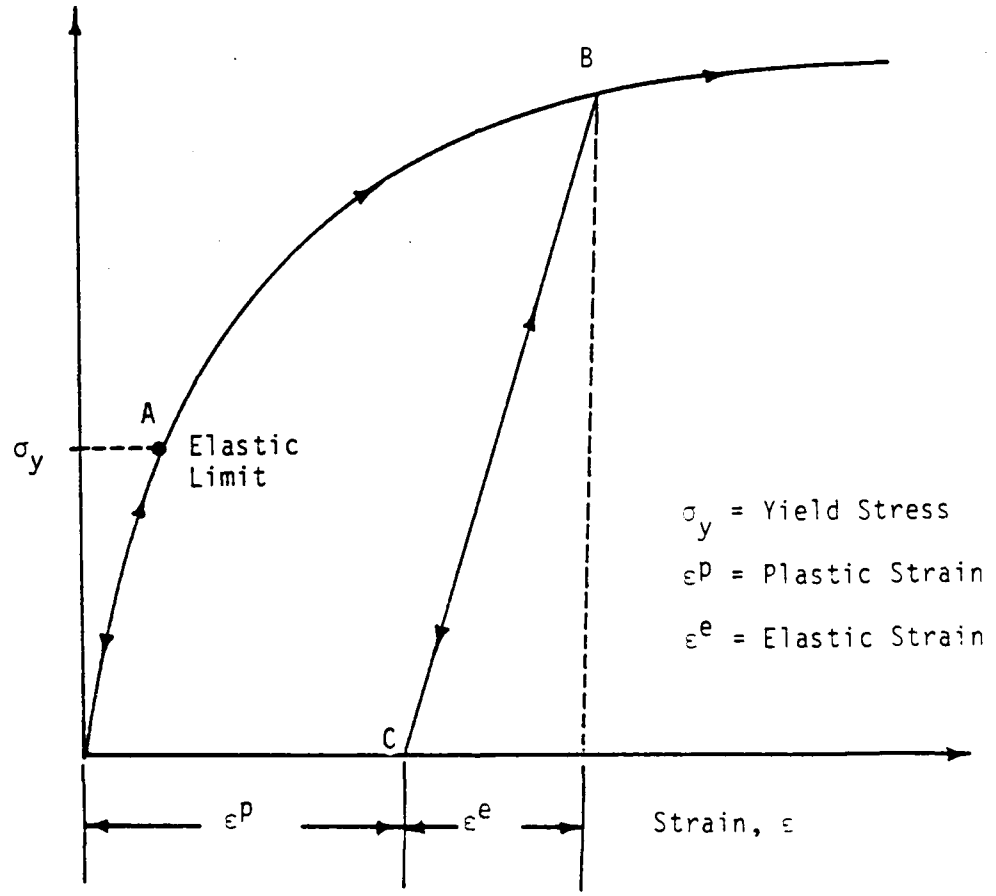

Figure 5.1. Typical Uniaxial Stress-Strain Response in Elasto-Plastic Deformation.

venient to define a scalar function, F, as the yield criterion. A general expression for hardening (softening) yield function F can be expressed [15, 16, 17, 22, 63, 31, 44, 73, 74, 7] as

$$F = F\ (J_i,\ I_i^p,\ K_j,\ a_m) \tag{5.2}$$

where J_i (i = 1,2,3) = invariant of the stress tensor, I_i^p (i = 1,2,3,4) = invariant of the plastic strain tensor, K_j (j = 1,2,3,4) = Joint or mixed invariants, $K_1 = \sigma_{ij}\ \varepsilon_{ij}^p$, $K_2 = \sigma_{ij}\ \sigma_{jk}\ \varepsilon_{ij}^p$, $K_3 = \sigma_{ij}\ \varepsilon_{ik}\ \varepsilon_{ki}^p$ and $K_4 = \sigma_{ij}\ \sigma_{jk}\ \varepsilon_{kl}^p\ \varepsilon_{li}^p$, a = scalar (tensor) valued internal state variable. Using index notation, invariants J_i and I_i^p are defined as

$J_1 = \sigma_{ii}$, $J_2 = 1/2\ \sigma_{ij}\ \sigma_{ij}$, $J_3 = 1/3\ \sigma_{ij}\ \sigma_{ij}\ \sigma_{ki}$;
$I_1^p = \varepsilon_{ii}^p$, $I_2^p = 1/2\ \varepsilon_{ij}^p\ \varepsilon_{ji}^p$, and $I_3^p = 1/3\ \varepsilon_{ij}^p\ \varepsilon_{jk}^p\ \varepsilon_{ki}^p$.

It should be mentioned here that when the joint invariants are not included, the principal directions of the stress and plastic strain tensor will be coincidental and represents a material which is isotropic initially and undergoes isotropic hardening.

5.2.2 Stress-Elastic Strain Relationship

For three dimensional bodies, the generalized Hooke's law for a linear elastic isotropic material can be written in the incremental form [22, 38, 39] as

$$de_{ij}^e = \frac{1 - 2\nu}{E}\ \delta_{ij}\ (d\sigma_{kk}) + \frac{dS_{ij}}{2G} \tag{5.3a}$$

Where $d\varepsilon_{ij}^e$ = elastic part of the total incremental strain, $d\varepsilon_{ij}$,

δ_{ij} = Kronecker delta, $d\sigma_{kk}$ = incremental spherical or hydrostatic stress, dS_{ij} = incremental deviatoric stress tensor, E = Young's modulus, G = Shear modulus and ν = Poisson's ratio.

or

$$d\sigma_{ij} = C_{ijkl}\, d\varepsilon^{e}_{kl} \tag{5.3b}$$

Where $d\sigma_{ij}$ = incremental stress, C_{ijkl} = elastic constitutive relation tensor.

In the theory of plasticity, the strain increment $d\varepsilon_{ij}$ due to a stress increment $d\sigma_{ij}$ can be decomposed into elastic and plastic components; here it must be assured that the strains are small [38]. Then

$$d\varepsilon_{ij} = d\varepsilon^{e}_{ij} + d\varepsilon^{p}_{ij} \tag{5.4}$$

Where superscripts 'e' and 'p' refer to elastic and plastic strain, respectively. Substituting for $d\varepsilon^{e}_{kl}$ in Eq. (5.3b) gives:

$$d\sigma_{ij} = C_{ijkl}\, (d\varepsilon_{kl} - d\varepsilon^{p}_{kl}) \tag{5.5}$$

5.2.3 Flow Rule

When the state of stress reaches the yield criterion f, the material undergoes plastic deformation; this is also called plastic flow. In the theory of plasticity [38, 39, 40] incremental plastic strain is defined by assuming the existence of a function, Q, called the plastic potential. In general,

the plastic potentional, Q, is a function of the state of stress, σ_{ij}, and the incremental plastic strain is proportional to the gradient of Q. Then the increments of the plastic strain can be expressed as

$$d\varepsilon^{p}_{ij} = d\lambda \frac{\partial Q}{\partial \sigma_{ij}} \tag{5.6}$$

which is referred to as the normality rule; here, $d\lambda$ is a positive scalar factor of proportionality. For some materials, the plastic potential function, Q, and the yield function, f, can be assumed to be the same. Such materials are considered to follow the "associative flow rule" of plasticity. However, for many geological materials, the yield function f and the plastic potential function Q are often different. These materials are considered to follow "non associative flow rules" of plasticity [22, 53, 49, 62, 58, 71, 23, 6]. In this dissertation, only associative plasticity concept is utilized.

5.2.4 Harding Rule

As seen in Fig. 5.1 a real material shows some increase in stress even after the elastic limit. This can be work or strain hardening. If a material is assumed to experience no hardening, then it is called perfectly plastic. Classical Tresca, Von Mises, Mohr-Coulomb, and Drucker-Prager yield criteria belong to this category. Here the shape, size, and orientation of the yield surface remain unchanged during plastic

straining as shown in Fig. 5.2a. Hardening rules are intended to define the process of strength gain in a material due to permanent straining in comparison to perfectly plastic response. In the theory of plasticity, there are three kinds of hardening rules: i) Isotropic hardening, ii) Kinematic hardening, and iii) Combination of isotropic and kinematic hardening. These hardening rules have been explained by Desai et al [22, 23a] and Faruque [32] in detail. In this section, these hardening rules will be explained briefly.

i) Isotropic Hardening

If the material behavior is not affected by orientation, it is called isotropic. Isotropic hardening takes place when the initial yield surface in the stress space expands uniformly without changing its shape or form during plastic flow and the center of the yield surface remains the same during the expansion. The initial yield surface f_0 is often defined as the locus of stress states when the first yielding occurs. A typical isotropic hardening in stress space is shown in Fig. 5.2a.

ii) Kinematic Hardening

This hardening rule was introduced by Ishlinski [40] and Prager [61, 60] and is known as Prager's kinematic hardening rule. Here the shape and size

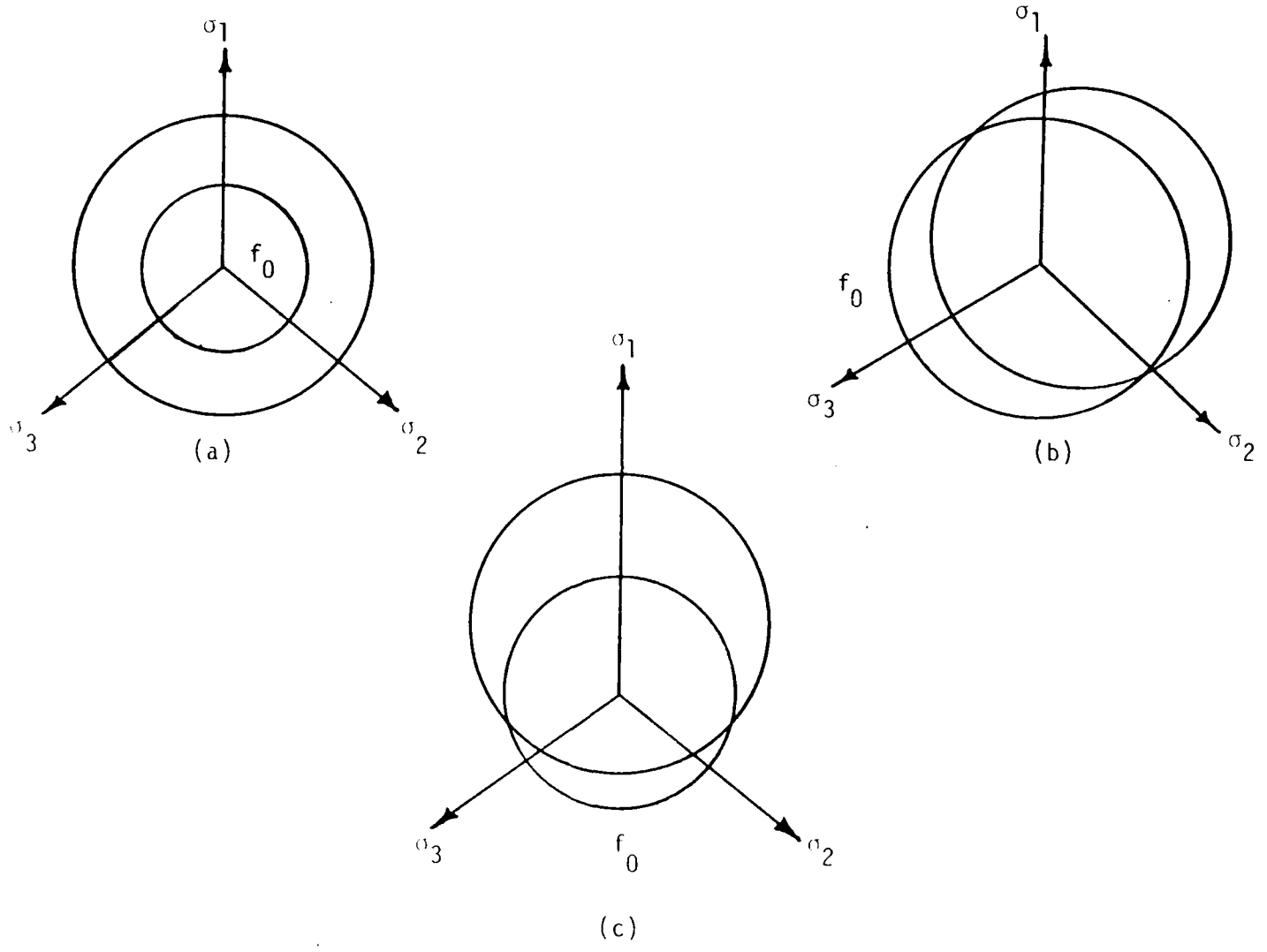

Figure 5.2. Plasticity Models: (a) Isotropic Hardening; (b) Kenenatic Hardening; (c) Combination of Isotropic and Kinematic Hardening.

of the yield surface remain the same but the yield surface can translate in the direction of the plastic strain increment in the stress space without rotation. A typical kinamatic hardening in stress space is shown in Fig. 5.2b.

iii) Combination of Isotropic and Kinematic Hardening

This hardening rule involves changes in size, shape and orientation of the yield surface. It is assumed that the yield surface expands as well as translates in the stress space. Also, the shape of the yield surface may not remain the same. A typical anisotropic hardening in stress space is shown in Fig. 5.2c.

5.3 Some Plasticity Models for Geological Materials

In this section, a brief review of classical plasticity as well as new plasticity models to characterize nonlinear and inelastic behavior of geological materials will be described.

5.3.1 Tresca Yield Criterion [80]

According to this criterion, yielding will initiate when the maximum value of the extreme shear stress is reached. One of the major drawbacks of the Tresca yield criterion is that it does not include the effect of the intermediate principal stress. Figs. 5.3a and 5.3b show geometric representation of Tresca yield condition in two and three dimensions, respectively.

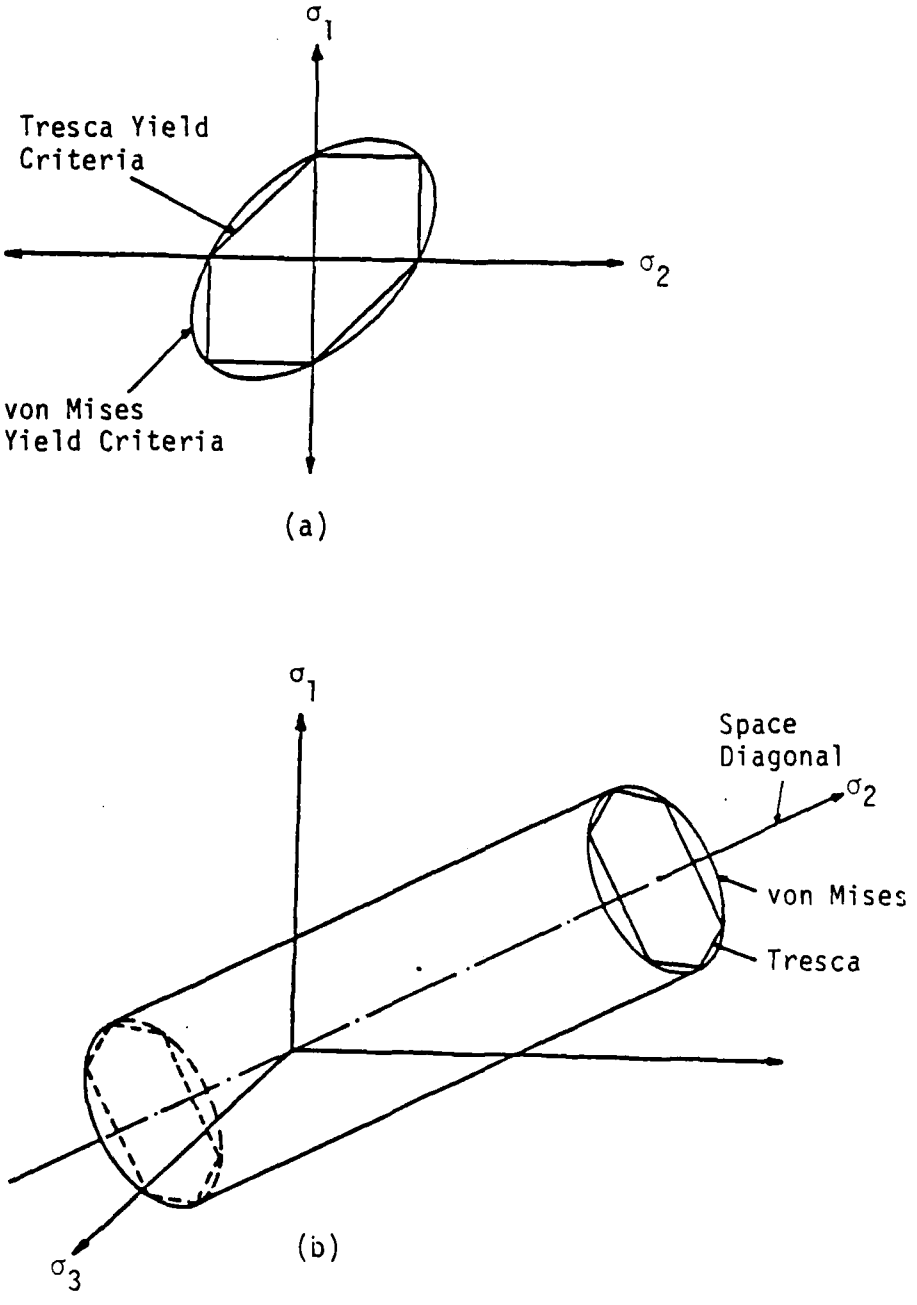

Figure 5.3. Schematic of Tresca and von Mises Yield Conditions: (a) in Two-Dimensional Stress Space; (b) in the Principal Stress Space.

It is seen from Figs. 5.3a and 5.3b that Tresca yield criterion plots as a discontinuous surface which poses difficulty when associated plasticity is adopted. Other major drawback of Tresca yield criterion is that the yield strength in tension and compression has been assumed to be equal.

5.3.2 Von Mises Yield Criterion [81]

The Von Mises Yield Criterion can be expressed as

$$F = \sqrt{J_{2D}} - k = 0 \tag{5.7}$$

where

$$J_{2D} = 1/6\ [(\sigma_1 - \sigma_2)^2 + (\sigma_2 - \sigma_3)^2 + (\sigma_3 - \sigma_1)^2] \tag{5.8a}$$

or

$$J_{2D} = 3/2\ \tau_{oct}^2 \tag{5.8b}$$

and k is the strain hardening parameter. In pricipal stress space, this yield criterion plots as a right circular cylinder centered on the hydrostatic axis. Figs. 5.3a and 5.3b show geometric representation of Von Mises yield conditions in two and three dimensions, respectively. For the hardening behavior, the radius of the yield surface will increase when the stress state is such that the yield surface is reached as deformation occurs. Thus the dependence on the parameter k. This criterion is seen to be independent of hydrostatic pressure as well as shear stress determination. The yielding of metals is described farily well by the Von Mises Criterion. However, for a material such as

concrete or rocks, the yield or ultimate (failure) strength shows a dependence on J_1 and J_3 implying that the Von Mises Criterion would not be valid for representing the strength of concrete and rock materials.

5.3.3 Mohr-Coulomb Failure Criterion

According to the Mohr-Coulomb Criterion, the shear strength increases with increasing normal stress on the failure plane:

$$\tau = c + \sigma \tan \phi \tag{5.9a}$$

or

$$\tau = c + \left(\frac{\sigma_1 - \sigma_3}{2}\right) \tan \phi \tag{5.9b}$$

Where τ is the shear stress on the failure plane, c the cohesion of the material, σ the normal effective stress on the failure surface, ϕ the angle of internal friction, σ_1 major principal stress and σ_3 minor principal stress. Fig. 5.4 shows the cross-section of the Mohr-Coulomb yield criterion on the π-plane which passes through the origin of the principal stress space. Eq. (5.9) represents an irregular hexagonal pyramid in the stress space as seen in Fig. 5.4. It is evident from Eq. (5.9) that the Mohr-Coulomb criteria does not include the effect of the intermediate principal stress.

5.3.4 Drucker-Prager Yield Criterion [4]

Extended Von Mises yield Criteria is proposed by Drucker and Prager where all the principal stresses are considered.

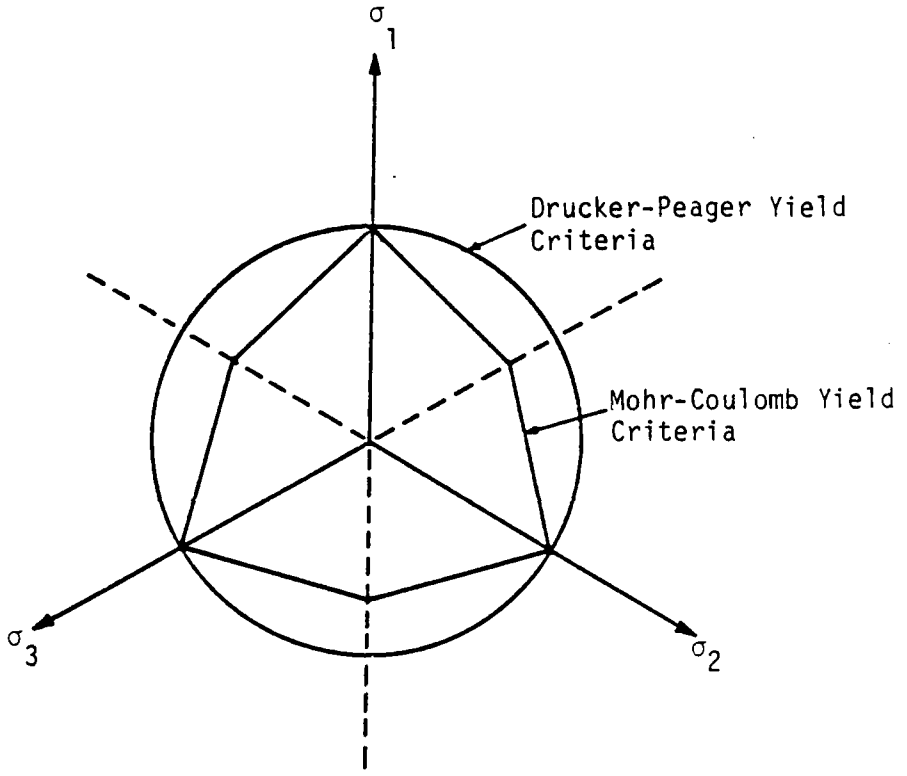

Figure 5.4. Mohr-Coulomb and Drucker-Prager Yield Criteria on π-Plane.

Drucker-Prager yield criteria can be expressed as:

$$F = \sqrt{J_{2D}} - \alpha J_1 - k = 0 \tag{5.10}$$

where

$$J_1 = \sigma_1 + \sigma_2 + \sigma_3 = 3\,\sigma_{oct} \tag{5.11}$$

with J_{2D} given by Eq. (5.8a). α and k are the material constants. Note that this yield function reduces to the Von Mises cylinder for $\alpha = 0$ (purely cohesive materials). Eq. (5.10) represents a right circular cone in principal stress space, centered on the hydrostatic axis as shown in Fig. 5.5. On the π-plane, it plots as a circle and is shown in Fig. 5.4. As shown on the failure surface, the Drucker-Prager criterion does include the effect of the hydrostatic pressure. However, as in the Von Mises criterion, the dependence on J_3 (or Lode angle, Θ) is not incorporated. This can be seen in the π-plane because the Drucker-Prager surface plots as a circle.

The Drucker-Prager failure criterion is more realistic than the Von Mises criterion for describing the failure of plain concrete and rocks. However, it is still deficient in many aspects As seen in Chapter 3 and 4, plain concrete and soapstone exhibit a strong stress path as well as confining pressure dependency. In the octahedral plane for instance, the ultimate (failure) envelope is definitely non-circular. Therefore any criterion used to predict the ultimate failure of these

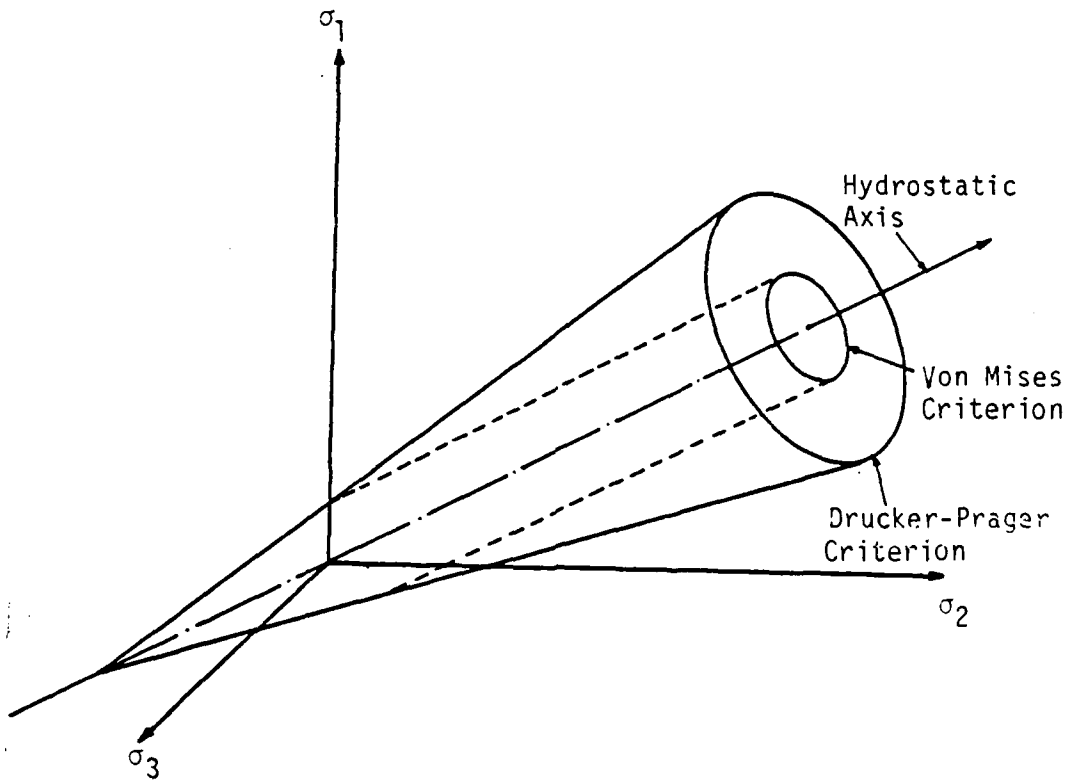

Figure 5.5. Von Mises and Drucker-Prager Yield Criteria in Principal Stress Space.

materials cannot neglect the dependency on J_1 and J_3 (σ_{oct} and Θ) as is done in the Von Mises Criterion or simply J_3 as in the Drucker-Prager Criterion.

5.3.5 William-Warnke Five-Parameter Failure Criterion [84]

In the model developed by William and Warnke for the triaxial failure surface of concrete type materials, the failure envelope is fully described in the principal stress space by assuming isotropic material behavior. It is basically a cone with curved meridians and a non-circular section as shown in Fig. 5.6. Since isotropic material behavior is assumed, only a sextant of the principal stress need be considered for the mathematical model, the rest will be symmetric. The surface is represented by hydrostatic and deviatoric sections. The hydrostatic section forms a meridinal plane, containing the hydrostatic axis as an axis of revolution. It can be represented in τ_{oct} - σ_{oct} stress space as shown in Fig. 5.7 where the hydrostatic axis lies along the abscissa. The deviatoric section lies in a plane perpedicular to the hydrostatic axis, described by Polar Coordinates r and Θ as shown in Fig. 5.8.

The failure surface function F (σ) for the five-parameter model is expressed as:

$$F(\sigma) = F(\sigma_a, \tau_a, \Theta) = \frac{1}{r(\sigma_a, \Theta)} \frac{\tau_a}{|f_{cu}|} - 1 \qquad (5.12)$$

$$= 0 \text{ for material failure}$$

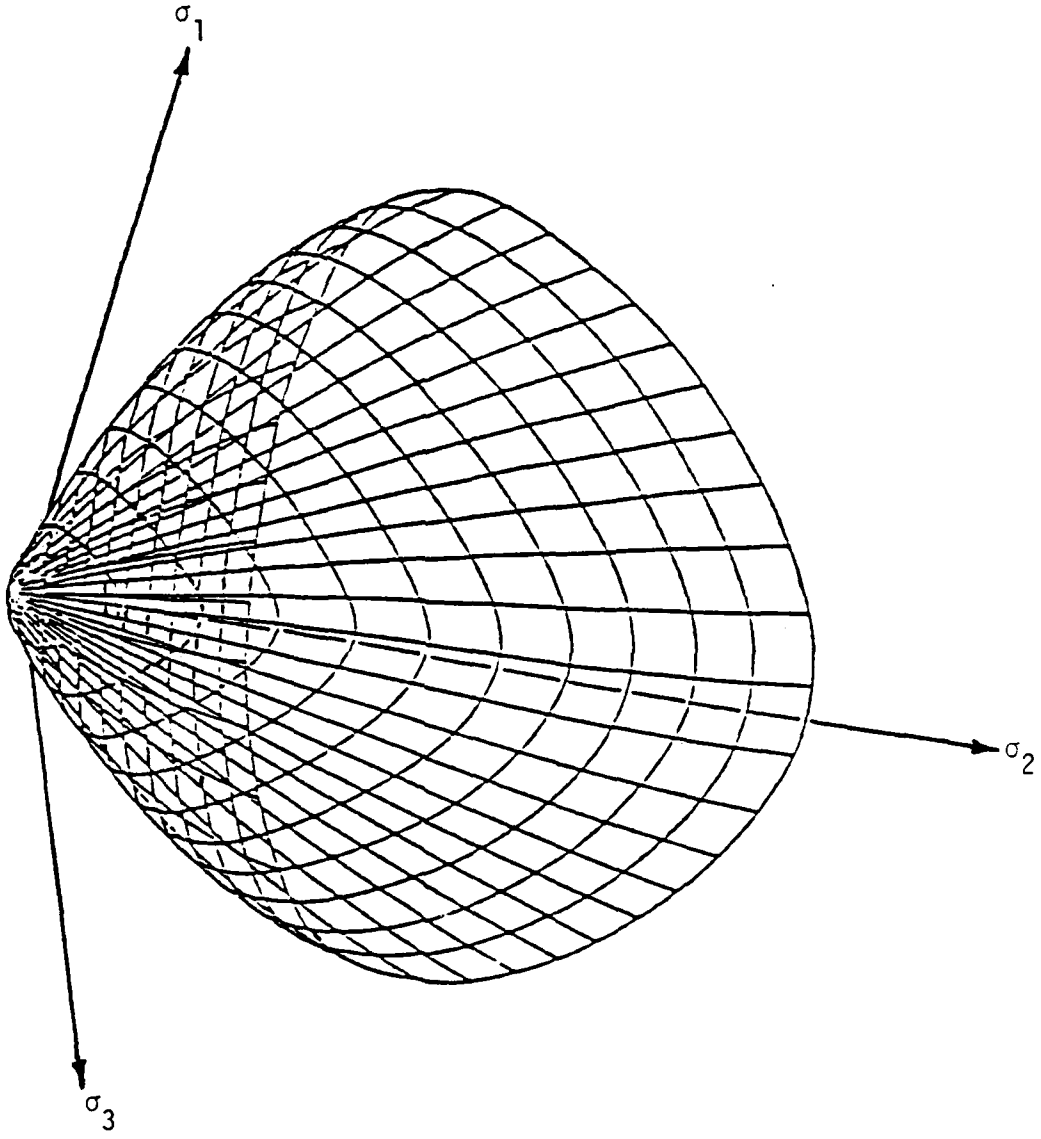

Figure 5.6. Failure Surface for Plain Concrete {Willam, et al [83 & 84]}

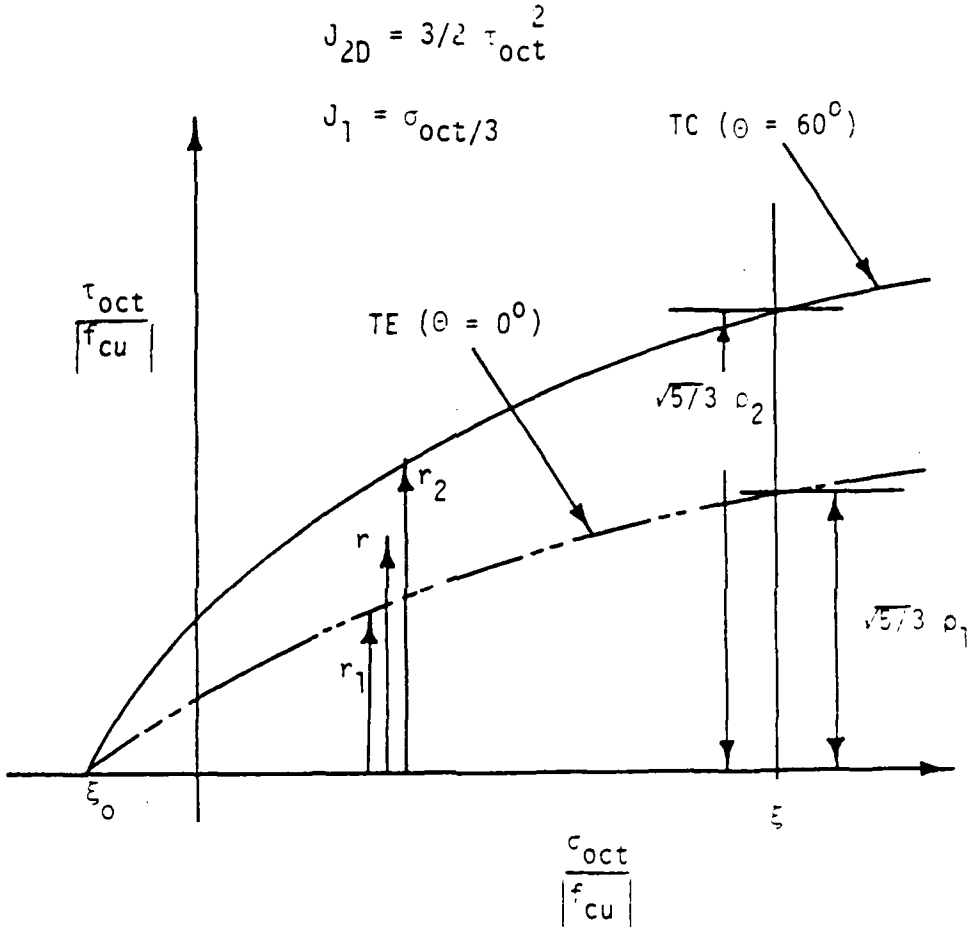

Figure 5.7. τ_{oct} - σ_{oct} or Hydrostatic Section of Proposed Willam-Warnke Failure Surface.

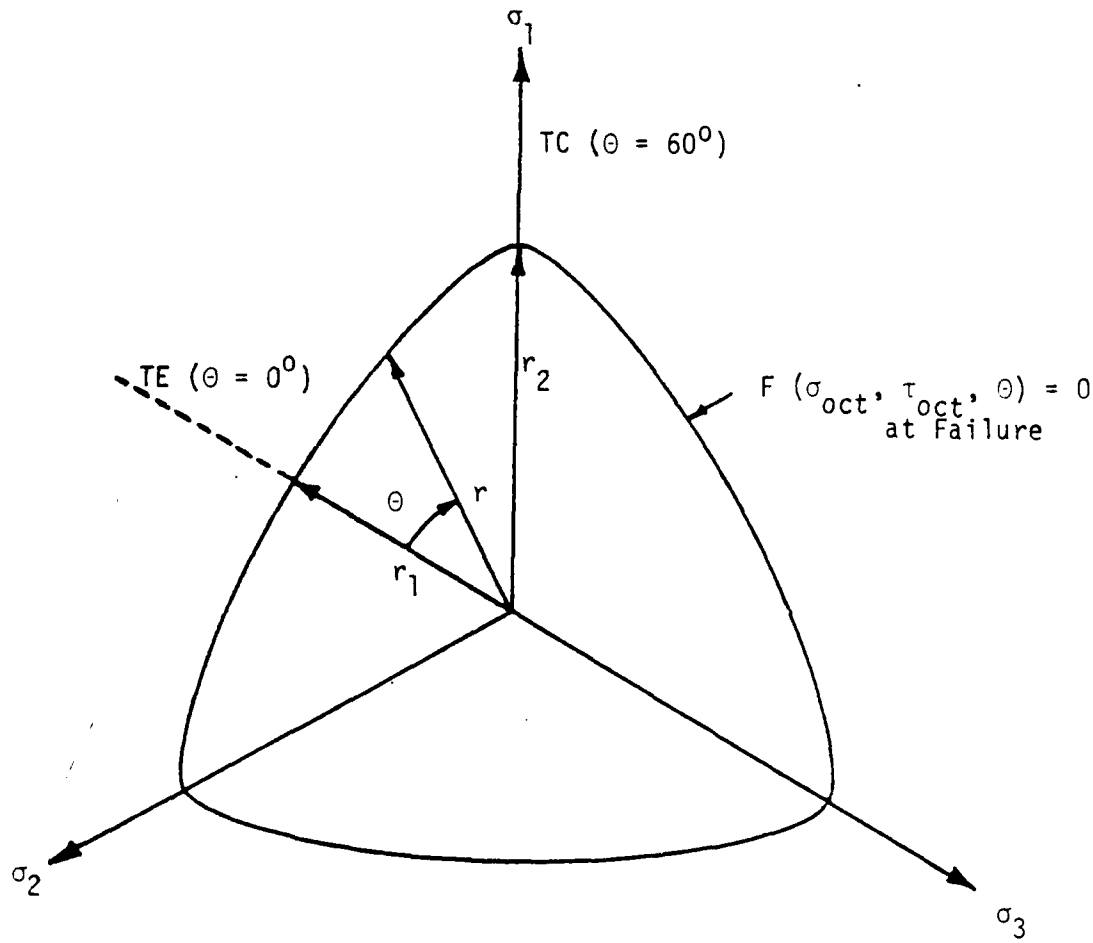

Figure 5.8. Deviatoric or Octahedral Section of Proposed Willam-Warnke Failure Surface.

where

σ_a = average normal stress

$$= 1/3\ (\sigma_1 + \sigma_2 + \sigma_3) \qquad (5.13)$$

$$= \sigma_{oct}$$

τ_a = average shear stress

$$= \frac{1}{\sqrt{15}} [(\sigma_1 - \sigma_2)^2 + (\sigma_2 - \sigma_3)^2 + (\sigma_3 - \sigma_1)^2]^{1/2} \qquad (5.14)$$

and

f_{cu} = uniaxial compression strength
(used for normalization)

William and Warnke assumed tension positive when formulating their failure criterion.

For materials such as concrete and rocks, the yield or failure show a dependence on tensile strength, f_t, implying that the Willam and Warnke would not be good enough for representing the strength of concrete and rock materials since the failure criterion does not include the effect of tensile strength.

5.3.6 Critical State Model [65]

This model is based on the observation that on a deviatoric stress (q) vs. mean pressure (p) plot, the ultimate failure points lie on the straight line, which is defined as the critical state line. After reaching a critical state, there will not be any further volume changes. Fig. 5.9 shows a typical critical state line on q-p plane where q is the difference between the major and the minor principal stresses, and p is the confining pressure.

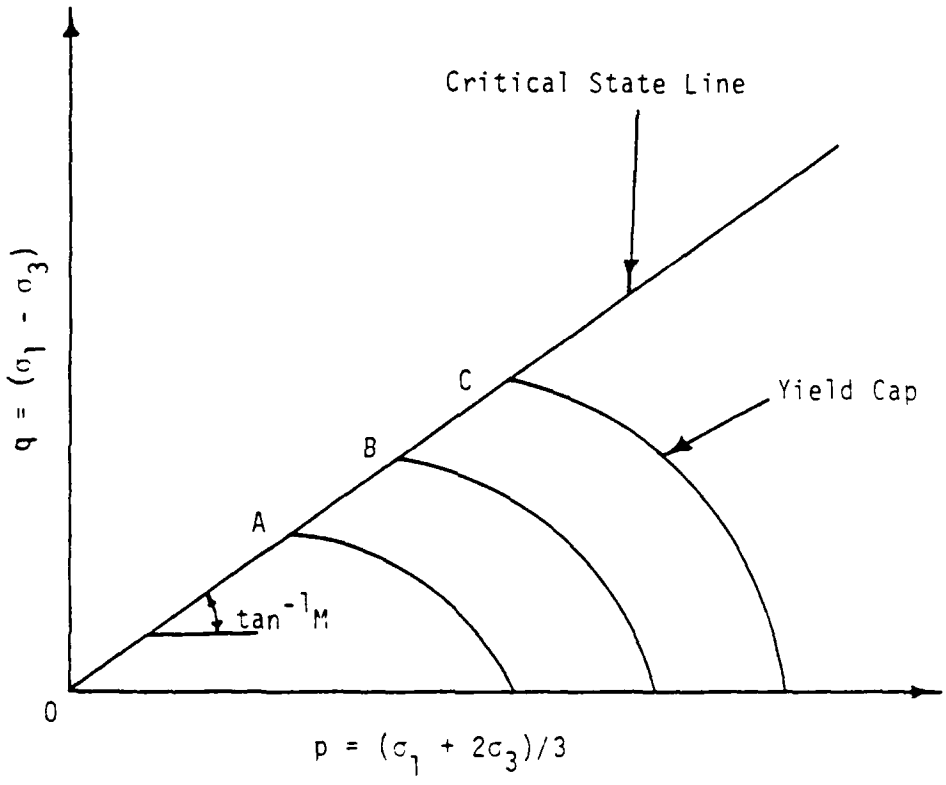

Figure 5.9. Critical State Line and the Yielding Caps on q - p Plane.

In addition to the failure envelope, functions have been developed to describe the yielding characteristics of geological material. These yield functions represent yield surfaces of constant plastic volumetric strain. Below a yield surface material is assumed to be elastic. Beyond the yield surface the material experiences plastic strains.

The modified Camclay yield function [64] can be written as:

$$F = q^2 - M^2 P_o P + M^2 P^2 = 0 \qquad (5.14)$$

where M is the slope of the critical state line on the q-P plot, and Po is the hardening parameter. This yield function represents a portion of an ellipse between the failure envelope and the mean pressure (P) axis that corresponds to yield locus, as shown in Fig. 5.9. The hardening parameter, P_o, varies for each yield surface although it is constant along each individual yield surface.

It is observed experimentally that the linear failure surface and circular shape of the yielding cap may not compare with the experimental data with reasonable accuracy. Subsequently, several extensions and modifications of the Cap model are proposed for geological materials by Dimaggio and Sandler [24]; Sandler and Rubin [60]; Roscoe, Schofield and Worth [65]; Lade [45];

Desai, Phan and Sture [21]

5.3.7 Model Proposed by Lade

The following three-parameter failure criterion for concrete proposed by Lade [2] stems from a general, three dimensional failure criterion previously developed by Lade [45] for cohesionless soils. The criterion is expressed in terms of stress invariants and involves three materials parameters describing the three independent characteristics for a concrete failure surface: the opening angle of the failure surface or friction angle, (2) the curvature of the failure surface in planes containing the hydrostatic axis, i.e. curved meridians, and (3) the tensile strength.

The failure surface function $F(\sigma)$ for this three-parameter criterion is expressed in terms of the first and third stress invariants as follows:

$$F(\sigma) = \left(\frac{J_1^3}{J_3} - 27\right)\left(\frac{J_1}{P_a}\right)^m - \eta_1 \qquad (5.15)$$

$$= 0 \text{ for material failure}$$

where

$$J_1 = \bar{\sigma}_1 + \bar{\sigma}_2 + \bar{\sigma}_3 \qquad (5.16)$$

$$J_3 = \bar{\sigma}_1 \cdot \bar{\sigma}_2 \cdot \bar{\sigma}_3 \qquad (5.17)$$

P_a = atmospheric pressure (positive) in the same unit as the stress

$\bar{\sigma}$'s are defined as translated the principal stress space along

the hydrostatic axis to include effect of tensile strength in Lade's failure criterion.

5.3.8 Model Proposed by Desai

Desai [15] chose a number of truncated form of F (J_1, $J_2^{1/2}$, $J_3^{1/3}$), Eq. (6.1), and evaluated them at ultimate (stress) condition for four different materials and for different stress paths. It may be mentioned that the ultimate condition is defined by the asypmtotic value of stress in the stress-strain response curve, as shown in Fig. 3.39. Of all the forms Desai [15] used, the form of eq. (6.5) essentially showed an invariant value of C at the ultimate condition for all the materials. A single yield surface (function) here is used instead of two or multiple yield surfaces. A comprehensive description of Desai's model is given in the following chapter.

CHAPTER 6

PROPOSED CONSTITUTIVE MODELS

6.1 Introduction

Characterization of stress-deformation behavior of concrete and rocks have been a subject of active research for a long time. Linear elastic, nonlinear (piecewise linear) elastic, elastic-plastic and endochronic models have been proposed and used by various investigators and the literature on the subject is very widespread.

The necessity of new developments in the area of constitutive modelling stems from the fact that none of the available models is general enough to provide a basis to characterize the behavior of different classes of materials under a variety of loading conditions. Thus, different constitutive models are required for different materials as well as for different histories of loadings. The techniques proposed by Desai [15, 23] can provide significant flexibility in terms of choosing appropriate yield conditions for plasticity-based constitutive laws. It should be noted here that some of the terms in the polynomial can be discarded at the outset, depending upon particular characteristics of given materials.

The major objective is to present a general model to characterize ultimate failure and hardening responses in the context of the theory of plasticity for concrete and rocks.

6.2 Polynomial Representation of the Yield Condition

The yield functions used in the past, Refs. [25, 29, 37, 69], can be considered to be polynomial functions expressed in terms of stress components or invariants of the stress tensor. Desai [15] proposed the following general functions as a complete polynomial in J_1, $J_2^{1/2}$, and $J_3^{1/3}$:

$$\begin{aligned} F(J_1,J_2^{1/2},J_3^{1/3}) = {} & \alpha_0+\alpha_1 J_1+\alpha_2 J_2^{1/2}+\alpha_3 J_3^{1/3}+ \\ & \alpha_4 J_1^{2}+\alpha_5 J_1 J_2^{1/2}+\alpha_6 J_2+\alpha_7 J_1 J_3^{1/3}+ \\ & \alpha_8 J_2^{1/2} J_3^{1/3}+\alpha_9 J_3^{1/3}+\alpha_{10} J,^{3}+ \qquad (6.1) \\ & \alpha_{11} J_1^{2} J_2^{1/2}+\alpha_{12} J_1^{2} J_3^{1/3}+\alpha_{13} J_1 J_2+ \\ & \alpha_{14} J_1 J_3^{2/3}+\alpha_{15} J_2 J_3^{1/3}+\alpha_{16} J_2^{2/3}+ \\ & \alpha_{17} J_2^{1/2} J_3^{2/3}+\alpha_{18} J_3+ \\ & \alpha_{19} J_1 J_2^{1/2} J_3^{1/3}+..... \end{aligned}$$

Where J_1, J_2, J_3 are the three stress invariants given by

$$J_1 = \sigma_{ii} \qquad (6.2a)$$

$$J_2 = 1/2\ \sigma_{ij}\ \sigma_{ji} \qquad (6.2b)$$

$$J_3 = 1/3\ \sigma_{ij}\ \sigma_{jk}\ \sigma_{ki} \qquad (6.2c)$$

the fractional powers of J_2 and J_3 are adopted to render the material response functions or constants to be dimensional. The function

in Eq. (6.1) can also be expressed in terms of J_{2D} and J_{3D}, the second and third invariants of the deviatoric stress tensor respectively. It may be noted that the yield function can be expanded up to any desired order. The constants, α_i ($i = 1,2...,n$ in Eq. (6.1) are material response functions. In general, all the material response functions can be expressed in terms of the history of deformation as well as a number of other tensor-valued and scalar-valued internal variables. Thus, α_i ($i = 1,2,...,n$) can be expressed as:

$$\alpha_i = \alpha_i \left(\int d\varepsilon_{mn}^p,\ W^p,\ a_{ij} \ldots . \eta_1,\ \eta_2 \ldots . \eta_N\right) \qquad (6.3)$$

Where $\int d\varepsilon_{ij}^p$ = history of plastic strain, $W^p = \int \sigma_{ij}\, d\varepsilon_{ij}^p$ = plastic work, a_{ij} = tensor-valued internal state variables, and $\eta_1, \eta_2 \ldots \eta_N$ = scalar-valued internal state variables.

Eq. (6.1) can be considered a special and simplified case of the general representation proposed by various investigators, Rivlin and Ericksen [63], Green and Naghdi [35], Shrivastava et al [72], Baker and Desai [7] and Sawczuk [67]. For instance, for an initially isotropic material, F can be expressed [15, 17, 23, 16] as

$$F = F(J_i,\ I_i^p,\ K_J,\ a_m) \qquad (6.4)$$

Where I_i^p ($i = 1,2,3$) = invariants of plastic strain tensor ε_{ij}^p, K_j ($J = 1,2,3,4$) are joint or mixed invariants of the stress and plastic strain tensor and a_m ($m = 1,2,....n$) are (scalar) valued functions such as plastic work. It has been shown that inclusion

of K_j can permit (induced) anisotropy during plastic straining [7, 37]. Equation (6.1) investigated herein is a special case of Eq. (6.4) in which F is expressed in terms of J_i with yielding and hardening behavior incorporated in the coefficient α_i which are treated either as material constants or response functions in terms of trajectories of total, volumetric and deviatoric plastic strain. The material is assumed to experience isotropic hardening; hence, K_j are not included at this time.

Desai [15] chose a number of truncated forms of $F(J_1, J_2 J_3)$ and evaluated them at ultimate (stress) condition for four different materials and for different stress paths. It may be noted that the ultimate condition is defined by asymptotic value of the stress in the stress-strain response curve. Of all the forms Desai [15] used, the form

$$\frac{J_1 J_3^{1/3}}{J_2} = C \tag{6.5}$$

essentially showed an invariant value of C at the ultimate conditions for all the materials. It is important to note here that the form given by Eq. (6.5) is not the only form which assumes an invariant value at ultimate condition. It is possible to construct a number of other such forms by choosing appropriate terms from the polynomial given by Eq. (6.1).

It was observed in Ref. [15] that the yield functions used in criteria such as Tresca, Van Mises, Mohr-Coulomb, Drucken Prager,

critical state and cap are truncated forms of F, Eq. (6.1). Also, the models recently derived by Lade [45] and Matsouka and Nakai [50] from laboratory observations for soils are also truncated forms of Eq. (6.1); modified forms of the former are also recently used to describe behavior of concrete [47, 70].

6.3 Proposed Constitutive Model

A number of investigators have proposed models for defining the failure behavior of concrete [77]. One of the early models was proposed by Kupfer and Gerstle [43] and involves (separate) definitions of failure surfaces for biaxial tension, biaxial compression, and tension--compression zones. Argyris et al [3, 5], Kotsovos and Newman [41], Ottosen [57], Willam and Wamke [83], Lade [48] and Traina et al [79, 78] and others have proposed models for describing failure behavior of concrete and rocks.

Willam and Warnke's model requires five parameters to define failure envelope and is expressed in term of average hydrostatic stress ($J_{1/3}$), average measure of octahedral shear stress ($\tau_a = 2/5\ \sqrt{J_{2D}}$) and a measure of lode angle Θ ($\cos 3\Theta = \sqrt{3}\, J_{3D}/J_{2D}$ The four parameter model by Ottosen [57] involves use of quantities proportioned to octahedral shear stress ($\tau_o = \sqrt{2}\ \sqrt{J_{2D}}/\sqrt{3}$), mean normal stress ($J_{1/3}$), and the angle Θ shown in Fig. 1.

Lade [48] proposed application of a model with F expressed in terms J_1, J_2 and J_3 for predicting failure behavior of concrete. Schreyer [79] proposed a modification of Lade's model that permits

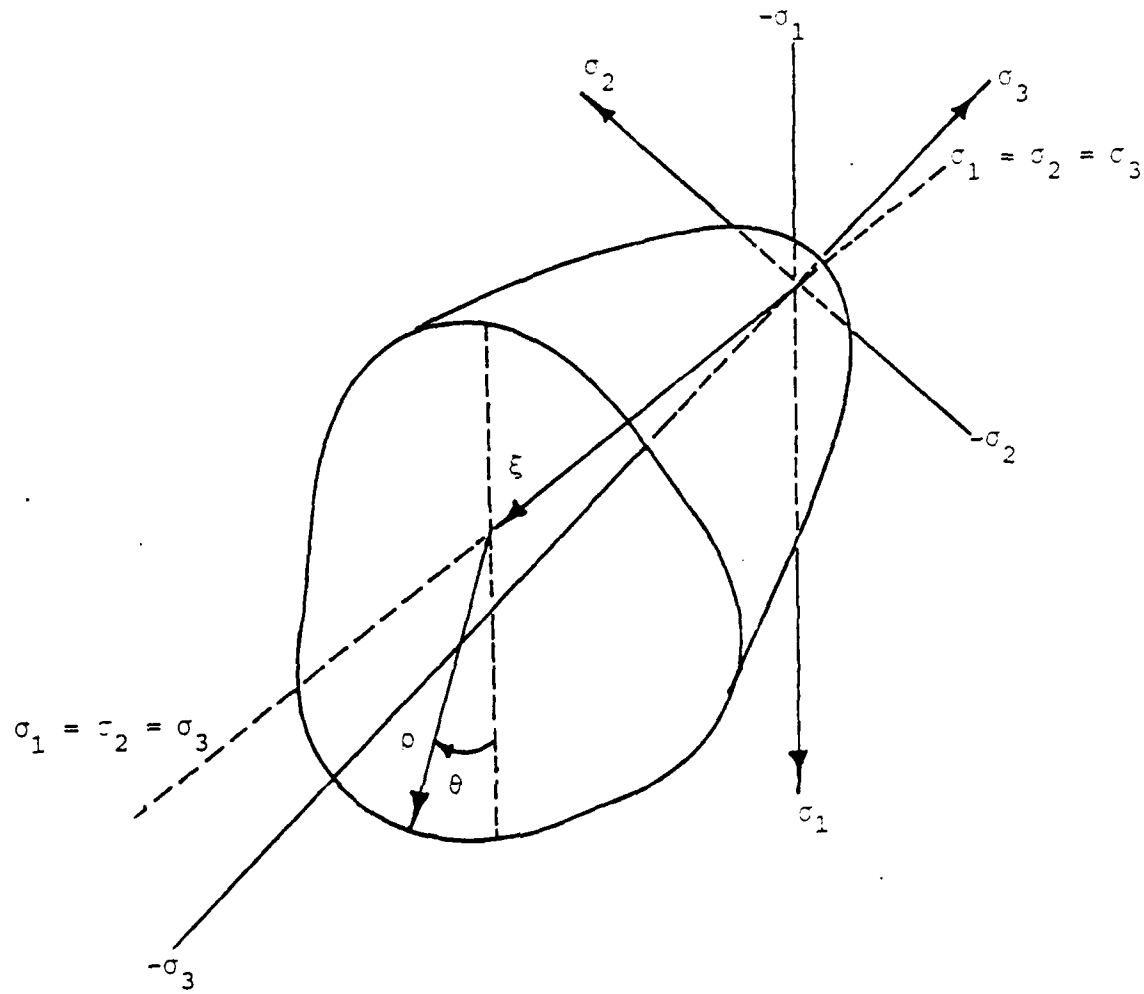

Figure 6.1. Triaxial Strength Surface in Principal Stress Space.

yield surface to intersect J_1-axis.

Elastic-plastic models for describing the hardening response of concrete and rocks have been proposed and used by various researchers: Mroz [54], Sudain and Schnobrich [75], Kupfer and Gerstle [43], Wu [86], Chen and Chen [12], Argyrin et al [4, 3, 5], Byukozlurk [11], Andenaes et al [2], Murray et al [55], and Chen and Ting [14]. Plasticity models including fracturing (and strain-softening) are proposed by Dougill [26, 27] Bazant and Kim [8] and Bazant [9, 10]. In the case of the hardening behavior, these concepts involve definition of initial yield surface representing the elastic limit, and then subsequent loading, yield or cap surface representing continuously yielding behavior of concrete and rocks. The final yield surface in the failure or fracture surface is often defined as the state of stress at which the change in volume is zero.

The yield function F is often expressed in terms of J_1 and J_2 (or J_{3D}); the models by Lade [48] and Traina et al [79] involve the invariant J_3 also. Bazant's [9, 10] model to include fracturing is based on two loading or yield surfaces, one expressed in terms of σ_{ij} and a hardening parameter, whereas the second in terms of ε_{ij} and another hardening parameter. This model possesses a number of useful capabilities such as effect of mean pressure ($J_{1/3}$) resulting in elastic or plastic volume change, strain-softening,

plastic volume change due to shear, and failure behavior; it is capable of capturing behavior for different loading paths like torsion-compression, uniaxial, and nonproportional triaxial.

One of the major drawbacks of all these models is that the yielding is controlled by two separate yield functions which intersect each other with a slope discontinuity. This results in nonuniqueness of the normals at the points of intersection. In the associated theory of plasticity, the incremental plastic strain is assumed to be normal to the yield surface at the loading point. Thus, the direction of incremental plastic strain is not defined at the point of intersection of two yield surfaces (see Fig. 6.2) This problem can be eliminated if a single yield surface (function) is used instead of two yield surfaces.

The definition of J_3 used in Eq. (6.4) is different from $J_3 = \sigma_1 \sigma_2 \sigma_3$ often used. This is because if one of the (principal) stresses is zero or near zero, $J_3 = \sigma_1 \sigma_2 \sigma_3$ may cause (computational) difficulties [15]. A modified form of the model presented previously [15, 16, 17, 19] to account for certain behavioral aspects of concrete and rocks is developed and presented herein. In the following descriptions, the major attention is given to the modification.

It may be noted that in the isotropic hardening plasticity theory, the initial yield surface expands continously until the ultimate or failure state is reached. However, the shape of the surface

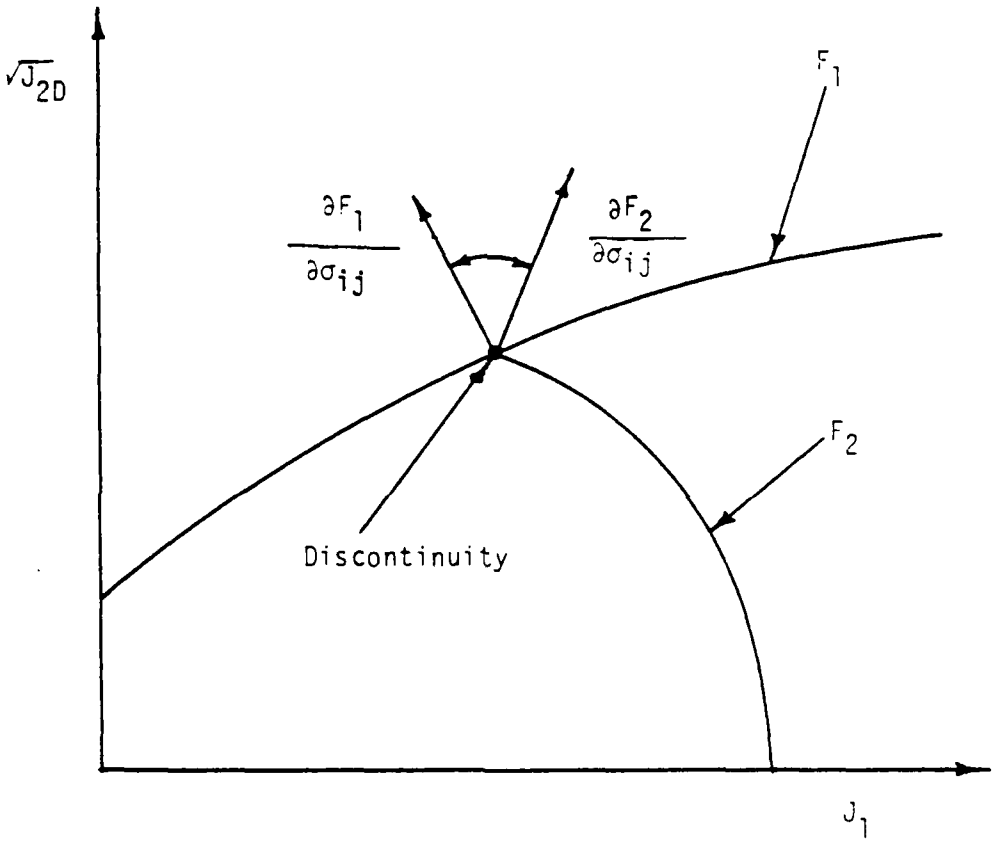

Figure 6.2. Typical Example of Two Yield Surface Plasticity Model.

remain unchanged. Geological materials such as soils, rocks and concrete exhibit plastic response even when the applied load is small. This means that hardening starts from the very beginning and the material continues to harden plastically until failure is reached. This hardening process is described by the hardening law of plasticity theory and will be discussed later.

One of the functions used to define yield in the context of incremental plasticity for describing behavior of soils [15, 16, 17, 19, 23a], on the basis of the form given by Eq. (6.1), is given by

$$F = J_{2D} - F_b F_s \tag{6.6}$$

where J_{2D} is the second invariant of the deviatoric stress tensor, F_b is the basic function and F_s is the shape function.

A special form of Eq. (6.6) is given by:

$$F(J_1, J_{2D}, J_{3D}) = J_{2D} - (-\alpha J_1^{\eta} + \gamma J_1^2)(1 - \beta S_r)^m = 0 \tag{6.7}$$

where α, β, γ, η are response functions, $S_r = J_{3D}^{1/3}/J_{2D}^{1/2}$ is a stress ratio where J_{3D} is the third invariant of deviatoric stress tensor. The functionals β, γ, η are assumed to be material constants, $m = -1/2$ for many geological materials, and α is assumed to be the growth (hardening or softening) function.

Based on the Eq. (6.7), a new constitutive model is proposed to describe both failure and yielding of pressure sensitive materials such as concrete and rocks. The model agrees with the experimental evidence regarding the shapes of yield surfaces on various planes. Moreover, both ultimate failure and yielding are defined

by a single yield surface.

In order for the ultimate criterion given by Eq. (6.7), originally formulated for cohesionless soils [19, 23a], to be applicable to concrete and rocks, the cohesion and tensile strength sustained by concrete and rocks must be included. This is done by translating the principal stress space along the hydrostatic axis as shown in Fig. 6.3 by the addition of a constant stress $R = a.p_a$ added to the normal stresses. The modified function is given by:

$$J_{2D} - (-\alpha J_1^{\,n} + \gamma J_1^{\,2})\,(1 - \beta S_r)^{-1/2} = 0 \qquad (6.8)$$

where

$$J_1 = \sigma_1^* + \sigma_2^* + \sigma_3^* \qquad (6.9a)$$

$$J_{2D} = 1/6\,[(\sigma_1^* - \sigma_2^*)^2 + (\sigma_2^* - \sigma_3^*)^2 + (\sigma_1^* - \sigma_3^{\,*})^2] \qquad (6.9b)$$

$$J_3 = 1/3\,(\sigma_1^{*3} + \sigma_2^{*3} + \sigma_3^{*3}) \qquad (6.9c)$$

$$J_{3D} = J_3^* = 2/3\,J_1^*\;J_{2D}^* - \frac{1}{27}\,J_1^{*3} \qquad (6.10)$$

The corresponding normal stresses σ_1^*, σ_2^* and σ_3^* in Eqs. (6.9 and 6.10) at ultimate state are expressed as

$$\sigma_1^* = \sigma_1 + R \qquad (6.11a)$$

$$\sigma_2^* = \sigma_2 + R \qquad (6.11b)$$

$$\sigma_3^* = \sigma_3 + R \qquad (6.11c)$$

$$R = aP_a \qquad (6.12)$$

where a = dimensionless number and p_a = atmospheric pressure. For cohesionless materials, R = 0, and the function at ultimate in Eq. (6.8) reduces to that in Eq. (6.7).

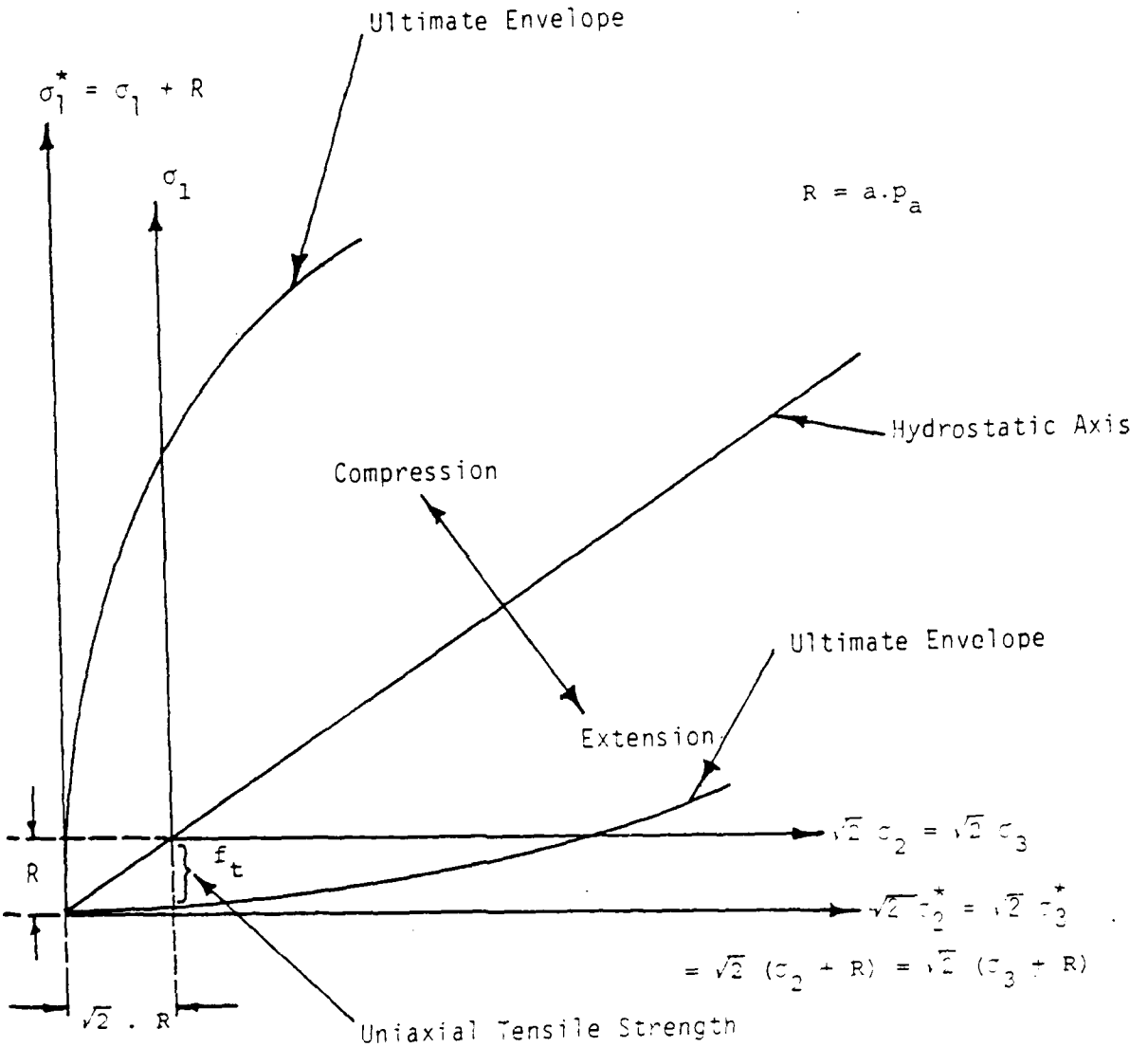

Figure 6.3. Translation of Principal Stress Space Along Hydrostatic Axis to Include Effect of Tensile Strength in Ultimate Criterion.

It is observed experimentally that the shape of the yield locus of materials such as concrete and rocks on the π-plane (or octahedral planes) changes continuously with J_1. It is found then at high pressures, the yield locus plots almost like a circle. As the confining pressure (J_1) is decreased, the shape of the yield locus gradually changes towards a triangle with smooth rounded corners [48]. At the limit, when $J_1 = 0$ the yield locus becomes triangular with vanishing rounded corners. Fig. 6.4 shows typical yield luci at the limits as well as during transition.

Consider that β in Eq. (6.8) is a function of J_1 defined by

$$\beta = \beta_o e^{-\beta_1 J_1} \tag{6.13}$$

where β_o and β_1 are material constants. It is seen from Eq. (6.13) that when $J_1 = 0$, $\beta = \beta_o$ and as $J_1 \to \infty$, $\beta \to 0$.

Plots of the proposed yield function on the $\sqrt{J_{2D}} - J_1$ (for TC, SS, TE), π, octahedral, triaxial and biaxial planes are shown in Figs. 6.5 (a,b,c) through 6.9 respectively, for the soapstone described subsequently.

6.3.1 Properties of the Proposed Yield Function

The model proposed here is expressed in terms of J_1, J_{2D}, J_{3D} with hardening defined by using various measures of plastic strain. Some of the distinguishing features of the proposed model are stated in the following page:

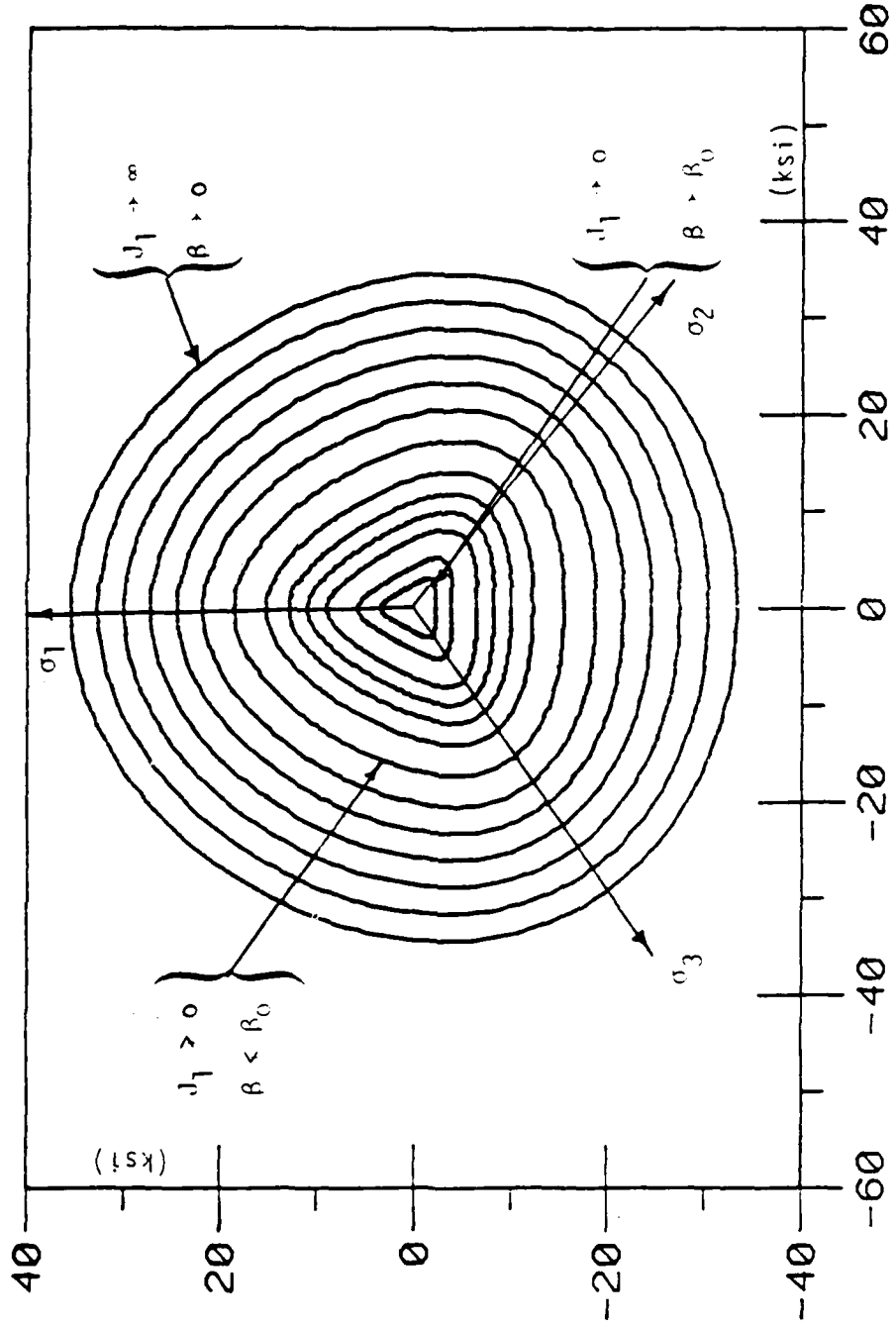

Figure 6.4. Typical Proposed Yield Loci at the Limits As Well As During Transition on the Octahedral Plane for Various J_1.

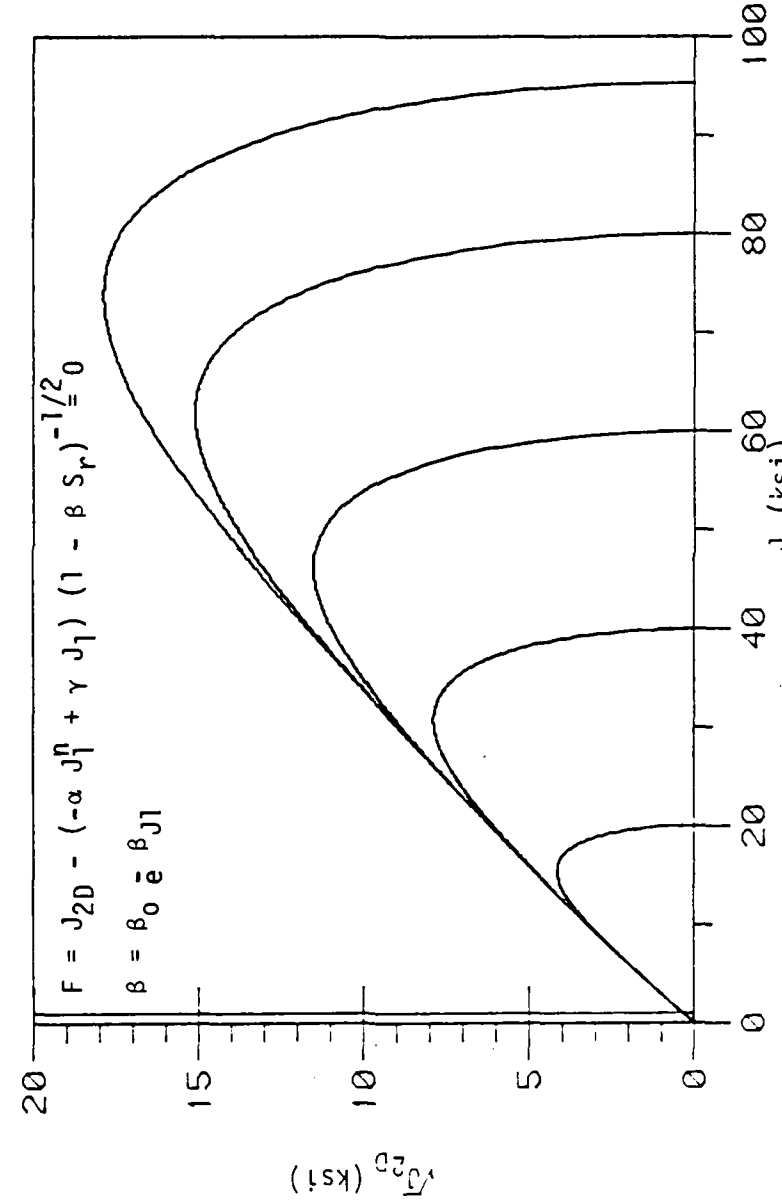

Figure 6.5a. Plot of the proposed Yield Function in $\sqrt{J_{2D}}$ - J_1 Plane for Triaxial Compression (TC) Test, (θ=-30°), for various α.

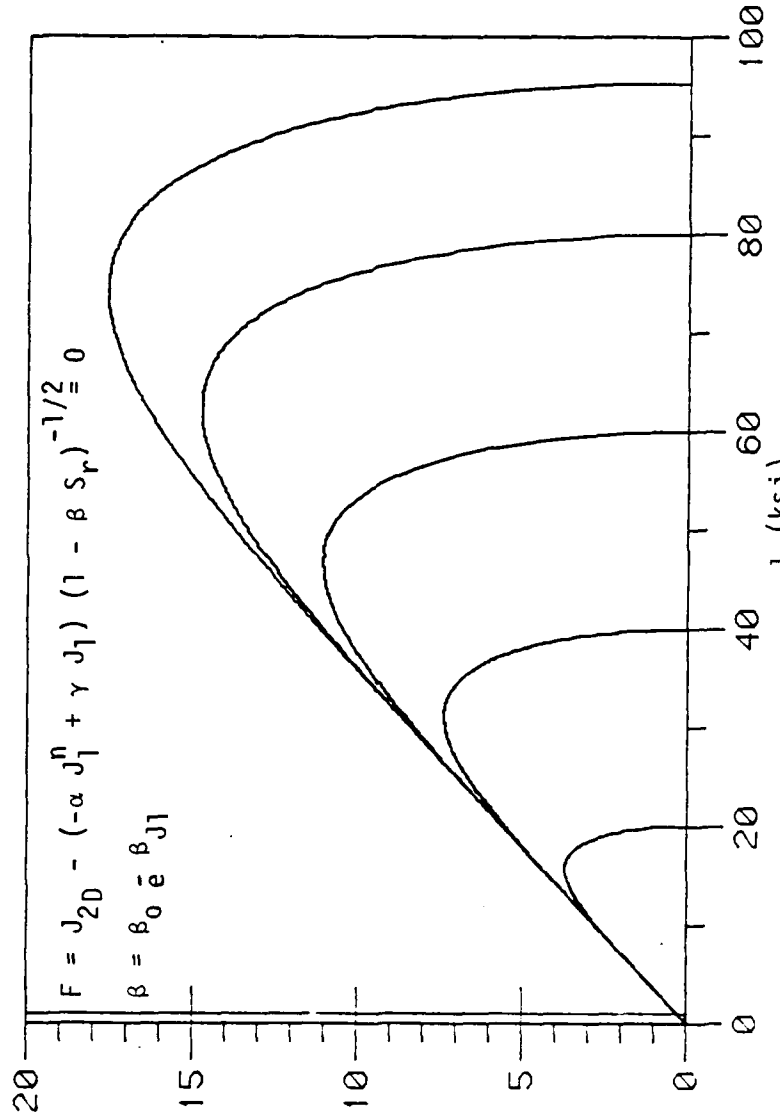

Figure 6.5b. Plot of the Proposed Yield Function in $\sqrt{J}_{2D}$ - J_1 Plane for Simple Shear (SS) Test, ($\theta=0^0$), for various ξ.

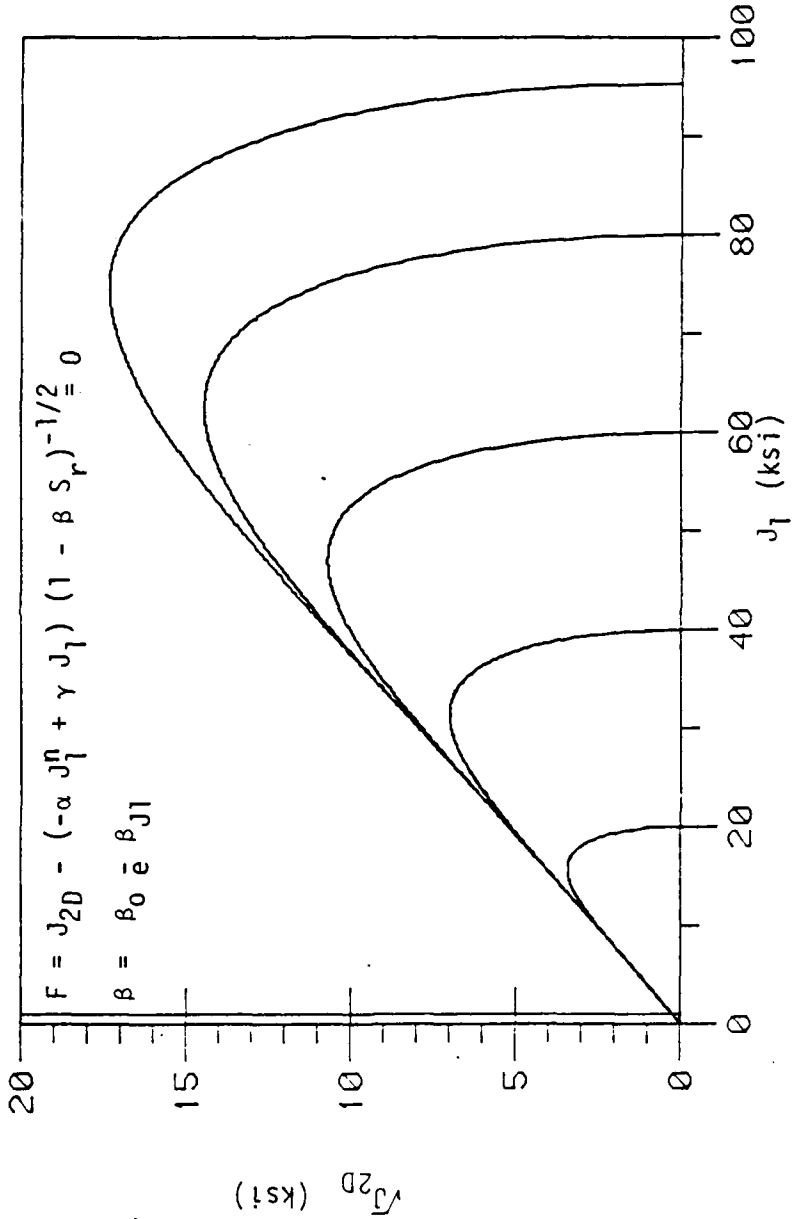

Figure 6.5c. Plot of the Proposed Yield Function in $\sqrt{J_{2D}}$ - J_1 Plane for Triaxial Extension (TE) Test, ($\theta=30^0$), for various α.

$$F \equiv J_{2D} - (-\alpha J_1^n + \gamma J_1)(1 - \beta S_r)^{-1/2} = 0$$

$$\beta = \beta_o e^{-\beta J_1}$$

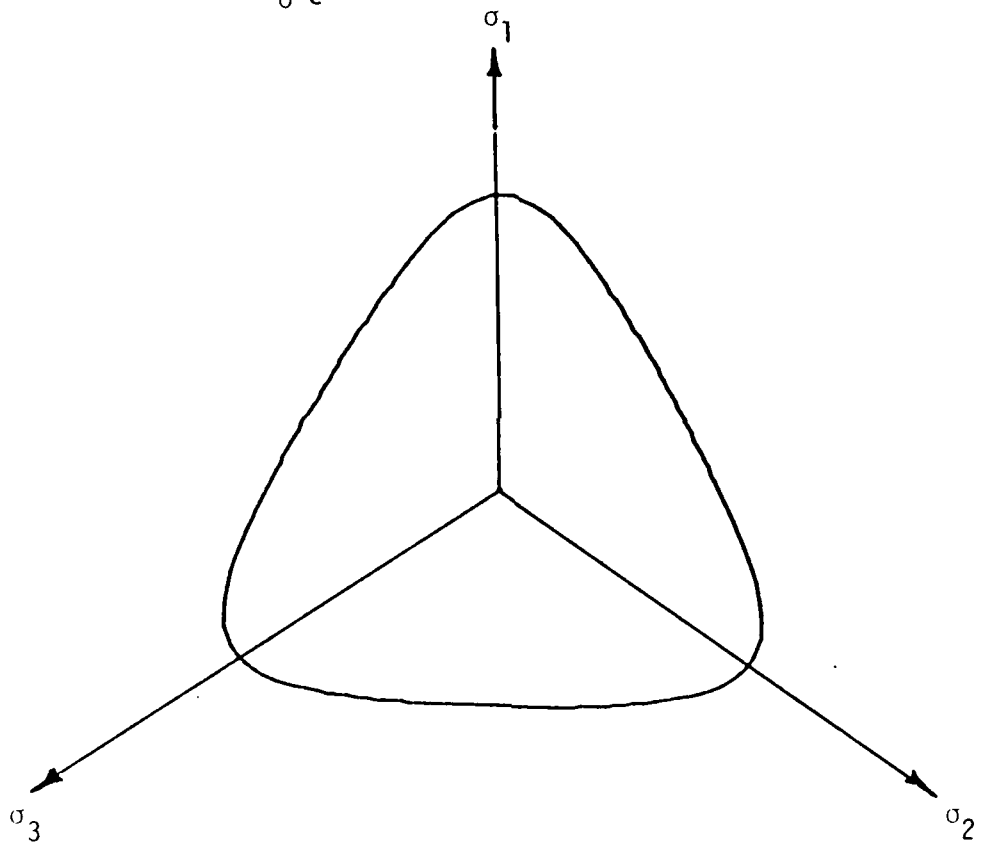

Figure 6.6. Plot of the Proposed Yield Function in π-Plane ($J_1 = 0$).

$$F \equiv J_{2D} - (-\alpha J_1^n + \gamma J_1)(1 - \beta S_r)^{-1/2} = 0$$

$$\beta = \beta_o e^{-\beta J1}$$

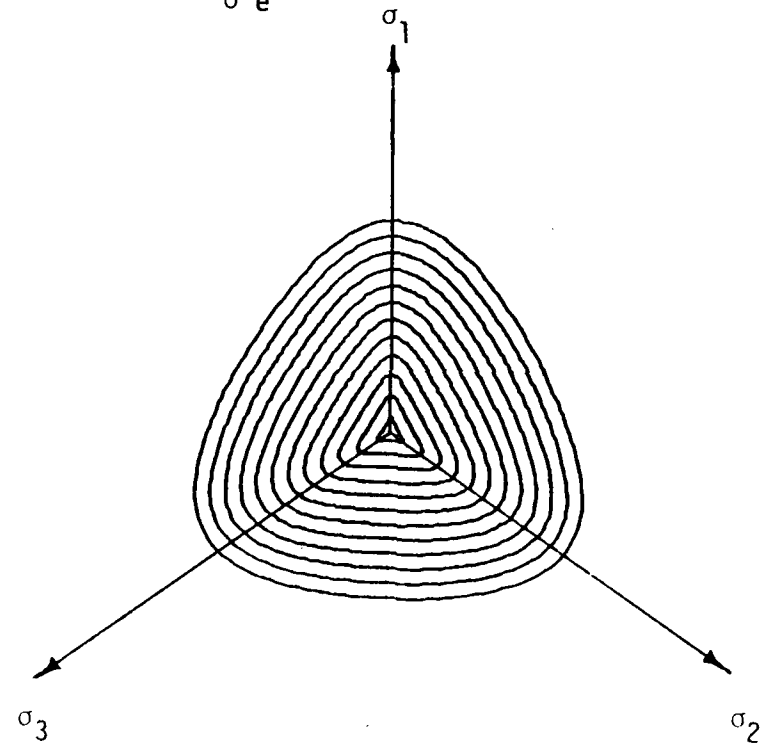

Figure 6.7. Typical Sections of the Yield Surface on the Octahedral Plane for Various J_1.

$$F \equiv J_{2D} - (-\alpha J_1^{n} + \gamma J_1)(1 - \beta S_r)^{-1/2} = 0$$

$$\beta = \beta_o e^{-\beta J_1}$$

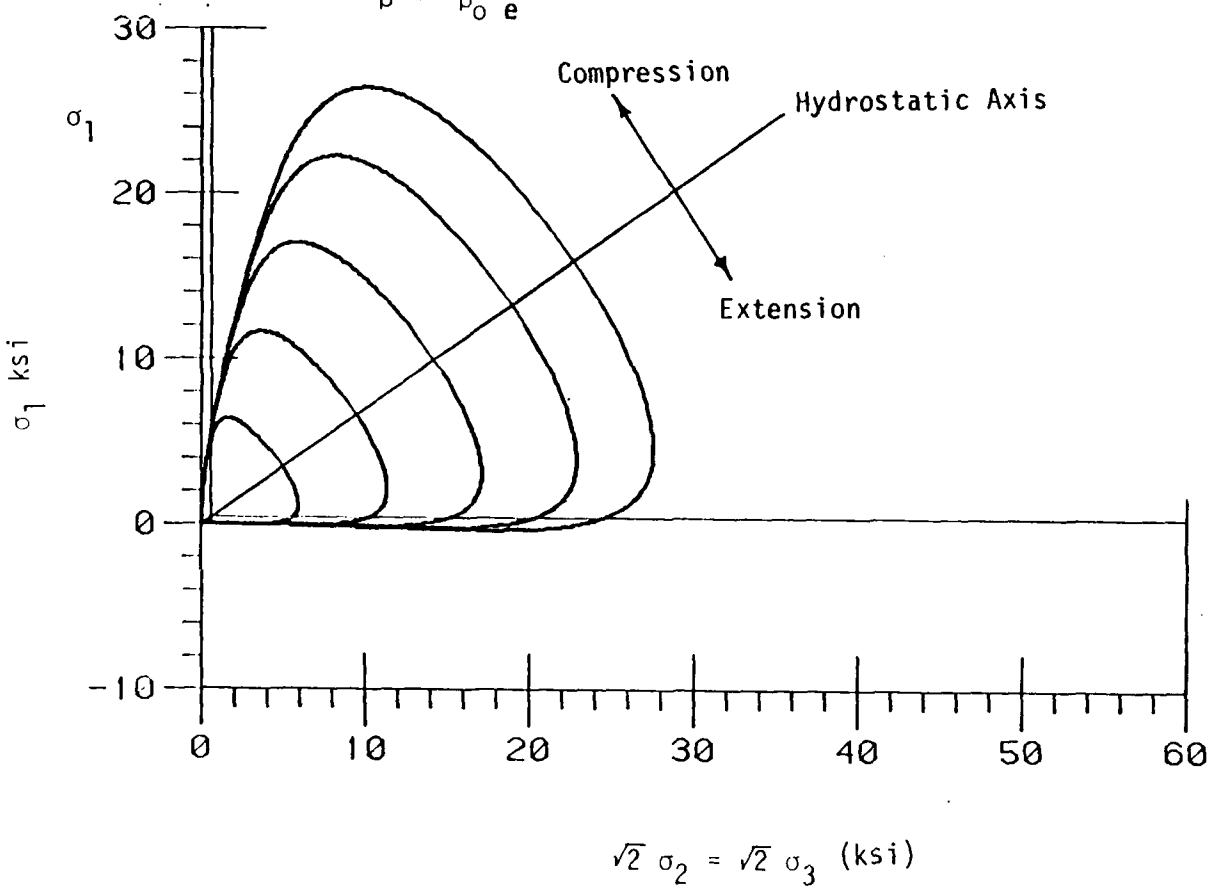

Figure 6.8. Plot of the Proposed Yield Function in Triaxial Plane.

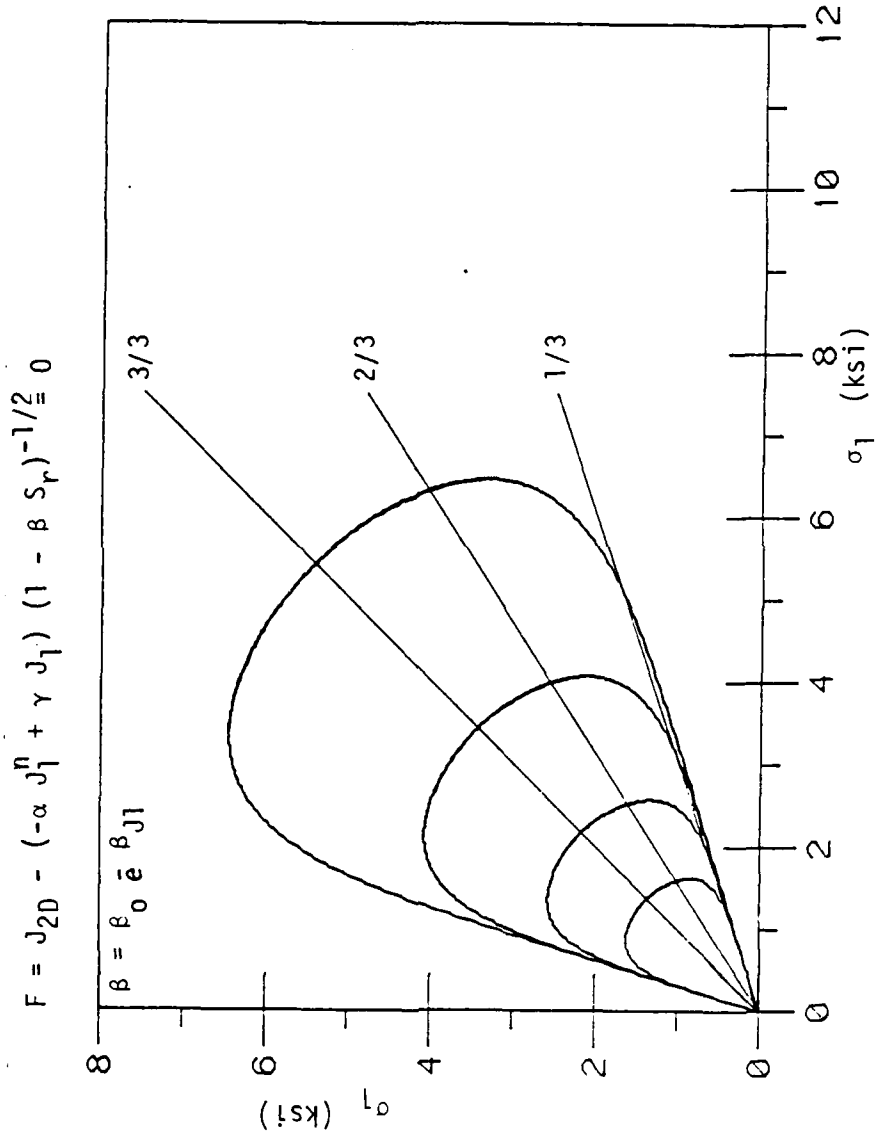

Figure 6.9. Plot of the Proposed Yield Function in Biaxial Plane for various α, (σ_3=0).

(1) Figure 6.5-6.9 show that the proposed model involves only one continuous surface which describes yield or loading surfaces by a single function, which also describes the ultimate behavior; as stated earlier, the traditional failure is defined in the proposed model by one of the functions with $\beta = \beta_f \leq \beta_u$.

(2) Because only one function defines the entire behavior (hardening and ultimate), the number of required parameters is smaller than the previous multi-surface models.

(3) Since intersections (singularities) of two or more surfaces are avoided, the model is easier to implement for numerical computations.

(4) The function F (Eq. 6.9) plots continuous and convex in the stress spaces, Fig. 6.5-6.9 for both hardening and ultimate responses of many (geological) materials. Moreover, it intersects the J_1-axis at right angles. As a result, it can be implemented in the context of the classical theory of plasticity based on the stability criterion [29].

(5) Material like rocks, concrete, broken rock, aggregate and ballast, and materials experiencing fracturing and softening near the ultimate condition for low confining pressure, can exhibit nonconvex yield surfaces; this response is similar to the star-shaped (ultimate) yield surfaces observed for metals [85]. This may be partly due to the fact that the ultimate strength for these conditions under certain stress paths such as extension, Fig. 6.5c can be much lower than that under other (compression) stress paths.

(6) A single definition of growth function ξ can simulate hardening (described subsequently) and include the effects of stress path, volume change and coupling of shear and volumetric responses. As a result, the model is simplified significantly.

6.3.2 Growth Function, α

The response function α is called the growth or evolution function. In general, the functional form of α can be written in the following form:

$$\alpha = \alpha \left(\int d\varepsilon_{ij}^{p},\ W^{p},\ a_{ij} \ldots,\ \eta_1,\ \eta_2, \ldots \eta_N,\ T\right) \tag{6.14}$$

the arguments of α are defined in Eq. 6.3. The variable T in eq. 6.14 is the temperature. In general, a large list of history dependent parameters can be chosen to express the growth function α. In this study, however, α will be made function of single parameter, ξ,

$$\xi = \int (d\varepsilon_{ij}^{p}\ d\varepsilon_{ij}^{p})^{1/2} \tag{6.15}$$

where ξ is the trajectory of plastic strain in a nine-dimensional Eulidean space formed by the components of the incremental plastic strain tensor. The parameter ξ contains both volumetric and deviatoric plastic deformations. Thus ξ can be split into two parts as [17]

$$\xi_D = \int (de_{ij}^{p}\ de_{ij}^{p})^{1/2} \tag{6.16}$$

$$\xi_V = \frac{1}{\sqrt{3}} \int d\varepsilon_{kk}^{p} \tag{6.17}$$

where ξ_D and ξ_V are the deviatoric and volumetric part of ξ, respectively and de_{ij}^{p} is the incremental deviatoric plastic strain

tensor defined by:

$$de_{ij}^{p} = de_{ij}^{p} - 1/3\ de_{kk}^{p}\ \delta_{ij} \tag{6.18}$$

with these definitions of ξ, we can now define α in the form:

$$\alpha = \frac{a_1}{\xi^{\eta_1}} \tag{6.19}$$

where a_1 and η_1 are the material constants associated with plastic hardening.

Typical plots of $\sqrt{J}_{2D}$ - J_1 of various α are shown in Fig. 6.5. It is seen that the yield surface plots convex on the $\sqrt{J}_{2D}$ - J_1 plane. Such convexity is required to ensure stability of the material in the plastic range.

It is mentioned earlier that the parameters ξ_V and ξ_D are the volumetric and the deviatoric part of the total plastic strain trajectory, ξ. Now consider two ratios, r_V and r_D, such that:

$$r_V = \frac{\xi_V}{\xi} \tag{6.20a}$$

$$r_D = \frac{\xi_D}{\xi} \tag{6.20b}$$

The ratio, r_V, describes the plastic volume change behavior under a general loading history. The ratio, r_D, describes the deviatoric behavior of the material point during inelastic straining. Figures 6.10 and 6.11 show the plots of r_D - r_V for a plain concrete and soapstone (described subsequently). It can be seen that irrespective of the stress path followed, the relation between r_V and r_D can be assumed to be essentially invariant. For an isotropic material that hardens isotropically, the relation

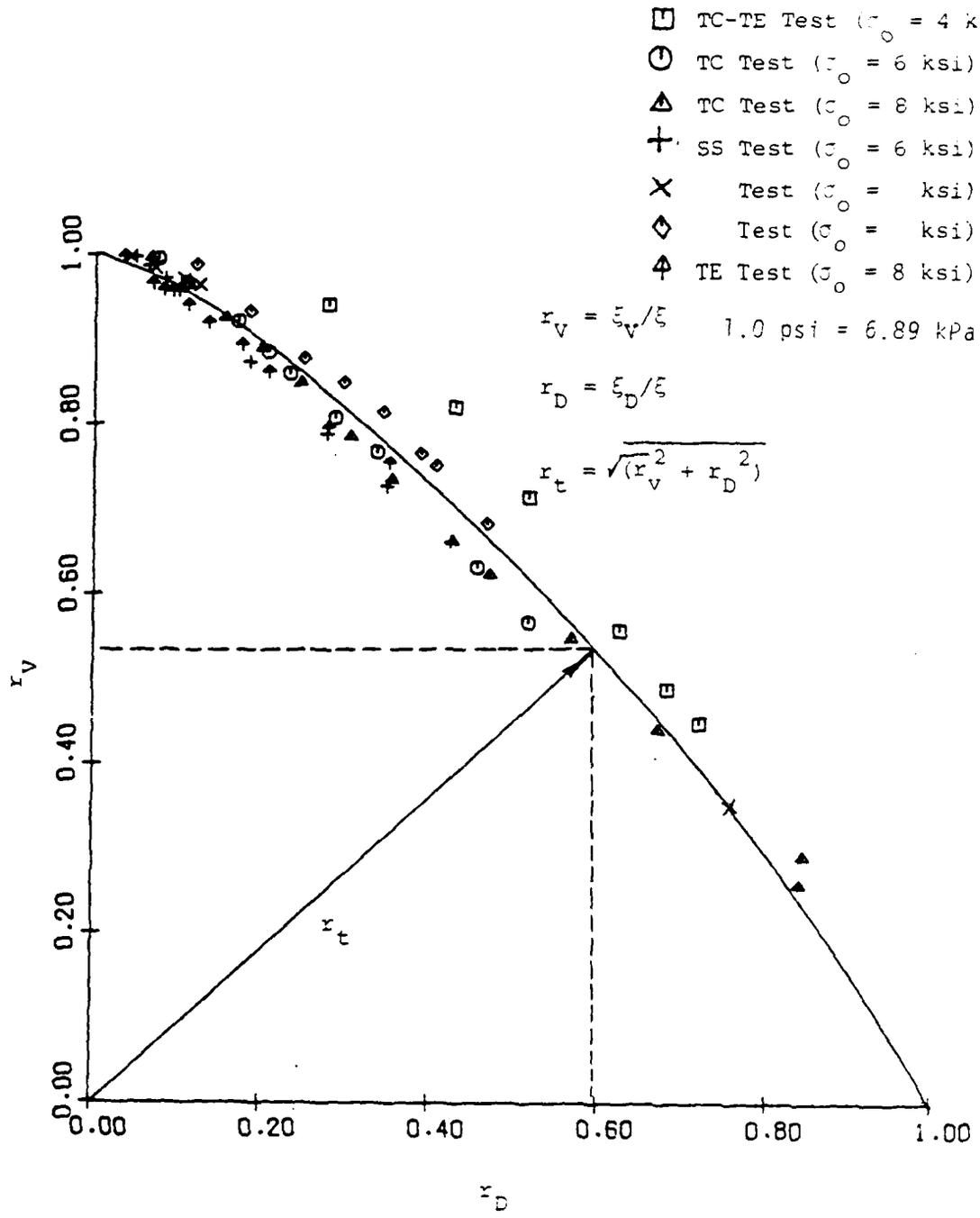

Figure 6.10. r_v - r_D Plot Obtained from a number of Triaxial Tests for the Plain Concrete.

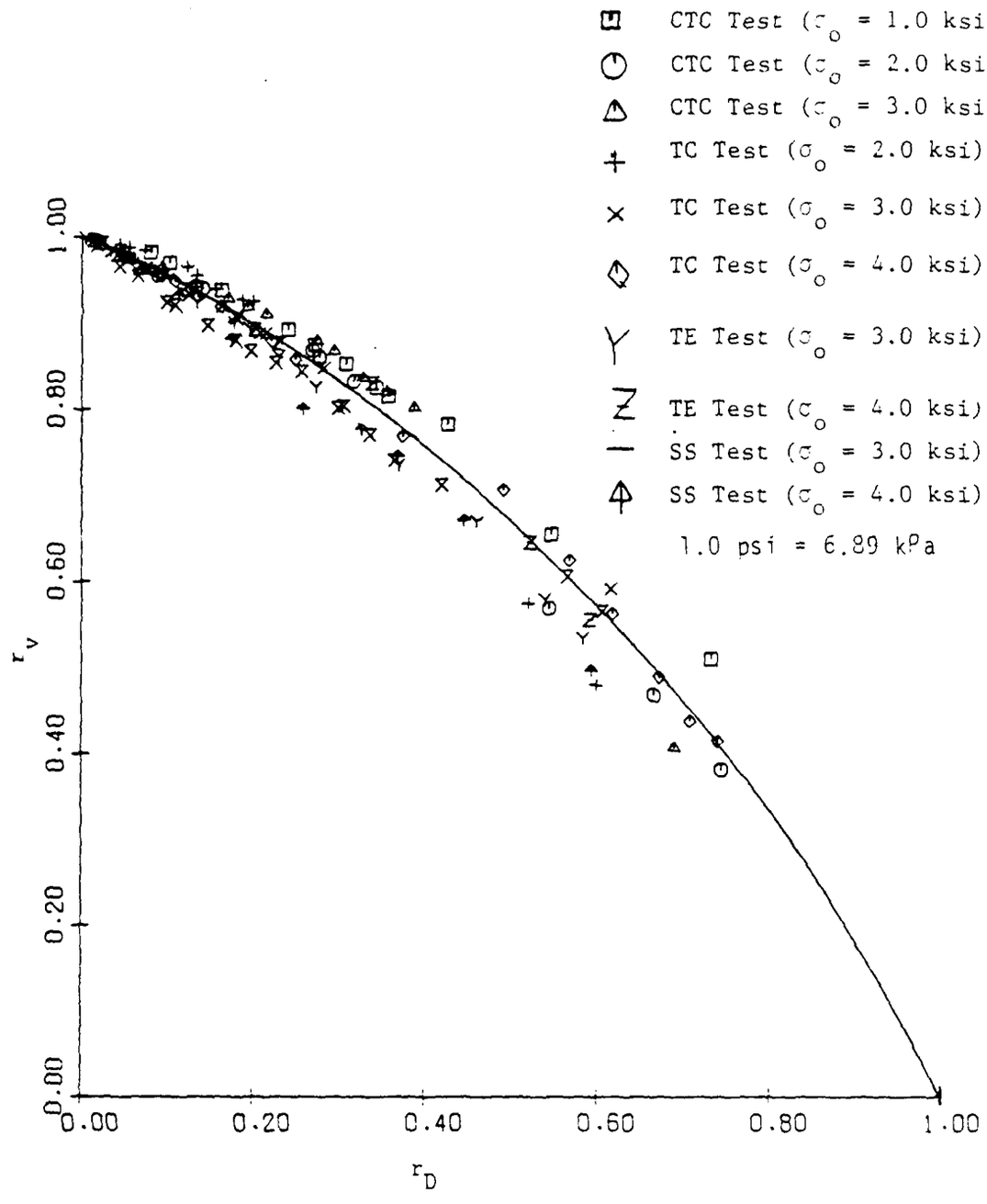

Figure 6.11. r_v - r_D Plot Obtained from a Number of Triaxial Tests for the Soapstone.

is bonded by unity. At the end of HC, $r_D = 0$ and $r_V = 1$, near the ultimate (or in the case of nonfrictional materials) $r_V \rightarrow 0$, and $r_D \rightarrow 1$.

6.3.3 Elastic-Plastic Constitutive Relations

The principles of continuity and consistency in Drucker's postulate [29] enable one to decompose an incremental strain tensor into elastic part and plastic part (assuming small strain) as

$$d\varepsilon_{ij} = d\varepsilon_{ij}^{e} + d\varepsilon_{ij}^{p} \tag{6.21}$$

where the superscripts e and p refer to elastic and plastic, respectively. The stress-elastic strain relationship can be written in form:

$$d\sigma_{ij} = C_{ijkl}\, de_{kl}^{e} \tag{6.22}$$

where C_{ijkl} is the elastic constitutive relation tensor. $d\varepsilon_{kl}^{e}$ is elastic part of the total incremental strain $d\varepsilon_{kl}$. Substituting for $d\varepsilon_{kl}^{e}$ in this equation gives:

$$d\sigma_{ij} = C_{ijkl}\, (d\varepsilon_{kl} - d\varepsilon_{kl}^{p}) \tag{6.23}$$

In general, the yield function may be written as:

$$F = F\,(\sigma_{ij},\, d\varepsilon_{ij}^{p}) \leq 0 \tag{6.24}$$

with equality during yielding and negative during unloading. With the assumption of the normality principle and associated flow rule, the incremen of plastic strain must be normal to the yield surface;

hence

$$d\varepsilon^{p}_{ij} = d\lambda \frac{\partial F}{\partial \sigma_{ij}} \tag{6.25}$$

Where $d\lambda$ is the unknown hardening parameter giving the magnitude of the plastic strain increments, with the direction governed by the normality rule. The consistancy condition [28, 18] is given by equality,

$$dF = 0 \tag{6.26}$$

Thus, the consistency condition can be restated as

$$dF = \frac{\partial F}{\partial \sigma_{ij}} d\sigma_{ij} + \frac{\partial F}{\partial \varepsilon_{ij}} p \, d\varepsilon_{ij}^{p} = 0 \tag{6.27}$$

After rearranging, it can be written as:

$$\frac{\partial F}{\partial \sigma_{ij}} d\sigma_{ij} = - \frac{\partial F}{\partial \varepsilon_{ij}} p \, d\varepsilon_{ij}^{p} \tag{6.28}$$

substituting the Eq. (6.23) and (6.25) in (6.28)

$$\frac{\partial F}{\partial \sigma_{ij}} C_{ijkl} (d\varepsilon_{kl} - d\varepsilon_{kl}^{p}) = - \frac{\partial F}{\partial \varepsilon_{ij}} p \, d\lambda \frac{\partial F}{\partial \sigma_{ij}} \tag{6.29}$$

or

$$d\lambda \left(\left[- \frac{\partial F}{\partial \varepsilon_{ij}} p \frac{\partial F}{\partial \sigma_{ij}} \right] + \frac{\partial F}{\partial \sigma_{ij}} \frac{\partial F}{\partial \sigma_{kl}} C_{ijkl} \right) = \frac{\partial F}{\partial \sigma_{ij}} C_{ijkl} \, d\varepsilon_{kl} \tag{6.30}$$

So the scalar parameter of proportionality can be written as:

$$d\lambda = \frac{\frac{\partial F}{\partial \sigma_{ij}} C_{ijkl} \, d\varepsilon_{kl}}{\left(\frac{\partial F}{\partial \sigma_{ij}} \frac{\partial F}{\partial \sigma_{kl}} C_{ijkl} - \frac{\partial F}{\partial \sigma_{ij}} \frac{\partial F}{d\varepsilon_{ij}} p \right)} \tag{6.31}$$

Equation (6.31) when substituted back in Eqs. (6.22) and (6.25) yields:

$$d\sigma_{ij} = C_{ijkl} \left(d\varepsilon_{kl} - d\lambda \frac{\partial F}{\partial \sigma_{ij}}\right) \tag{6.32}$$

or

$$d\sigma_{ij} = \left(C_{ijkl} - \frac{C_{rskl} \frac{\partial F}{\partial \sigma_{kl}} \frac{\partial F}{\partial \sigma_{ij}} C_{ijkl}}{\frac{\partial F}{\partial \sigma_{ij}} C_{ijkl} \frac{\partial F}{\partial \sigma_{kl}} - \frac{\partial F}{\partial \varepsilon_{ij}^{p}} \frac{\partial F}{\partial \sigma_{ij}}}\right) d\varepsilon_{kl} \tag{6.33}$$

or

$$d\sigma_{ij} = \left(C_{ijkl}^{e} - C_{ijkl}^{p}\right) d\varepsilon_{kl} \tag{6.34}$$

This can be rewritten as:

$$d\sigma_{ij} = C_{ijkl}^{e-p} d\varepsilon_{kl} \tag{6.35}$$

where C_{ijkl}^{e-p} is known as the elasto-plastic constitutive tensor.

$\frac{\partial F}{\partial \sigma_{ij}}$ and $\frac{\partial F}{\partial \varepsilon_{ij}^{p}}$ must be evaluated from a given yield function.

$\frac{\partial F}{\partial \sigma_{ij}}$ in Eqs. (6.31) and (6.32) can be expanded by the chain rule.

$$\frac{\partial F}{\partial \sigma_{ij}} = \left(\frac{\partial F}{\partial J_1} \frac{\partial J_1}{\partial \sigma_{ij}}\right) + \left(\frac{\partial F}{\partial J_{2D}} \frac{\partial J_{2D}}{\partial \sigma_{ij}}\right) + \left(\frac{\partial F}{\partial J_{3D}} \frac{\partial J_{3D}}{\partial \sigma_{ij}}\right) \tag{6.36}$$

or gradient of F with respect to σ_{ij} can be expressed as:

$$\frac{\partial F}{\partial \sigma_{ij}} = \frac{\partial F}{\partial J_1} S_{ij} + \frac{\partial F}{\partial J_{2D}} S_{ij} + \frac{\partial F}{\partial J_{2D}} \left(S_{ik} S_{kj} - 2/3 J_{2D} S_{ij}\right) \tag{6.37}$$

where δ_{ij} = Kronecker's delta and S_{ij} = deviatoric stress tensor.

6.4 Determination of Material Constants

6.4.1 General

The proposed model has a number of material constants including the Young's modulus, E, poisson's ratio, ν, shear modulus, G, and bulk modulus, K. Determination of such constants for any material requires a comprehensive series of laboratory tests with number of loading, unloading and reloading cycles.

The proposed constitutive model is, in general, applicable for any pressure sensitive material. In this dissertation, however, only concrete and rocks will be considered.

Seven different concretes and rocks are considered here to obtain the material constants associated with the proposed constitutive model. These are i) a plain concrete under low confining pressures, ii) a plain concrete under high confining pressure, iii) Steel Fiber Reinforced Concrete, iv) Soapstone, v) Sandstone, vi) Westerly Granite, and vii) Dunham Dolomite. The stress-stain responses for plain concrete under low confining pressure and soapstone are presented in Chapter 3 and 4, respectively. The test data for the plain concrete under high confining pressure is adopted from Scavuzzo et al [68]. The test data for the steel fiber reinforced concrete is taken from Egging [30]. The test data for the sandstone is taken from Nishida et al [56]. The test data for this westerly granite and dunham dolomite are taken from Mogi [52].

6.4.2 Procedure for Determining Material Constants

There are nine material constants associated with proposed model as described in Eq. (6.9). These constants can be classified into three categories:

1) Elastic Constants
   E, ν or G, K

2) Constants for Hardening Yielding
   R, n, β_o, β_1, γ

3) Constants for Hardening
   a_1, η_1

Elastic Constants

There are two elastic constants for an isotropic material, Young's modulus, E and poisson's ratio, ν. It may be noted that bulk modulus, K and shear modulus, G, may also be used. It will be assumed that unloading and reloading is elastic. Thus E and ν can be found from the slope of the unloading-reloading curves. Although any test can be used for this purpose, only the hydrostatic compression test and conventional triaxial compression tests will be used to determine E, ν. When the hydrostatic compression test data is plotted as mean pressure vs. volumetric strain, the slope of the unloading-reloading curve gives the bulk modulus, K, where K is related to E and ν through the following equation:

$$K = \frac{E}{3(1-2\nu)} \tag{6.38}$$

To obtain E and ν explicitly, a second equation is needed. To determine appropriate values for shear modulus, G, plots of octahedral

shear stress vs. octahedral shear strain are used. The slope of the unloading-reloading of the τ_{oct} - γ_{oct} curve represents a value equal to twice the shear modulus. From these plots a weighted average value of shear modulus, G, was determined. G is related to E and ν through the following equation:

$$G = \frac{E}{2(1 + \nu)} \tag{6.39}$$

using Eq. (6.38) and (6.39), E and ν can be obtained explicitly.

Response Function, n.

The value of n can be determined at the state of stress (in the experiment) at which the dialation occurs, that is, volume change is zero. At this state, from Eq. (6.8)

$$\frac{J_{2D}}{J_1^2} = [- \alpha J_1^{(n-2)} + \gamma] F_s \tag{6.40}$$

Also at dialation point

$$\frac{\partial F}{\partial J_1} = 0 \tag{6.41}$$

or

$$- (- \alpha n J_1^{(n-1)} + 2\gamma J_1) F_s = 0$$

or

$$J_1 = \left(\frac{2\gamma}{\alpha n}\right)^{\left(\frac{1}{n-2}\right)} \tag{6.42}$$

from Eqs. (6.40) and (6.42)

$$1 - \frac{2}{n} = \frac{\frac{J_{2D}}{J_1^2}}{F_s \gamma} \tag{6.43}$$

from which n is obtained.

For materials such as concrete and rocks we can use the following procedure to determine n from a number of stress paths. At ultimate failure Eq. (6.40) can be written as:

$$\left(\frac{J_{2D}}{J_1^2}\right)_{\text{ultimate}} = \gamma F_s \tag{6.44}$$

At dialation point using Eq. (6.43) we obtain:

$$\left(\frac{J_{2D}}{J_1^2}\right)_{\text{dialation}} = \left(1 - \frac{2}{n}\right) F_s \gamma \tag{6.45}$$

Dividing Eqs. (6.44) and (6.45) and substituting for:

$$\frac{\left(\frac{J_{2D}}{J_1^2}\right)_{\text{dialation}}}{\left(\frac{J_{2D}}{J_1^2}\right)_{\text{ultimate}}} = S$$

or

$$\frac{\left(\frac{\tau_{oct}^2}{J_1^2}\right)_{\text{dialation}}}{\left(\frac{\tau_{oct}^2}{J_1^2}\right)_{\text{ultimate}}} = S$$

thus

$$S = \frac{(1 - \frac{2}{n})\, F_s \gamma}{\gamma F_s} = (1 - \frac{2}{n}) \tag{6.46}$$

n value obtained from different stress paths (for different initial confining pressure) will, in general, be different. Thus an average value of n will be calculated.

The Effect of the Tensile Strength, R.

If the uniaxial tensile strength, f_t, is not determined experimentally, Hannant [36], Lade [48] and Mitchell [51] gives an approximate formula relating f_t to the unconfined compression strength, f_{cu}, through the following formula:

$$f_t = T.P_a \left(\frac{f_{cu}}{P_a}\right) \qquad \text{(compression positive)} \tag{6.47}$$

where T and t are dimensionless numbers, and P_a is atmospheric pressure in the same units as those of f_t and f_{cu}. Values of T and t have been determined [51, 82, 48] for several frictional materials and listed in Table 6.1. Once f_t is known, the value of R can be computed. From studes conducted by Lade [23], R was found to be 0.3% to 1.4% greater than f_t. In other words:

$$1.003 f_t \leq R \leq 1.014\ f_t \tag{6.48a}$$

or

$$1.003\ f_t \leq a p_a \leq 1.014\ f_t \tag{6.48b}$$

with the estimated value of R, the resulting stresses in Eqs. (6.11) are calculated and then substituted into the expression the stres.

TABLE 6.1
VALUES OF PARAMETERS T AND t FOR
VARIOUS TYPES OF FRICTIONAL MATERIALS

MATERIAL	T	t	REFERENCE
Cemented Soils	-0.37	0.88	Mitchell [51]
Concrete & Mortar	-0.61	0.67	Wastiels [82]
Igneous Rocks	-0.53	0.70	Lade [48]
Metamorphic Rocks	-0.00082	1.6	Lade [48]
Sedimentary Rocks	-0.22	0.75	Lade [48]
Ceramics	-1.0	0.73	Lade [48]

invariants given in Eqs. (6.9 and 6.10).

Determination of β_o and β_1

Consider the yield condition at ultimate failure which $\alpha \to 0$. Then Eq. (6.8) reduces to:

$$J_{2D} - (\gamma J_1^2)\,(1 - \beta S_r)^{-1/2} = 0 \tag{6.49}$$

Now consider a TC (or CTC) and a TE (or RTE) test at $J_1 = \sigma_1+\sigma_2+\sigma_3 = C$ where the values of C defines specific octahedral planes.

If $(J_{2D})_{TC}$ and $(J_{2D})_{TE}$ are the respective shear strengths (at ultimate), we can write from Eq. (6.49)

$$(J_{2D})_{TC} - \frac{\gamma J_1^2}{(1 - \beta S_r)_{TC}^{1/2}} = 0$$

or

$$\frac{(J_{2D})_{TC}\,(1 - \beta S_r)_{TC}^{1/2} - \gamma J_1^2}{(1 - \beta S_r)_{TC}^{1/2}} = 0$$

Since $(1 - \beta S_r)$ is not zero. Then

$$(J_{2D})_{TC}\,(1 - \beta S_r)_{TC}^{1/2} = \gamma J_1^2 \tag{6.50}$$

Similarly

$$(J_{2D})_{TE}\,(1 - \beta S_r)_{TE}^{1/2} = \gamma J_1^2 \tag{6.51}$$

Since the right sides of Eqs. (6.50) and (6.51) are equal, for a given octahedral plane, we can write:

$$(J_{2D})_{TC}\,(1 - \beta S_r)_{TC}^{1/2} = (J_{2D})_{TE}\,(1 - \beta S_r)_{TE}^{1/2} \tag{6.52}$$

or

$$\frac{(J_{2D})_{TC}}{(J_{2D})_{TE}} = \frac{(1 - \beta S_r)^{1/2}_{TE}}{(1 - \beta S_r)^{1/2}_{TC}}$$

or

$$\frac{(J_{2D})^2_{TC}}{(J_{2D})^2_{TE}} = \frac{(1 - \beta S_r)_{TE}}{(1 - \beta S_r)_{TC}} \tag{6.53}$$

After rearranging Eq. (6.53) we can write:

$$\beta = \frac{[(J_{2D})^2_{TC} - (J_{2D})^2_{TE}]}{[(S_r J_{2D}^2)_{TC} - (S_r J_{2D}^2)_{TE}]} \tag{6.54}$$

It is evident from Eq. (6.54) that β can be determined for any pair of tests (TC and TE) if the stresses at ultimate (failure) are known. Also from Eq. (6.13)

$$\beta = \beta_o \, e^{-B_1 J_1}$$

taking natural log on both sides of Eq. (6.13), one obtains:

$$\ln(-\beta) = \ln(-\beta_o) - \beta_1 J_1 \tag{6.55}$$

Equation (6.55 represents a straight line when plotted in $\ln(-\beta)$ - J_1 space as shown in Fig. 6.12. Then β_o and β_1 are obtained from the intersection and slope of the straight line, respectively. The following steps are required to obtain β_o and β_1 from the laboratory tests:

a) Consider N pair of tests at different values of J_1.

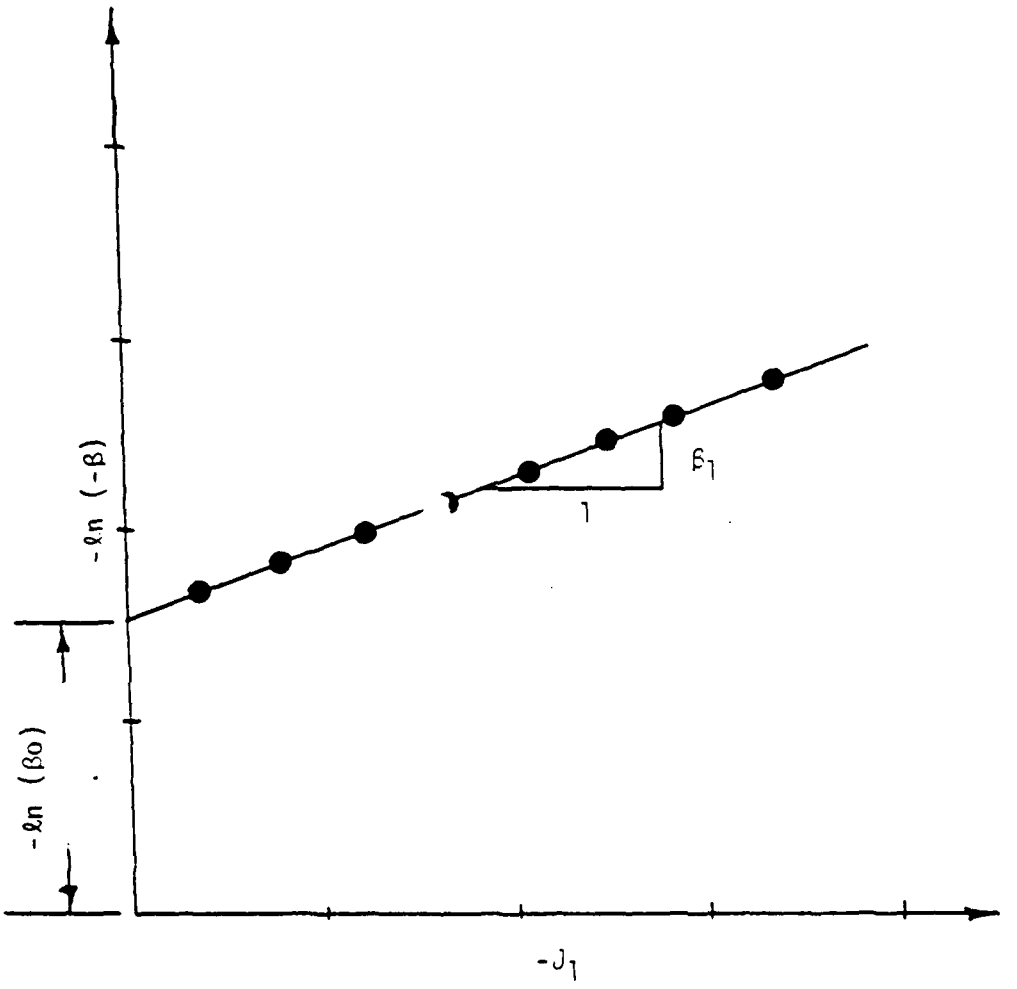

Figure 6.12. Schematic Plot to Determine the Material Constants β_0 and β_1.

Each pair is composed of one TC (or CTC) and one TE (or RTE) test at some confining pressure.

b) For each pair of test, compute β at ultimate from Eq. (6.54).

c) Since J_1 is known for each pair of tests, compute - ln (- β) and - J_1 and locate it on the (- ln (- β) - (- J_1)) space as shown in Fig. 6.12. There will be N number of such points.

d) Draw a best fit straight line (in a least square sense) through these points (see Fig. 6.12) and extrapolate backward to intersect with the ordinate, - ln (- β).

e) The constant β_1 is simply the slope of this line. β_o is computed from the intercept with the ordinate which is equal to - ln (- β).

Determination of γ

The following procedure may be used to compute γ from conventional laboratory test data:

a) The equation of the yield surface at ultimate can be written as

$$J_{2D} = \gamma J_1^2 (1 - \beta S_r)^{-1/2}$$

$$\gamma J_1^2 = J_{2D} (1 - \beta S_r)^{1/2} \qquad (6.56)$$

or may be written as

$$m = \gamma J_1^2 \qquad (6.57)$$

where

$$m = [J_{2D} (1 - \beta S_r)^{1/2}] .$$

Since β known, m can be determined for any test if the stresses at ultimate are known.

b) Consider a number of tests at various confining pressure (J_1). Compute m and J_1^2 for each test using the known stresses at ultimate.

c) Since m and J_1^2 for each tests are known (at ultimate), locate this point on the m - J_1^2 space as shown in Fig. 6.13. If N number of tests are included, there will be N such points.

d) Draw a best fit straight line through the experimental points such that it also passes through the origin (See Fig. 6.13).

e) γ is obtained from the slope of this line.

Determination of a_1 and η_1

The growth function, Eq. (6.19), after taking natural log of both sides can be written as:

$$\eta_1 \ln (\xi) + \ln (\alpha) = \ln (a_1) \qquad (6.58)$$

Equation (6.53) can now be used to determine η_1 and a_1. The following steps are involved in the calculation of η_1 and a_1.

a) Consider the stress-strain curve from one test (a TC test) as shown in Fig. 6.14. A number of points, say N, are selected on the loading portion of the

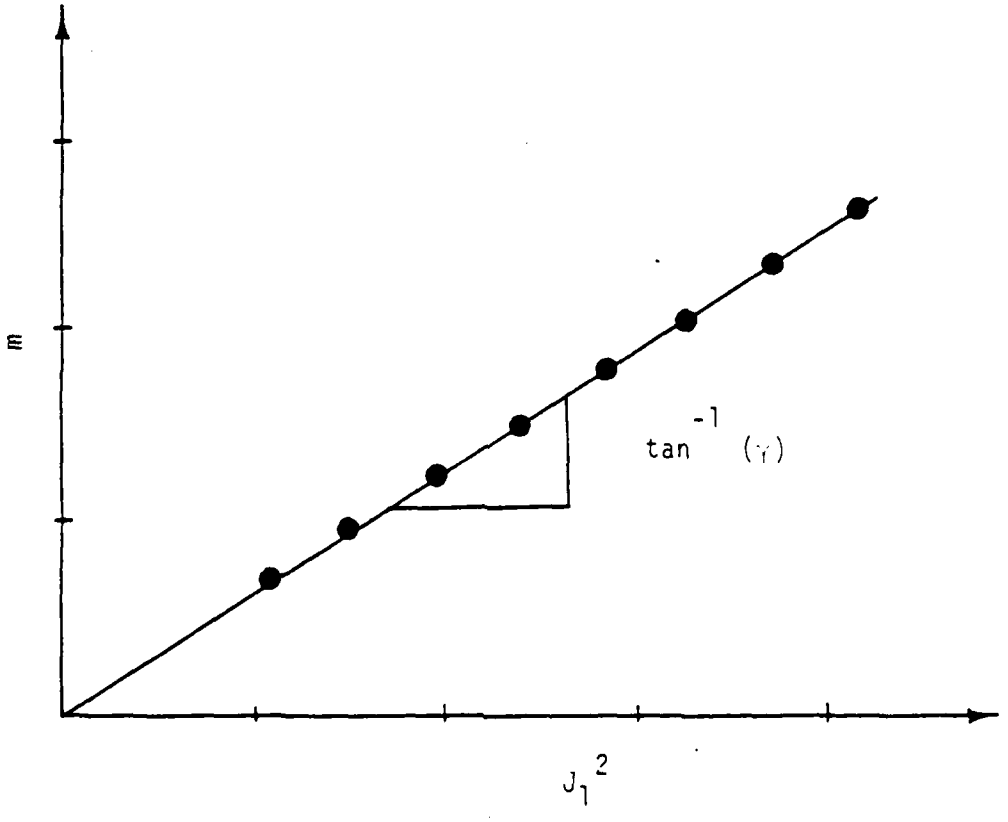

Figure 6.13. Schematic Plot to Determine the Material Constant γ.

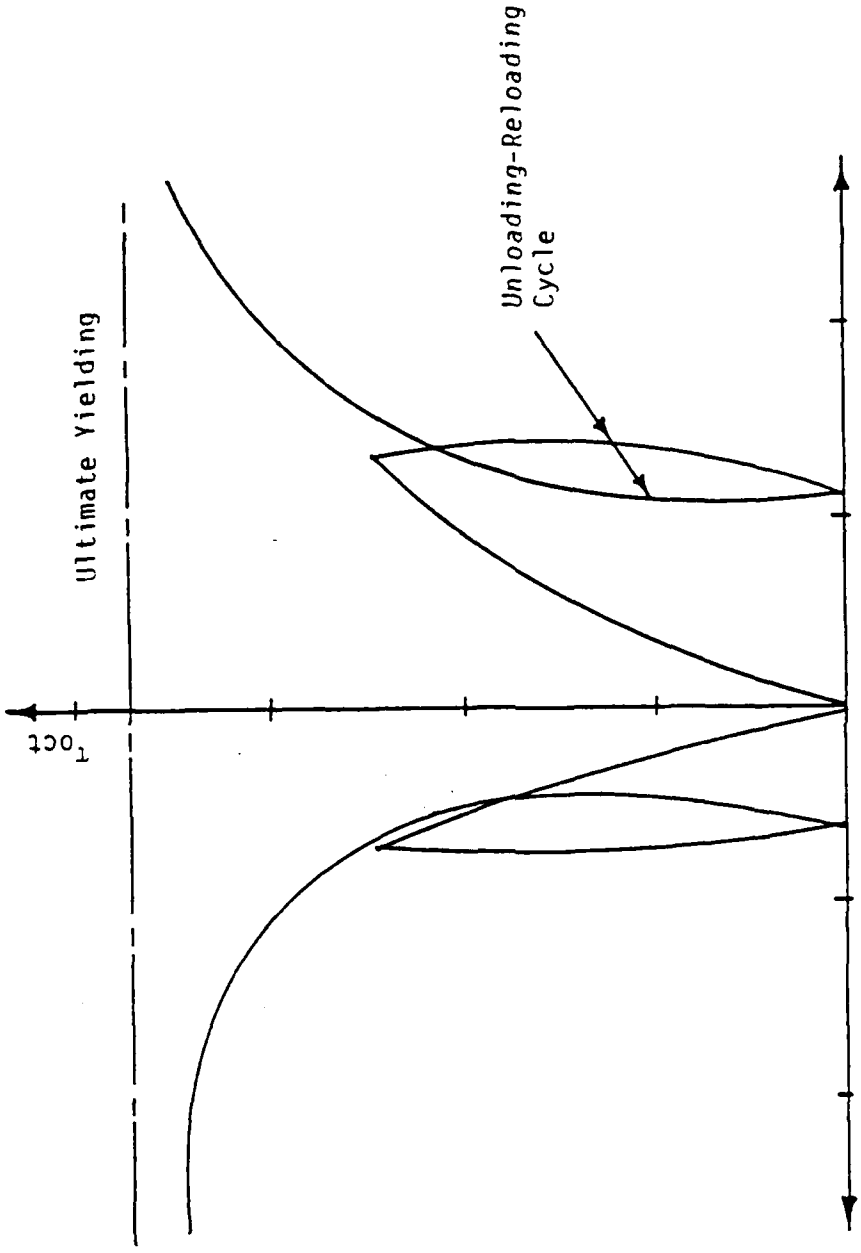

Figure 6.14. Typical Stress-Strain Response Curves for a Triaxial Compression (TC) Test.

stress-strain curve and the stresses, σ_i (i = 1,2,3) and the corresponding strains, ε_i (i = 1,2,3) at each point are noted.

b) Using the slopes of the unloading-reloading curves, ε_i^p (i = 1,2,3) are obtained at each point where the superscript p denotes plastic. From ε_i^p (i = 1,2,3), the incremental plastic strain $\Delta\varepsilon_i^p$ (i = 1,2,3) between any two adjacent points is obtained.

c) At every point, $\Delta\xi$ is then calculated using the incremental plastic strain, $\Delta\varepsilon_i{}^p$ (i = 1,2,3), where

$$\Delta\xi = \{(\Delta\varepsilon_1{}^p)^2 + (\Delta\varepsilon_2{}^p)^2 + (\Delta\varepsilon_3{}^p)^2\}^{1/2} \qquad (6.59)$$

d) Total ξ at j th point is then calculated according to the following equations:

$$\xi_j = \xi_o + \sum_{i=1}^{j} \Delta\xi^i \qquad (6.60)$$

where j refers to the point at which the quantities are calculated. $\Delta\xi^i$ in Eq. (6.55) denotes the ith increments of ξ. ξ_0 is the value of ξ corresponding to initial confining pressure, σ_0, at which shearing started.

e) The stress invariants J_1, J_{2D}, J_{3D} are computed at each of N points from the known stresses, σ_i (i = 1,2,3).

f) The magnitude of α is then calculated from the yield

condition at each point using the equation:

$$\alpha = \frac{[(\gamma J_1^2) - J_{2D}(1 - \beta S_r)^{1/2}]}{J_1^n} \qquad (6.61)$$

g) For each point, compute - ln (ξ) and ln (α) and locate this point on the - ln (ξ) vs. ln (α) space. If total number of tests is M, then a total of number of points will be obtained. A typical plot N x M is shown in Fig. 6.15.

h) For each available test, plots of - ln (ξ) vs. ln (α) yield the value of α_1 from the intercept along the ordinate and η_1 from the slope of the straight line (see Fig. 6.15). The values of η_1 and a_1 are averaged from available tests.

The general procedure outlined above may be used for hand calculation. The process, however, can be tedious and time

6.5 Material Constants for Plain Concrete Under Low Confining Pressure

Description of this plain concrete is given in section 2.2.1. The test results are presented in Chapter 3. Eleven tests, including the hydrostatic compression (HC) test, are used to obtain the material constants associated with the proposed model. Tests

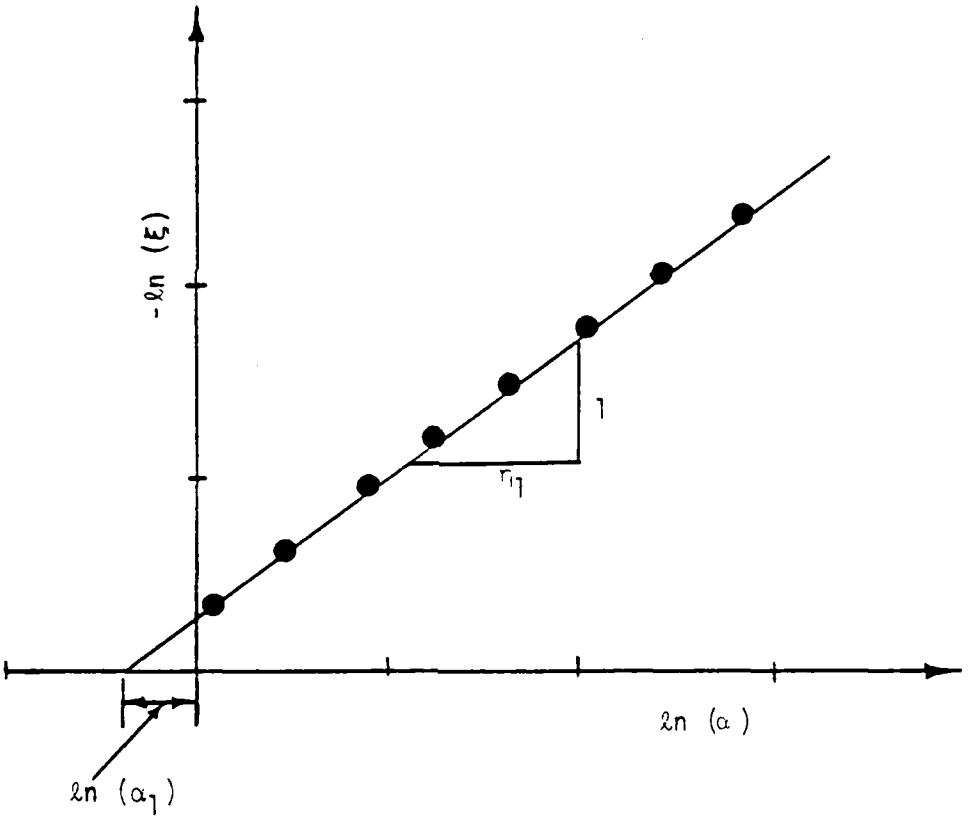

Figure 6.15. Schematic Plot to Determine the Hardening Constants α_1 and n_1.

(from Table 3.2 are used to find material constants as shown in Fig. 6.16. Figure 6.16 shows the plot which provides the values of n_1 and a_1. It may be noted that the plots are obtained from the computer. Thus, no hand calculations are used to obtain the constant for hardening. β_0 and β_1 are determined from Fig. 6.17.

The constants for plain concrete was obtained by here-going procedures. TABLE 6.2 shows values of the material constants from various stress path tests as previously discussed.

6.6 Material Constants for Colorado Plain Concrete Under High Confining Pressure

The plain concrete tested by Scavuzzo et al [68] has properties of cement: sand: gravel = 1:3.16:3.19, and cement: water = 1.2. Also f_c = 3650 psi (25.17 MPa), uniaxial compressive strength with 3x6 in. (7.62x15.24 cm) cylinders at 28 days.

For multiaxial testing 4x4x4 inch (10.16x10.16x10.16 Cm) cubical specimens were used. The testing program consisted of TC, TE and SS, Fig. 2.10, tests with initial hydrostatic pressures of $\sigma_0 = \frac{J_1}{3}$ = 4, 6 and 8 Ksi (27.58, 41.37 and 55.16 MPa). All specimens were first loaded in HC up to σ_0 and then subjected to deviatoric cyclic loading along TC, TE or SS path with increasing octahedral shear stress to failure. Tests with circular stress path involving hydrostatic, monotonic loading to 4 and 8 ksi, followed by deviatoric stress along the triaxial compression path

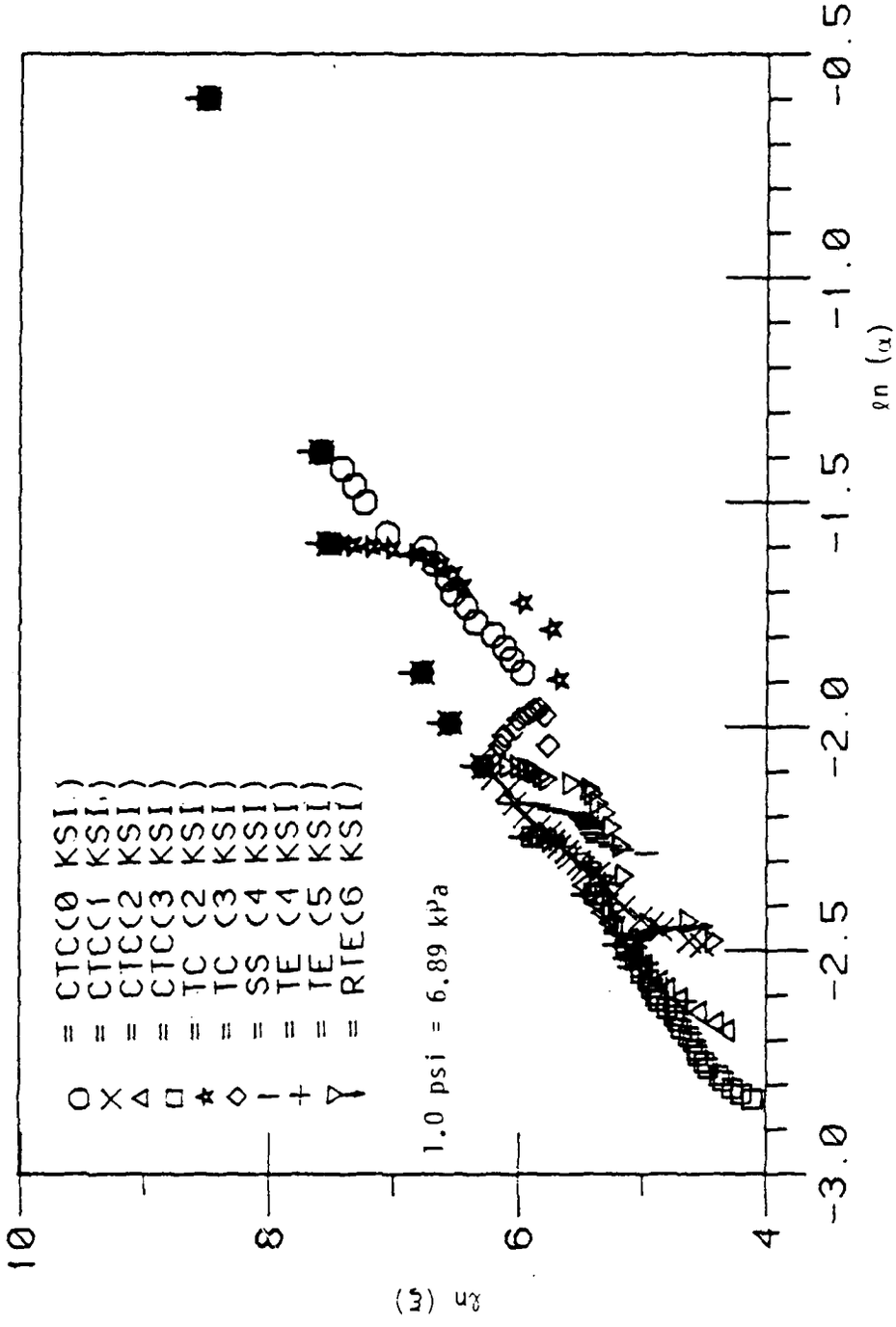

Figure 6.16. Plot of $-\ln(\varepsilon)$ vs. $\ln(\alpha)$ from Tests Under Different Stress Paths for Plain Concrete.

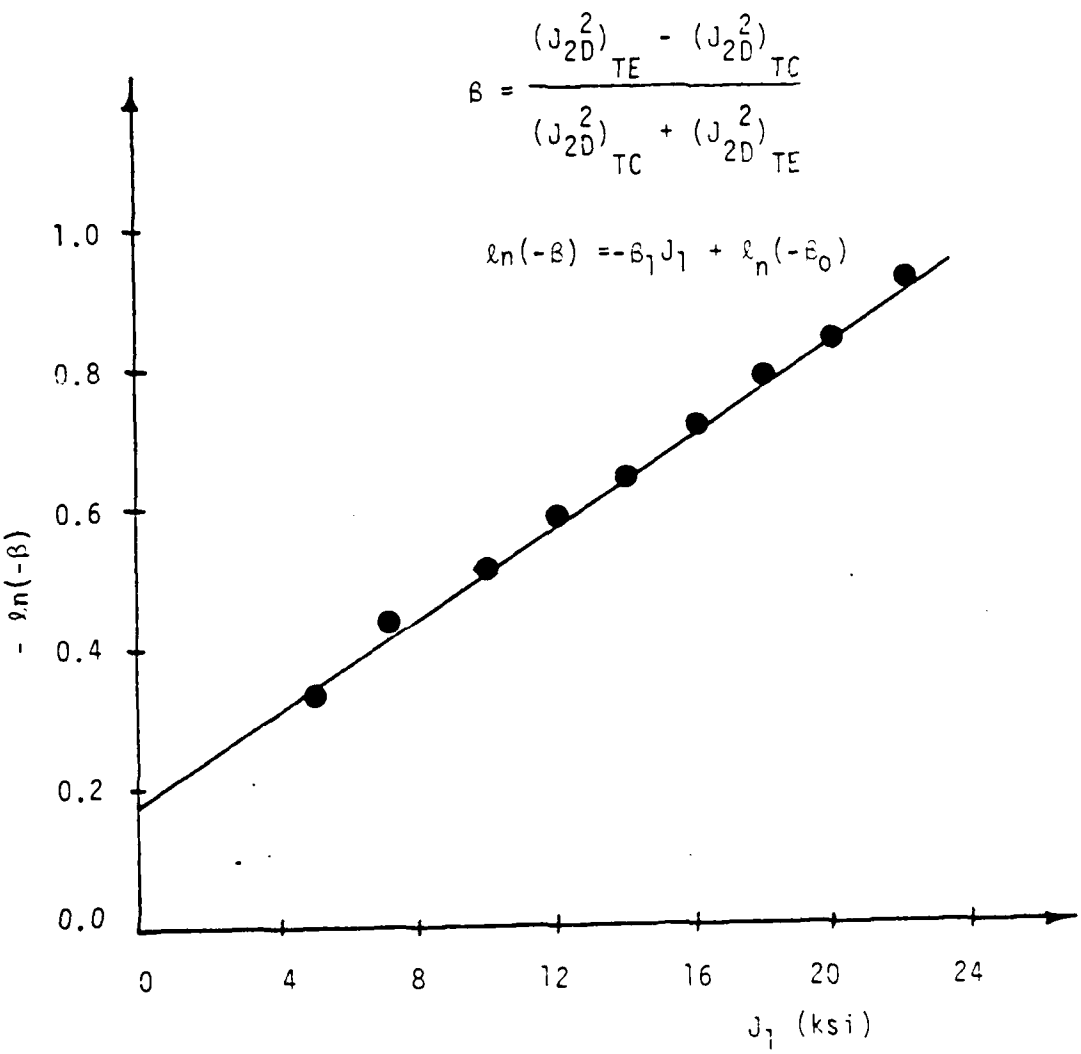

Figure 6.17. Plot of $-\ln(-\varepsilon)$ vs. J_1 to Determine Material Constants ε_0 and β_1 for Plain Concrete.

TABLE 6.2
MATERIAL CONSTANTS FOR PLAIN CONCRETE
FROM DIFFERENT STRESS PATH TESTS

MATERIAL CONSTANT FOR PLAIN CONCRETE			
		ENGLISH UNITS	SI UNITS
ELASTIC CONSTANTS	K	487.80 ksi	3363.8 MPa
	G	440.36 ksi	3036.3 MPa
	E	1012.82 ksi	6983.4 MPa
	ν	0.154	0.154
CONSTANTS FOR ULTIMATE YIELDING	δ=3R	1.1833 ksi	8.1589 MPa
	γ	.1130	.1130
	β_0	-0.8437	-0.8437
	β_1	0.0270	0.0270
	n	7.0	7.0
CONSTANTS FOR HARDENING	η_1	0.4388	0.4388
	a_1	0.9321×10^{-2}	0.9321×10^{-2}

in the specified circle, Fig. 2.11, were also performed.

Seven tests with different stress paths are used to obtain the elastic constants, ultimate and hardening parameters for plain concrete. Tests are used to find material constants as shown in Fig. 6.18. Figure 6.18 shows the computer plot which is used to obtain η_1 and a_1. β_o and β_1 are determined from Fig. 6.19

TABLE 6.3 shows values of the material constants for Coloardo plain concrete.

6.7 Material Constants for SFRC-UC

The properties of SFRC-UC tested by Egging [30] are as follows:

Mix

The concrete mix generally used in SFRC was a high strength design which was mixed with various sizes of randomly distributed steel fibers.

Uniaxial Compression Strength

f_c = 9200 psi (63.43 MPa)

Uniaxial Tensile Strength

T =-935 psi (6.57 MPa)

with 3x6 (7.62x15.24 cm) cylinders at 28 days.

For multiaxial testing 4x4x4 inch (10.16x10.16x10x16 cm) cubical specimens were used. The testing program consisted of TC, TE and SS tests with initial hydrostatic pressures of 4,6 and 8 ksi (27.58, 41.37 and 55.16 MPa). All specimens were loaded in the same manner as the Colorado plain concrete.

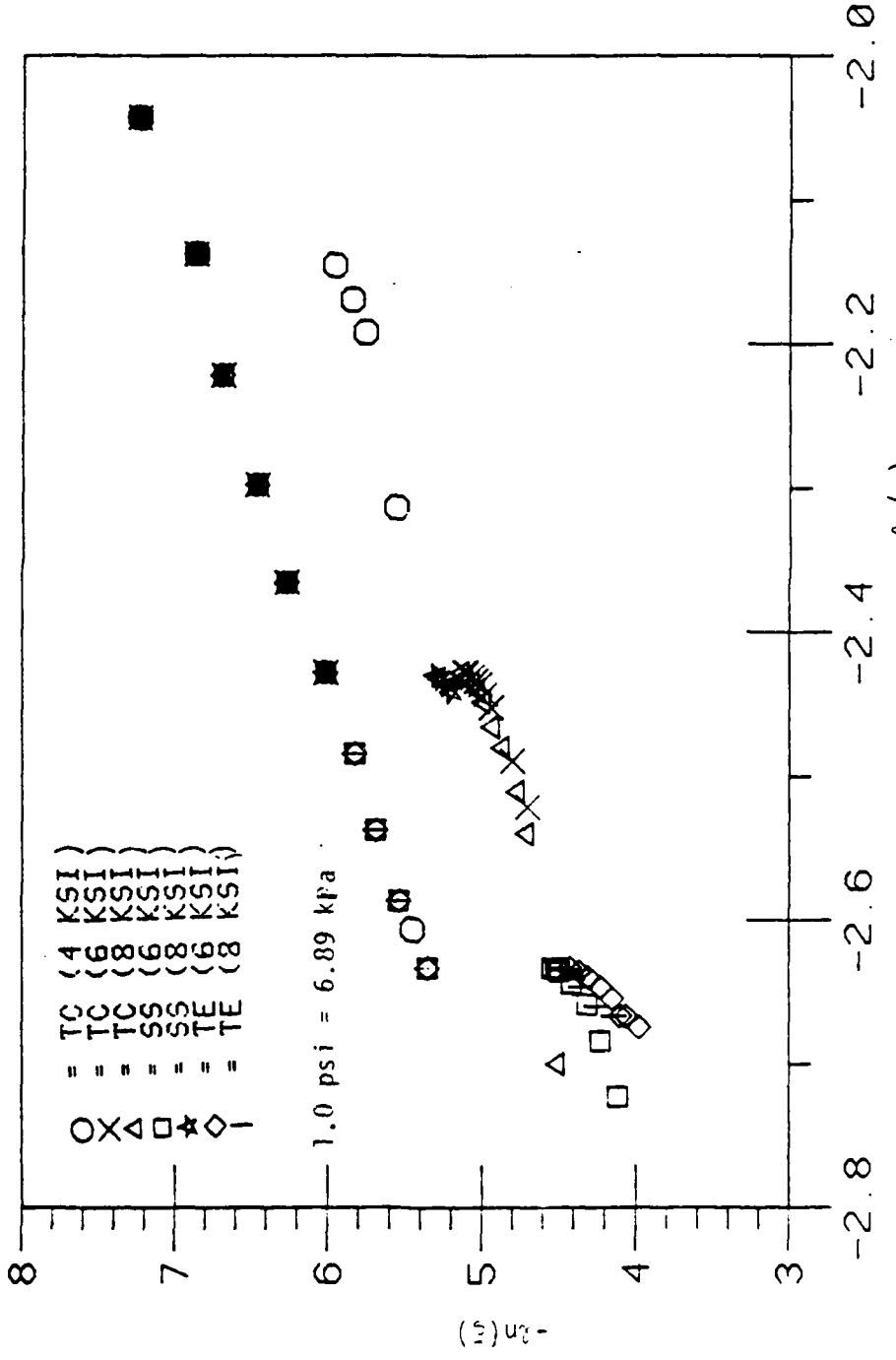

Figure 6.18. Plot of $-\ln(\xi)$ vs. $\ln(\alpha)$ from Tests Under Different Stress Paths for Colorado Plain Concrete.

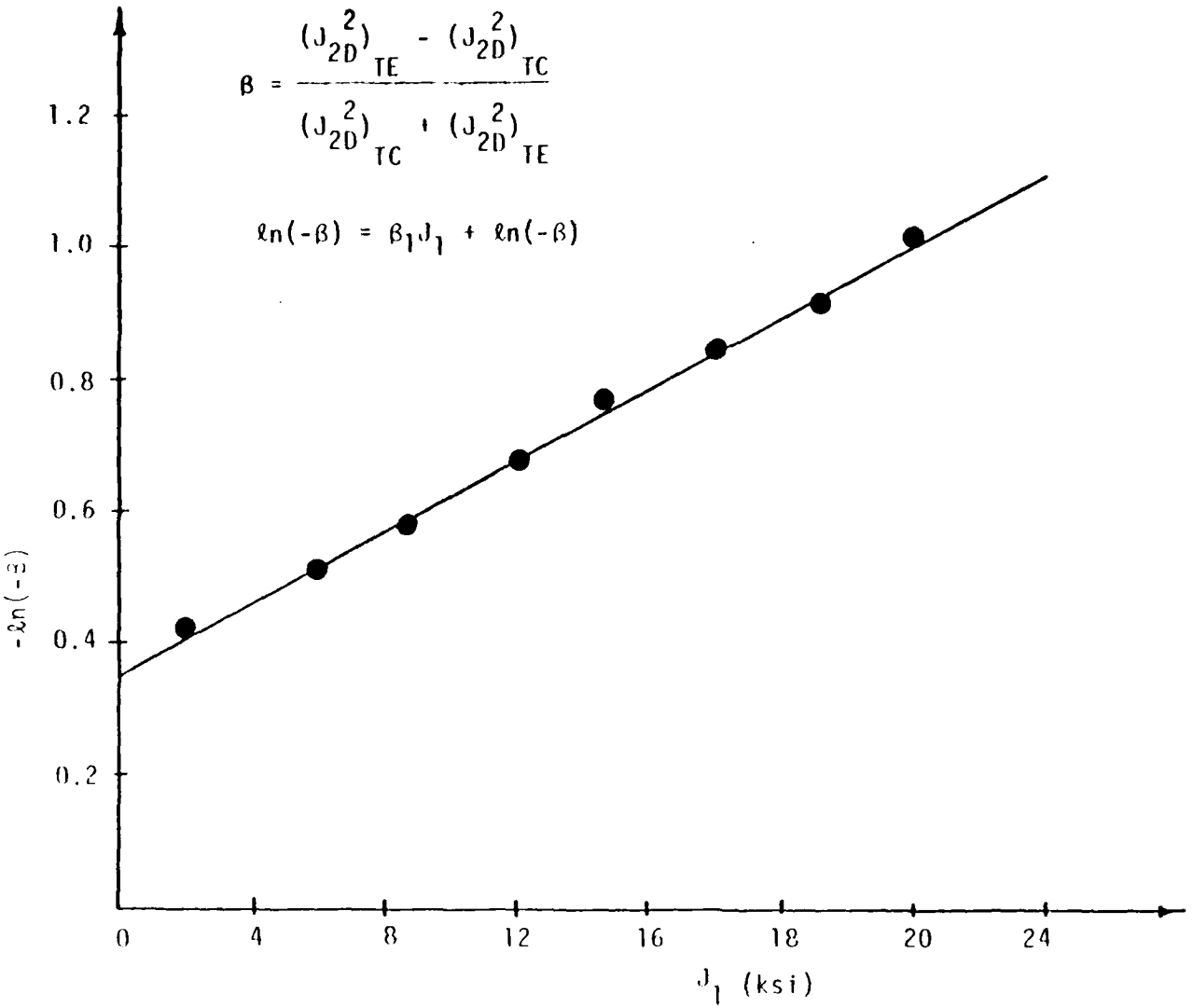

Figure 6.19. Plot of $-\ln(-\beta)$ vs. J_1 to Determine Material Constants β_0 and β_1 for Colorado Plain Concrete.

TABLE 6.3
MATERIAL CONSTANTS FOR COLORADO PLAIN CONCRETE
FROM DIFFERENT STRESS PATH TESTS

MATERIAL CONSTANT FOR COLORADO PLAIN CONCRETE			
		ENGLISH UNITS	SI UNITS
ELASTIC CONSTANTS	K	1762 ksi	12148.3 MPa
	G	1608.7 ksi	11092. MPa
	E	3700 ksi	25511.5 MPa
	ν	0.15	0.15
CONSTANTS FOR ULTIMATE YIELDING	δ=3R	1.0776 ksi	7.4 MPa
	γ	0.07882	0.07882
	β_0	-0.60319	-0.60319
	β_1	0.0314	0.0314
	n	7.0	7.0
CONSTANTS FOR HARDENING	r_1	0.153907	0.153907
	a_1	0.362863×10^{-1}	0.362863×10^{-1}

Nine various stress path tests were used to find material constants. Tests are used to find material constants as shown in Fig. 6.20. Figure 6.20 shows the computer plot which is used to obtain η_1 and α_1. β_0 and β_1 are determined from Fig. 6.21

TABLE 6.4 shows values of the material constants for SFRC-UC.

6.8 Material Constants for Soapstone

Description of the soapstone is given in Section 2.2.2. The test results are presented in Chapter 4.

Eleven tests, including the hydrostatic compression test, are used to obtain the material constants. Tests (from TABLE 4.1) are used to find material constants as shown in Fig. 6.22. Fig. 6.22 shows the plot which provides the values of η_1 and α_1. β_0 and β_1 are determined from Fig. 6.23.

TABLE 6.5 shows values of the material constants for soapstone.

6.8 Material Constants for Sandstone

Description of sandstone and failure criterion in octahedral planes with results of tests is given by Nishida et al [56] f_c = 9.393 ksi (64.72 MPa), uniaxial compression strength, is given by Kulhawy [42]. For generalized triaxial testing 1.57x1.57x1.57 inch (4x4x4 cm) cubical specimens were used.

Fifteen tests with different stress paths, seven TC tests with confining pressure σ_0 = 14.22, 20.06, 28.02, 34.71, 41.82, 48.74

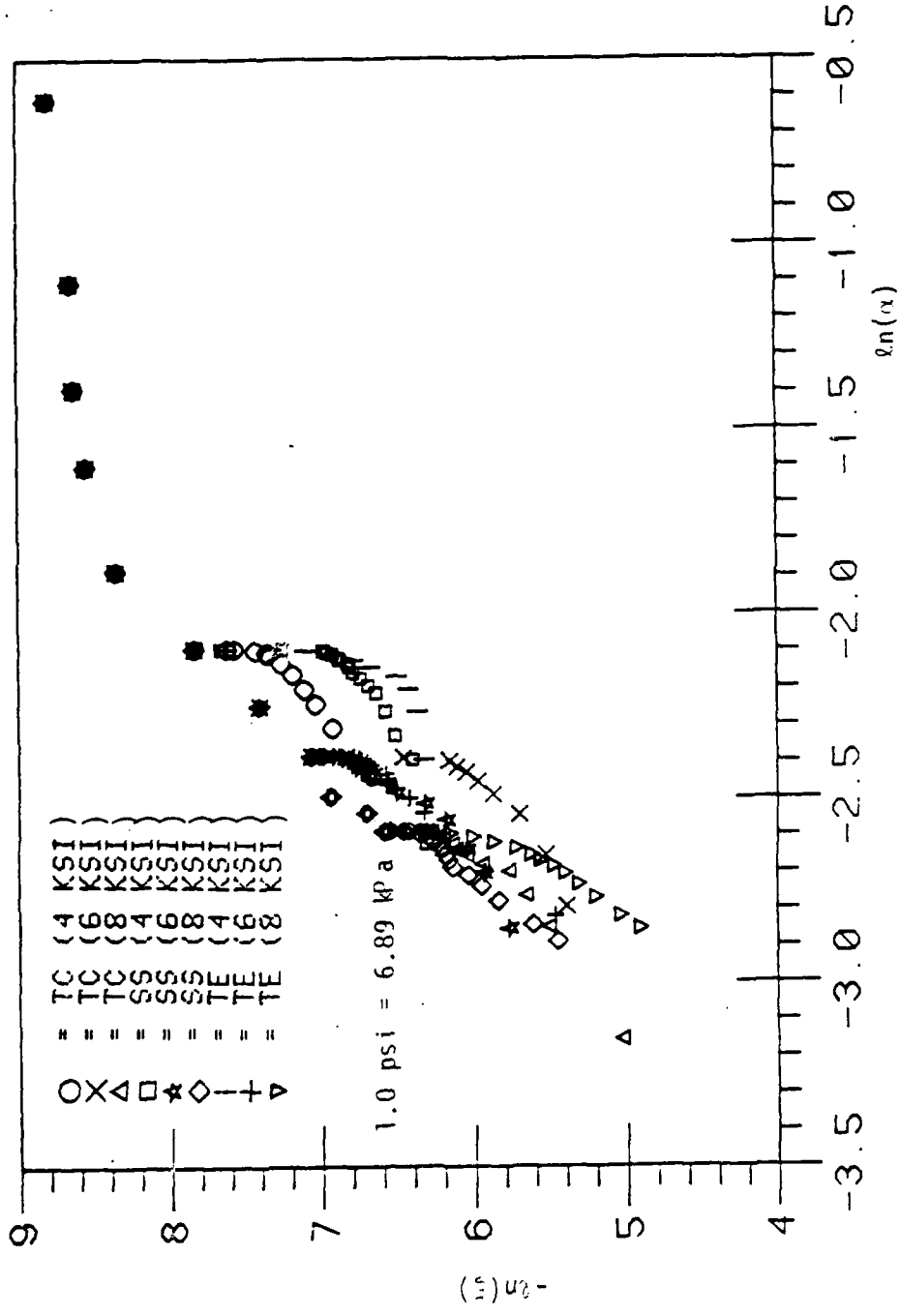

Figure 5.20. Plot of $-\ell n(\xi)$ vs. $\ell n(\alpha)$ from Tests Under Different Stress Paths for SFRC-UC.

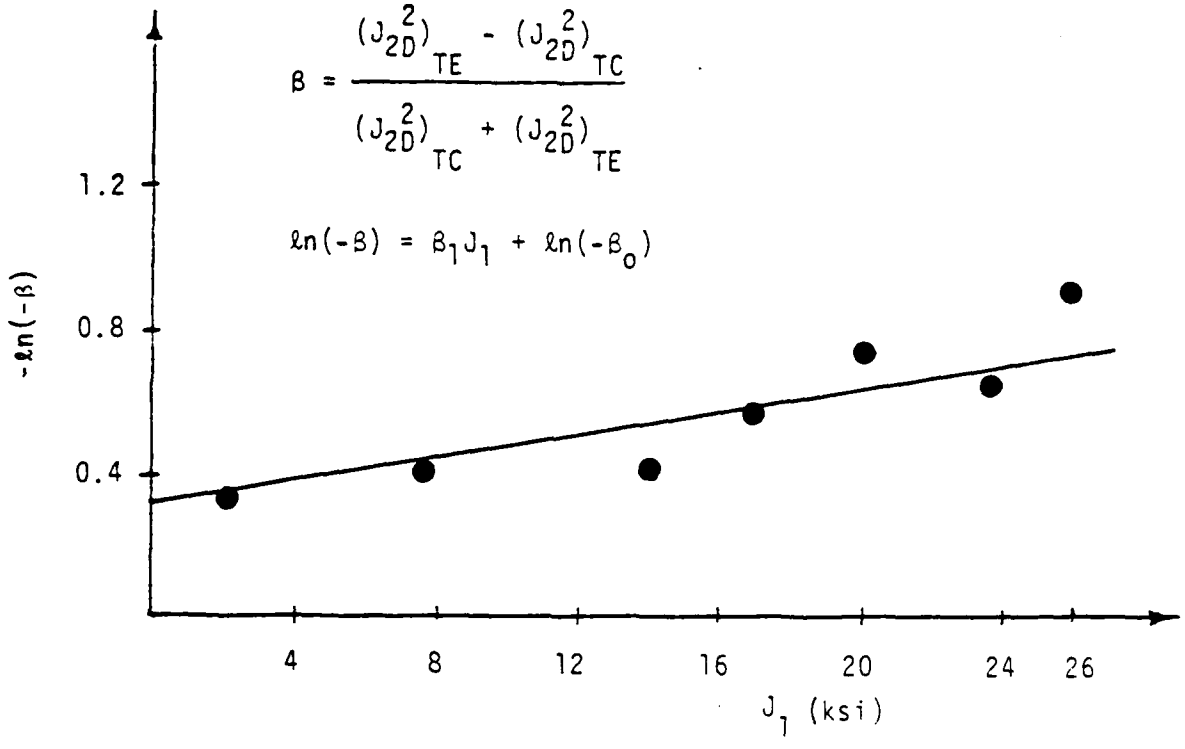

Figure 6.21. Plot of $-\ln(-\beta)$ vs. J_1 to Determine Material Constants β_0 and β_1 for SFRC-UC.

TABLE 6.4
MATERIAL CONSTANTS FOR SFRC-UC
FROM DIFFERENT STRESS PATH TESTS

MATERIAL CONSTANT FOR SFRC-UC			
		ENGLISH UNITS	SI UNITS
ELASTIC CONSTANTS	K	936 ksi	6453.7 MPa
	G	1177 ksi	8115.4 MPa
	E	2487 ksi	17147.9 MPa
	ν	0.0568	0.0568
CONSTANTS FOR ULTIMATE YIELDING	δ=3R	2 ksi	1.38 MPa
	γ	0.1079	0.1079
	β_0	-0.70778	-0.70778
	β_1	0.01639	0.01639
	n	7.0	
CONSTANTS FOR HARDENING	n_1	0.448750	0.448750
	a_1	0.451937×10^{-2}	0.451937×10^{-2}

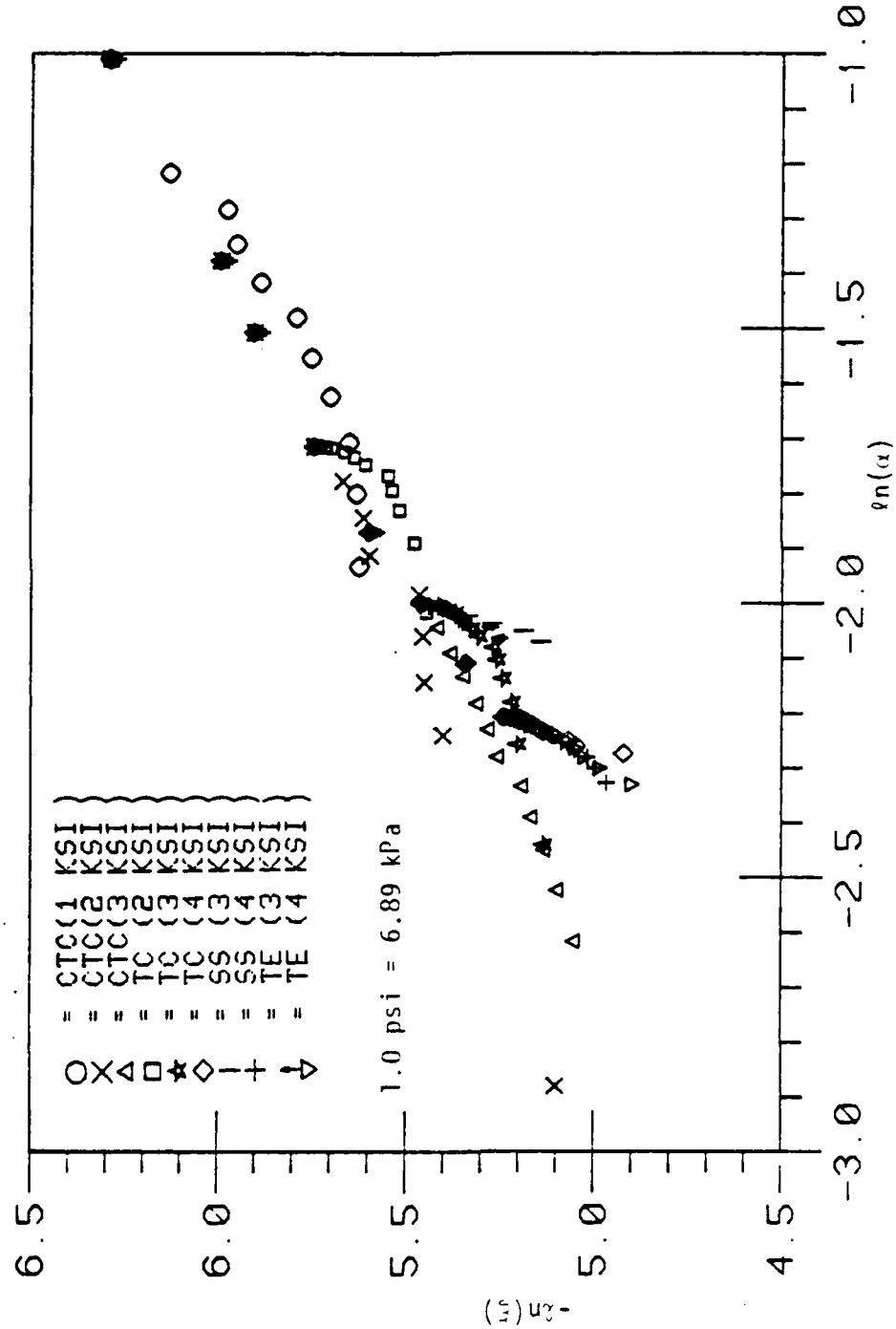

Figure 6.22. Plot of $-\ell n(\xi)$ vs. $\ell n(\alpha)$ from Tests Under Different Stress Paths for Soapstone.

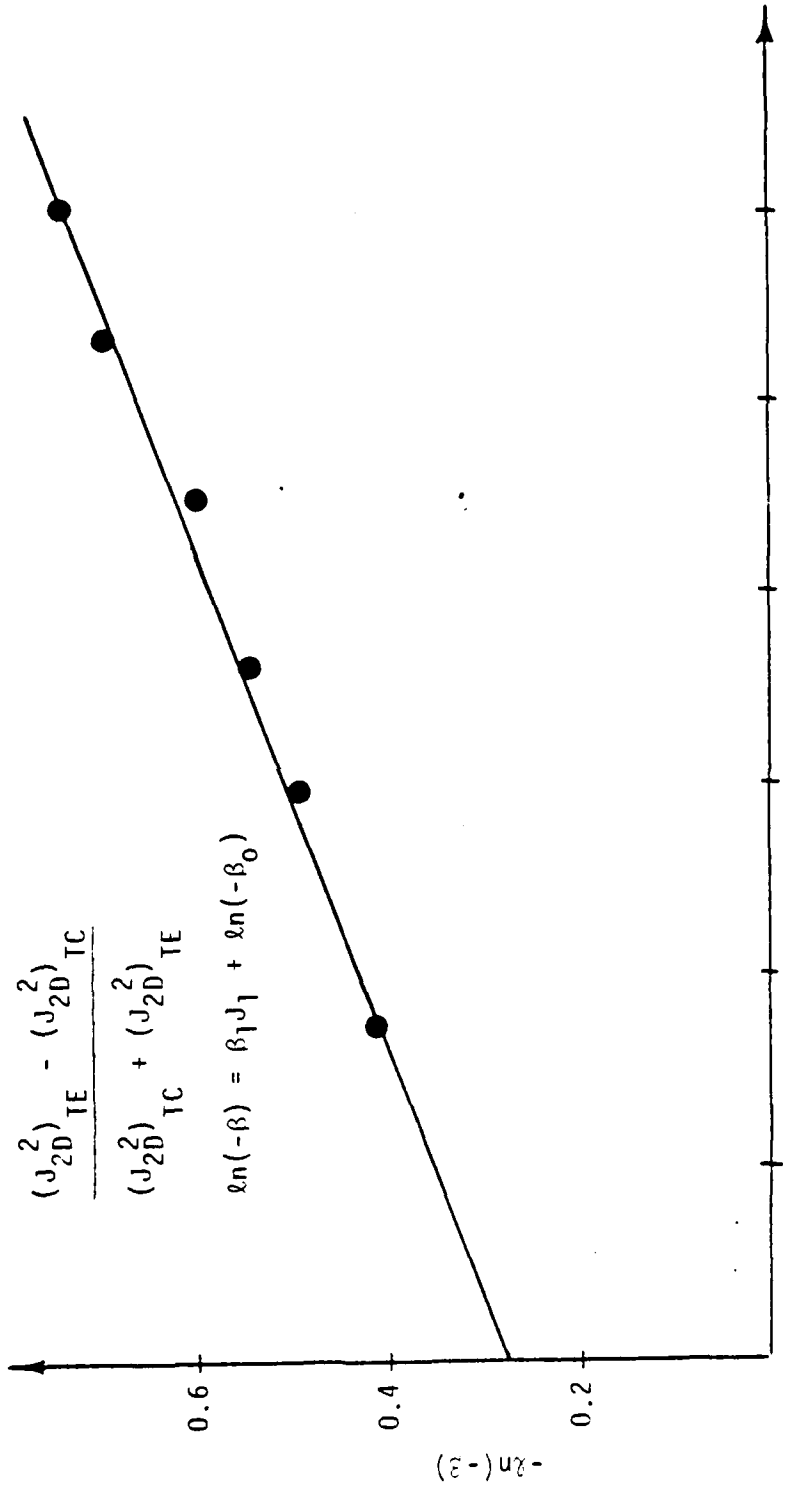

Figure 5.23. Plot of -ℓn vs. J_1 to Determine Material Constants β_o and β_1 for Soapstone.

TABLE 6.5
MATERIAL CONSTANTS FOR SOAPSTONE
FROM DIFFERENT STRESS PATH TESTS

MATERIAL CONSTANT FOR SOAPSTONE			
		ENGLISH UNITS	SI UNITS
	K	449.51 ksi	3099.37 MPa
	G	614.99 ksi	4240.4 MPa
	E	1327.39 ksi	9152.4 MPa
	ν	0.0792	0.0792
	$\delta=3R$	0.46 ksi	3.2 MPa
	γ	0.0468	0.0468
	β_0	-0.74922	-0.74922
	β_1	0.0465	0.0465
	n	7.0	7.0
	n_1	0.747	0.747
	a_1	0.177×10^{-2}	0.177×10^{-2}

and 56.0 ksi (98.05, 138.31, 193.20, 239.33, 288.35, 336.06 and 386.12 MPa) and eight TE tests with confining pressure σ_o = 21.72, 28.2, 34.66, 42.15, 48.46, 54.96, 64.73 and 70.56 Ksi (149.76, 194.44, 238.98, 290.62, 334.13, 378.95, 446.31 and 486.51 MPa), are used to find ultimate parameters. Also three tests, two TC tests with confining pressure σ_o = 28.45 ksi (196.16 MPa), are used to find hardening parameters. Fig. 6.24 shows the plot which provides the values of n_1 and a_1. β_o and β_1 are determined from Fig. 6.25.

TABLE 6.6 shows values of the material constants for sandstone.

6.10 Material Constants for Westerly Granite

Description of westerly granite (Igneous Rock) is given by [52]. All specimens were taken from a single block of rock. Compression specimens were circulars with 0.63 inch (1.6 cm) in diameter and 1.97 inch (5.0 cm) long. Extension specimens were from 0.92 to 1.0 inch (2.30 to 2.54 cm) in diameter and 1.97 inch (5.0 cm) long. f_c = 42.698 ksi (294.19 MPa).

Twelve tests with different stress paths, six CTC tests with confining pressures σ_o = 0., 1.86, 2.47, 3.77, 6.09 and 8.41 ksi (σ_o = 0, 12.82, 17.02, 25.98, 41.96, 57.94 MPa) and six RTE with confining pressures σ_o = 44.67, 50.47, 61.78, 73.10, 79.99, 85.71 ksi (σ_o = 307.8, 347.7, 425.7, 503.7, 551.1, 590.5 Mpa), are used to find ultimate parameters for

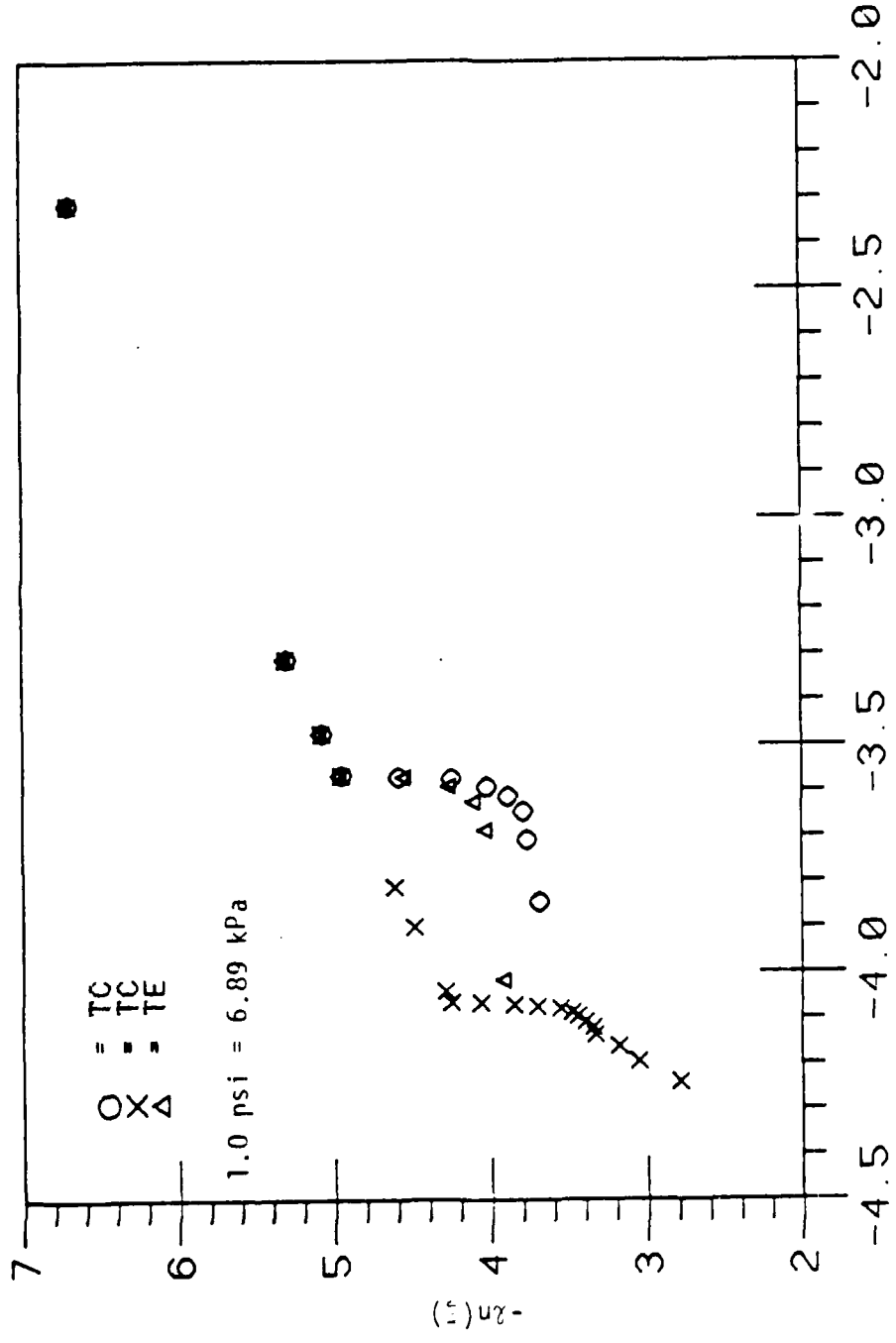

Figure 5.24. Plot of $-\ln(\varepsilon)$ vs. $\ln(\alpha)$ From Test Under Different Stress Paths for Sandstone.

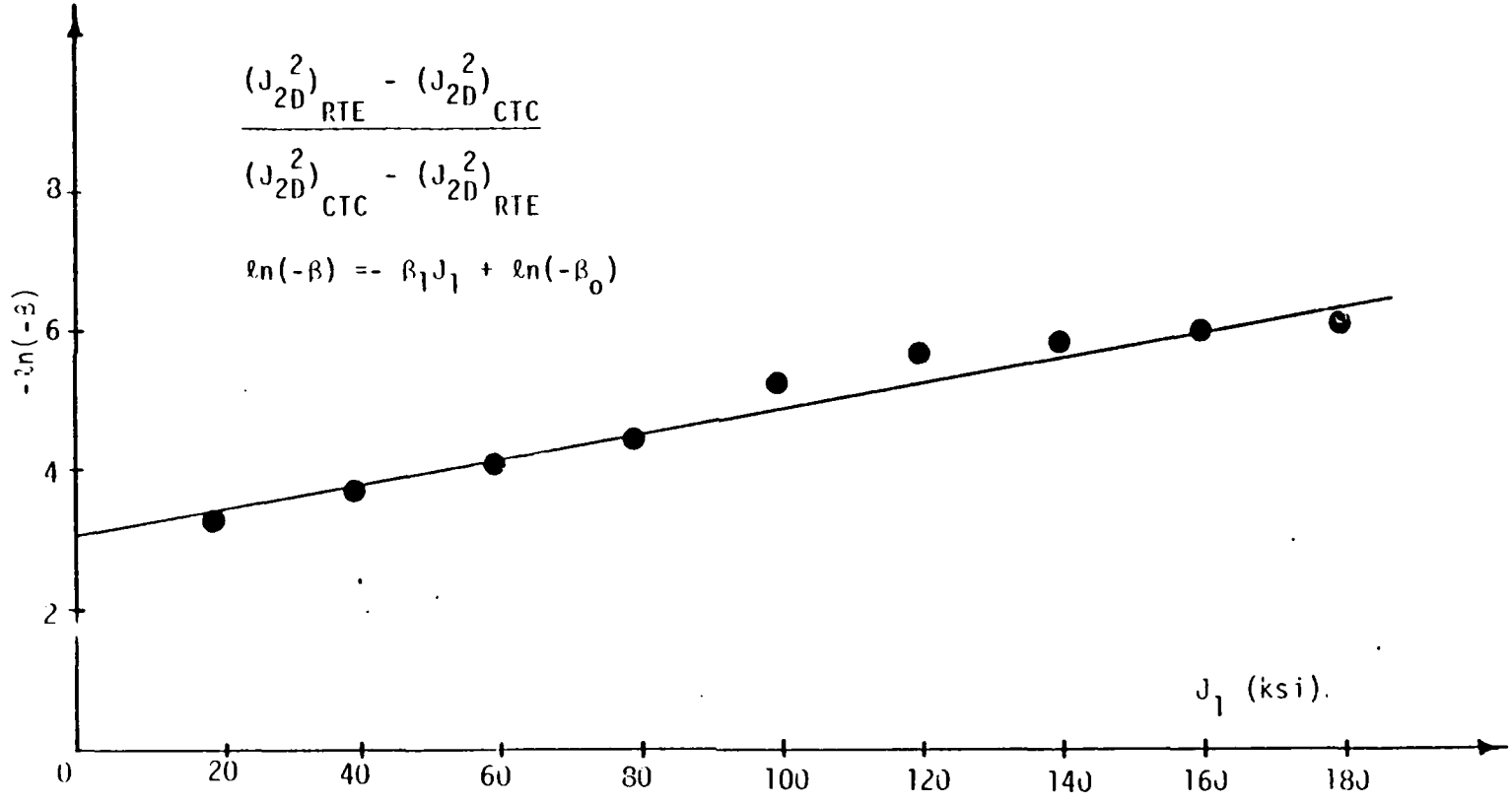

Figure 6.25. Plot of $-\ell n(-\beta)$ vs. J_1 to Determine Material Constants β_o and β_1 for Sandstone.

TABLE 6.6
MATERIAL CONSTANTS FOR SANDSTONE
FROM DIFFERENT STRESS PATH TESTS

MATERIAL CONSTANT FOR SANDSTONE			
		ENGLISH UNITS	SI UNITS
ELASTIC CONSTANTS	K	1581.23 ksi	10902.6 MPa
	G	1666.7 ksi	11491.9 MPa
	E	3700.1 ksi	25512.2 MPa
	ν	0.11	0.11
CONSTANTS FOR ULTIMATE YIELDING	$\delta=3R$	1.251 ksi	8.626 MPa
	γ	0.0774	0.0774
	β_0	-0.76721	-0.76721
	β_1	0.0019	0.0019
	n	7.2	7.2
CONSTANTS FOR HARDENING	η_1	0.345303	0.0345303
	a_1	0.4663×10^{-2}	0.4663×10^{-2}

westerly grainie. Stress-strain responses for these tests were not available to determine the elastic constants and hardening parameters.

Constants for Ultimate Yielding

The value of the material constants for westerly granite are given below:

$\delta = 3R = 5.706$ ksi (39.343 MPa)

$\gamma = 0.14460$

$\beta_0 = 0.81058$

$\beta_1 = 0.0025$

$n_1 = 7.2$

Fig. 6.26 shows the plot which provides the values of β_0 and β_1.

6.11 Material Constants for Dunham Dolomite

Description of Dunham Dolomite (sedimentary rock) is given by [52]. All specimens were taken from a single block of rock. Compression specimens were circulars with 0.63 inch (1.6 cm) in diameter and 1.97 inch (5.0 cm) long. Extension specimens were taken from 0.92 to 1.0 inch (2.30 to 2.54 cm) in diameter and 1.97 inch (5. cm) long. fc = 31.472 ksi (217.0 MPa).

Sixteen tests with different stress paths, six CTC tests wi : confining pressures σ_0 = 12.06, 17.84, 18.66, 22.46, 24.71 and 28.19 ksi (83.15, 123.01, 128.66, 154.86, 170.38 and 194.37 MPa and ten RTE with confining pressures σ_0 = 21.29, 25.98,

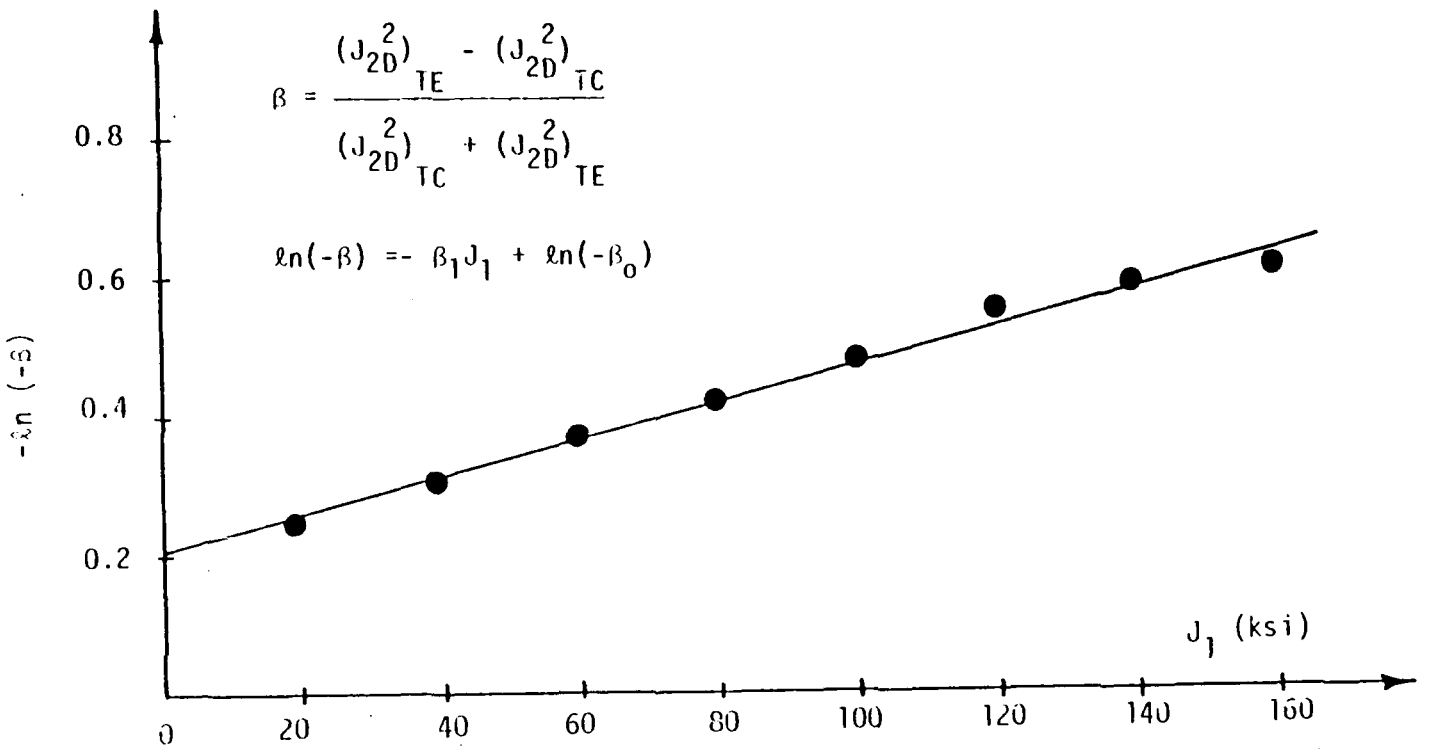

Figure 6.26. Plot of $-\ell n(-\beta)$ vs. J_1 to Determine Material Constants β_o and β_1 for Westerly Granite.

29.88, 31.39, 36.99, 39.56, 42.55, 43.51, 49.21 and 54.187 ksi (146.79, 179.13, 206.02, 216.43, 255.05, 272.77, 293.38, 300.0, 339.30 and 373.62 MPa), are used to find ultimate parameters for Dunham Dolomite. Stress-strain responses for these tests were not available to determine the elastic and hardening constants.

Constant for Ultimate Yielding

The value of the material constants for Dunham Dolomite are given below:

$\delta = 3R = 3.096$ ksi (21.35 MPa)

$\gamma = 0.1303$

$\beta_0 = 0.83166$

$\beta_1 = 0.00405$

β_0 and β_1 are determined from Fig. 6.27.

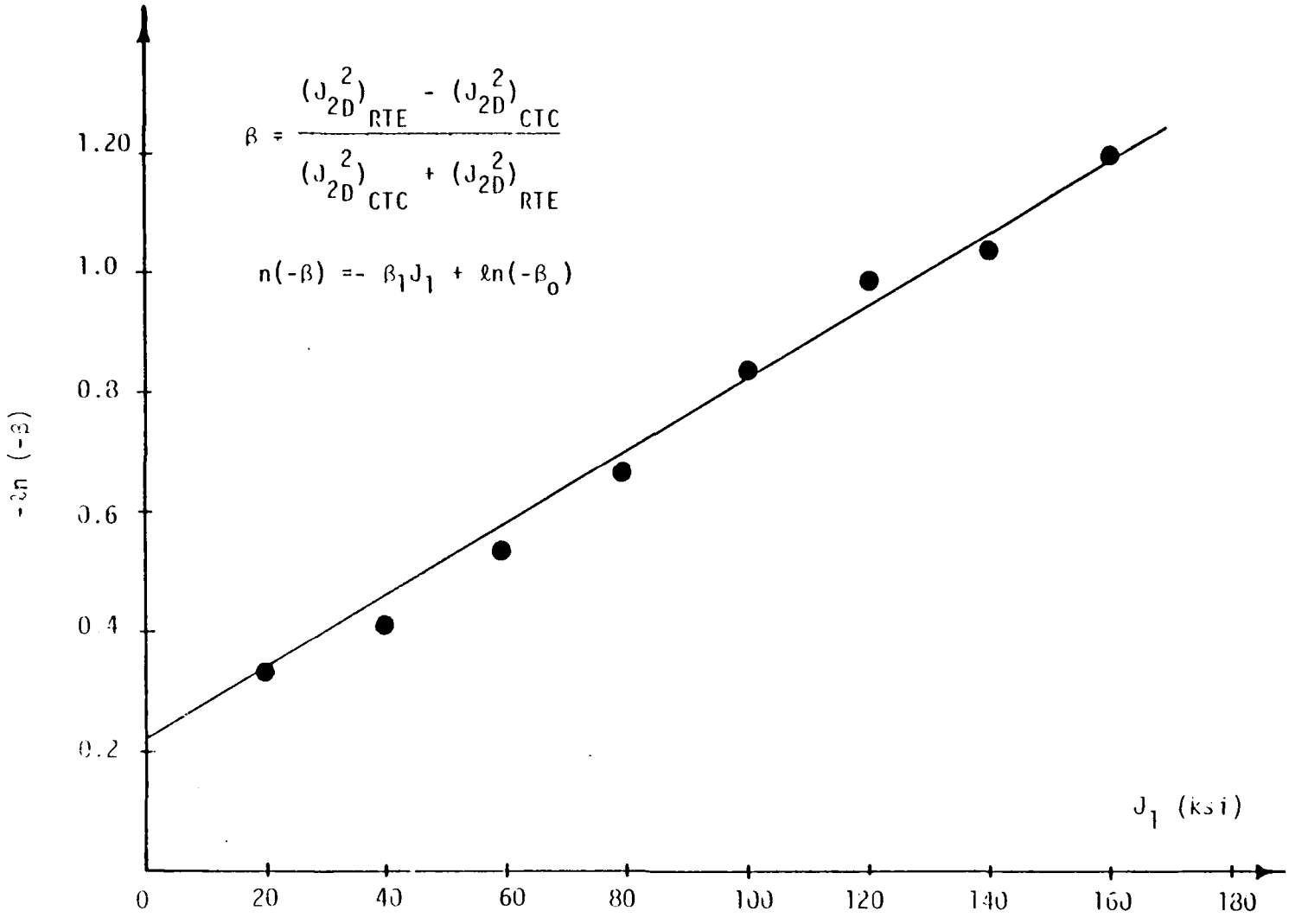

Figure 6.27. Plot of $-\ell n(-\beta)$ vs. J_1 to Determine Material Constants β_0 and β_1 for Dunham Dolomite.

AD-A174 451 CONSTITUTIVE MODELLING OF CONCRETE AND ROCKS UNDER MULTIAXIAL COMPRESSIVE (U) ARIZONA UNIV TUCSON DEPT OF CIVIL ENGINEERING M R SALAMI ET AL 04 SEP 86 4/5

UNCLASSIFIED AFOSR-TR-86-2014 AFOSR-83-0256 F/G 8/7 NL

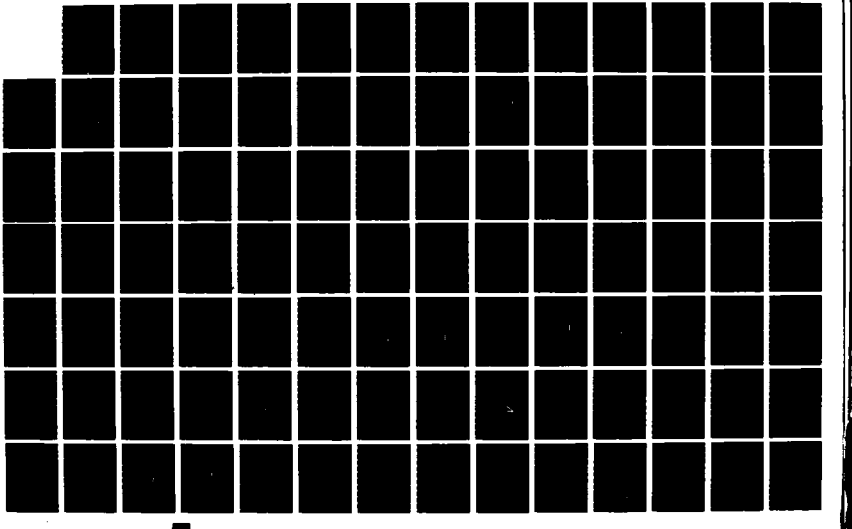

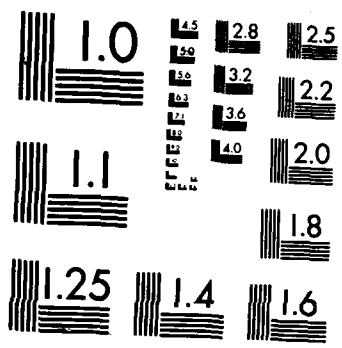

CHAPTER 7

VERIFICATION OF PROPOSED MODEL

7.1 Introduction

In this chapter, the verification of the model with respect to the ubical triaxial test data for a number of different concretes and rocks is presented. The parameters obtaaned in Chapter 6 will be used to back predict the strengths and the stress-strain responses obtained from laboratory tests for plain concrete, Colorado plain concrete, SFRC-UC, soapstone, sandstone, Westerly Granite and Dunham Dolomite.

The incremental constitutive equation is used on the basis of the normality rule of plasticity and the consistency condition $dF = 0$ as:

$$\{d\sigma\} = [C^{ep}] \{d\varepsilon\} \tag{7.1}$$

where $\{d\sigma\}$, $\{d\varepsilon\}$ = vectors of incremental stress and strain components, respectively, and $[C^{ep}]$ = constitutive matrix containing the foregoing material constants. In order to predict the behavior under a given stress path, Eq. (7.1) is integrated along that path starting from the initial hydrostatic state.

A computer procedure is developed using Fortran IV language to perform the numerical integration in Eq. (7.1). Some of the important features of this integration routine are discussed in detail by Faruque [32].

7.2 Verification with Respect to Plain Concrete

The material constants for this plain concrete under low confining pressure are given in TABLE 6.2. The description of the plain concrete is given in Chapter 2. The computer procedures are used to back-predict some of the ultimate envelopes, strengths and stress-strain responses curves obtained from the cubical triaxial tests.

7.2.1 $\sqrt{J_{2D}}$ - J_1 Plane

From Eq. (6.3), the predicted ultimate (failure) envelope in J_{2D} - J_1 plane was calculated and compared with the experimentally determined strength values. These comparisons are shown in Fig. 7.1, 7.2 and 7.3 for the Triaxial Compression (TC), Simple Shear (SS) and Triaxial Extension (TE) tests, respectively. Good correlation is shown between predicted and experimental results.

7.2.2 Octahedral, Triaxial, Biaxial, and π Planes

From Eq. (6.8), the predicted ultimate envelope was calculated and compared with the experimentally determined strength values. The predicted envelopes are shown in Figs. 7.4 and 7.5 for the octahedral and triaxial planes, respectively. The proposed model is seen to represent the data very well.

The predicted ultimate envelope has the required shape, i.e. curved in the triaxial planes and a triangular section

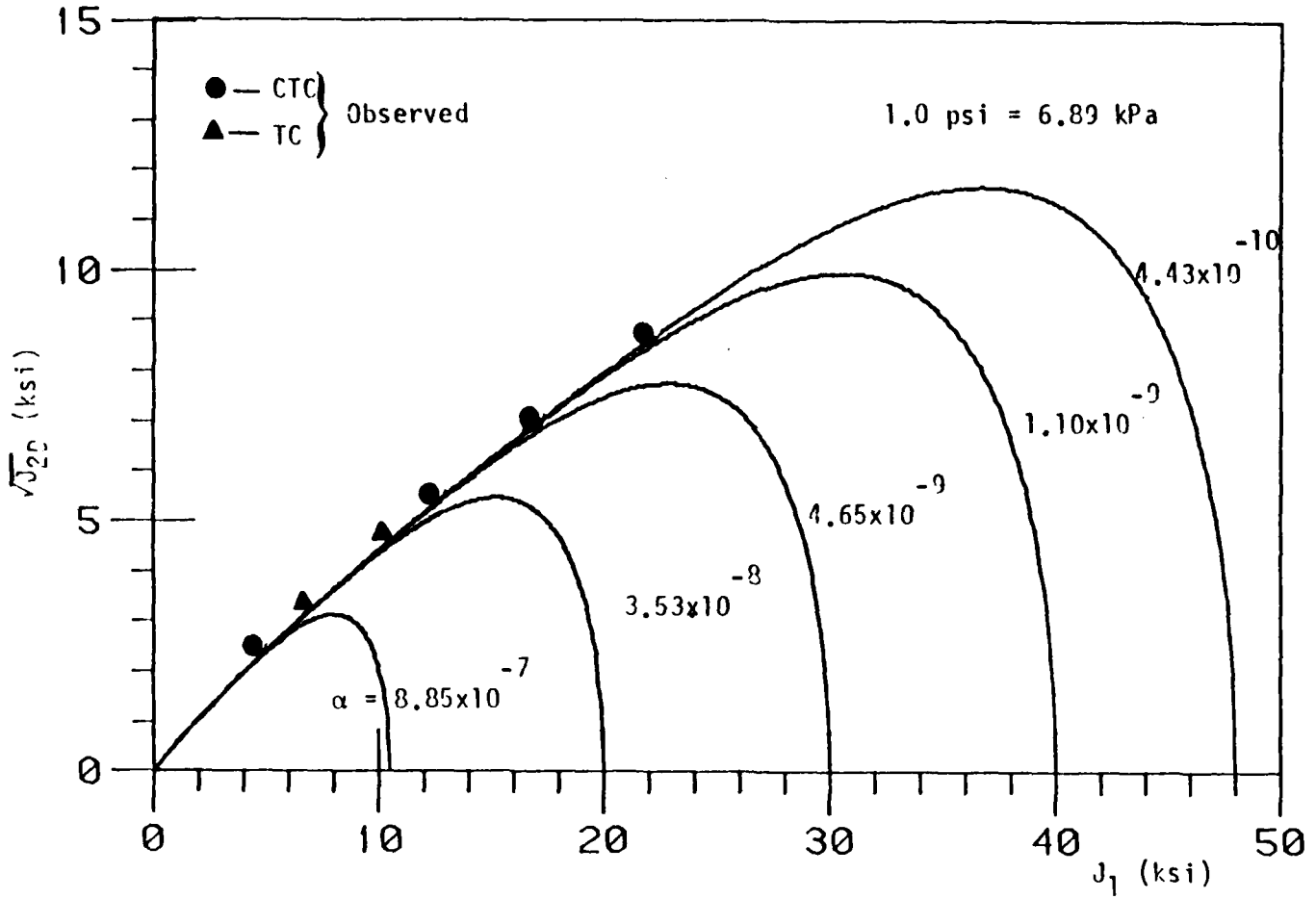

Figure 7.1. Predicted Ultimate and Pre-Ultimate Envelopes in $\sqrt{J_{2D}}$ - J_1 Plane for Conventional Triaxial Compression (CTC) and Triaxial Compression (TC) Tests, ($\theta = -30^0$), for Plain Concrete.

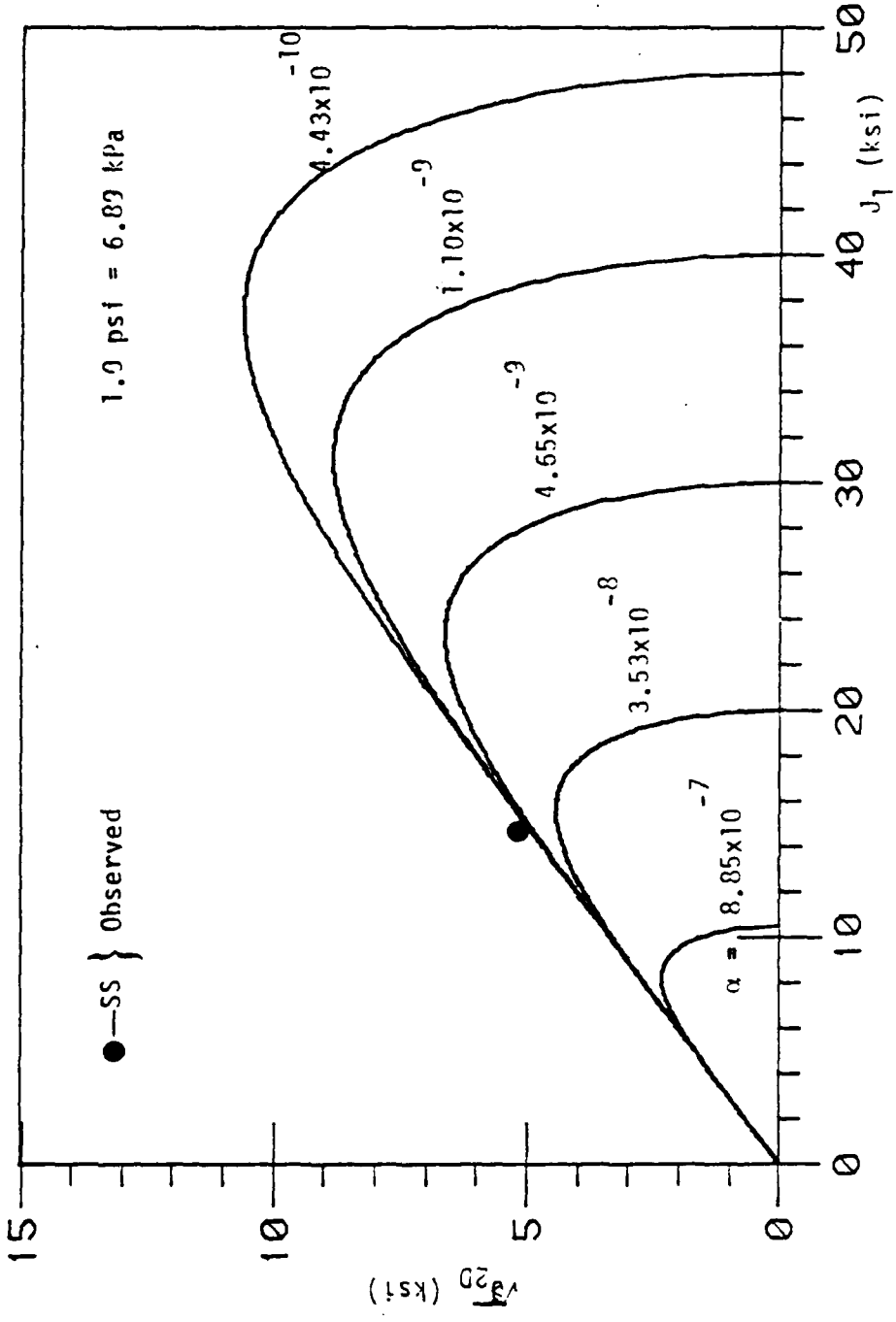

Figure 7.2. Predicted Ultimate and Pre-Ultimate Envelopes in $\sqrt{J_{2D}}$ - J_1 Plane for Simple Shear (SS) Test, ($\theta = 0^0$), for Plain Concrete.

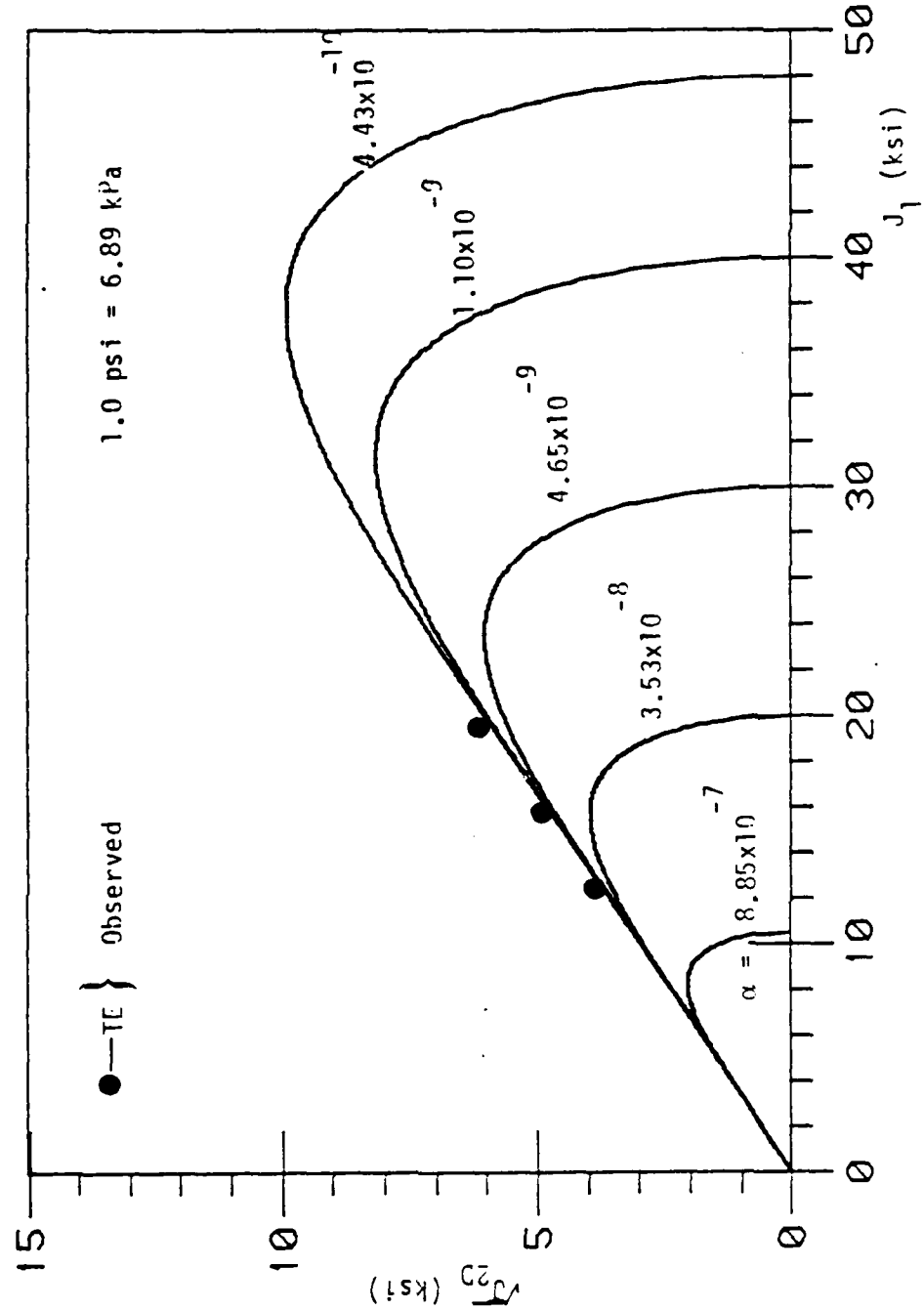

Figure 7.3. Predicted Ultimate and Pre-Ultimate Envelopes in $\sqrt{J_{2D}}$ - J_1 Plane for Triaxial Extension (TE) Test, ($\theta = 30^0$), for Plain Concrete.

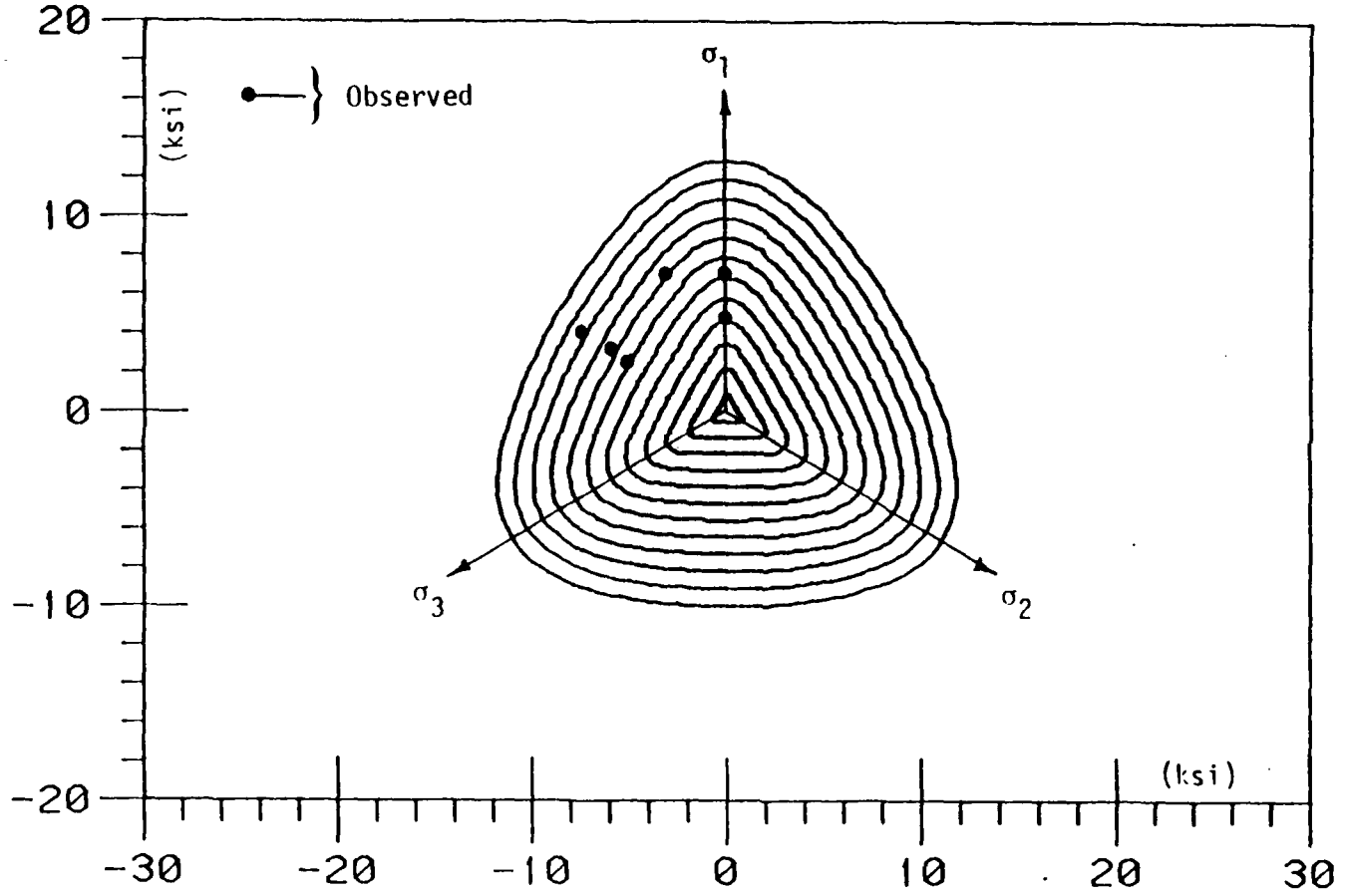

Figure 7.4. Variations of Cross-Sectional Shapes in Octahedral Planes (J_1 = 1,3,5,7,9,11,13,15,17,21,23 and 25 ksi), (1.0 psi = 6.89 kPa), for predicted ultimate surface for plain concrete.

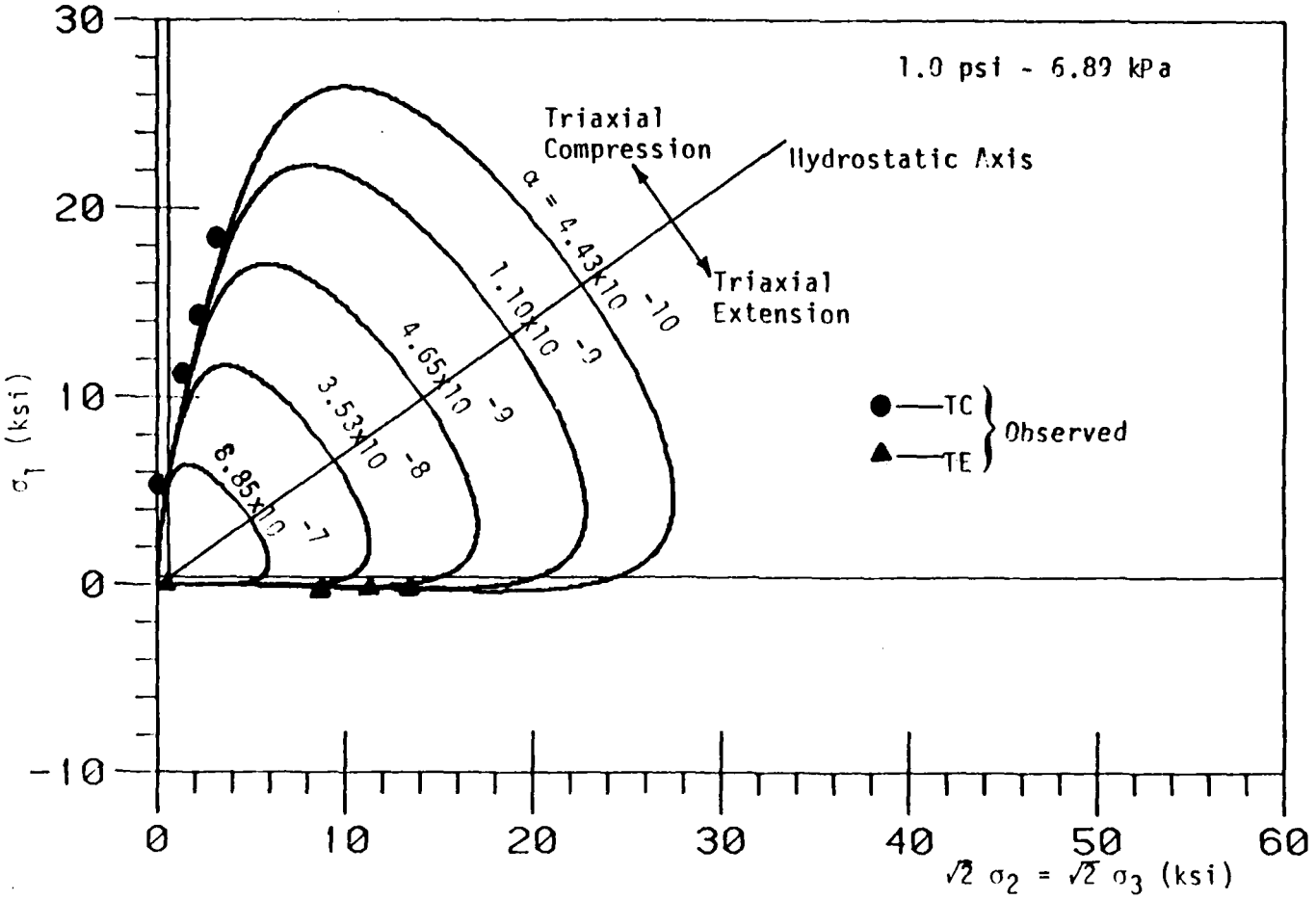

Figure 7.5. Predicted Ultimate and Pre-Ultimate Envelopes in Triaxial Plane for Plain Concrete.

with rounded corners in the octahedral plane. It is seen in Fig. 7.4 and 7.7, as the confining pressure (J_1) is increased, the shape of the yield envelope gradually changes from triangle with smooth rounded corners to a circle (at very high confining pressure).

Fig. 7.6 shows the biaxial ultimate envelope predicted using proposed constitutive model. It is for reference only since no experimental biaxial strength data was obtained.

Predicted ultimate envelope on the π-plane is shown in Fig. 7.7.

7.2.3 Strength Behavior

Based on the predicted strength envelope, Fig. 7.5, predicted values of the uniaxial compressive strength, f_{cu}, equi-biaxial compressive strength, f_{cb}, and uniaxial tensile strength, f_t, can be calculated. These predicted strengths are:

$$f_{cu} = 5077 \text{ psi } (35 \text{ MPa}) \qquad (7.2)$$

$$f_{cb} = 16862 \text{ psi } (116.3 \text{ MPa})$$

$$f_t = -389 \text{ psi } (-2.68 \text{ MPa}) \qquad \text{(Compression Positive)}$$

The values of f_{cu} and f_t compared to unconfined compression strength, f_{cu}, and tensile strength, f_t, based on tests with cubical specimens of 4x4x4 inch (10.16x10.16x10.16 cm) in multiaxial test device and Eq. (6.47), respectively. These values were:

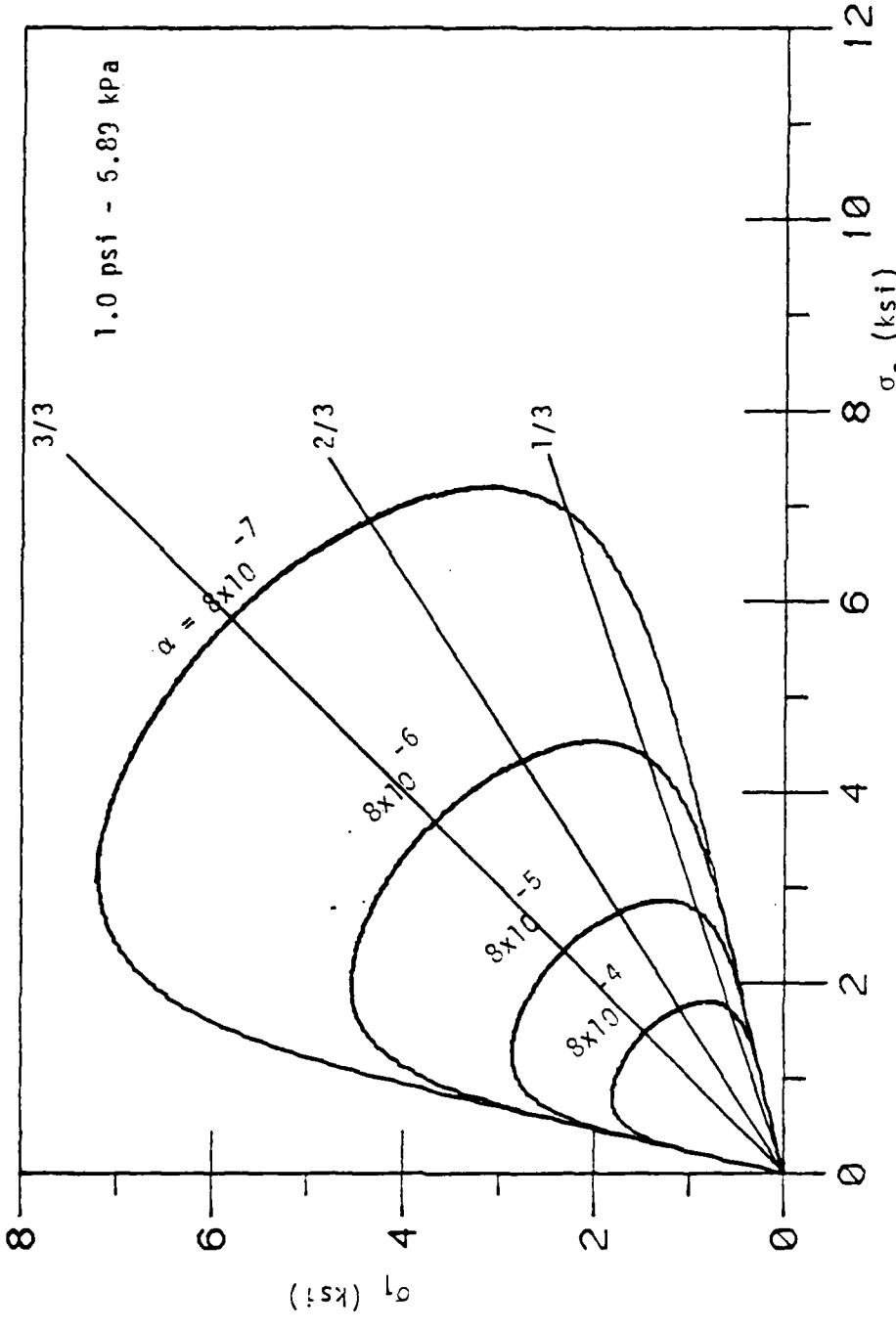

Figure 7.6. Predicted Biaxial Ultimate and Pre-Ultimate Envelopes ($\sigma_3 = 0$) Based on Proposed Model for Plain Concrete.

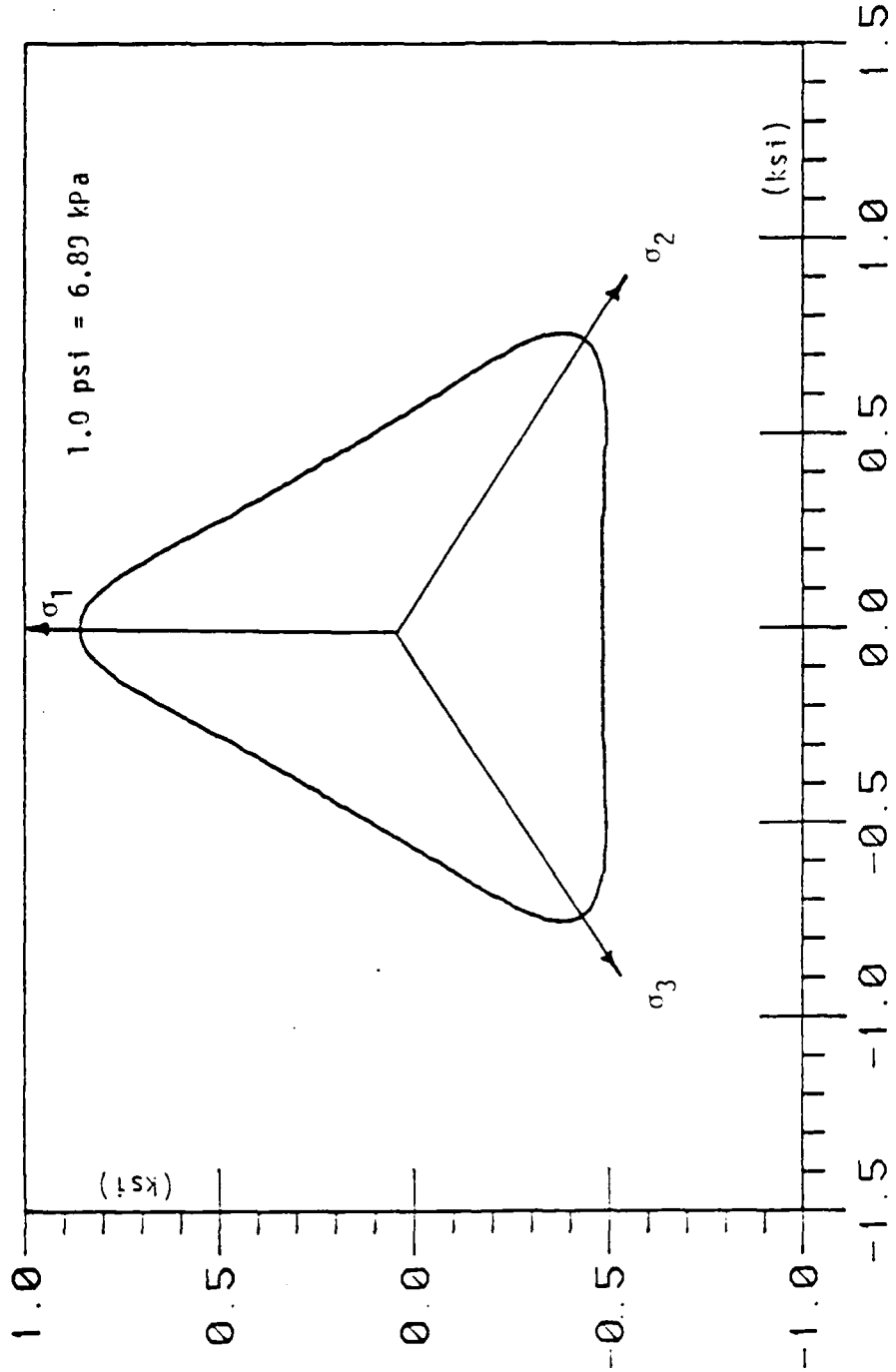

Figure 7.7. Predicted Ultimate Surface in π-Plane for Plain Concrete.

$$f_{cu} = 4503 \text{ psi } (31.05 \text{ MPa}) \qquad (7.3)$$

$$f_t = -\ 389 \text{ psi } (-2.68 \text{ MPa}) \qquad \text{(Compression Positive)}$$

The differences between these predicted and observed strengths may be attributed to the effect of specimen types and boundary conditions.

Based on the predicted ultimate envelope, Fig. 7.5, predicted values of the $\sqrt{J_{2D}}$ for TC on π-plane ($\Theta = -30^{o}$) SS ($\Theta = 0^{o}$) and TE ($\Theta = 30^{o}$) can be calculated. These predicted values are:

$$\begin{aligned} (\sqrt{J_{2D}})_{TC} &= 0.634 \text{ ksi } (4.37 \text{ MPa}) \\ (\sqrt{J_{2D}})_{SS} &= 0.404 \text{ ksi } (2.786 \text{ MPa}) \\ (\sqrt{J_{2D}})_{TE} &= 0.347 \text{ ksi } (2.393 \text{ MPa}) \end{aligned} \qquad (7.4)$$

Eqs. (7.4) can be expressed as the ratio of different stress paths on the π-plane:

$$R_1 = \frac{(\sqrt{J_{2D}})_{TC}}{(\sqrt{J_{2D}})_{TE}} = 1.83$$

$$R_2 = \frac{(\sqrt{J_{2D}})_{SS}}{(\sqrt{J_{2D}})_{TE}} = 1.165 \qquad (7.5)$$

$$R_3 = \frac{(\sqrt{J_{2D}})_{TC}}{(\sqrt{J_{2D}})_{SS}} = 1.57$$

Note that $(\sqrt{J_{2D}})_{TC}$ is almost twice of $(\sqrt{J_{2D}})_{TE}$ (Eqs. 7.4) plotted in π-plane. This may be partly due to the fact that ultimate strength for plain concrete under extension stress path is much lower than that under comparison stress path.

7.2.4 Stress-Strain Behavior for Test Used for Finding Material Constants

Figure 7.8 shows the comparison of the prediction and observation for a typical HC test; the agreement between the prediction and observation is satisfactory. Figures 7.9, 7.10, 7.11 and 7.12 show the comparison of the predictions and observations for the stress-strain responses for one (CTC) test, one (TC) test, one (SS) test, and one (TE). Initial confining pressure for the (CTC), (TC), (SS) and (TE) tests are 1 ksi (6.895 MPa), 3 ksi (20.69 MPa), 4.5 ksi (31.03 MPa) and 4 ksi (27.58 MPa), respectively. It is evident from Figs. 7.9, 7.10, 7.11 and 7.12 that the predictions from the model compare fairly well with experimental results.

7.2.5 Volumetric Responses Behavior

The volumetric strain, ε_v, is plotted with respect to axial strain, ε_1. Figs. 7.13, 7.14, 7.15 and 7.16 show ε_v - ε_1 plots for one CTC (σ_o - 1 ksi) test, one TC (σ_o = 3 ksi) test, one SS (σ_o = 4.5 ksi) and one TE (σ_o = 4 ksi) test. Experimental results are also shown on the same plots. It is evident from

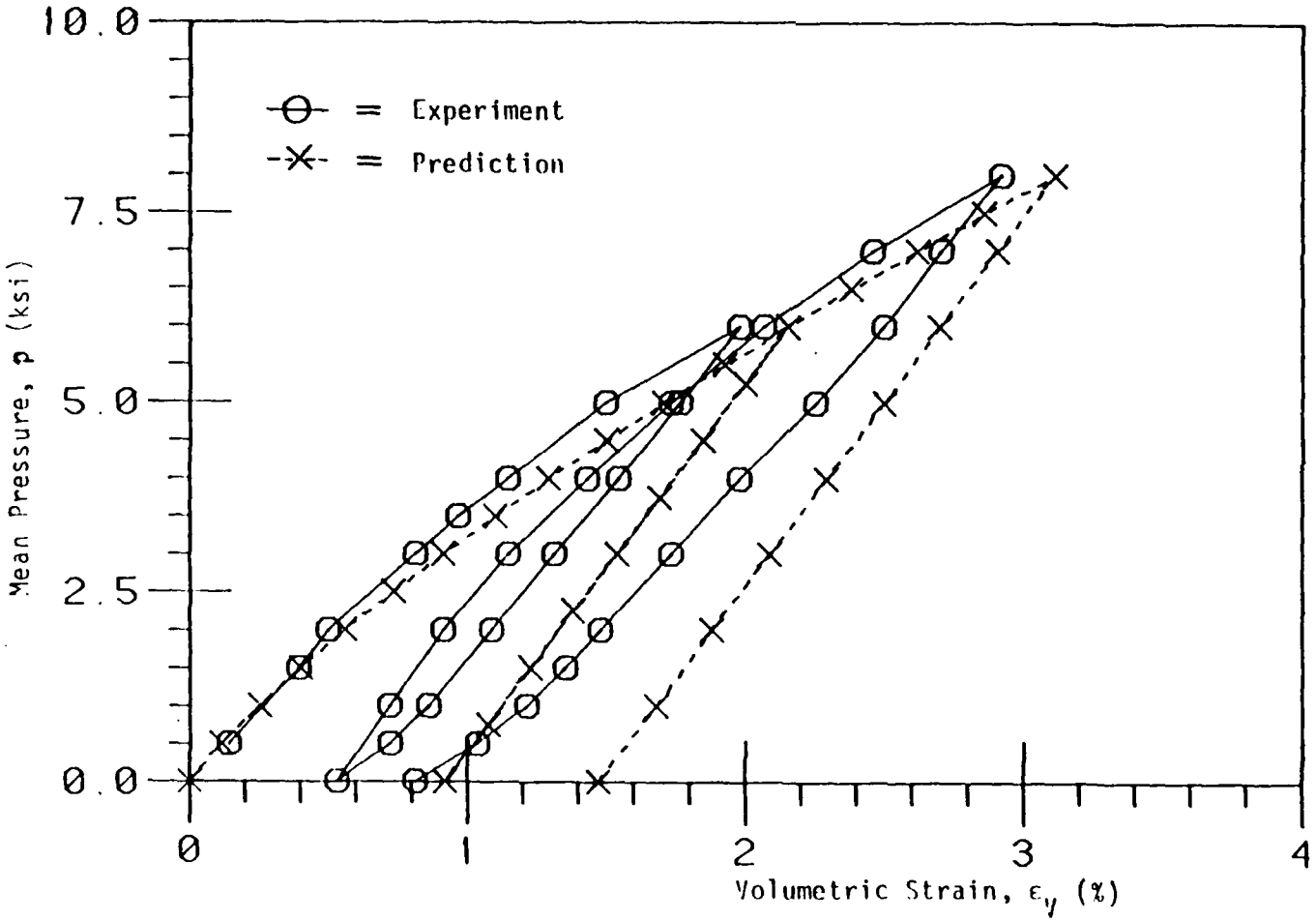

Figure 7.8. Comparison of Stress-Strain Responses of Hydrostatic Compression (HC) Test for Plain Concrete (σ_o = 8. ksi), (1.0 psi = 6.89 kPa)

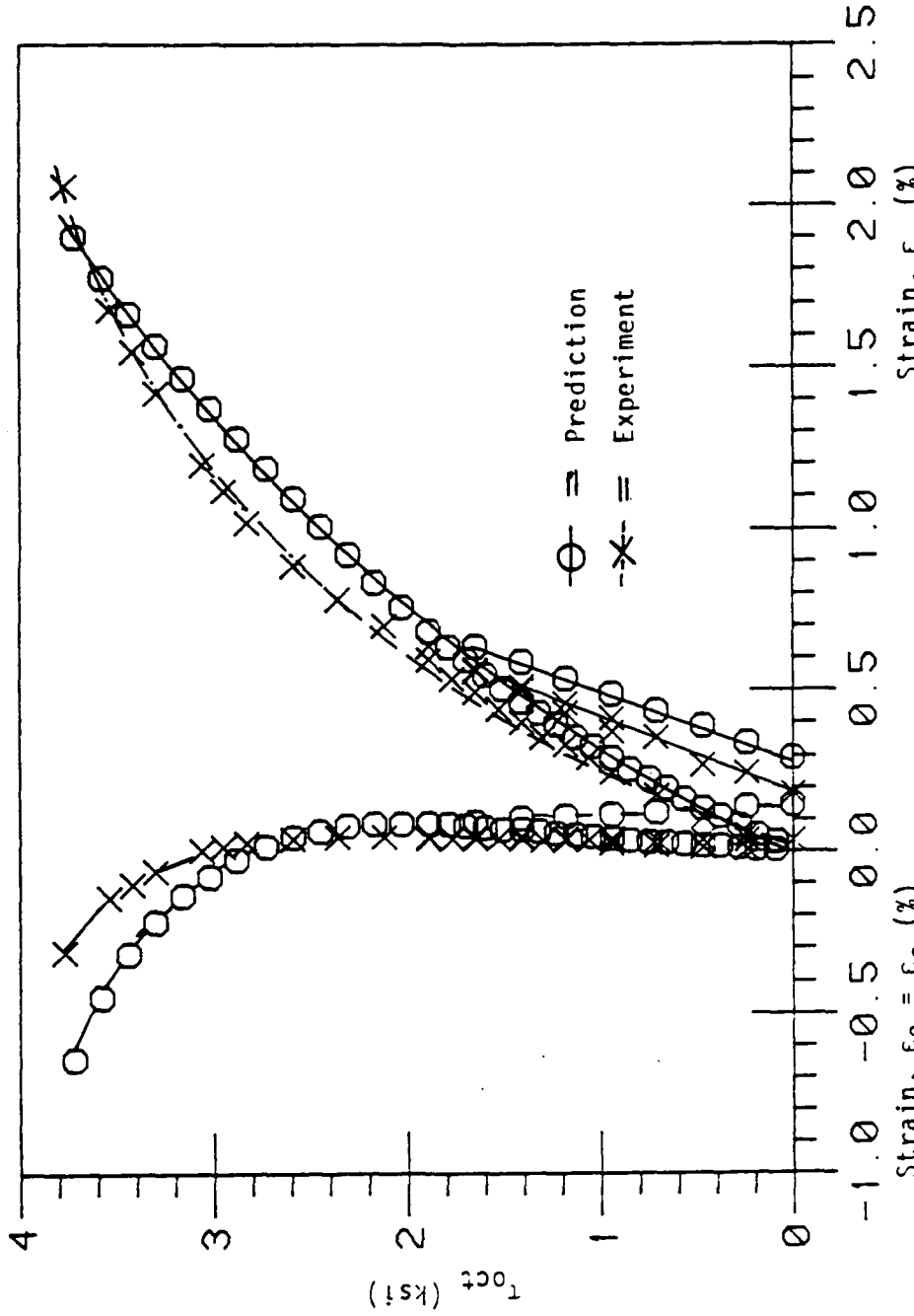

Figure 7.9. Comparison of Stress-Strain Responses of Conventional Triaxial Compression (CTC) Test for Plain Concrete (σ_o = 1.0 ksi), (1.0 psi = 6.89 kPa)

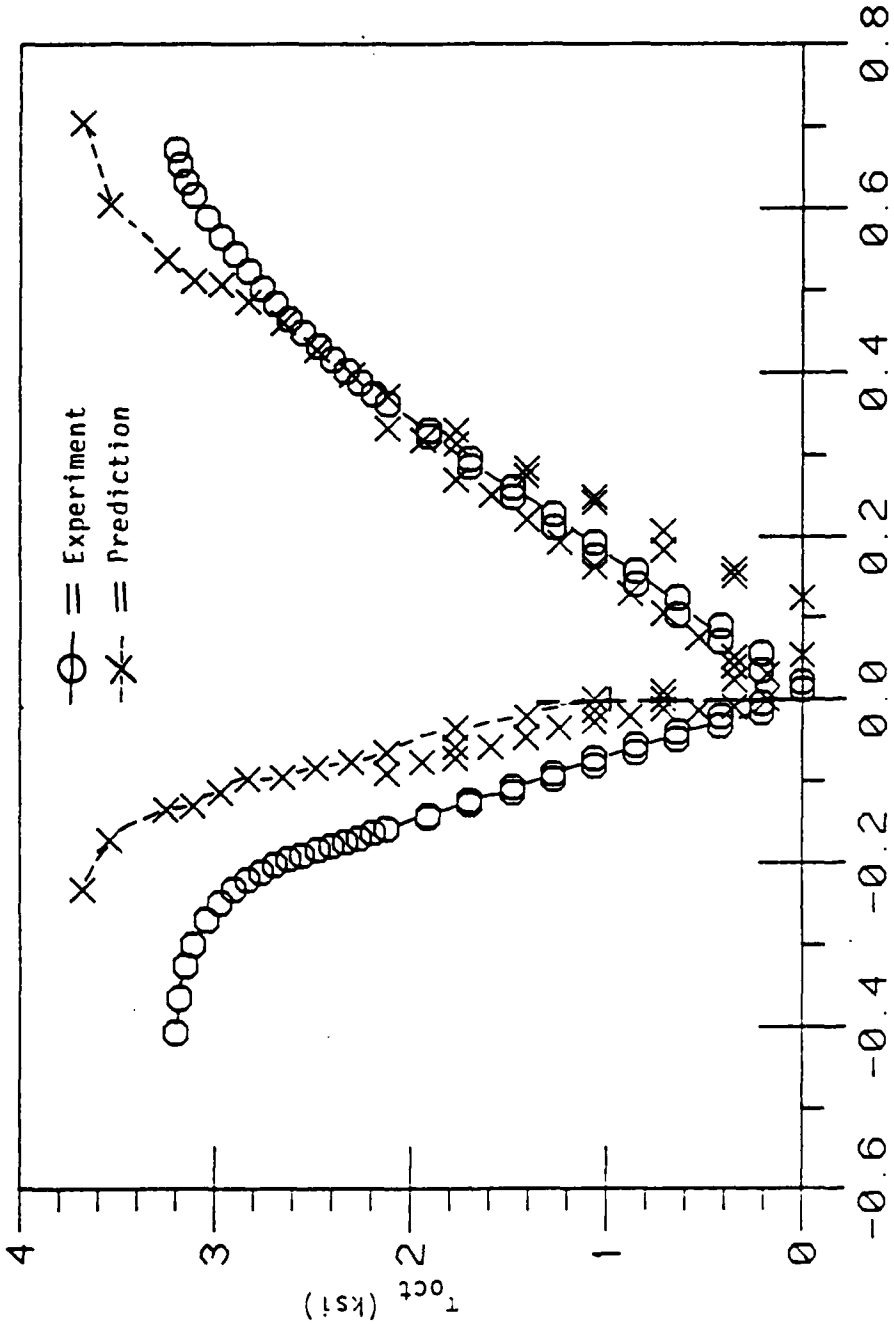

Figure 7.10. Comparison of Stress-Strain Responses of Triaxial Compression (TC) Test for Plain Concrete (σ_o = 3.9 ksi), (1.0 psi = 6.89 kPa).

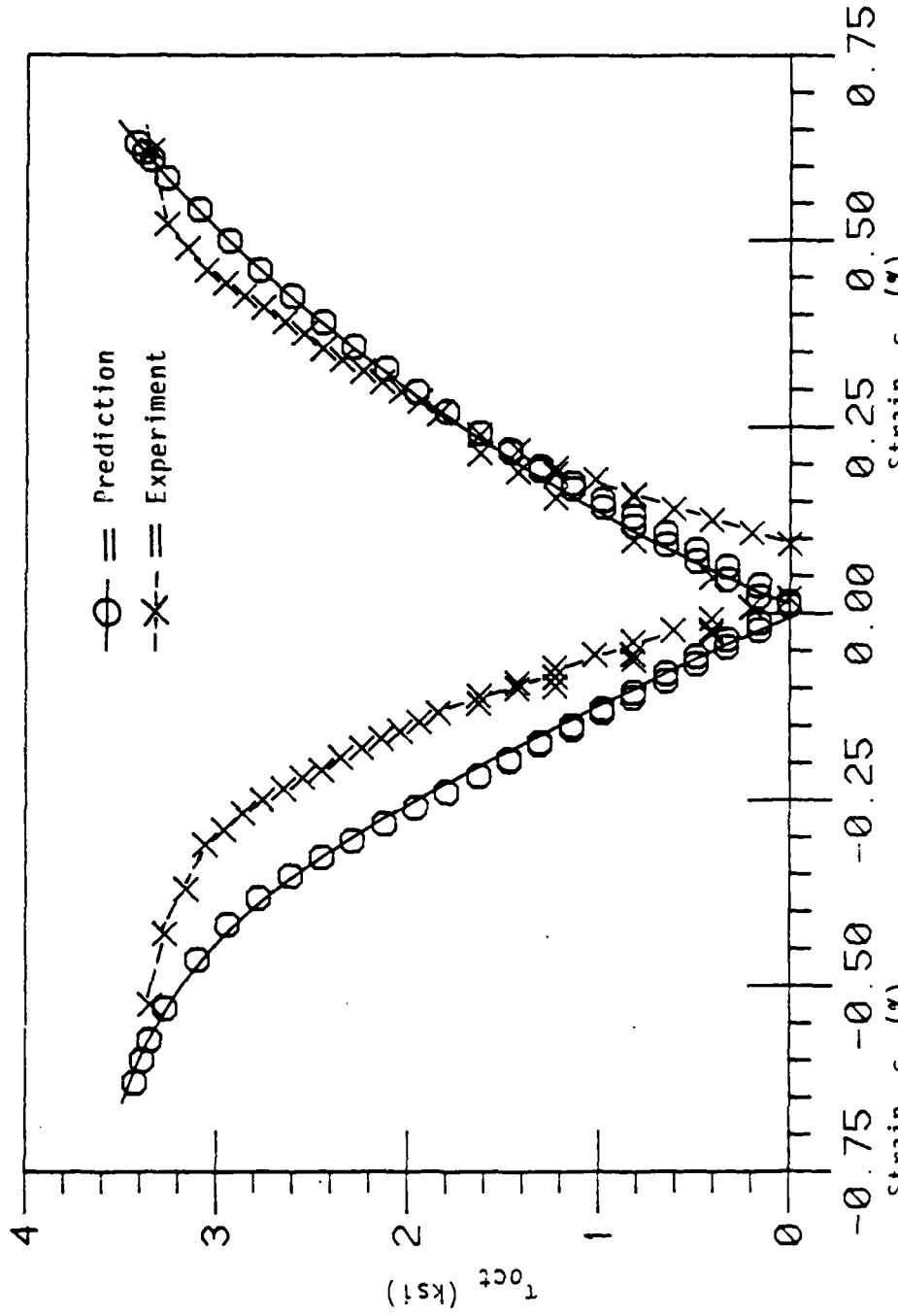

Figure 7.11. Comparison of Stress-Strain Responses of Simple Shear (SS) Test for Plain Concrete (σ_o = 4.5 ksi), (1.0 psi = 6.89 kPa).

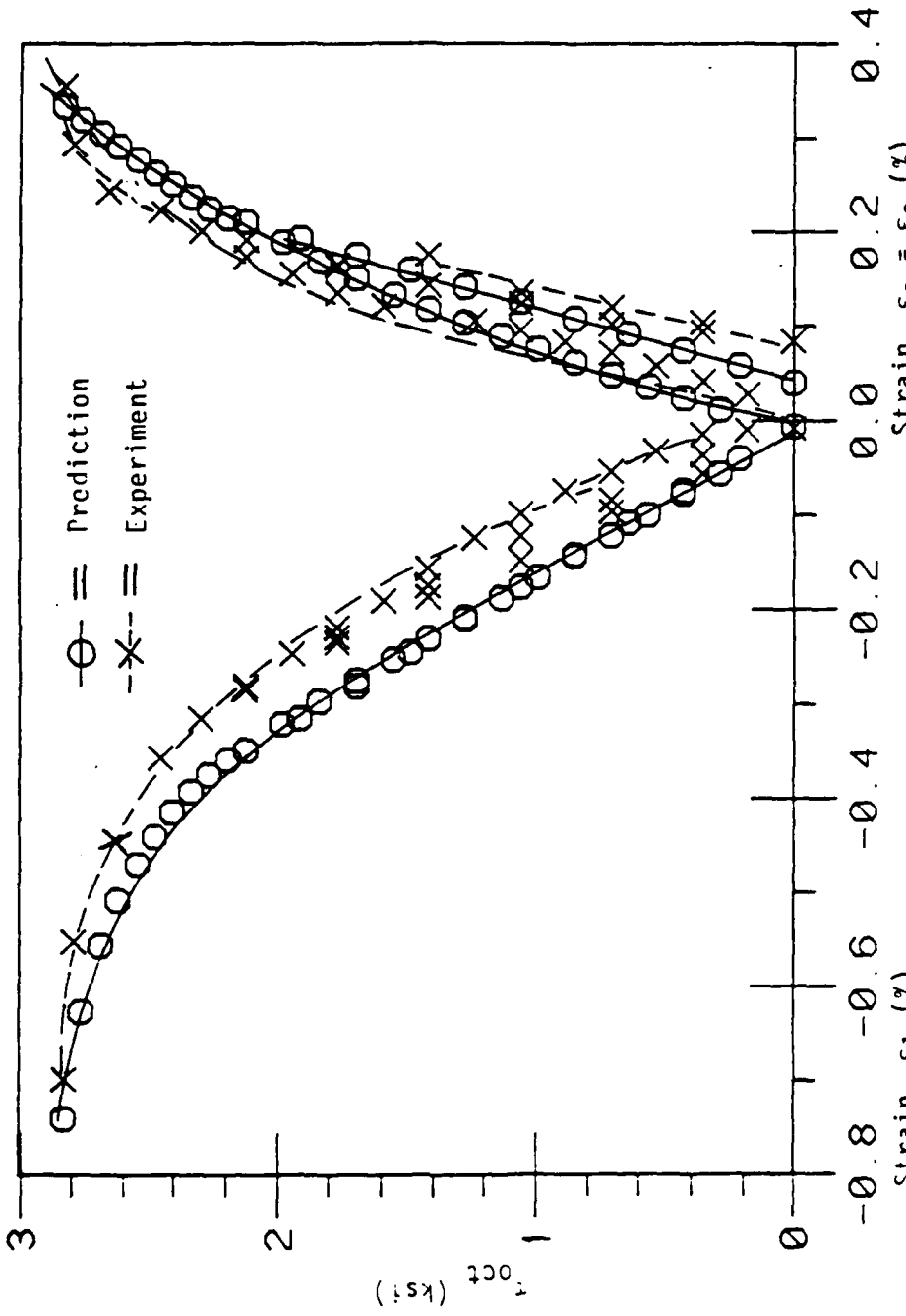

Figure 7.12. Comparison of Stress-Strain Responses of Triaxial Extension (TE) Test for Plain Concrete (σ_o = 4.0 ksi), (1.0 psi = 6.89 kPa)

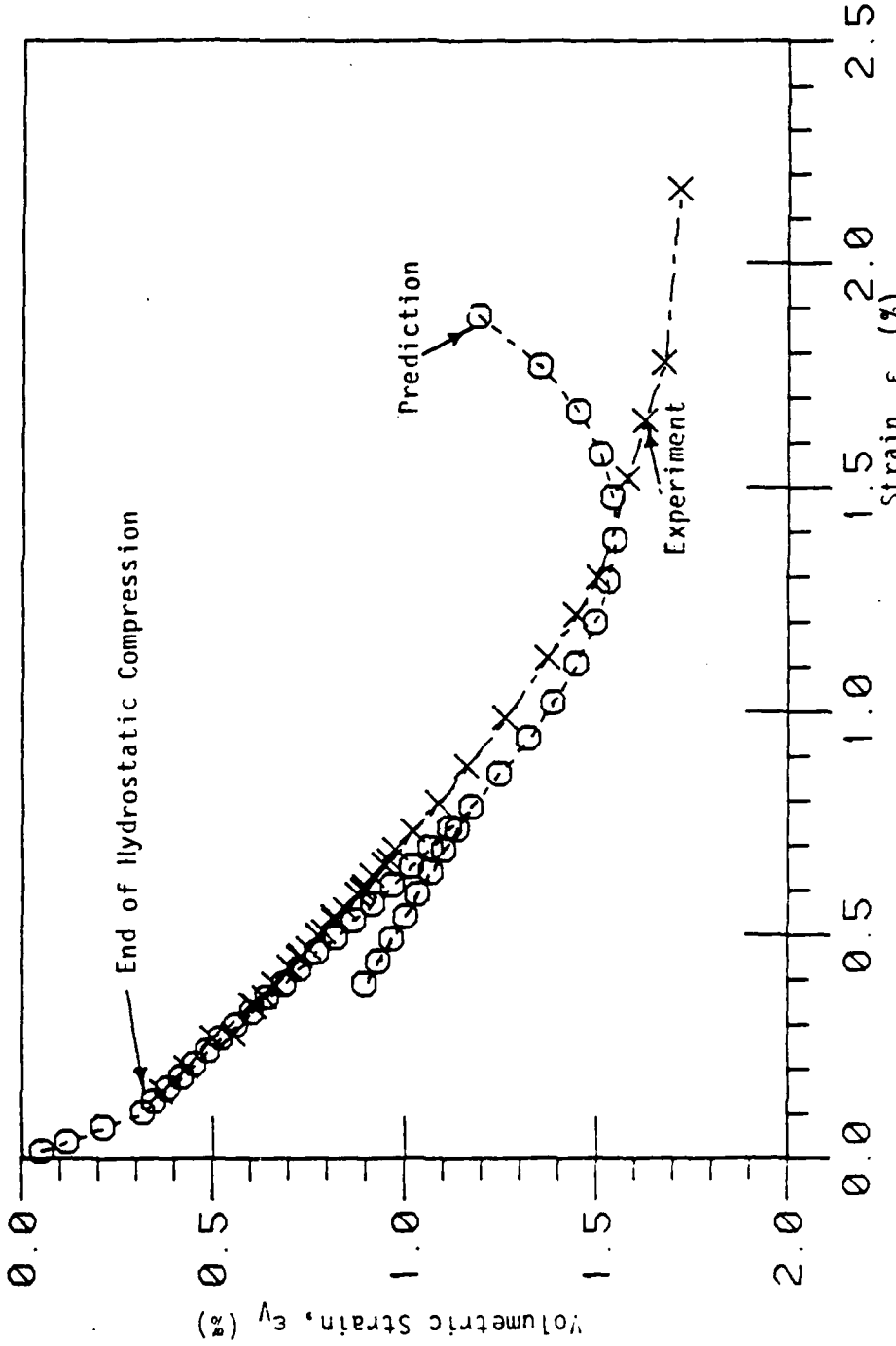

Figure 7.13. Comparison of Volumetric Response of Compression Triaxial Compression (CTC) Test for Plain Concrete (σ_o = 1.0 ksi), (1.0 psi = 6.89 kPa).

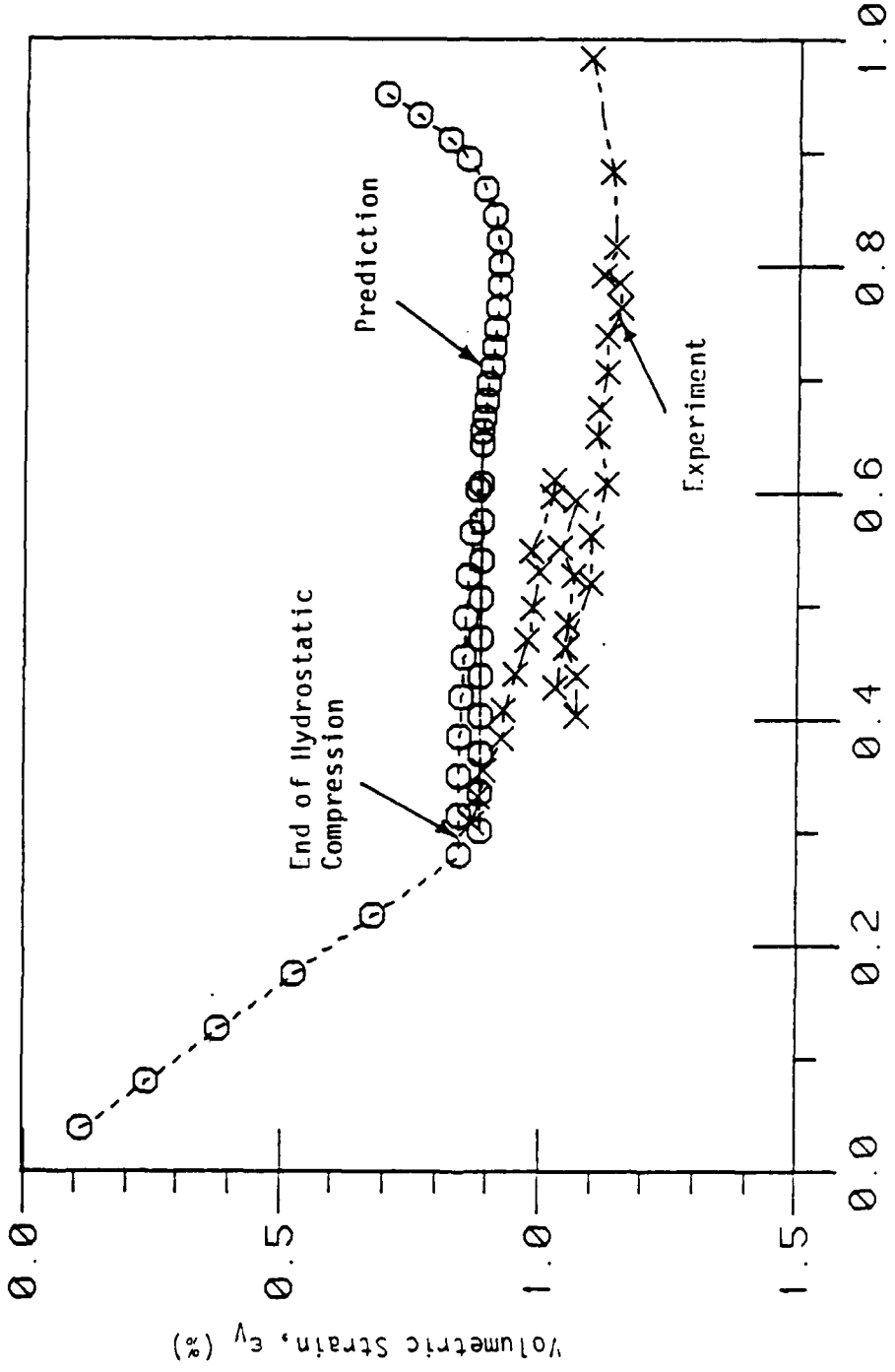

Figure 7.14. Comparison of Volumetric Response of Triaxial Compression (TC) Test for Plain Concrete (σ_o = 3.0 ksi), (1.0 psi = 6.89 kPa).

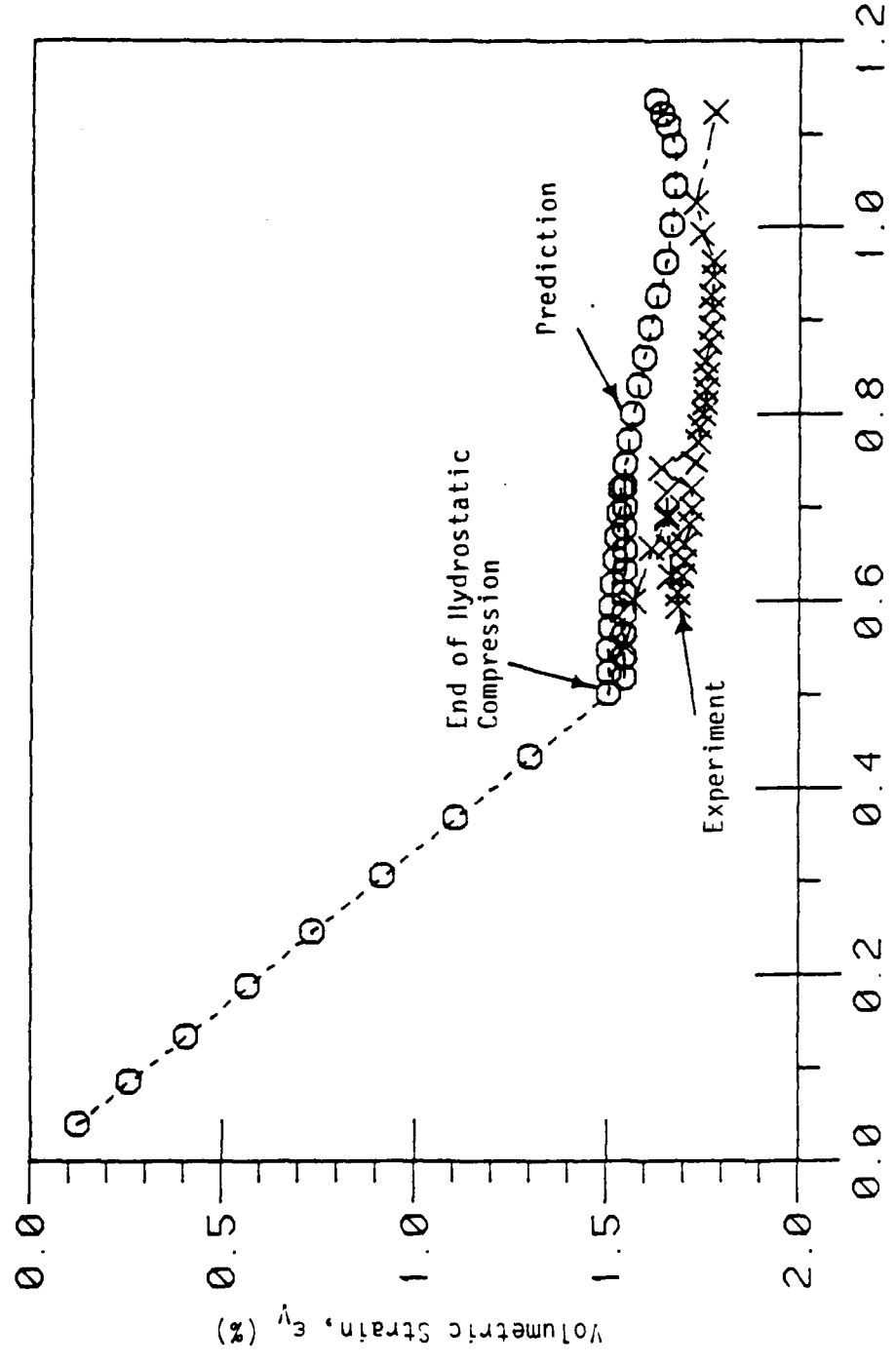

Figure 7.15. Comparison of Volumetric Response of Simple Shear (SS) Test for Plain Concrete (σ_o = 4.5 ksi), (1.0 psi = 6.89 kPa).

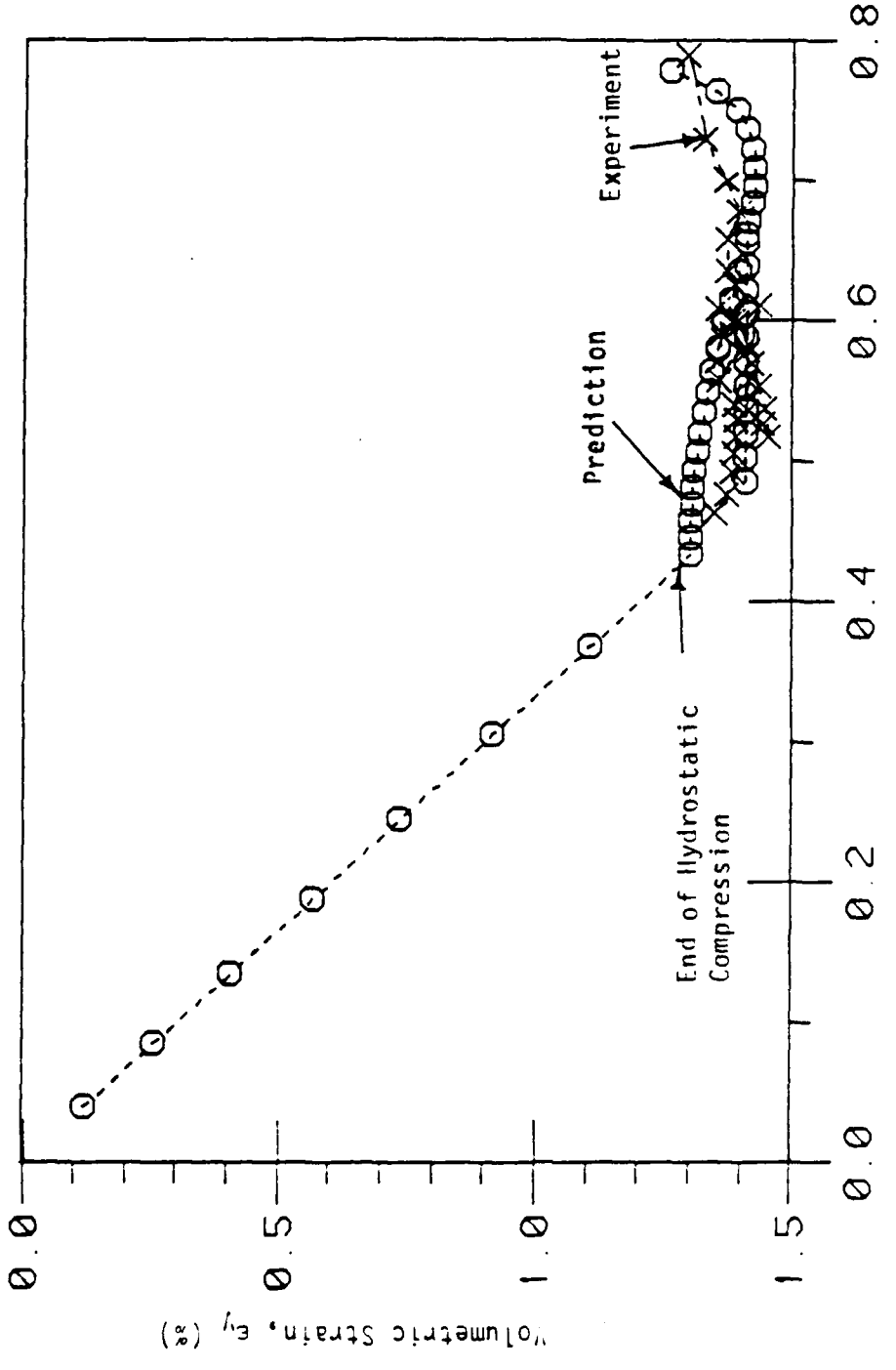

Figure 7.16. Comparison of Volumetric Response of Triaxial Extension (TE) Test for Plain Concrete (σ_o = 4.0 ksi), (1.0 psi = 6.89 kPa).

these plots that the predictions compare fairly well with the experimental data.

7.2.6 Circular Stress Path and Proportional Loading Tests Not Used for Finding Material Constants

Figures 7.17 and 7.18 show the comparison of the predictions and the observations for a circular stress path test and a proportional loading (R = 1/3) test which are not used to determine the material constants. It is seen from Figs. 7.17 and 7.18 that a good agreement is achieved between the predictions and the observations.

7.3 Verification with Respect to Colorado Plain Concrete

The material constants for this plain concrete under high confining pressure are given in TABLE 6.3. The description of the plain concrete is presented in Chapter 6. A number of ultimate envelopes, strengths and stress-strain response curves are predicted and compared with the experimental results.

7.3.1 $\sqrt{J_{2D}}$ - J_1 Plane

Figures 7.19, 7.20 and 7.21 show the comparison of the predictions and observations of ultimate envelopes in $\sqrt{J_{2D}}$ - J_1 plane, for (TC) test, (SS) test and (TE) test, respectively. The proposed model is seen to represent the data very well.

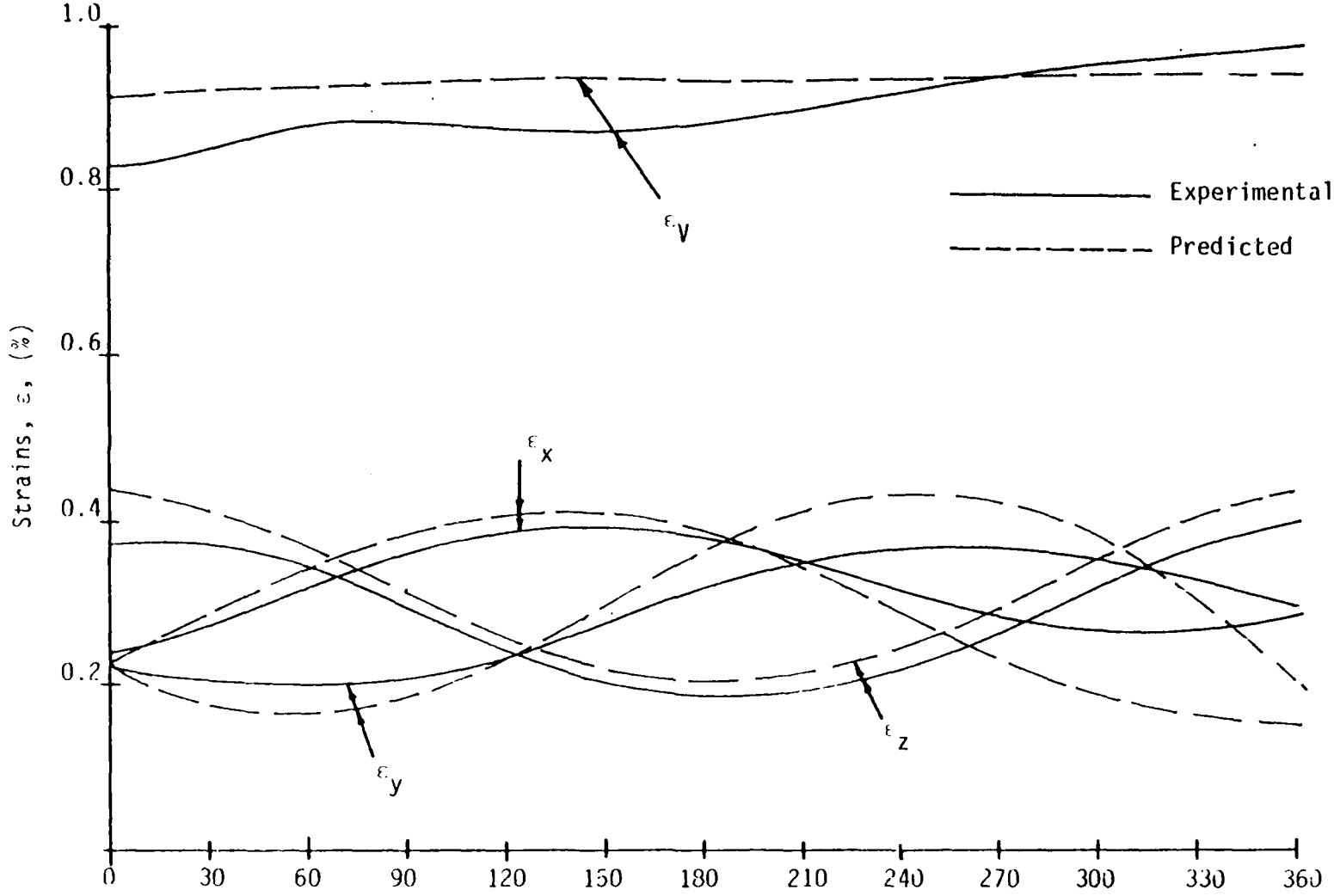

Figure 7.17. Comparison of Principal Strain at Volumetric Strain-Angle of Similarity Responses of Circular Path (CPS) Test for Plain Concrete (σ_{oct} = 4.0 ksi at τ_{oct} = 1.0 ksi), (1.0 psi = 6.89 kPa)

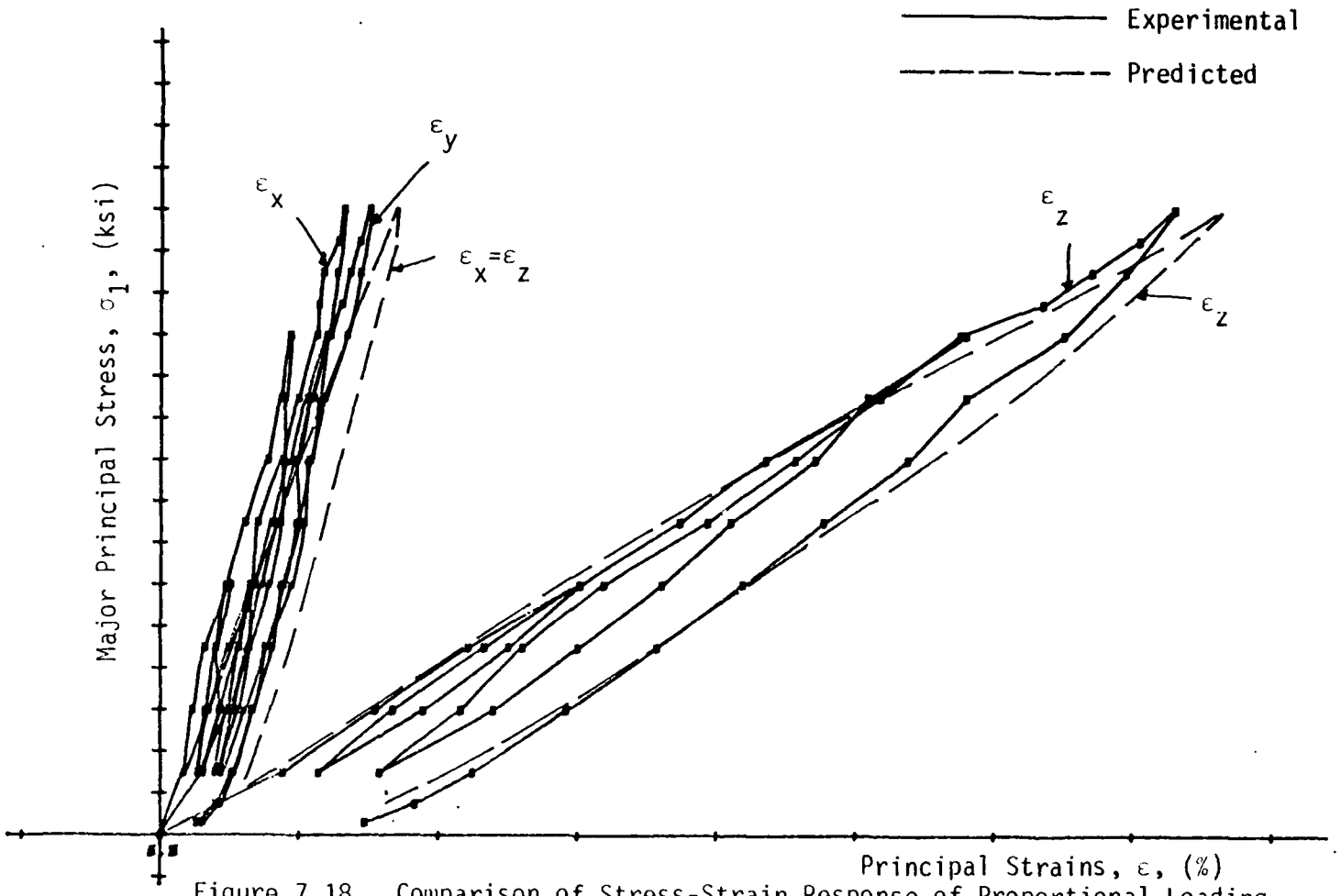

Figure 7.18. Comparison of Stress-Strain Response of Proportional Loading (PL) Test for Plain Concrete (R = 1/3), (1.0 psi = 6.89 kPa)

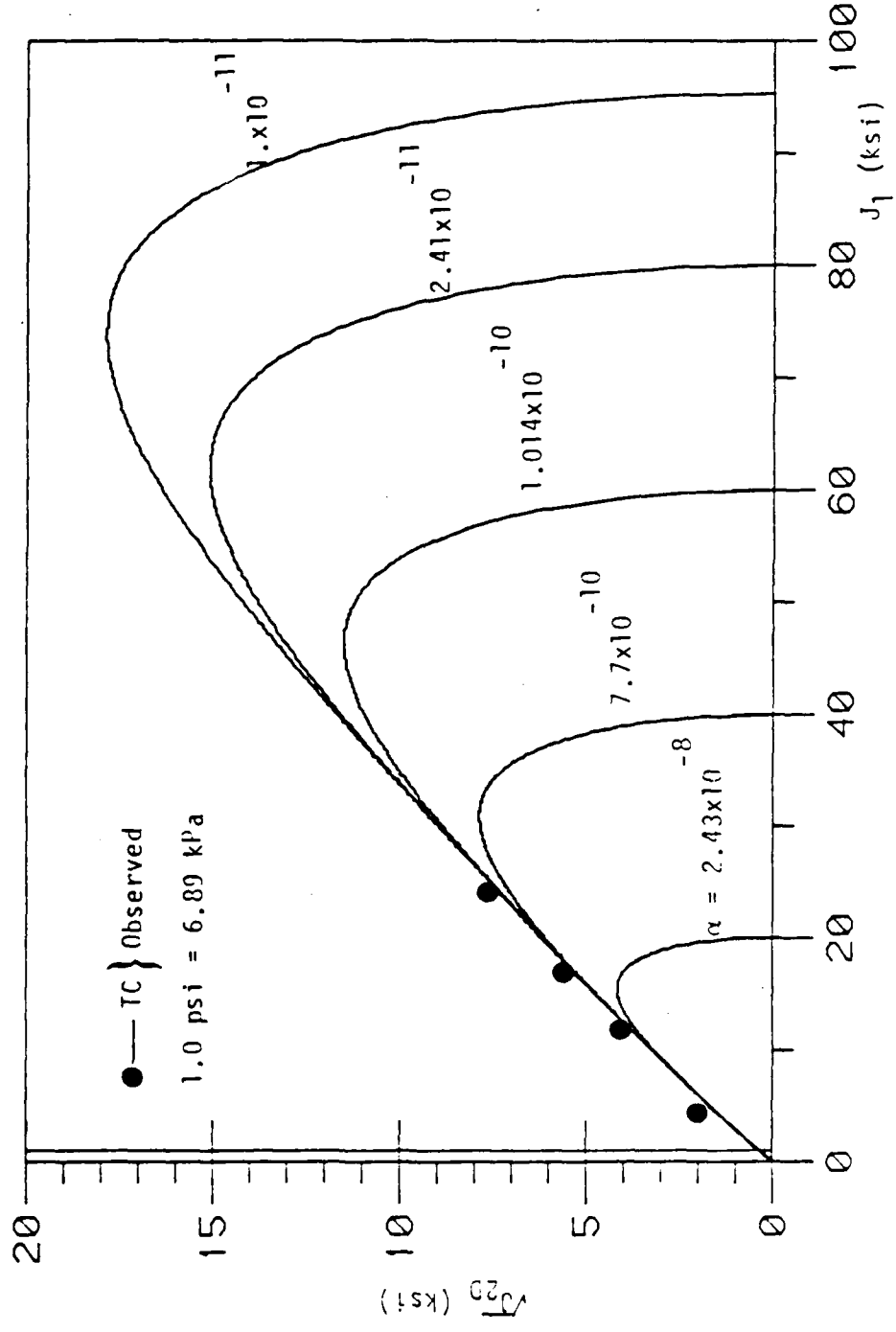

Figure 7.19. Predicted Ultimate and Pre-Ultimate Envelopes in $\sqrt{J_{2D}}$ - J_1 Plane for Triaxial Compression (TC) Test, ($\theta = -30^0$), for Colorado Plain Concrete.

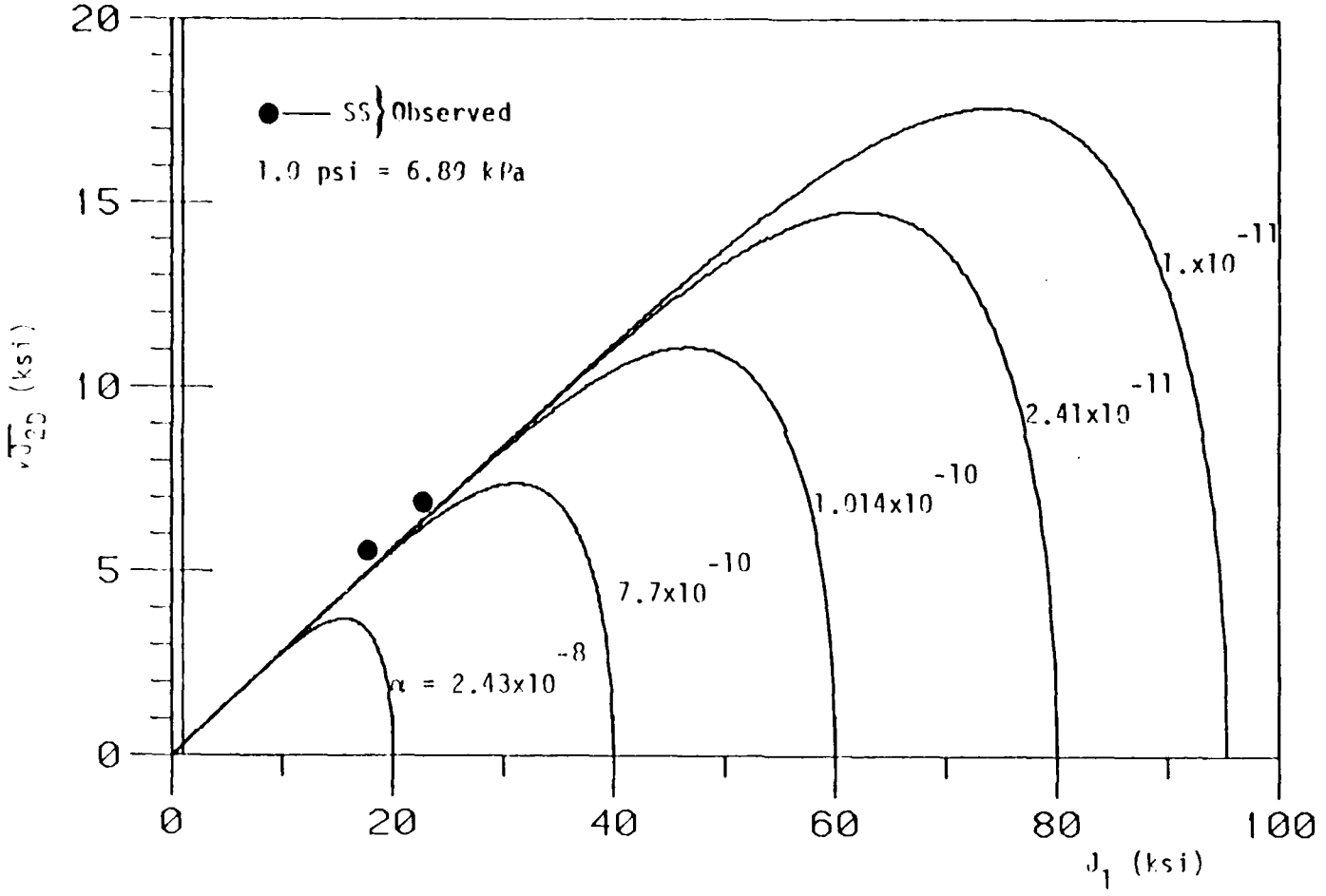

Figure 7.20. Predicted Ultimate and Pre-Ultimate Envelopes in $\sqrt{J_{2D}}$ - J_1 Plane for Simple Shear (SS) Test ($\theta = 0^0$), for Colorado Plain Concrete.

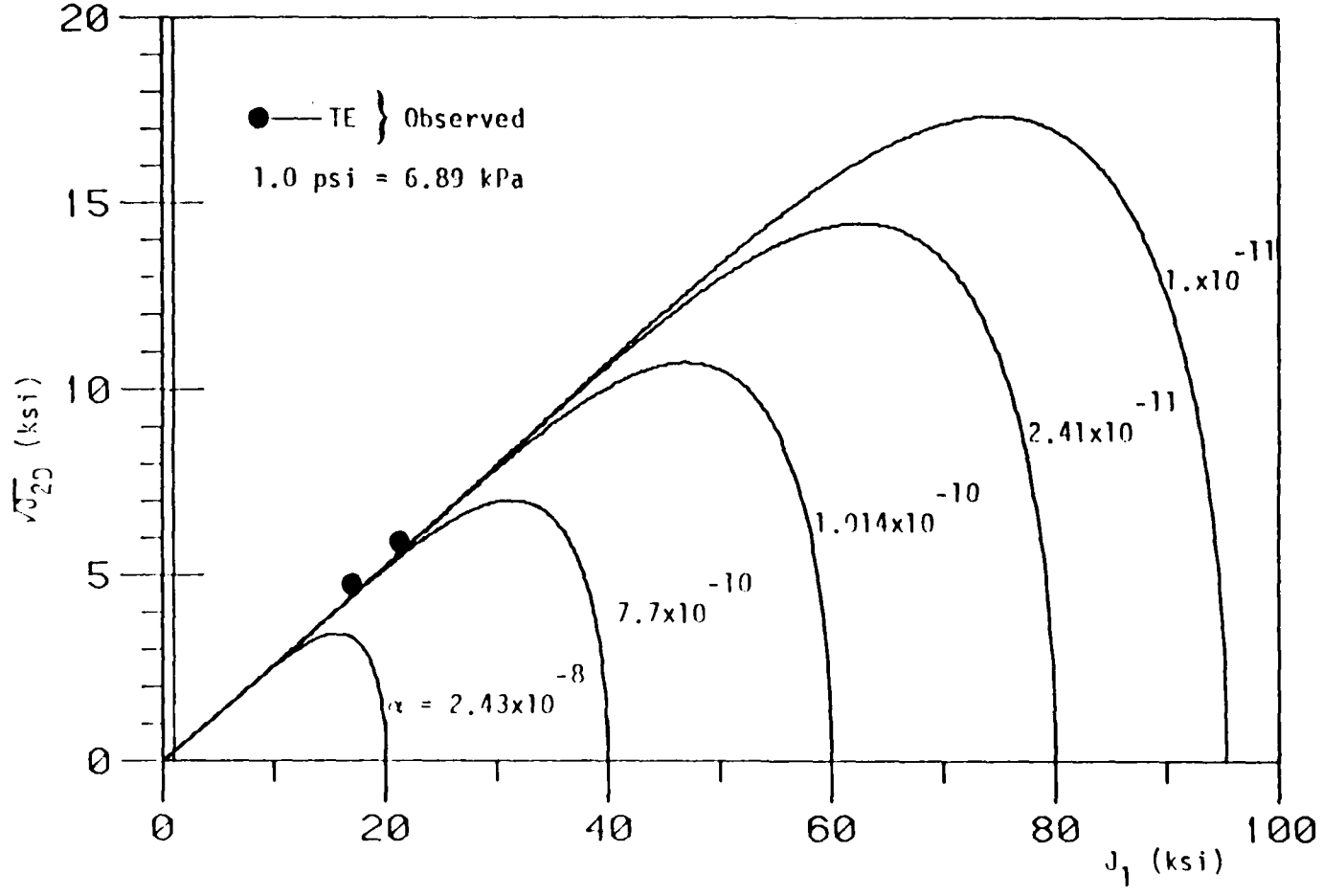

Figure 7.21. Predicted Ultimate and Pre-Ultimate Envelopes for Triaxial Extension (TE) Test, ($\theta = 30^{o}$), for Colorado Plain Concrete.

7.3.2 Octahedral, Triaxial, Biaxial and π-Planes

From Eq. (6.8), the predicted ultimate envelope was calculated and compared with the experimentally determined strength values. These comparisons are shown in Figs. 7.22 and 7.23 for the octahedral and triaxial planes, respectively. It is evident from these plots that the predictions compare well with the experimental data.

Fig. 7.24 shows the biaxial ultimate envelope predicted using proposed constitutive model. It is for reference only since no experimental biaxial strength data was obtained.

Predicted ultimate envelope on the π-plane is shown in Fig. 7.25.

7.3.3 Strength Behavior

Based on the predicted strength envelope, Fig. 7.23, predicted values of the uniaxial compressive strength, f_{cu}, equibiaxial compressive strength, f_{cb}, and uniaxial tensile strength, f_t, can be calculated. These predicted strengths are:

$$f_{cu} = 3800 \text{ psi } (26.2 \text{ MPa}) \tag{7.6}$$

$$f_{cb} = 3490 \text{ psi } (58.51 \text{ MPa})$$

$$f_t = -354 \text{ psi } (-2.44 \text{ MPa}) \quad \text{(Compression Positive)}$$

The values of f_{cu} and f_t compared to unconfined compression strength, f'_c, and tensile strength, f_t, based on tests with cylindrical specimens of 3x6 in. (7.62x15.24 cm) and Eq. (5.17),

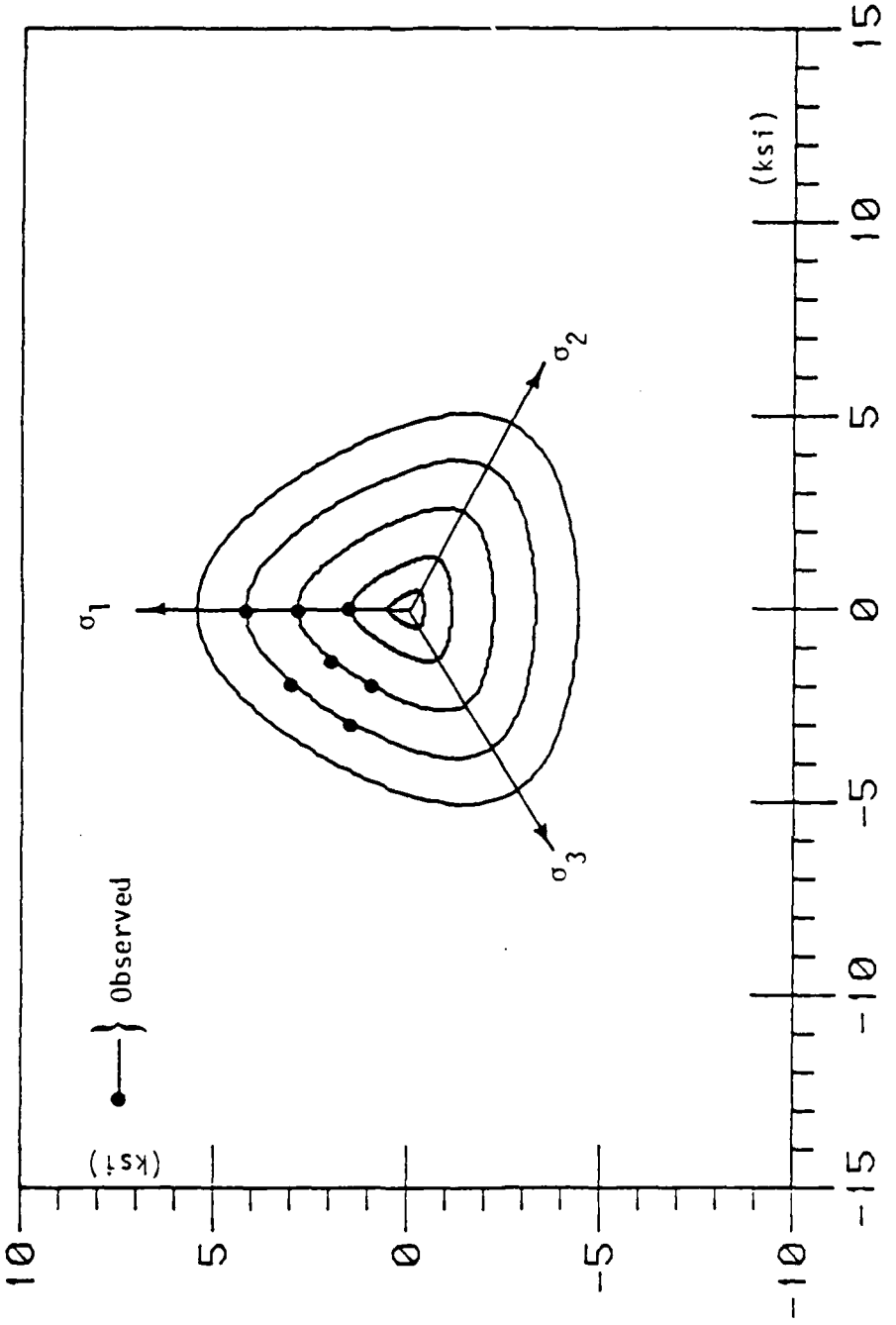

Figure 7.22. Variation of Cross-Sectional Shapes in Octahedral Planes (J_1 = 1,13,19,25 and 31 ksi), (1.0 psi - 6.89 kPa), for predicted ultimate surface for Colorado Plain Concrete.

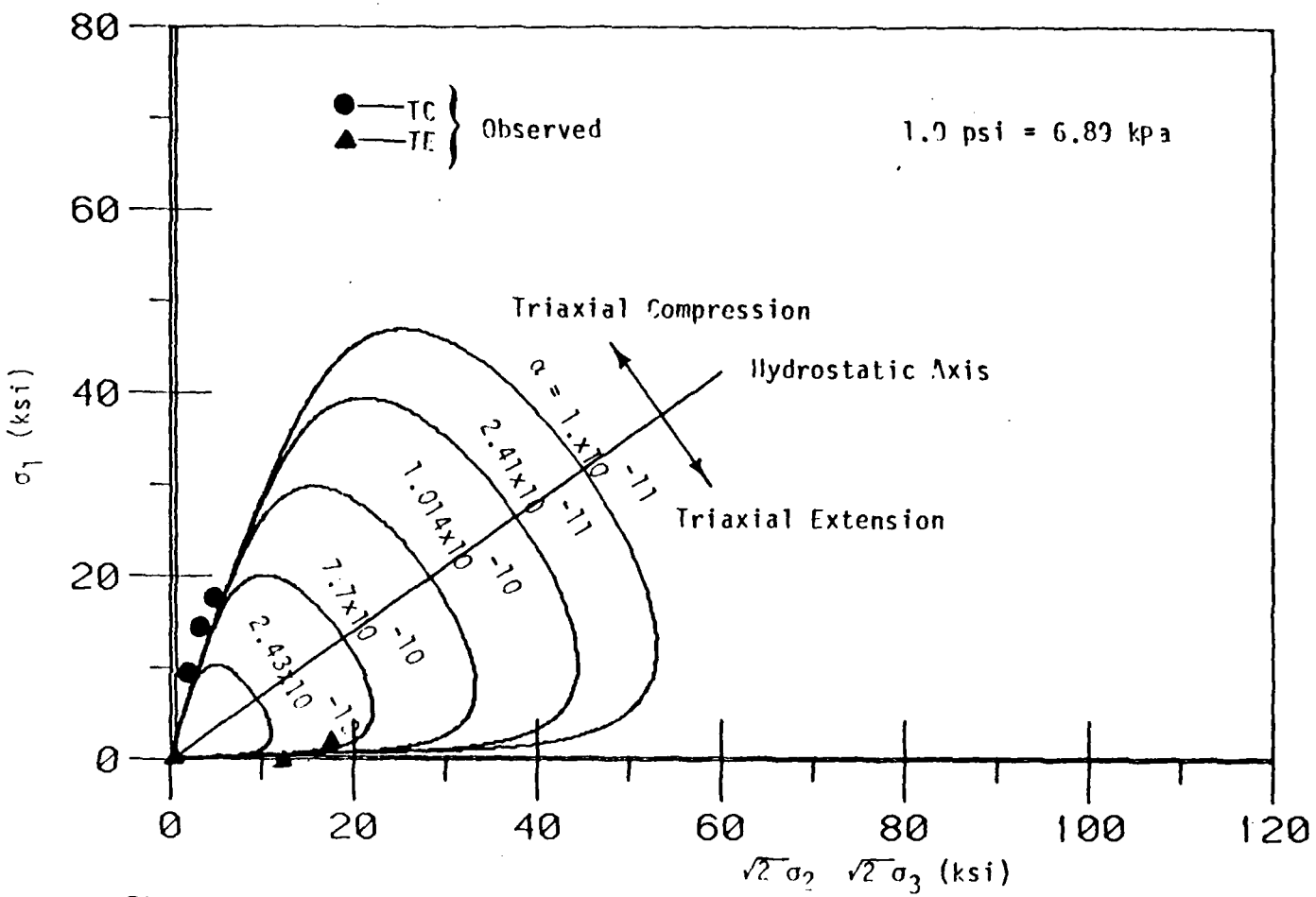

Figure 7.23. Predicted Ultimate and Pre-Ultimate Envelopes in Triaxial Plane for Colorado Plain Concrete.

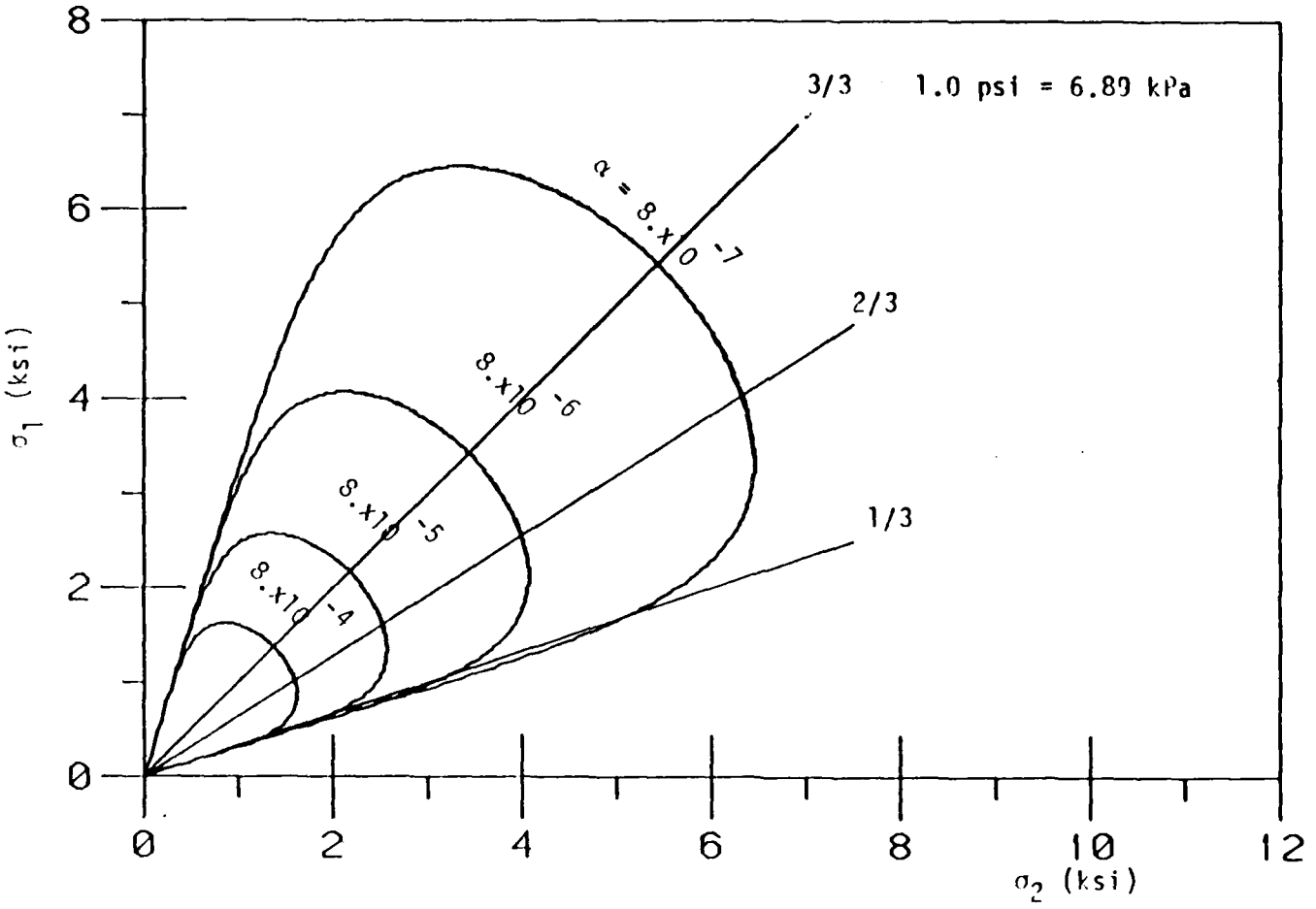

Figure 7.24. Predicted Biaxial Ultimate and Pre-Ultimate Envelopes (σ_3 = 0) Based on Proposed Model for Colorado Plain Concrete.

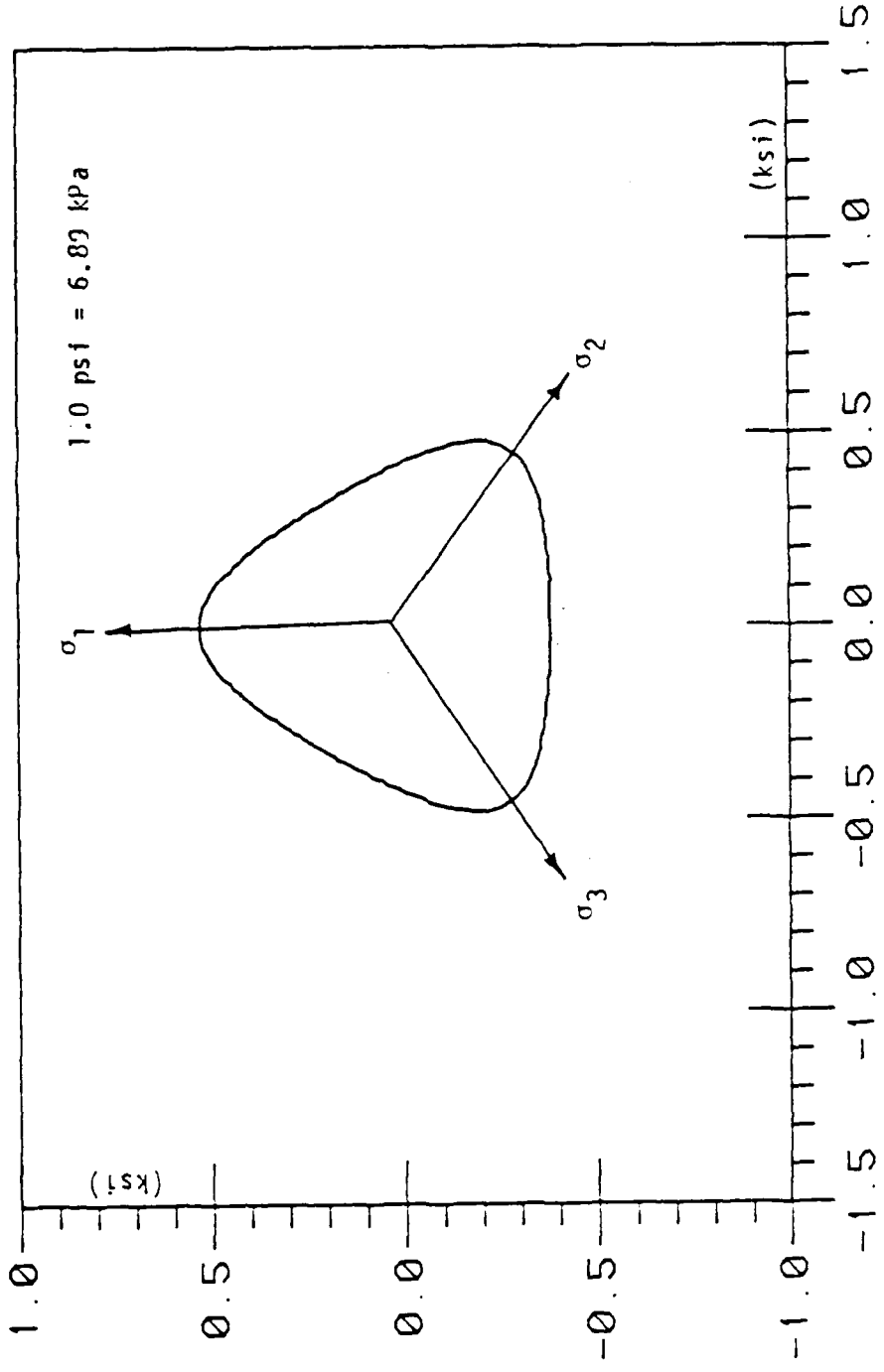

Figure 7.25. Predicted Ultimate Surface in π-Plane for Colorado Plain Concrete.

respectively. These values were:

$$f'_c = 3954 \text{ psi } (27.26 \text{ MPa}) \qquad (7.7)$$

$$f_t = -\ 354 \text{ psi } (-2.44 \text{ MPa}) \qquad \text{Compression Positive)}$$

It is evident from Eqs. (7.6) and (7.7) that the predictions compare well with the experimental strengths.

Based on the predicted ultimate envelope, Fig. 7.25, predicted values of the $\sqrt{J_{2D}}$ on the π-plane for TC ($\theta = -30^o$) SS ($\theta = 0^o$) and TE ($\theta = 30^o$) can be calculated. These values are:

$$(\sqrt{J_{2D}})_{TC} = 0.45 \text{ ksi } (3.1 \text{ MPa})$$

$$(\sqrt{J_{2D}})_{SS} = 0.30 \text{ ksi } (2.07 \text{ MPa}) \qquad (7.8)$$

$$(\sqrt{J_{2D}})_{TE} = 0.25 \text{ ksi } (1.72 \text{ MPa})$$

Ratios of Eqs. (7.8) can be expressed as:

$$R_1 = \frac{(\sqrt{J_{2D}})_{TC}}{(\sqrt{J_{2D}})_{TE}} = 1.80$$

$$R_2 = \frac{(\sqrt{J_{2D}})_{SS}}{(\sqrt{J_{2D}})_{TE}} = \qquad (7.9)$$

$$R_3 = \frac{(\sqrt{J_{2D}})_{TC}}{(\sqrt{J_{2D}})_{SS}} = 1.50$$

One can see that $(\sqrt{J_{2D}})_{TC}$ is almost twice $(\sqrt{J_{2D}})_{TE}$ (Eqs. 7.8) when plotted in π-plane as it is expected for pressure sensitive materials.

7.3.4 Stress-Strain Behavior for Test Used for Finding Material Constants

Figure 7.26 shows the comparison between the predicted and observed stress-strain responses for a hydrostatic compression (HC) test. It is seen that the comparison is good.

Figures 7.27, 7.28 and 7.29 show the comparison of the pre- for Triaxial Compression (TC), Simple Shear (SS) and Triaxial Extension (TE) tests, respectively. For the (TC), (SS) and (TE), the initial confining pressure is σ ksi (41.37 "Pa). It is evident from Figs. 7.27, 7.28 and 7.29 that the predictions from the proposed model compare well with the experimental results.

7.3.5 Volumetric Responses Behavior

Figures 7.30, 7.31 and 7.32 show plots of $\varepsilon_V = \varepsilon_1$ for one TC (σ_o = 6 ksi) test, one SS (σ_o = 6 ksi) test and one TE (σ_o = 6 ksi) test. It is evident from these plots that the correlation between the proposed model predictions and observations is satisfactory.

7.3.6 Circular Stress Path Test Not Used for Finding Material Constants

Figure 7.33 shows the comparison of the predictions and the observations for a circular stress path test which is not

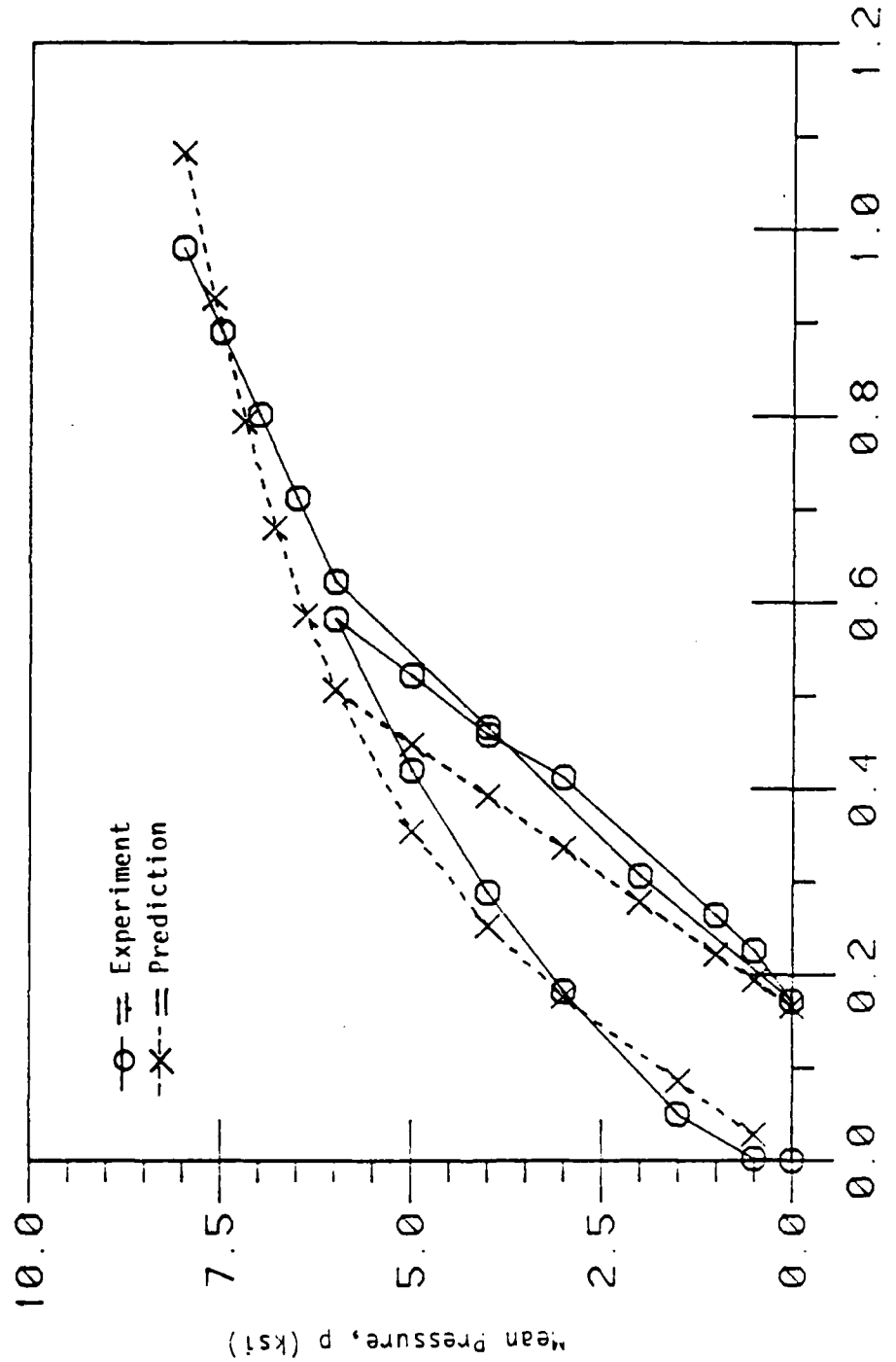

Figure 7.26. Comparison of Stress-Strain Responses of Hydrostatic Compression (HC) Test for Colorado Plain Concrete (σ_o = 8.0 ksi), (1.0 psi = 6.89 kPa).

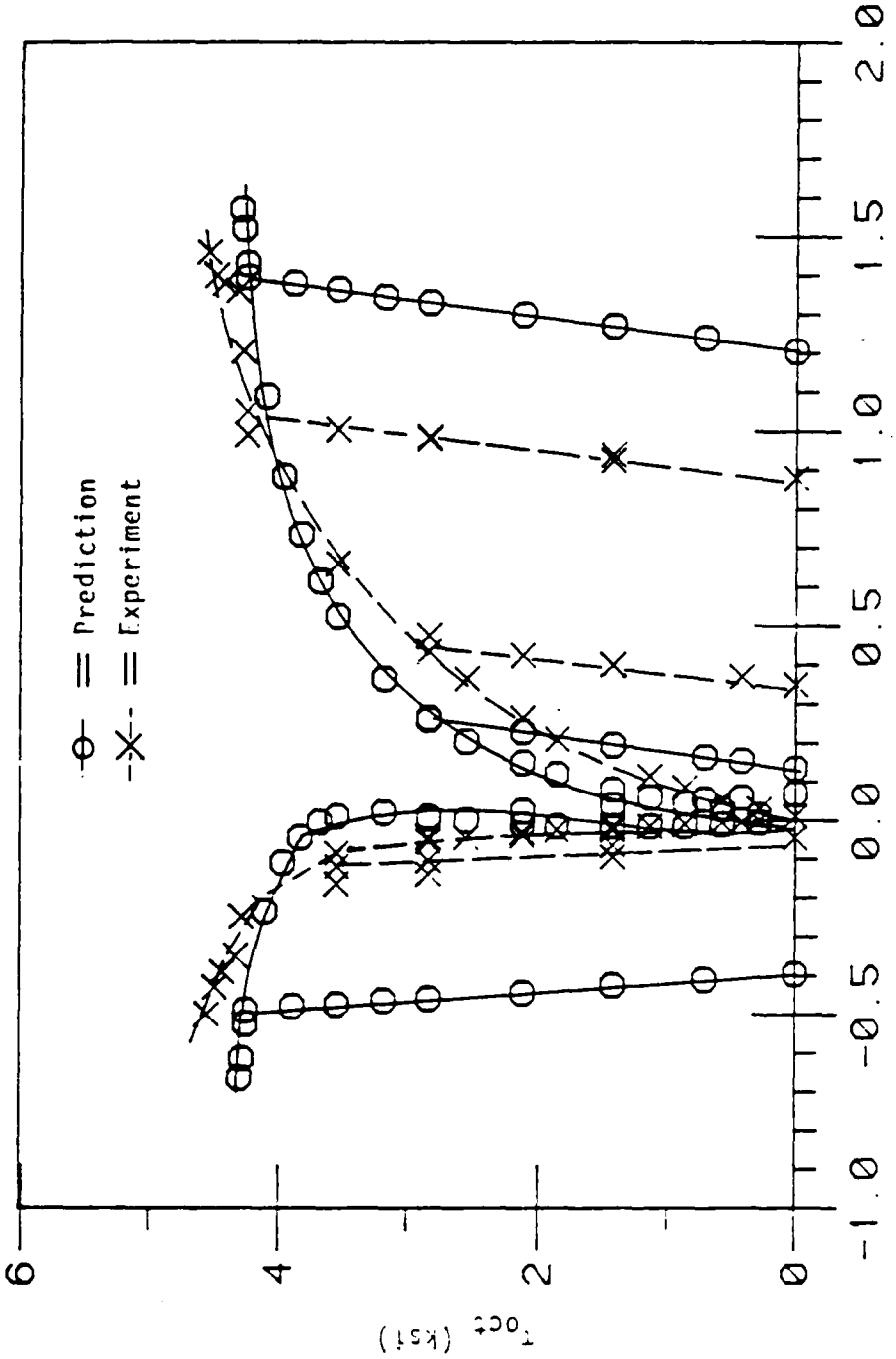

Figure 7.27. Comparison of Stress-Strain Responses of Triaxial Compression (TC) Test for Colorado Plain Concrete (σ_o = 6.0 ksi), (1.0 psi = 6.89 kPa).

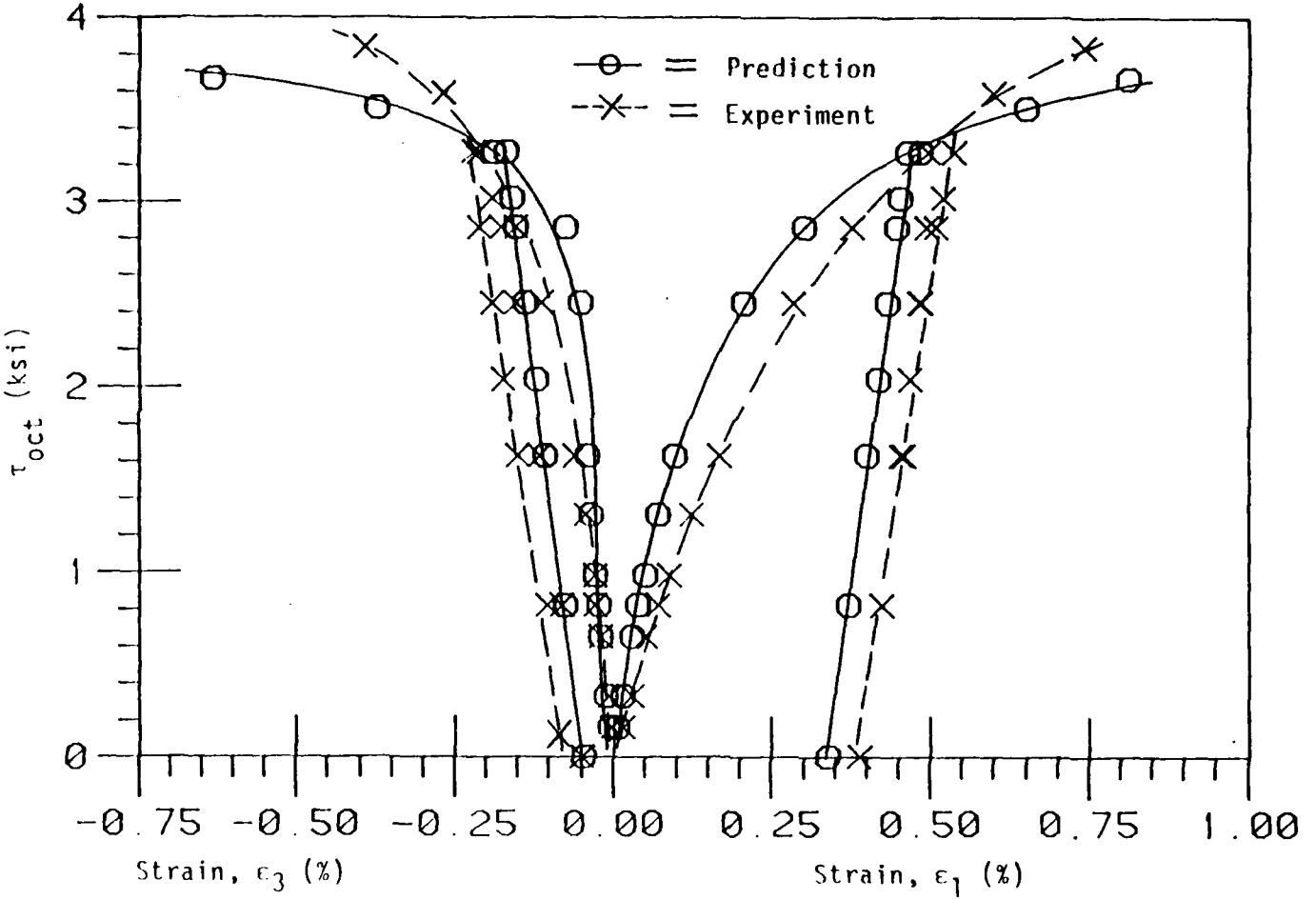

Figure 7.28. Comparison of Stress-Strain Responses of Simple Shear (SS) for Colorado Plain Concrete (σ_o = 6.0 ksi), (1.0 psi = 6.89 kPa).

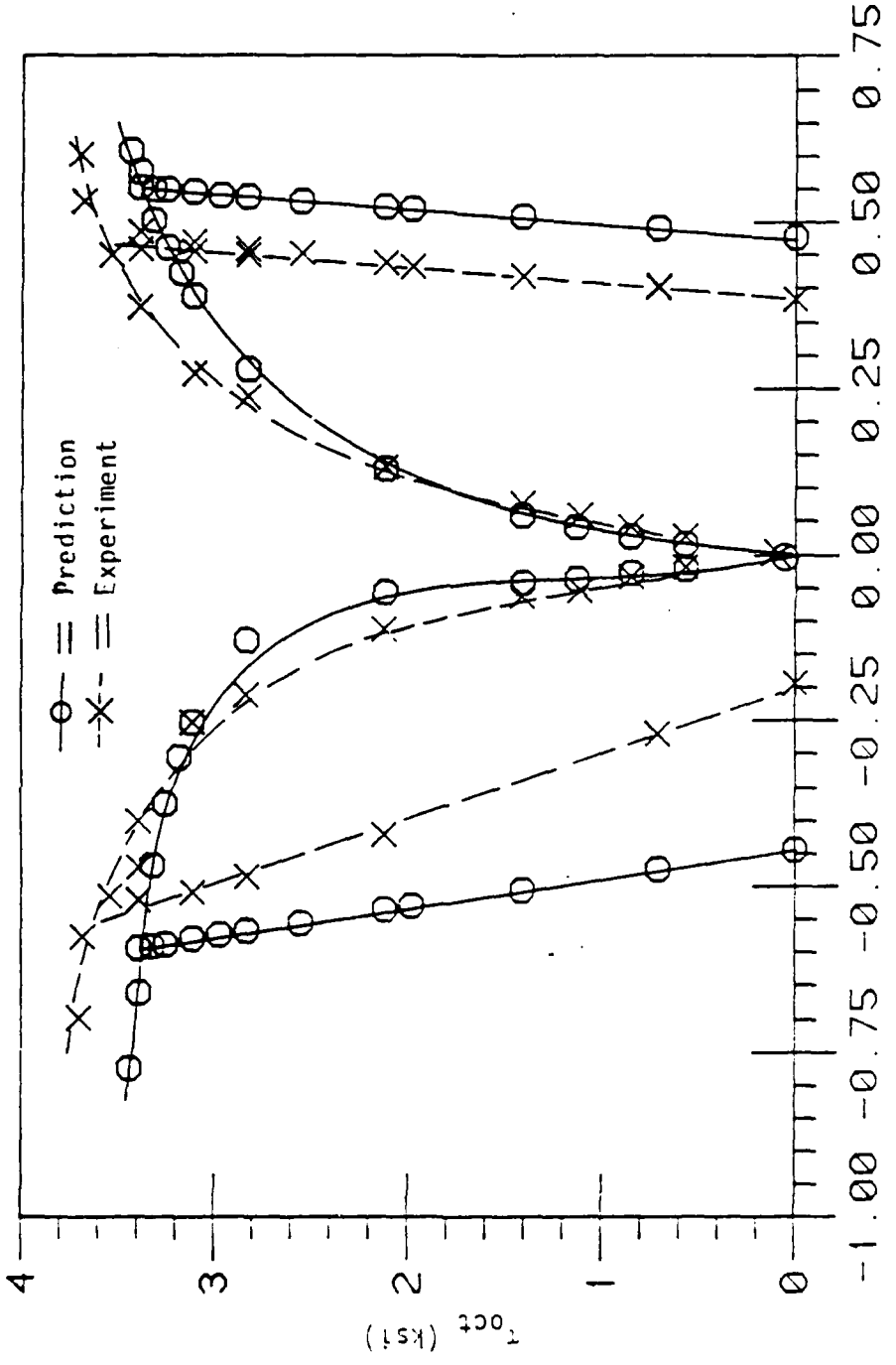

Figure 7.20. Comparison of Stress-Strain Responses of Triaxial Extension (TE) Test for Colorado Plain Concrete (σ_o = 6.0 ksi), (1.0 psi = 6.89 kPa).

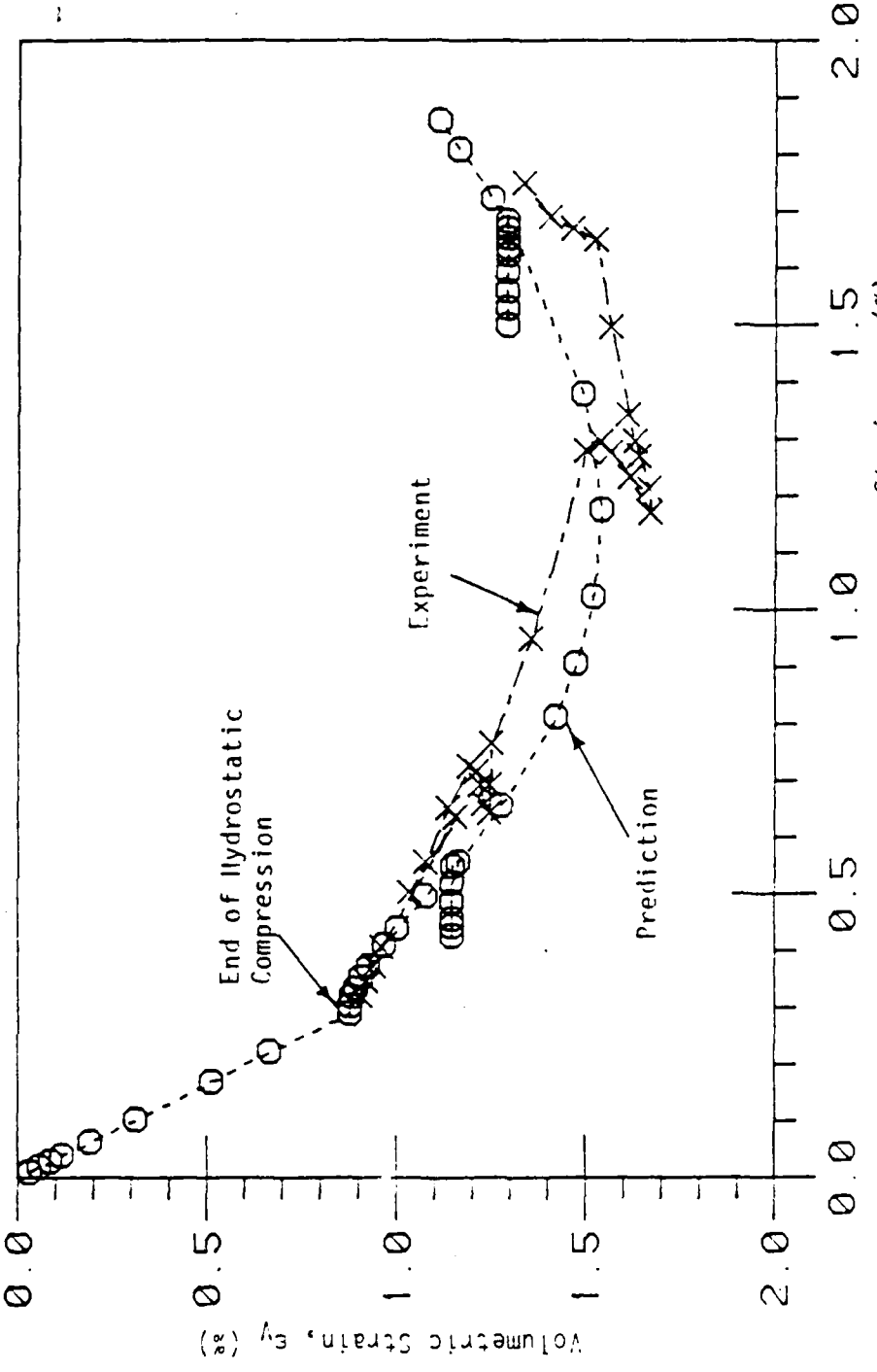

Figure 7.30. Comparison of Volumetric Response of Triaxial Compression (TC) Test for Colorado Plain Concrete (σ_o = 6.0 ksi), (1.0 psi = 6.89 kPa).

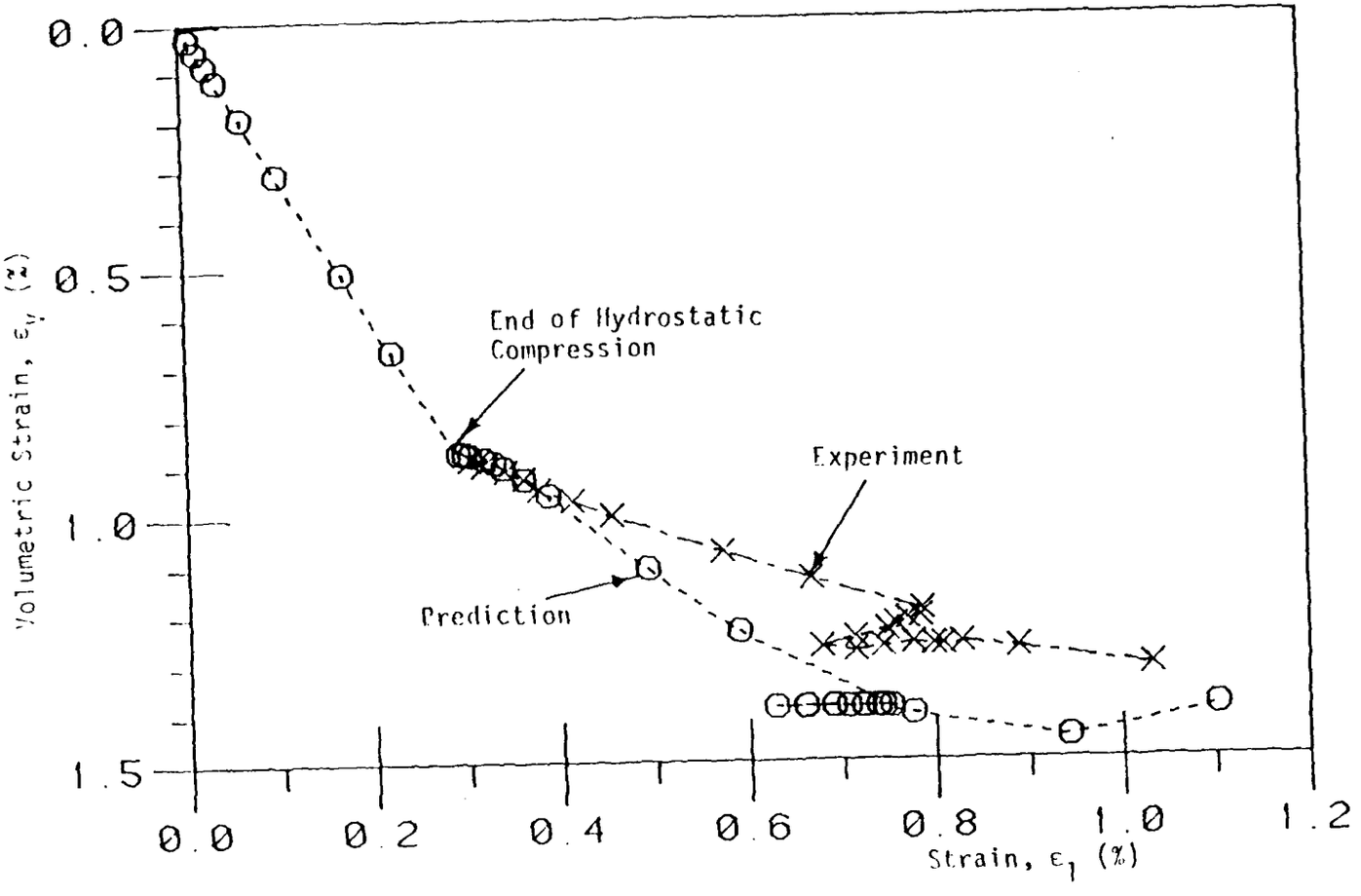

Figure 7.31. Comparison of Volumetric Response of Simple Shear (SS) Test for Colorado Plain Concrete (σ_0 = 6.0 ksi), (1.0 psi = 6.89 kPa).

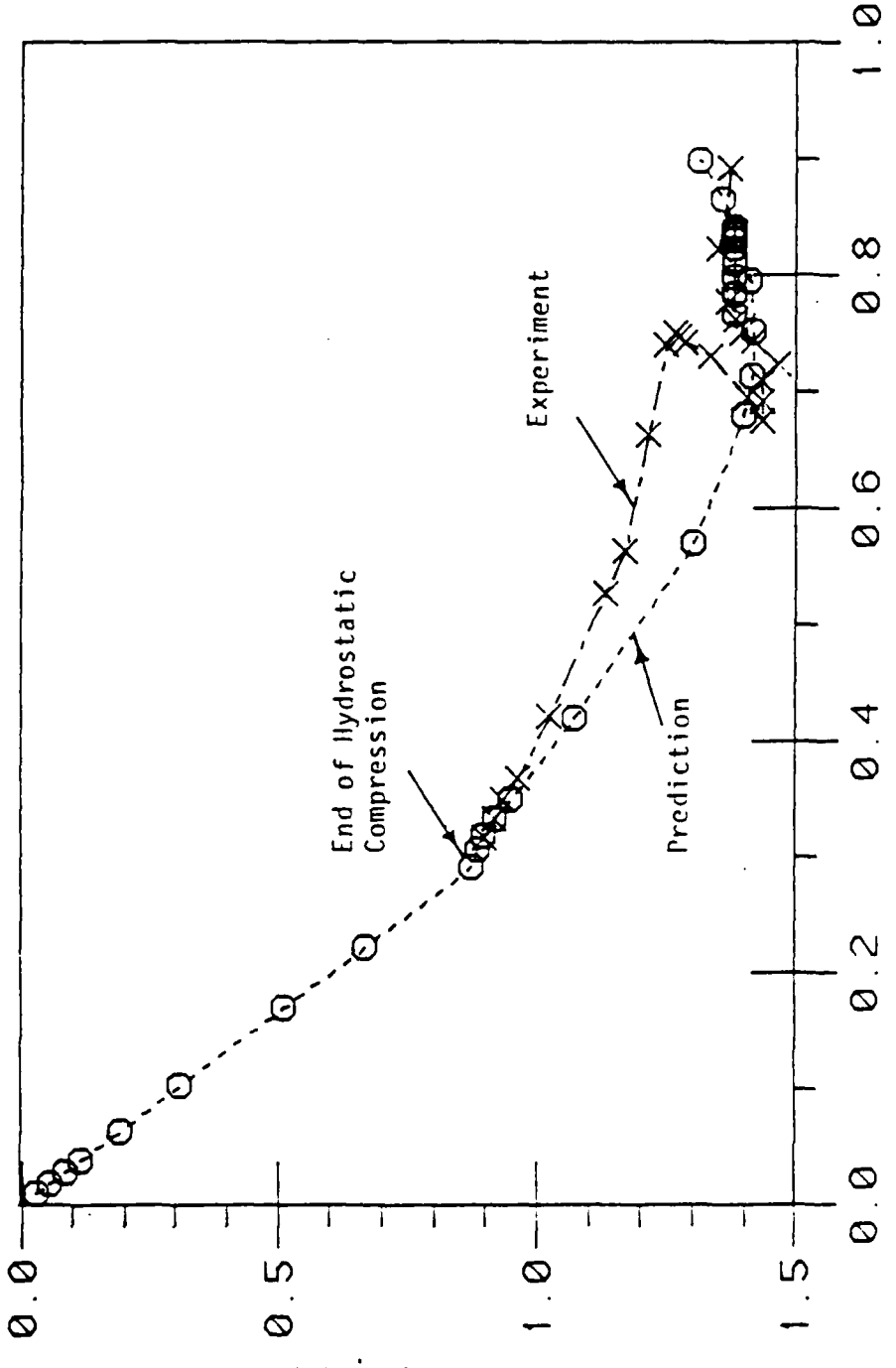

Figure 7.32. Comparison of Volumetric Response of Triaxial Extension (TE) Test for Colorado Plain Concrete (σ_o = 6.0 ksi), (1.0 psi = 6.89 kpa).

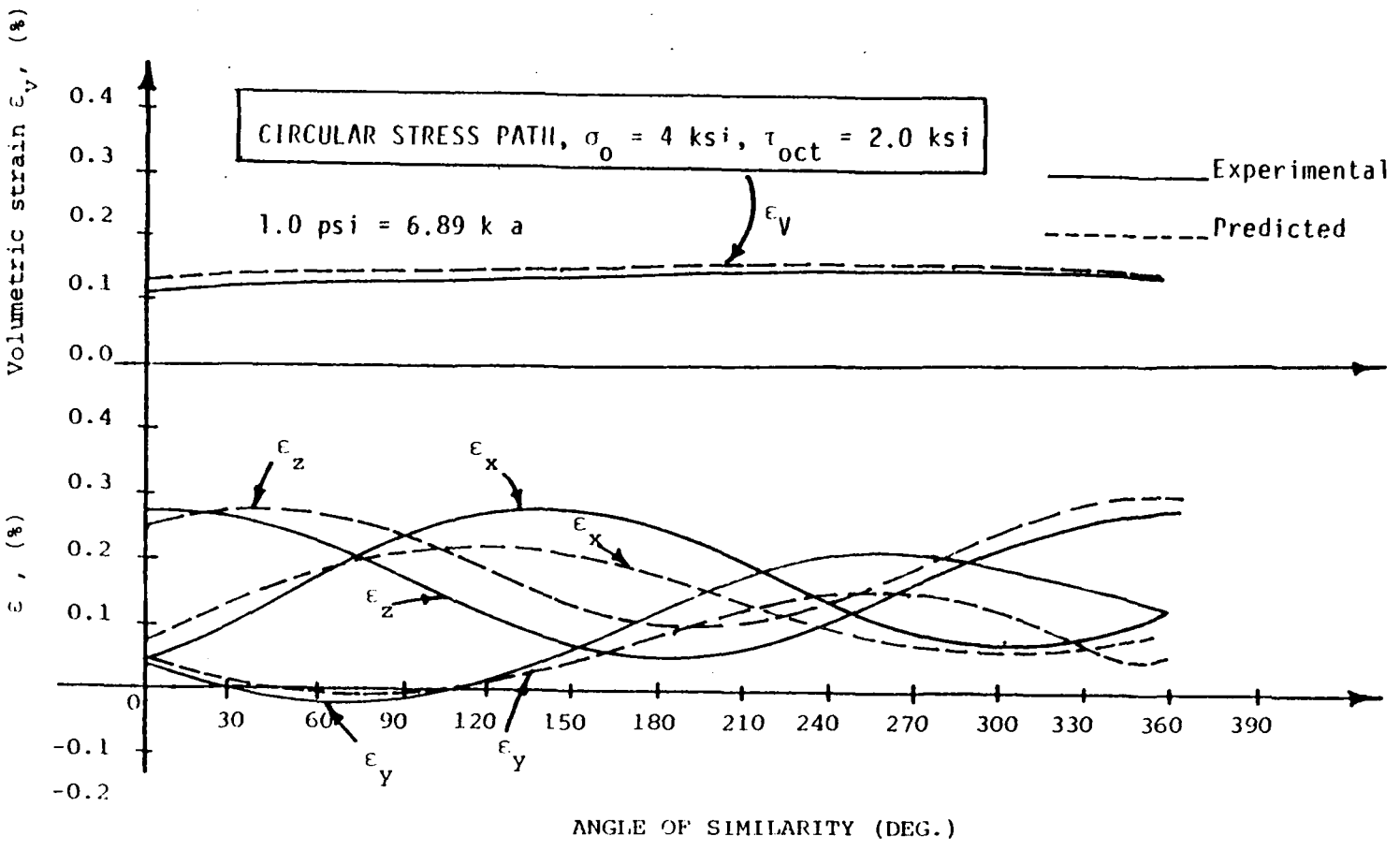

Figure 7.33. Comparison of Principal Strain and Volumetric Strain-Angle of Similarity Responses of Circular Path (CSP) Test for Colorado Plain Concrete.

used to determine the material constants. It is seen from Fig. 7.33 that a good agreement is achieved between the predictions and the observations.

The material constants for SFRC-UC (steel fiber reinforced concrete--University of Colorado) are given in TABLE 6.4. The description of the SFRC-UC is presented in Chapter 6. Ultim te envelopes, strengths and a number of stress-strain response curves are predicted and compared with the experimental results.

7.4.1 $\sqrt{J_{2D}}$ - J_1 Plane

Figures 7.34, 7.35 and 7.36 show the comparison of the predictions and observations of ultimate envelopes, in $\sqrt{J_{2D}}$ - J_1 plane, for (TC), (SS) and (TE) tests, respectively. It is evident from these figures that the model predictions are in close agreement with observations.

7.4.2 Octahedral, Triaxial, Biaxial and π-Planes

Figures 7.37 and 7.38 show the comparison of the predictions and observations of ultimate envelopes for octahedral and triaxial planes, respectively. It is evident from these plots that predictions compare well with the experimental data.

Figure 7.39 shows the biaxial ultimate envelope predicted using proposed model. It is for reference only since no experimental biaxial strength data was obtained.

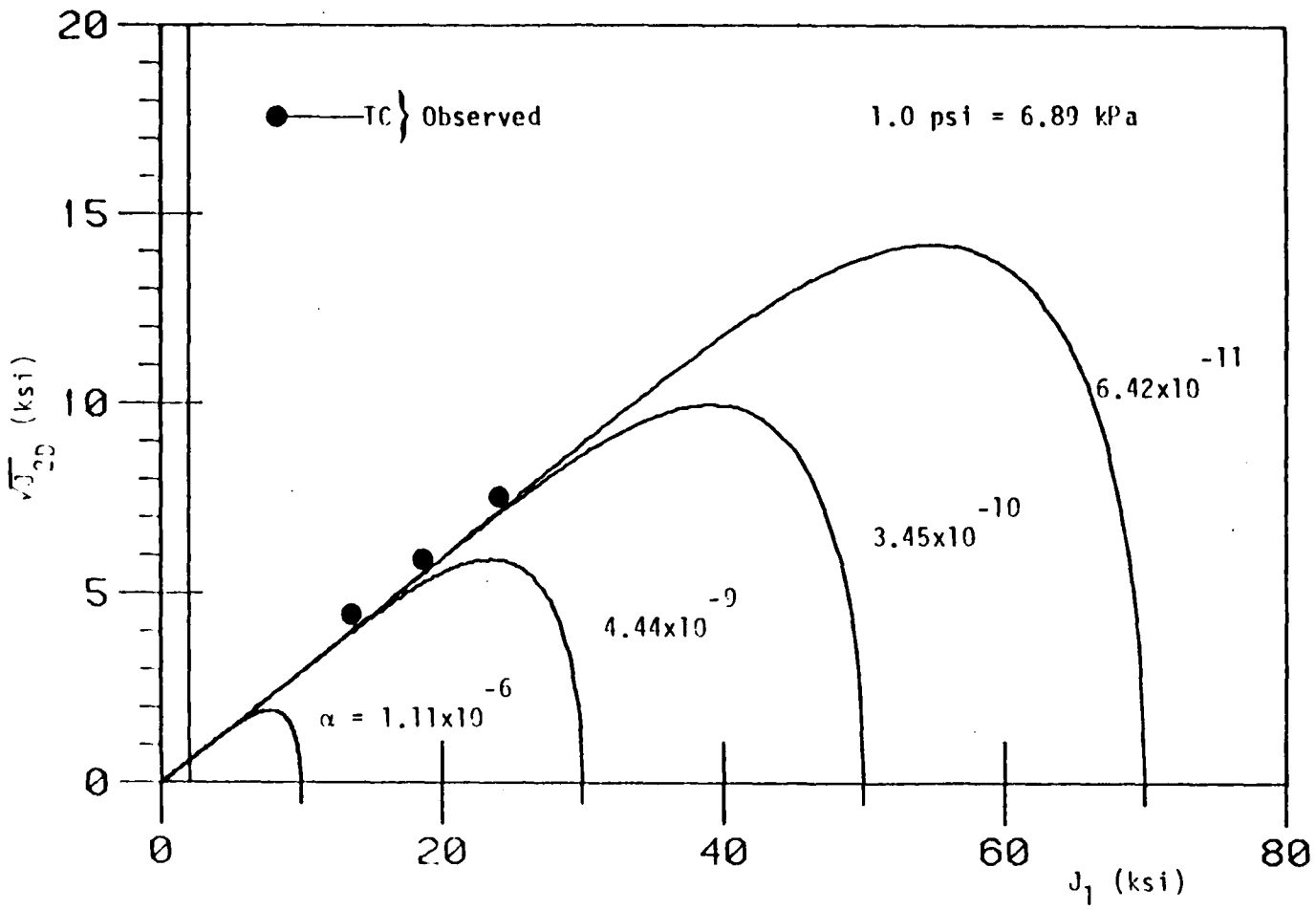

Figure 7.34. Predicted Ultimate and Pre-Ultimate Envelopes in $\sqrt{J_{2D}}$ - J_1 Plane for Triaxial Compression (TC) Test, ($\theta = -30^0$), for SFRC-UC.

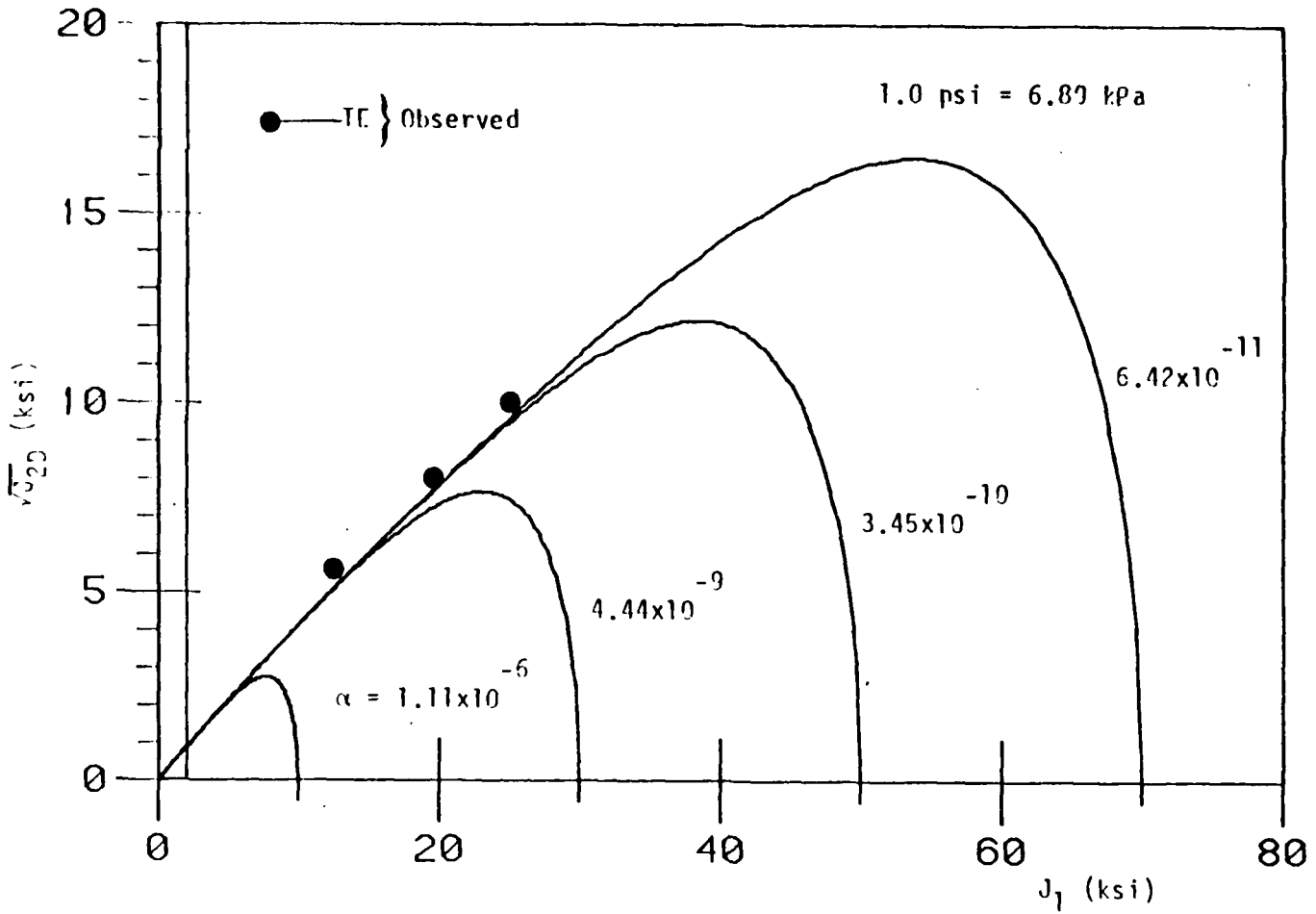

Figure 7.35. Predicted Ultimate and Pre-Ultimate Envelopes in $\sqrt{J_{2D}}$ - J_1 Plane for Triaxial Extension (TE) Test, ($\theta = 30^0$), for SFRC-UC.

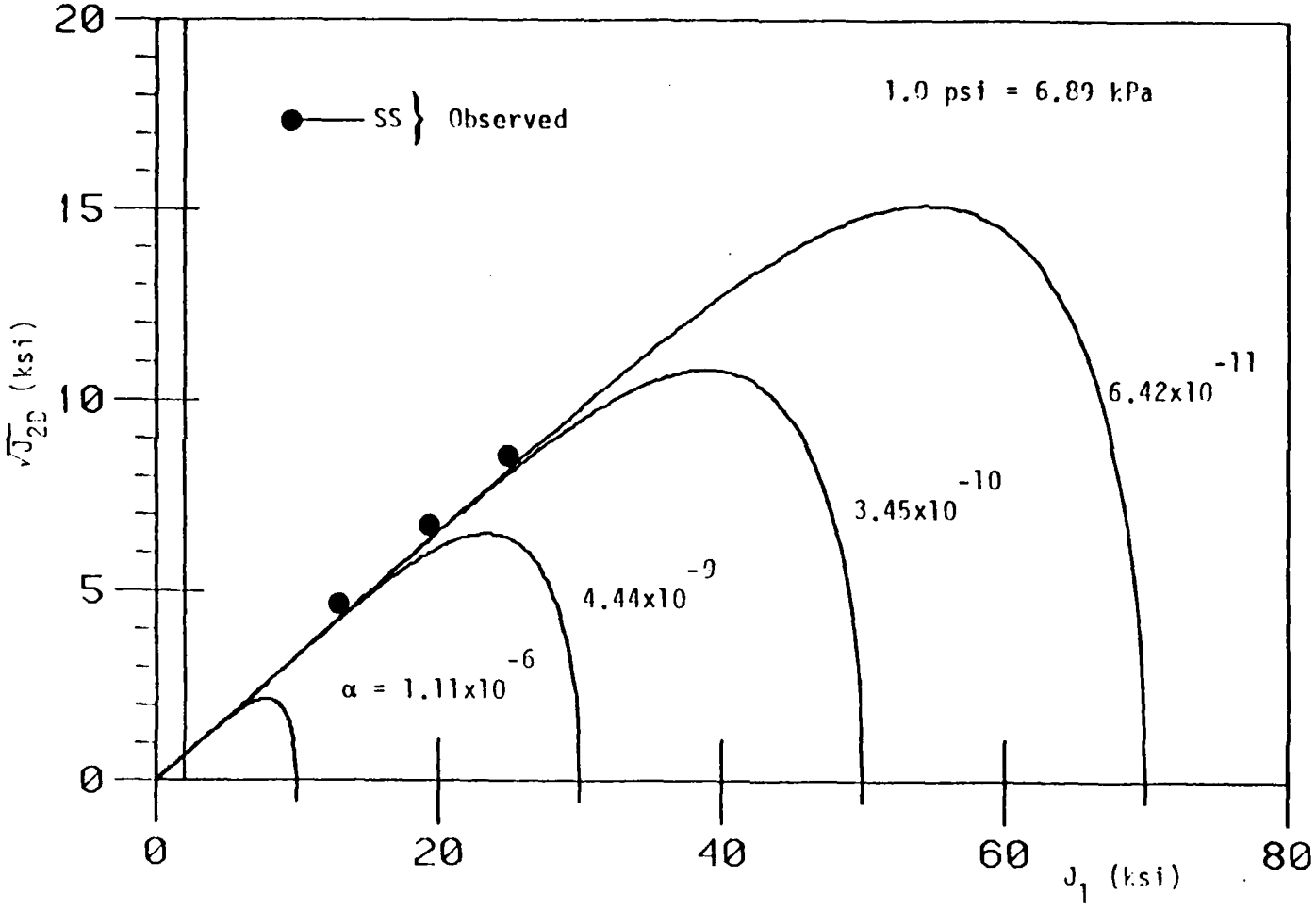

Figure 7.36. Predicted Ultimate and Pre-Ultimate Envelopes in $\sqrt{J_{2D}} - J_1$ Plane for Simple Shear (SS) Test, ($\theta = 0^0$), for SFRC-UC.

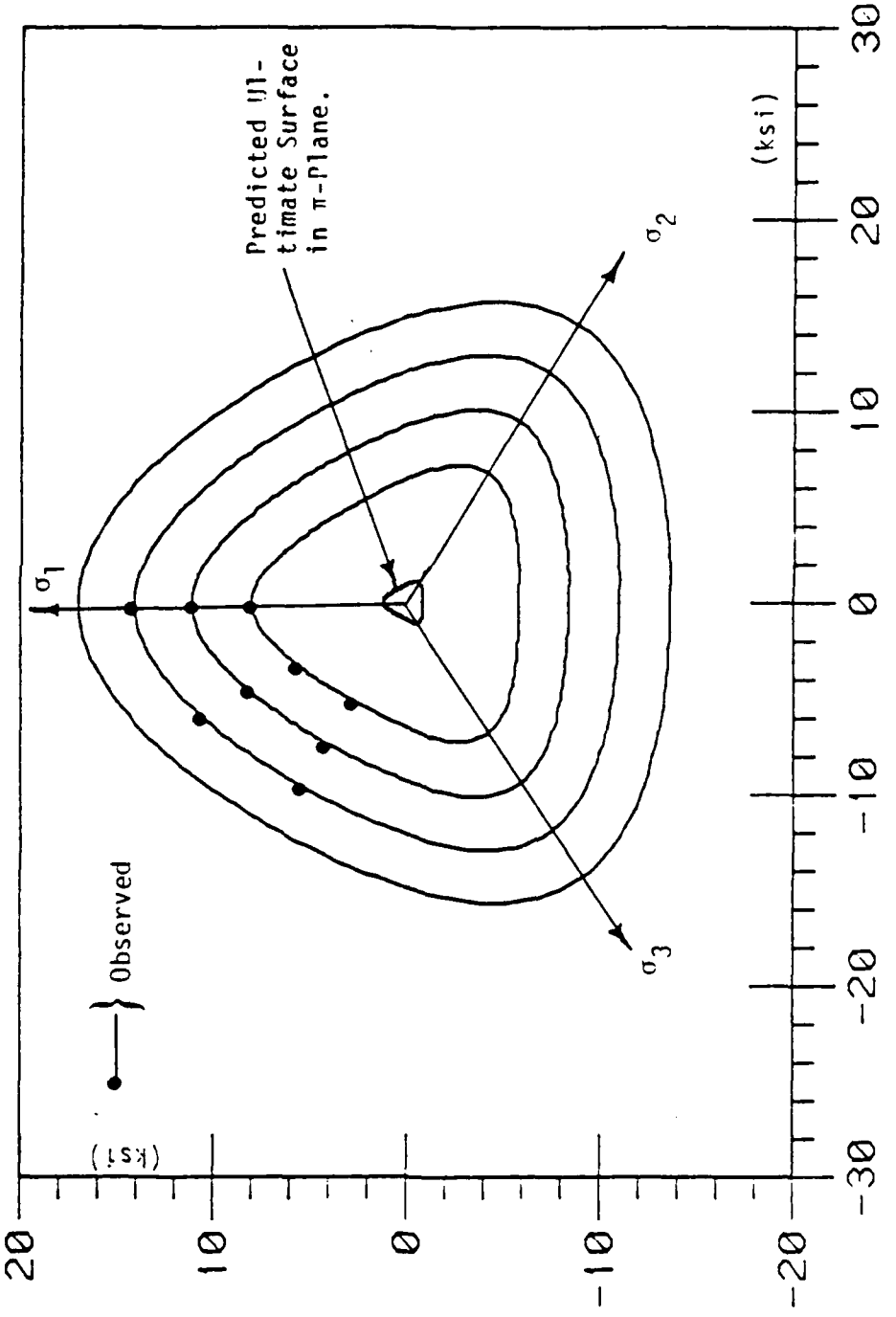

Figure 7.37. Variation of Cross-Sectional Shapes in Octahedral Planes (J_1 = 2,14,20,26,32 ksi), 1.0 psi = 6.89 kPa), for Predicted Ultimate Surface for SFRC-UC.

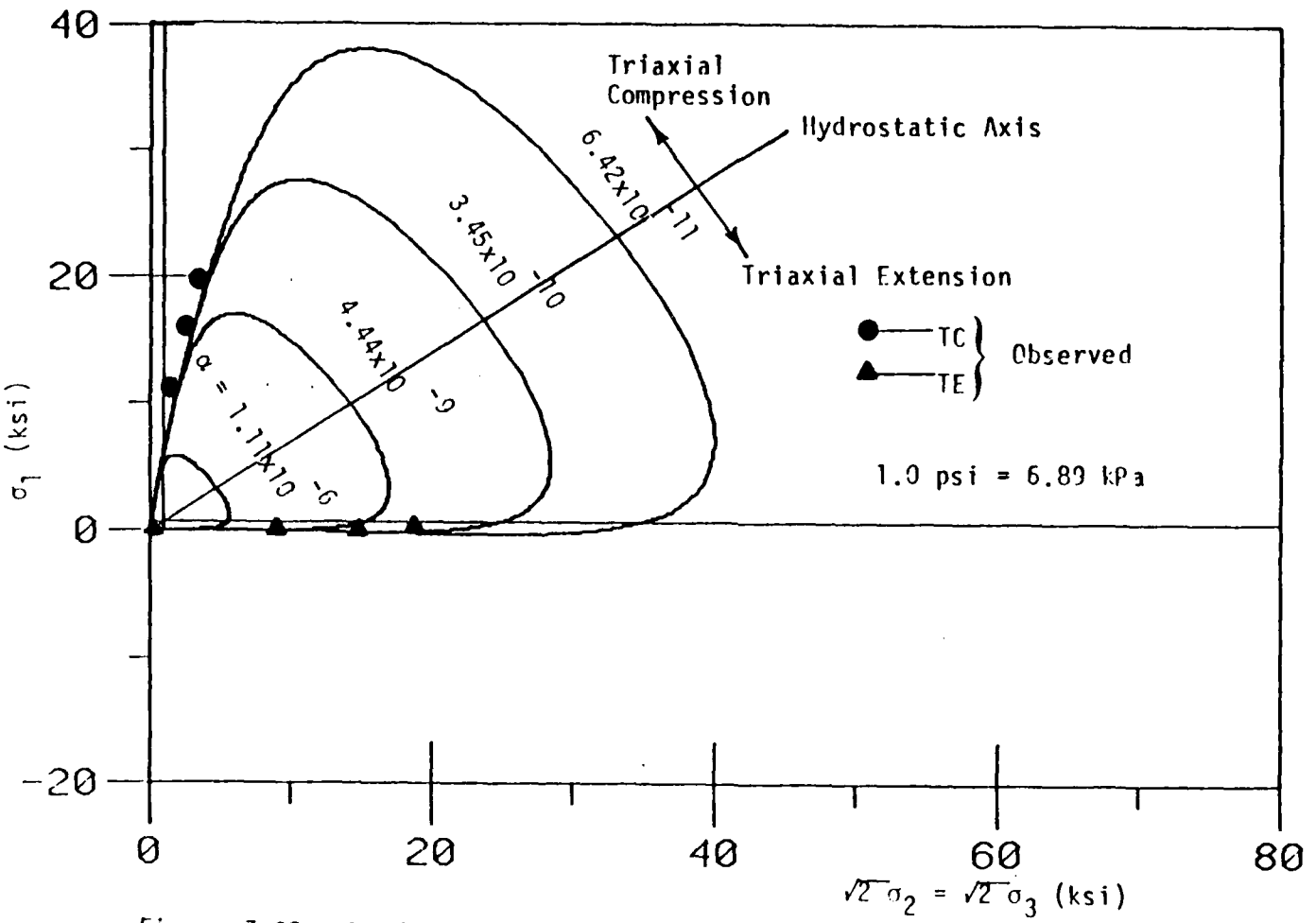

Figure 7.38. Predicted Ultimate and Pre-Ultimate Envelopes in Triaxial Plane for SFRC-UC.

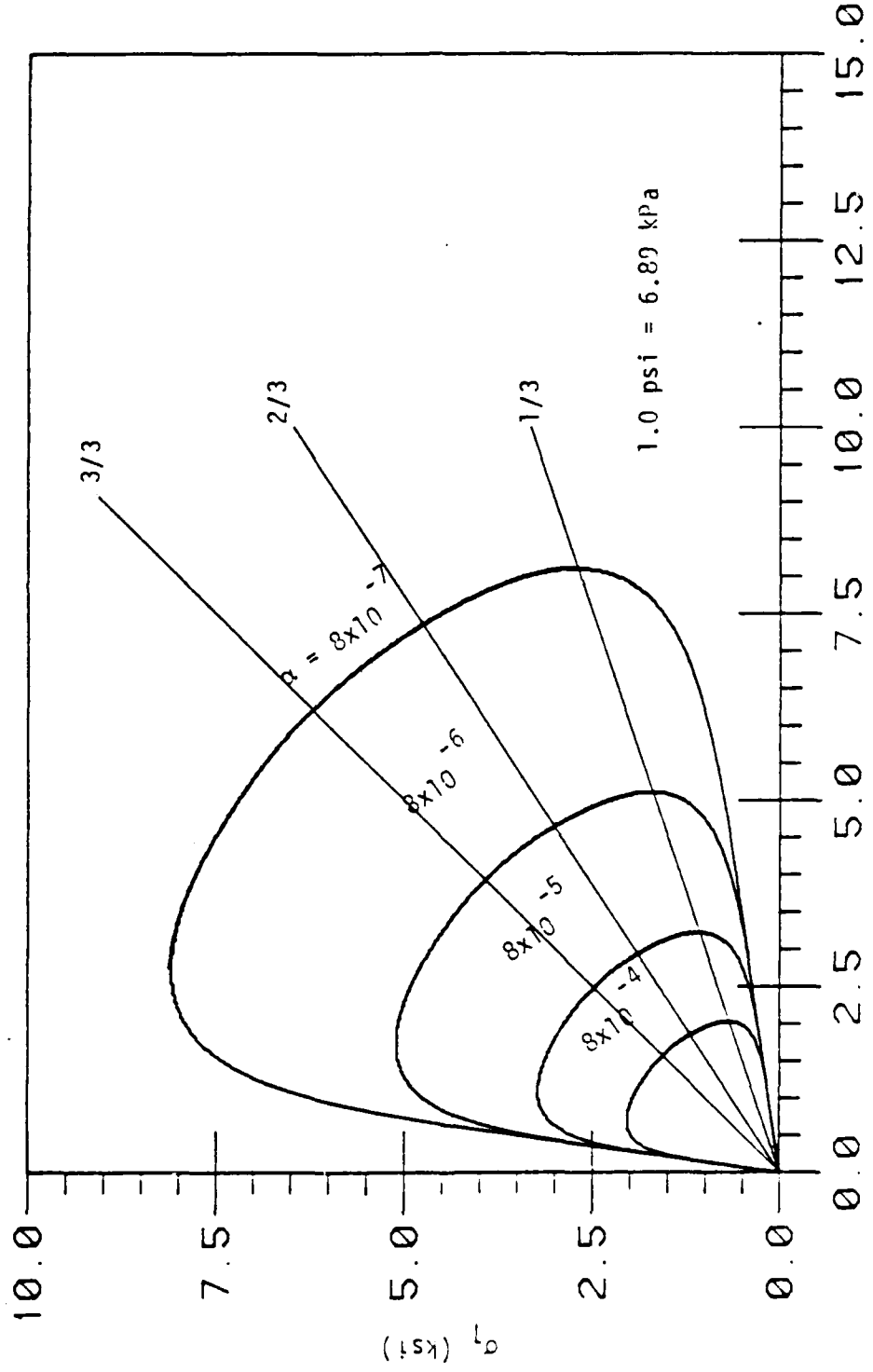

Figure 7.39. Predicted Biaxial Ultimate and Pre-Ultimate Envelopes ($\sigma_3 = 0$) Based on Proposed Model for SFRC-HC.

Predicted ultimate envelope on the π-plane is shown in Fig. 7.37.

7.4.3 Strength Behavior

Based on the predicted strength envelope, Fig. 7.38, predicted values of the uniaxial compressive strength, f_{cu}, equibiaxial compressive strength, f_{cb}, and uniaxial tensile strength, f_t, can be calculated. These predicted strengths are:

f_{cu} = 7330 psi (50.56 Mpa)

f_{cu} = 24395.2 psi (168.20 (7.10)

f_t = - 656 psi (-4.52 MPa) (Compression Positive)

The values of f_{cu} and f_t compared to unconfined compression strength, f'_c, and tensile strength, f_t, based on tests with cylindrical specimens of 3x6 in. (7.62x15.24 cm) and Eq. (6.47), respectively. These values are:

f'_c = 9200 psi (63.43 MPa) (7.11)

f_t = -556 psi (-4.52 MPa) (Compression Positive)

The differences between these predicted and observed strengths may be attributed to the effect of specimen type and boundary conditions.

Based on the predicted ultimate envelope, Fig. 7.39, predicted values of the $\sqrt{J_{2D}}$ on the π-plane for TC (θ = - 30°) SS (θ = 0°) and TE (θ = 30°) can be calculated. These values are:

$$(\sqrt{J_{2D}})_{TC} = 0.96 \text{ ksi } (6.62 \text{ MPa})$$
$$(\sqrt{J_{2D}})_{SS} = 0.69 \text{ ksi } (4.76 \text{ MPa}) \quad (7.12)$$
$$(\sqrt{J_{2D}})_{TE} = 0.58 \text{ ksi } (4.0 \text{ MPa})$$

Ratios of Eqs. (7.12), on the π-plane, can be expressed as

$$R_1 = \frac{(\sqrt{J_{2D}})_{TC}}{(\sqrt{J_{2D}})_{TE}} = 1.66$$

$$R_2 = \frac{(\sqrt{J_{2D}})_{SS}}{(\sqrt{J_{2D}})_{TE}} = 1.19 \quad (7.13)$$

$$R_3 = \frac{(\sqrt{J_{21}})_{TC}}{(\sqrt{J_{2D}})_{SS}} = 1.39$$

From Eqs. (7.12) and (7.13), one can see that $(\sqrt{J_{2D}})_{TC}$ is almost twice $(\sqrt{J_{2D}})_{TE}$ (Eqs. 7.12) when plotted in π-plane as it is expected for SFRC-UC.

7.4.4 Stress-Strain Behavior for Test Used for Finding Material Constants

Figure 7.40 shows the comparison between the predicted and observed stress-strain responses for a hydrostatic compression (HC) test. It is seen from Fig. 7.40 that the prediction from the proposed model compare fairly well with the experimental result.

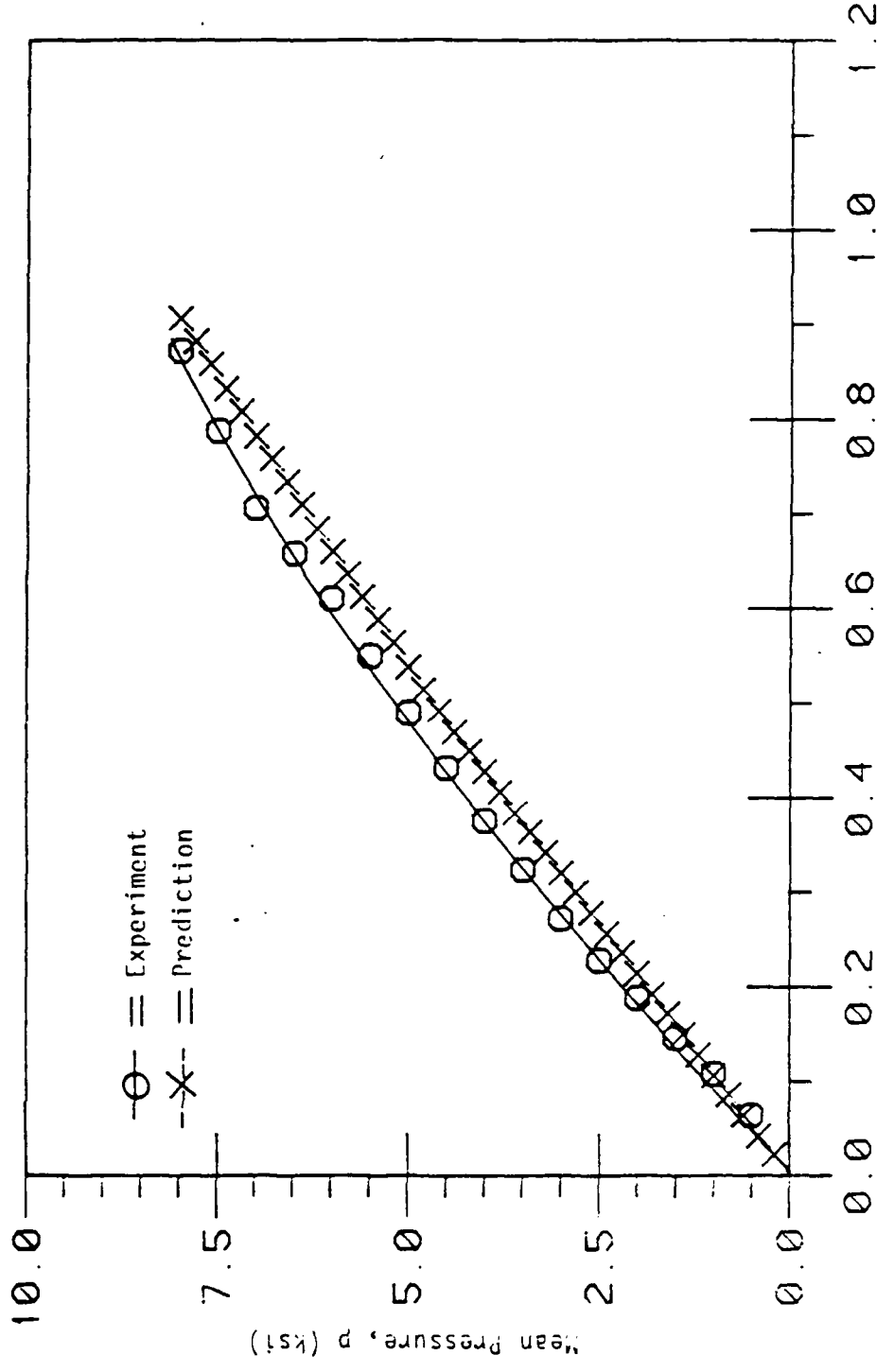

Figure 7.40. Comparison of Stress-Strain Responses of Hydrostatic Compression (HC) Test for SFRC-HC (σ_o = 8.0 ksi), (1.0 psi = 6.89 kPa).

Figures 7.41 through 7.46 show the comparison of predictions and observations for the stress-strain responses for two (TC) tests, two (SS) tests, and two (TE) tests. For the (TC), (SS) and (TE) tests, the initial confining pressures are 4 and 6 ksi (27.58 and 41.37 MPa). It is evident from Figs. 7.41 through 7.46 that the predictions from the model compare well with the experimental results.

7.4.5 Volumetric Responses Behavior

Figures 7.47 through 7.52 show plots of $\varepsilon_v - \varepsilon_1$ for two TC (σ_o = 4 and 6 ksi) tests, two SS (σ_o = 4 and 6 ksi) tests and two TE (σ_o = 4 and 6 ksi) tests. It is evident from Figs. 7.47 through 7.52 that the proposed model predictions are in close agreement with the observations.

The material constants for soapstone are given in TABLE 6.5. The description of the soapstone is presented in Chapter 2. Ultimate envelopes, strengths and a number of stress-strain response curves are predicted and compared with the experimental results. These results are presented below.

7.5.1 $\sqrt{J_{2D}} - J_1$ Plane

Figures 7.53, 7.54 and 7.55 show the comparison of the predictions and observations of ultimate envelopes, in $\sqrt{J_{2D}} - J_1$ plane, for (TC), (SS) and (TE) tests, respectively. It is

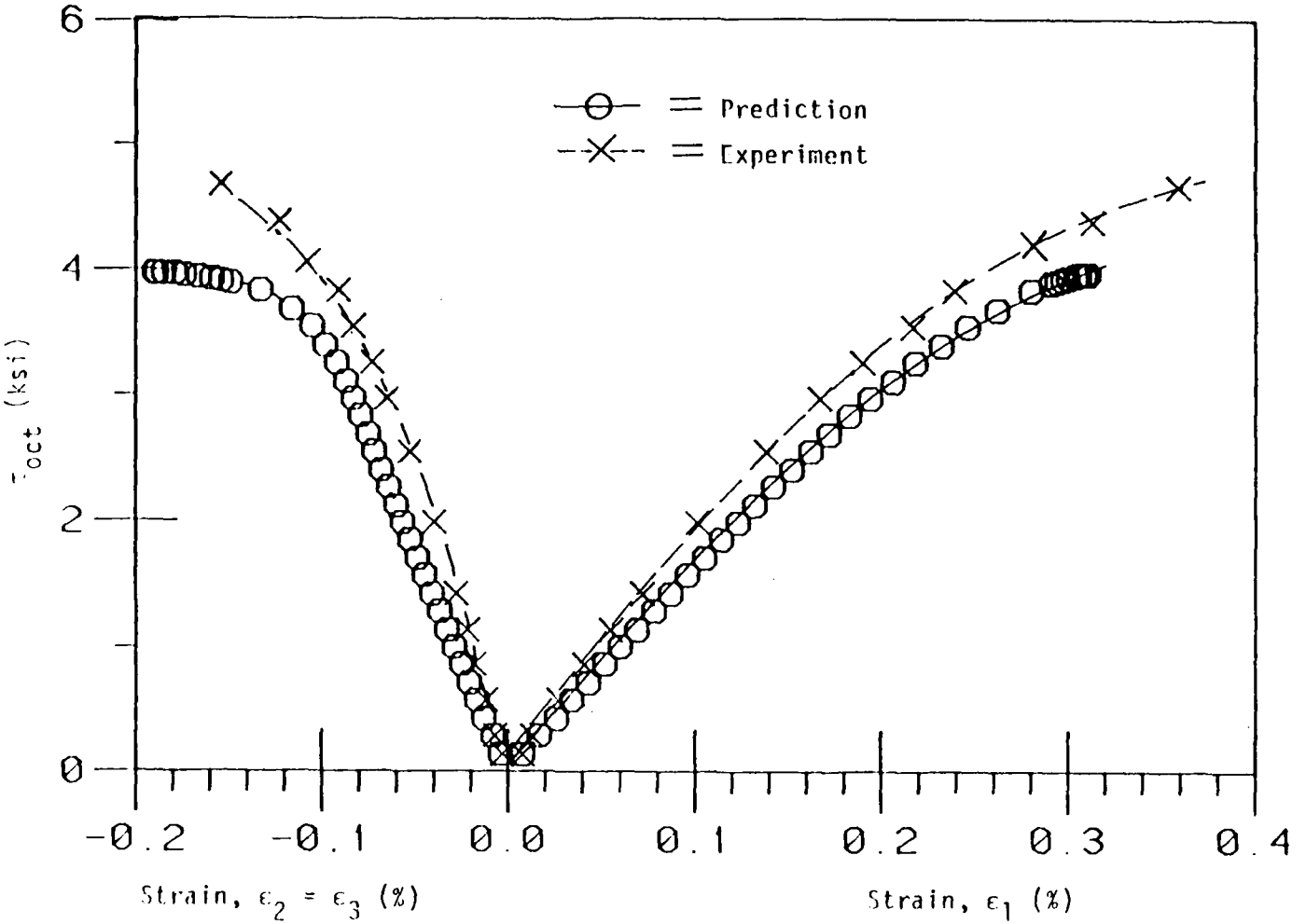

Figure 7.41. Comparison of Stress-Strain Responses of Triaxial Compression (TC) Test for SFRC-UC (σ_o = 4.0 ksi), (1.0 psi = 6.89 kPa).

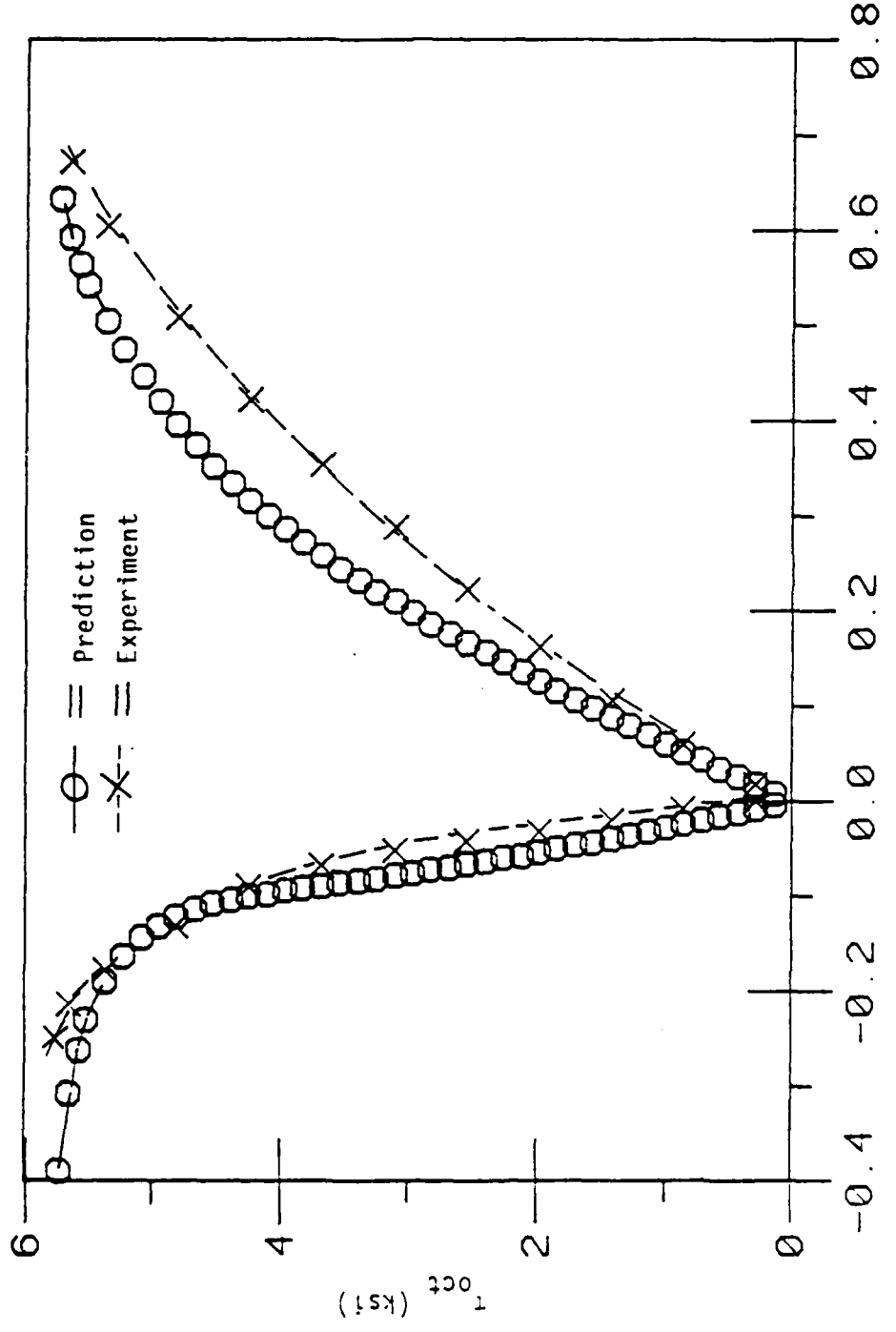

Figure 7.42. Comparison of Stress-Strain Response of Triaxial Compression (TC) Test for SFRC-UC (σ_o = 6.0 ksi), (1.0 psi = 6.89 kPa).

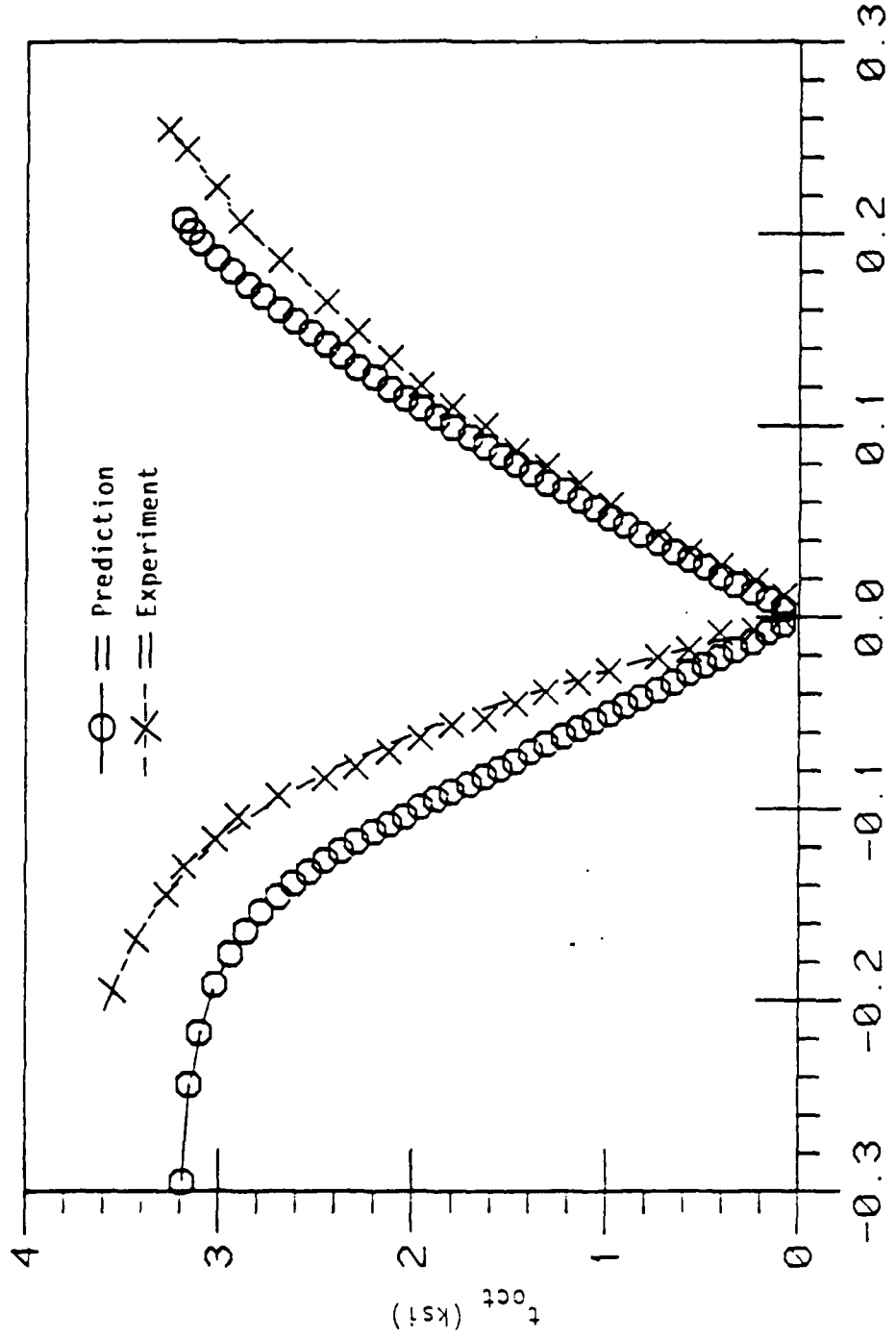

Figure 7.43. Comparison of Stress-Strain Responses of Simple Shear (SS) Test for SFRC-UC (σ_o = 4.0 ksi), (1.0 psi = 6.89 kPa).

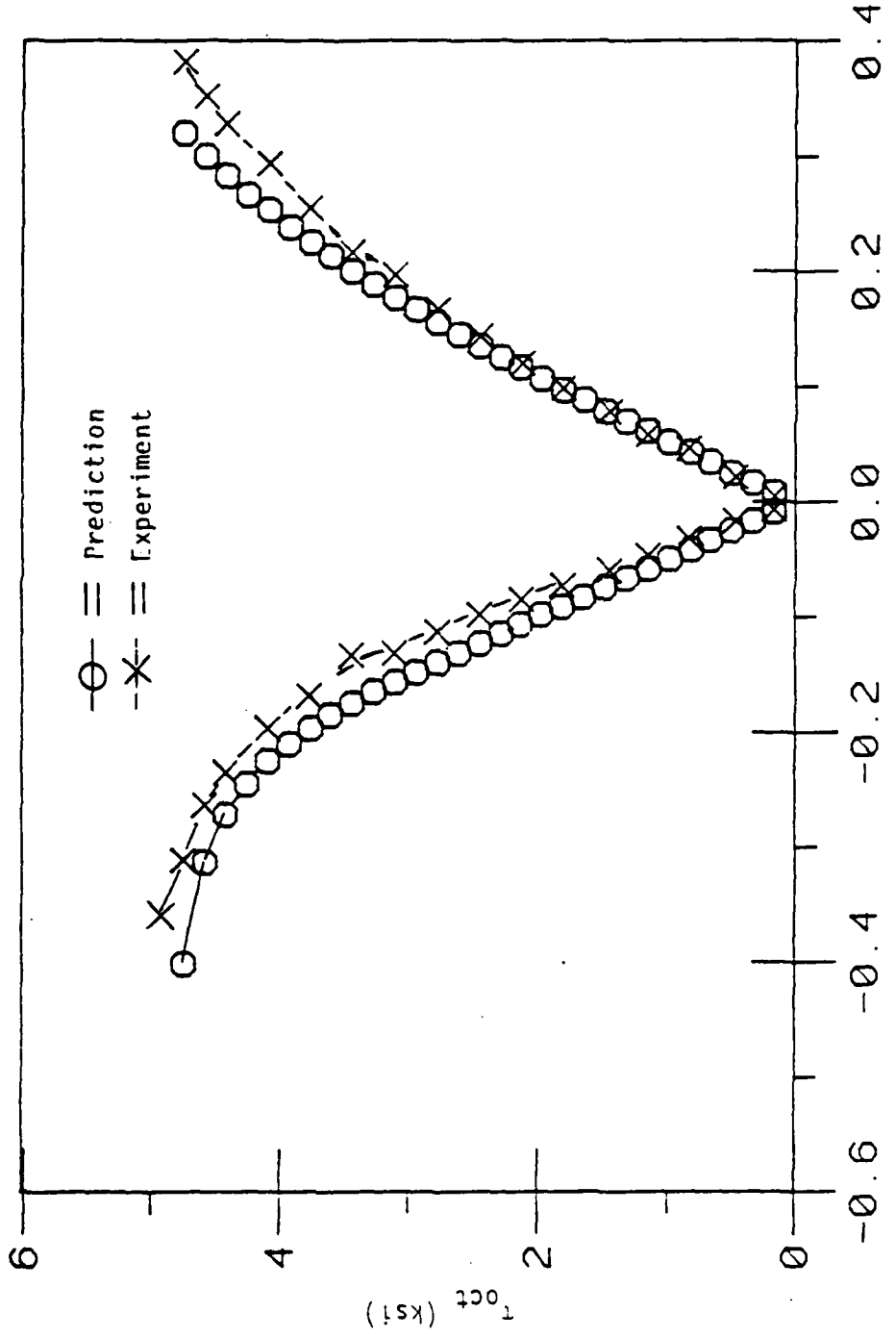

Figure 7.44. Comparison of Stress-Strain Responses of Simple Shear (SS) Test for SFRC-IIC (σ_o = 6.0 ksi), (1.0 psi = 6.89 kPa).

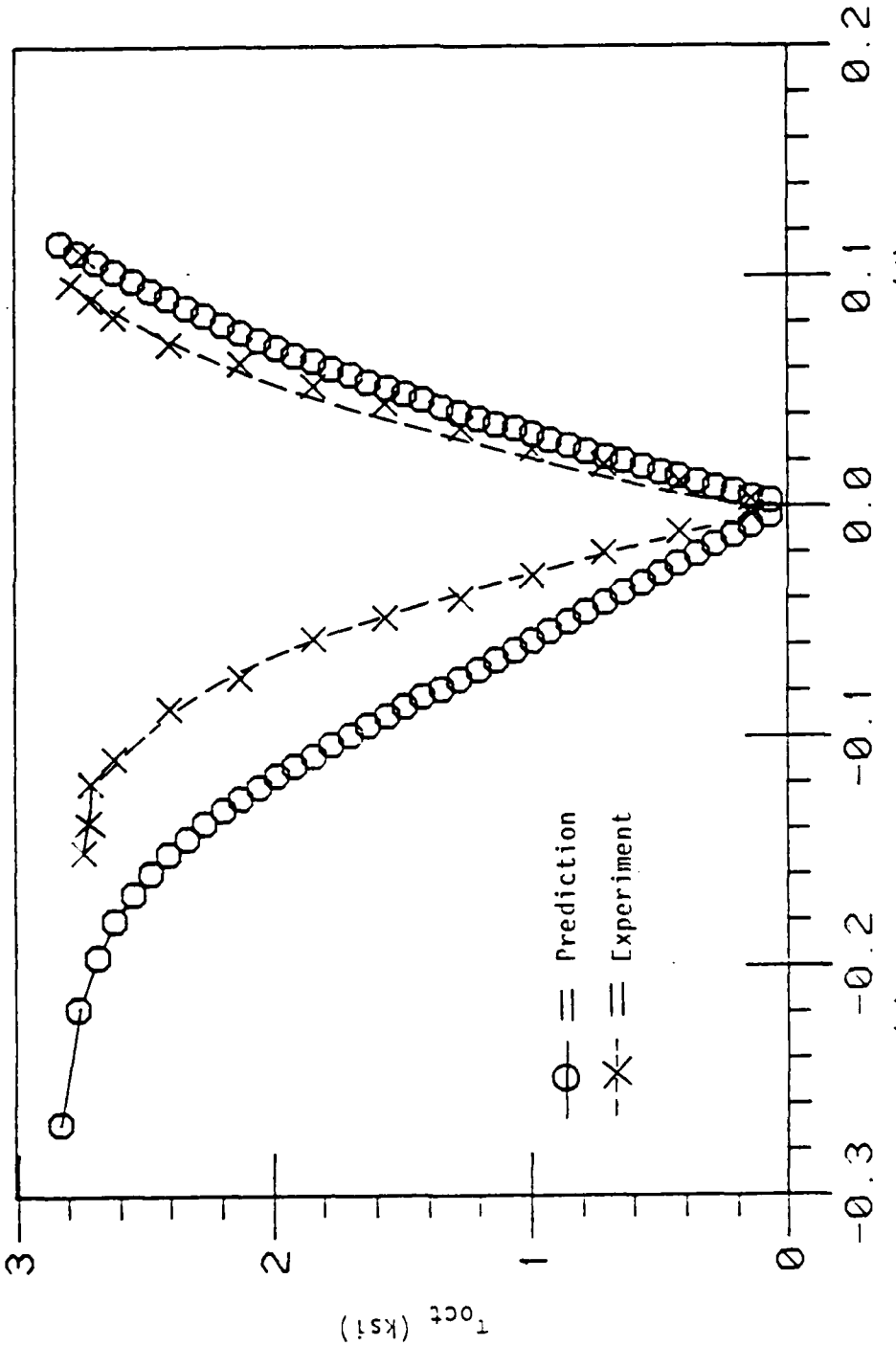

Figure 7.45. Comparison of Stress-Strain Responses of Triaxial Extension TE) Test for SFRC-IIC (σ_o = 4.0 ksi), (1.0 psi = 6.89 kPa).

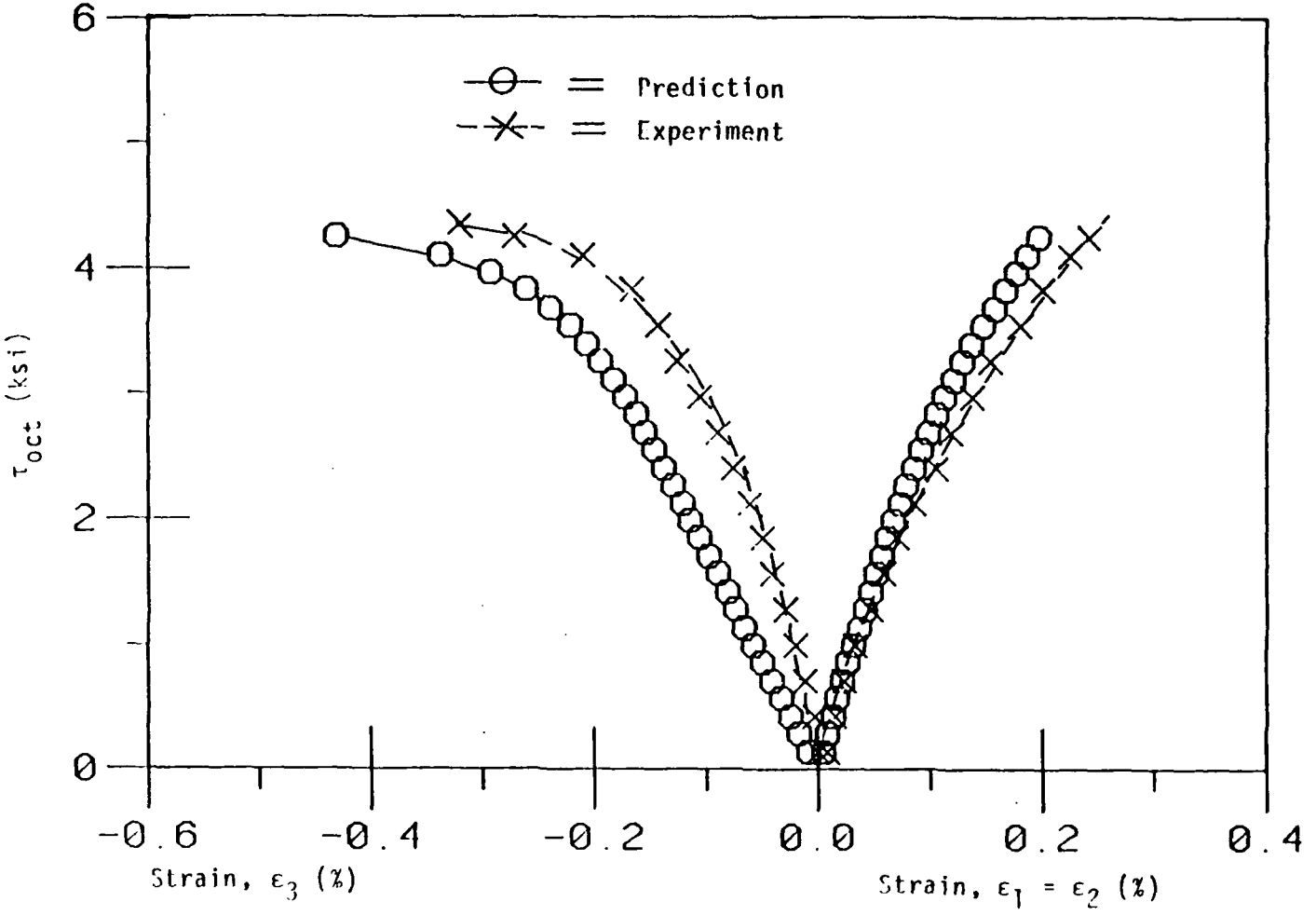

Figure 7.46. Comparison of Stress-Strain Responses of Triaxial Extension (TE) Test for SFRC-UC (σ_o = 6.0 ksi), (1.0 psi = 6.89 kpa).

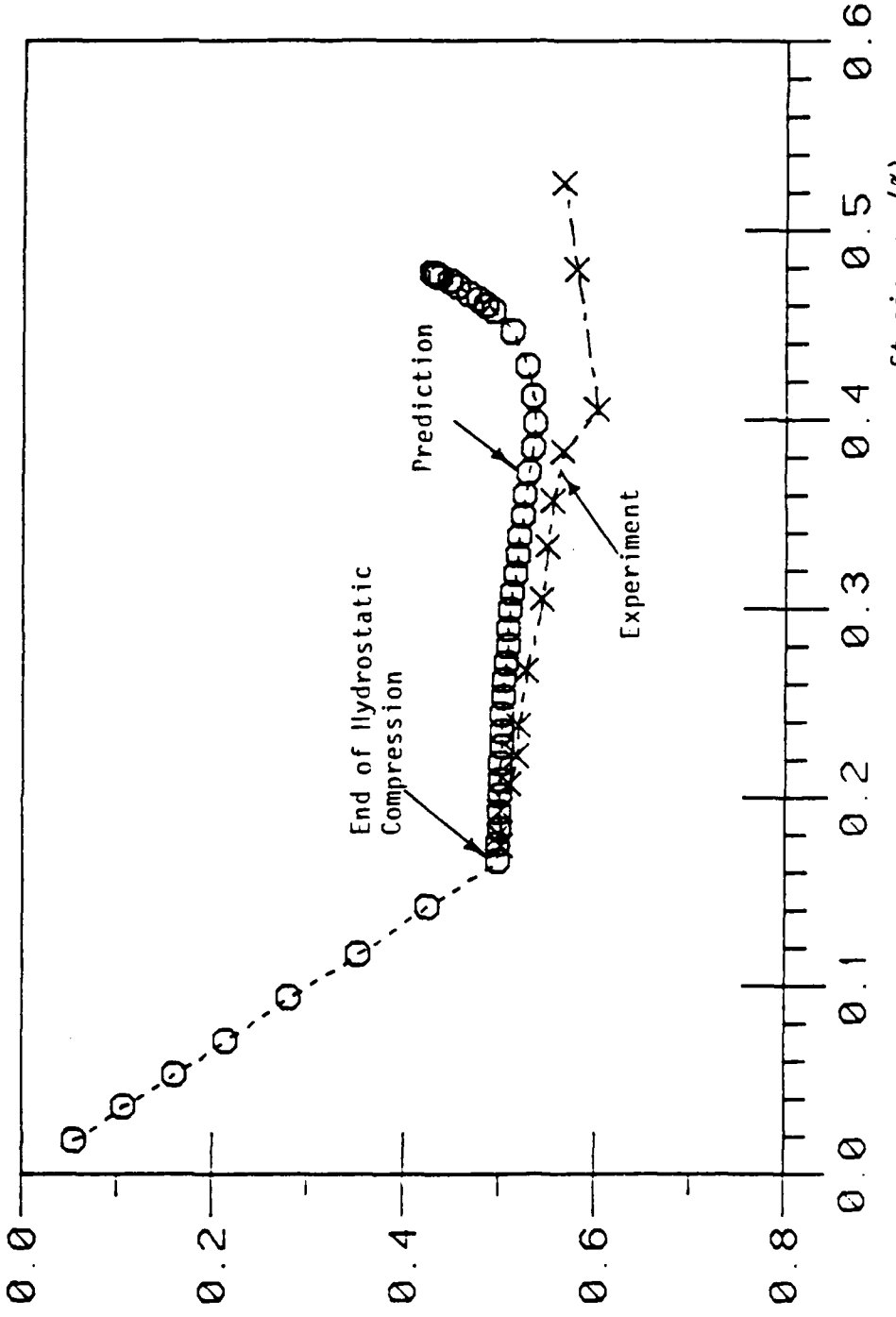

Figure 7.47. Comparison of Volumetric Response of Triaxial Compression TC) Test for SFRC-UC (σ_o = 4.0 ksi), (1.0 psi = 6.89 kPa).

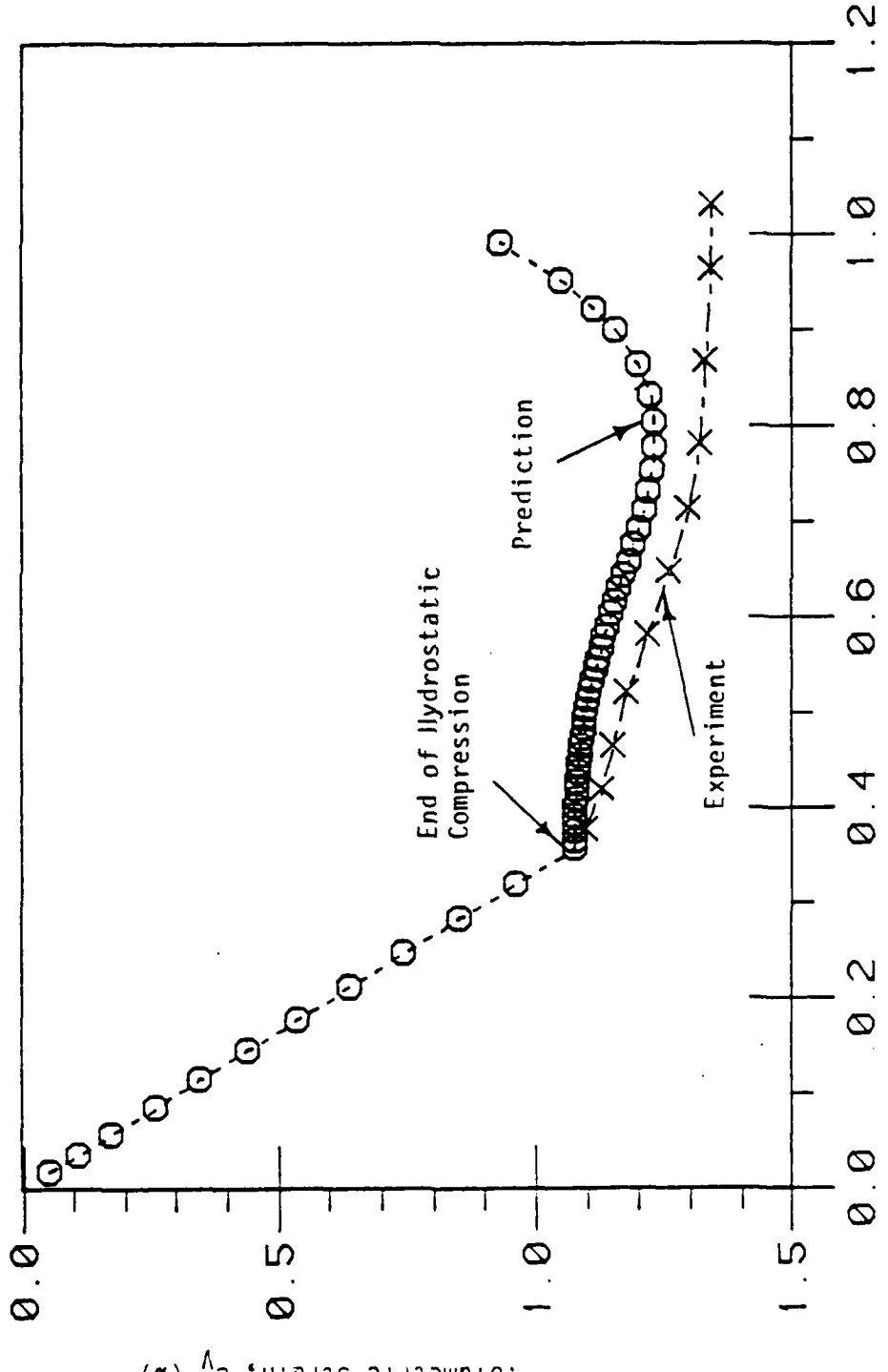

Figure 7.48. Comparison of Volumetric Response of Triaxial Compression (TC) Test for SFRC-UC (σ_o = 6.0 ksi), (1.0 psi = 6.89 kPa).

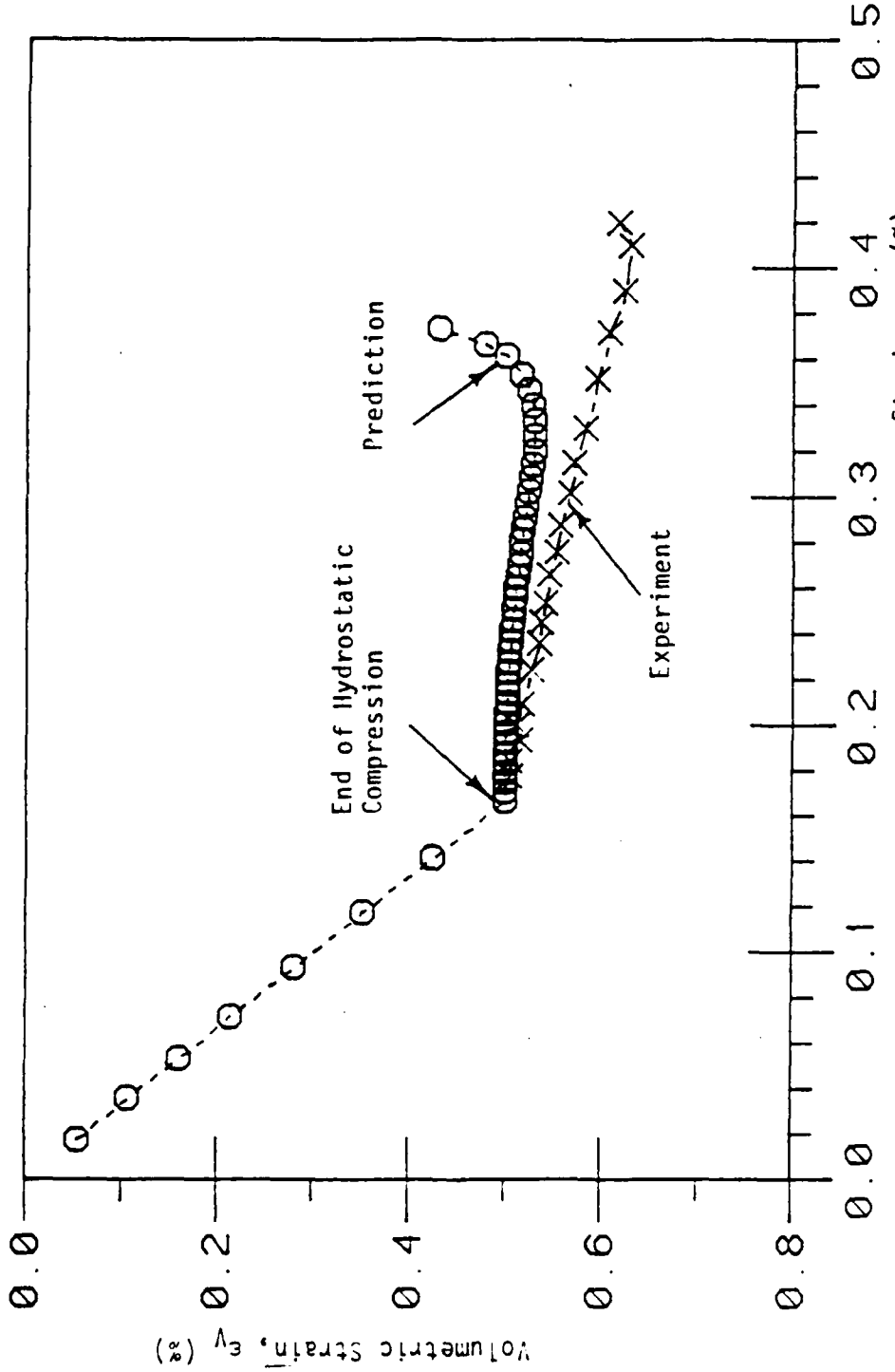

Figure 7.49. Comparison of Volumetric Response of Simple Shear (SS) Test for SFRC-UC (σ_o = 4.0 ksi), (1.0 psi = 6.89 kPa).

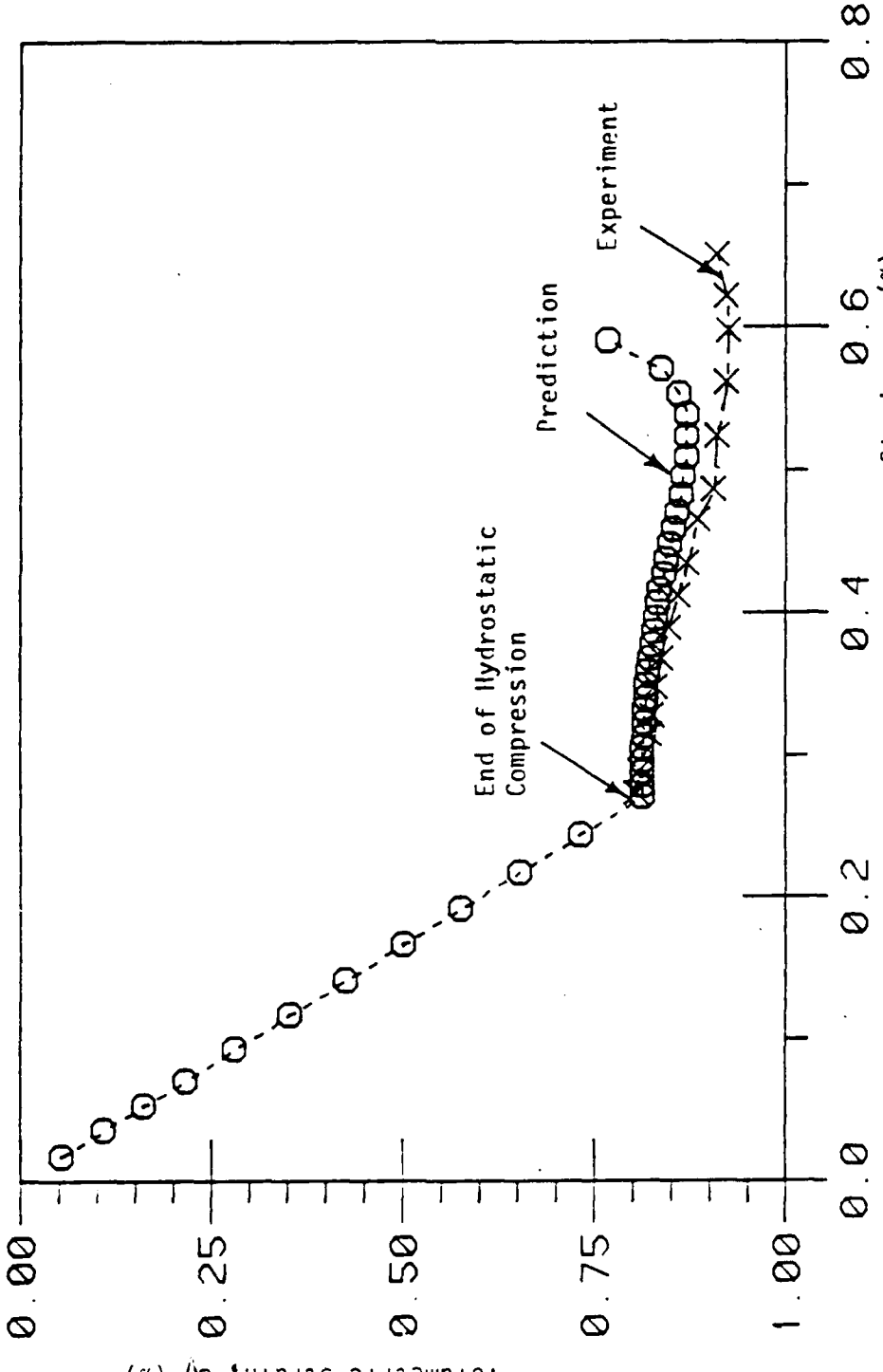

Figure 7.50. Comparison of Volumetric Response of Simple Shear (SS) Test for SFRC-UC (σ_o = 6.0 ksi), (1.0 psi = 6.89 kPa).

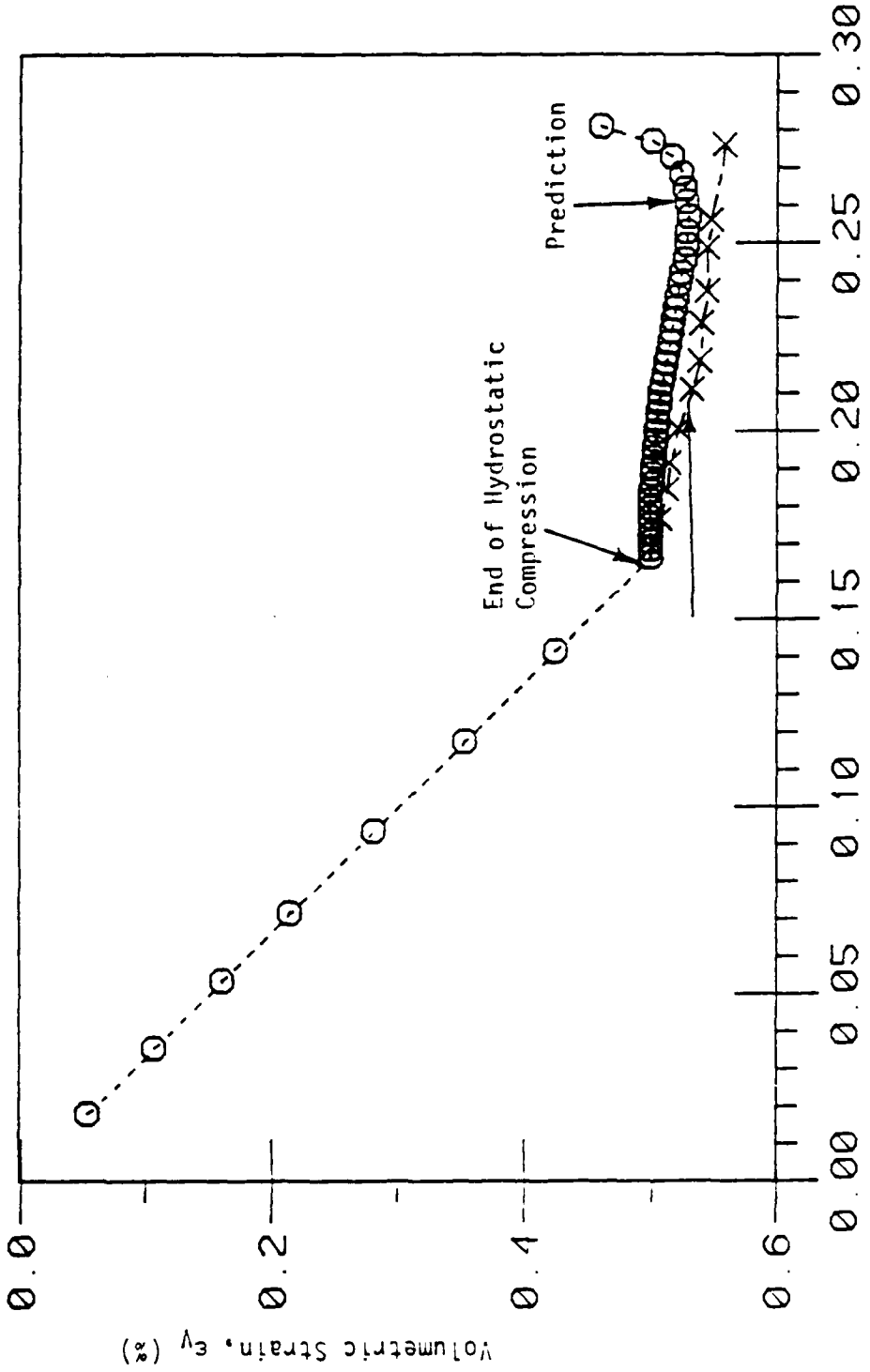

Figure 7.51. Comparison of Volumetric Response of Triaxial Extension (TE) Test for SFRC-UC (σ_o = 4.0 ksi), (1.0 psi = 6.89 kPa).

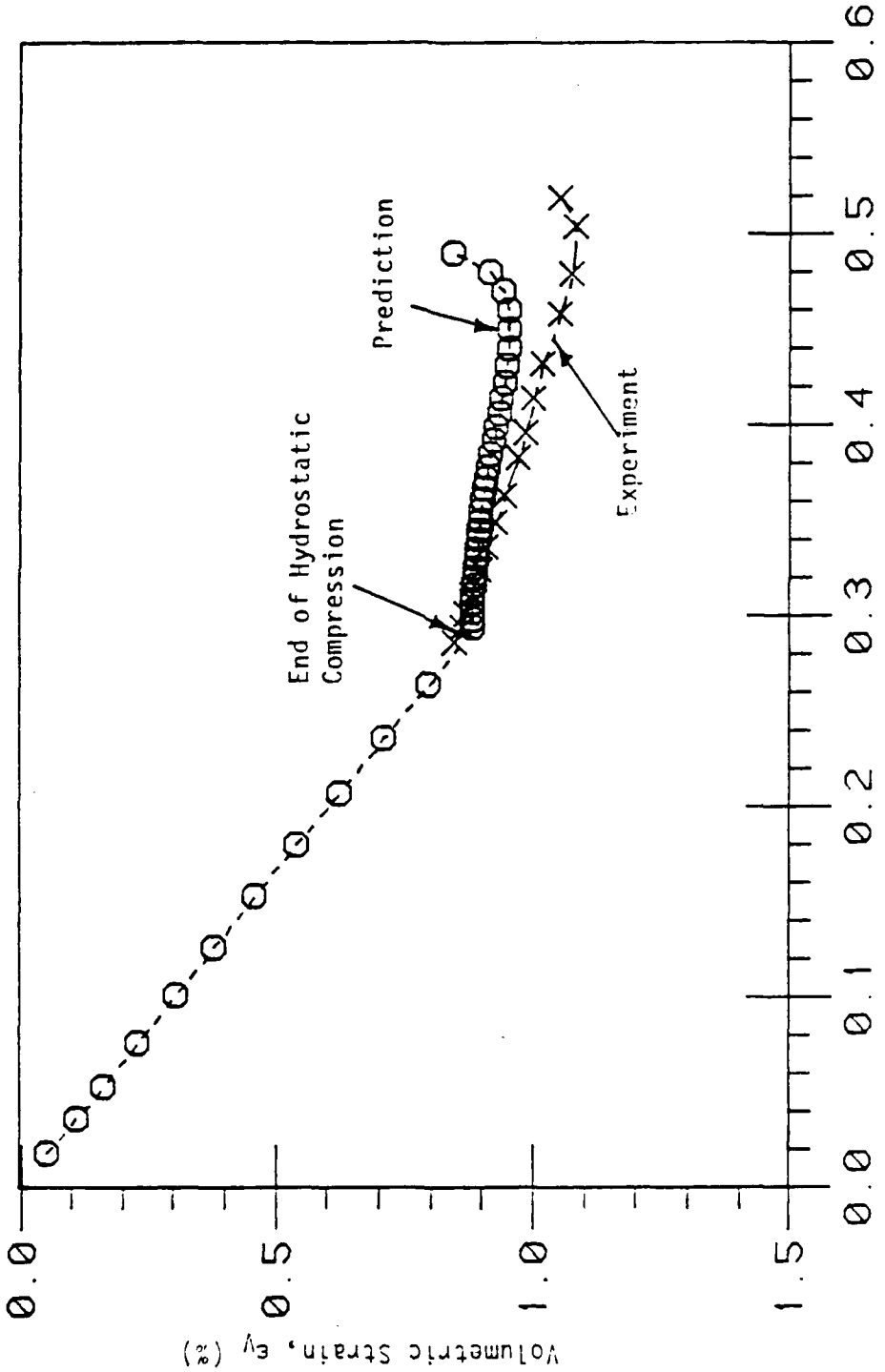

Figure 7.52. Comparison of Volumetric Response of Triaxial Extension (TE) Test for SFRC-UC (σ_o = 6.0 ksi), (1.0 psi = 6.89 kPa).

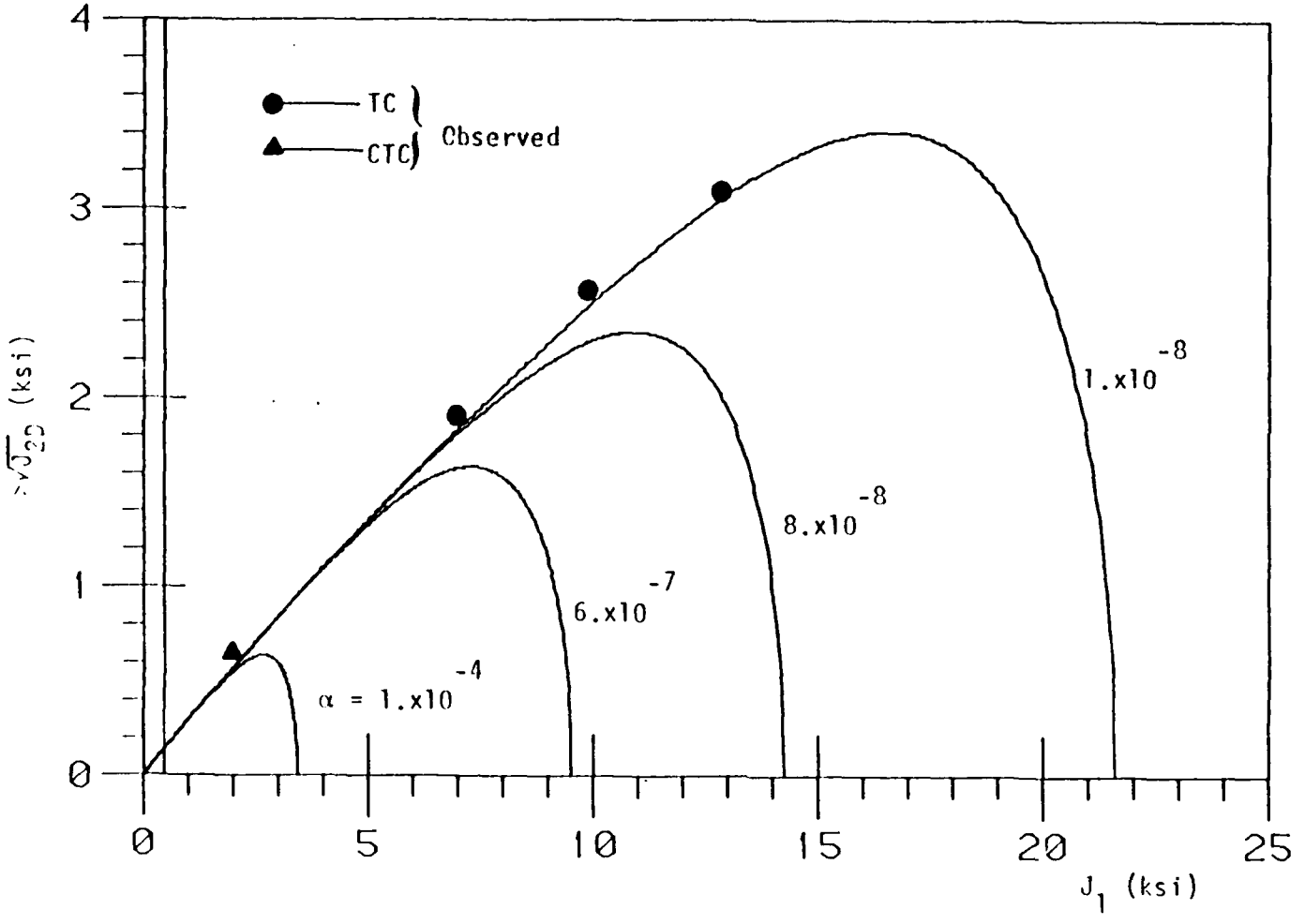

Figure 7.53. Predicted Ultimate and Pre-Ultimate Envelopes in $\sqrt{J_{2D}}$ - J_1 Plane for Convention Triaxial Compression (CTC) and Triaxial Compression (TC), ($\theta = -30^{o}$), for Soapstone.

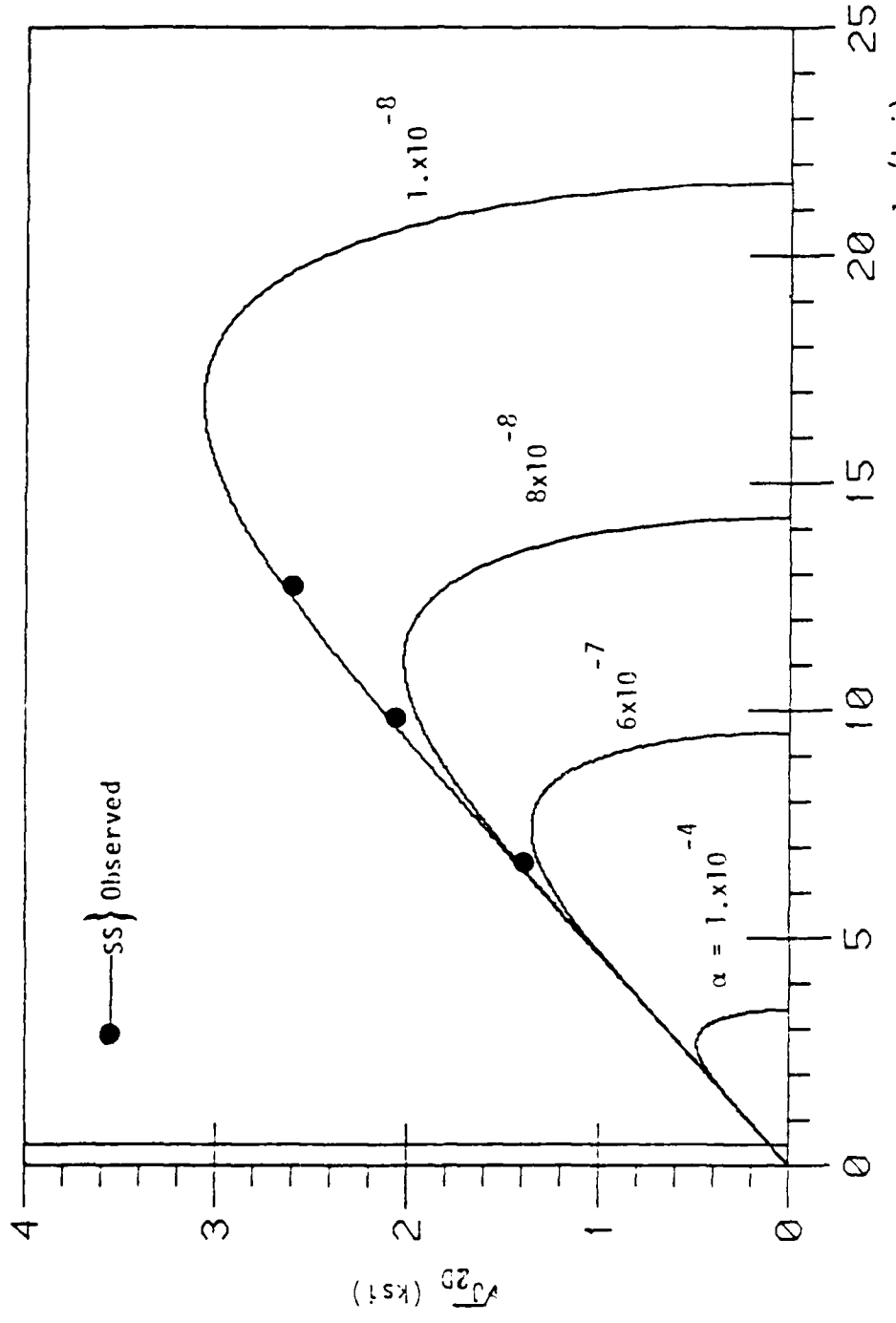

Figure 7.54. Predicted and Pre-Ultimate Envelopes in $\sqrt{J_{2D}}$ - J_1 Plane for Simple Shear (SS) Test, ($\theta = 0^0$), For Soapstone.

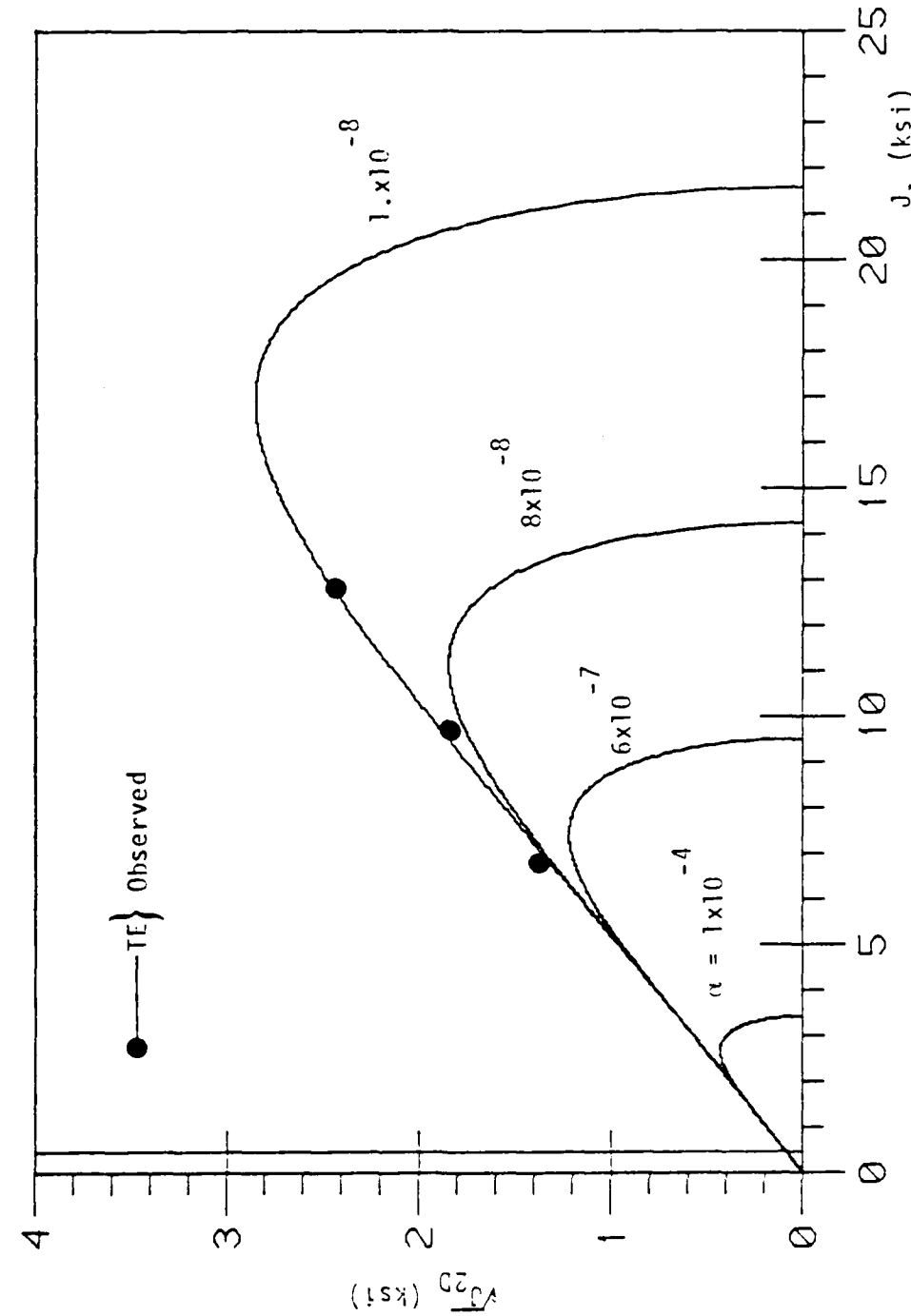

Figure 7.55. Predicted Ultimate and Pre-Ultimate Envelopes in $\sqrt{J_{2D}}$ - J_1 Plane for Triaxial Extension (TE), $\phi = 30^0$), for Soapstone.

evident from Figs. 7.53 through 7.55 that the model predictions compare well with the experimental data.

7.5.2 Octahedral, Triaxial, Biaxial and π-Planes

Figures 7.56 and 7.57 show the comparison of the predictions and observations of ultimate envelopes for octahedral and triaxial planes, respectively. It is evident from these Figs. that the model predictions compare well with the experimental results.

Figure 7.58 shows the biaxial ultimate envelope predicted using proposed model. It is for reference only since no experimental biaxial strength data was obtained.

Predicted ultimate envelope on π-plane is shown in Fig. 7.59.

7.5.3 Strength Behavior

Based on the predicted strength envelope, Fig. 7.57, predicted values of the uniaxial compressive strength, f_{cu}, equibiaxial compressive strength, f_{cb}, and uniaxial tensile, f_t, can be calculated. These predicted strengths are:

$$f_{cu} = 940 \text{ psi } (6.51 \text{ MPa})$$
$$f_{cb} = 1270 \text{ psi } (8.78 \text{ MPa}) \qquad (7.14)$$
$$f_t = 160 \text{ psi } (-1.08 \text{ MPa}) \qquad \text{(Compression Positive)}$$

The values of f_{cu} and f_t compared to unconfined compression strength, f'_{cu}, and tensile strength, f_t, based on tests with

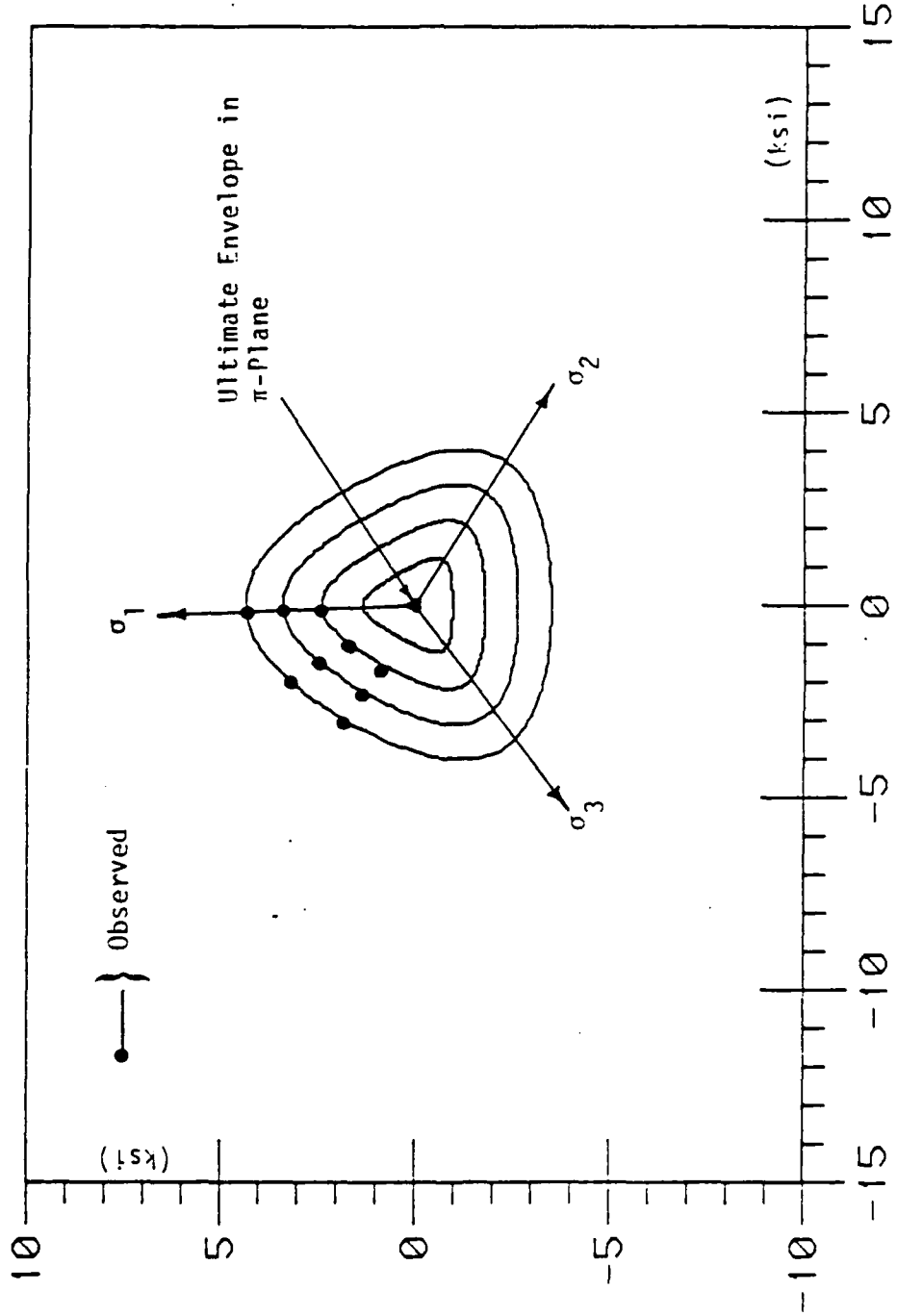

Figure 7.56. Variation of Cross-Sectional Shapes in Octahedral Planes (J_1 = .46, 3.46, 6.46, 9.46 and 12.46 ksi), (1.0 psi = 6.89 kPa), for Predicted Ultimate Surface for Soapstone.

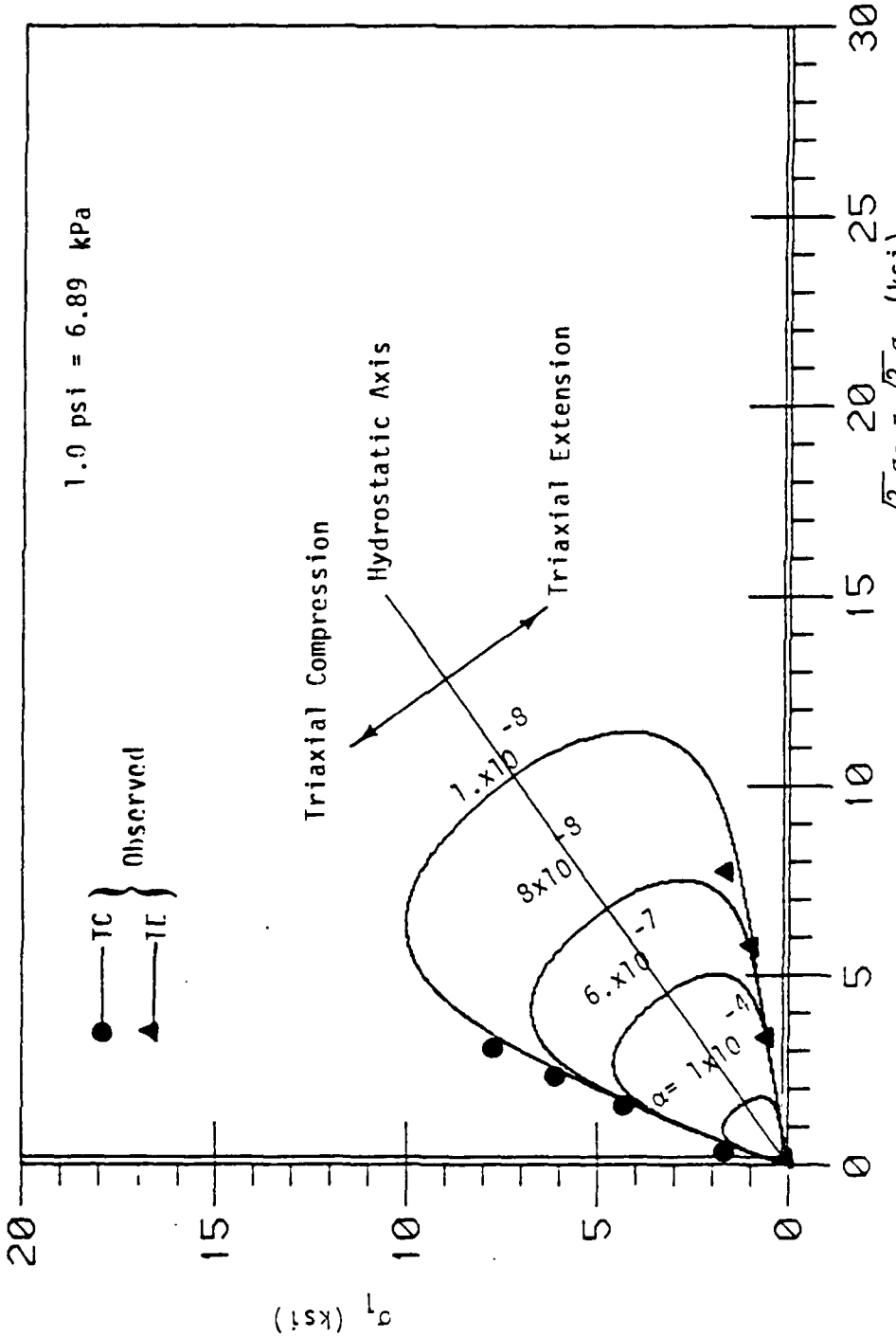

Figure 7.57. Predicted Ultimate and Pre-Ultimate Envelopes in Triaxial Plane for Soapstone.

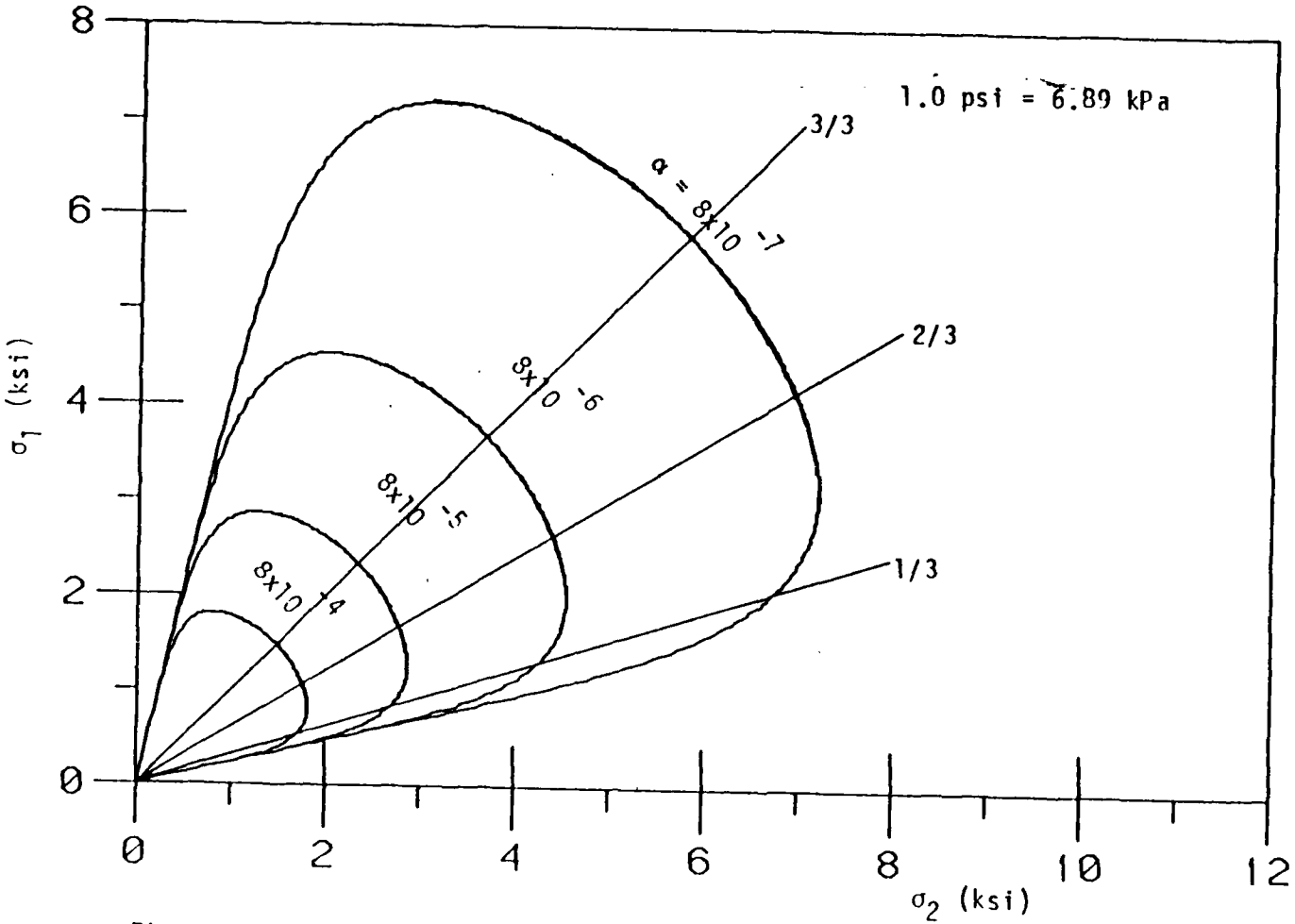

Figure 7.58. Predicted Biaxial Ultimate and Pre-Ultimate Envelopes ($\sigma_3 = 0$) Based on Proposed Model for Soapstone.

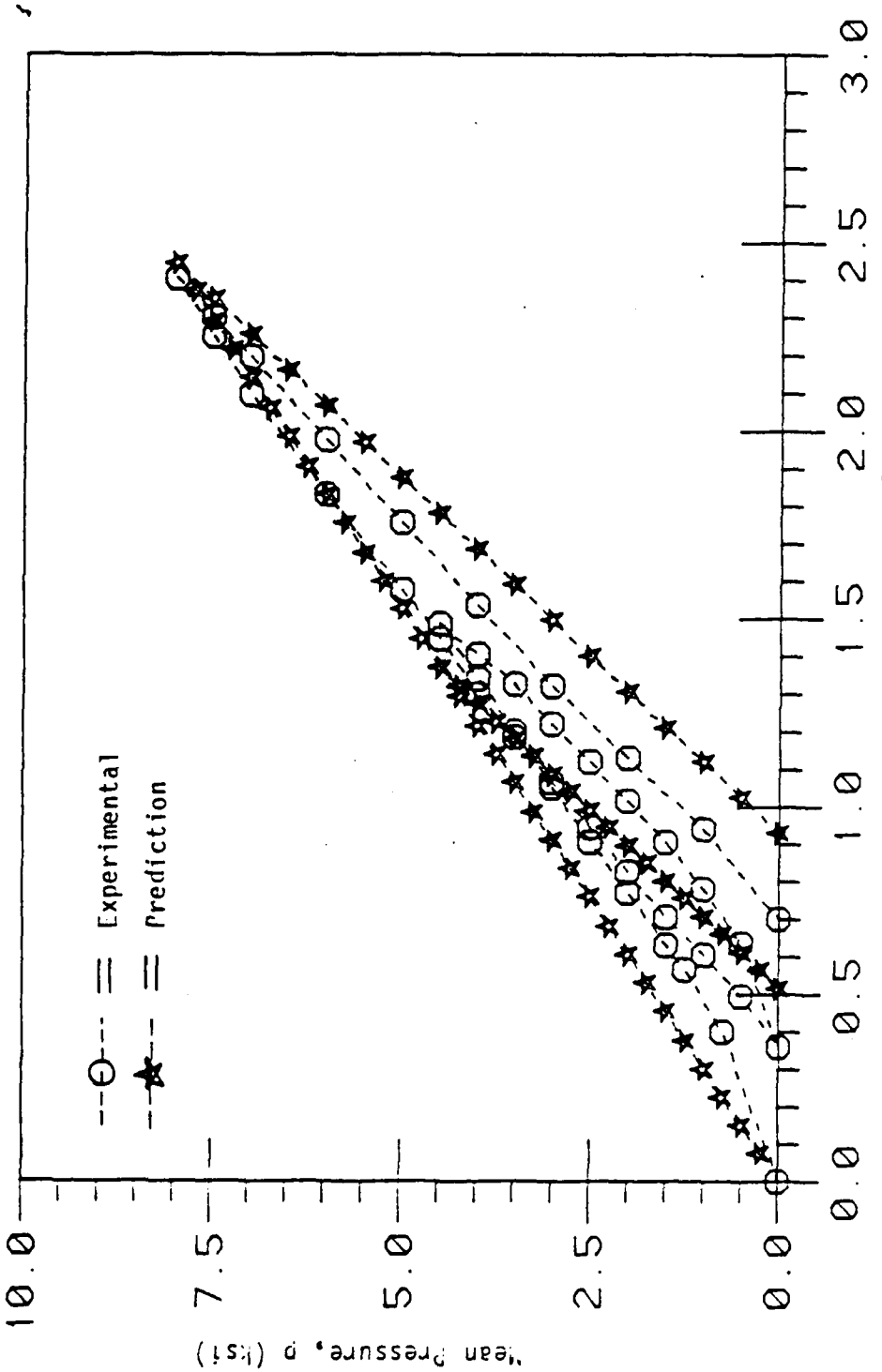

Figure 7.59. Comparison of Stress-Strain Responses of Hydrostatic Compression (HC) Test for Soapstone (σ_o = 8.0 ksi), (1.0 psi = 6.89 kPa).

cubical specimen of 4x4x4 in. (10.16x10.16x10.16 cm) in multiaxial test device and Eq. (6.47), respectively. These values are:

$$f'_{cu} = 1200 \text{ psi } (8.27 \text{ MPa}) \qquad (7.15)$$

$$f_t = -160 \text{ psi } (-1.08 \text{ MPa}) \qquad \text{(Compression Positive)}$$

It is evident from Eqs. (7.14) and (7.15) that the correlation between the proposed model predictions and observations is reasonable.

Based on the predicted ultimate envelope, Fig. 7.56, predicted values of the $\sqrt{J_{2D}}$ on the π-plane for TC ($\theta = -30^o$), SS ($\theta = o$) and TE ($\theta = 30^o$) can be calculated. These values are:

$$(\sqrt{J_{2D}})_{TC} = 0.73 \text{ ksi } (5.03 \text{ MPa})$$

$$(\sqrt{J_{2D}})_{SS} = 0.54 \text{ ksi } (3.72 \text{ MPa}) \qquad (7.16)$$

$$(\sqrt{J_{2D}})_{TE} = 0.42 \text{ ksi } (2.90 \text{ MPa})$$

Ratios of Eqs. (7.16), on the π-plane, can be expressed as

$$R_1 = \frac{(\sqrt{J_{2D}})_{TC}}{(\sqrt{J_{2D}})_{TE}} = 1.74 \qquad \text{(as } R_1 \to 2.0\text{, the shape of ultimate envelope in } \pi\text{-plane becomes a triangle)}$$

$$R_2 = \frac{(\sqrt{J_{2D}})_{SS}}{(\sqrt{J_{2D}})_{TE}} = 1.29 \qquad (7.17)$$

$$R_3 = \frac{(\sqrt{J_{2D}})_{TC}}{(\sqrt{J_{2D}})_{SS}} = 1.35$$

From Eqs. (7.16) and (7.17), one can see that the predicted ultimate envelope has the required shape, a triangular section with rounded corner in the π-plane.

7.5.4 Stress-Strain Behavior for Test Used for Finding Material Constants

Figure 7.59 shows the comparison between the predicted and observed stress-strain response curves for a hydrostatic compression (HC) test. It is seen from Fig. 7.60 that the prediction from the model compare fairly well with the experimental results.

Figures 7.61 through 7.65 show the comparison of predictions and observations for the stress-strain responses for two (CTC) tests, one (TC) test, one (SS) test and one (TE) test. Initial confining pressures for (CTC) tests are 1 and 3 ksi (6.895 and 20.69 MPa). For the (TC) test, the initial confining pressure is 2 ksi (13.79 MPa). For the (TE) and (SS) tests, the initial confining pressure is 3 ksi (20.69 MPa). It is evident from Figs. 7.61 through 7.65 that the predictions from the proposed model compare very well with experimental results.

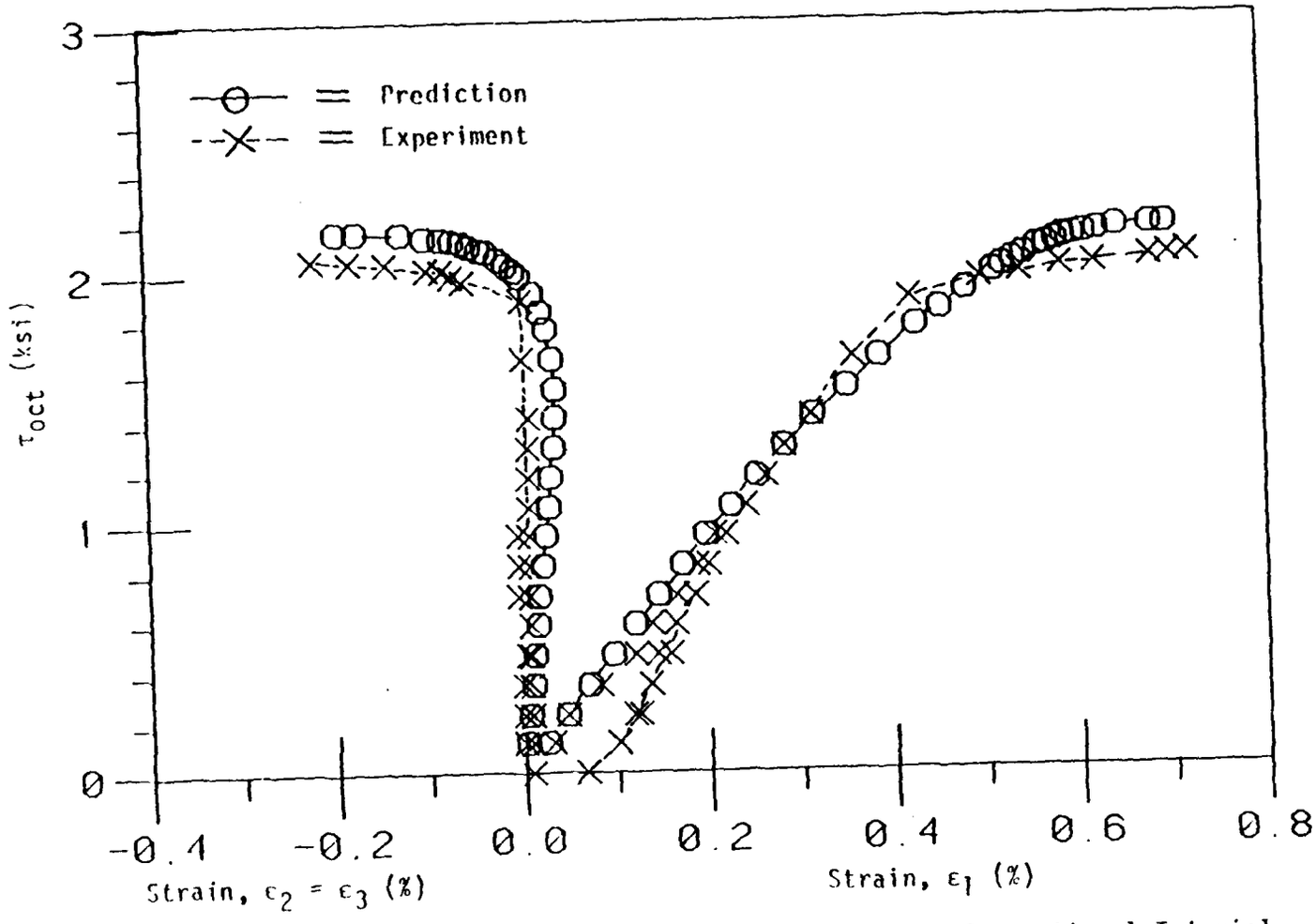

Figure 7.60. Comparison of Stress-Strain Responses of Conventional Triaxial Compression (CTC) Test for Soapstone (σ_0 = 1.0 ksi), (1.0 psi = 6.89 kPa).

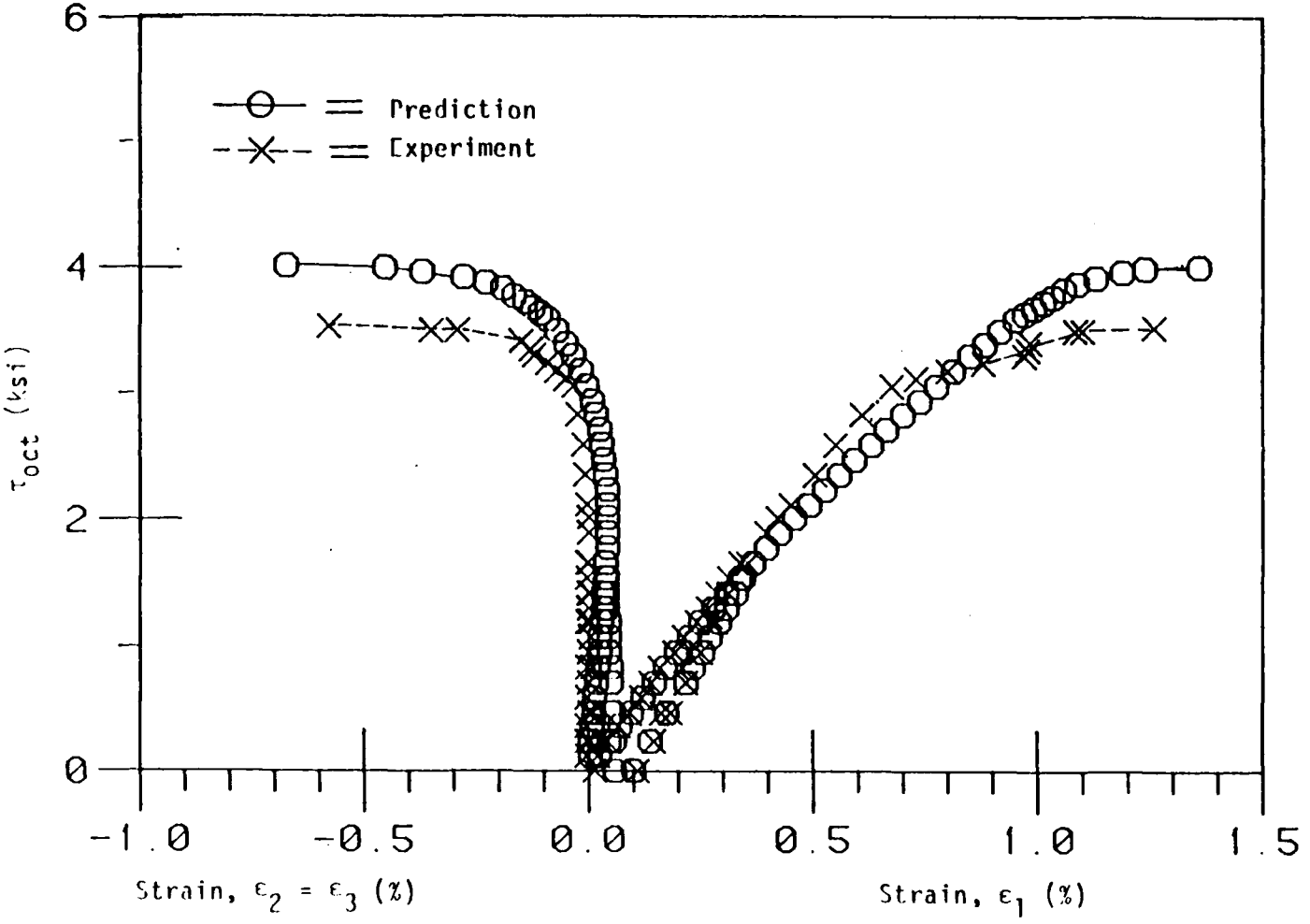

Figure 7.61. Comparison of Stress-Strain Responses of Conventional Triaxial Compression (CTC) Test for Soapstone (σ_o = 3.0 ksi), (1.0 psi = 6.89 kPa).

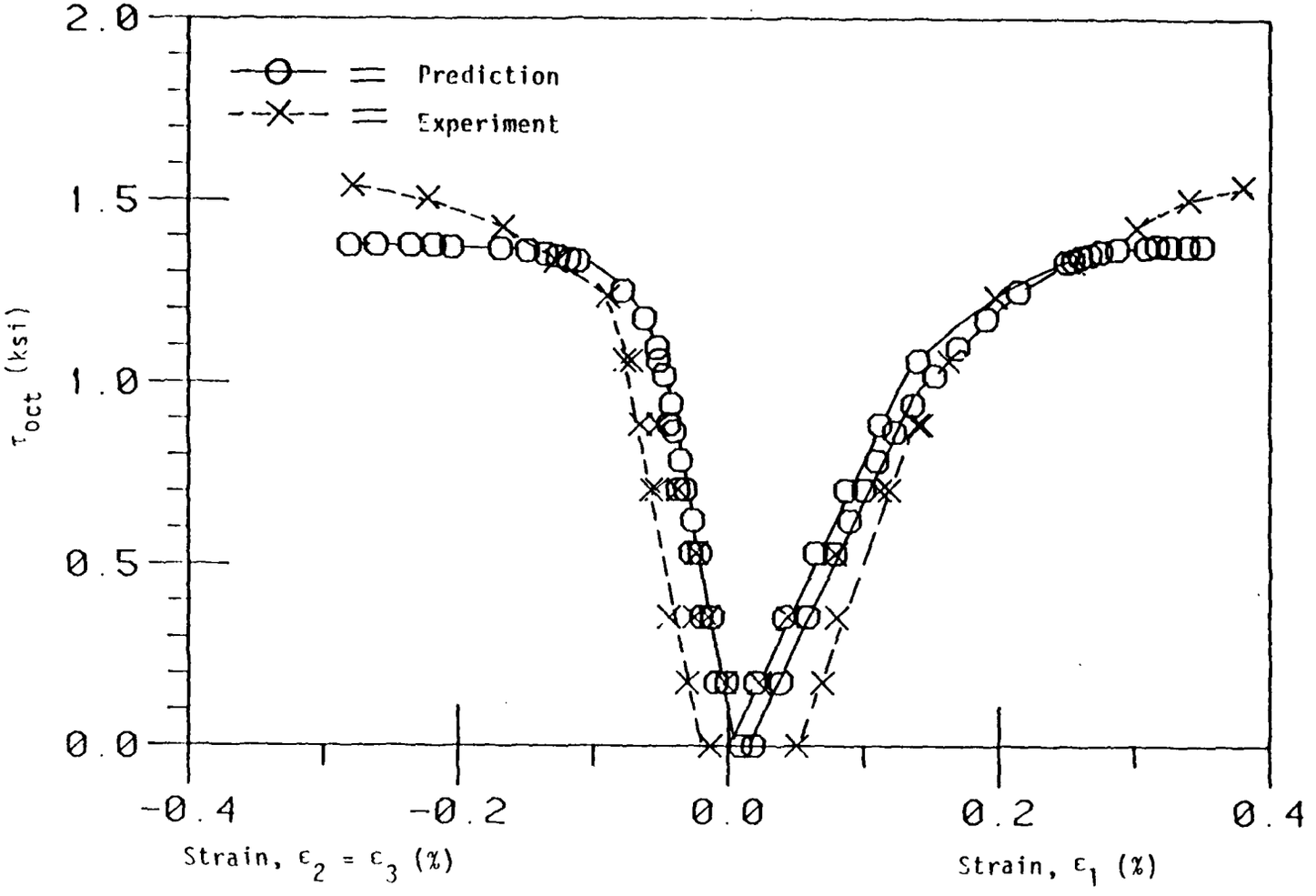

Figure 7.62. Comparison of Stress-Strain Responses of Triaxial Compression (TC) Test for Soapstone (σ_o = 2.0 ksi), (1.0 psi = 6.89 kPa).

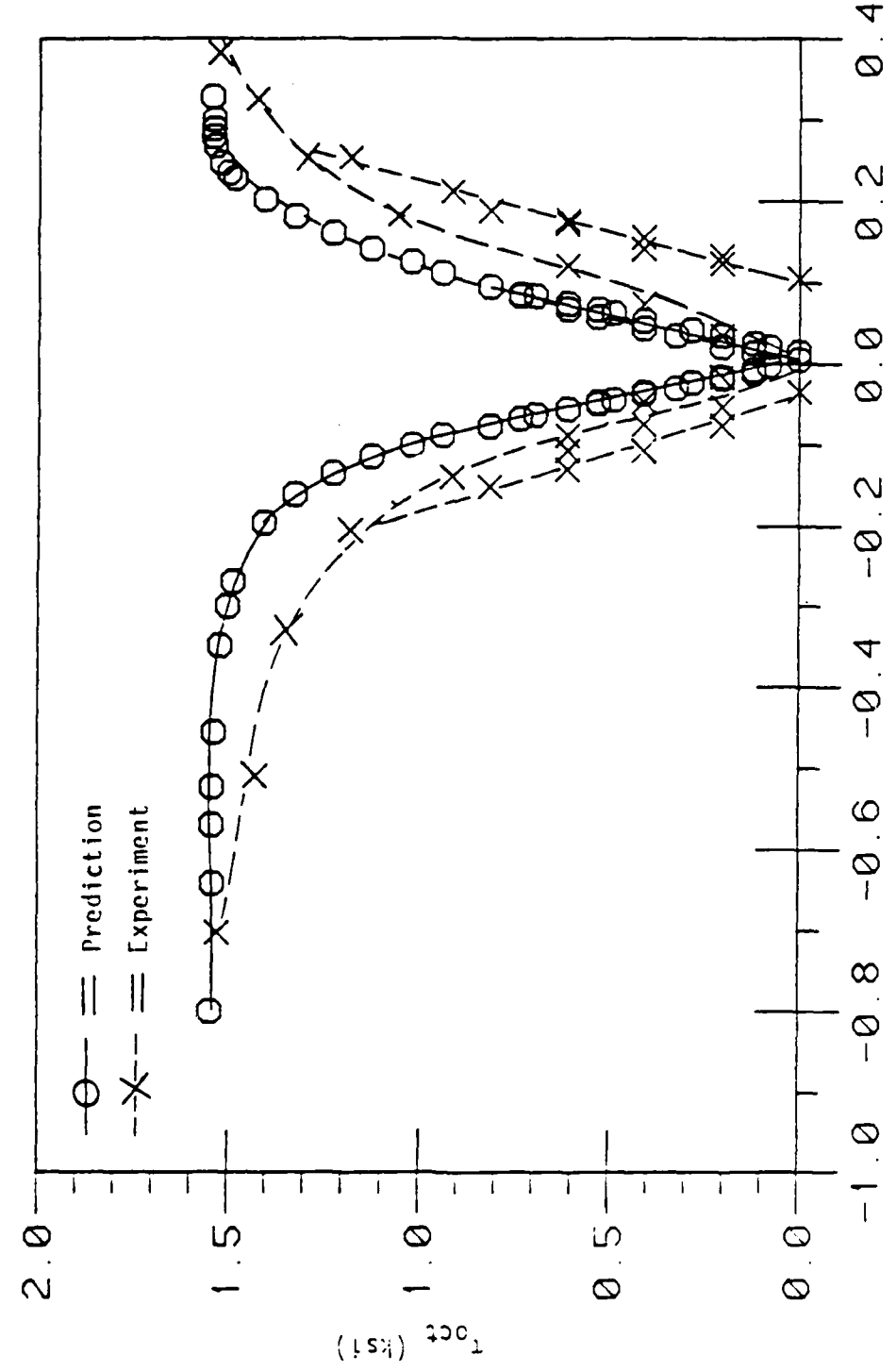

Figure 7.63. Comparison of Stress-Strain Responses of Simple Shear (SS) Test for Soapstone (σ_o = 3.0 ksi), (1.0 psi = 6.89 kpa).

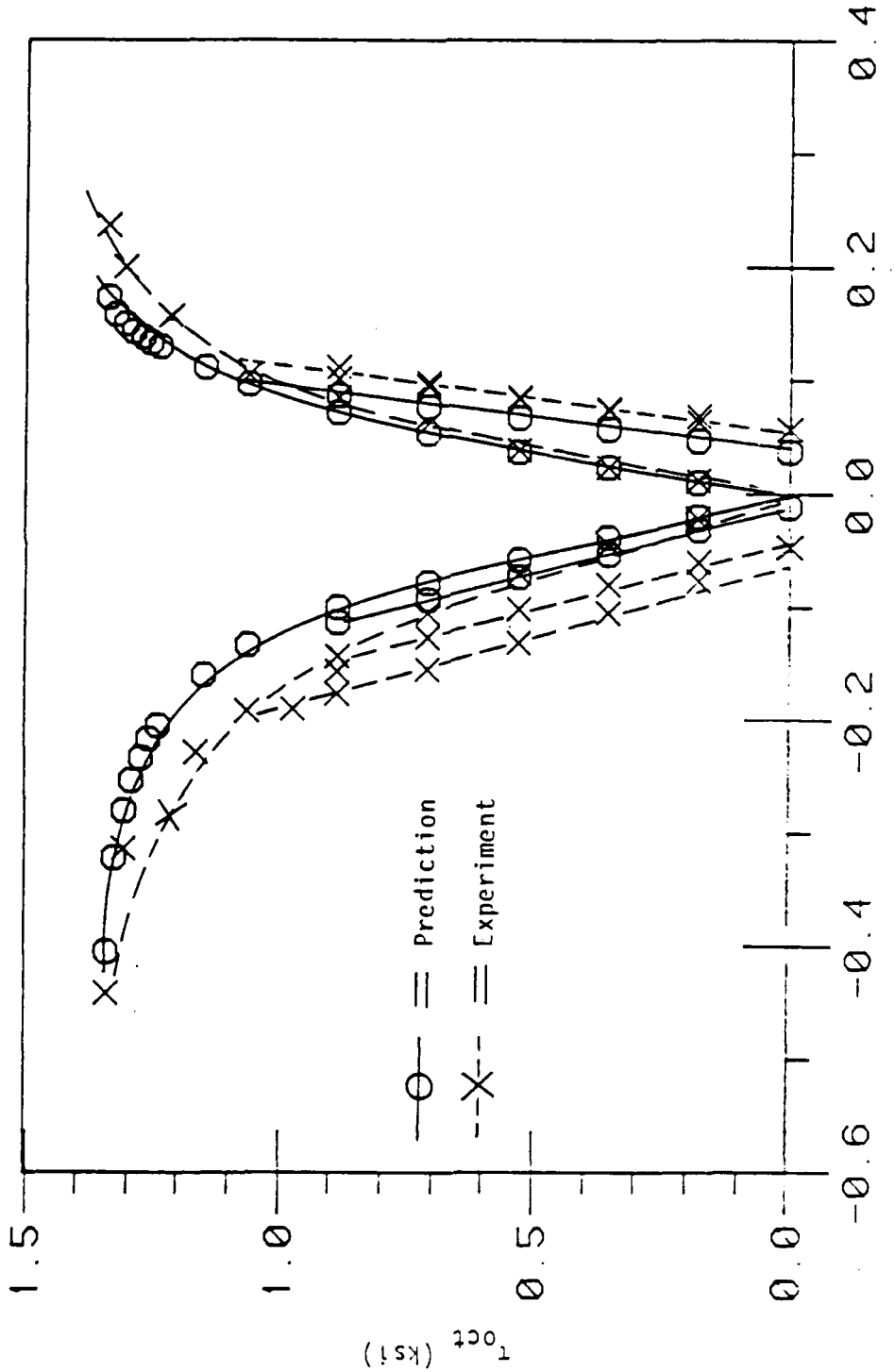

Figure 7.64. Comparison of Stress-Strain Responses of Triaxial Extension (TE) Test for Soapstone (σ_o = 3.0 ksi), (1.0 psi = 6.89 kPa).

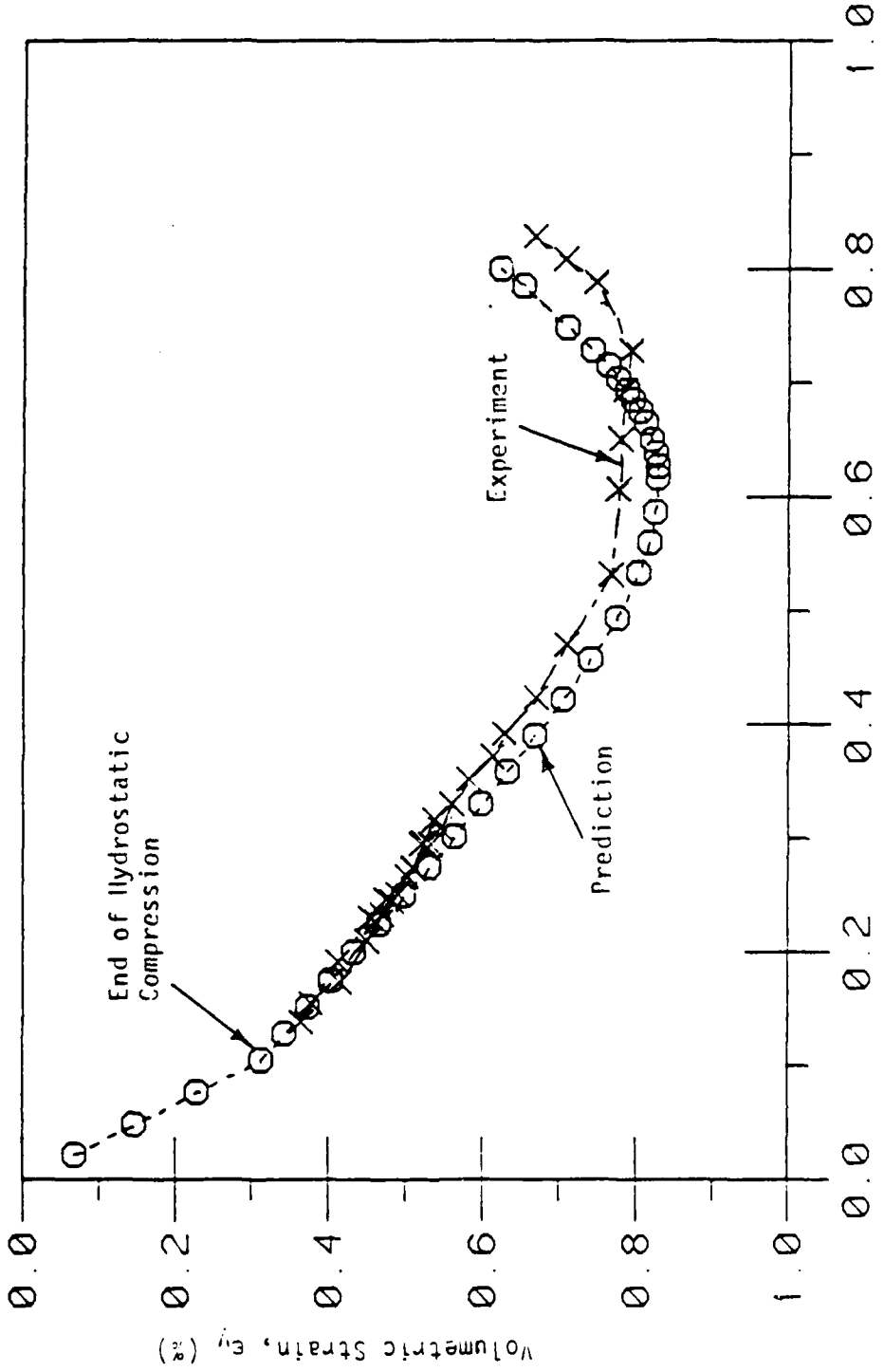

Figure 7.65. Comparison of Volumetric Response of Conventional Triaxial Compression (CTC) Test for Soapstone (σ_o = 1.0 ksi), (1.0 psi = 6.89 kPa).

7.5.5 Volumetric Responses Behavior

Figures 7.65 through 7.69 show plots of $\varepsilon_v - \varepsilon_1$ for two CTC (σ_o = 1 and 3 ksi) tests, one TC (σ_o = 2 ksi) test, one SS (σ_o = 3 ksi) test and TE (σ_o = 3 ksi) test. It is evident from Figs. 7.56 through 7.69 that the models compare very well with the experimental results.

7.5.6 Circular Stress Path Test Not Used for Finding Material Constants

Figure 7.70 shows the comparison of the predictions and the observations for a circular stress path which was not used to determine the material constants. It is seen from Fig. 7.70 that a good agreement is achieved between the predictions and observations.

The material constants for sandstone are given in TABLE 6.5. The description of the sandstone is presented in Chapter 6. Ultimate envelopes, strengths and a number of stress-strain response curves are predicted and compared with the experimental results, as presented below.

7.6.1 $\sqrt{J_{2D}} - J_1$ Plane

Figures 7.71, 7.72 and 7.73 show the comparison of the predictions and observations of ultimate envelopes, in $\sqrt{J_{2D}} - J_1$ plane, for (TC), (SS) and (TE) tests, respectively. It

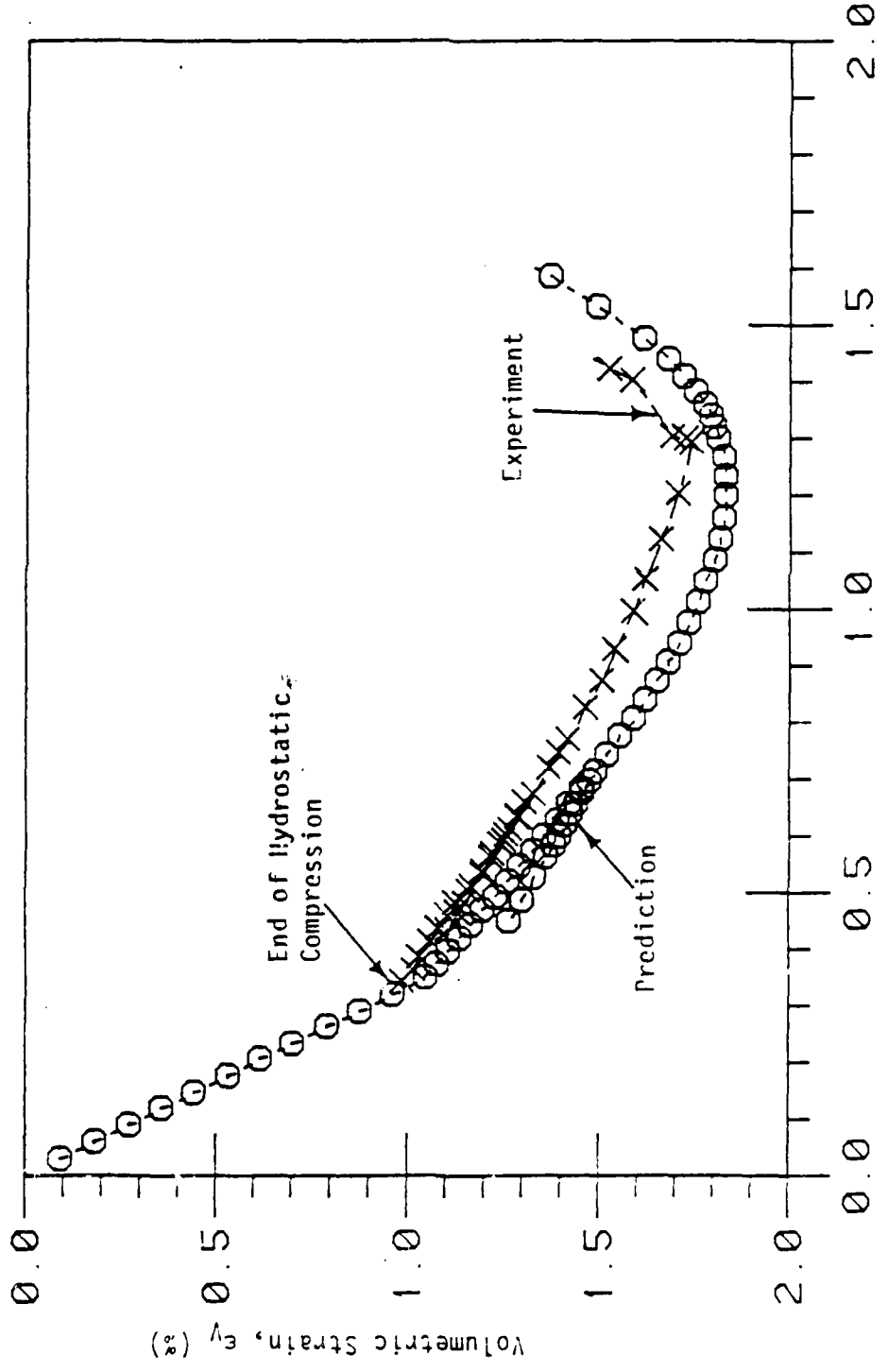

Figure 7.66. Comparison of Volumetric Response of Conventional Triaxial Compression (CTC) Test for Soapstone (σ_o = 3.0 ksi), 1.0 psi = 6.89 kPa).

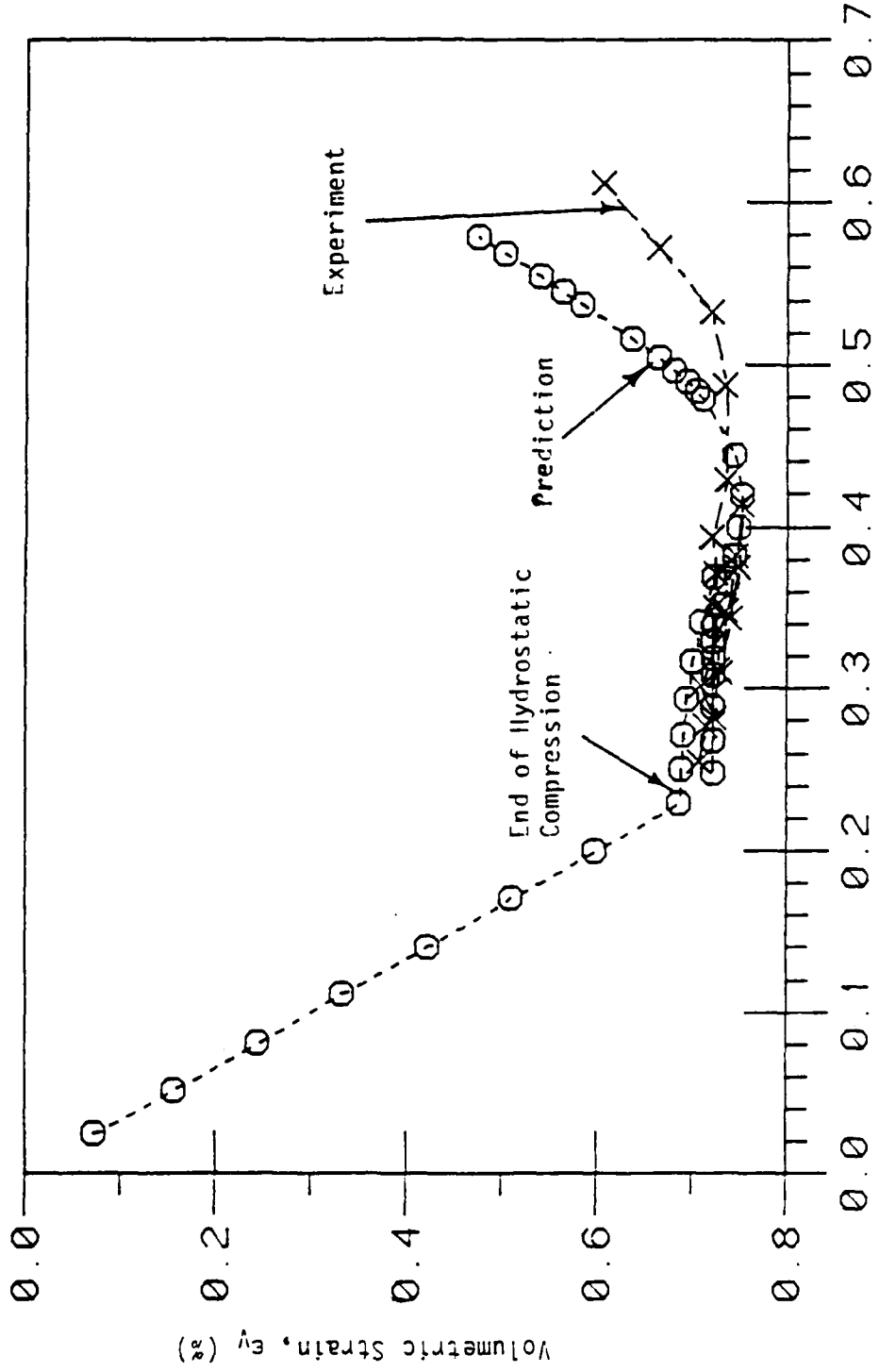

Figure 7.67. Comparison of Volumetric Response of Triaxial Compression (TC) for Soapstone (σ_o = 2.0 ksi), (1.0 psi = 6.89 kPa).

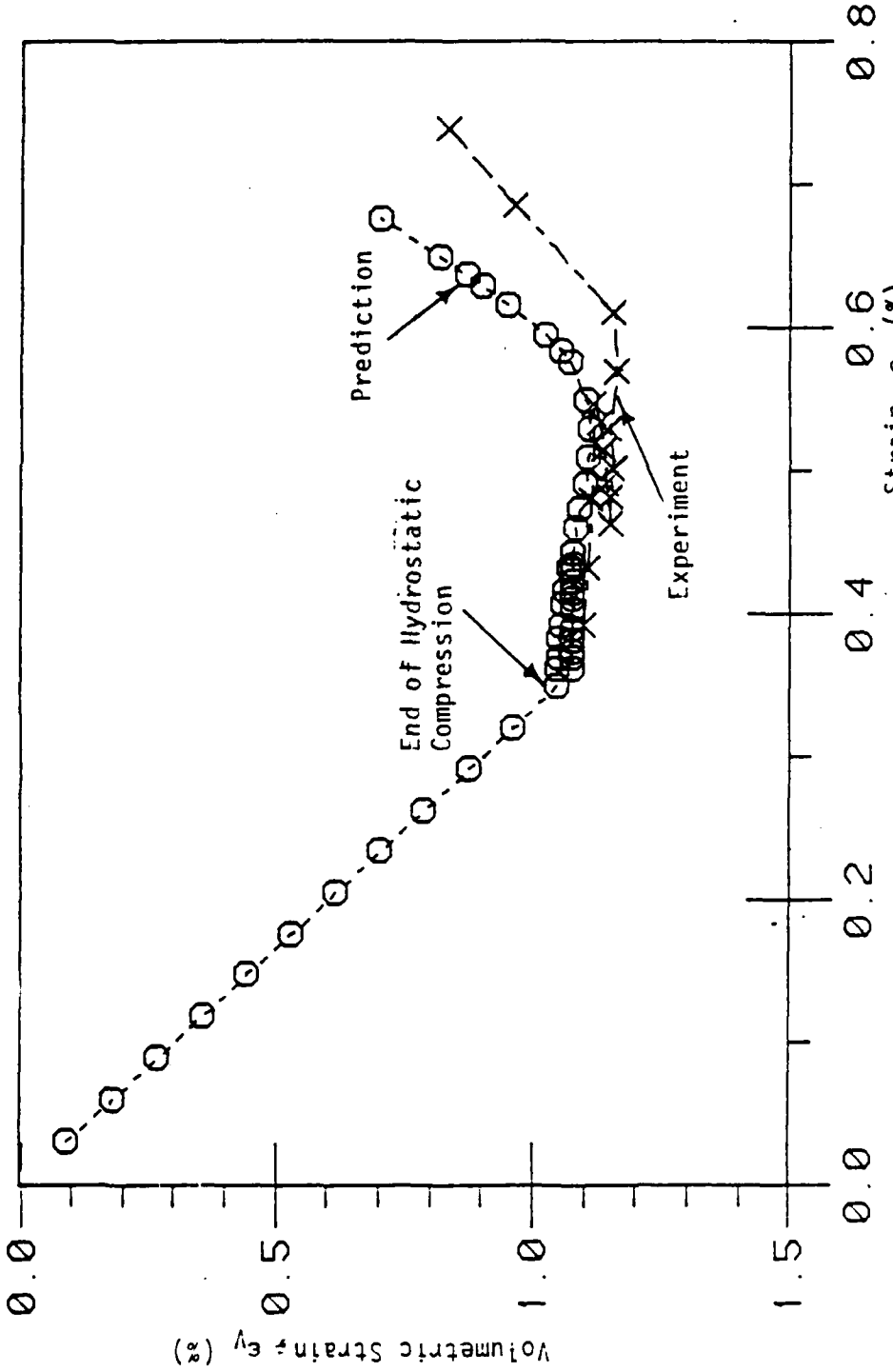

Figure 7.68. Comparison of Volumetric Response of Simple Shear (SS) Test for Soapstone (σ_o = 3.0 ksi), (1.0 psi = 6.89 kPa).

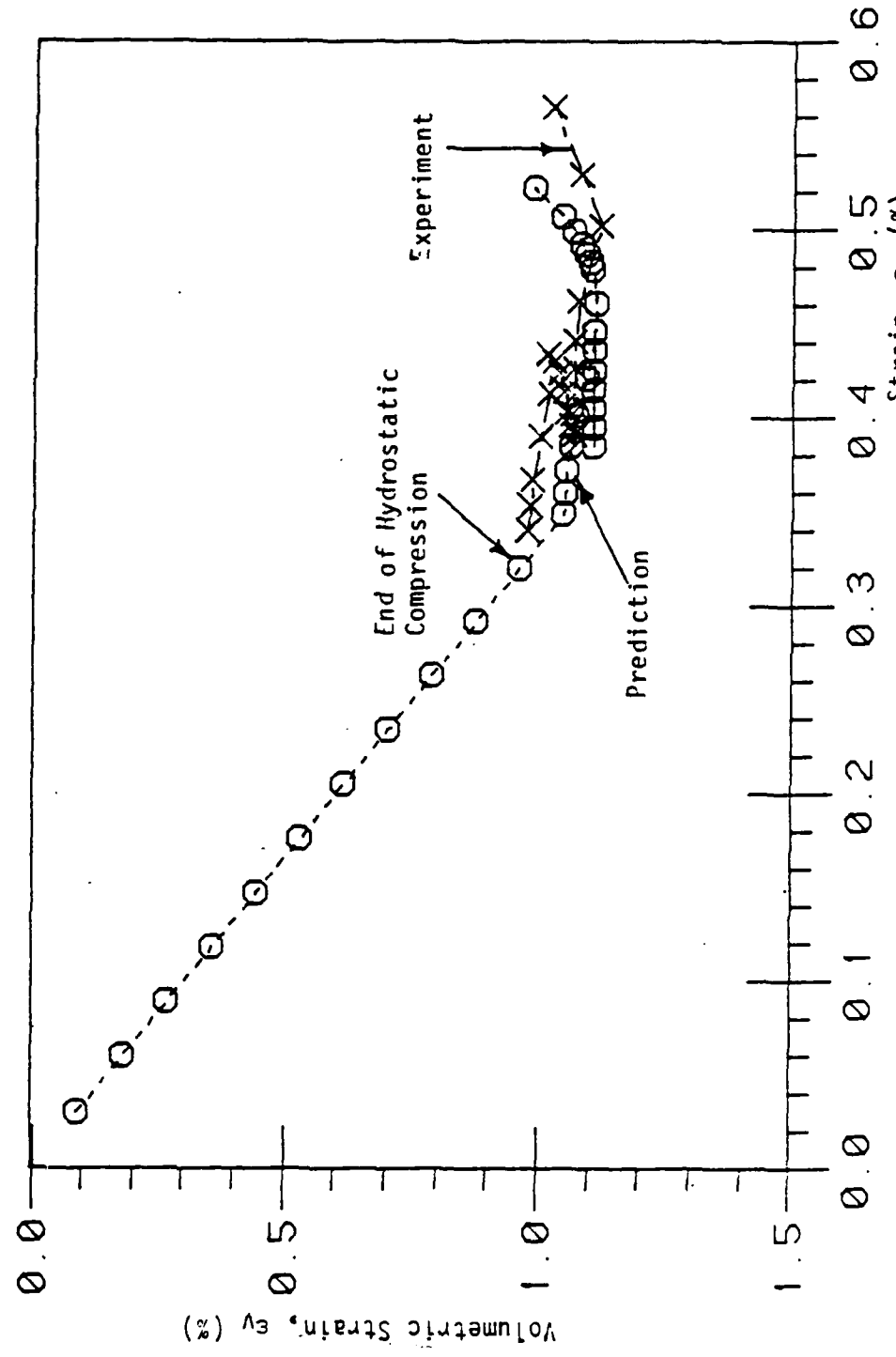

Figure 7.69. Comparison of Volumetric Response of Triaxial Extension (TE) Test for Soapstone (σ_o = 3.0 ksi), (1.0 psi = 6.89 kpa).

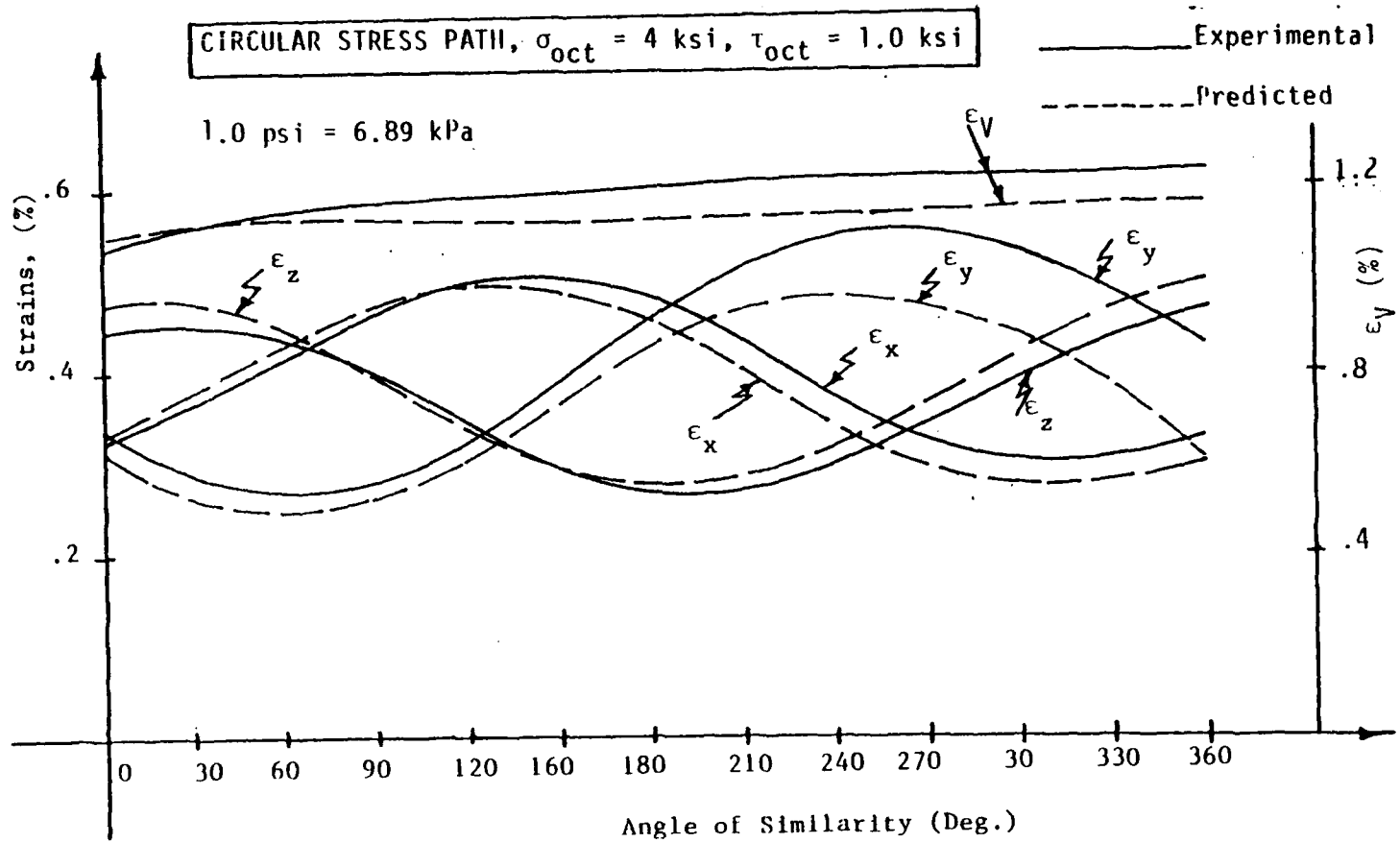

Figure 7.70. Comparison of Principal Strain and Volumetric Strain-Angle of Similarity Responses of Circular Path (CSP) Test for Soapstone.

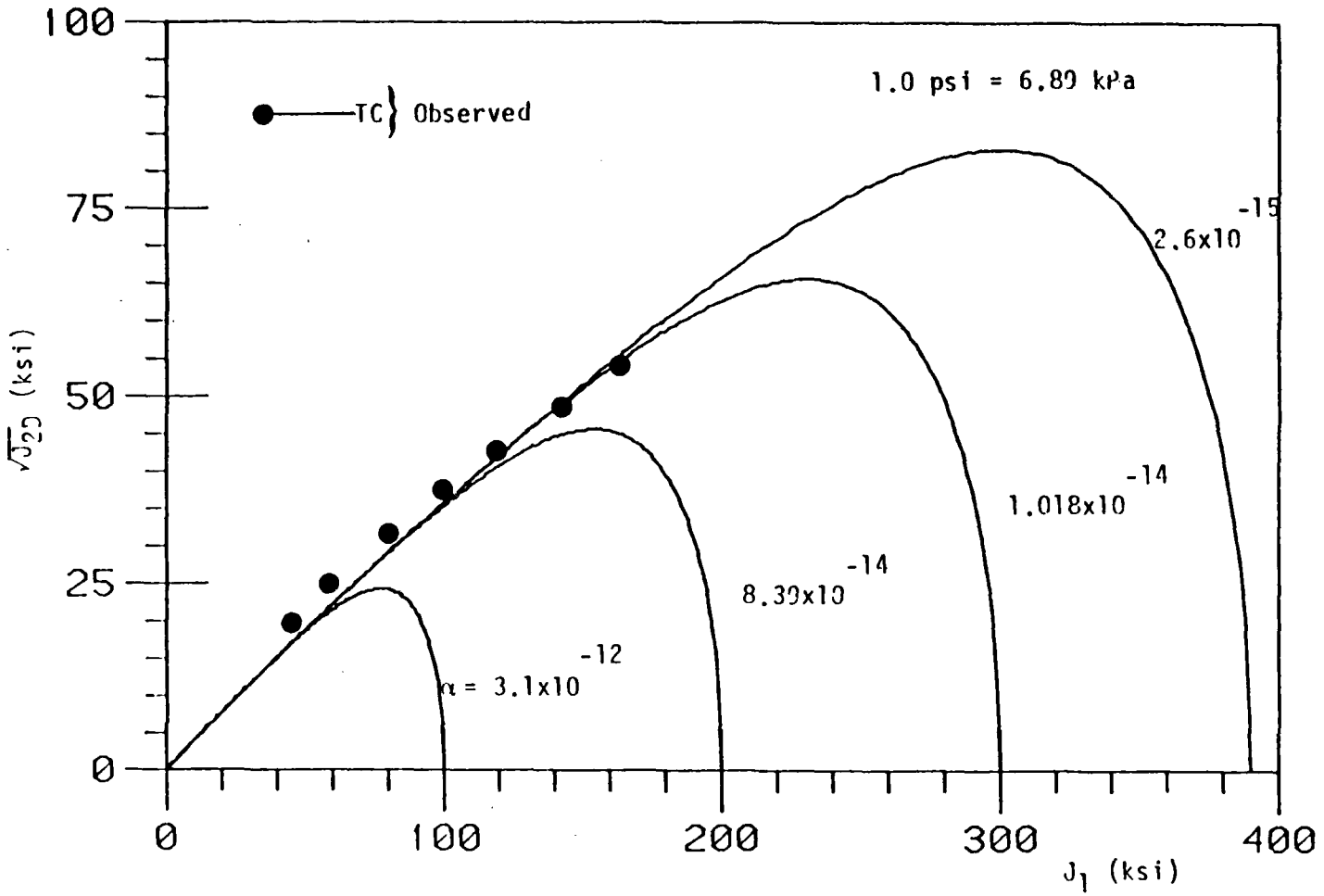

Figure 7.71. Predicted Ultimate and Pre-Ultimate Envelopes in $\sqrt{J_{2D}}$ - J_1 Plane for Triaxial Compression (TC) Test, ($\theta = 30^0$), for Sandstone.

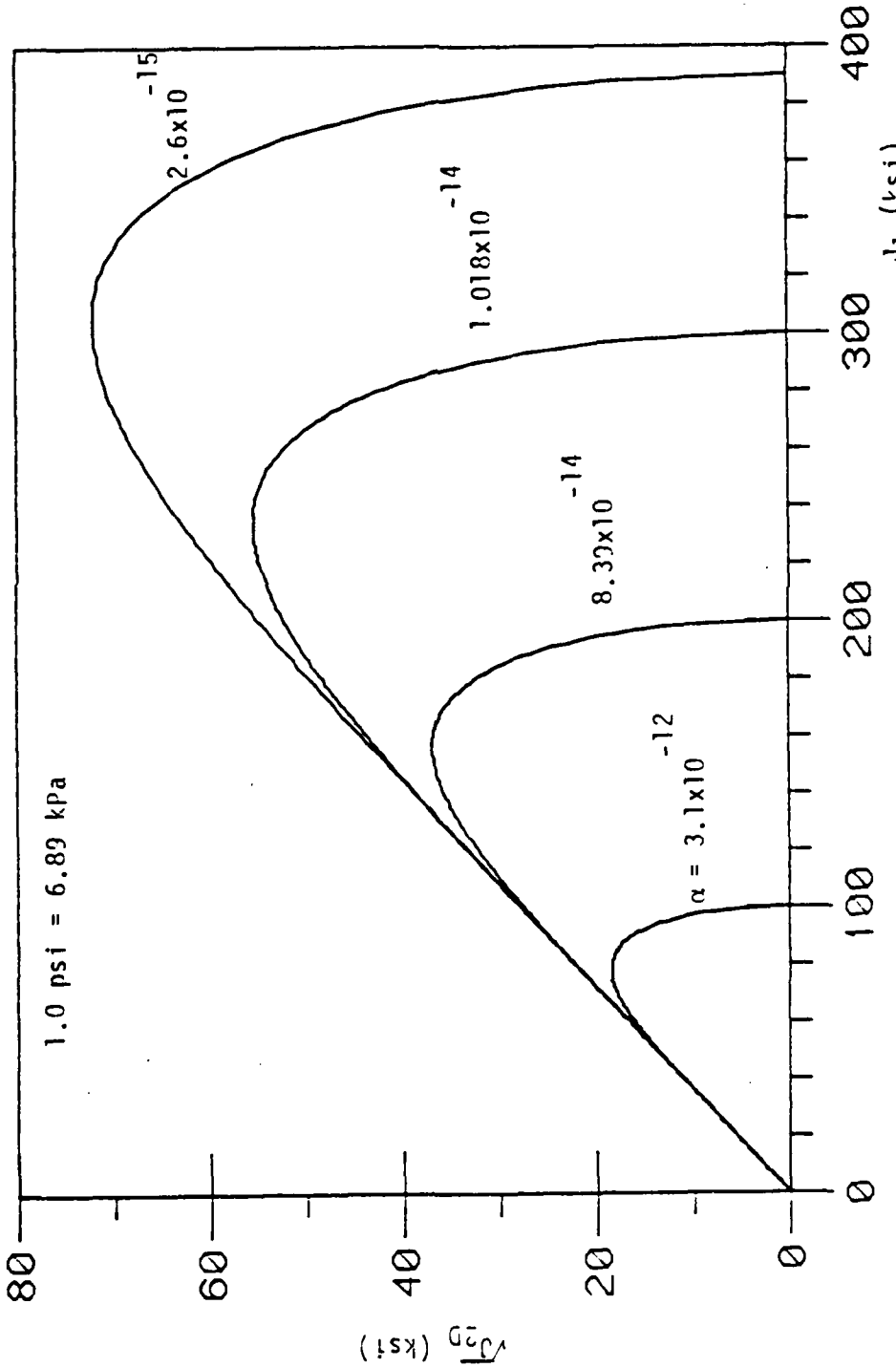

Figure 7.72. Predicted Ultimate and Pre-Ultimate Envelopes in $\sqrt{J_{2D}}$ - J_1 Plane for Simple Shear (SS) Test, ($\theta = 0^0$, for Sandstone.

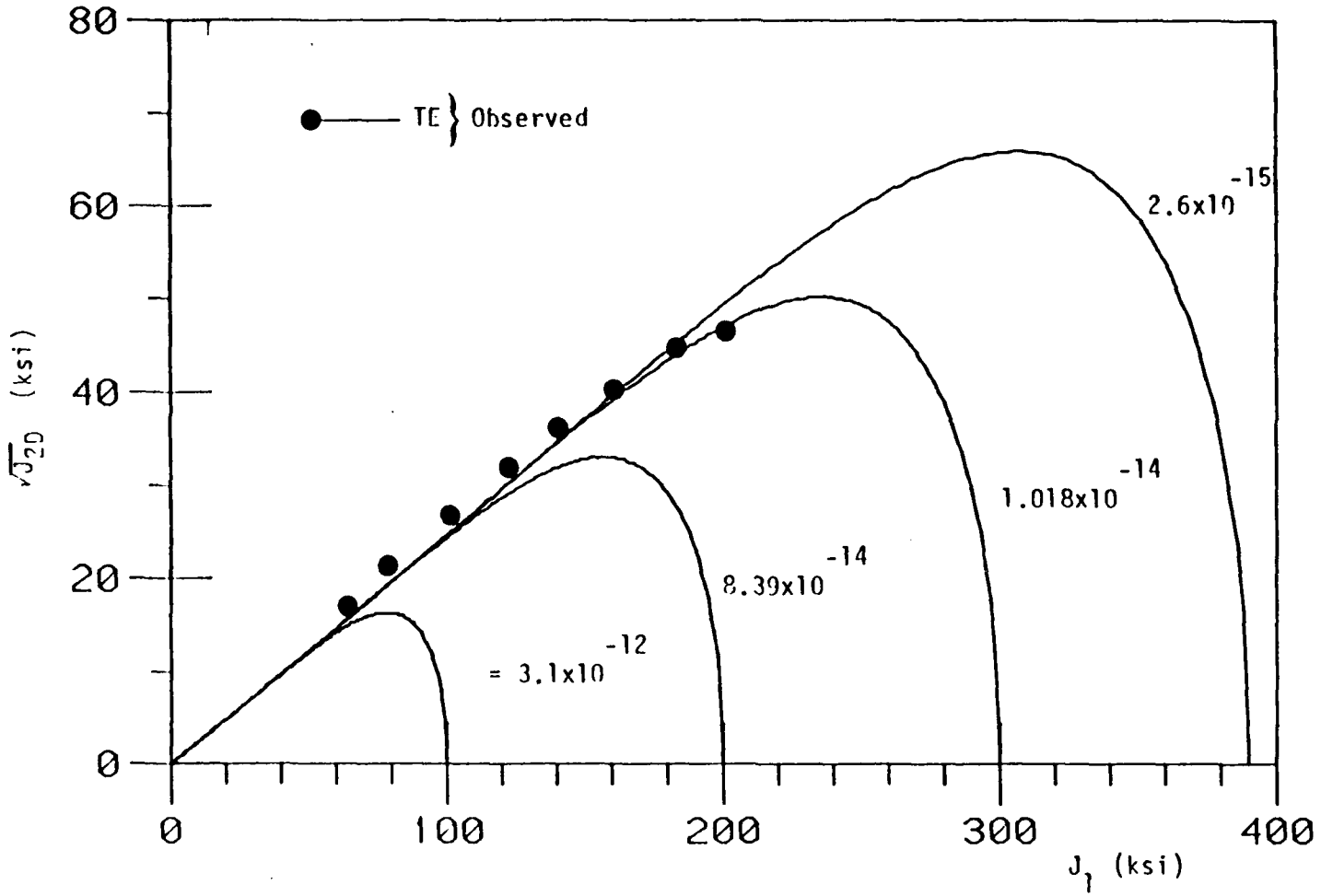

Figure 7.73. Predicted Ultimate and Pre-Ultimate Envelopes in $\sqrt{J_{2D}}$ - J_1 Plane for Triaxial Extension (TE) Test, (θ = 30°), for Sandstone.

is evident from these Figures that the proposed model predictions compare well with the experimental data.

7.6.2 Octahedral and Triaxial Planes

Figures 7.74 and 7.75 show the comparison of the predictions and observations of ultimate envelopes for octahedral and triaxial planes, respectively.

Predicted ultimate envelope on π-plane also is shown in Fig. 7.75.

7.6.3 Strength Behavior

Based on the predicted envelope, Fig. 7.75, predicted values of the uniaxial compressive strength, f_{cu}, equi-biaxial compressive strength, f_{cb}, and uniaxial tensile, f_t, can be calculated. These predicted strengths are:

$$f_{cu} = 10.48 \text{ ksi } (72.23 \text{ MPa})$$
$$f_{cb} = 13.58 \text{ ksi } (93.61 \text{ MPa}) \qquad (7.18)$$
$$f_t = 0.411 \text{ ksi } (-2.83 \text{ MPa}) \qquad \text{(Compression Positive)}$$

the values of f_{cu} and f_t compared to unconfined compression strength, f'_c, and tensile strength, f_t, based on tests with cylindrical specimens of 3x6 in. (7.62x15.24 cm) and Eq. (6.47), respectively. These values are:

$$f'_c = 9.804 \text{ ksi } (67.60 \text{ MPa}) \qquad (7.19)$$
$$f_t = 0.411 \text{ ksi } (-2.83 \text{ MPa}) \qquad \text{(Compression Positive)}$$

It is evident from Eqs. (12.18 and (12.19) that the predictions

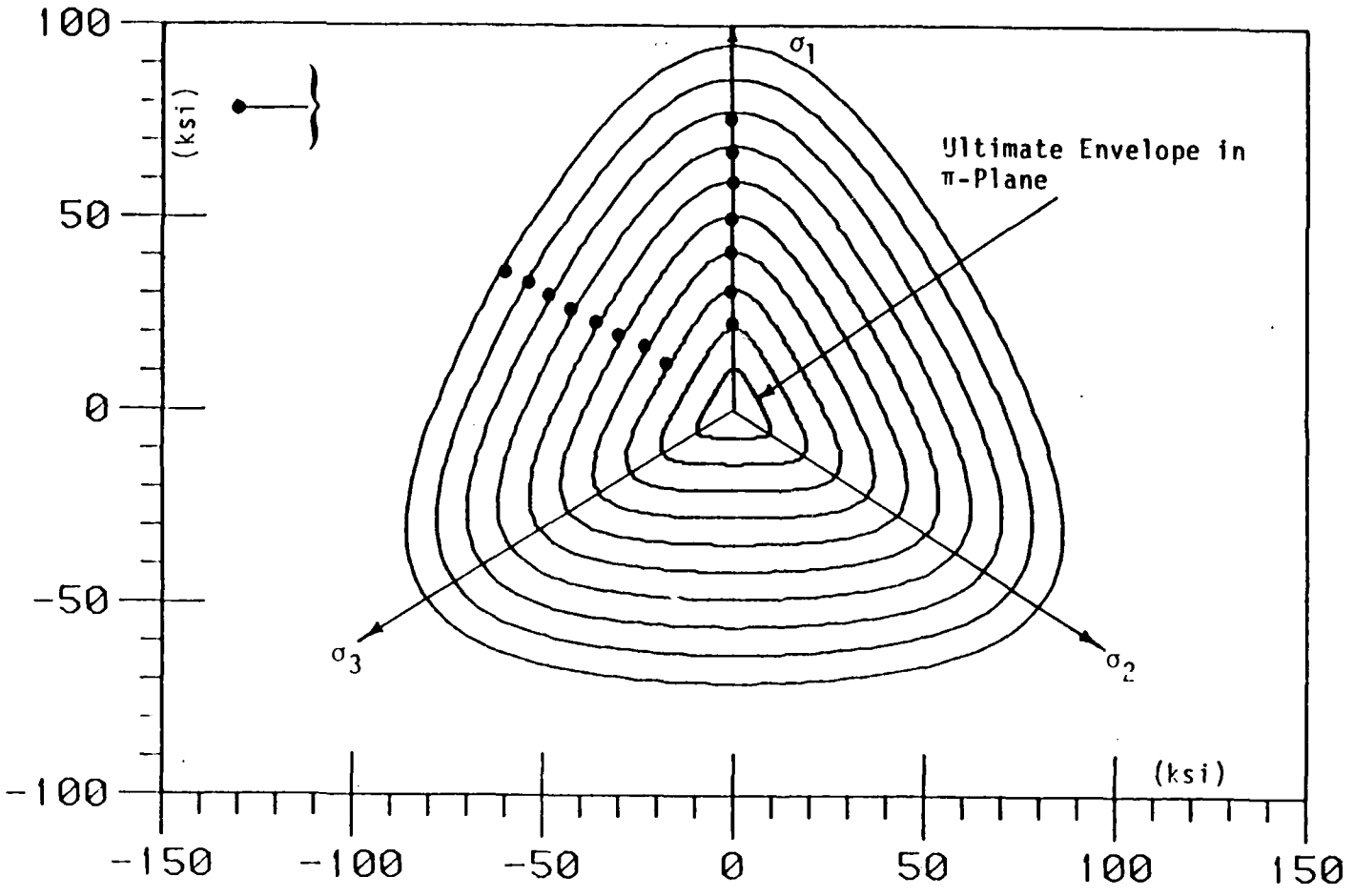

Figure 7.74. Variation of Cross-Sectional Shapes in Octahedral Planes (J_1 = 1.25,20,40,60,80,100,120,140,160 and 200 ksi), 1.0 psi = 6.89 kPa), for Predicted Ultimate Surface for Sandstone.

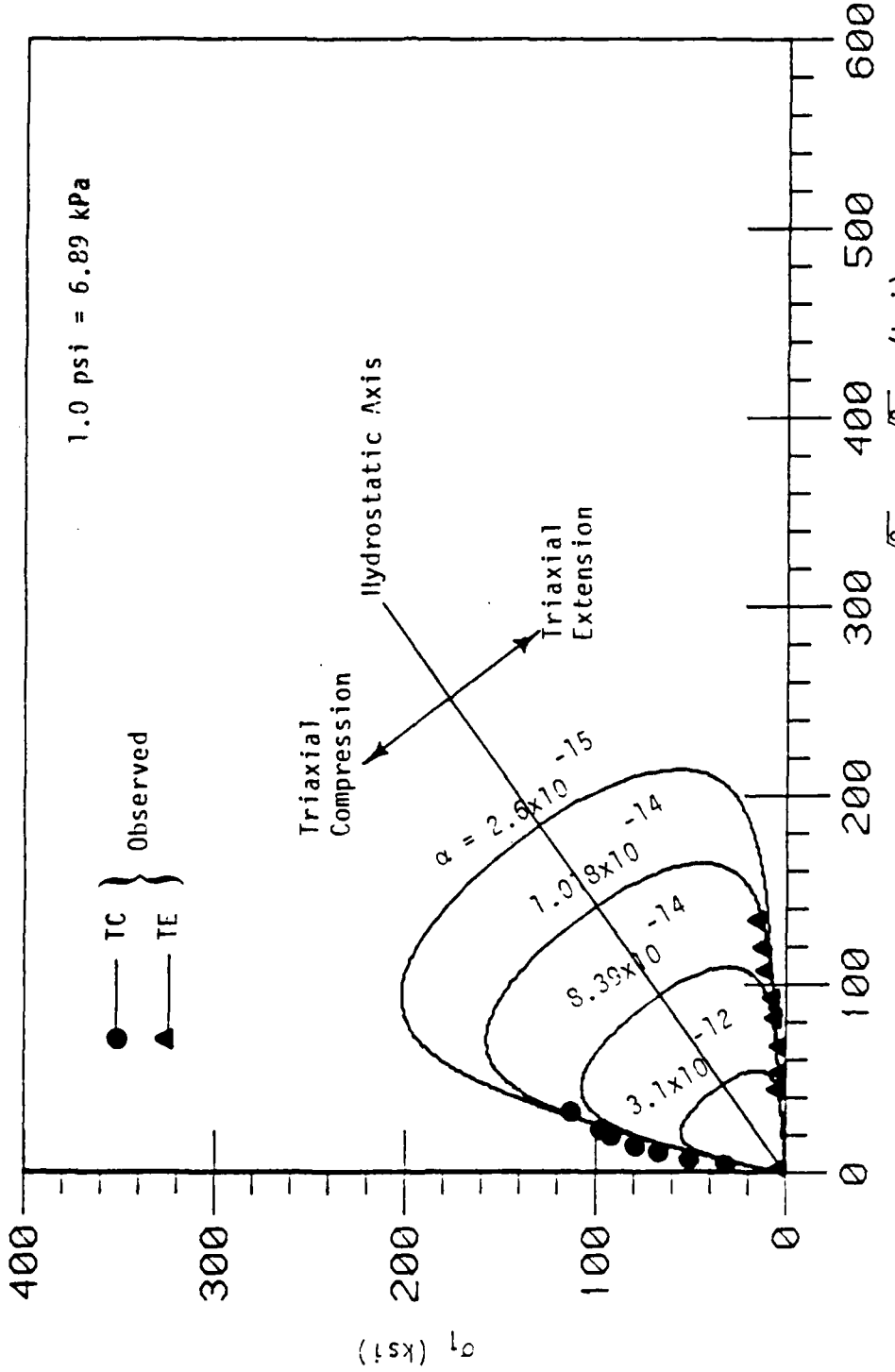

Figure 7.75. Predicted Ultimate and Pre-Ultimate Envelopes in Triaxial Plane for Sandstone.

compare very well with the experimental results.

Based on the predicted ultimate envelope, Fig. 7.74 predicted values of the J_{2D} on the π-plane for TC ($\Theta = -30^{o}$), SS ($\Theta = 0^{o}$) and TE ($\Theta = 30^{o}$) can be calculated. These values are:

$$(\sqrt{J_{2D}})_{TC} = 0.865 \text{ ksi } (5.96 \text{ MPa})$$

$$(\sqrt{J_{2D}})_{SS} = 0.603 \text{ ksi } (4.16 \text{ MPa}) \qquad (7.21)$$

$$(\sqrt{J_{2D}})_{TE} = 0.523 \text{ ksi } (3.61 \text{ MPa})$$

Ratios of Eqs. (7.21), on the π-plane, can be expressed as

$$R_1 = \frac{(J_{2D})_{TC}}{(J_{2D})_{TE}} = 1.65$$

$$R_2 = \frac{(J_{2D})_{SS}}{(J_{2D})_{TE}} = 1.15 \qquad (7.22)$$

$$R_3 = \frac{(J_{2D})_{TC}}{(J_{2D})_{SS}} = 1.43$$

It is seen from Eqs. (7.21) and (7.22) that the predicted ultimate envelope has the required shape, a triangular section with rounded corner in the π-plane.

7.6.4 Stress-Strain Behavior for Tests Used for Finding Material Constants

Figure 7.76 shows the comparison between predicted and constructed (knowing E and ν of sandstone and based on theory of elasticity) stress-strain response curves for hydrostatic compression (HC) test. It is seen from Fig. 7.76 that the prediction from model compared very well with the constructed result.

Figures 7.77 through 7.79 show the comparison of predictions and observations for the stress-strain responses for two compression tests (strain control test) and one extension test (strain control test). Initial confining pressures for compression tests are 28.45 and 56.899 ksi (196.16 and 292.32 MPa). For the extension test, the initial confining pressure is 28.45 ksi (196.16 MPa). It is evident from Figs. 7.77 through 7.79 that the predictions from the proposed model compare very well with experimental results.

7.6.5 Volumetric Responses Behavior

Figures 7.80 through 7.82 show the compression of predictions and observations for $\varepsilon_v - \varepsilon_1$ responses for two compression (σ_0 = 28.45 and 56.899 ksi) tests and one extension (σ_0 = 28.45 ksi). It is evident from these plots that the predictions compare well with the experimental data.

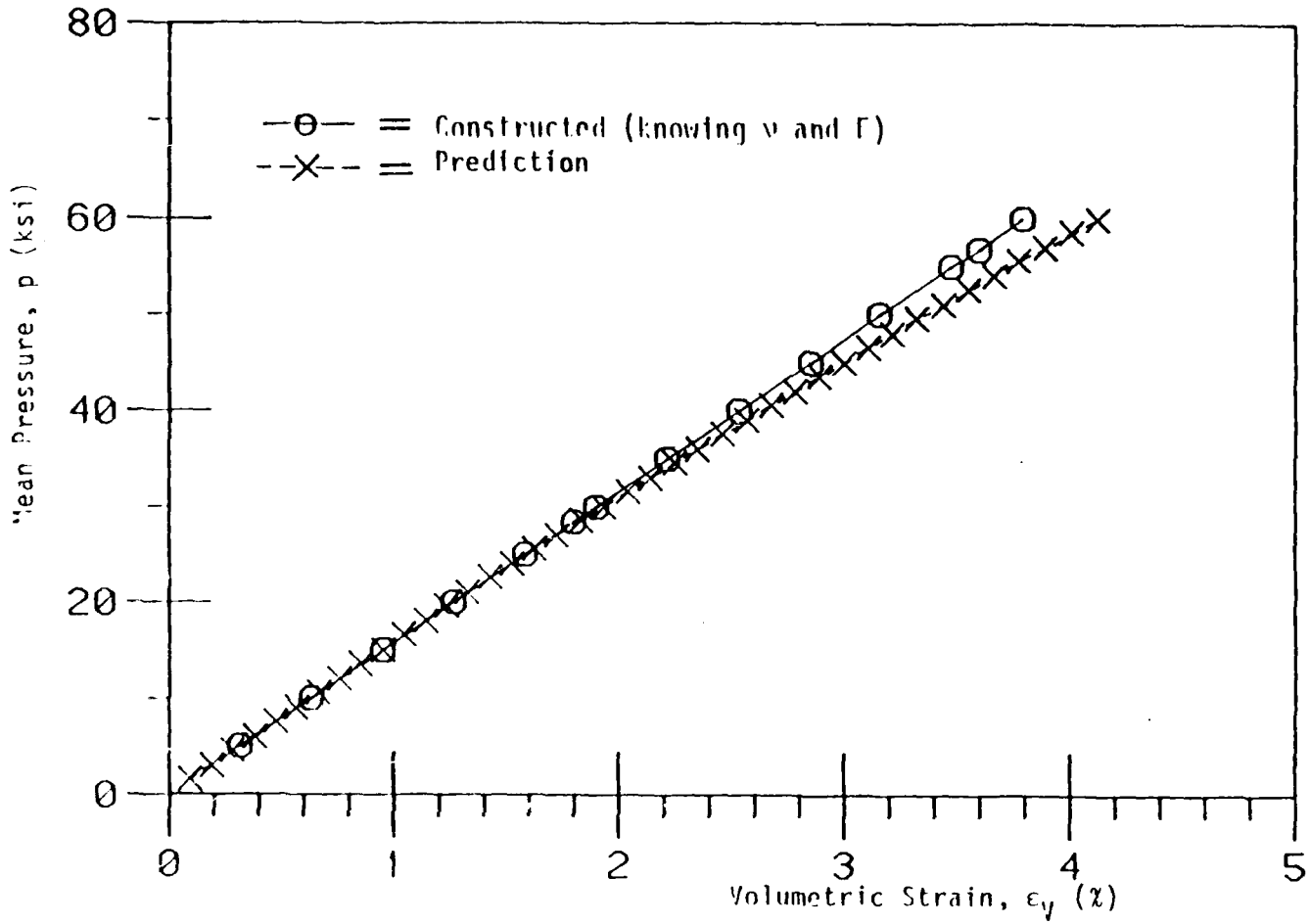

Figure 7.76. Comparison of Stress-Strain Responses of Hydrostatic Compression (HC) Test for Sandstone (σ_o = 8.0 ksi), (1.0 psi = 6.89 kPa).

AD-A174 451 CONSTITUTIVE MODELLING OF CONCRETE AND ROCKS UNDER MULTIAXIAL COMPRESSIVE (U) ARIZONA UNIV TUCSON DEPT OF CIVIL ENGINEERING M R SALAMI ET AL 04 SEP 86 5/5

UNCLASSIFIED AFOSR-TR-86-2014 AFOSR-83-0256 F/G 8/7 NL

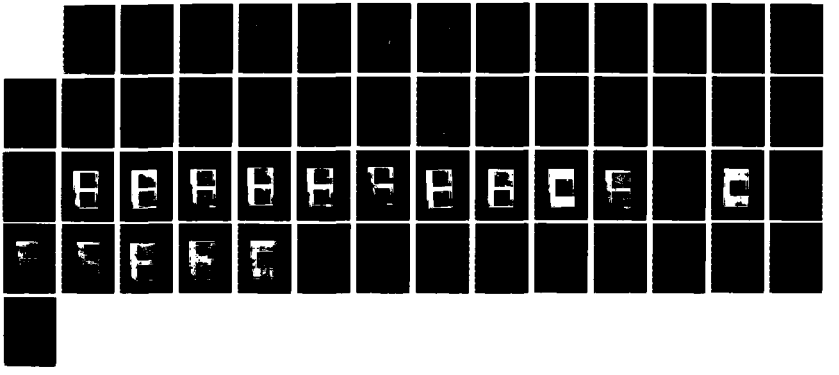

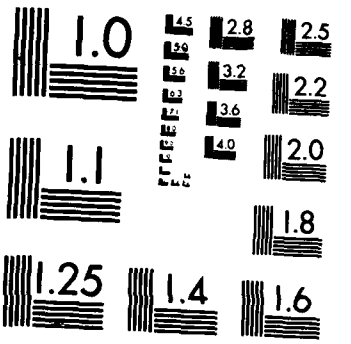

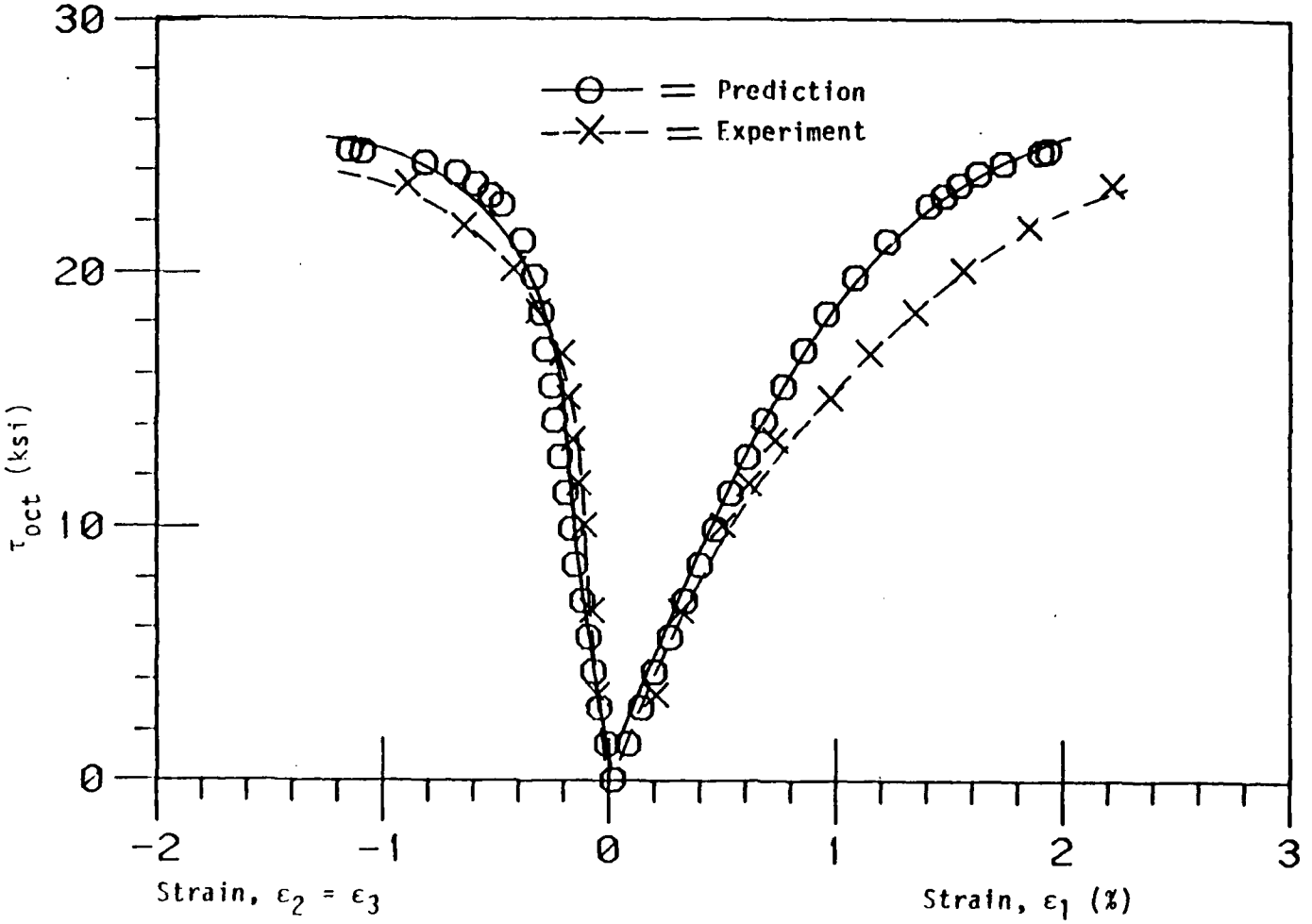

Figure 7.77. Comparison of Stress-Strain Responses of Triaxial Compression (Strain Control) Test for Sandstone (σ_o = 28.45 ksi), (1.0 psi = 6.89 kPa).

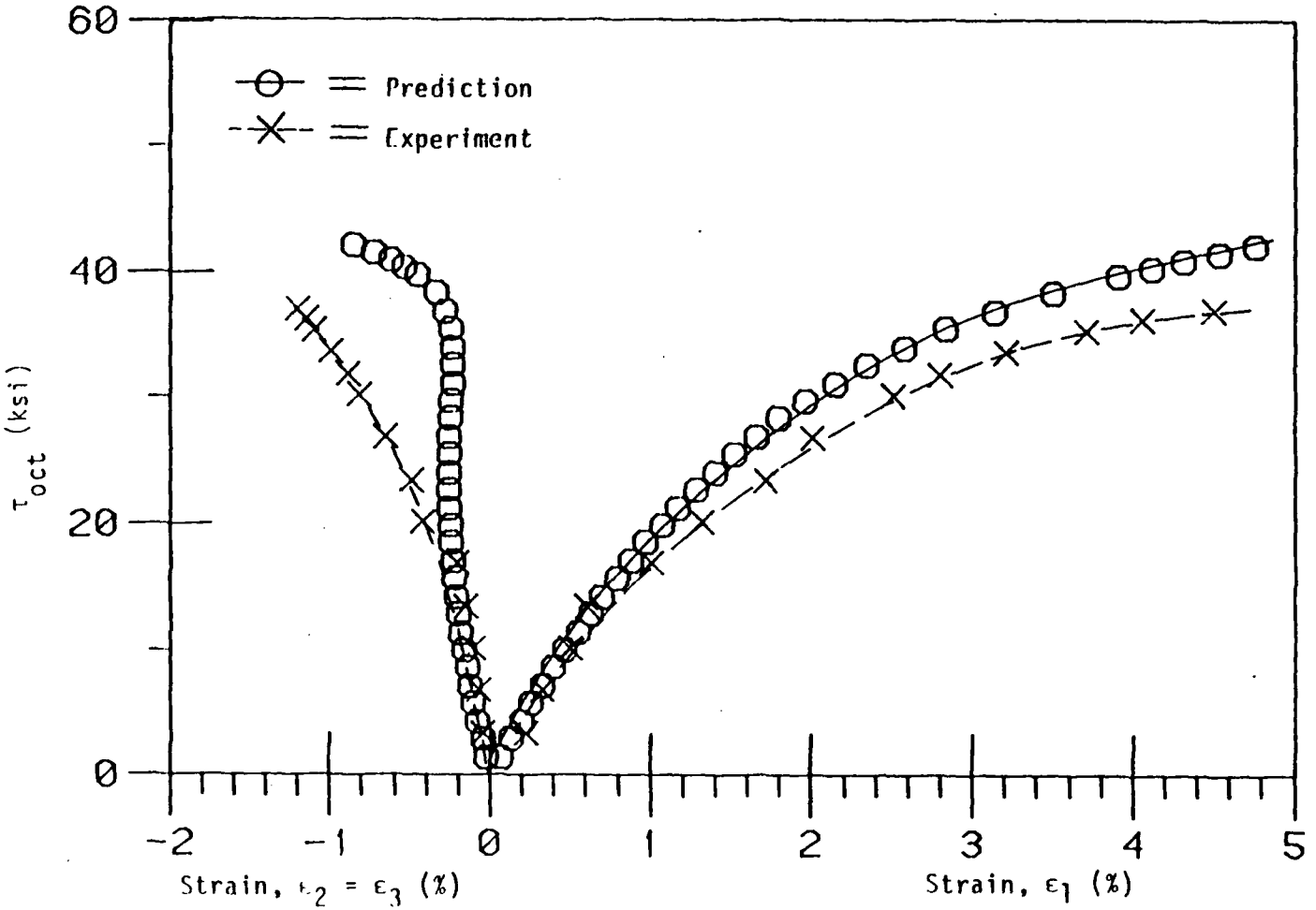

Figure 7.78. Comparison of Stress-Strain Responses of Triaxial Compression (Strain Control) Test for Sandstone (σ_o = 56.899 ksi), (1.0 psi = 6.89 kPa).

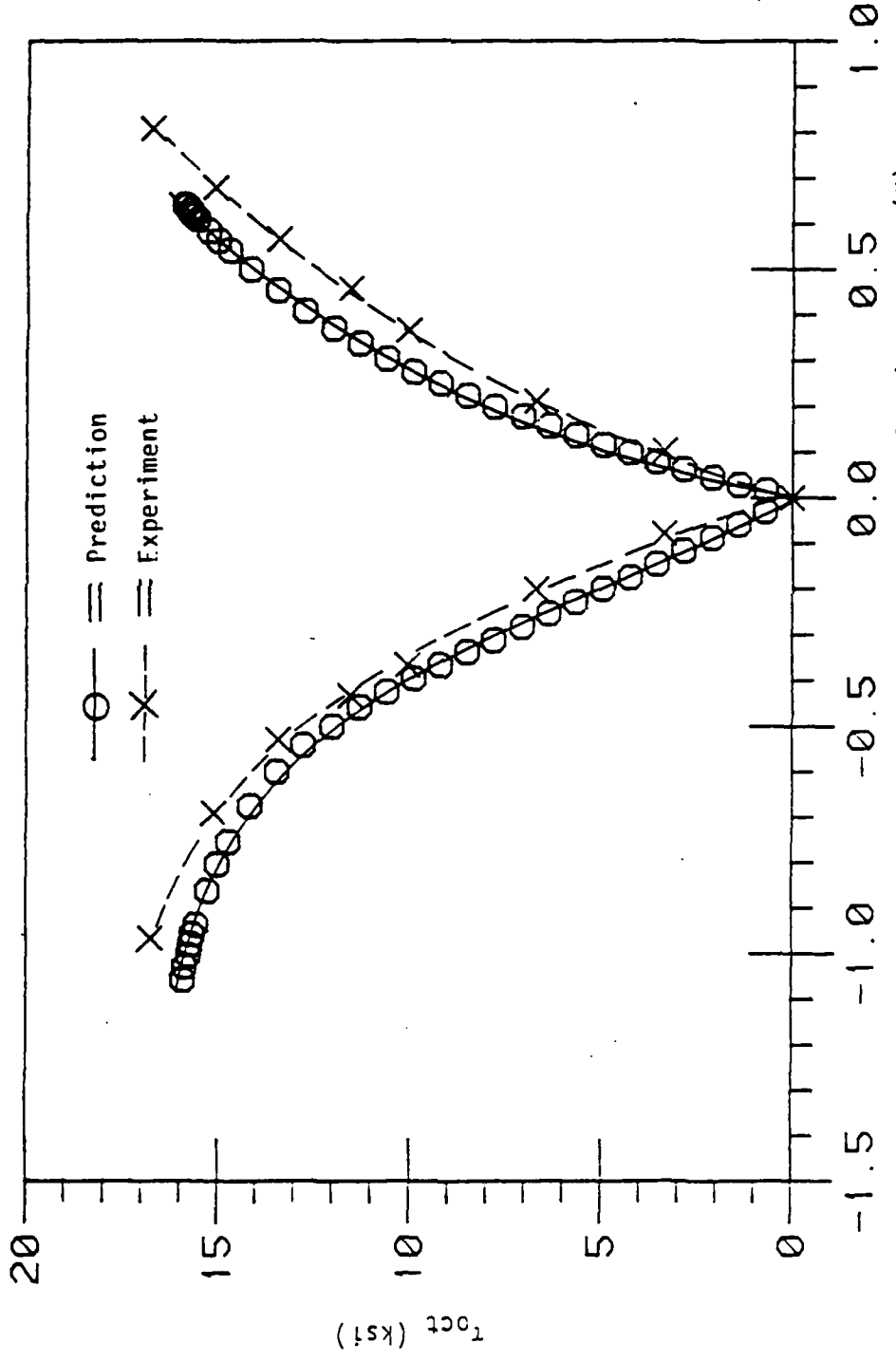

Figure 7.79. Comparison of Stress-Strain Responses of Triaxial Extension (Strain Control), Test for Sandstone (σ_o = 28.45 ksi), (1.0 psi = 6.89 kPa).

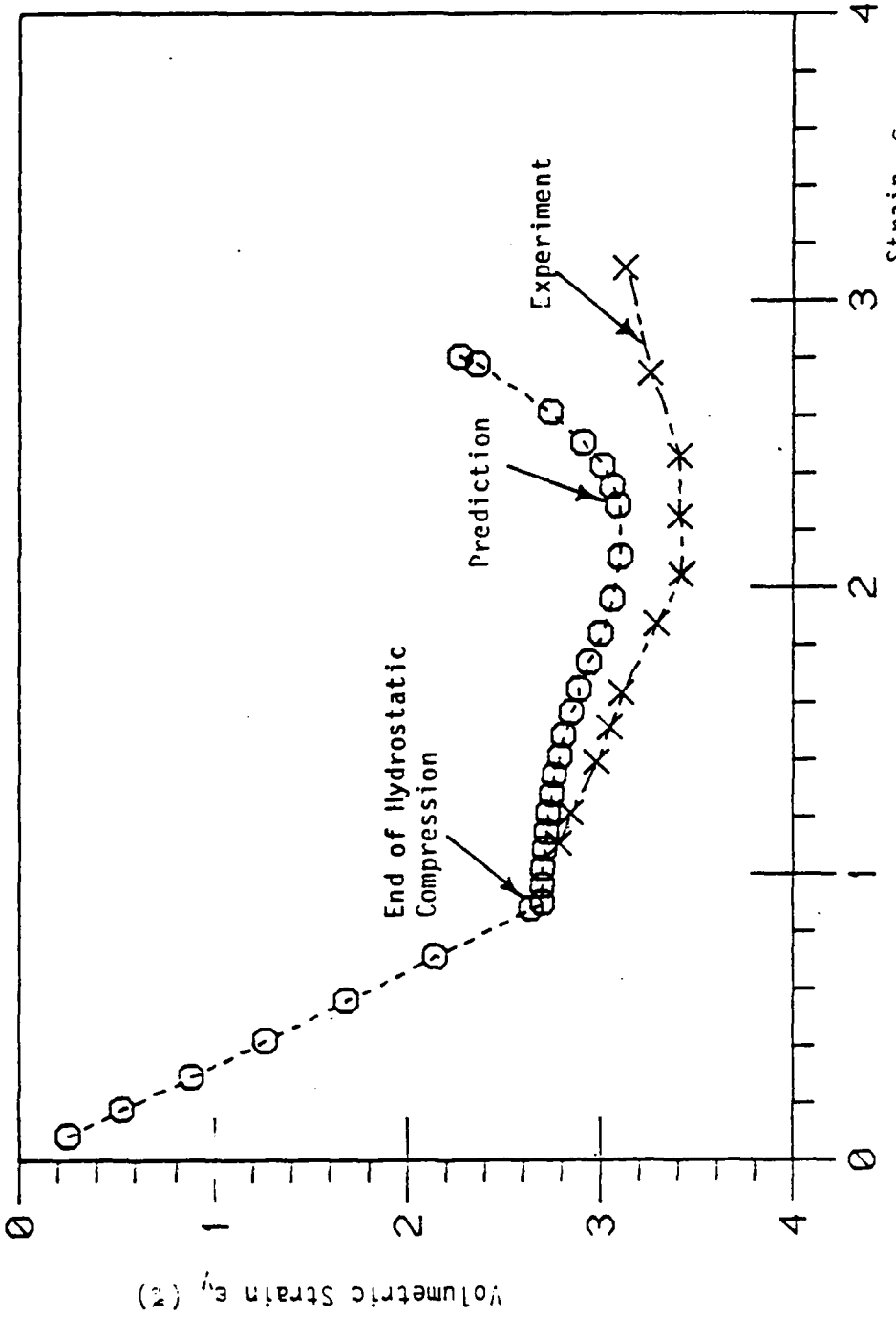

Figure 7.80. Comparison of Volumetric Response of Triaxial Compression (Strain Control) Test for Sandstone (σ_0 = 28.45 ksi), (1.0 psi = 6.89 kPa).

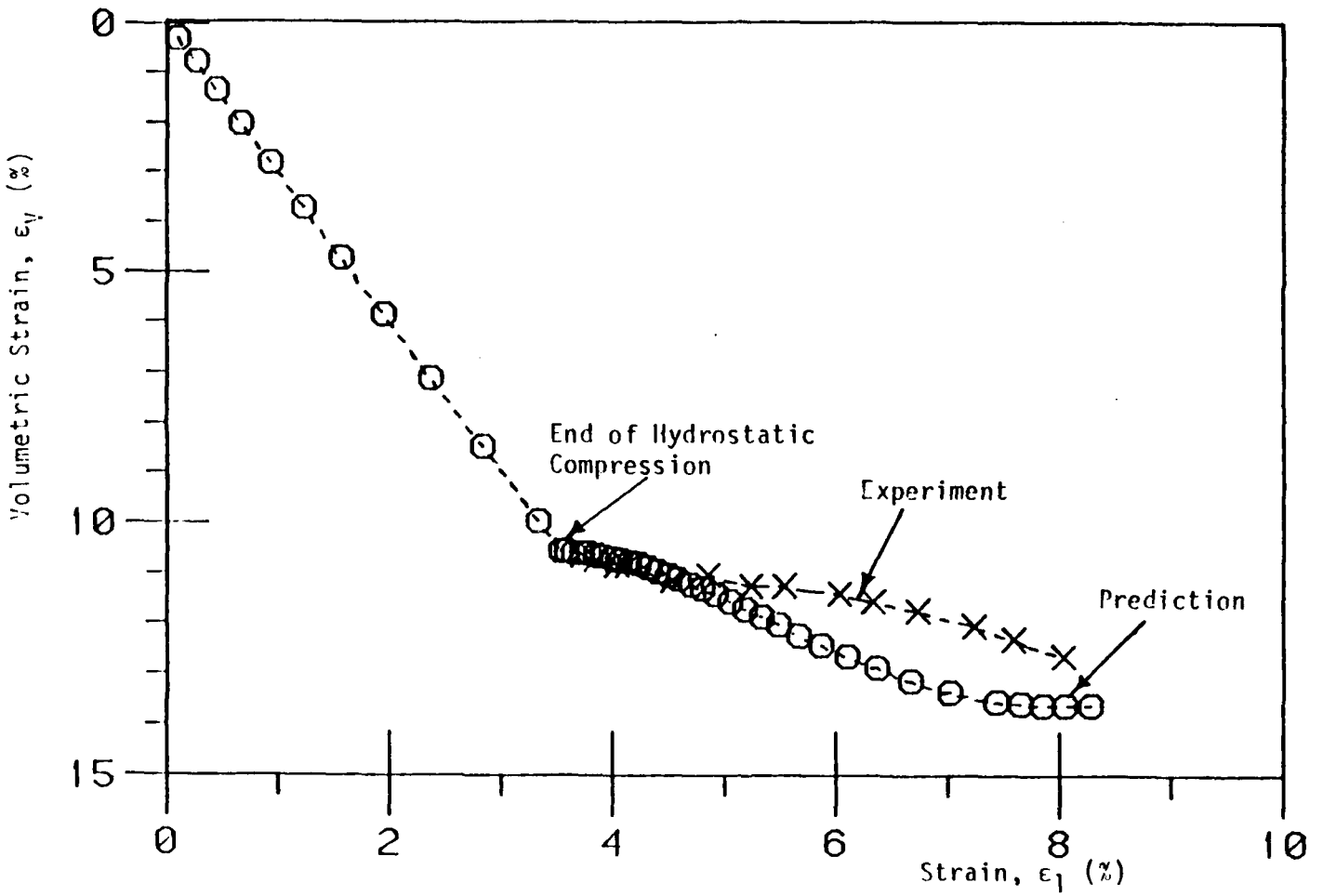

Figure 7.81. Comparison of Volumetric Response of Triaxial Compression (Strain Control) Test for Sandstone (σ_o = 56.899 ksi), (1.0 psi = 6.89 kPa).

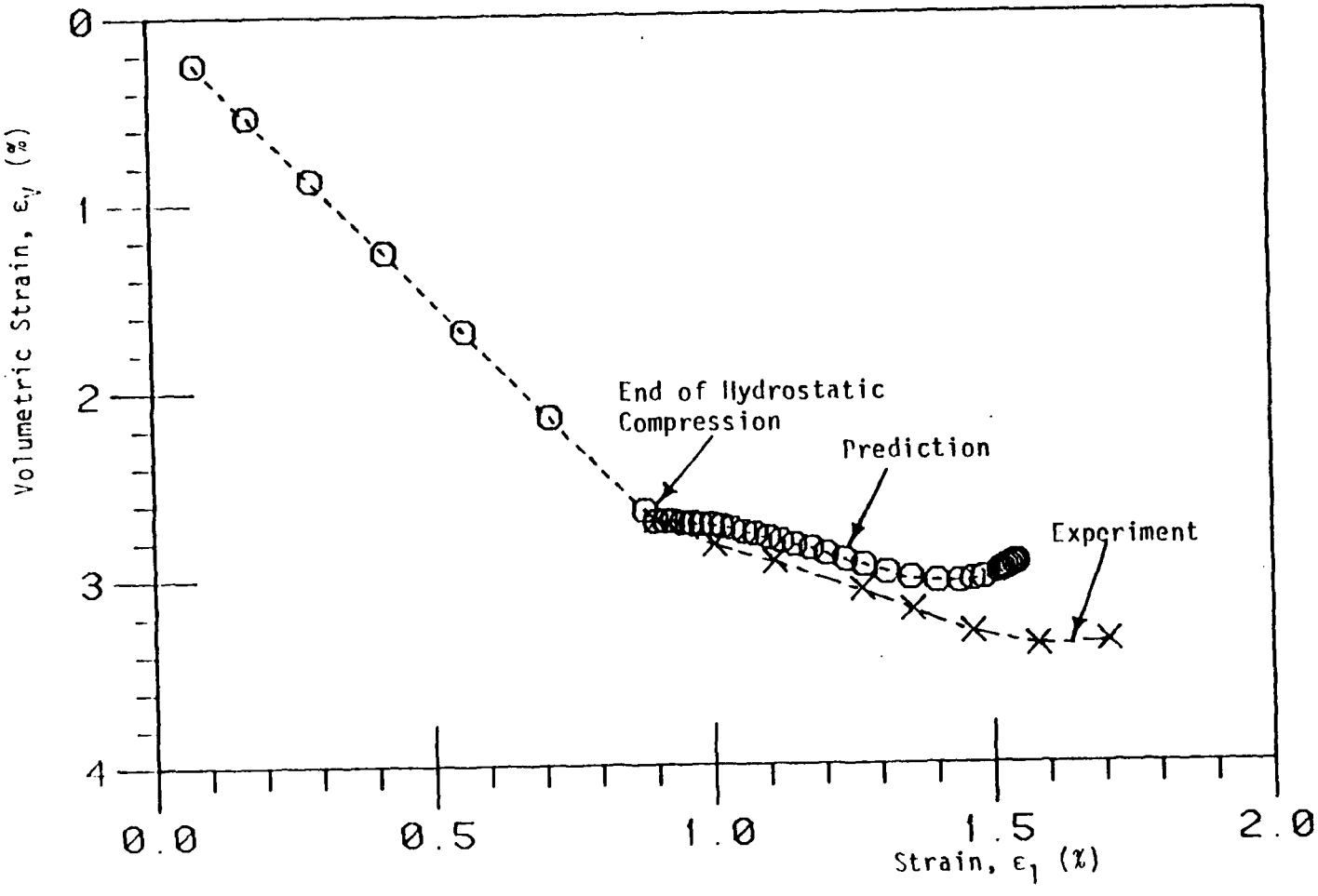

Figure 7.82. Comparison of Volumetric Response of Triaxial Extension (Strain Control) Test for Sandstone (σ_o = 28.45 ksi), (1.0 psi = 6.89 kPa).

The material constants for Westerly Granite are given in section 6.10. The description of the Westerly Granite is presented in Chapter 6. Ultimate envelopes and strengths are predicted and compared with the experimental results.

7.7.1 $\sqrt{J_{2D}}$ - J_1 Plane

Figures 7.83 through 7.85 show the comparison of the predictions and observations of ultimate envelopes, in $\sqrt{J_{2D}}$ - J_1 plane, (CTC), (SS) and (RTE) tests, respectively. It is evident from Fig. 7.83 through 7.85 that the model predictions compare well with the experimental data.

7.7.2 Octahedral and Triaxial Planes

Figures 7.86 and 7.87 show the comparison of the predictions and observations of ultimate envelopes for octahedral and triaxial planes, respectively. It is seen from these Figs. that the proposed model predictions compare well with the experimental results.

Predicted ultimate envelope on the π-plane also is shown in Fig. 7.87.

7.7.3 Strength Behavior

Based on the predicted envelope, Fig. 7.87 predicted values of the uniaxial compressive strength, f_{cu}, equi-biaxial

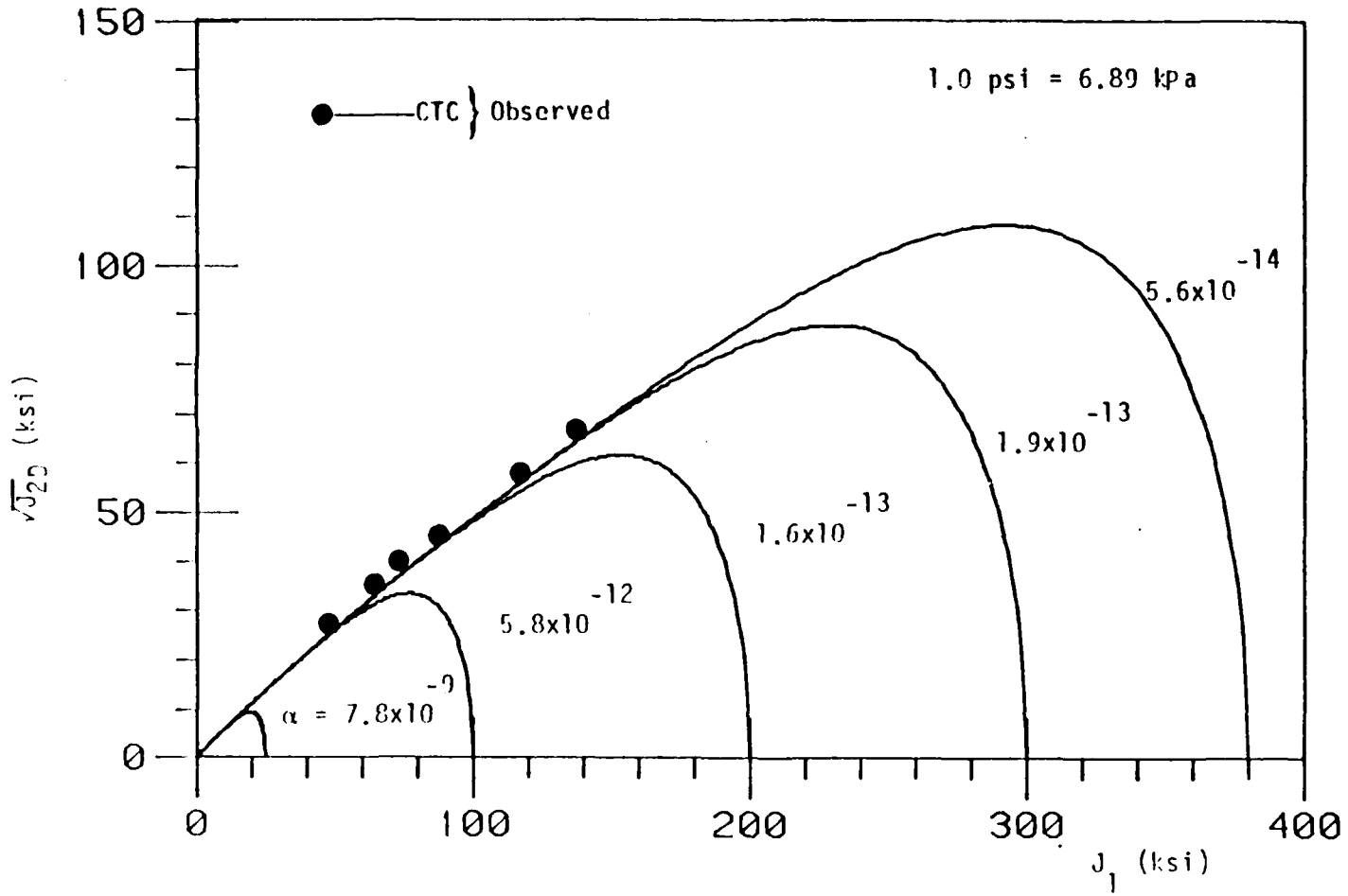

Figure 7.83. Predicted Ultimate and Pre-Ultimate Envelopes in $\sqrt{J_{2D}}$ - J_1 Plane for Conventional Triaxial Compression (CTC) Test, ($\theta = -30^{o}$), for Westerly Granite.

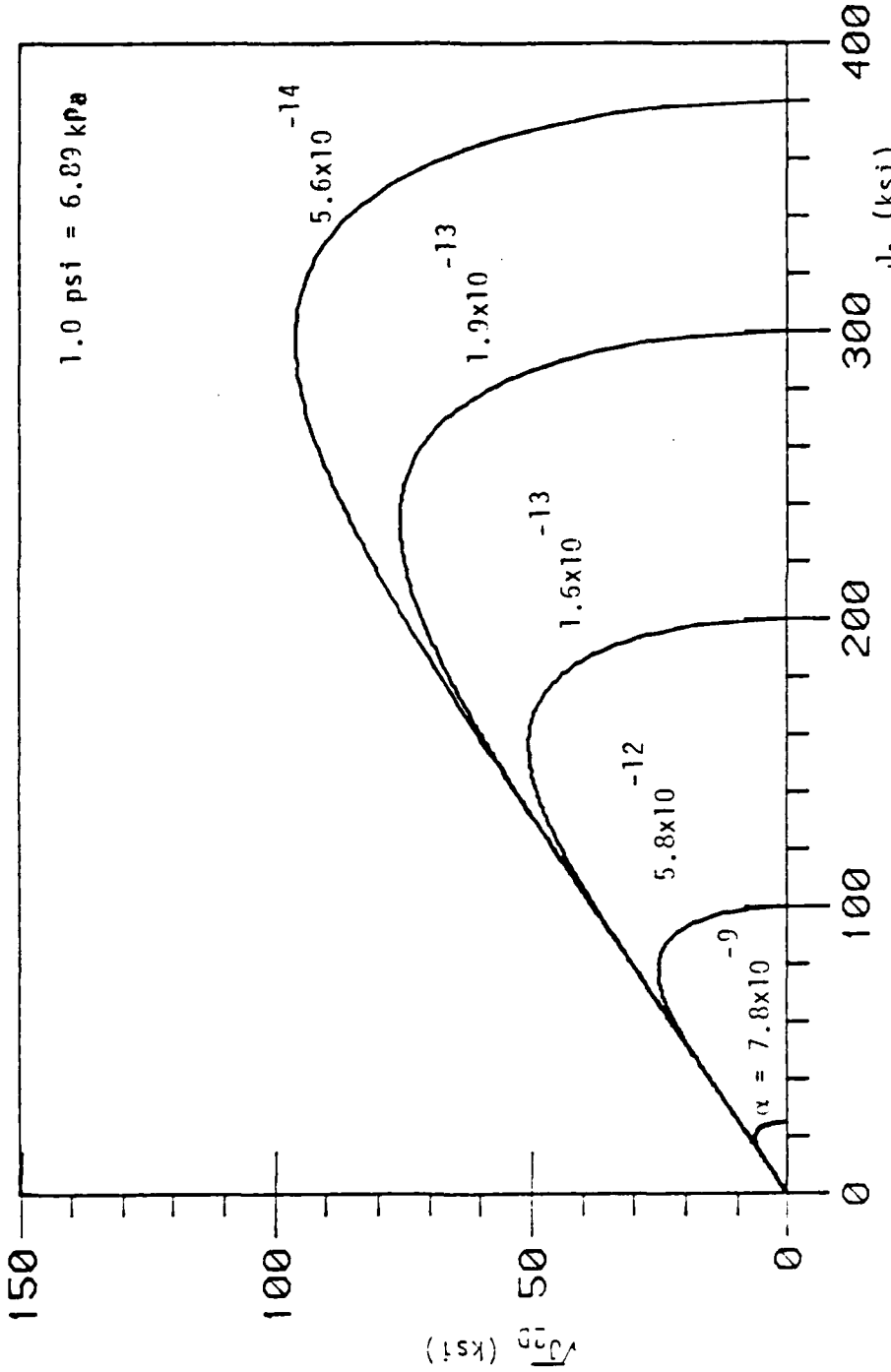

Figure 7.84. Predicted Ultimate and Pre-Ultimate Envelopes in $\sqrt{J_{2D}}$ - J_1 for Simple Shear (SS) Test, ($\theta = 0^0$), for Westerly Granite.

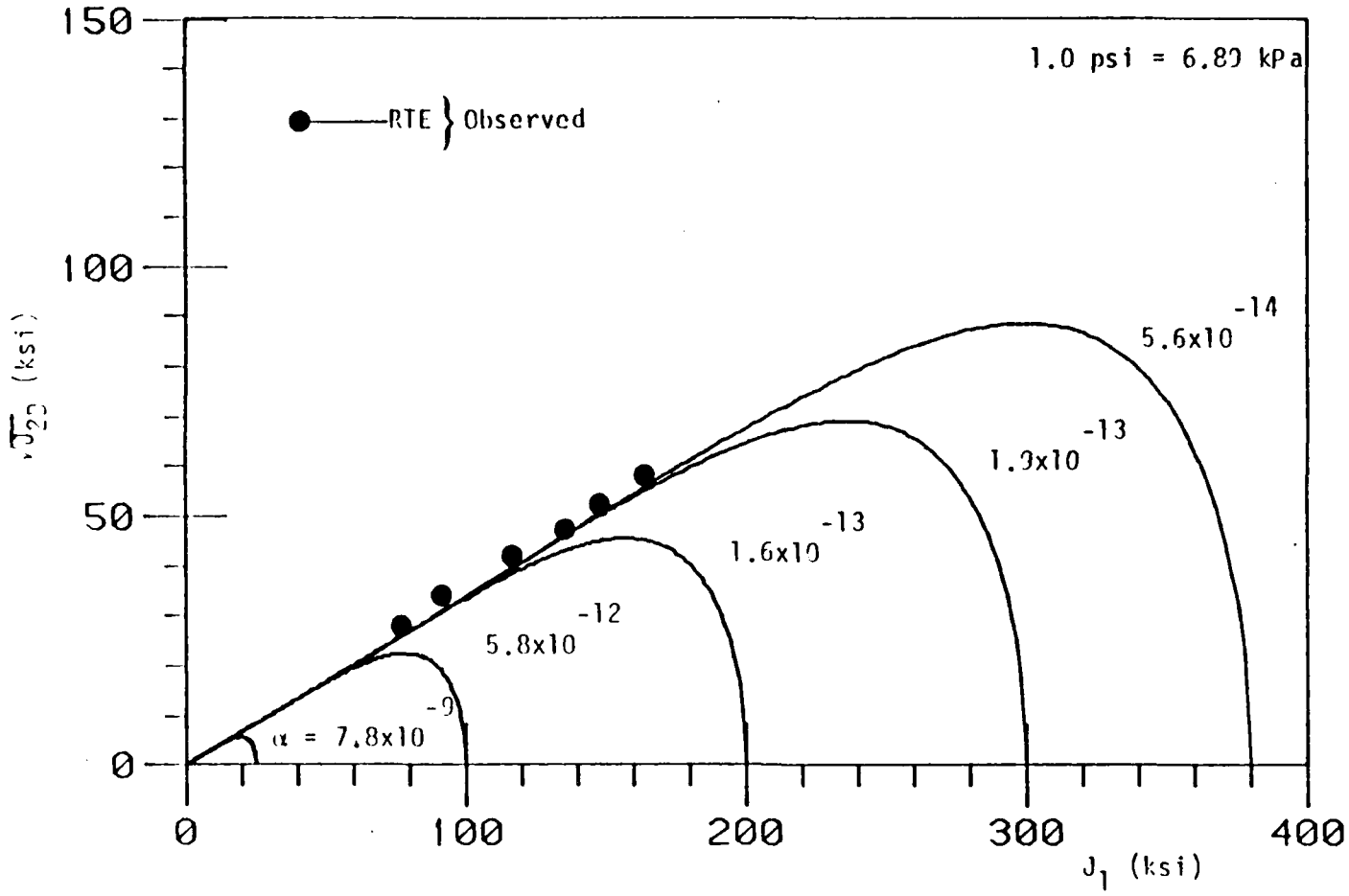

Figure 7.85. Predicted Ultimate and Pre-Ultimate Envelopes in $\sqrt{J_{2D}} - J_1$ Plane for Reduced Triaxial Extension (RTE) Test, ($\theta = 30^0$), for Westerly Granite.

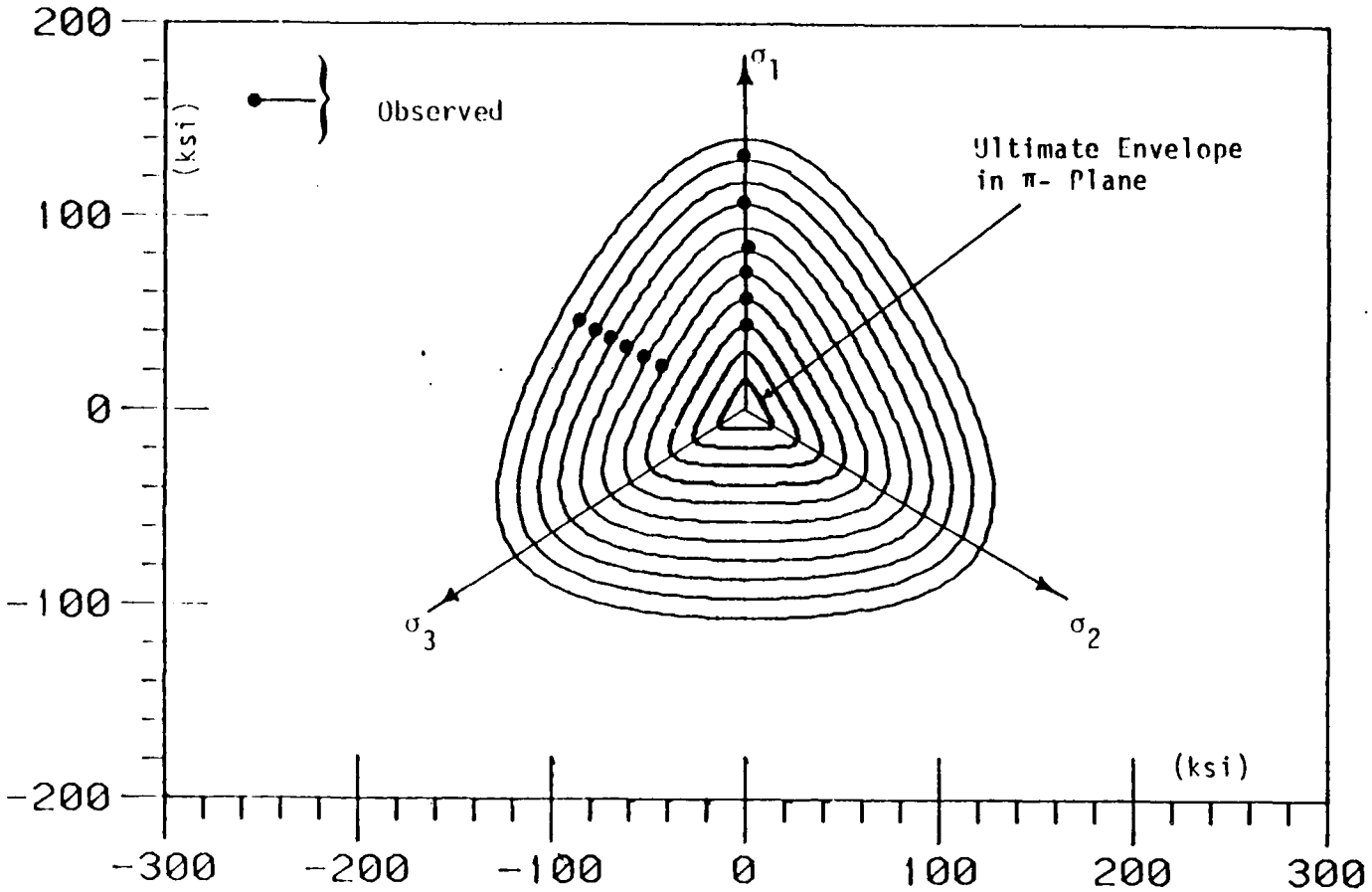

Figure 7.86. Variation of Cross-Sectional Shapes in Octahedral Planes (J_1 = 5.7,20,40,60,80,100,120,140,160,180 and 200 ksi), 1.0 psi = 6.89 kpa) for Predicted Ultimate Surface for Westerly Granite.

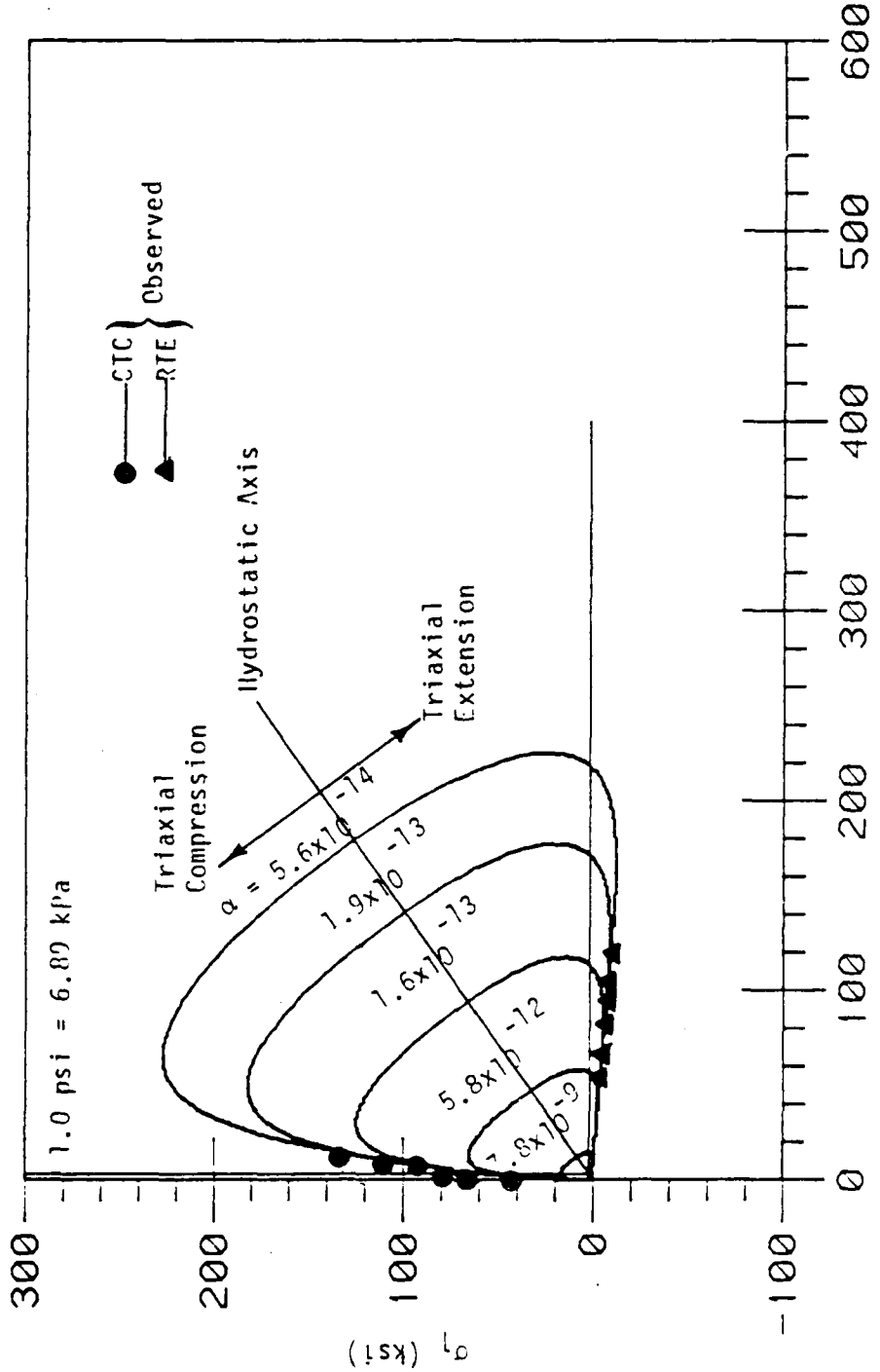

Figure 7.87. Predicted Ultimate and Pre-Ultimate Envelopes in Triaxial Plane for Westerly Granite.

compressive strength, f_{cb}, and uniaxial tensile, f_t, can be calculated. These predicted strengths are:

$$f_{cu} = 46.15 \text{ ksi } (318.23 \text{ MPa})$$

$$f_{cb} = 153.66 \text{ ksi } (1059.48 \text{ MPa}) \qquad (7.23)$$

$$f_t = -1.876 \text{ ksi } (-12.94 \text{ MPa}) \qquad \text{(Compression Positive)}$$

The values of f_{cu} and f_t compared to unconfined compression strength, f'_c, and tensile strength, f_t, based on tests with cylindrical specimens of 0.63x1.97 in. (1.6x5.0 cm) and Eq. (6.46), respectively. These values are:

$$f'_c = 42.698 \text{ ksi } (294.4 \text{ MPa}) \qquad (7.24)$$

$$f_t = -1.876 \text{ ksi } (-12.94 \text{ MPa}) \qquad \text{(Compression Positive)}$$

It is evident from Eqs. (7.23) and (7.24) that the predictions compare well with the experimental results. The differences between these predicted and observed strengths may be attributed to effect of specimen types and boundary conditions.

Based on the predicted ultimate envelope, Fig. 7.87, predicted values of the $\sqrt{J_{2D}}$ on the π-plane for CTC ($\theta = -30^o$), SS ($\theta = 0^o$) and RTE ($\theta = 30^o$) can be calculated. These values are:

$$(\sqrt{J_{2D}})_{CTC} = 3.0 \text{ ksi } (20.68 \text{ MPa})$$

$$(\sqrt{J_{2D}})_{SS} = 2.0 \text{ ksi } (13.79 \text{ MPa}) \qquad (7.25)$$

$$(\sqrt{J_{2D}})_{RTE} = 1.732 \text{ ksi } (11.94 \text{ MPa})$$

Ratios of Eqs. (7.25), on the π-plane, can be expressed as

$$R_1 = \frac{(\sqrt{J_{2D}})_{CTC}}{(\sqrt{J_{2D}})_{RTE}} = 1.73$$

$$R_2 = \frac{(\sqrt{J_{2D}})_{SS}}{(\sqrt{J_{2D}})_{RTE}} = 1.15 \qquad (7.26)$$

$$R_3 \quad \frac{(\sqrt{J_{2D}})_{CTC}}{(\sqrt{J_{2D}})_{SS}} = 1.50$$

It is evident from Eqs. (7.25) and (7.26) that the predicted envelope has a triangular section with rounded corner in π-plane.

The material constants for Dunham Dolomite are given in Section 6.11. The description of the Dunham Dolomite is presented in Chapter 6. Ultimate envelopes and strengths are predicted and compared with the experimental results.

7.8.1 $\sqrt{J_{2D}}$ - J_1 Plane

Figures 7.88 through 7.90 show the comparison of the predictions and observations of ultimate envelopes, in $\sqrt{J_{2D}}$ - J_1 plane, (CTC), (SS) and (RTE) tests, respectively. It is seen from these Figs. that the proposed model predictions compare

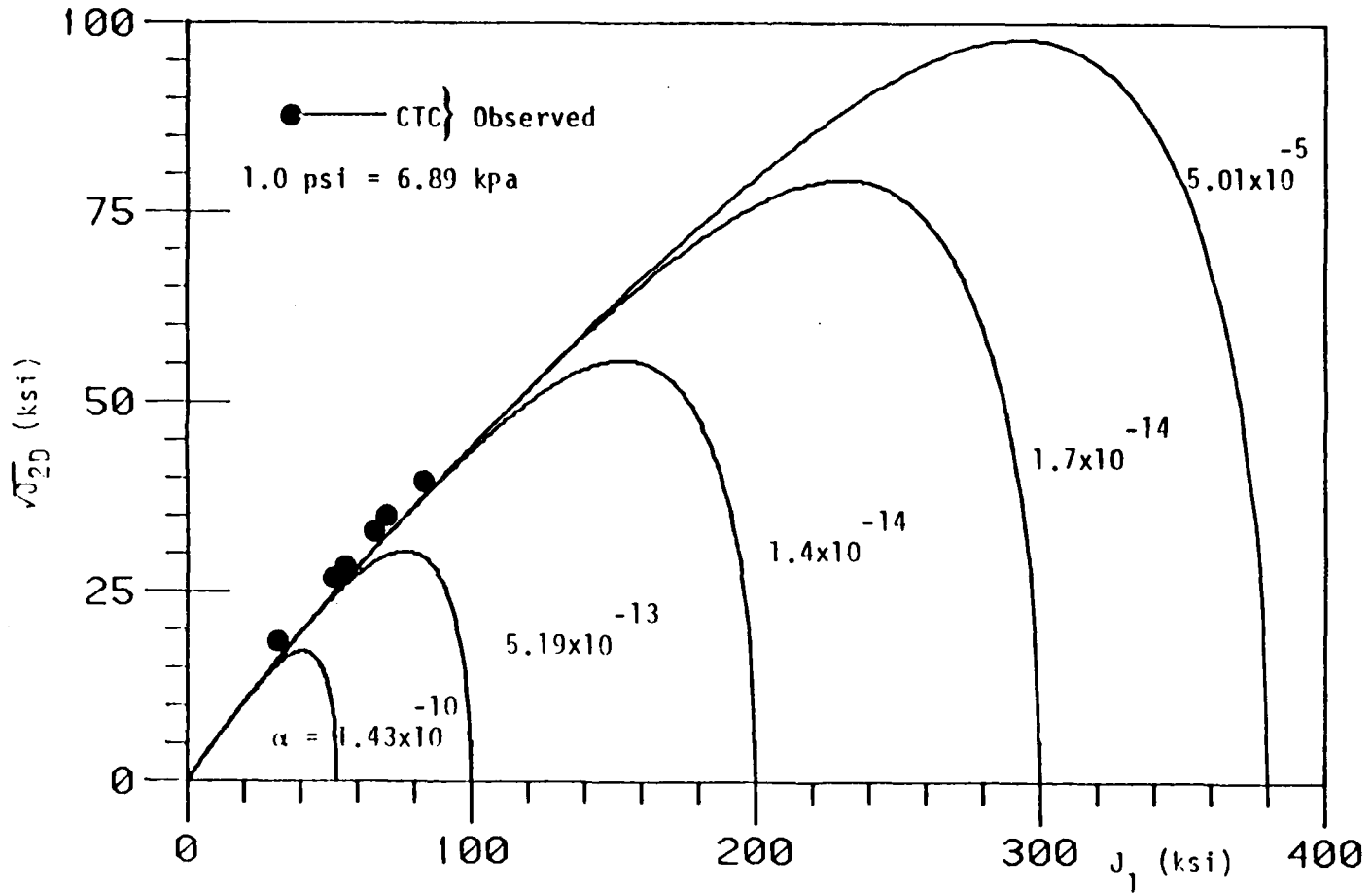

Figure 7.88. Predicted Ultimate and Pre-Ultimate Envelopes in $\sqrt{J_{2D}}$ - J_1 Plane for Conventional Triaxial Compression (CTC) Test, ($\theta = -30^{o}$), for Dunham Dolomite.

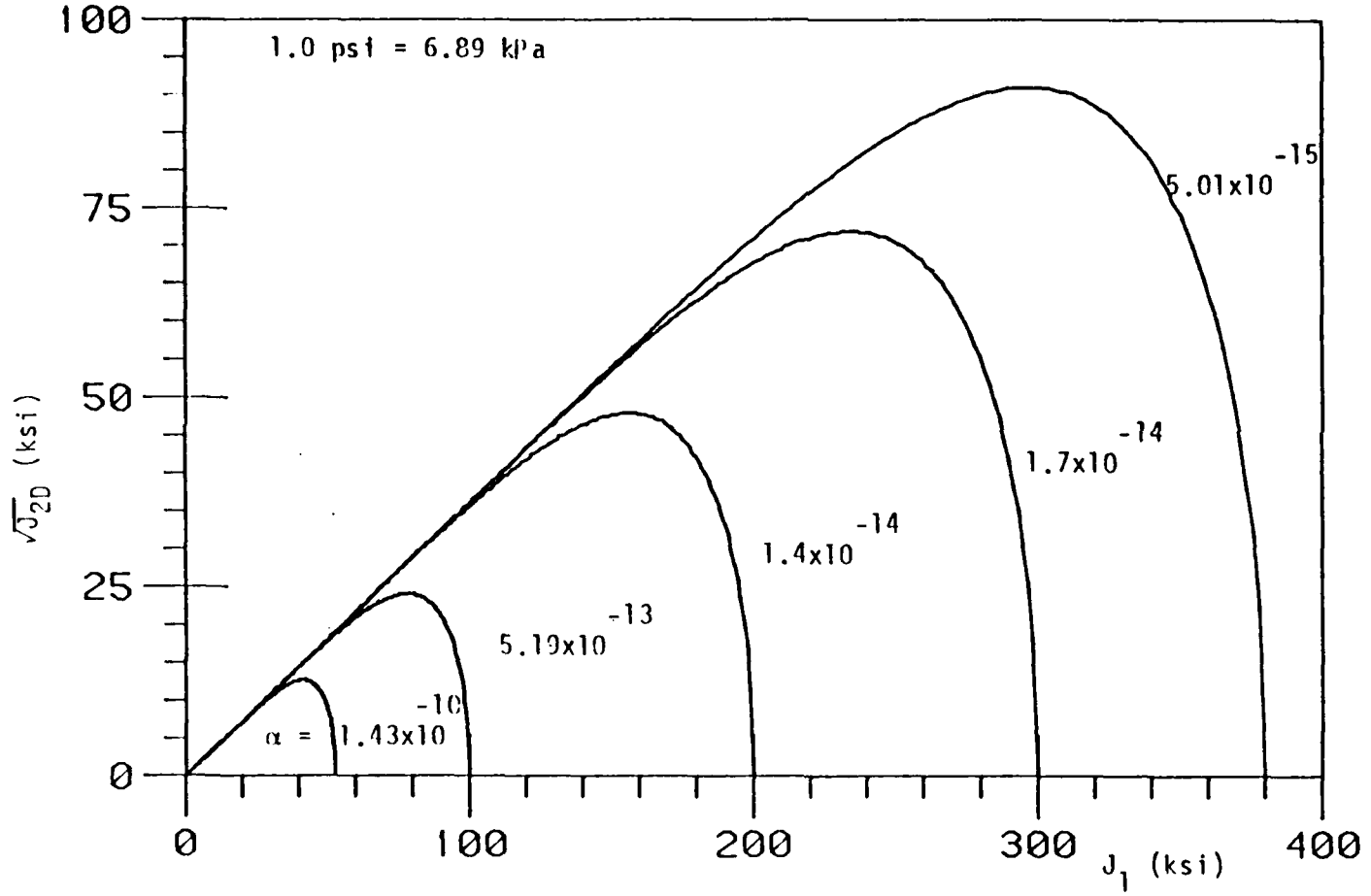

Figure 7.89. Predicted Ultimate and Pre-Ultimate Envelopes in $\sqrt{J_{2D}}$- J_1 Plane for Simple Shear (SS) Test, ($\theta = 0^0$), for Dunham Dolomite.

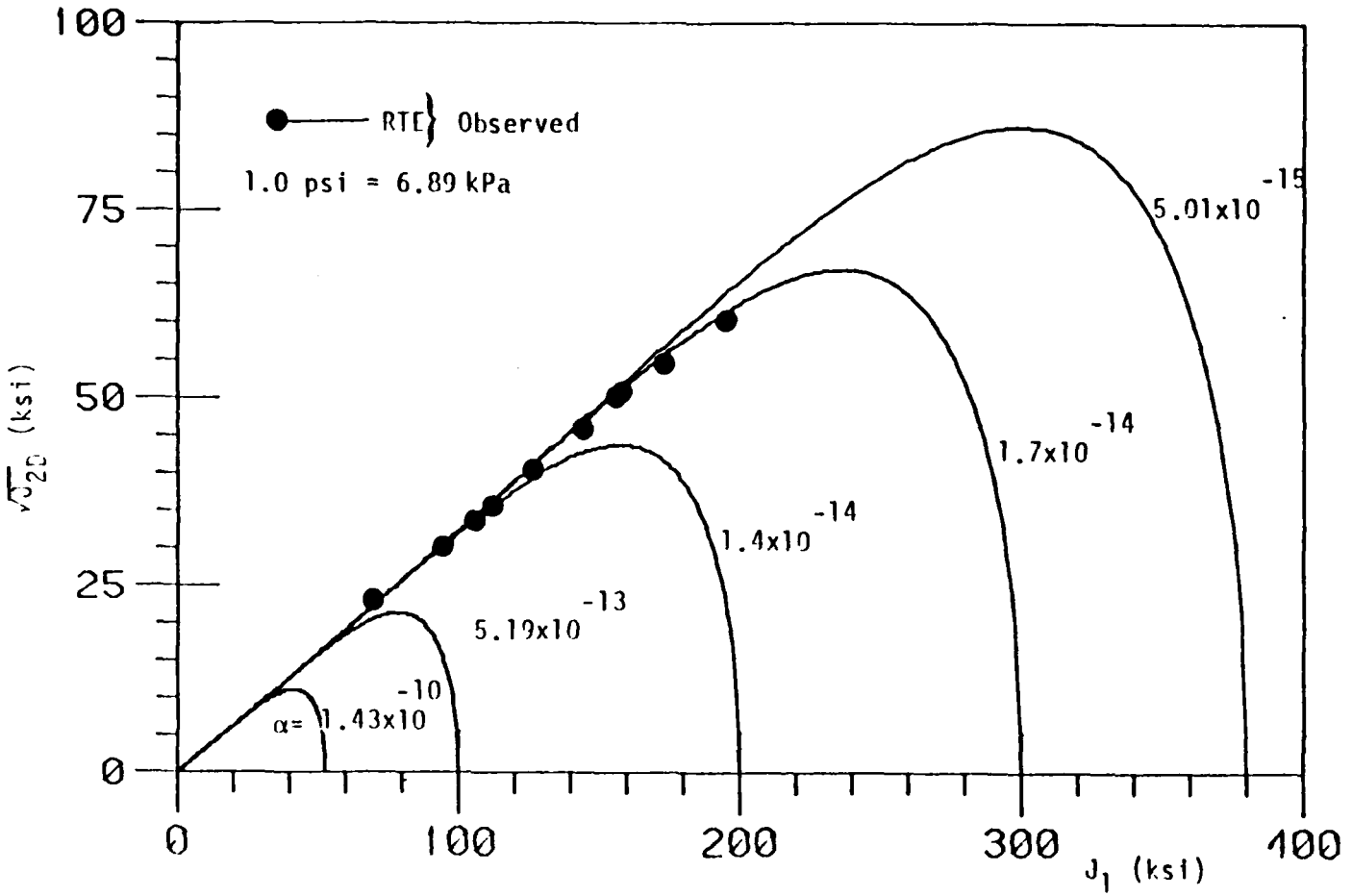

Figure 7.90. Predicted Ultimate and Pre-Ultimate Envelopes in $\sqrt{J_{2D}}$ - J_1 Plane for Reduced Triaxial Extension (RTE) Test, ($\theta = 30^{o}$), for Dunham Dolomite.

well with the experimental data.

7.8.2 Octahedral and Triaxial Planes

Figures 7.91 and 7.92 show the comparison of the predictions and observations of ultimate envelopes for octahedral and triaxial planes, respectively. It is seen from these Figs. that the correlation between the model predictions and observations is reasonable.

Predicted ultimate envelope on the π-plane is shown in Fig. 7.91.

7.8.3 Strength Behavior

Based on the predicted envelope, Fig. 7.92 predicted values of the uniaxial compressive strength, f_{cu}, equi-biaxial compressive strength, f_{cb}, and uniaxial tensile, f_t, can be calculated. These predicted strengths are:

$$f_{cu} = 30.77 \text{ ksi } (212.15 \text{ MPa})$$
$$f_{cb} = 146.86 \text{ ksi } (1012.6 \text{ MPa}) \qquad (7.27)$$
$$f_t = -1.0179 \text{ ksi } (-7.018 \text{ MPa}) \qquad \text{(Compression Positive)}$$

The values of f_{cu} and f_t compared to unconfined compression strength, f'_c, and tensile strength, f_t, based on tests with cylindrical specimens of 0.63x1.97 in. (1.6x5.0 cm) and Eq. (6.47), respectively. These values are:

$$f'_c = 31.472 \text{ ksi } (216.999 \text{ MPa}) \qquad (7.28)$$
$$f_t = -1.0179 \text{ ksi } (-7.018 \text{ MPa}) \qquad \text{(Compression Positive)}$$

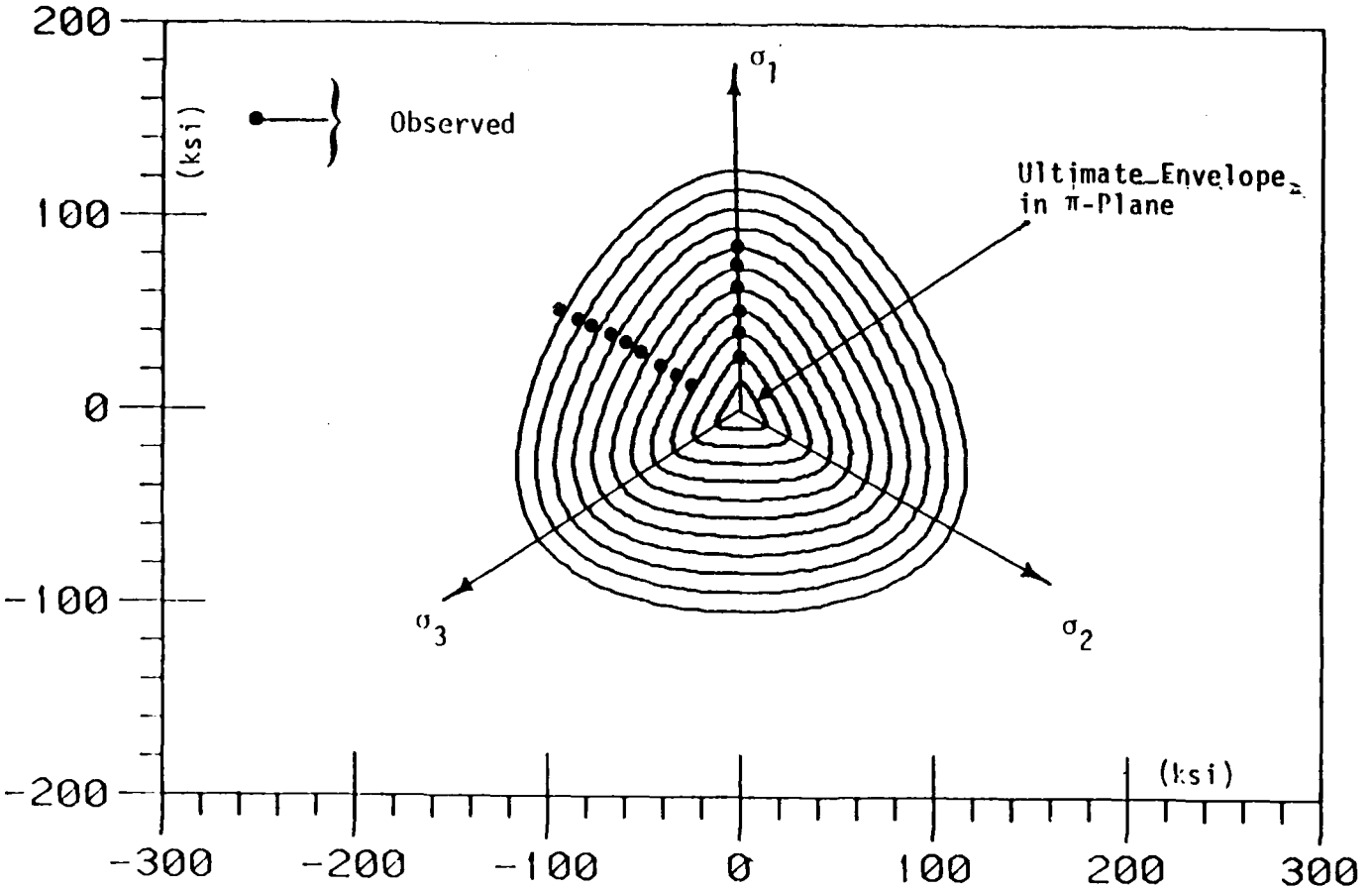

Figure 7.91. Variation of Cross-Sectional Shapes in Octahedral Planes (J_1 = 3.1,20,40,80,100,120,140,160,180 and 200 ksi), (1.0 psi = 6.89 kPa) for Predicted Ultimate Surface for Dunham Dolomite.

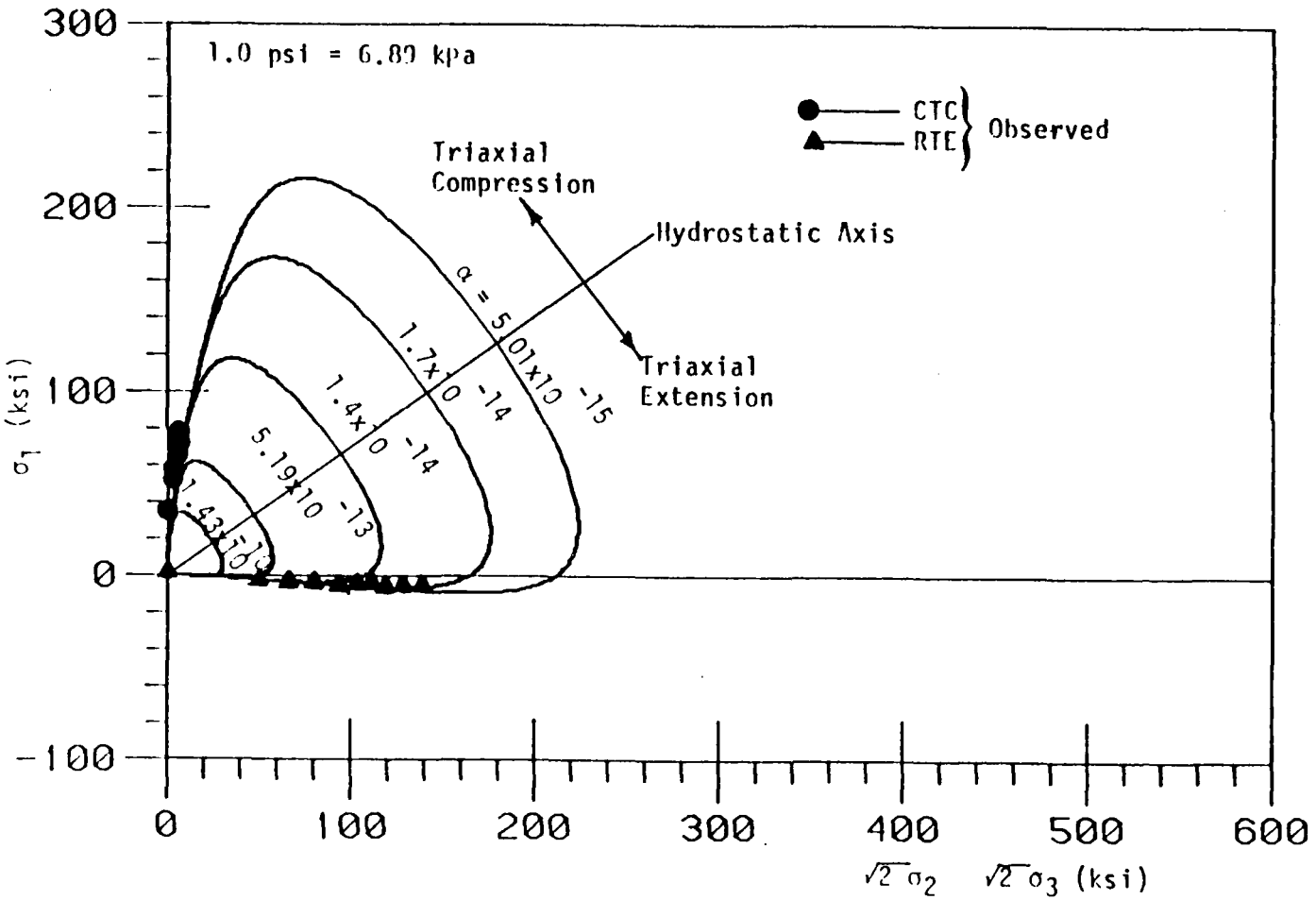

Figure 7.32. Predicted Ultimate and Pre-Ultimate Envelopes in Triaxial Plane for Dunham Dolomite.

It is evident from Eqs. (12.27) and (12.28) that the predictions compare very well with the experimental results.

Based on the octahedral ultimate envelope, Fig. 7.91, predicted values of the $\sqrt{J_{2D}}$ on π-plane for CTC (θ=- 30°), SS (θ= 0°) and RTE (θ= 30°) can be calculated. These values are:

$$(\sqrt{J_{2D}})_{CTC} = 1.177 \text{ ksi } (8.115 \text{ MPa})$$

$$(\sqrt{J_{2D}})_{SS} = 0.762 \text{ ksi } (5.254 \text{ MPa}) \qquad (7.29)$$

$$(\sqrt{J_{2D}})_{RTE} = 0.656 \text{ ksi } (4.523 \text{ MPa}) \quad \text{(Compression Positive)}$$

Ratios of Eqs. (7.29), on the π-plane, can be expressed as

$$R_1 = \frac{(\sqrt{J_{2D}})_{CTC}}{(\sqrt{J_{2D}})_{RTE}} = 1.794$$

$$R_2 = \frac{(\sqrt{J_{2D}})_{SS}}{(\sqrt{J_{2D}})_{RTE}} = 1.162 \qquad (7.30)$$

$$R_3 = \frac{(\sqrt{J_{2D}})_{CTC}}{(\sqrt{J_{2D}})_{SS}} = 1.545$$

It is evident from Eqs. (7.29) and (7.30) that the predicted envelope has a triangular section with rounded corner in π-plane.

7.9 Comments

Seven different concretes and rocks were considered for the verification of the proposed model. The material constants associated with the proposed model were determined for each concrete and rock using a number of different straight line stress path tests for that concrete or rock. These material constants were used to back-predict ultimate, pre-ultimate, strengths and the stress-strain responses of a selected number of tests for every concrete and rock. It is evident from these back-predictions that the proposed model can represent the responses of pressure sensitive materials such as concrete and rock with reasonable accuracy.

CHAPTER 8

SUMMARY, CONCLUSIONS AND RECOMMENDATIONS FOR FUTURE WORK

8.1 Summary

In this study a series of tests were performed on plain concrete and soapstone. The purpose of these tests was to acquire some understanding of the constitutive behavior of plain concrete and soapstone subjected to general and complex load histories, and the results of these tests were used to calibrate the proposed constitutive model for predicting the strength and behavior of plain concrete and soapstone under multiaxial compressive loads.

The proposed model has a number of material constants. Laboratory tests were performed to determine these material constants. Besides plain concrete and soapstone, test data for Colorado plain concrete, SFRC-UC, sandstone, Weterly Granite and Dunham Dolomite is also used [68, 30, 56, 52, 52]. Details of the parameter determination are given in Chapter 6. Material constants for different concretes and rocks are given in Chapter 6. These constants are then used to back-predict the ultimates, strengths and stress-strain response.

8.2 Conclusions

Many conclusions are drawn from the investigation presented herein. First of all, under multiaxial compression, the material's

deformational and strength response is strongly stress path and confining pressure dependent resulting in an ultimate (failure) envelope.

Appropriate constitutive laws are required to obtain reasonable solutions for many problems in geomechanics. Available constitutive models may not adequately characterize the behavior of concretes and rocks. Thus, new and improved constitutive models are necessary.

The proposed model can provide a simple and efficient way to define continuous yielding and hardening behavior. Since it involves only a single function to define both the ultimate yield and pre-ultimate yielding, it is intended to be simple compared to previously used two surface models [45, 69] that involve two separate functions. Since the proposed yield function is continuous, it also avoids the singularity point at the intersection of two functions in the previous models, thus reducing the difficulties associated with computer implementation. The ultimate criterion involves only four independent material constants. The material constants can be simply determined from simple tests such as uniaxial compression and triaxial compression or biaxial compression tests. For the purpose of including value of tensile strength in ultimate criterion for frictional materials, it is necessary to include the uniaxial

tensile strength in the material constant determination. A simple expression for evaluation of uniaxial tensile strength on the basis of the uniaxial compression strength is given by Lade [48].

The proposed constitutive model provides a continuous and convex plot in $\sqrt{J_{2D}}$ - J_1, octahedral and triaxial planes, Thus, the normal to yield surface at any point can be defined uniquely. Many available plastic models represent the yielding process by two separate surfaces which intersect each other with slope discontinuity; that is, the normal at the point of intersection is non unique. This gives rise to difficulty when associated plasticity laws are used..

The proposed model is verified with respect to the triaxial tests on a number of different concretes and rocks. Ultimate, strength, stress-strain behavior and volumetric behavior are compared. It is seen that the proposed model provides satisfactory predictions for observed behavior under a variety of stress paths.

The proposed model predictions are shown in Chapter 7. The correlation between the experimental results and analytical predictions are very good and provide a simple approach for developing constitutive models for concrete and rock.

8.3 Recommendations for Future Work

At the time this research on concrete and rock was conducted, the ability to determine the uniaxial tensile strength of a cubical specimen was not possible because the cubical device used to perform the tests employ fluid cushion compressive type loading only. The additional equipment to apply tensile stresses to a cubical specimen is required. Also, tests with low confining pressure and in combined tension-compression regimes are needed in order to elucidate the response of concrete and rock under this type of loading.

The general polynomial function, Eq. (6.1), permits choice of a number of approximate (truncated) forms which may be used instead of the proposed model. Further work is necessary to establish these alternatives and to explore their capabilities fully.

APPENDIX A

MULTIAXIAL TESTING 4X4X4 IN. (10.16X10.16X10.16 CM) CUBICAL SPECIMEN OF PLAIN CONCRETE AFTER TESTING

Figure A-1. Plain Concrete Specimens Under Hydrostatic Compression (HC) Testing (σ_o = 8 ksi), (1.0 psi = 6.89 kpa).

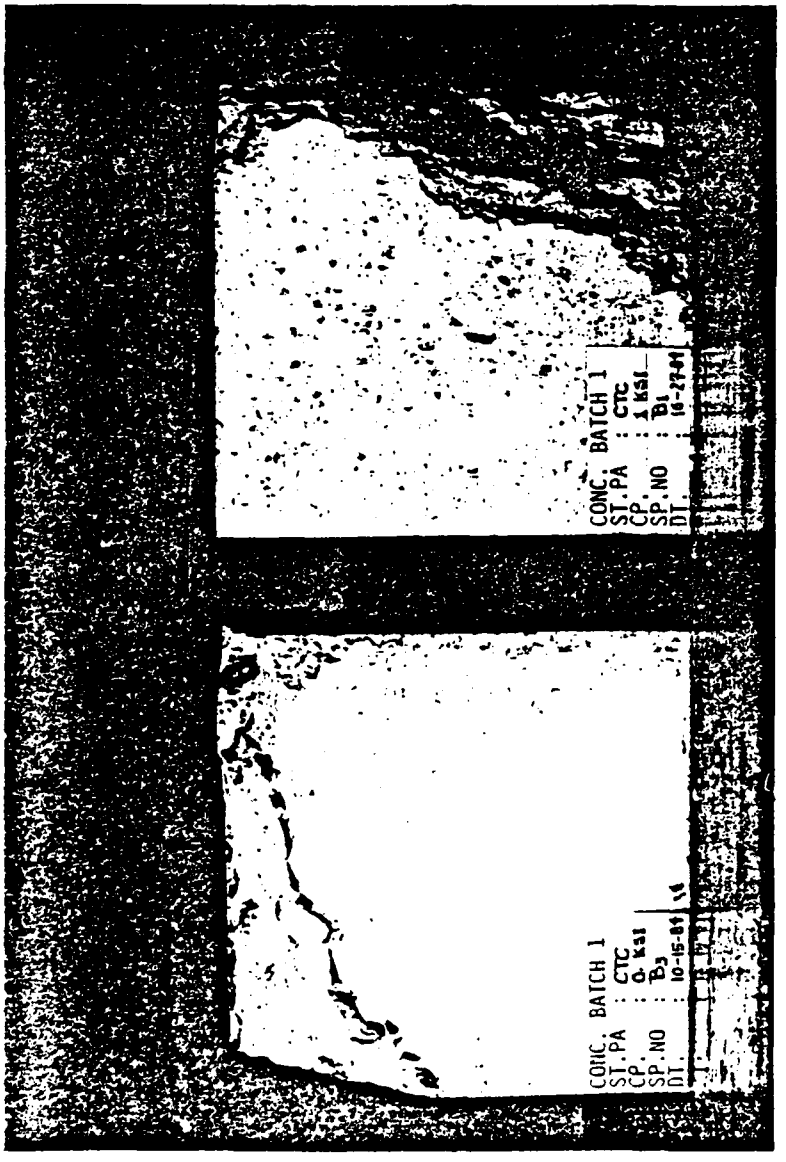

Figure A-2. Failed Plain Concrete Specimens Under Conventional Triaxial Compression (CTC) Testing (σ_o = 0 and 1 ksi), (1.0 psi = 6.89 kpa).

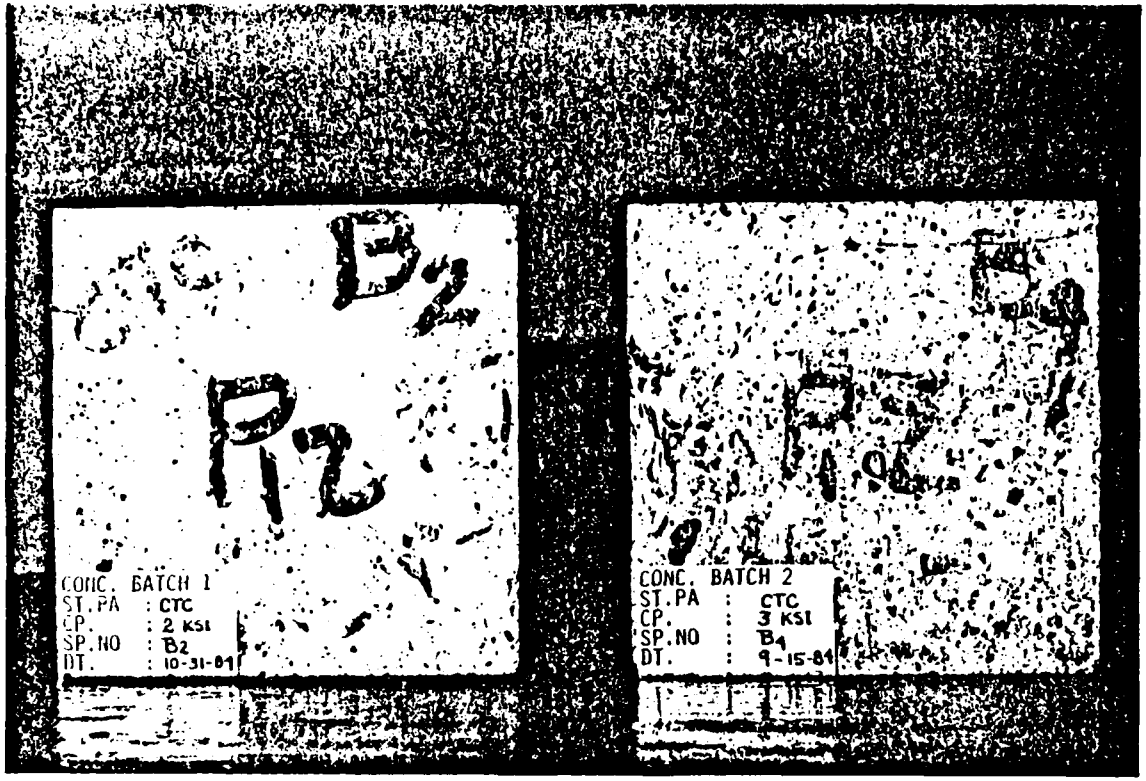

Figure A-3. Failed Plain Concrete Specimens Under Conventional Triaxial Compression (CTC) Testing (σ_o = 2 and 3 ksi), (1.0 psi = 6.89 kpa).

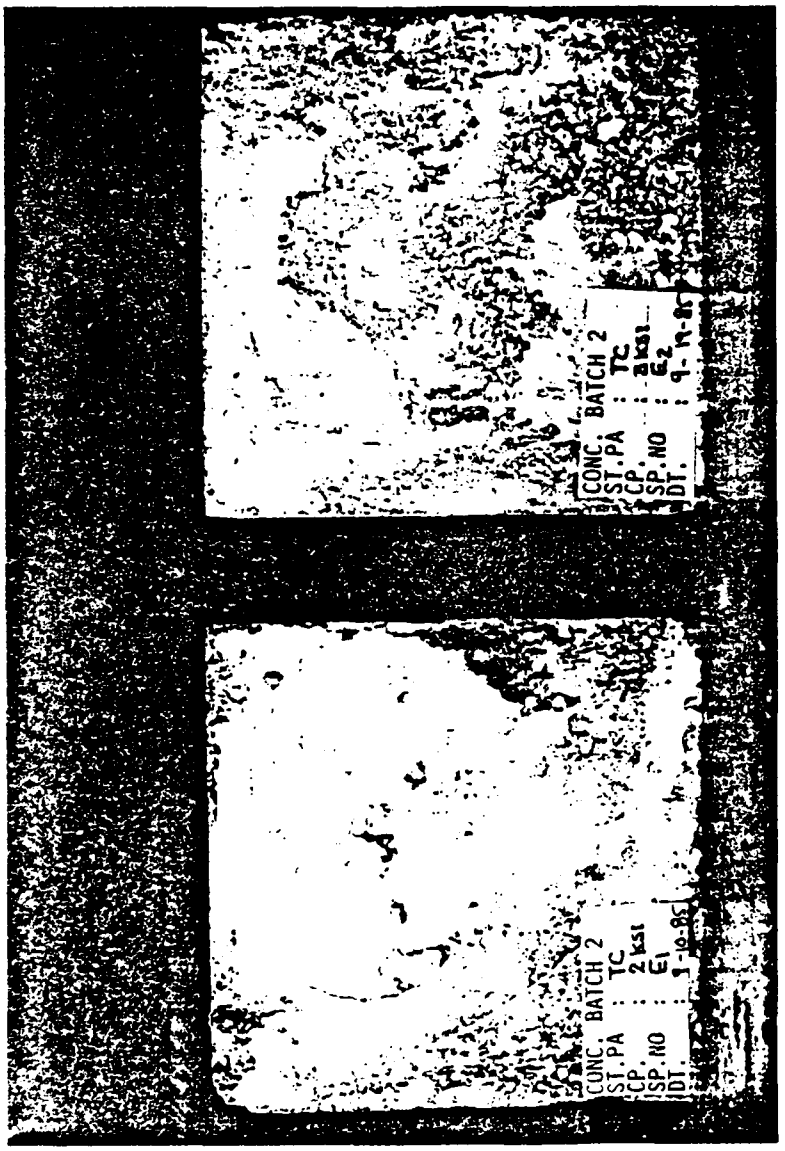

Figure A-4. Failed Plain Concrete Specimens Under Triaxial Compression (TC) Testing (σ_o = 2 and 3 ksi), (1.0 psi = 6.89 kpa).

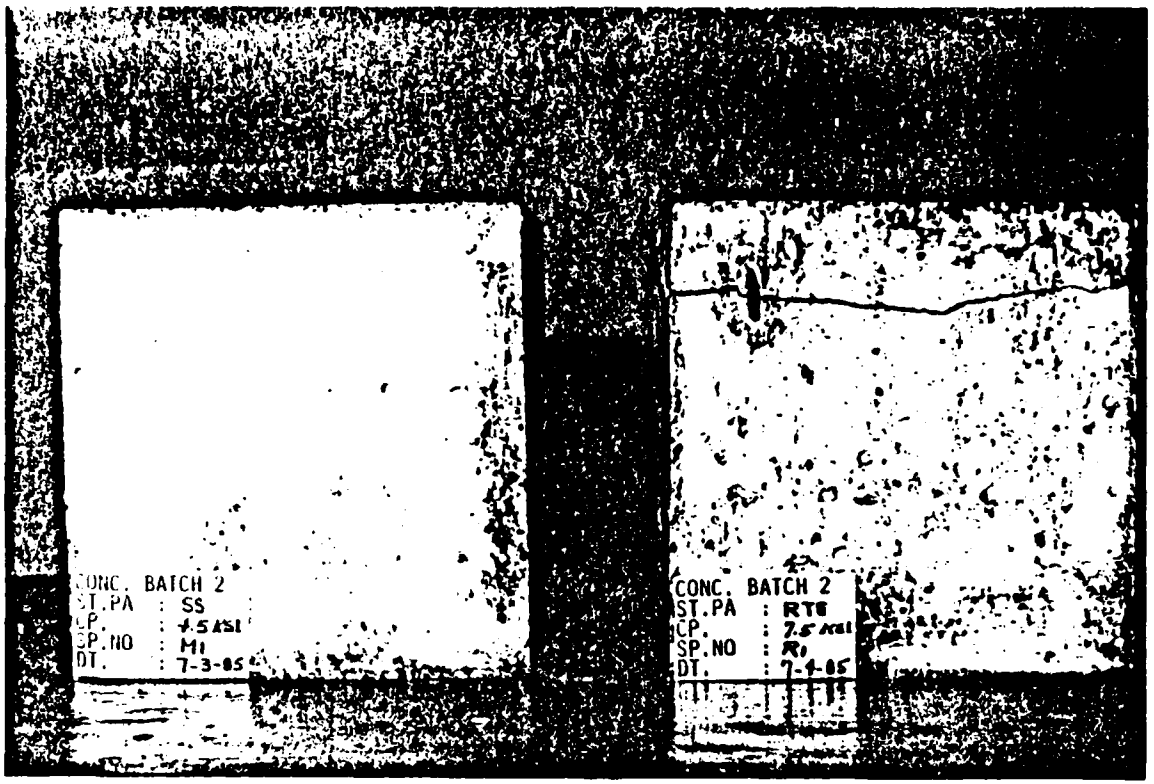

Figure A-5. Failed Plain Concrete Specimens Under Simple Shear (SS) and Reduced Triaxial Extension (RTE) Testing (σ_0 = 4.5 and 7.5 ksi, respectively), (1.0 psi = 6.89 kpa).

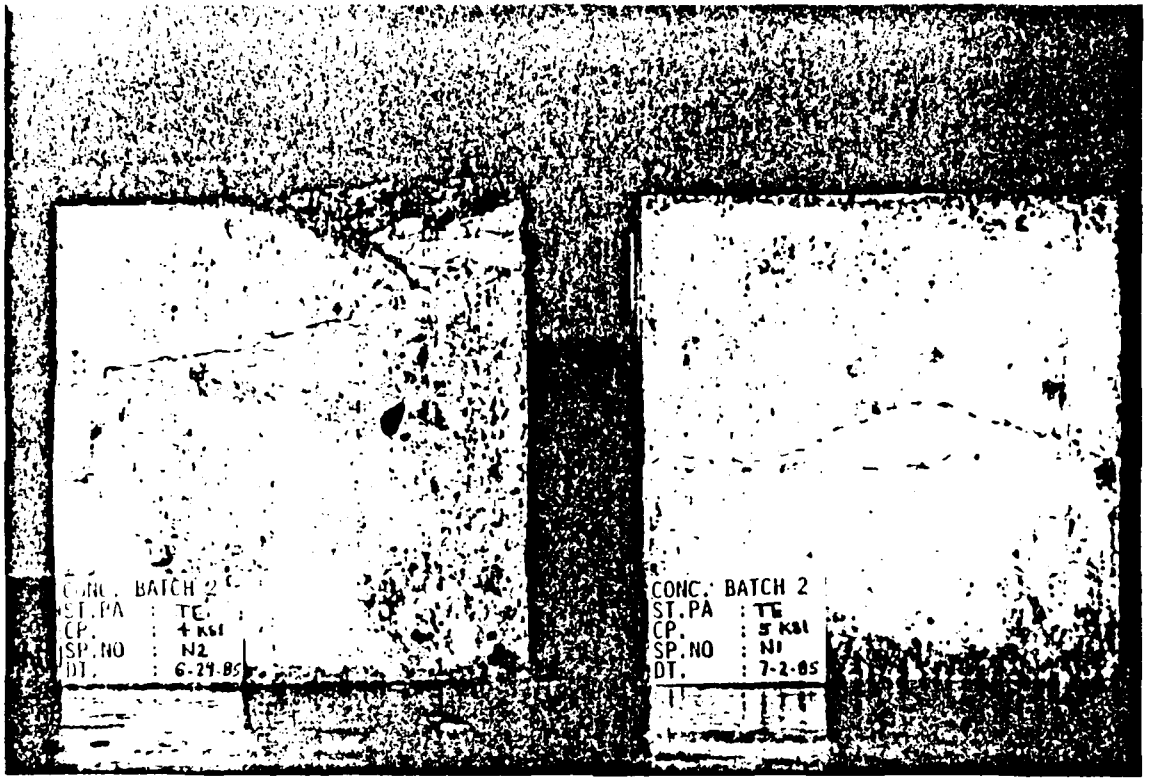

Figure A-6. Failed Plain Concrete Specimens Under Triaxial Extension (TE) Testing (σ_o = 4 and 5 ksi), (1.0 psi = 6.89 kpa).

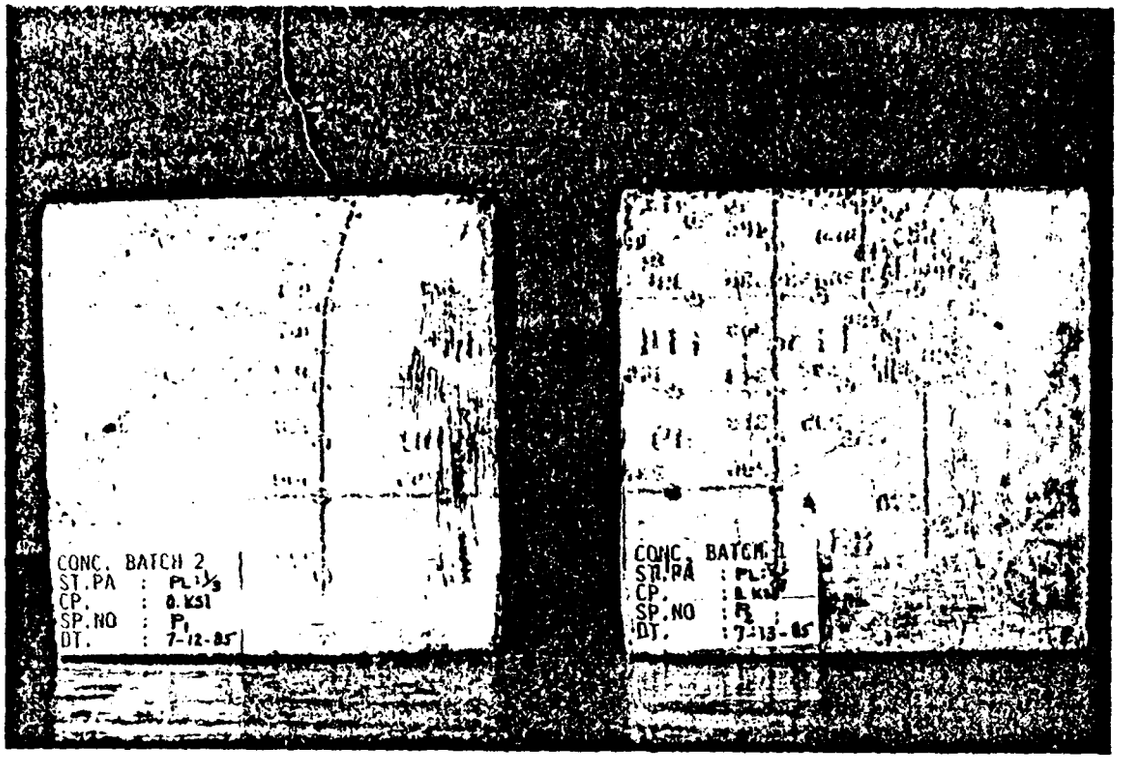

Figure A-7. Plain Concrete Specimens Under Proportional Loading (PL) Testing (R = 1/3 and 2/3).

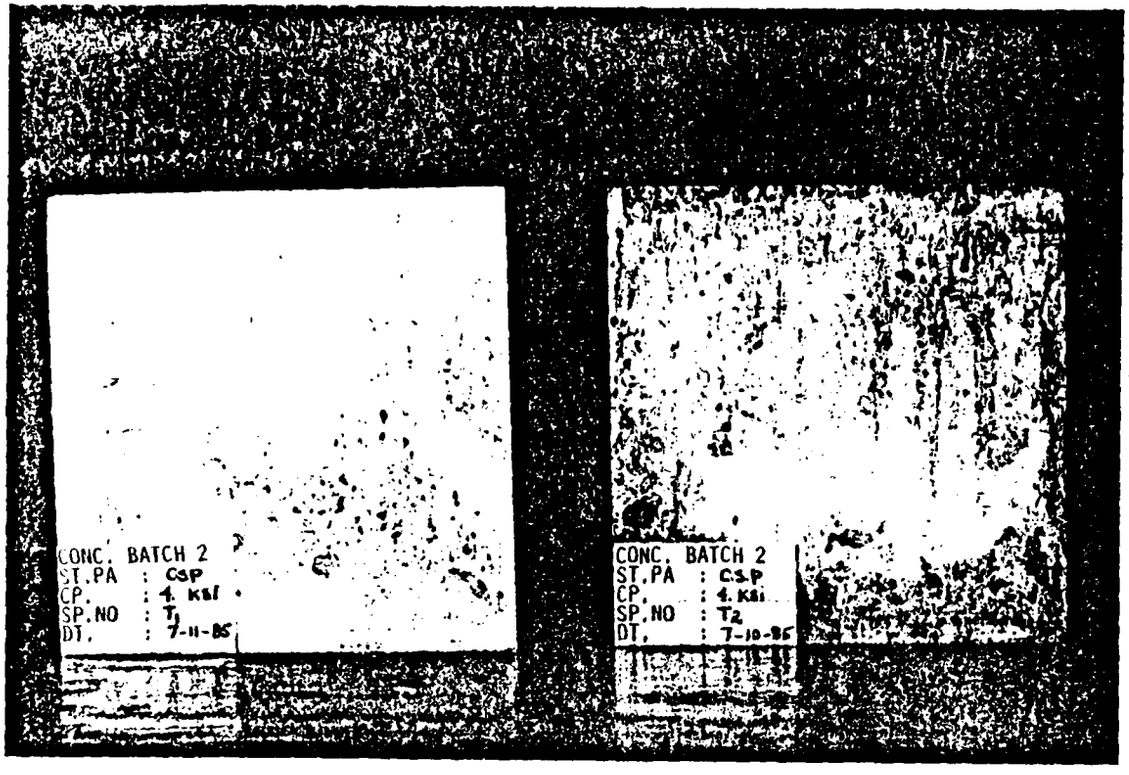

Figure A-8. Plain Concrete Specimens Under Circular Stress Path (CSP) Testing ($\sigma_o = 4$, $T_{oct} = 1$ and $\sigma_o = 4$, $\tau_{oct} = 1.5$ ksi), (1.0 psi = 6.89 kpa).

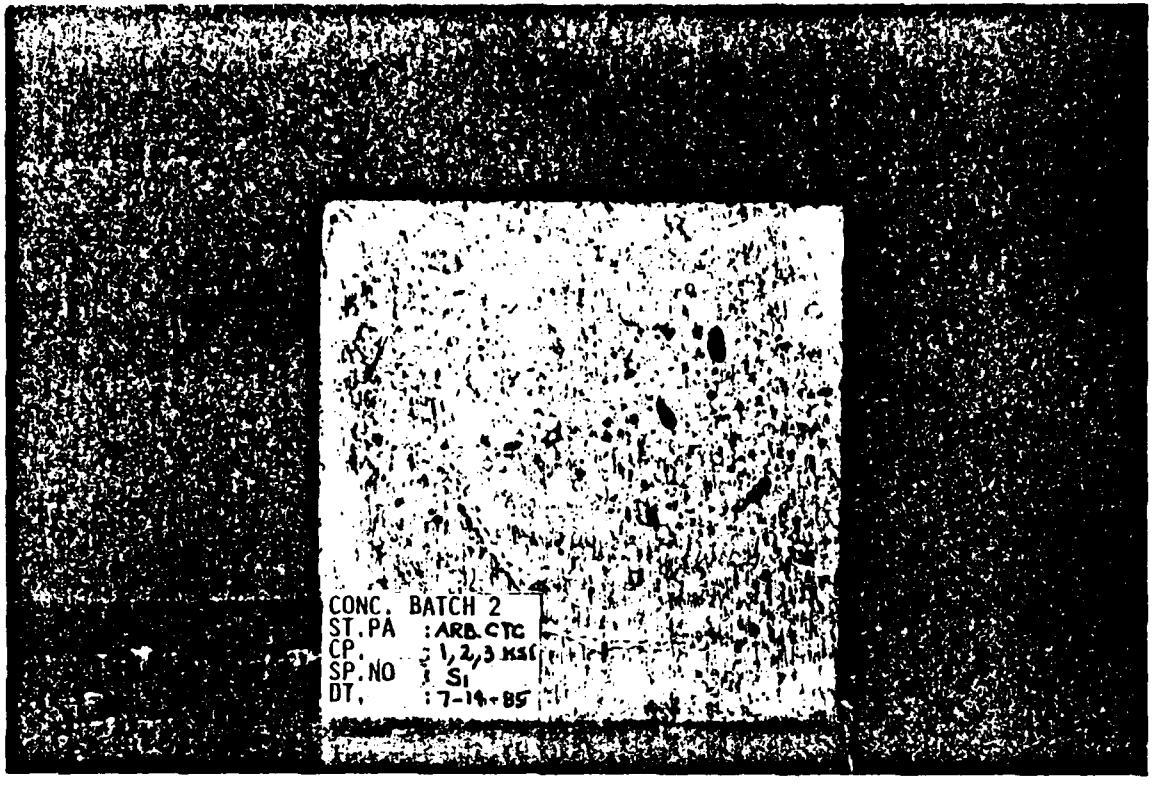

Figure A-9. Plain Concrete Specimen Under Conventional Triaxial Compression (CTC) Testing with Three Different Confining Pressures (σ_0 = 1, 2 and 3 ksi), (1.0 psi = 6.89 kpa).

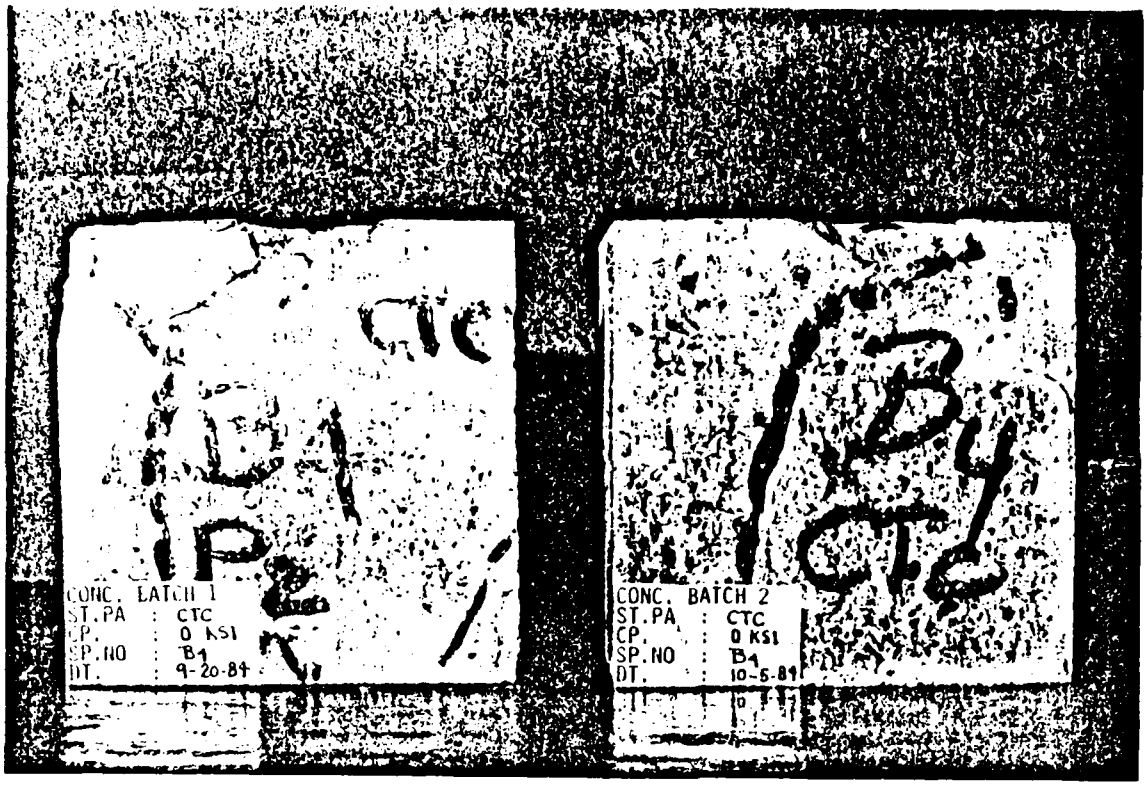

Figure A-10. Failed Plain Concrete Specimens Under Conventional Triaxial Compression (CTC) Testing (σ_o = 0 ksi), (1.0 psi = 6.89 kpa).

APPENDIX B

MULTIAXIAL TESTING 4X4X4 IN. (10.16X10.16X10.16 CM) CUBICAL SPECIMEN OF SOAPSTONE AFTER TESTING

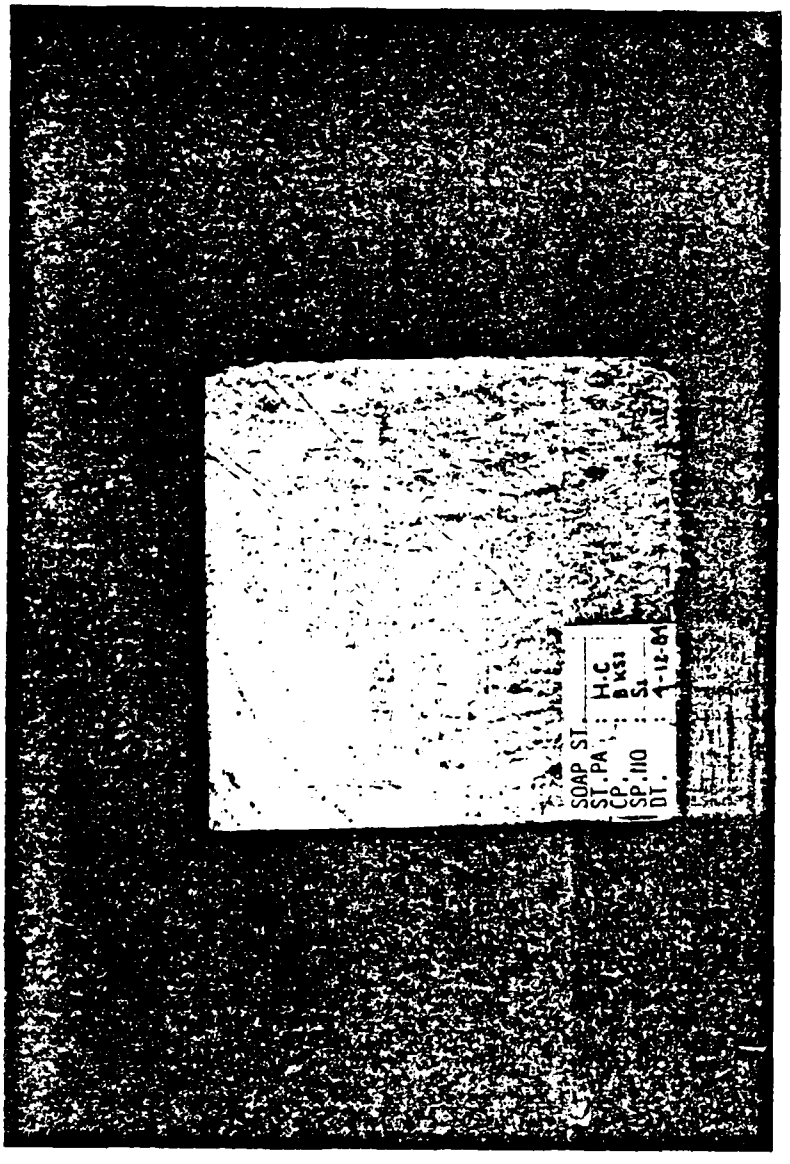

Figure B-1. Soapstone Specimen Under Hydrostatic Compression (HC) Testing (σ_0 = 8 ksi), (1.0 psi = 6.89 kpa).

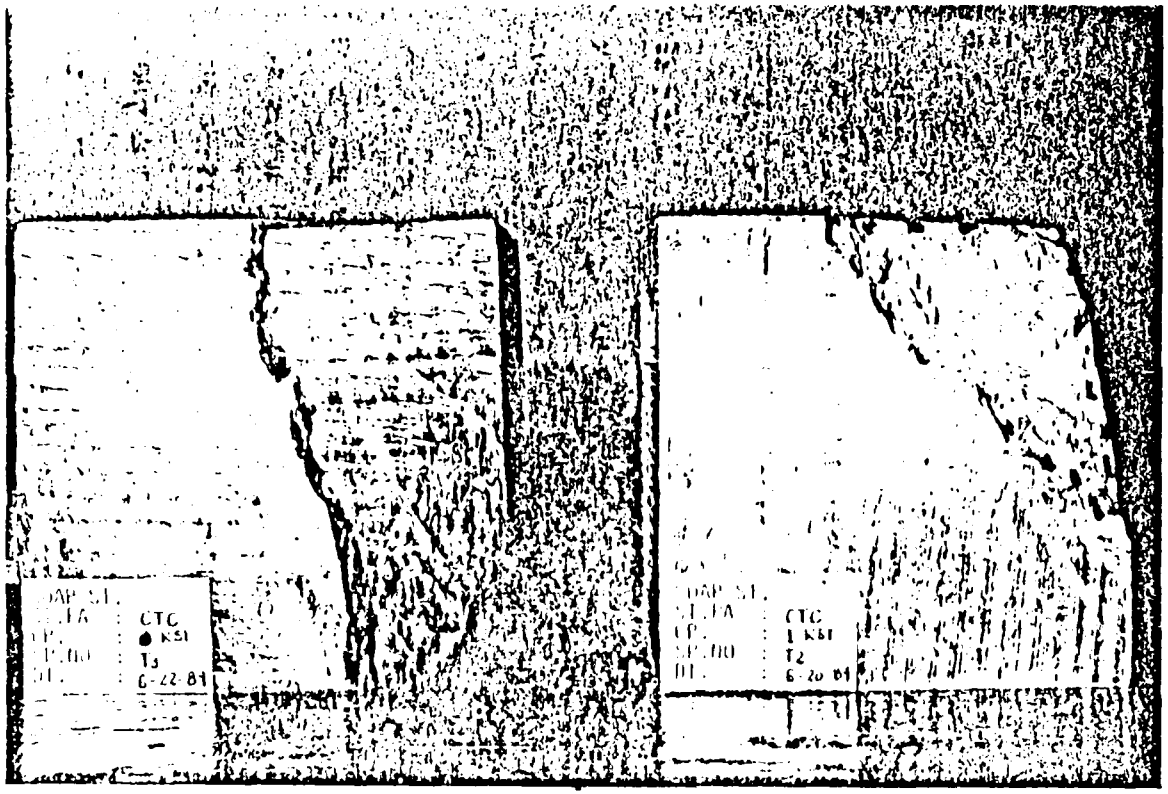

Figure B-2. Failed Soapstone Specimens Under Conventional Triaxial Compression (CTC) Testing (σ_0 = 0 and 1 ksi), (1.0 psi = 6.89 kpa).

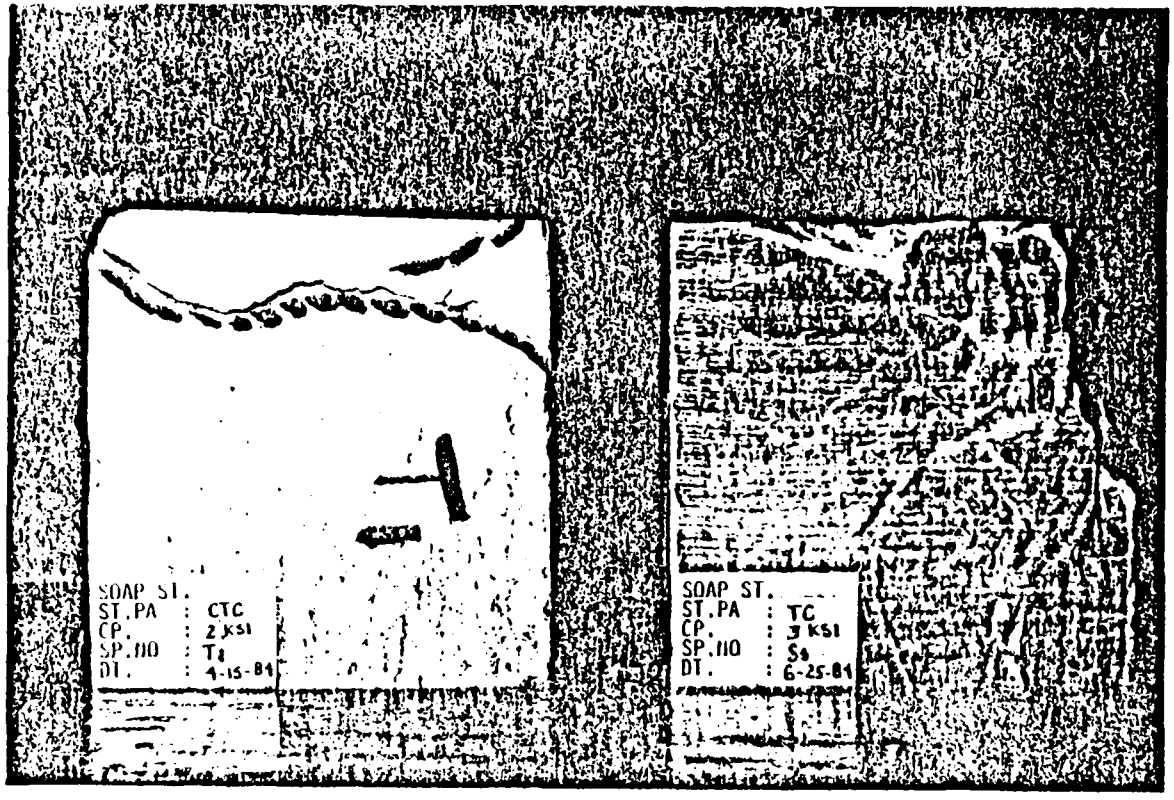

Figure B-3. Failed Soapstone Specimens Under Conventional Triaxial Compression (CTC) Testing (σ_0 = 2 and 3 ksi), (1.0 psi = 6.89 kpa).

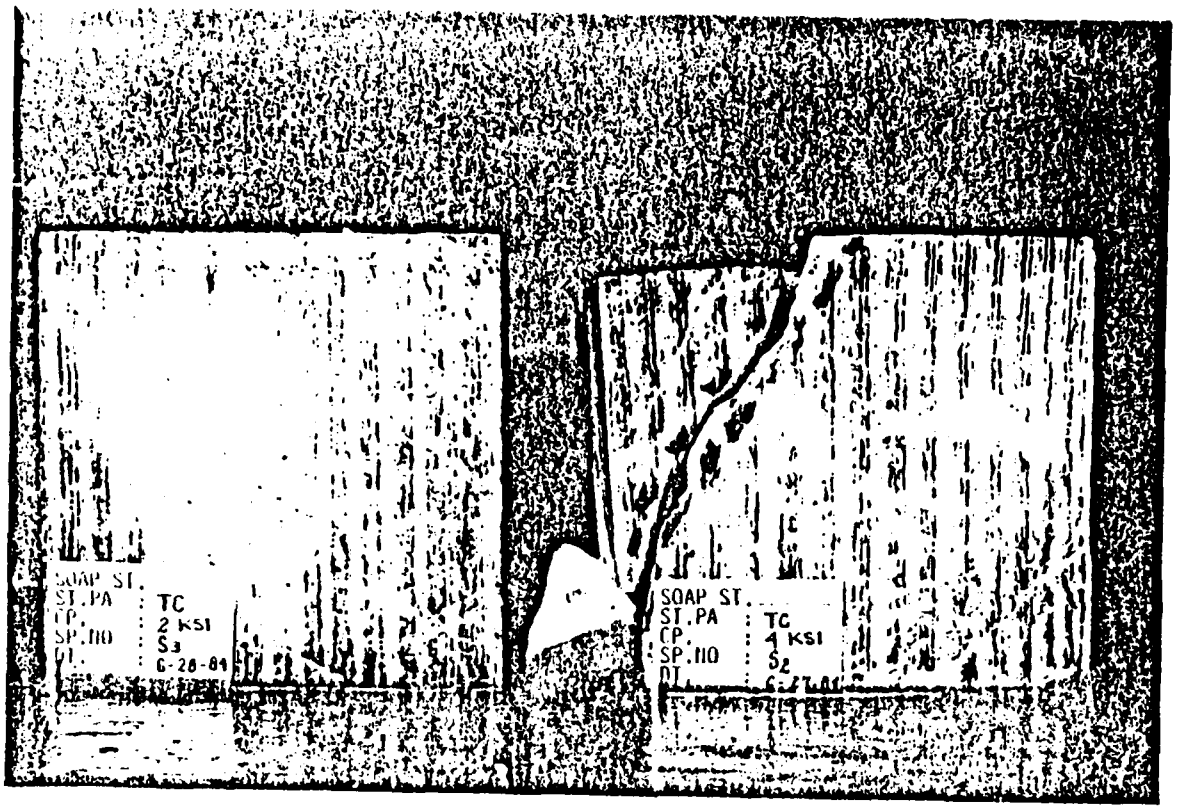

Figure B-4. Failed Soapstone Specimens Under Triaxial Compression (TC) Testing (σ_0 = 2 and 4 ksi), (1.0 psi = 6.89 kpa).

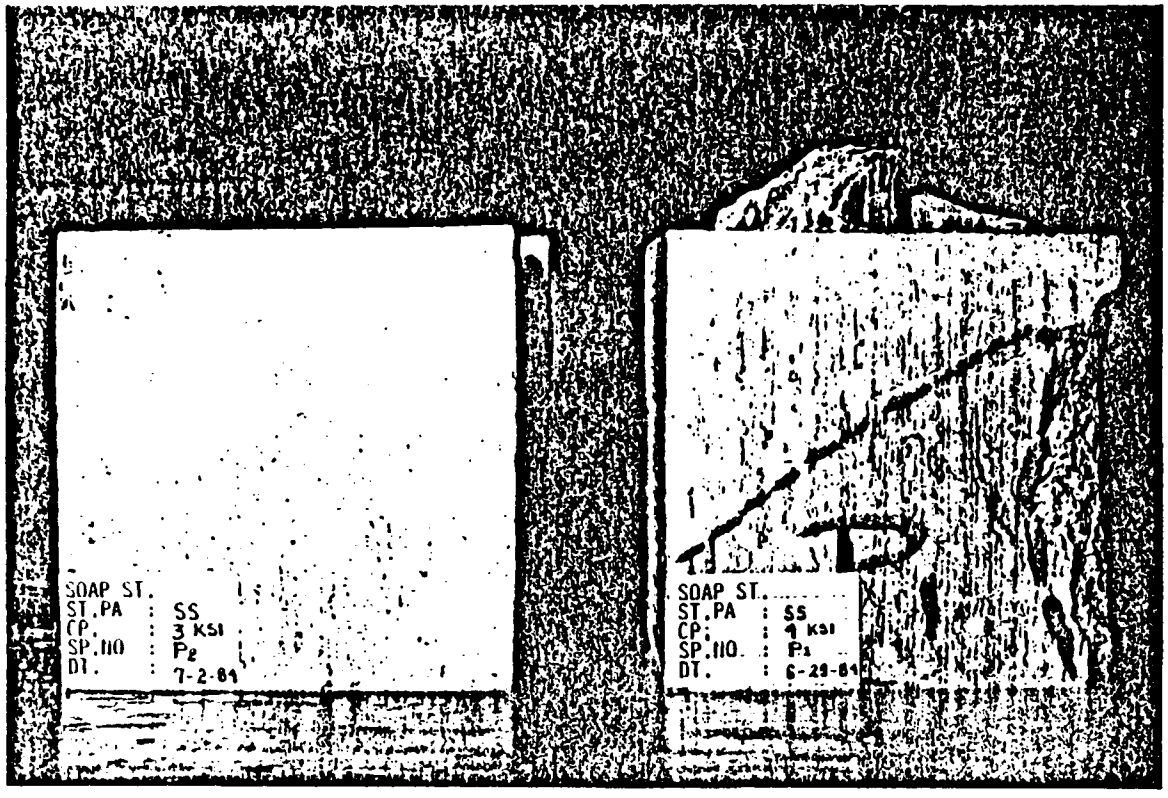

Figure B-5. Failed Soapstone Specimens Under Simple Shear (SS) Testing (σ_0 = 3 and 4 ksi), (1.0 psi = 6.89 kpa).

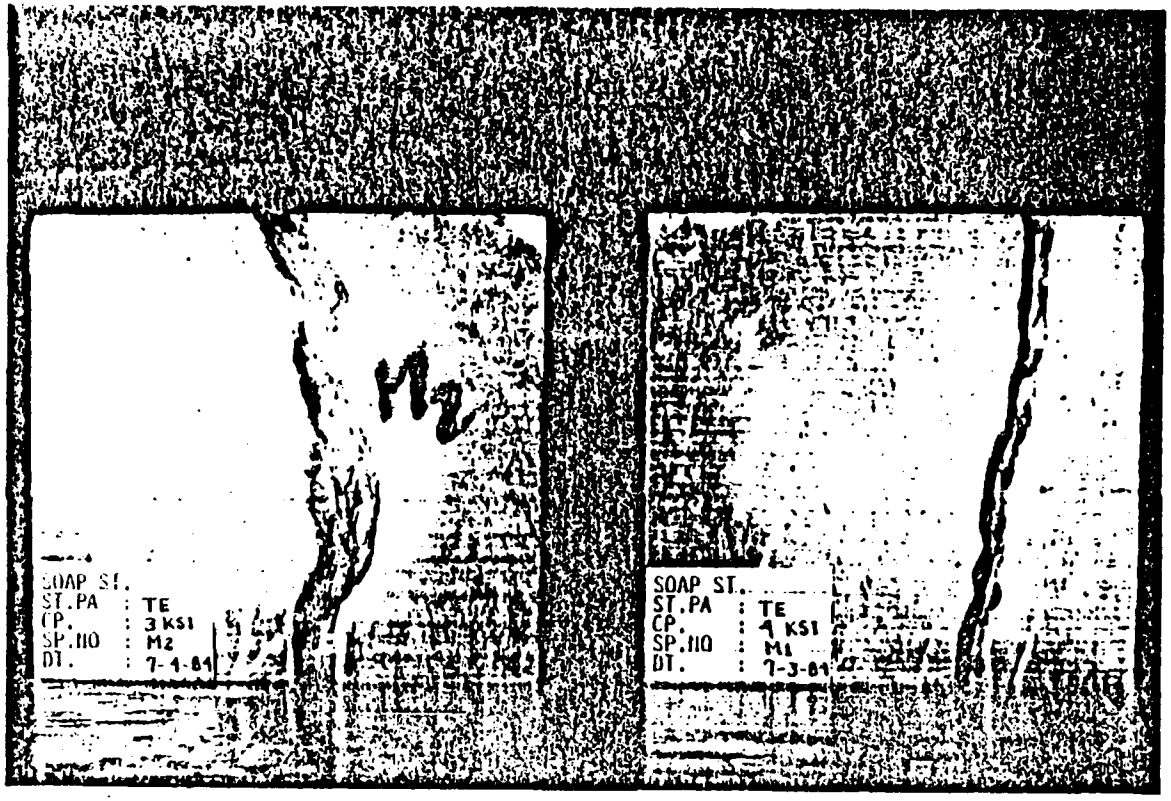

Figure B-6. Failed Soapstone Specimens Under Triaxial Extension (TE) Testing (σ_o = 3 and 4 ksi), (1.0 psi = 6.89 kpa).

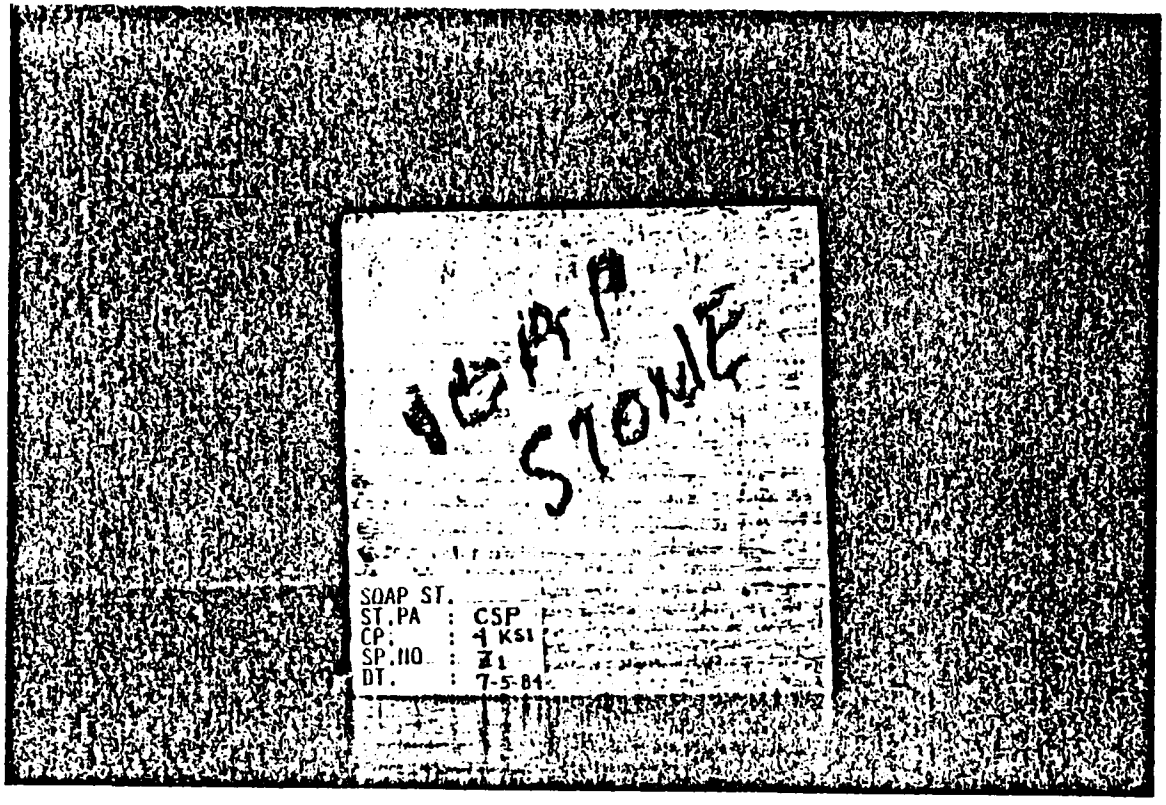

Figure B-7. Soapstone Specimen Under Circular Stress Path (CPS) Testing (σ_o = 4 and τ_{oct} = 1 ksi), (1.0 psi = 6.89 kpa).

LIST OF REFERENCES

1. American Society for Testing and Materials (ASTM), Annual Book of ASTM Standards, Part 14, published by ASTM, 1975.

2. Andenaes, E., Gerstle, K. and Ko, H. Y., "Response of Mortar and Concrete to Biaxial Compression," Journal of Engineering Mechanics Division, ASCE, Vol. 103, No. EM4, August 1977, pp. 515-525.

3. Argyris, J. H., Faust, G., and Willam, K. J., "Finite Element Modelling of Reinforced Concrete Structures," Introductory Report, IABSE Colloquium on "Advanced Mechanics of Reinforced Concrete," Delft, June 2-4, 1984.

4. Argyris, J. H., Faust, G., Szimmat, J., Wanke, E. P. and Willam, K. J., "Recent Developments in the Finite Element Analysis of Prestressed Concrete Reactor Vessels, " Nuclear Engineering and Design, Vol. 28, 1974, pp. 42-75.

5. Argyris, J. H., Faust, G. and Willam, K. J., "Limit Load Analysis of Thick-Walled Concrete Structures--A finite Element Approach to Fracture," Computer Methods in Applied Mechanics and Engineering, Vol. 8, North Holland Co., 1976, pp. 215-243.

6. Baker, R., and Desai, C. S., "Consequences of Deviatoric Normality in Plasticity with Isotropic Strain Hardening," Int. J. Num. Analyt. Method in Geomech., Vol. 6, No. 3, 1982.

7. Baker, R. and Desai, C. S., "Induced Anisotropy During Plastic Straining," Report, Department of Civil Engineering, Virginia Tech, Blacksburg, VA 1981.

8. Bazant, Z. P. and Kim, S. S., "Plastic-Fracturing Theory for Concrete," Journal of the Engineering Mechanics Division, Proceedings, American Society of Civil Engineers, Vol. 105, June 1979, pp. 407-428 with errata in Vol. 106.

9. Bazant, Z. P., "Work Inequalities for Plastic-Fracturing Materials," Int. Journal of Solids and Structures, Vol. 16, 1980, pp. 873-901.

10. Bazant, Z. P., "Endochronic Inelasticity and Incremental Plasticity," Int. Journal of Solids and Structures, Vol. 14, 1978, pp. 691-714.

11. Buyukozturk, O., "Nonlinear Analysis of Reinforced Concrete Structures," Computer and Structures, Vol. 7, 1977, pp. 149-156.

12. Chen, A. C. T. and Chen, W. F., "Constitutive Relation for Concrete," Journal of the Engineering Mechanics Division, ASCE, Vol. 101, No. EM4, August 1975, pp. 465-481.

13. Chen, W. F., "Plasticity in Reinforced Concrete," McGraw-Hill Book Co., New York, 1982.

14. Chen, W. F. and Ting, E. C., "Constitutive Models for Concrete Structures," Journal of the Engineering Mechanics Division, ASCE, Vol. 106, No. EM1, Feb. 1980, pp. 1-19.

15. Desai, C. S., "A General Basis for Yield, Failure and Potential Functions in Plasticity," Int. J. Num. Analyt. Methods in Geomech., Vol. 4, 1980, pp. 361-375.

16. Desai, C. S. and Faruque, M. O., "A Generalized Basis for Modelling Plastic Behavior of Materials," Proc., Int. Conf. on Const. Laws for Eng. Mat.: Theory and Application, Univ. of Arizona, Tucson, AZ, 1983.

17. Desai, C. S. and Faruque, M. O., "A Constitutive Model for Geological Materials," J. Eng. Mech. Div., ASCE, Vol. 110, No. 9, Sept. 1984, pp. 1391-1408.

18. Desai, C. S., and Faruque, M. O., "A Generalized Basis for Modelling Plastic Behavior of Materials," Proc., Int. Conf. on Const. Laws for Eng. Mat: Theory and Application, Univ. of Arizona, Tucson, AZ, 1983.

19. Desai, C. S., Frantziskonis, G. N. and Somasundarm, S., "Constitutive Modelling for Geological Materials," Proceedings, 5th Int. Conf. on Num. Meth. in Geomech., Nagoyo, Japan, April 1985.

20. Desai, C. S., and Janardhanam, R. and Sture, S., "A High Capacity Truly Triaxial Device and Application," J. Geotech Testing, ASTM, 1980.

21. Desai, C. S., Phan, H. V., and Sture, S., "Procedure, Selection and Application of Plasticity Models for Soil," Int. J. Num. Analyt. Methods in Geomech., Vol. 5, No. 3, 1981, pp. 295-311.

22. Desai, C. S. and Siriwardane, H. J., "Constitutive Laws for Engineering Materials," Prentice-Hall, Inc., Englewood Cliffs, NJ, 1983.

23. Desai, C. S., and Siriwardane, H. J., "A Concept of Correction Functions to Account for Non-Associative Characteristics of Geologic Media," Int. J. Num. Analyt. Methods in Geomech., Vol. 4, 1980, pp. 377-387.

23a. Desai, C. S., Somasundarm, S. and Frantziskonis, G. N., "A Hierarchical Approach to Constitutive Modelling of Geologic Materials," Int. J. Num. Analyt. Methods in Geomech., Vol. 10, No. 2, 1986.

24. DiMaggio, F. L., and Sandler, I. S., "Material Model for Granular Soil," J. Eng. Mech. Div., ASCE, Vol. 97, EM3, 1971, pp. 935-950.

25. DiMaggio, F. L. and Sandler, I. S., "Material Model for Granular Soils," J. Eng. Mech. Div., ASCE, Vol. 97, EM3, 1971, pp. 935-950.

26. Dougill, J. W., "Some Remarks on Path Independence in the Small in Plasticity," Quarterly of Applied Mathematics, Vol. 32, 1975, pp. 233-243.

27. Dougill, J. W., "On Stable Progressively Fracturing Solids," ZAMP (Zeitschrift fur Angewandte Mathematik und Physik), Vol. 27, Papc. 4, 1976, pp. 423-437.

28. Drucker, D. C., "A More Fundamental Approach to Plastic Stress-Strain Relations," Proc., 1st U.S. Natl. Cong. Appl. Mech., Chicago, IL, 1951, pp. 487-491.

29. Drucker, D. C. and Prager, W., "Soil Mechanics and Plastic Analysis of Limit Design," Quart. Appl. Math., Vol. 10, No. 2, 1952.

30. Egging, D. E., "Constitutive Relations for Randomly Oriented Steel Fiber Reinforced Concrete Under Multiaxial Compression Loading," M.S. Thesis, University of Colorado, Dept. of Civil, Environmental and Architectural Engineering, 1982.

31. Eringen, A. C., "Nonlinear Theory of Continuous Media," McGraw-Hill Book Company, New York, 1962.

32. Faruque, M. O., "Development of a Generalized Constitutive Model and its Implementation in Soil-Structure Interaction," Ph.D. Dissertation, University of Arizona, Tucson, AZ, 1983.

33. Gerstle, K. H., Linse, D. L., Bertacchi, P., Kotsovos, M. D., Ko, H. Y., Newman, J. B., Rossi, P., Schickert, G., Taylor, M. A., Traina, L. A. and Zimmerman, R. M., "Strength of Concrete Under Multiaxial Stress States," Douglas McHenry International Symposium on Concrete and Concrete Structures, American Concrete Institute, Publication sp-55, pp. 103-131, sp 55-5.

34. Gerstle, K. H., Aschl, H., Bellotti, R., Bertacchi, P., Kotsovos, M.D., Ko, H. Y., Linse, D. H., Newman, J. B., Rossi, P., Schickert, G., Taylor, M. A., Traina, L. A., Winkler, H. and Zimmerman, R. M., "Behavior of Concrete Under Multiaxial Stress States," Journal of the Engineering Mechanics Division, ASCE, Vol. 106, No. EM6, Proc. Paper 15945, Dec. 1980, pp. 1383-1403.

35. Green, A. E. and Naghdi, P. M., "A General Theory of an Elastic-Plastic Continuum," Arch. of Rat. Mech. and Analysis, Vol. 18, No. 4, 1965, pp. 252-281.

36. Hannant, D. J., "Nomograms for the Failure of Plain Concrete Subjected to Short-Term Multiaxial Stresses," The Structural Engineer, Vol. 52, No. 5, May 1974, pp. 151-165.

37. Hill, R., "The Mathematical Theory of Plasticity," Oxford Univ. Press, Oxford, U.K., 1980.

38. Hill, R., "The Mathematical Theory of Plasticity," Oxford Univ. Press, London, 1950.

39. Hodge, P. G., "The Theory of Piecewise Linear Isotropic Plasticity," IUTAM Coloq., Madrid, Spain, 1955.

40. Ishlinski, A. Yu., "General Theory of Plasticity with Linear Strain Hardening," Urk. Mat. Zu., Vol. 6, 1954, pp. 314.

41. Kotsovos, M. D. and Newman, J. B., "Generalized Stress-Strain Relations for Concrete," Journal of the Engineering Mechanics Division, ASCE, Vol. 104, No. EM4, Proc. Paper 13922, Aug. 1978, pp. 845-856.

42. Kulhawy, F. H., "Stress Deformation Properties of Rock and Rock Discontinuities," Engng. Geol. 9., 1975, pp. 327-350.

43. Kupfer, H. B. and Gerstle, K. H., "Behavior of Concrete Under Biaxial Stresses," Journal of Engineering Mechanics Division, ASCE, Vol. 99, No. EM4, Proc. Paper 9917, Aug. 1973, pp. 852-866.

44. Leigh, D. C., "Nonlinear Continum Mechanics," McGraw-Hill Book Company, New York, 1968.

45. Lade, P. V., "Elastic-Plastic Stress-Strain Theory for Cohesionless Soil with Curved Yield Surface," Int. J. Solids and Struc., Vol. 13, 1977, pp. 1019-1035.

46. Lade, P. V., "Failure Criterion for Frictional Materials," Proc., Int. Conf. on Constitutive Laws for Engineering Materials, Univ. of Arizona, Tucson, AZ, Jan. 1983.

47. Lade, P. V., "Failure Criterion for Frictional Materials, "Proc., Int. Conf. on Constitutive Laws for Engineering Materials, Univ. of Arizona, Tucson, AZ, Jan. 1983.

48. Lade, P. V., "Three-Parameter Failure Criterion for Concrete," Journal of the Engineering Mechanics Div. ASCE, Vol. 108, No. EM5, Proc. Paper 17383, Oct. 1982.

49. Lade, P. V., "Elastic-Plastic Stress-Strain Theory for Cohesionless Soil with Curved Yield Surfaces," Report, UCLA-ENG-7594, Univ. of Calif., Los Angeles, CA, Nov. 1975.

50. Matsuoka, H. and Nakai, T., "Stress-Deformation and Strength Characteristics of Soil Under Three Different Principal Stresses," Proc., Japan Soc. Civil Engrs., No. 232, 1974, pp. 59-70.

51. Mitchell, J. K., "The Properties of Cement-Stabilized Soil," Proc., Workshop on Materials and Methods for Low Cost Road, Rail and Reclamation Weeks, Leura, Australia, September 1976, pp. 365-404.

52. Mogi, K., "Effect of the Intermediate Principal Stress on Rock Failure," Journal of Geophysical Research, Vol. 72, No. 20, April 1967, pp. 5117-5130.

53. Mroz, Z., "Non-Associated Flow Laws in Plasticity," J. De McCanique, Vol. 2, No. 1, 1963, pp. 21-41.

54. Mroz, Z., "Mathematical Models of Inelastic Concrete Behavior," Inelasticity and Non-Lincarity in Structural Concrete, M. Z. Cohn, ed., University of Waterloo Press, Waterloo, Ontario, Canada, Study No. 8, 1972, pp. 47-72.

55. Murray, D. W., Chitnuyanondh, L., Agha, K. Y. and Wong, C., "A Concrete Plasticity Theory for Biaxial Stress Analysis," Journal of Engineering Mechanics Division, ASCE, Vol. 105, No. EM6, December 1979, pp. 989-1006.

56. Nishida, T., Esaki, T., Aoki, K. and Kimura, T., "On the Stress Loci by Strain Controlled Tests of Sandstone Under Generalized Triaxial Stress," Report, Research Institute of Industrial Science, Kyushu University, Japan, 1984.

57. Ottosen, N. S., "A Failure Criterion for Concrete," Journal of the Engineering Mechanics Division, ASCE, Vol. 103, No. EM4, Aug. 1977, pp. 527-535.

58. Ohashi, Y., Kawashima, K. and Yokochi, T., "Anisotropy Due to Plastic Deformation of Initially Isotropic Mild Steel and its Analytical Formulations," J. Mech. Phys. Solids, Vol. 23, 1975, pp. 277-294.

59. Peterson, N. V., "Soapstone Industry in Southwest Oregon," The Ore Bin, Vol. 40, No. 9, Sept. 1978.

60. Prager, W., "A New Method of Analyzing Stresses and Strains in Work-Hardening Plastic Solids," J. Appl. Mech., Vol. 78, 1956.

61. Prager, W., and Hodge, P. G., Jr., "Theory of Perfectly Plastic Solids," John Wiley and Sons, 1951.

62. Prevost, J. H., "Mathematical Modelling of Monotonic and Cyclic Undrained Clay Behavior," Int. J. Num. Analyt. Methods in Geomech., Vol. 1, 1977, pp. 196-216.

63. Rivilin, R. S. and Ericksen, J. L., "Stress-Deformation Relations for Isotropic Materials," J. Rational Mech. Anal., Vol. 4, 1955, pp. 355-425.

64. Roscoe, K. H. and Burland, J. B., "On the Generalized Stress-Strain Behavior of 'Wet' Clays," Engineering Plasticity, Heyman, J., and Leckie, F. A., eds., Cambridge University Press, 1968.

65. Roscoe, K. H., Schofield, A. N. and Worth, C. P., "On the Yielding of Soils," Geotechnique, Vol. 8, No. 1, March 1958.

66. Sandler, I. S. and Rubin, D., "An Algorithm and a Modular Subroutine for the Cap Model," Int. J. Num. Analyt. Methods in Geomech., Vol. 3, 1979.

67. Sawczuk, A., "On Modelling of Nonlinear Mechanical Response of Materials," Proc. Prager Symp. on Mech. of Geomaterials, Northwestern Univ., Evanston, IL, Sept. 1983.

68. Scavuzzo, R., Cornelius, H. V., Gerstle, K. H. Ko, H. Y. and Stankowski, T., "Stress-Strain Curve for Concrete Under Multiaxial Load Histories," Report, University of Colorado, Dept. of Civil, Environmental and Architectural Eng., Aug. 1983.

69. Schofield, A. N. and Wroth, C. P., "Critical State Soil Mechanics," McGraw-Hill, London, 1968.

70. Schreyer, H. L. and Bobcock, S. M., "A Viscoplastic Representation for Concrete," Proc. Int. Conf. on Const. Laws for Eng. Mat., eds. C. S. Desai and R. H. Gallagher, Univ. of Arizona, Tucson, 1983, pp. 451-456.

71. Shiratori, E., Ikegami, K., and Yoshida, F., "Analysis of Stress-Strain Relations by Use of an Anisotropic Hardening Plastic Potential," J. Mech. Phys. Solids, Vol. 27, 1979, pp. 213-229.

72. Shrivastava, H. P., Mroz, Z. and Dubey, R. N., "Yield Criterion and the Hardening Rule for a Plastic Solid," Ziet. Angew. Math. Mech., Band 53, Heft, 10, 1973, pp. 625-633.

73. Spencer, A. J. M., "Theory of Invariants," Continuum Physics, ed. A. C. Eringen, Vol. I, 1971, pp. 239-353.

74. Spencer, A. J. M. and Rivlin, R. S., "Finite Integrity Bases for Five or Fewer Symmetric 3x3 Matrices," Arch. Rational Mech. Anal., Vol. 2, 1959, p. 435.

75. Suidan, M. and Schnobrich, W. C., "Finite Element Analysis of Reinforced Concrete," Journal of the Structural Division, ASCE, Vol. 99, No. ST10, October 1973, pp. 2109-2122.

76. Strue, S., "An Improved Multiaxial Cubical Cell and its Application to the Testing of Anisotropic Materials," M.S. Thesis, University of Colorado, Dept. of Civil, Environmental and Architectural Eng., 1983.

77. Task Committee, Finite Element Analysis of Reinforced Concrete, "Chap. 2 in Committee on Concrete and Masonry Structures," Structural Div., ASCE, New York, NY, 1982, pp. 34-137.

78. Traina, L. A., "Experimental Stress-Strain Behavior of a Low Strength Concrete Under Multiaxial States of Stress," Final Report, AFWL-TR-82-92, New Mexico Engineering Research Institute, University of New Mexico, Jan. 1983.

79. Traina, L. A., Babcock, S. M., and Schreyer, H. L., "Reduced Experimental Stress-Strain Results for A Low-Strength Concrete Under Multiaxial State of Stress," Final Report, AFWL-TR-83-3, New Mexico Engineering Research Institute, University of New Mexico, May 1983.

80. Tresca, H., "Memoire Sur Leconlement des Corps Solides," Mem. Press par Dis. Savants 18, 1868, pp. 733-799.

81. Von Mises, R., "Mechanick der Festen Korper im Plastisch Deformablen Zustand," Gottinger Nachrichten, Math. - Phys. Kl, 1913, pp. 582-592.

82. Wasliels, J., "Behavior of Concrete Under Multiaxial Stresses," A Review, Cem. Concr. Res. 9, 1979, pp. 35-44.

83. Willam, K. J. and Warnke, E. P., "Constitutive Model for the Triaxial Behavior of Concrete," Int. Assoc. of Bridge and Structural Engineers, Seminar on Concrete Structures Subjected to Triaxial Stresses, Paper III-1, Bergamo, Italy, May 17-19, 1974.

84. Willam, K. J. and Warnke, E. P., "Constitutive Model for the Triaxial Behavior of Concrete," International Association for Bridge and Structural Engineers, (IABSE), Report 19-21, 1974-1975, seminar, "Concrete Structures Subjected to Triaxial Stresses," ISMES-Bergamo-1974, Proceeding, organized by the Italian Group of IABSE & ISMES (Instituto Sperimentale Modeli E Structture), Session III, Reports on General Subject, pp. III-1 to III-30.

85. Wilkins, M. K., Streit, R. D. and Raugh, J. E., "Cumulative-Strain-Damage Model of Ductile Fracture: Simulation and Prediction of Engineering Fracture Test," Report No. UCRL-53058, Lawrence Livermore Lab., Univ. of Calif., Berkeley, Calif., 1980.

86. Wu, H. C., "Dual Failure Criterion for Plain Concrete," Journal of the Engineering Mechanics Division, ASCE, Vol. 100, No. EM6, Dec. 1974, pp. 1167-1181.